RUSSIAN ACADEMY OF SCIENCES

INSTITUTE FOR PROBLEMS IN MECHANICAL ENGINEERING

**Proceedings of the XL Summer School – Conference**

# ADVANCED PROBLEMS IN MECHANICS

# A P M 2 0 1 2

## St. Petersburg

## July 2 – 8, 2012

**http://apm-conf.spb.ru**

**St. Petersburg, 2012**

# GENERAL INFORMATION SCIENTIFIC COMMITTEE AND EDITORIAL BOARD

# PREFACE

Dear Reader,

in this book you will find the Proceedings of the Summer School Conference "Advanced Problems in Mechanics (APM) 2012". The conference had been started in 1971. The first Summer School was organized by Prof. Ya.G. Panovko and his colleagues. In the early years the main focus of the School was on nonlinear oscillations of mechanical systems with a finite number of degrees of freedom. Since 1994 the Institute for Problems in Mechanical Engineering of the Russian Academy of Sciences organizes the Summer School. The traditional name of "Summer School" has been kept, but the topics covered by the School have been much widened, and the School has been transformed into an international conference. Now it is held under the patronage of the Russian Academy of Sciences. The topics of the conference cover now almost all fields of mechanics, being concentrated around the following main scientific directions:

— aerospace mechanics;
— computational mechanics;
— dynamics of rigid bodies and multibody dynamics;
— fluid and gas;
— mechanical and civil engineering applications;
— mechanics of media with microstructure;
— mechanics of granular media;
— nanomechanics;
— nonlinear dynamics, chaos and vibration;
— molecular and particle dynamics;
— phase transitions;
— solids and structures;
— wave motion.

The Summer School – Conference has two main purposes: to gather specialists from different branches of mechanics to provide a platform for cross-fertilization of ideas, and to give the young scientists a possibility to learn from their colleagues and to present their work. Thus the Scientific Committee encouraged the participation of young researchers, and did its best to gather at the conference leading scientists belonging to various scientific schools of the world.

We believe that the significance of Mechanics as of fundamental and applied science should much increase in the eyes of the world scientific community, and we hope that APM conference makes its contribution into this process.

We are happy to express our sincere gratitude for a partial financial support to Russian Foundation for Basic Research, Russian Academy of Sciences, and St. Petersburg Scientific Center. This support has helped substantially to organize the conference and to increase the participation of young researchers.

We hope that you will find the materials of the conference interesting, and we cordially invite you to participate in the coming APM conferences. You may find the information on the future "Advanced Problems in Mechanics" Schools Conferences at our website:

**http://apm-conf.spb.ru**

With kind regards,

Co-Chairmen of APM 2012

Dmitri A. Indeitsev, Anton M. Krivtsov

# Contents

# Functionally invariant solutions of nonlinear Klein-Gordon equation

E. L. Aero A. N. Bulygin Yu. V. Pavlov
bulygin_an@mail.ru

**Abstract**

New approach to the integration of nonlinear Klein-Gordon equation is given. Solutions $U(x, y, z, t)$ are searched in the form of a composite function $U = f(W)$. It is assumed that $W(x, y, z, t)$ simultaneously satisfies to two partial differential equations and $f(W)$ to the self-similar nonlinear ordinary differential equation. Functionally invariant solutions are constructed for $W$ which contain arbitrary function $F(\alpha)$. Ansatz $\alpha(x, y, z, t)$ may be found as a root of linear algebraic equation of variables $(x, y, z, t)$ with coefficients in the form of arbitrary functions of $\alpha$. Particular expressions of ansatz $\alpha$ are found. Proposed approach is illustrated by the solution of sine-Gordon equation.

## 1 Introduction

Nonlinear Klein-Gordon (NKG) equation

$$\frac{\partial^2 U}{\partial x^2} + \frac{\partial^2 U}{\partial y^2} + \frac{\partial^2 U}{\partial z^2} - \frac{1}{v^2}\frac{\partial^2 U}{\partial t^2} = V'(U) \tag{1}$$

plays the fundamental role in the modern natural sciences. Here $V'(U)$ is a nonlinear function of $U$, prime denotes differentiation with respect to the argument. Equation (1) with $V'(U) = \exp U$ pioneered in the theory of surfaces of constant curvature. It was solved by Liouville [1]. To the present time are studied cases when $V'(U)$ has a form of truncated exponential, Taylor, Fourier and $\operatorname{sh} nU$, $\operatorname{ch} nU$ $(n = 1, 2, \ldots)$ series. Equation (1) with $V'(U)$ in the form of sum of exponents describes the oscillations of the chain of nonlinear pendulums [2] (Toda's chain). NKG equation with cubic nonlinearity $V'(U) = U^3 - U$ is used in the field theory models [3]. Function $V'(U) = \sin U$ defines sine-Gordon equation (SG). It brings into existence one of the most beautiful and universal object of the modern scientific studies — soliton. SG equation has extremely wide area of applications: modeling of nonlinear lattice [4, 5], orientational structure of liquid crystals [6], orientation of spins in ferromagnetic materials [7], propagation of fluxons in Josephson transitions [8], propagation of perturbations in macromolecules [9], processes in the Earth's crust [10], surface metrics [11], and many others. A lot of studies in mathematics, applied and theoretical physics have been devoted to the equations with $V'(U) = p_1 \sin U + p_2 \sin 2U$ (double sine-Gordon (DSG)) and $V'(U) = p_1 \sin U + p_2 \sin 2U + p_3 \sin 3U$ (triple sine-Gordon (TSG)). In the theory of nonlinear lattice dynamics DSG describes cardinal transformation of the near atomic order, lattice fragmentation produced by large deformations, defect creation and propagation of dislocations [12, 13]. In the nonlinear optics DSG equation is modeling propagation of short light impulses in the fivefold degenerated media [14, 15]. TSG

equation is used in the studies of magnetoelastic waves in ferromagnets such as garnet ferrites [16]. There are papers devoted to study of NKG equations with $V'(U)$ represented by the sum of $\operatorname{sh} nU$ and $\operatorname{ch} nU$ [17]. A lot of studies have been devoted to the development of mathematical methods for solving NKG equations. Fundamental results have been obtained both in integration of NKG equation of special forms and general forms of $V'(U)$. Robust methods of computational study of NKG equations are developed [7].

However new approach to the construction of NKG equations solutions is of great interest because new solutions allow to understand more deeply the nature of nonlinear equations' solutions and could find application to the description of physical phenomena and technological processes.

Method of functionally invariant NKG equations solutions construction is proposed hereafter. Basic concepts of the method have been stated in the papers [18, 19]. Authors' papers [20]–[25] are devoted to the construction of functionally invariant solutions of SG, DSG and TSG equations.

## 2 New approach to the construction of exact solutions for nonlinear Klein-Gordon equation

We seek the solution of NKG equation in the form of a composite function $U = f[W(x, y, z, t)]$. Then equation (1) takes a form

$$f''\left[\left(\frac{\partial W}{\partial x}\right)^2+\left(\frac{\partial W}{\partial y}\right)^2+\left(\frac{\partial W}{\partial z}\right)^2-\frac{1}{v^2}\left(\frac{\partial W}{\partial t}\right)^2\right]+$$
$$+f'\left[\frac{\partial^2 W}{\partial x^2}+\frac{\partial^2 W}{\partial y^2}+\frac{\partial^2 W}{\partial z^2}-\frac{1}{v^2}\frac{\partial^2 W}{\partial t^2}\right]=V'(f). \tag{2}$$

Assume that function $W(x, y, z, t)$ simultaneously satisfies to two equations

$$\left(\frac{\partial W}{\partial x}\right)^2+\left(\frac{\partial W}{\partial y}\right)^2+\left(\frac{\partial W}{\partial z}\right)^2-\frac{1}{v^2}\left(\frac{\partial W}{\partial t}\right)^2=P(W), \tag{3}$$

$$\frac{\partial^2 W}{\partial x^2}+\frac{\partial^2 W}{\partial y^2}+\frac{\partial^2 W}{\partial z^2}-\frac{1}{v^2}\frac{\partial^2 W}{\partial t^2}=Q(W), \tag{4}$$

and $f(W)$ is the solution of nonlinear ordinary differential equation

$$P(W)\,f''+Q(W)\,f'=V'(f). \tag{5}$$

Here $P(W)$ and $Q(W)$ are arbitrary functions.

Integration of equations (3)–(5) in the general form is not easier than solving the original equation (1). However for particular form of functions $P(W)$ and $Q(W)$ exact solutions of the equations (3)–(5) could be found and therefore of the equation (1).

**2.1.** Assume that

$$P(W)=W^2, \qquad Q(W)=W. \tag{6}$$

Then equations (3)–(5) take the form

$$\left(\frac{\partial W}{\partial x}\right)^2+\left(\frac{\partial W}{\partial y}\right)^2+\left(\frac{\partial W}{\partial z}\right)^2-\frac{1}{v^2}\left(\frac{\partial W}{\partial t}\right)^2=W^2, \tag{7}$$

$$\frac{\partial^2 W}{\partial x^2}+\frac{\partial^2 W}{\partial y^2}+\frac{\partial^2 W}{\partial z^2}-\frac{1}{v^2}\frac{\partial^2 W}{\partial t^2}=W, \tag{8}$$

$$W^2 f''+W f'=V'(f). \tag{9}$$

Equation (9) after change of variable

$$\zeta=\ln W \tag{10}$$

is reduced to the well known equation of nonlinear mathematical pendulum

$$\frac{d^2 f}{d\zeta^2}=V'(f), \tag{11}$$

which has first integral

$$\frac{df}{\sqrt{E+V(f)}}=\pm\sqrt{2}\,d\zeta. \tag{12}$$

Therefore for the case (6) equation (5) is integrated and function $f(W)$ is found at least in the form of quadrature.

Function $W(x,y,z,t)$ could be found using the method of construction of functionally invariant solutions of wave equation [18, 19]. Assume that

$$W=e^{\varphi}V(x,y,z,t), \qquad \varphi=a_1x+a_2y+a_3z-\sigma v^2 t. \tag{13}$$

Here $(a_1,a_2,a_3,\sigma)$ are arbitrary constants. Then if

$$a_1^2+a_2^2+a_3^2=1+\sigma^2v^2, \tag{14}$$

function $V(x,y,z,t)$ must simultaneously satisfy to three equations:

$$a_1\frac{\partial V}{\partial x}+a_2\frac{\partial V}{\partial y}+a_3\frac{\partial V}{\partial z}+\sigma\frac{\partial V}{\partial t}=0, \tag{15}$$

eikonal type equation

$$\left(\frac{\partial V}{\partial x}\right)^2+\left(\frac{\partial V}{\partial y}\right)^2+\left(\frac{\partial V}{\partial z}\right)^2-\frac{1}{v^2}\left(\frac{\partial V}{\partial t}\right)^2=0 \tag{16}$$

and wave equation

$$\frac{\partial^2 V}{\partial x^2}+\frac{\partial^2 V}{\partial y^2}+\frac{\partial^2 V}{\partial z^2}-\frac{1}{v^2}\frac{\partial^2 V}{\partial t^2}=0. \tag{17}$$

We seek function $V(x,y,z,t)$ in the form

$$V(x,y,z,t)=F(\alpha). \tag{18}$$

Here $F(\alpha)$ is an arbitrary function. Ansatz $\alpha(x,y,z,t)$ is the root of the equation

$$x\,l(\alpha)+y\,m(\alpha)+z\,n(\alpha)-v^2tp(\alpha)+g(\alpha)=0, \tag{19}$$

where $(l(\alpha),\ m(\alpha),\ n(\alpha),\ p(\alpha),\ g(\alpha))$ are arbitrary functions of $\alpha$.

Function $V(x,y,z,t)$ in the form (18) will be a solution of the equation (15), provided that algebraic equation

$$a_1l+a_2m+a_3n=v^2\sigma p, \tag{20}$$

is satisfied, and satisfy to equations (16), (17), if

$$l^2 + m^2 + n^2 = v^2 p^2. \tag{21}$$

**2.2.** Solution of NKG equation could be obtained also by other methods. Assume that

$$P(W) = 1, \qquad Q(W) = 0. \tag{22}$$

Then $f(W)$ will coincide with $f(\zeta)$, if to change argument $\zeta$ to $W$, and

$$W(x, y, z, t) = \varphi + F(\alpha). \tag{23}$$

Here $\varphi(x, y, z, t)$ is given by (13), and $F(\alpha)$ is an arbitrary function of $\alpha$. Ansatz $\alpha(x, y, z, t)$ is still the root of equation (19).

Also

$$W(x, y, z, t) = x\, a_0(\alpha) + y\, b_0(\alpha) + z\, c_0(\alpha) - t\, v^2 d_0(\alpha) + e_0(\alpha), \tag{24}$$

will be the solution of equations (3), (4), (22) with equation (19) for the ansatz if

$$\begin{aligned} &a_0(\alpha) = \int l(\alpha)\, d\alpha, \quad b_0(\alpha) = \int m(\alpha)\, d\alpha, \quad c_0(\alpha) = \int n(\alpha)\, d\alpha, \\ &d_0(\alpha) = \int p(\alpha)\, d\alpha, \quad e_0(\alpha) = \int g(\alpha)\, d\alpha, \end{aligned} \tag{25}$$

and conditions

$$a_0^2 + b_0^2 + c_0^2 = 1 + v^2 d_0^2, \tag{26}$$

$$(a_0')^2 + (b_0')^2 + (c_0')^2 = v^2 (d_0')^2 \tag{27}$$

are fulfilled.

## 3 Finding of ansatz $\alpha(x, y, z, t)$

For different solutions ansatz $\alpha(x, y, z, t)$ is found from the equation (19) which contains more unknown coefficients than number of algebraic equations to be satisfied by them. Therefore ansatz $\alpha$ is not defined uniquely. Not touching on the finding of general expression for $\alpha$, we note some simple particular cases.

**a)** $l = vpx_1, \quad m = vpx_2, \quad n = vpx_3, \quad g = -vp\alpha,$ (28)

$$\alpha = xx_1 + yx_2 + zx_3 - v^2 t. \tag{29}$$

Constants $x_1, x_2, x_3$ depend on $(v, \sigma, a_1, a_2, a_3)$ and new constant $f_0$ assuming that in general expressions for $(x_1, x_2, x_3)$ $\cos f(\alpha) = \cos f_0$:

$$\begin{aligned} x_1 &= \frac{v}{\sqrt{a_1^2 + a_2^2 + a_3^2}} \Big[\cos\delta \cos C \cos f_0 + \sin\delta \sin f_0 + v\sigma \cos A\Big], \\ x_2 &= \frac{v}{\sqrt{a_1^2 + a_2^2 + a_3^2}} \Big[\sin\delta \cos C \cos f_0 - \cos\delta \sin f_0 + v\sigma \cos B\Big], \\ x_3 &= \frac{v}{\sqrt{a_1^2 + a_2^2 + a_3^2}} \Big[-\sin C \cos f_0 + v\sigma \cos C\Big]. \end{aligned} \tag{30}$$

Here

$$\cos A = \frac{a_1}{\sqrt{a_1^2+a_2^2+a_3^2}}, \quad \cos B = \frac{a_2}{\sqrt{a_1^2+a_2^2+a_3^2}}, \quad \cos C = \frac{a_3}{\sqrt{a_1^2+a_2^2+a_3^2}}, \tag{31}$$

$$\cos\delta = \frac{a_1}{\sqrt{a_1^2+a_2^2}}, \qquad \sin\delta = \frac{a_2}{\sqrt{a_1^2+a_2^2}}. \tag{32}$$

**b)** $l = vpx_1, \quad m = vpx_2, \quad n = vpx_3, \quad f(\alpha) = \alpha, \quad g = 0.$ (33)

In the second case $\alpha$ is the root of the trigonometrical equation

$$\eta\cos\alpha + \xi\sin\alpha + v\sigma\zeta = 0\,, \tag{34}$$

$$\begin{aligned}
\eta &= (x-u_1t)\cos\delta\cos C + (y-u_2t)\sin\delta\cos C - (z-u_3t)\sin C\,,\\
\xi &= (x-u_1t)\sin\delta - (y-u_2t)\cos\delta\,,\\
\zeta &= (x-u_1t)\cos A + (y-u_2t)\cos B + (z-u_3t)\cos C,
\end{aligned} \tag{35}$$

where

$$u_1 = \frac{1}{\sigma}\sqrt{1+v^2\sigma^2}\,\cos A, \quad u_2 = \frac{1}{\sigma}\sqrt{1+v^2\sigma^2}\,\cos B, \quad u_3 = \frac{1}{\sigma}\sqrt{1+v^2\sigma^2}\,\cos C.$$

From (34) we find that

$$\alpha = -(-1)^n\left[\arcsin\frac{\eta}{\sqrt{\xi^2+\eta^2}} + \arcsin\frac{v\sigma\zeta}{\sqrt{\xi^2+\eta^2}}\right] + n\pi\,, \tag{36}$$

$n = 0, \pm1, \ldots$

Ansatz $\alpha$ as it follows from (36) is defined if

$$-1 \le \frac{v\sigma\zeta}{\sqrt{\xi^2+\eta^2}} \le 1\,. \tag{37}$$

Domain (37) is the exterior of cones with axis directed along the vector $\mathbf{a} = a_1\mathbf{i}+a_2\mathbf{j}+a_3\mathbf{k}$, and vertex of cone (at $t = 0$) coincides with the origin of coordinates. With changing of time cones move along the vector $\mathbf{a}$ with the speed $\mathbf{u} = u_1\mathbf{i} + u_2\mathbf{j} + u_3\mathbf{k}$. Cone opening is defined by the parameter $v\sigma$. Plane 1 is shown on the Fig. 1. It moves parallel to itself and perpendicular to the vector $\mathbf{a}$. It is described by the equation $a_1x + a_2y + a_3z - \sigma v^2t = 0$. Plane 2 touches cone side surface. Its equation is $x_1x + x_2y + x_3z - v^2t = 0$.

**c)** $l = vp\cos\theta\cos\phi, \quad m = vp\cos\theta\sin\phi, \quad n = vp\sin\theta, \quad g = 0.$ (38)

Here $(p, \theta, \phi)$ are arbitrary functions of $\alpha$. Equation (21) is identically satisfied. Equation (20) relates $\theta(\alpha)$ with $\phi(\alpha)$. We seek function $\theta(\alpha)$ from (19) which takes the form

$$N\sin^2\theta - 2Q\sin\theta + M = 0. \tag{39}$$

From (39) one can find that

$$\sin\theta_1(\alpha) = \frac{Q-\sqrt{Q^2-MN}}{N}, \quad \sin\theta_2(\alpha) = \frac{Q+\sqrt{Q^2-MN}}{N}, \tag{40}$$

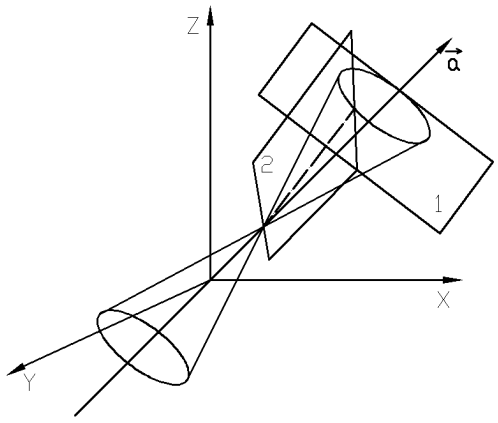


Figure 1: Domain of ansatz definition (37).

$$Q^2 - MN = (s^2 - \varphi^2)(xa_2 - ya_1)^2, \quad s^2 = x^2 + y^2 + z^2 - v^2t^2,$$
$$N = (a_1^2 + a_2^2 + a_3^2)(x^2 + y^2 + z^2) - (a_1x + a_2y + a_3z)^2, \tag{41}$$
$$Q = v\left[a_3\sigma(x^2 + y^2 + z^2) - (a_3t + z\sigma)(a_1x + a_2y + a_3z) + (a_1^2 + a_2^2 + a_3^2)zt\right]$$

**d**) $l = \cos\phi, \quad m = \sin\phi, \quad n = \operatorname{sh}\psi, \quad \mathrm{vp} = \operatorname{ch}\psi, \quad \mathrm{g} = 0,$ (42)

where $\phi(\alpha), \psi(\alpha)$ are arbitrary functions of $\alpha$. Equation (21) is identically satisfied. Equation (20) relates $\phi(\alpha)$ with $\psi(\alpha)$. Equation (19) takes the form

$$M\cos^2\gamma + 2Q\sin\gamma\cos\gamma + N\sin^2\gamma = 0, \quad \gamma(\alpha) = \delta - \phi(\alpha). \tag{43}$$

Here

$$Q^2 - MN = \left(\frac{z\sigma v - vta_3}{\sigma^2v^2 - a_3^2}\right)^2 (s^2 - \varphi^2),$$
$$N = (x\sin\delta - y\cos\delta)^2 + \frac{(z\sigma v - vta_3)^2}{\sigma^2v^2 - a_3^2} \tag{44}$$
$$Q = \left(x\cos\delta + y\sin\delta + \frac{za_3 - \sigma v^2 t}{\sigma^2v^2 - a_3^2}\sqrt{a_1^2 + a_2^2}\right)(x\sin\delta - y\cos\delta).$$

From (43) one can find that

$$\operatorname{tg}\gamma_1(\alpha) = \frac{\sqrt{\mathrm{Q}^2 - \mathrm{MN}} - \mathrm{Q}}{\mathrm{N}}, \quad \operatorname{tg}\gamma_2(\alpha) = -\frac{\sqrt{\mathrm{Q}^2 - \mathrm{MN}} + \mathrm{Q}}{\mathrm{N}}. \tag{45}$$

It should be kept in mind concerning the choice of given ansatzs $\alpha(x, y, z, t)$ that since we seek the solution $V(x, y, z, t)$ in the form of arbitrary function $F(\alpha)$ then $V(x, y, z, t)$ remains the solution if $\alpha$ is changed to the arbitrary function $\chi(\alpha)$.

For cases (22), (24)

**a**) $a_0 = \cos\psi_0, \quad b_0 = \sin\psi_0, \quad c_0 = \operatorname{tg}\alpha, \quad \mathrm{vd}_0 = \operatorname{tg}\alpha, \quad \psi_0 = \mathrm{const},$
$$W = x\cos\psi_0 + y\sin\psi_0 + F(z - vt), \tag{46}$$

**b)** $a_0 = \dfrac{\operatorname{ch}\alpha}{\operatorname{sh}\alpha}\cos\psi_0, \quad b_0 = \dfrac{\operatorname{ch}\alpha}{\operatorname{sh}\alpha}\sin\psi_0, \quad c_0 = 1, \quad vd_0 = \dfrac{\operatorname{ch}\alpha}{\operatorname{sh}\alpha},$
$W = z + F(x\cos\psi_0 + y\sin\psi_0 - vt),$ (47)

**c)** $a_0 = 1, \quad b_0 = \operatorname{tg}\alpha, \quad c_0 = \operatorname{tg}\alpha\operatorname{sh}\psi_0, \quad \mathrm{vd}_0 = \operatorname{tg}\alpha\operatorname{ch}\psi_0,$
$W = x + F(y + z\operatorname{sh}\psi_0 - \mathrm{vt}\operatorname{ch}\psi_0).$ (48)

Here $F(\alpha)$ is arbitrary function of the given argument.

# 4 Solution of NKG equation for particular form of the function $V'(U)$

We illustrate new approach to the solving of NKG equation on the example of the integration of SG equation. If $V'(U) = \sin U$ then $F(\zeta)$ is given by the integral (12)

$$\int \frac{df}{\sqrt{E - \cos f}} = \pm\sqrt{2}(\zeta + \zeta_0). \tag{49}$$

Certain form of the solution $U = f(\zeta)$ is defined by the value of integration constant $E$:

$$U = 4\operatorname{arctg} e^{\pm(\zeta+\zeta_0)}, \qquad E = 1, \tag{50}$$

$$U = \pm 2\operatorname{arctg}\left[\sqrt{1-k^2}\,\frac{\operatorname{sn}\left[\frac{1}{k}(\zeta+\zeta_0), k\right]}{\operatorname{cn}\left[\frac{1}{k}(\zeta+\zeta_0), k\right]}\right], \qquad E > 1, \tag{51}$$

$$U = \pm 2\operatorname{arctg}\frac{\operatorname{dn}\left[(\zeta+\zeta_0), k\right]}{k\operatorname{sn}\left[(\zeta+\zeta_0), k\right]}, \qquad 0 < E < 1. \tag{52}$$

Solution (51) could be written in another form, namely

$$U = \pi - 2\operatorname{am}\left[K(k) - F(\psi, k),\, k\right], \quad \psi = \pm\operatorname{am}\left[\frac{1}{k}(\zeta+\zeta_0), k\right]. \tag{53}$$

Here $\operatorname{sn}(\zeta, k)$, $\operatorname{cn}(\zeta, k)$, $\operatorname{dn}(\zeta, k)$ are elliptic sine, cosine and Jacobi delta-function correspondingly, $F(\psi, k)$ and $K(k)$ — incomplete and complete elliptic integrals, and $\operatorname{am}(\zeta, k)$ — Jacobi amplitude. Solution (53) is obtained from (51) using well known relation between incomplete elliptic integrals of the first kind

$$F(\phi, k) + F(\psi, k) = K(k), \tag{54}$$

with arguments related by the condition

$$\sqrt{1-k^2}\operatorname{tg}\phi\operatorname{tg}\psi = 1. \tag{55}$$

Solutions (51), (53) coincide in the period $0 < \zeta < 2K(k)$ and are different in the extension of the solution outside the period. Function (51) is extended periodically and (53) increases monotonically in the form of the "ladder". Functions (50)–(53) have different pattern of change. Solution (50) asymptotically tends to limits $(0, 2\pi)$. It is shown at the left of Fig. 2 where is shown graph of $U(x, z)$ for the solution (50) with

$$W = x\cos\psi_0 + y\sin\psi_0 + 2\sin(z - vt). \tag{56}$$

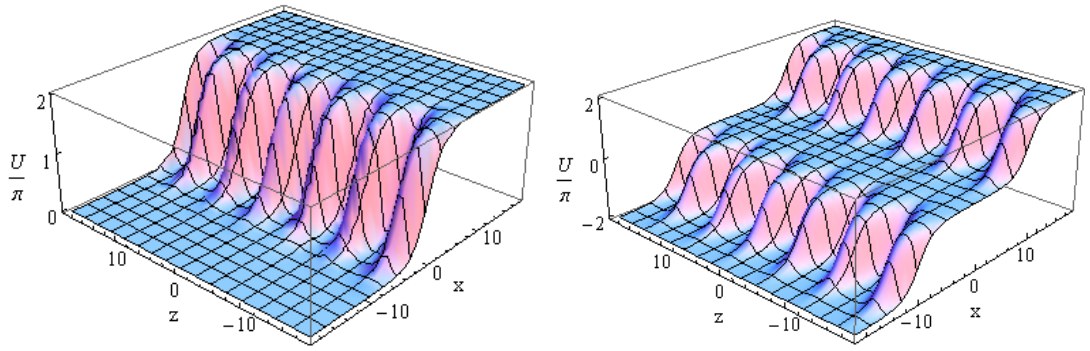


Figure 2: Graphs of solutions (50) at the left, and (53) at the right at $y = 0, t = 0$, $\psi_0 = \pi/4$, $k = 0.99999, \zeta_0 = 0$.

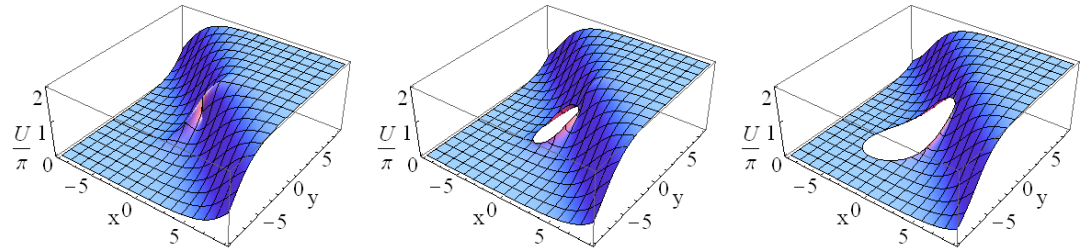


Figure 3: Graphs of solution (50) with ansatz (40) at $z = 0$ and $t = 0$ (at the left), $t = 1$ (at the centre), $t = 2$ (at the right); $v = 1$, $\sigma = 0.5$, $\zeta_0 = 0.1$, $a_1 = a_2 = 0.56, a_3 = 0.79$.

Graph has a form of kink with transition domain modulated by the periodic function.

Function (53) as mentioned above increases monotonically and its graph with the same function $W$ is shown at the right of Fig. 2. Solutions (51), (52) change periodically achieving maximum value $U = \arccos E$. On the Fig. 3 are shown graphs of solutions (50) with ansatz $\sin\theta_1(\alpha)$ (40). Note that for the given ansatz real solution exists not for all $(x, y, z, t)$. Domains where real solution does not exist correspond to the gaps on the graph. With increase of time such domains increase for the given solution.

## 5 Conclusion

We note finally:

1) New approach to the integration of NKG equation is proposed relating to the $(3+1)$ equation. However it could be easily extended on the spaces of any dimension $(n + 1)$. Moreover it has been shown in [26] that with increase of $n$ number of possible algebraic equations having ansatz $\alpha(x, y, z, \ldots, t)$ as root increases, also increase the number of arbitrary functions in the anzatz equation. For the three dimensional space equation (19) is unique [19].

2) New approach allows to find the solution at least in the form of quadrature for any nonlinear integrable function $V'(U)$. For the particular form of functions $V'(U)$ represented by the truncated exponential, ( sh nU, ch nU), Taylor, and Fourier series solution of NKG equation is reduced to the calculation and inversion of algebraic, elliptic, ultraelliptic and Abel integrals with genus defined by the number of summands.

## Acknowledgements

*This work was supported by RFBR, grant 10-01-00243-a.*

## References

[1] J. Liouville. Journal de mathématiques pures et appliquées, 1-re série, **18**, (1853) 71–72.

[2] M. Toda. J. Phys. Soc. Jpn. **22**, (1967) 431–436.

[3] N. N. Bogoliubov, D. V. Shirkov. Quantum Fields. Benjamin-Cammings, Massachusetts, 1983.

[4] E. L. Aero, A. N. Bulygin. Mech. Solids. **42**, No. 5, (2007) 807–822.

[5] E. L. Aero, J. Engrg. Math., **55**: 1–4 (2006), 81–95.

[6] P. G. de Gennes. The Physics of Liquid Crystals. Clarendon, Oxford, 1974.

[7] R. Dodd, J. Eilbeck, J. Gibbon, H. Morris. Solitons and Nonlinear Wave Equations. Academic Press, New York, 1982.

[8] K. Lonngren and A. Scott, eds. Solitons in Action. Acad. Press, New York (1978).

[9] A. S. Davydov. Solitons in Bioenergetics [in Russian]. Naukova Dumka, Kiev, 1986.

[10] V.G. Bykov. Nonlinear Wave Processes in Geological Media [in Russian]. Dalnauka, Vladivostok, 2000.

[11] P. L. Chebyshev. Uspekhi Matem. Nauk **1**, N 2, (1946) 38–42.

[12] E. L. Aero, A. N. Bulygin. Mechanics of Solids, **45**, No. 5, (2010) 670–688.

[13] E. L. Aero, A. N. Bulygin. *in* "Mechanics of Generalized Continua. One Hundred Years After the Cosserats", Eds. G.A. Maugin, A.V. Metrikine, Advances in Mechanics and Mathematics, Vol.21, Springer, 2010, pp.121–130.

[14] G. L. Lamb, Jr. Rev. Mod. Phys. **43**, (1971) 99–124.

[15] S. Duckworth, R. K. Bullough, P. J. Caudrey, J. D. Gibbon. Phys. Lett. A **57**, (1976) 19–22.

[16] R. M. Vakhitov, O. G. Ryakhova. Technical Physics **50**, (2005) 1021–1025.

[17] A.-M. Wazwaz. Chaos, Solitons and Fractals **33**, (2007) 703–710.

[18] H. Bateman. The Mathematical Analysis of Electrical and Optical Wave-Motion On the Basis of Maxwell's Equations. Cambridge Univ. Press, Cambridge, 1915.

[19] S. L. Sobolev. Tr. Fiz.-Mat. Inst. Steklova, **5**, (1934) 259–264.

[20] E. L. Aero, A. N. Bulygin, Yu. V. Pavlov. Teor. Matem. Fiz. **158**, No. 3, (2009) 370–377 [English transl.: Theor. Math. Phys. **158**(3), (2009) 313–319].

[21] E. L. Aero, A. N. Bulygin, Yu. V. Pavlov. Nelineinii Mir **7**, N 7, (2009) 513–517.

[22] E. L. Aero, A. N. Bulygin, Yu. V. Pavlov. Proc. Int. Conf. “Days on Diffraction 2010”, Saint Petersburg, Russia, p. 10–15.

[23] E. L. Aero, A. N. Bulygin, Yu. V. Pavlov. Proc. Int. Conf. “Days on Diffraction 2011”, St.Petersburg, Russia, p. 5–10.

[24] E. L. Aero, A. N. Bulygin, Yu. V. Pavlov. Proc. XXXIX Summer School – Conference “Advanced Problems in Mechanics”, St. Petersburg (Repino), 2011, p. 10–20.

[25] E. L. Aero, A. N. Bulygin, Yu. V. Pavlov. Differentsial'nye Uravneniya **47** (2011) 1428–1438 [English transl.: Differential Equations **47** (2011) 1442–1452].

[26] N. P. Erugin. Uch. Zap. Leningrad Univ. Vyp. **15**, N 96, (1948) 101–134.

*E. L. Aero, A. N. Bulygin, Yu. V. Pavlov,*
*Institute of Problems in Mechanical Engineering, RAS,*
*61 Bol'shoy, V.O., Saint Petersburg, 199178, Russia*

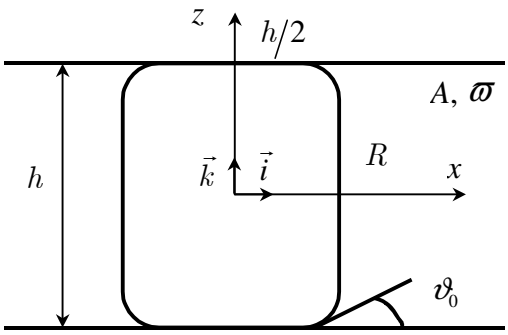


Figure 1: Geometry of a problem.

# The influence of contact angle's hysteresis on the cylindrical drop's dynamics

Aleksey Alabuzhev
alabuzhev@mail.ru

**Abstract**

The forced oscillations of a cylindrical drop are considered in the present work. The drop is suspended in the different fluid and confined by two parallel rigid plates, subjected to vibrations. The vibration axis is perpendicular to the symmetry axis. The amplitude of vibrations is small in comparison with the drop radius. The equilibrium contact angle is right. The specific boundary conditions, assumed by Hocking (1987), is applied to take into account: the contact line starts to slide only when the deviation of the contact angle exceeds a certain critical value. As a result, the stick-slip dynamics can be observed.

## 1 Problem statement

This investigation assumes that a drop with a density $\rho_i^*$ is suspended in a fluid of different density $\rho_e^*$. In the absence of external forces the drop has cylindrical shape with radius $R^*$. The system is confined between two parallel rigid plates, subjected to vibrations perpendicular to the drop axis (fig.1). In the absence of vibrations a contact angle between a lateral surface of a drop and bounding plate equals $\pi/2$. The thickness of the layer is h. The equilibrium contact angle between the lateral surface of drop and the rigid plate is $\theta_0$.

The vessel is closed at the infinity and undergoes high-frequency oscillations according to the law $\underline{r}=\underline{R}+\mathrm{A}\underline{j}\cos(\omega \mathrm{t})$ ($\underline{r}$, $\underline{R}$ are the radius - vectors of an arbitrary point of a drop surface in the plane parallel to the rigid plates (horizontal plane) in the presence and absence of vibrations, respectively, A is the amplitude of vibrations, $\underline{j}$ is the unit vector in a horizontal plane). The vibration amplitude A is small as compared to R. It is assumed, that the lateral surface of the drop is $r = R + \zeta(\alpha, z, t)$ where $\alpha$ is the polar angle.

Velocity of motion of a contact line is assumed to be proportional to a deviation of a contact angle from equilibrium value [1]:

$$\zeta_t = \begin{cases} \Lambda(\gamma - \gamma_0), & \gamma > \gamma_0 \\ 0, & |\gamma| < \gamma_0 \\ \Lambda(\gamma + \gamma_0), & \gamma < -\gamma_0 \end{cases} \quad (1)$$

The following quantities are chosen as the scales: time - $\sqrt{(\rho_e^* + \rho_i^*)h^2R/\sigma}$, length - $R$, height - h, potential of velocity - $\mathrm{A}\sqrt{\sigma R/((\rho_e^* + \rho_i^*)h^2)}$, density -$\rho_e^* + \rho_i^*$, pressure - $A\sigma/h^2$, deviations of the drop surface - A.

$$p = -\rho\left(\varphi_t + \frac{1}{2}\varepsilon(\nabla\varphi)^2\right), \Delta\varphi = 0, \quad (2)$$

$$r = 1 + \varepsilon\zeta\,[\underline{n}\cdot\nabla\varphi] = 0, F_t + \varepsilon\nabla\varphi\cdot\nabla F = 0, [p] = -\operatorname{div}\underline{n}, \quad (3)$$

$$z = \pm\frac{1}{2} : veck\cdot\nabla\varphi = 0 \quad (4)$$

$$z = \pm\frac{1}{2}, r = 1 + \varepsilon\zeta : \zeta_t = \begin{cases} \lambda(\gamma - \gamma_0), & \gamma > \gamma_0 \\ 0, & |\gamma| < \gamma_0 \\ \lambda(\gamma + \gamma_0), & \gamma < -\gamma_0 \end{cases} \quad (5)$$

Here $\underline{v} = \nabla\varphi$ - velocity potential, $F = r - R - \epsilon\zeta(\alpha, z, t)$ - drop surface, $p$ - pressure, $\underline{n} = \frac{\nabla F}{|\nabla F|}$ - normal vector, $\underline{k}$ - unit vector of $z$-axis, $\gamma(t) = \mp\zeta_z|_{z=\pm1/2}$ - contact line's deviation from equilibrium position, $\zeta$ - surface deviation of equilibrium shape. The effective boundary condition (5) shows that the contact line is fixed, if the absolute value of the deviation of the surface is less than some characteristic value of $\gamma_0$. The square brackets denote the jump in value at the interface between the external fluid and the drop in the index of the unknown functions are denoted derivatives with respect to relevant variables. The boundary problem (2)-(5)contains the following dimensionless parameters: small vibration amplitude - $\epsilon = A/R$, capillary parameter $\lambda$=$\Lambda\sqrt{h^2R(\rho_e^* + \rho_i^*)/\sigma}$, the ratio of radius to height - $b = R/h$, density of internal fluid - $\rho = \rho_i^*/(\rho_e^* + \rho_i^*)$, density of external fluid - $\rho = \rho_e^*/(\rho_e^* + \rho_i^*)$.

## 2 Method of solution

Despite the fact that the boundary condition (5) makes the problem (2)-(5) is nonlinear, the solutions for the functions $\varphi$, $\zeta$, $p$ can be represented as a series (see [2]-[4]):

$$\varphi_i = \sum_{k=0}^{\infty} a_k(t)\,\mathrm{I}_0\left((2k+1)\pi br\right)\sin(2k+1)\pi z, \quad (6)$$

$$\varphi_e = \sum_{k=0}^{\infty} b_k(t)\,\mathrm{K}_0\left((2k+1)\pi br\right)\sin(2k+1)\pi z, \quad (7)$$

$$\zeta = \sum_{k=0}^{\infty} c_k(t)\sin(2k+1)\pi z, \quad (8)$$

$$p_i = -\rho_i\left(\varphi_{it} + \omega^2 z\cos\omega t\right), p_e = -\rho_e\left(\varphi_{et} + \omega^2 z\cos\omega t\right), \quad (9)$$

$$b_k(t) = a_k(t)\frac{\mathrm{I'}_0\left((2k+1)\pi b\right)}{\mathrm{K'}_0\left((2k+1)\pi b\right)}, a_k(t) = \frac{c_{kt}(t)}{\mathrm{I}_0\left((2k+1)\pi b\right)}. \tag{10}$$

On the other hand, using the normal stress balance condition (3) , the solution of the surface deviation $\zeta$ can be written as:

$$\zeta = \frac{b\gamma}{\cos\left(\frac{1}{2b}\right)}\sin\left(\frac{z}{b}\right) + \sum_{k=0}^{\infty}\left(\frac{c_{ktt}}{\Omega_k^2} + \frac{(\rho_i-\rho_e)\omega^2 g_k\cos\omega t}{1-(2k+1)^2\pi^2 b^2}\sin\left((2k+1)\pi z\right)\right) \tag{11}$$

Here $g_k = \left(2(-1)^k\right)\Big/\left((2k+1)^2\pi^2\right)$ is Furie expansion coefficient of function $z$ on basic functions $\sin\left((2k+1)\pi z\right)$, $\Omega_k$ - eigen frequencies of cylindrical drop with free contact line:

$$\Omega_{mk}^2 = \frac{m^2-1+4\pi^2b^2k^2}{F_{mk}}R^i_{mk\,r}(1), \tag{12}$$

where$L_k$ =$m = 0, 1, 2, ...$ - azimuthal number, $k = 0, 1, 2, ...$ - wave number, $R^i_{m0}(r) = r^m$, $R^e_{m0}(r) = r^{-m}$,

$$R^i_{mk}(r) = \mathrm{I}_m(2\pi bkr)$$

for $k \geqslant 1$, $R^e_{mk}(r) = \mathrm{K}_m(2\pi bkr)$ for $k \geqslant 1$, $\mathrm{I}_m$, $\mathrm{K}_m$ - modified Bessel functions , $F_{mk} = \rho R^i_{mk}(1) - R^i_{mk\,r}(1)\,R^e_{mk}(1)/R^e_{mk\,r}(1)$, $R^{i,e}_{mk\,r}(r) = d\,R^{i,e}_{mk}(r)\Big/dr$ - subscript $r$ is derivative on radius $r$. In our solution $m = 0$.

Comparing the solutions 8 and 11 for $\zeta$, we obtain a system of ordinary differential equations for unknown amplitudes $c_k(t)$:

$$c_{ktt} + \Omega_k^2 c_k = \Omega_k^2 S_k\gamma - \Omega_k^2 L_k\cos\omega t, \tag{13}$$

where $S_k = bf_k\,\mathrm{ces}\left(\frac{1}{2b}\right)$, $L_k = \frac{(\rho_i-\rho_e)\omega^2 g_k}{(2k+1)^2\pi^2b^2-1}$, $f_k = \frac{2b(-1)^k}{(2k+1)^2\pi^2b^2-1}\cos\left(\frac{1}{2b}\right)$, $f_k$ - Furie expansion coefficient of function $\sin\left(z/b\right)$.

Equation (13) must be solved together with 95). Note that the series for $\zeta$ converges very slowly. However, the eigen frequencies $\Omega_k$ are growing rapidly, therefore, from some $k$, can neglect the first term on the left side of equation (5) as compared with the rest, ie . $c_k \approx S_k\gamma - L_k\cos\omega t$. Thus, using a finite sum and the solution of (8), we obtain

$$\begin{aligned}\zeta_t &= \sum_{k=0}^{N} c_{kt}\sin\left((2k+1)\pi z\right) + \sum_{k=N+1}^{\infty}\left(S_k\gamma_t + L_k\omega\sin(\omega t)\right)\sin\left((2k+1)\pi z\right) = \\ &= \sum_{k=0}^{N} D_{kt}\sin\left((2k+1)\pi z\right),\end{aligned} \tag{14}$$

where $D_k = c_k + S_k\gamma - L_k\cos(\omega t)$. Substituting (14) into (5), we obtain the equation for $\lambda$:

$$\gamma_t = \frac{\left(-\sum\limits_{k=0}^{N}(-1)^k c_{kt} + \sum\limits_{k=0}^{N}(-1)^k L_k\omega\sin(\omega t) - \begin{cases}\lambda(\gamma-\gamma_0), & \gamma > \gamma_0\\ 0, & |\gamma| < \gamma_0\\ \lambda(\gamma+\gamma_0), & \gamma < -\gamma_0\end{cases}\right)}{\sum\limits_{k=0}^{N}(-1)^k S_k}. \tag{15}$$

The system of differential equations (13), (15) was solved using the method of Gear.

## 3 Results

The boundary condition of Hocking (5) shows that the contact line is fixed, if the contact angle does not exceed a certain critical value. Otherwise, the contact line moves. Figures (2-3) shows the areas in which the contact line is moving or at rest.

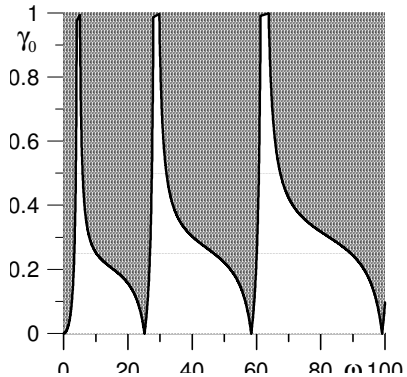


Figure 2: The diagram of contact line motion on the plane ($\omega$, $\gamma_0$), $\rho_i = 0.3$, $b = 1$. The solid lines are determined by the condition and separate the domains of oscillations with the fixed contact line, in gray and with the contact line moving in the stick-slip regime

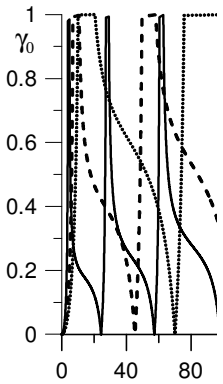


Figure 3: The diagram of contact line motion on the plane ($\omega$, $\gamma_0$), ($\rho_i = 0.7$). $b = 1$ - solid, $b = 1.5$ - dashed, $b = 2$ - dotted.

Figures (4-5) show the dependence of the oscillation amplitude of the frequency of the external influence of the capillary for different values of the parameter and the critical value of contact angle. Previously, it was found that in the absence of hysteresis are forcing frequencies at which the contact line is not moving. In the presence of hysteresis, the contact line is not moving in a certain range of frequencies. By increasing the contact angle values characteristic time during which the contact line is not moving, growing, and the frequency range in which it is in motion, is shrinking.

## 4 Conclusion

The effect of contact angle hysteresis on the dynamics of liquid drops in equilibrium has the form of a cylinder and axially bounded by two parallel solid surfaces under the action of axial vibration. The equilibrium contact angle between the side surface of the droplets and solid surfaces is assumed to be straight. Considered their own and forced vibrations of the drop. The influence of the dynamics of the contact line was taken into account by an effective boundary condition, allowing the contact angle hysteresis. Due to the dissipative nature of the effective boundary condition there is a stable regime of nonlinear oscillations. There is evidence to reject the surface and the frequency characteristics depending on the constant Hawking, and the characteristic value of the contact angle. Previously, it was found that in the absence of hysteresis are forcing frequencies at which the contact line is not moving. In the presence of hysteresis, the contact line is not moving in a certain range of frequencies. By increasing the contact angle values characteristic time during which the contact line is not moving, growing, and the frequency range in which it is in motion, is shrinking. For large values of the constant Hawking, when the contact line is

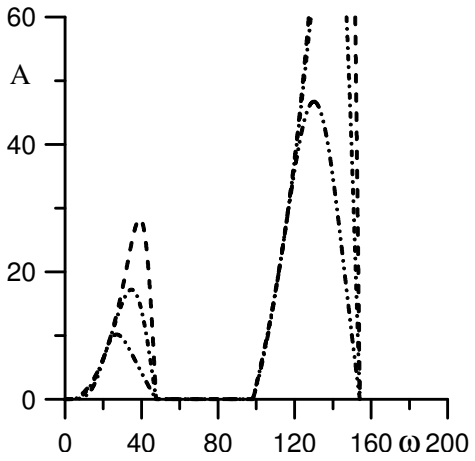


Figure 4: Amplitude-frequency response ($\gamma_0 = 1$).$\lambda = 3$ - dotted line, $\lambda = 5$ - dash-dotted, $\lambda = 10$ - dashed-2-dotted

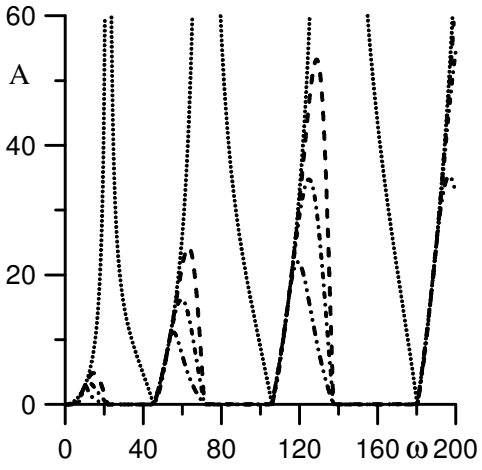


Figure 5: Amplitude-frequency response ($\gamma_0 = 10$).$\lambda = 0$ - dotted line, $\lambda = 3$ - dashed, $\lambda = 5$ - dash-dotted, $\lambda = 10$ - dash-2-dotted

weakly interacts with the substrate and the dissipation is small, the possible existence of resonances.

## Acknowledgements

*The work was supported by the President RF grant MK-2368.2011.1*

## References

[1] Hocking L.M. The damping of capillary-gravity waves at a rigid boundary. J. Fluid Mech., 1987, v.179, pp.253-266.

[2] Alabuzhev A.A., Lyubimov D.V. Effect of the contact-line dynamics on the natural oscillations of a cylindrical droplet. Journal of Applied Mechanics and Technical Physics. 2007. V. 48. No 5. P. 686-693.

[3] Fayzrakhmanova I., Straube A. Stick-slip dynamics of an oscillated sessile drop // Phys. Fluids 2009. V. 21, 072104.

[4] Irina S. Fayzrakhmanova, Arthur V. Straube, and Sergey Shklyaev. Bubble dynamics atop an oscillating substrate: Interplay of compressibility and contact angle hysteresis. Phys. Fluids 23, 102105 (2011).

*Aleksey A. Alabuzhev, ICMM UB RAS, Perm, Russia*

# Cyclic strength of metallic materials and thin walled structures under the attack of corrosive media

Alexander R. Arutyunyan Robert A. Arutyunyan
Robert.Arutyunyan@paloma.spbu.ru

**Abstract**

To describe the corrosion fatigue crack growth, the modified Paris-Erdogan equation is presented. When formulating this equation the following consideration was taken into account. The involvement of an aggressive environment in fatigue crack growth depends on a complex interaction between chemical, mechanical and metallurgical factors. The total crack extension rate under corrosion fatigue conditions is approximated by a simple superposition of the crack growth rate in an inert atmosphere and the crack extension rate due to aggressive environment. The Paris-Erdogan equation is applied to describe the crack growth rate in an inert atmosphere. To formulate the crack extension rate due to aggressive environment it was assumed that the corrosive degradation of material is described by the first order chemical equation, where the stress intensity factor is considered to control the chemical reaction. The modified Paris-Erdogan equation was solved for different values of material parameters. The received crack propagation relations were used to formulate the fatigue strength criterions for metallic specimen with a crack and thin walled structures. Any engineering structure contains a certain numbers of initial micro cracks. Under the cyclic stress and corrosion environment they start to develop. Two periods of crack propagation can be distinguished: the initial, prolonged period, when the size of a crack reaches the critical value, and the period of rapid progressing. This is the way how the dominating crack is formed. However, it is not possible to indicate the time and place of its formation. So the strength of the structure can't be estimated by the traditional methods of design, so the probabilistic methods must be applied. In this paper the probabilistic corrosive fatigue failure criterion, based on corresponding crack growth rate, is developed. The crack growth and fatigue failure curves according to the presented theoretical relations are constructed. They are in good agreement with the basic experimental results of the response of metallic materials to the attack of corrosive media.

Financial support of the Russian Foundation for Basic Research (Grant N 12-08-00594) is gratefully acknowledged.

The fatigue crack propagation law in inert environments is defined by the Paris-Erdogan equation [1]

$$\frac{dl}{dN} = C\,(\Delta K)^m\,, \tag{1}$$

where $\Delta K$ is stress intensity factor range, $C$, $m$ are material variables, $l$ is current value of the crack length, $N$ - the loading cycles.

Equation (1) covers the linear (in $\log(dl/dN) - \log(\Delta K)$ coordinates) part of full fatigue crack propagation diagram (curve 1 in Fig. 1).

When formulating the kinetic equation for the fatigue corrosive crack growth, the following consideration was taken into account [2, 3]. The involvement of an aggressive environment in fatigue crack growth depends on a complex interaction between chemical,

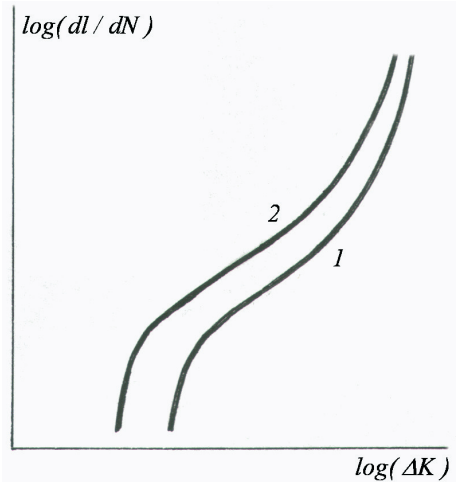


Figure 1: Kinetic diagrams of fatigue failure: for inert media (curve 1), for corrosive media (curve 2).

mechanical and metallurgical factors which leads to the intensification of the crack growth rate as it is shown in Fig. 1 (curve 2). Compare the curves 1 and 2 in Fig. 1 we can see that for the large values of $\Delta K$ the influence of corrosive media on the crack growth rate is negligible. Opposite, for the small values of $\Delta K$ the influence of corrosive media on the crack growth rate is significant. To describe these experimental effects the total crack extension rate under corrosion fatigue conditions is approximated by a simple superposition [3, 4] of the crack growth rate in an inert atmosphere and the crack extension rate due to aggressive environment

$$\frac{dl}{dN} = C\,(\Delta K)^m + \frac{d\gamma}{dN}, \tag{2}$$

where $\gamma$ is the current depth of crack due to corrosive material degradation at the tip of a crack.

To formulate the crack extension rate due to aggressive environment it was assumed that the corrosive degradation of material is described by the first order chemical equation, where the stress intensity factor is considered to control the chemical reaction

$$\frac{d\gamma}{dN} = F(\Delta K)\; N^{\beta}, \tag{3}$$

where $F$ is a function of $\Delta K$ and $\beta$ is a constant. Further we will consider the power relation for the function $F$: $F(\Delta K) = K_1(\Delta K)^{\alpha}$ ($K_1$ and $\alpha$ are constants).

Taking $\alpha = m$ and introducing (3) into (2), we will receive the following kinetic equation

$$\frac{dl}{dN} = (\Delta K)^m \left(C + K_1 N^{\beta}\right). \tag{4}$$

Further, we will consider the propagation of a small through thickness crack in a large plane specimen, for which $\Delta K = \Delta\sigma\sqrt{\pi\, l}$ ($\Delta\sigma$ is stress range). Introducing this value of stress intensity factor range into (4) we will have

$$\frac{dl}{dN} = (\Delta\sigma)^m \pi^{m/2} l^{m/2} \left(C + K_1 N^{\beta}\right). \tag{5}$$

For $\Delta\sigma = Const$, $l = l_0$ at $N = 0$ the solution of equation (5) is

$$l = \left[ \frac{2-m}{2} (\Delta\sigma)^m \pi^{m/2} \left( CN + K_1 \frac{N^{\beta+1}}{\beta+1} \right) + l_0^{\frac{2-m}{2}} \right]^{\frac{2}{2-m}}. \tag{6}$$

If $K_1 = 0$ from (6) follows the Paris-Erdogan relation for the propagation of fatigue crack in inert environments

$$l = \left[ \frac{2-m}{2} (\Delta\sigma)^m \pi^{m/2} CN + l_0^{\frac{2-m}{2}} \right]^{\frac{2}{2-m}}. \tag{7}$$

Compare the relations (6) and (7), one can see that the crack grows more intensive in corrosive media than in inert media. In Fig. 2 the theoretical crack growth curves according to the relations (7) (curve 1) and (6) (curve 2) are presented.

Let's consider the fatigue strength criterions for a metallic specimen with a crack in corrosive and inert media. Taking $l = l_*$ ($l_*$ is final crack size at failure) in (7) and (6) we will receive the corresponding failure criterion for the inert media

$$(\Delta\sigma)^m CN = \frac{2\left( l_*^{\frac{2-m}{2}} - l_0^{\frac{2-m}{2}} \right)}{(2-m)\pi^{m/2}}. \tag{8}$$

and for the corrosive media

$$(\Delta\sigma)^m \left( CN + K_1 \frac{N^{\beta+1}}{\beta+1} \right) = \frac{2\left( l_*^{\frac{2-m}{2}} - l_0^{\frac{2-m}{2}} \right)}{(2-m)\pi^{m/2}}. \tag{9}$$

In Fig. 3 in $\log(\Delta\sigma) - \log N$ coordinates are presented the theoretical fatigue fracture curves according to criterions (8) (curve 1) and (9) (curve 2). As it follows from this figure for the relatively large values of $\Delta\sigma$ the influence of corrosive media on the fatigue failure is negligible, while for the small values of $\Delta\sigma$ the influence of corrosive media on the fatigue failure is significant.

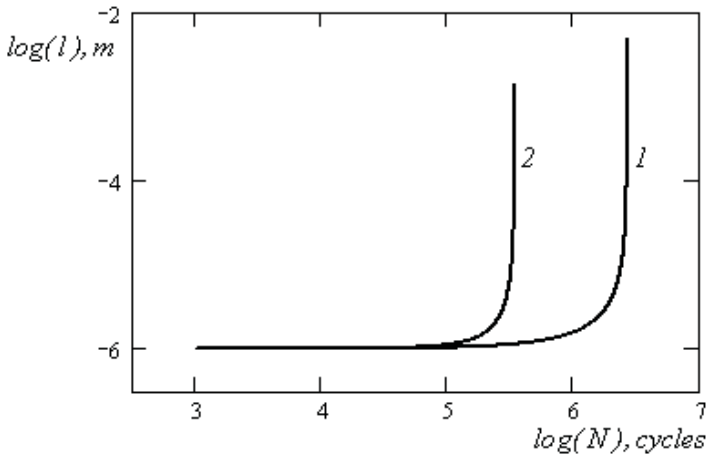


Figure 2: The crack growth curves according to the relations (7) (curve 1) and (6) (curve 2), $\Delta\sigma = 150\ MPa$.

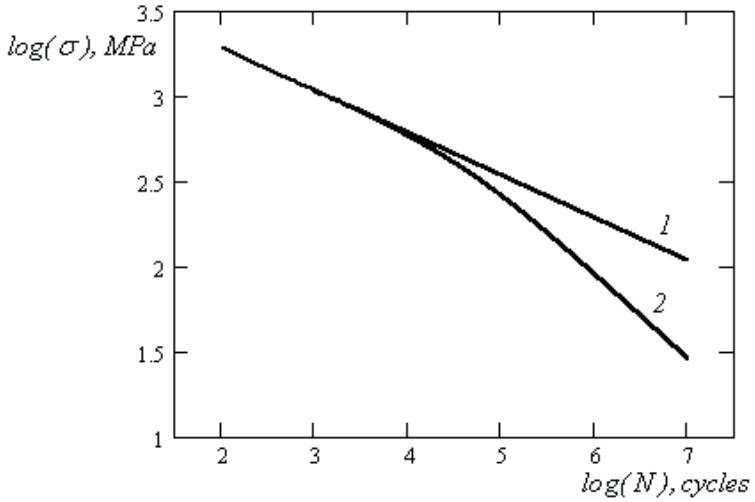


Figure 3: The theoretical fatigue failure curves according to criterions (8) (curve 1) and (9) (curve 2).

When formulating the probability fatigue fracture model we will take into account the following assumptions [5, 6]. An engineering structure is considered as a statistical system containing $n$ initial micro cracks $l_{0i}$ ($l_{0i} \le l_i \le l_*$, $i = \overline{1,\ n}$).

Let's assume that the cracks size distribution is random and is defined by the Poisson's law

$$G(l) = \frac{e^{-\lambda\, l_{0i}} - e^{-\lambda\, l_i(N)}}{e^{-\lambda\, l_{0i}} - e^{-\lambda\, l_*}}, \tag{10}$$

where $\lambda$ is a constant.

We assume also that the number of cycles to failure $N$ is random one and defined by the Poisson's law. It follows from (10) by introducing into it the value of crack length $l$ defined by the relation (6). Under the cyclic loading and corrosive media cracks are developed and the failure of structure follows when the size of a crack reaches the critical value. The corresponding number of cycles $N = \min(N_i)$ (where $N_i$ is the number of cycles to failure for the individual $i$-th crack). So we have the minimal value distribution problem for the random variable $N_i$. Such distribution was considered by Gumbel [7]

$$H(N) = 1 - \left[1 - G(N)\right]^n. \tag{11}$$

For the great number of cracks instead of formula (11) the following asymptotic relation can be used [7, 8]

$$H(N) \approx 1 - \exp\left[-nG(N)\right]. \tag{12}$$

Going to the reliability function $R(N)$ we will have

$$R(N) = 1 - H(N) = \exp\left\{-n\frac{e^{-\lambda\, l_{0i}} - e^{-\lambda\, l_i(N)}}{e^{-\lambda\, l_{0i}} - e^{-\lambda\, l_*}}\right\}. \tag{13}$$

For the given reliability level $R_*$ the following failure criterion can be derived from formula (8)

$$(\Delta\sigma)^m \left(CN + K_1\frac{N^{\beta+1}}{\beta+1}\right) = \frac{2}{(2-m)\pi^{m/2}}\left[\left(\frac{1}{\lambda}\ln\left(\frac{1}{B}\right)\right)^{\frac{2-m}{2}} - l_{0i}^{\frac{2-m}{2}}\right], \tag{14}$$

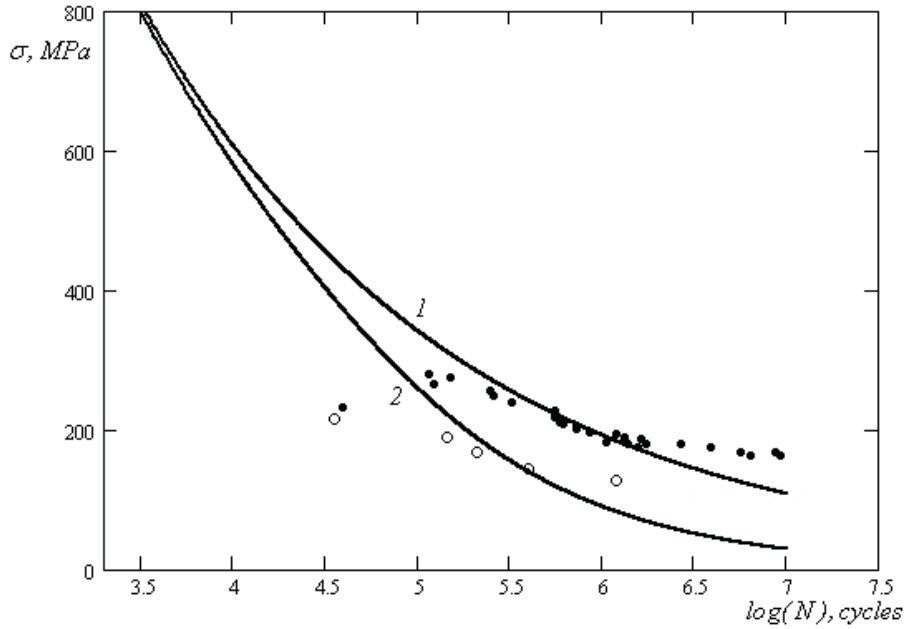


Figure 4: Theoretical fatigue failure curves according to the criterions (15) (curve 1) and (14) (curve 2). By points are shown the experimental results [9].

where $B = e^{-\lambda l_{0i}} + \dfrac{e^{-\lambda l_{0i}} - e^{-\lambda l_*}}{n} \ln R_*$.

Taking $K_1 = 0$ in (14), we will have the failure criterion for the inert media

$$(\Delta\sigma)^m CN = \frac{2}{(2-m)\pi^{m/2}} \left[ \left( \frac{1}{\lambda} \ln \left( \frac{1}{B} \right) \right)^{\frac{2-m}{2}} - l_{0i}^{\frac{2-m}{2}} \right], \qquad (15)$$

In Fig. 4 in $\sigma - \log(N)$ coordinates are presented the theoretical fatigue failure curves according to criterions (15) (curve 1) and (14) (curve 2). The points correspond to the experimental results [9].

To draw the theoretical curves in Fig. 2-4 the following values of parameters were used: $C = 7,5 \cdot 10^{-11}[m \cdot cycles]^{-1} \cdot [MPa]^{-4}$, $l_* = 10^{-1}m$, $l_{0i} = 10^{-6}m$, $m = 4$, $\lambda = 5[m]^{-1}$, $\beta = 1$, $K_1 = 3 \cdot 10^{-15}[m]^{-1} \cdot [cycles]^{-2} \cdot [MPa]^{-4}$, $n = 20$, $R_* = 0,8$.

## References

[1] Paris P., Erdogan F. A critical analysis of crack propagation laws // Journal of Basic Engineering. Trans. ASME. Series D. 1963. 85. N 4. P. 528-534.

[2] Scully J.C. The fundamental of corrosion. Pergamon Press. Oxford. New York et al. 1975. 224p.

[3] Hertzberg, Richard W. Deformation and fracture mechanics of engineering materials. John Wiley & Sons, Inc. 1989. 680p.

[4] Arutyunyan R.A., Denisova A.A. The growth of corrosion cracks and the fatigue fracture criterion // Vestnik S.-Petersburg University. Ser. 1. Vipusk 3. N 17. P. 60-64. (in Russian).

[5] Arutyunyan R.A. A probability corrosion fracture model // Probl. Prochnosty. 1988. N 12. P. 106-108. (in Russian).

[6] Arutyunyan R.A. A probability fatigue fracture model of complex systems // Doklady Russian Academy of Science. 1993. V. 332. 3. N 12. P. 317-318. (in Russian).

[7] Gumbel E.J. Statistics of extremes. Columbia University Press. New York. 1958. 450p.

[8] Bolotin V.V. Probabilistic methods in structural mechanics. Moscow. Stroyisdat. 1965. 279p. (in Russian).

[9] S.E. Stanzl-Tschegg, H. Mayer. Fatigue and fatigue crack growth of aluminium alloys at very high numbers of cycles // International Journal of Fatigue. 2001. V. 23. Supplement 1. P. 231-237.

*Alexander R. Arutyunyan, Robert A. Arutyunyan, St.-Petersburg State University, Faculty of Mathematics and Mechanics, Saint Petersburg, Petrodvoretz, Universytetskii prospect, 28, 198504, Russia*

# Fracture energy consumption in speed loading experiments

Robert A. Arutyunyan Kira S. Yakimova
Robert.Arutyunyan@paloma.spbu.ru

**Abstract**

The nonlinear damage summation law expressed in terms of relative values of energy consumption is proposed. For the verification of the damage summation law the experiments on the plane specimens made of polymethylmetacrylate under the several values of speed loading were carried out. As it follows from the experiments the deviation from the linear damage law is essential and the value of the fracture energy depends on the application sequence of speed loading. For example, for two levels of speed loading ($1mm/min$ and $8mm/min$) the energy consumption at fracture is minimal, when the speed of initial loading is equal to $1mm/min$. So from the received experimental results follow that the energy consumption at fracture is dependent on the regimes of speed loading and they should be taken into account in design and exploitation of different equipments for processing and milling the solid materials.

Financial support of the Russian Foundation for Basic Research (Grant N 11-08-00763) is gratefully acknowledged.

In many practical applications such as building industry, mining and processing, food industry, pulp and paper industry and others the most important problem is to define the regimes of loading with the minimal fracture energy consumption. In many of mentioned industries the energy consumptions for fracture are significant and not well grounded. To solve the problem it is necessary to compare the different regimes of loading and find those with the optimal value of energy consumption for fracture, so they can be recommended in the designing and running of different processing and fracture equipments.

To estimate the optimal energy consumption for fracture, the energy consumptions in different loading programs are compared. The energy consumptions are defined in accordance with the damage summation law, expressed in terms of relative value of energy consumption [1]. If the sum of the relative value of energy consumption is less one then the energy consumption is optimal. So we can define the reliable boundary of optimal value of the fracture energy.

The notion of damages and the linear laws of summation of damages [2-5] were considered in the beginning of the last century as applied to fatigue fracture by Palmgren (1924) and fracture under creep condition by Robinson (1938) and Baily (1935). Miner (1945) formulated a linear law of summation of damages for the case of alternation of cyclic and prolonged static loadings. In the case of the multi stage fatigue loading a specimen is tested by the stress $\sigma_1$ during $N_1$ cycles, after that it is tested by the stress $\sigma_2$ during $N_2$ cycles up to fracture, etc. At stress level $\sigma_k$ the specimen is tested up to fracture at the number of cycles $N_k$. If $N_{iR}$ $(i = 1, 2, ..., k)$ is the number of cycles to fracture under the action of stress $\sigma_i$, then the relations $N_1/N_{1R}, N_2/N_{2R}, ..., N_i/N_{iR}, ..., N_k/N_{kR}$ are the fractions of damage during the first, second and $k$-th stages of loading cycles.

The same way can be introduced the damage concept for the case of speed loading experiments. Let during the time $t_1$ a specimen is tested under the speed level $V_1$ after

that it is tested during the time $t_2$ under the speed level $V_2$ up to fracture and so on. If $t_{iR}$ $(i = 1, 2, ..., n)$ are the time to fracture at the speed level $V_i$ in sustained loading, so the relations $t_1/t_{1R}, t_2/t_{2R}, ..., t_i/t_{iR}, ..., t_n/t_{nR}$ are the fractions of damage in the processes of the first, the second and the $n$ stages of speed loadings.

The linear law of summation of damages during alternation of different speed loadings can be expressed as

$$\sum_{1}^{n} \frac{t_i}{t_{iR}} = 1. \tag{1}$$

If $n = 2$, then the linear damage summation law is

$$\frac{t_1}{t_{1R}} + \frac{t_2}{t_{2R}} = 1. \tag{2}$$

In our experiments, carried out under the action of different speed loading regimes, the systematic deviations from the linear damage summation law (2) were established. In this connection, the non linear modifications of the linear damage summation law will be considered. In particular,

$$\left(\frac{t_1}{t_{1R}}\right)^m + \left(\frac{t_2}{t_{2R}}\right)^m = a, \tag{3}$$

where $m$, $a$ are constants.

As it was mentioned, in many applications the problem is to choose the regimes of loading with the minimal consumptions of the fracture energy, so they can be recommended in the designing and running of different processing and fracture equipments.

To find such loading regimes we will operate on the damage concept defined in terms of relative value of energy consumption and the damage summation law will be formulated using such definitions. In the case of relation (3) we have the following relation.

$$\left(\frac{W_1}{W_{1R}}\right)^m + \left(\frac{W_2}{W_{2R}}\right)^m = a, \tag{4}$$

where $W_1$, $W_2$ are the current values of energy, respectively, during the $V_1$ and $V_2$ speed levels loadings, $W_{1R}$, $W_{2R}$ are the values of energy consumption for fracture at speed levels $V_1$ and $V_2$ sustained loading.

The experimental evaluation of hypotheses of summation of damages was investigated in experiments for the specimen made of polymethylmetacrylate for two levels of speed loading $V_1 = 1mm/min$ and $V_2 = 8mm/min$. Experiments were carried out at room temperature for plane specimens of the following sizes: the length of the working part was 60 mm, the width was 10 mm, and the thickness was 5 mm. The speed loading were performed on Lloyd 30k PLUS machine.

Six specimens were used to define the energy consumptions for fracture in tension experiments at the speed levels $V_1$ and $V_2$ in sustained loading. The typical diagrams, received in these experiments are shown in Fig. 1.

The results of calculation of damage defined in terms of the relative value of energy consumption based on the experiments are shown in Fig. 2 and Tables 1, 2.

The solid circles in Fig. 2 correspond to the case when the initial loading is in $V_1$ regime, the cross marked points go to the case when the initial loading is in $V_2$ regime.

As it follows from Fig. 2 and Tables 1, 2, the energy consumption for fracture is minimal, when the speed of initial loading is equal $1mm/min$.

Table 1: The energy consumption during the alternation of two levels of speed loading ($V_1 = 1mm/min$ and $V_2 = 8mm/min$). First loading is in $V_1$ regime.

| $W_1/W_{1R}$ | $W_2/W_{2R}$ | $W_1/W_{1R} + W_2/W_{2R}$ |
|---|---|---|
| 0,127 | 0,883 | 1,010 |
| 0,125 | 0,501 | 0,626 |
| 0,135 | 0,754 | 0,889 |
| 0,010 | 2,029 | 2,039 |
| 0,011 | 1,335 | 1,346 |
| 0,395 | 0,304 | 0,699 |
| 0,371 | 0,312 | 0,683 |
| 0,048 | 1,375 | 1,423 |
| 0,054 | 0,759 | 0,813 |
| 0,238 | 0,498 | 0,736 |
| 0,225 | 1,203 | 1,428 |

Table 2: The energy consumption during the alternation of two levels of speed loading ($V_1 = 1mm/min$ and $V_2 = 8mm/min$). First loading is in $V_2$ regime.

| $W_2/W_{2R}$ | $W_1/W_{1R}$ | $W_2/W_{2R} + W_1/W_{1R}$ |
|---|---|---|
| 1,461 | 0,078 | 1,539 |
| 2,133 | 0,080 | 2,213 |
| 1,222 | 0,127 | 1,349 |
| 0,019 | 1,083 | 1,102 |
| 0,020 | 0,715 | 0,735 |
| 0,620 | 0,349 | 0,969 |
| 0,592 | 0,634 | 1,226 |
| 0,080 | 0,733 | 0,813 |
| 0,166 | 0,634 | 0,800 |
| 0,199 | 0,688 | 0,887 |
| 0,251 | 0,651 | 0,902 |
| 0,366 | 0,532 | 0,898 |
| 0,368 | 0,472 | 0,840 |

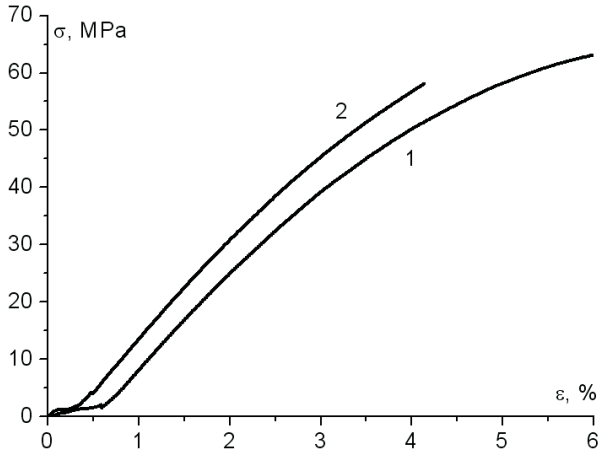


Figure 1: Tension stress-deformation diagrams: at the speed levels $V_1$ (curve 1) and $V_2$ (curve 2).

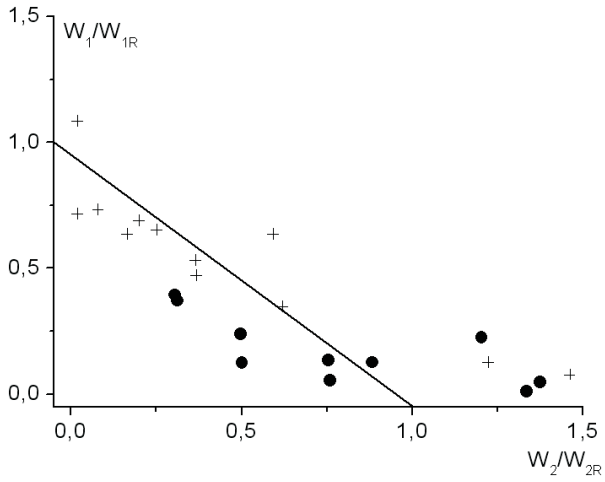


Figure 2: Accumulation damages by the energy consumption during the alternation of two levels of speed loading ($V_1 = 1mm/min$ and $V_2 = 8mm/min$). • - first loading is in $V_1$ regime, + - first loading is $V_2$ in regime.

## Conclusions

The nonlinear damage summation law expressed in terms of relative values of energy consumption in speed loading experiments is suggested.

To estimate the optimal energy consumption, energy consumptions for fracture for two levels of speed loading ($V_1 = 1mm/min$ and $V_2 = 8mm/min$) were defined. It is shown, that the energy consumption at fracture is minimal, when the speed of initial loading is equal to 1 mm/min.

The received results may be used in designing and running of different processing and fracture equipments.

## References

[1] Arutyunyan R.A. Optimization of energy consumption for fracture of solids // Doklady Russian academy of science. 2010. Vol. 434. N 2. P. 182-185.

[2] Palmgren A. The fatigue life of ball-bearings // Zeitschrift. VDI. 1924. Vol. 68. P. 339-341.

[3] Robinson E.L. Effect of temperature variation on the long rupture strength of steels // Trans. ASME. 1952. Vol. 74. N 5. P. 777-781.

[4] Baily R.W. The utilization of creep test data in engineering design // The institution of mechanical engineers. Proceedings. 1935. Vol. 131. P. 131-269.

[5] Miner M.A. Cumulative damage in fatigue // Journal of Applied Mech. ASME. 1945. Vol. 12. N 9. P. 159-164.

*Robert A. Arutyunyan, Universitetskii pr., 28, Faculty of Mathematics and Mechanics Saint Petersburg State University, Saint Petersburg, Petrodvoretz, 198504, Russia.*

# Nonlocal optimization of multi-layered spaced shields

Nikolay V. Banichuk Svetlana Yu. Ivanova Evgeny V. Makeev
banichuk@ipmnet.ru

**Abstract**

The study concerns the problems of optimal design of shields structures produced from various given materials. The number of materials is supposed to be finite and consequently the admissible design set consists of separate discrete values. The impactor was modelled as a short axisymmetrical rigid body that strikes the compound structure consisting of a system of solid plates. The ballistic limit velocity is taken as a performance criterion of the designed layered structure that has to be maximized under some constraints. Best distributions of given materials are found and presented.

## 1 Introduction

The problems of penetration of rigid projectiles (strikers) into deformable media at supersonic entry velocities and the problems of optimal design of layered shield structures are of significant practical and theoretical importance.

Wide survey on the mechanics of penetration of projectiles into targets was presented by Backman and Goldsmith [1] and Goldsmith [2] (taking into account complicated conditions). Bivin et al. [3], [4] devoted their study to determination of the dynamic characteristics of deformed media by the method of penetration. Cavitation and the influence of head shape in attack of thick targets by non-deformable projectiles was investigated by Hill [5]. Cavitation for vertical input of strikers into elastic-plastic media was also investigated by Bivin [6]. Experimental aspects of considered problems are described in the book [7]. Laboratory scale penetration experiments into geological targets up to impact velocities of 2.1 km/sec were studied by Forrestal et al. [8]. Experimental and theoretical results on the problem of penetration into layered materials are contained in the paper of Bivin [9].

Some shape optimization problems have been solved for rigid striker penetrating into deformable media and published by Ben-Dor et al. [10] - [14] and Banichuk et al. [15] - [17], Ostapenko et al. [18], [19]. Some problems of optimization for homogeneous shield structures and for the structure of a layered slab with the penetration of a rigid striker (in the case of normal impact) were studied by Aptukov [20], Aptukov and Pozdeev [21], Aptukov et al. [22] - [24]. In [20], [22] Aptukov et al. considered cylindrical and cone-nosed impactors and determined the optimal distribution of the mechanical characteristics of a non-homogeneous plate using Pontryagin's maximum principle. In [23] (Aptukov et al.) solved the discrete problems of optimization of a layered plate when the shield was consisted of several layers of different materials which were chosen from a given set. In the monograph [24] these investigations were summarized by Aptukov et al. Note that in [21], [22] the problem of optimization of layered structure was investigated using linear relation between dynamical rigidity $H_d$ and the material density $\rho$: $H_d = c_1\rho + c_2$ ($c_1$, $c_2$ - material constants). As a result piece-wise constant optimal design (layered structure) has been found. Kanibolotsky and Urzhumtsev published a book [25], devoted to analysis and design

of layered structures, where they included the results concerning the optimization of shield structure under impact.Alyokhin and Urzhumtsev [26] devoted their studies to optimization of layered mechanical systems including the problems of penetration of projectiles into layered structures. In the book [27] Ben-Dor, Dubinsky and Elperin studied as the problems of shape optimization of impactors penetrating into ductile, concrete and some composite media as the problems of investigation of ballistic properties. The third part of the book is devoted to optimization of multi-layered shields including spaced and two-component ceramic shields. In the recent book [28] Bazhenov and Kotov presented important results on dynamical contact interaction of rigid bodies and deformable solids.

All mentioned problems devoted to optimization of shield structures were investigated using necessary extremum conditions and local search. In the given below investigation we present global approach to finding non-local optimal layered shield structures. We consider a multi-component armor consisting of a system of solid homogeneous plates. The impactor is modelled as a short cylindrical rod that strikes the compound plate. It is suppose that the compound plate breaks progressively into a cone of fractured materials. The goal of this paper is to determine the layered structure that provide the maximum of the ballistic limit velocity considered as optimized functional.

## 2 Basic relations

We consider a multi-layered structure that is consisted from $n$ homogeneous layers (plates) made of $r$ different given materials ($n$, $r$ - given numbers). Suppose that materials of these plates occupy the intervals $x_i \le x \le x_{i+1}$ in the normal to the plate direction, such that $x_{i+1} = x_i + \Delta_i$, $x_0 = 0$, $x_n = L$, $i = 0, 1, ..., n-1, n$ where $\Delta_i$ - thickness of the plate with number $i$ and $L = \sum \Delta_i$ - thickness of composed structure. Material properties of the layer with number $i$ are characterized by two constants: $A_0^i$ (dynamical hardness)and $A_2^i$ (density) which correspond to the material with number $s$, i.e. $A_0^i,\ A_2^i \in \{A_{0s},\ A_{2s}\}$, $s = 1, 2, ..., r$. Properties of the whole shield structure will be described by piece-wise constant functions $A_0(x)$, $A_2(x)$ such that $A_0 = A_0^i$, $A_2 = A_2^i$, $x \in [x_i, x_{i+1})$. For convenience the following piece-wise constant function $t = t(x)$, $x \in [0, L]$, $t \in \{t_s = s\}$ is introduced and natural parametrization of structural properties is used: $A_0\left(t(x)\right)_{t=t_s=s} = A_0^i$, $A_2\left(t(x)\right)_{t=t_s=s} = A_2^i$. To evaluate the "cost" of the material used in the considered multi-layered shield structure we take the integral functional

$$K(t) = \int_0^L k\left(t(x)\right) dx \tag{1}$$

where $k\left(t(x)\right)$ is the density of material ($k(t(x)) \equiv \rho(x)$) or the material cost per unit of length.

Penetration of the rigid striker into multi-layered structure is described by the following differential equation and boundary (initial) condition at $x = 0$:

$$Mv\frac{dv}{dx} = D, \quad (v)_{x=0} = v_{imp}, \quad D = -\pi R^2\left(A_0 + \kappa A_2 v^2\right) \tag{2}$$

where $R$ is the radius of cylindrical striker and $\kappa$ - coefficient characterizing the flatness of the striker nose ([26], [29]). If the initial penetration with $v(0) = v_{imp}$ is such that $v(x) > 0$, $0 \le x < L$, $(v)_{x=L} = 0$ then the impact velocity is called "ballistic limit velocity" $v(0) = v_{imp} = v_{BLV}$ and is taken as a main characteristic of the layered structure. In what follows it will be considered as an optimized functional

$$J(t) = v_{BLV}(t) \tag{3}$$

To evaluate the ballistic limit velocity (impact velocity $v_{imp} = v_{BLV}$) we introduce new space variable $\xi$: $\xi = L - x$, $(d\xi = -dx)$ and transform the initial-value problem (2) to the following form

$$\frac{dv^2}{d\xi} = \beta\left(\alpha + v^2\right), \quad \left(v^2\right)_{\xi=0} = 0, \quad \alpha = A_0/(kA_2), \quad \beta = 2\pi r^2 A_2/M \tag{4}$$

Determination of the velocity distribution $v(\xi)$ is performed for $0 \le x \le L$ using equal spaced nodes $\xi_i$: $\xi_{i+1} = \xi_i + \Delta$, $i = 0, 1, ..., n$ and the following notation $\alpha(t(\xi))_{t=t_s} = \alpha_i$, $\beta(t(\xi))_{t=t_s} = \beta_i$, $\xi \in [\xi_i, \xi_{i+1})$, $(v^2)_{\xi=\xi_0=0} = 0$, $(v^2)_{\xi=\xi_N=L} = v^2_{BLV}$. After integration of ordinary differential equation (4) with respect to $\xi$ for $\xi \in [\xi_i, \xi_{1+1}]$ we will have

$$\ln\left[(\alpha_i + v^2_{i+1})/(\alpha_i + v^2_i)\right] = \mu_i \tag{5}$$

Here $\mu_i = \beta_i \Delta\xi$, $\Delta\xi = \xi_{i+1} - \xi_i$, $i = 0, 1, ..., n$; $v_0 = 0$ , $v_N = v_{BLV}$. Performing elementary algebraic transformations we obtain the following relation between $v^2_i$ and $v^2_{i+1}$:

$$v^2_{i+1} = \alpha_i \left[\left((1 + \frac{v^2_i}{\alpha_i}\right)\exp(\mu_i) - 1\right] \tag{6}$$

## 3 Genetic algorithm for finding global optimal design of shield structure

Considered problem consists in optimization of multi-layered space shield structure such that the piece-wise constant function $t(x)$ maximizes the ballistic limit velocity $v_{BLV}$ under constraint imposed on the cost (mass or weight or other important characteristics) functional $K(t)$ i.e.

$$J_* = J(t_*) = \max_t v_{BLV}(t), \quad K(t) \le K_0 \tag{7}$$

Here $K_0$ is given problem parameter. To solve formulated problem of maximization of $v_{BLV}(t)$ and finding of global optimal design (distribution of layers and materials) taking into account presented isoperimetric inequality (7) we apply the penalty function approach based on maximization of adjoint functional $J^a$:

$$J^a(t) = J(t) - \lambda(K(t) - K_0), \quad \lambda = \begin{cases} 0, & if \quad K(t) - K_0 \le 0, \\ \lambda_0 > 0, & if \quad K(t) - K_0 > 0 \end{cases} \tag{8}$$

where $\lambda_0$ - positive penalty multiplier.

Solution of the problem of the functional $J^a(t)$ maximization for various given values of the problem parameter $K_0$ ("cost" of materials) is performed with the help of a genetic algorithm (GAS [30]). We suppose that the interval [0, $L$] of variable $\xi$ is divided by the node points $\xi_i$, $i = 0, 1, ..., n$ into $N$ equal parts of the length $\Delta x = L/n$. For each subinterval the parameters $A_0$ and $A_2$ take the values corresponding to the chosen materials. Populations under consideration consist of $N$ individuals represented admissible piece-wise homogeneous shield structure. The number $N$ is supposed to be even and is kept constant in the population renewal process. Each $j$ -individual of the population is described by the set of values (elements) $t(j, i)$ representing the design variable for corresponding subinterval $x_i \le x \le x_{i+1}$. The "best" individual, i.e. the set $t(j, i)$ maximizing the augmented functional $J^a$ is sought by using the genetic algorithm.

The first step of the algorithm consists in initialization of population that is assigned random values taken from [1,...,$r$] to each element $t(j,i)$. For created individuals ($j$=1,...,$N$) of initial population we compute augmented functional $J^a$ and find the individual having the maximal value of the functional. Using initial data for the next steps of the algorithm it is possible to determine new population consisting of $N$ individuals and to perform in what follows successive maximization of the functional $J^a$.

At the second step of the algorithm we perform successive selection of $N/2$ individual pairs - "parents" to obtain $N/2$ pairs of individuals - "children", those constitute the new population. Selection of the first parent ("a") is performed by the following manner. Some natural number $N^T < N$ is chosen and then $N^T$ individuals are selected by the random way. From this set of individuals we preserve and use only one individual having the maximal value of augmented functional $J^a$. Similarly we find the second parent ("b") and put together the first pair of individuals. All together we compose $N/2$ of such pairs.

The third step of the algorithm consists in obtaining of two children from each parent pair of individuals. To this purpose we take some constant value from the interval [0,1], that is called as crossover probability $p_{CO}$. Then for each parent pair it is generated random number $p_r$ from interval [0,1] and random number $m$ from [0,...,n-1]. If it is appeared that $p_r \leq p_{CO}$ then the values of design variables (elements) of children for $i$=0,...,$m$ are copied from their parents "a" and "b", but the meaning of these elements (for $i$=$m+1$,...,$n-1$) are obtained with the help of crossover. The latter means that for child "a" we copy the values of the corresponding elements of the parent "b" and vice versa. Successive sorting of all parent pairs and performing of described operations lead to obtaining of $N$ individuals - children, that compose new population.

The fourth step of the algorithm consists in mutation of obtained new population. This step is necessary not to stick at the local maximum of the considered functional. To realize the mutation procedure we take some small enough ($\sim 0.01$) parameter $p_m$ (probability of mutation). Then for all elements of each individual of the population we generate the random number $p_r$ from the interval [0,1]. If $p_r \leq p_m$ then the value of design variable for considered element is replaced by the arbitrary value, satisfying given constraints (from 1 to $r$). For obtained new population we compute the functionals $J^a$ for all numbers $j$ and select the best individual. Then we go to the second step of applied algorithm. Note that if the best child from new population is appeared to be worse then the best parent from previous population then we replace it by this parent. Thus the finding process of global maximum will be monotonic.

## 4 Numerical results

Optimal distributions of materials $t(x)$ have been determined for different values of the problem parameters with the help of described genetic algorithm. The parameters of computational process have been taken as $n = 20$, $N = 10$, $N^T = 4$, $p_{CO} = 0.5$, $p_m = 0.05$. Calculations were complicated after generation of 10000 populations.Characteristics of materials considered as admissible for optimal design of nonhomogeneous shield structure are taken from [29], [31]. The following materials were considered:

s=1 - aluminun $(A_{01} = 350 \cdot 10^6\ N/m^2, \quad A_{21} = 2765\ kg/m^3)$
s=2 - soft steel $(A_{02} = 1850 \cdot 10^6\ N/m^2, \quad A_{22} = 7830\ kg/m^3)$
s=3 - copper $(A_{03} = 910 \cdot 10^6\ N/m^2, \quad A_{23} = 8920\ kg/m^3)$
s=4 - duraluminum $(A_{04} = 1330 \cdot 10^6\ N/m^2, \quad A_{24} = 2765\ kg/m^3)$

The results of numerical solution are presented in Fig.1 for the following problem parameters: $L = 0.1m$, $R = 0.005m$, $M = 0.05kg$, $\kappa = 1$, $\lambda_0 = 10^6\ m^3/kg \cdot sec$. The variant (a) corresponds to the optimal structure when the constraint on the shield mass is not

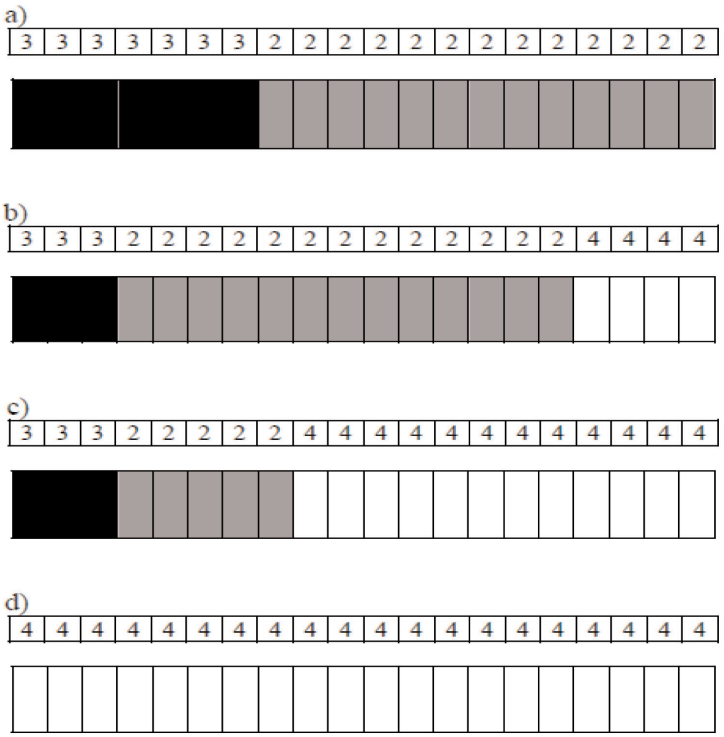


Figure 1: Optimal material distributions

taken into account. In this case the optimal structure is composed of two layers: the first in the order of penetration - copper ($s = 3$), the second - steel ($s = 2$). The ballistic limit velocity $v_{BLV} = 1630\ m/sec$, $K = 816\ kg/m^2$. The variants (b) and (c) correspond to the values of mass constraint per unit of shield square $K_0 = 700\ kg/m^2$ and $K_0 = 500\ kg/m^2$, respectively. The third layer - duraluminum ($s = 4$) is presented in the optimal structures (b) and (c). The values of shield mass and the ballistic limit velocity are: $K = 698\ kg/m^2$, $v_{BLV} = 1468\ m/sec$ for the case (b) and $K = 495\ kg/m^2$, $v_{BLV} = 1133\ m/sec$ for the case (c). The optimal structure (d) for $K_0 = 300\ kg/m^2$ has the only layer - duraluminum ($s = 4$) with $K = 276\ kg/m^2$ and $v_{BLV} = 815\ m/sec$. From the obtained results it is follows that the inertial properties of shield material ($A_2$ - density) are more actual for the high velocities of strikers and heavy materials must be presented in front layers of the optimal structures. For low velocities the dynamical hardness of materials $A_0$ will be more actual.

## 5 Some notes and conclusions

In the paper we presented formulation and analysis of the problem of optimization of multi-layered shield structures that dynamically interacted with rigid axisymmetric bodies (strikers, impactors) and characterized by such functionals as ballistic limit velocity, mass of the shield structure and its "cost" and other.

In the previous publications devoted multi-layered structures the finding of the best solutions have been performed in frame of "local" search. It means that the mathematical programming methods of local extremum finding or necessary optimality conditions of the optimal control theory have been used in these studies to find optimal design. In contrast to

them we developed the procedure of global optimal finding based on evolutionary stochastic methods (genetic algorithm).

Note also that in proposed paper we developed the procedure of analytical integration of dynamic equation for each separate homogeneous plate that gave us possibility to perform rigorous evaluation of ballistic limit velocity in effective manner (in the sense of computational time consumption for integration that must be performed each considered admissible variant of multi-layered shield structure).

## Acknowledgements

*The work is performed under financial support of RFBR (grant 11-08-00030-a), RAS Program 13, Program of Support of Leading Scientific Schools (grant 3288.2010.1).*

## References

[1] Backman M.E., Goldsmith W. The mechanics of penetration of projectiles into targets. Internat. Engng. Sci. 1978, Vol.16, N.1, p.1-99.

[2] Goldsmith W. Non-ideal projectile impact on targets. Intern. J. Impact Engng. 1999, Vol. 22, N. 2-3, p.95-395.

[3] Bivin Yu.K., Viktorov V.V. and Kovalenko B.Ya. Determination of the dynamic characteristics of soil by the method of penetration. Izv. Akad. Nauk SSSR, MTT, 1980, N.3, p.105-110.

[4] Bivin Yu.K., Kolesnikov V.A. and Flitman L.M. Determination of mechanical properties of a medium by the method of dynamic insertion. Izv. Akad. Nauk SSSR, MTT, 1991, N.4, p.155-164.

[5] Hill R. Cavitation and the influence of headshape in attack of thick targets by non-deformable projectiles. J. Mech. and Phys. Solids. 1980, Vol.28, N.5/6, p.249-263.

[6] Bivin Yu.K. Cavity for vertical input of rigid bodies into elastic-plastic medium. MTT, 1997, N.1, p.93-101.

[7] Ballistic machines and their applications in experimental studies. M.: Nauka, 1984.

[8] Forrestal M.J., Lee L.M. and Jenrette B.D. Laboratory-scale penetration experiments into geological targets up to impact velocities of 2.1 km/s. Trans. ASME, J. Appl. Mech. 1986, Vol.53, N.2, p.317-320.

[9] Bivin Yu.K. Penetration of rigid bodies into soil and layered medium. MTT, 2008, N.1, p.154-160.

[10] Ben-Dor, G., Dubinsky, A., Elperin, T. Shape optimization of high velocity impactors using analytical models. International Journal of Fracture, 1997, Vol.87, N.1, L7-L10.

[11] Ben-Dor, G., Dubinsky, A., Elperin, T. Optimal 3-D penetrating into layered targets. Theoretical and Applied Fracture Mechanics, 1997, Vol.27, N.3, p.161-166.

[12] Ben-Dor, G., Dubinsky, A., Elperin, T. Optimization of the shape of a penetrator taking into account plug formation. International Journal of Fracture, 2000, Vol.106, N.3, L29-L34.

[13] Ben-Dor, G., Dubinsky, A., Elperin, T. Shape optimization of a penetrator nose. Theoretical and Applied Fracture Mechanics, 2001, Vol.35, N.3, p.261-270.

[14] Ben-Dor, G., Dubinsky, A., Elperin, T. Numerical solutions for shape optimization of an impactor penetrating into semi-infinite target. Computers and Structures, 2003, Vol.81, N.1, p.9-14.

[15] Banichuk, N.V., Ivanova, S.Yu. Shape optimization of rigid 3-D high speed impactor penetrating into concrete shields. Mechanics Based Design of Structures and Machines, 2008, Vol.36, N.3, p.249-259.

[16] Banichuk, N.V., Ragnedda, F., Serra, M. On body shapes providing maximum depth of penetration. Structural and Multidisciplinary Optimization, 2009, Vol.38, N.3, p.491-498.

[17] N.V. Banichuk, S.Yu. Ivanova, F. Ragnedda and M. Serra. Multiobjective shape optimization of the rigid shell moving into a condensed media. Mechanics Based Design of Structures and Machines, 2012, Vol.40, N.1, p.73-82.

[18] Ostapenko, N.A., Romanenko, V.I., Yakunina, G.E. Optimum forms of the three-dimensioned bodies for penetration of dense media. Journal of Applied Mechanics and Technical Physics, 1994, Vol.4, p.515-521.

[19] Ostapenko, N.A., Yakunina, G.E. The shape of slender three dimensional bodies with maximum depth of penetration into dense media. Journal of Applied Mathematics and Mechanics, 1999, Vol.63, p.953-967.

[20] Aptukov, V.N. Optimal structure of inhomogeneous plate with continuous distributions of properties over the thickness. Mech. Solids, 1985, Vol.20, N.3, p.148-151.

[21] Aptukov, V.N. and Pozdeev, A.A. Some minimax problems of the technology and strength of constructions. Eng. Cybernatics, 1982, Vol.20, N.1, p.39-46.

[22] Aptukov, V.N., Petrukhin, G.I. and Pozdeev, A.A. Optimal deceleration of a rigid body by an inhomogeneous plate for the case of normal impact. Mech. Solids, 1985, Vol.20, N.3, p.155-160.

[23] Aptukov, V.N., Belousov, V.L. and Kanibolotsky, M.A. Optimization of the structure of a layered slab with the penetration of a rigid striker. Mech. composite Mat., 1986, Vol.22, N.2, p.179-183.

[24] Aptukov, V.N., Murzakaev, A.V. and Fonarev, A.V. Applied Theory of Penetration. Nauka, Moscow, 1992 (in Russian).

[25] Kanibolotsky M.A., Urzhumtsev Yu.S. Optimal Design of Layered Structures. Novosibirsk, Nauka, Sib. Department, 1989 (in Russian).

[26] Alyokhin V.V., Urzhumtsev Yu.S. Optimization of Layered Systems. Yakutsk, Publ. SD RAS, Sib., 2002, 178p. (in Russian).

[27] Ben-Dor, G., Dubinsky, A., Elperin, T. Applied High-Speed Penetration Dynamics. Dordrecht, The Netherland, Springer, 2006, 357p.

[28] Bazhenov, V.G. and Kotov, V.L. Mathematical Modelling of Non-stationary Processes of Impact and Penetration of Axisymmetric Bodies and Soil Media Properties Identification. PHYSMATLIT, Moscow, 2011, 208p. (in Russian).

[29] Vitman, F.F., Stepanov, V.A. Influence of deformation rate on the rear force for metals at striker velocities $10^2 - 10^3$ m/sec. In: Some Problems of Rigid Body Strength. Izd. Akad. Nauk SSSR, Moscow-Leningrad, 1959 (in Russian).

[30] Goldberg, D.E. Genetic Algorithms in Search, Optimization and Machine Learning. Addision-Westley Publ. Comp., inc. 1989.

[31] Vitman, F.F., Ioffe, B.S. A simple method of determining the dynamical hardness of metals using a double cone. Zavodskaja Laboratorija, 1948, Vol.14, N.6, p.727-732 (in Russian).

*Nickolay V. Banichuk, Prospekt Vernadskogo, 101, bld.1, Moscow, Russia*
*Svetlana Yu. Ivanova, Prospekt Vernadskogo, 101, bld.1, Moscow, Russia*
*Evgeny V. Makeev, Prospekt Vernadskogo, 101, bld.1, Moscow, Russia*

# Wear and tear of nominally fixed joints affected by vibration and percussive impacts

I. I. Blekhman L. I. Blekhman V. B. Vasilkov K. S. Ivanov
K. S. Yakimova
iliya.i.blekhman@gmail.com

**Abstract**

Vibrational conditions are very common for many of natural and artificial material processing devices such as grinding and rod mills, conical and jaw breakers, screening, conveying and feeding devices and also hydropower, construction and other machines. It is known, that vibration and percussive impact lead to increase of risk of facility parts breakdown and even catastrophes. Decrease in material durability under such impacts referred to as fatigue phenomenon is well investigated. However, wearing of parts of nominally fixed joints referred to as fretting-wear is not intimately examined. Wearing of this kind occurs in bolted-type connections, rotating bearings backs, rod-sleeve joints, leaf springs, gears, sockets and other junctions. This article deals with the fretting-wear effect on facility parts, and its origin consisting in relative micro- and occasionally macro-movability of junctions. The effect is considered in terms of simple physical models. Some recommendations on design and handling of relevant machinery are presented.

## 1 Introduction

A great number of minerals and waste products processing machines such as ball and rod mills, cone and jaw crushers, screens, conveyors and feeders, operate in presence of vibration and impact stress. It does also hydropower, construction and many other machines. Both the vibration and the impact stress are known to cause a severe risk of parts break-down or even industrial disasters. The phenomenon of material strength deterioration caused by fatigue is well studied. However, the same could not be said about another effect of importance, which is the wear of nominally fixed joints and parts subjected to aforementioned factors – the effect referred to as the fretting wear. Such a wear takes place in bolt connections, flange joints, roller bearing fit surfaces, bushing-shaft connections, leaf springs, gears, couplings and other devices. The byproducts of the wear remaining within the contact clearance increase the wear intensity. In addition the intensity tends to be increased due to water penetration in the contact area and electrochemical corrosion. The aforesaid effect has recently come into the focus of many researchers (see e.g. [1 - 4]). The aim of this paper is to emphasize the influence of the said effect, to study the physical nature of the wear believed to be caused by relative micro- or macromobility of joints, to investigate this effect in terms of simple physical models and to state some recommendations for the aforesaid devices design and exploitation.

## 2 The effect of vibration and impacts on the effective dry friction coefficients, microslip of adjacent parts

The effective coefficients of dry friction at rest $f_1$, i.e. the friction coefficients effective in presence of constant or slowly changing forces , tend to decrease under vibration reaching in some cases zero, i.e. the system behaves as if the dry friction disappears.

Let's consider a system consisting of a perfectly rigid body pressed against a rough surface with the force $N$ while a harmonic force $\Phi = \Phi_0 \sin \omega t$ acting independently, the latter being directed either lengthwise or perpendicular or transverse to the surface (Fig.1, a).

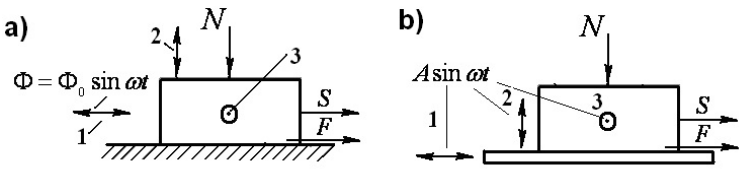


Figure 1: Illustration to definition of effective friction coefficients: a) Disturbing force effect: 1 – lengthwise force, 2 – perpendicular force, 3 – transverse force; b) Surface vibration effect: 1 – lengthwise vibration, 2 – perpendicular vibration, 3 – transverse vibration

Hence the effective coefficients of dry friction in rest, i.e. the friction coefficients in relation to body moving force $S$, will correspondingly have the following values [5, 6]:

$$f_1^{(=)} = f_1(1 - \frac{w}{f_1}), \qquad f_1^{(\perp)} = f_1(1 - w), \qquad f_1^{(\bullet)} = f_1\sqrt{1 - (w/f_1)^2}, \tag{1}$$

where $f_1$ – is "usual" coefficients of dry friction at rest , while

$$w = \Phi_0/N \tag{2}$$

–is called "coefficient of overload".

Formulas (1) remain valid for the case when force $\Phi$ is absent (Fig.1, b), but the surface will perform harmonic oscillations in corresponding directions according to the law $A \sin \omega t$ ($A$–amplitude, $\omega$–oscillation frequency). The coefficient of overstress is to be calculated using the formula :

$$w = mA\omega^2/N, \tag{3}$$

where $m$ – is body mass.

Finally, if normal force $N$ represents the weight of the body $mg$, then

$$w = A\omega^2/g. \tag{4}$$

The formulas (1) are valid only when coefficients $f_1^{(=)}$, $f_1^{(\perp)}$ and $f_1^{(\bullet)}$ are positive. With greater values of the overstress coefficient $w$ an apparent variation of friction mode takes place; in this case one may consider the effective coefficients of dry friction to be equal to zero.

The forecited formulas have been verified through experiments. They explain the effect of microslip in nominally fixed parts contacting by means of dry friction. The effect will be explained below in more details using three simple models.

Regarding the impact stress influenced systems, it was shown by D.M. Tolstoy experiments [7, 8], that even a comparatively slight action of impact stress may result in considerable reduction of the effective coefficients of dry friction $f_1^{(\perp)}$ even though for a very short time. During the experiments a ball of $0.45g$ mass when dropped from $4cm$ height on a body of $1176g$ mass caused diminishing of coefficient $f_1^{(\perp)}$ as compared to coefficient $f_1$ by 25 %. Theoretical explanation of this effect is given in papers [6, 9].

## 3 Model 1 – a solid body on a vibrating surface

Let us consider the simplest model representing vibration and impact action on contacting parts interacting through dry friction forces (Fig. 2, a).

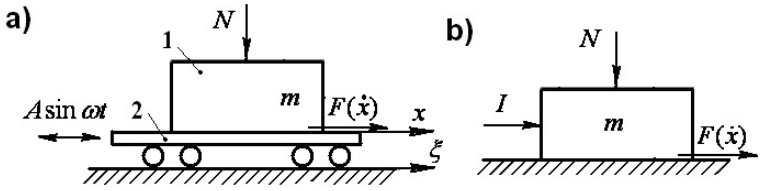


Figure 2: Solid body on a platform: a) – effect of vibrating platform , b) –effect of impact

A solid body 1 with mass $m$ is placed on a rigid platform 2, performing lengthwise oscillations according to the law:

$$\xi = A\sin\omega t, \tag{5}$$

where $\xi$ – is absolute coordinate of the platform, $A$ – amplitude, $\omega$– vibration frequency. A dry friction force $F$ appears between the body and the platform; the body is pressed against the platform by some constant force $N$, which may include the weight $mg$ of the body. The movement of the body in relation to the platform defined by coordinate $x$ associated with it can be described by the equation:

$$m\ddot{x} = mA\omega^2\sin\omega t + F(\dot{x}), \tag{6}$$

where

$$F(\dot{x}) = \begin{cases} -fN & for \quad \dot{x} > 0 \\ fN & for \quad \dot{x} < 0 \end{cases}$$
$$-Nf_1 < F(\dot{x}) < Nf_1 \quad for \quad \dot{x} = 0, \tag{7}$$

where $f$ and $f_1$ are coefficients of sliding and static dry friction correspondingly.

The stable periodic behavior determined by equation (6), were considered in detail in references [5, 6, 10]. Let us represent the results of this solution in a different form.

The mode of movements is assumed to depend on two nondimensional parameters:

$$w = \frac{mA\omega^2}{Nf}, \qquad w_1 = \frac{mA\omega^2}{Nf_1}. \tag{8}$$

Assuming $f = 0.7f_1$, which approximately corresponds to the actual ratio between these two coefficients for many materials, we obtain a single parameter $w = mA\omega^2/N$. Fig. 3 illustrates the body relative oscillation semi-range dependence on this parameter. When $w$ <1/0.7=1.43 the body moves together with the platform – there is no sliding friction between them (area I). When $\frac{1}{0.7} = 1.43 < w < \frac{1}{0.472} = 2.12$ the body slips alternatively forward and backward, stopping its movement for finite time periods after each change in the sliding direction (area II), while with $w$ >1/0.472=2.12 (area III) it slips, changing momentarily the direction of slippage.

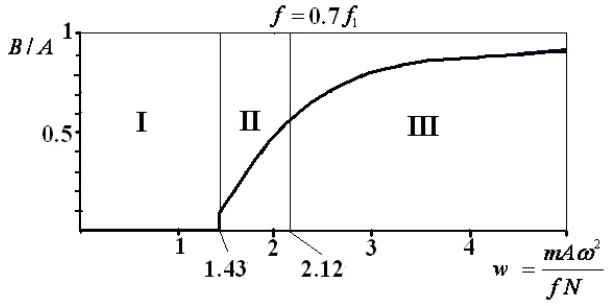


Figure 3: Dependance of the body oscillation half-swing on the overstress parameter

Increase of $w$ leads to increase of the half-swing $B$, which asymptotically approaches the oscillation amplitude value $A$ when $w \to \infty$.

The condition for no-slipping body behavior could be expressed by the following inequality:

$$f_1 N > mA\omega^2 \tag{9}$$

or alternatively, when $f = 0.7f_1$, by the inequality:

$$fN > 0.7mA\omega^2. \tag{10}$$

When the body with a mass $m$ is subjected to an impact with momentum $I$ (Fig. 2, b) it acquires velocity $v = I/m$. It results in a shift of the body to a distance $B_1$, which may be found from the equality $\frac{1}{2}mv^2 = fNB_1$, hence

$$B_1 = \frac{mv^2}{2fN} = \frac{I^2}{2fNm}. \tag{11}$$

It follows from the forecited expressions that whereas it is possible to avoid interfacial slippage of machine parts in vibration conditions by applying stronger interference $N$, it is not possible to avoid it in impact conditions even by a very tight interference.

## 4 Model 2 – a solid body with inner degree of freedom – influence of resonance effects

Let us consider a system extending model 1 by including a second body with mass $m_2$ placed inside the body with mass $m_1$, (see Fig. 4,a). The second body is joined to the first one using a flexible member and a damping member, $c$ and $\beta$ are a coefficient of rigidity and a damping coefficient correspondingly. The body $m_1$, as it is in the system

considered above, is placed on a platform, oscillating according to the law (5), the force $F(\dot{x})$ represents the dry friction arising between the body $m_1$ and the platform. The body $m_2$ can move with relatively to the body $m_1$ along the direction parallel to the plane of contact.

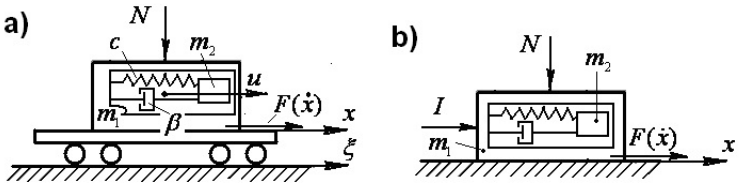


Figure 4: A solid body with inner degree of freedom a) Effect of vibrating platform, b) Effect of impact

The relative to the platform position of body $m_1$ is described by coordinate $x$, while the position of the body $m_2$ relative to the body $m_1$ is described by coordinate $u$; the latter is calculated from the position corresponding to that of unstrained flexible member.

Equations describing the motions of the system under consideration could be written in the following form:

$$m_1\ddot{x} = m_1 A\omega^2 \sin\omega t + cu + \beta\dot{u} + F(\dot{x}), \tag{12}$$

$$m_2\ddot{u} = m_2(A\omega^2 \sin\omega t - \ddot{x}) - cu - \beta\dot{u}, \tag{13}$$

where the friction force $F(\dot{x})$ is determined by expressions (7) as shown above.

It is of some difficulties to obtain the exact analytical solution of the non-linear system (12), (13). An approximate solution of a more general system is described in [11], where the object was to investigate vibrational displacement of bodies. In this paper we dwell upon periodic oscillation modes of motion and suggest some solutions based on the other assumptions. For that matter we take as a first approximation the assumption that the motion of the main body $m_1$ only slightly affects the motion of the body $m_2$. Then the value $m_2\ddot{x}$ in equation (13) can be neglected in comparison with the other values so that the equation takes the following form:

$$m_2\ddot{u} + \beta\dot{u} + cu = m_2 A\omega^2 \sin\omega t. \tag{14}$$

The solution of this equation corresponding to the forced steady-state oscillations could be described the following way:

$$u = Ak\sin(\omega t + \alpha), \tag{15}$$

where

$$k = \frac{\omega^2}{\sqrt{(\lambda^2 - \omega^2)^2 + 4n^2\omega^2}},$$

$$\frac{c}{m_2} = \lambda^2, \quad \frac{\beta}{m_2} = 2n, \quad \sin\alpha = -2\frac{n}{\omega}k, \quad \cos\alpha = \frac{\lambda^2 - \omega^2}{\omega^2}k. \tag{16}$$

Hence the equation (12) could be written in the form:

$$m_1\ddot{x} = m_1 A\omega^2 \sin\omega t + cAk\sin(\omega t + \alpha) + \beta\omega Ak\cos(\omega t + \alpha) + F(\dot{x}).$$

This equation can be also reformulated in the following form:

$$m_1\ddot{x} = m_1 A_1 \omega^2 \sin(\omega t + \varepsilon) + F(\dot{x}), \tag{17}$$

where

$$A_1 = A\sqrt{1 + 2k(\frac{\lambda_1^2}{\omega^2}\cos\alpha - 2\frac{n_1}{\omega}\sin\alpha) + k^2(\frac{\lambda_1^4}{\omega^4} + 4\frac{n_1^2}{\omega^2})}, \tag{18}$$

$\lambda_1^2 = \frac{c}{m_1}$, $2n_1 = \frac{\beta}{m_1}$, and $\varepsilon$ – some inessential constant which may be always reduced to zero by selecting the initial time point $t$. The equation (17) is congruent to the equation (6), obtained for one-mass system, so that it is possible to use the solution of the latter. Specifically, assuming $f = 0.7f_1$ it is possible to determine half-swing of oscillations $B = B_2$ using the Fig. 3, it is to be taken into account that the amplitude A value should be replaced with the amplitude $A_1$ value, which is determined by formula (18).

The solution obtained may be used for calculating an approximate solution. However, there is no special need for it because the solution accuracy can be checked using the software designed for the system (12), (13) equations investigation. Calculations performed using this software proved that the approximate solution provides quite a satisfactory accuracy.

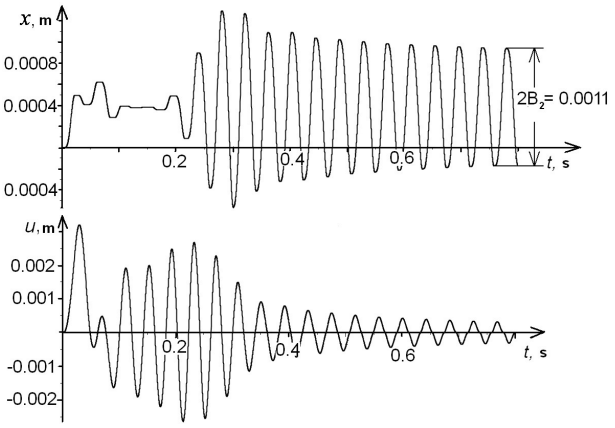


Figure 5: Graphs showing dependence of coordinates$x$ and $u$ on time t (Parameter values: $A = 0.001\ m$; $\omega = 150\ s^{-1}$; $A = 9 \cdot 10^4\ N/m$; $\beta = 30\ N \cdot s/m$; $\lambda_2 = 300\ s^{-1}$; $f = 0.5$; $m_1 = 3\ kg$; $m_2 = 1\ kg$; $N = 100\ N$)

Fig.5 illustrates dependence of the coordinates $x$ and $u$ on time $t$ and Fig. 6 shows oscillation half-swing $B_1$ versus oscillation frequency $\omega$. One can see that inner freedom degree can significantly enhance influence of vibration on the area of body $m_1$ sliding along the base plate when oscillation frequency $\omega$ approached the frequency of free oscillations $\lambda_2 = \sqrt{c/m_2}$ performed by $m_2$ body inside $m_1$ body. The same inference will be obtained when using formula (18) for calculations and Fig. 3 graph.

Formula (11) obtained for the Model 1, remains valid for the calculation of the body $m_1$ shift resulted from impact influence.

Similarly to the Model 1 case, it is possible to eliminate interfacial slippage of the mass $m_1$ by application of sufficiently high pressing force $N$. In impact condition such a microslip cannot be excluded even with a very tight fit.

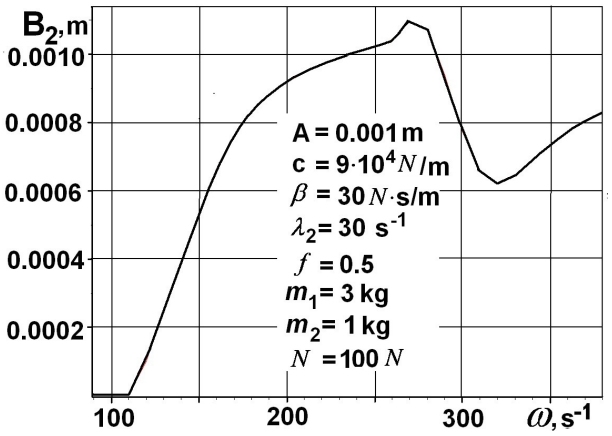


Figure 6: Amplitude of body $m_1$ oscillations versus induced oscillation frequency $\omega$

# 5 Model 3 – an elastic rod and a washer planted on it with initial strain

Compression fit is a widespread kind of machinery joints. The behavior of parts of such joints consisting, for example, from a rod and a washer tightly planted on it can be considered on the basis of the model representing a particular case of a so-called Chelomei pendulum. In work [15] it has been shown that in systems of this kind not only microslip could be observed, but also even vibrational translation.

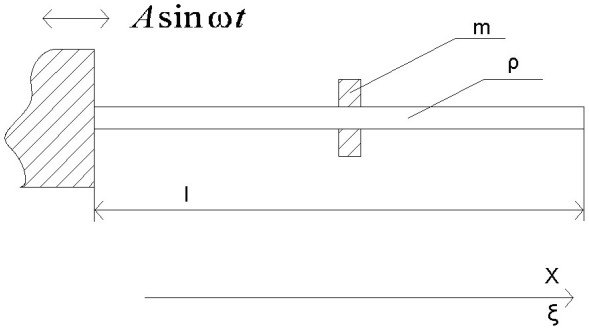


Figure 7: Model configuration

The system under consideration consists of elastic rod of length $l$ and rigid washer of mass $m$, planted on the rod with initial strain $\varepsilon^0$. The base of the rod is being vibrated, performing oscillations which could be written in fixed coordinates $\xi$:

$$\xi(t) = A\sin\omega t. \tag{19}$$

The equation of motion of the washer in the rod base bounded (moving) coordinate system could be written in the following form:

$$\begin{gathered} m\ddot{x} = mA\omega^2\sin\omega t + F_f(t,x,\dot{x}) \\ F_f = \begin{cases} -fN(t,x), & \dot{x} > 0 \\ -mA\omega^2\sin\omega t, & \dot{x} \equiv 0 \\ fN(t,x), & \dot{x} < 0 \end{cases} \end{gathered} \tag{20}$$

where $x$ is coordinate of the bar cross-section in the moving frame of reference associated with the oscillating base and at the same time coordinate of the washer near this section, $F_f$ - the friction force that occurs between the washer and the bar, m – the mass of the washer, A – the amplitude of the bar base oscillations, $\omega$ - their frequency, $f$- the friction coefficient, $N(t)$ - the elastic interaction force between the washer and the bar, the change of which is determined by its vibrational excitation. The frictional force is determined by Coulomb's law, not exceeding $|fN(t)|$ in absolute value, and balancing other effects at rest (in this case, the inertia force).

As it was shown in the publication [15], taking into account the initial strain or say the fit, with which the washer is planted on the rod, it is possible to write the friction force in the following form:

$$F_f = \begin{cases} -\eta f S_c E \left(\varepsilon_n^0 - \frac{\rho A\omega^2(l-x)}{2E}\sin\omega t\right), & \dot{x} > 0 \\ -mA\omega^2 \sin\omega t, & \dot{x} \equiv 0 \\ \eta f S_c E \left(\varepsilon_n^0 - \frac{\rho A\omega^2(l-x)}{2E}\sin\omega t\right), & \dot{x} < 0 \end{cases} \tag{21}$$

where $S_c$ is the area of the rod-washer contact, and $E$ is the rod's Young's modulus. It should be required that the following condition for $\varepsilon^0$ is met:

$$\varepsilon^0 \geq \frac{\rho A\omega^2 l}{2E} \tag{22}$$

Otherwise the washer could lose its fit on the rod and the behavior of the washer planted on the rod with a gap could be quite different from that under consideration.

Microslip and vibrational translation could be examined using methods presented in the book [5] for investigation of the problem of motion of a body on a rough inclined vibrating plane.

Considering the problem it is convenient to dissect the time axis into intervals so that the washer planted on the rod relatively resting inside each one of these intervals begins to slide in positive direction $I_+$, remains in the relative rest $I_0$, or begins to slide in negative direction $I_-$.

The motion in positive direction begins under the following conditions:

$$\begin{aligned} &\sin\omega t \ > \ z_+ \\ &z_+ = \frac{2\eta f S_c E \varepsilon_n^0}{A\omega^2\left(2m+\eta f \rho S_c(l-x)\right)} \end{aligned} . \tag{23}$$

Interval of motion in negative direction:

$$\begin{aligned} &\sin\omega t \ < \ z_- \\ &z_- = -\frac{2\eta f S_c E \varepsilon_n^0}{A\omega^2\left(2m-\eta f \rho S_c(l-x)\right)} \end{aligned} . \tag{24}$$

Under the following conditions

$$\begin{cases} \sin\omega t - z_+ < 0 \\ \sin\omega t - z_- > 0 \end{cases} \tag{25}$$

the washer remains in relative rest.

The behavior of the washer is considered to consist of a set of intervals of sliding in positive or negative direction and also relative rest intervals. It should be mentioned that

these intervals do not correspond one to one to the aforesaid intervals $I$. The motion of the washer could be described by the following expressions:

$$\dot{x}(t) = \mp\frac{fS_cE\varepsilon_n^0}{m}\left(t-t^*\right) - A\omega\left(1 \pm \frac{fS_c\rho(l-x)}{2m}\right)\left(\cos\omega t - \cos\omega t^*\right) + \dot{x}^* \tag{26}$$

$$\begin{aligned} x(t) = \mp\tfrac{fS_cE\varepsilon_n^0}{2m}\left(t-t^*\right)^2 + A\omega\left(1 \pm \tfrac{fS_c\rho(l-x)}{2m}\right)\cos\omega t^*\left(t-t^*\right) - \\ -A\left(1 \pm \tfrac{fS_c\rho(l-x)}{2m}\right)\left(\sin\omega t - \sin\omega t^*\right) + \dot{x}^*(t-t^*) \end{aligned} \tag{27}$$

Top marks are for the positive, and bottom marks are for a negative initial velocities, respectively, $t^*$ – is the interval beginning moment and $\dot{x}^*$ parameter is choosen to meet the interval initial conditions. After the stop $\dot{x}(t) = 0$ the washer switches to the mode, corresponding to the interval in which $t$ lies: $I_\pm$ or $I_0$.

The software developed using the algorithm described above could help also in calculation of the energy consumption or power of dissipative forces which could be useful in estimation of the wear. As described below the wear would be considered to be proportional to the power of dissipative forces. The diagram showing dependence of the power on overload coefficient is presented on the Fig. 8.

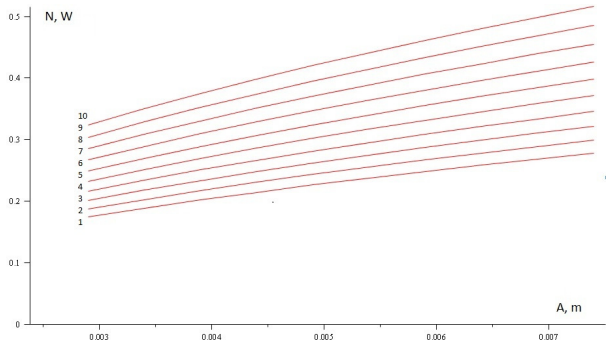


Figure 8: Friction force power versus the amplitude of the exitation dependance, each curve corresponds to fixed overload coefficient (from 10 - curve 1 to 12 - curve 10)

## 6 On some other Models

Among other models of no pertinence to the wear problem the flexible body models may be referred to [6, 9, 12, and 13]. Flexibility of adjacent bodies was taken into account in the theory of construction hysteresis [14]. If necessary such models can be used in evaluation of the wear caused by vibration.

## 7 Wear of nominally fixed joints in vibration and impact conditions

The energy consumed in interfacial slip of bodies during one vibration period $T = 2\pi/\omega$, amounts to $E_1 = 4fNB$, while energy consumption per second (i.e. power expense) is:

$$P = E_1/T = \frac{2}{\pi}fNB\omega. \tag{28}$$

Let us suppose that the energy consumed on overcoming friction in interfacial slip of adjacent parts is spent on corruption of these parts materials. To put it otherwise, let us assume that the rate of mass wear $W$ (kg/s), i.e. wear of material mass per second is proportional to the power $P$:

$$W = \kappa P = \frac{2\kappa}{\pi} f N B \omega. \tag{29}$$

Here the coefficient$\kappa$, having dimensionality $\frac{kg}{s}\frac{s}{Nm} = \frac{kg}{N}\frac{1}{m} = \frac{s^2}{m^2}$, represents a mass wear corresponding to $P = 1W$ energy consumption. This assumption is in agreement with so called Energy Theory of Wear [16–18], as well as with solid materials comminution practice (see below) and data on grinding media wear in a barrel mills ([19], p. 302).

Let us denote the area of contacting surface by $F$ and the rate of linear wear by $\Delta$. Then the following could be expressed:

$$W = \rho F \Delta, \qquad \Delta = \frac{W}{\rho F} = \frac{2\kappa f \sigma B \omega}{\pi \rho} (m/s), \tag{30}$$

where $\sigma = N/F$ – normal pressure between the adjacent parts. Knowing the rate of linear wear $\Delta$, the time $T_*$ required for the wear to reach a critical value $\delta$ could be readily estimated:

$$T_* = \delta/\Delta \text{ (c)} = \delta/3600 \cdot \Delta(h). \tag{31}$$

The value $\kappa$ in formulas (29), (30) can be treated as an empirically determined coefficient. Unfortunately, we failed to find the magnitude of this coefficient. So below we shall make attempt to estimate this coefficient at least roughly.

The quantity for $\varphi\ (D, d)$, representing the consumption of energy required for destruction of one kilogram of material from initial average size $D$ to a final size $d$, is well known in the theory of materials comminution [19, 20]. It is obvious that the quantity in consideration is reciprocal to the coefficient $\kappa$, i.e.

$$\varphi\ (D, d) = 1/\kappa\ \ (W \cdot s/kg = m^2/s^2) \tag{32}$$

As reported in papers [21, 22] the wear products of mating materials had 40–50 mcm sizes. Grinding ores in disk pulverizers to such size requires approximately about 2000 $kWh/t = 7.2\ 10^6\ W\ s/kg$ of energy $\varphi$. Taking into account the imperfect mechanism of treatment taken for the study and allowing for inefficiency of the friction wear we assume the actual consumption of energy to be much higher than it was observed and for that matter take the coefficient $\varphi$ by two orders higher, namely $\varphi \approx 10^9\ W\ s/kg$.

Supporting $\rho = 7.8 g/cm^3 = 7.8\ 10^3 kg/m^3$ , $f = 0.3$, $\sigma = 10 N/mm^2 = 10^7 N/m^2$ , $\omega$ =314 $s^{-1}$, $B = 1 mcm = 10^{-6}$ m and taking into account the formulas (30) and (31) we obtain $\Delta = \dfrac{2 \cdot 0.3 \cdot 10^7 \cdot 10^{-6} \cdot 314}{3.14 \cdot 10^9 \cdot 7.8 \cdot 10^3} = 0.769 \cdot 10^{-10}$ m/s and at $\delta = 1\ mm = 10^{-3}\ m$. Then we could evaluate $T_* = \delta/\Delta = \dfrac{10^{-3}}{0.769 \cdot 10^{-10}} = 1.3 \cdot 10^7$ s= $\dfrac{1.3 \cdot 10^6}{3600 \cdot 24} = 150$ days. In the case of the half-swing of sliding is taken as $B = 0.1\ mm = 10^{-4} m$, the time $T_*$ is reduced by 100 , i.e. will last only 1.5 days.

It is to be noted that in some cases the slip of parts subjected to impacts and vibration could be minimized or even eliminated through construction design or process improvements. For examples, engineering solutions regarding lowering design hysteresis are described in the books [14, 23], and RF Patent [24].

## 8 Some recommendations concerning design and exploitation of machines operating in vibration and impact conditions

1. It is essential that many of friction joints in mechanisms and structures designed for severe operation in conditions of vibrations and impacts should not be considered as fixed. It relates to bolt connections, flange joints and bushing-shaft connections of ball and rod mills, crushers, screens and power engineering machines.

2. Microslip of adjacent machine parts subjected to impacts and vibration has the effect of producing their wear; a unilateral displacement of parts is possible (for example self-loosening of threaded joints). In inadequate maintenance conditions this may entail the machine's failures and even the plant's shut downs.

3. In contrast to vibrational conditions where some interfacial slip of adjacent machine parts can be excluded by application of press fit, it is not possible to avoid the interfacial microslip in impact conditions even when using a very high pressure fit.

4. The slippage of machine parts caused by vibration and impacts in some cases can be diminished or even eliminated by introducing special design and process innovations.

5. When planning the maintenance schedule for adjacent parts and connections one should take into consideration that in line with the theory suggested here the wear rate of such parts tends to be increased even higher than in proportion to amplitude rise and is likely to be enhanced by higher oscillation frequency.

## 9 Conclusion

This paper deals with the effect of vibration and impacts on nominally fixed joints of machine parts, such as bolt and flange connections. Under the action of impacts and vibration (or oscillation) such components reveal so called micro mobility in relation to each other and thus are subjected to wear. A number of formulas have been obtained for two virtual models to describe the wear rate, the formulas contain a single empirical coefficient. In its physical sense that coefficient denotes a wear rate per a unit of energy spent on mutual slipping action. Based on the results obtained, some recommendations have been suggested with regard to design engineering and maintenance schedule of the machines in question.

## Acknowledgements

*The authors are pleased to express their acknowledgement to Y.A. Fadin for discussion and valuable remarks. This paper has been prepared under the Federal Sci-Tech/Programme (State Contract No.16.515.12.5002).*

## References

[1] Zhu M.H., Zhou Z.R. On the mechanisms of various fretting wear modes // Tribology International. 2011. Vol. 44. P. 1378–1388

[2] Yong Liu, Jin-Quan Xu, Yoshiharu Mutoh Evaluation of fretting wear based on the frictional work and cyclic saturation concepts // International Journal of Mechanical Sciences. 2008. Vol. 50. P. 897–904

[3] Helmi Attia A generalized fretting wear theory // Tribology International. 2009. Vol. 42. P. 1380–1388

[4] N.V. Perfilyeva Dynamic model for mechanical contact of relatively fixed joints. Doctor's Thesis – Tomsk, 2003. – 39 p.

[5] I.I. Blekhman, G.Y. Gzanelidze Vibrational displacement, M., Nauka, 1964. – 410 p.

[6] I.I. Blekhman Vibrational mechanics – M.: Physmatlit, 1994, 400 p. (in English: Blekhman I.I. Vibrational Mechanics. (Nonlinear Dynamic Effects, General Approach, Applications). – Singapore et al: – World Scientific Publishing Co., 2000. – 510 p.)

[7] D.M. Tolstoy Natural oscillations of a ram in relation to contact stiffness and their effect on friction //USSR Academy of Science Transactions, 1963. v.153, No 4. pp 820–824

[8] . D.M. Tolstoy, R.L. Kaplan On friction self-oscillations and friction force dependence on velocity //Theory of friction and wear. – M.: Nauka, 1965. pp. 44–83

[9] K.M. Ryspelov Study on operational reliability and improvement in maintenance of grinding equipment (exemplified by Djezkasgan MMC, Master's Degree Thesis – L., 1982.

[10] L.G. Loyzyansky, A.I. Lurie Theoretical mechanics, Part III. – L-M.: ONTI, 1934. 624 p.

[11] K.S. Yakimova Vibrational displacement in a two-mass vibrating system. / SSSR Academy of Sciences News., MTT. 1969, No 5. p. 20–30

[12] N.V. Florina A punch on a flexible support subjected to variable stresses and sliding. Master's Degree Thesis. L., 1964.

[13] L.V. Nikitin Statics and dynamics of solid bodies in conditions of external dry friction. - M.: Moscow Liceum, 1998. – 272 p.

[14] Ya.G. Panovko Mechanics of a solid body under strain.– M.: Nauka, 1985. – 288 p.

[15] Blekhman I.I., Ivanov K.S. On a Chelomey pendulum problem // Proc. of the XXXVII Summer School "Advanced Problems in Mechanics" (APM – 2009). St. Petersburg (Repino), June 30-July 5, 2009. – St. Petersburg, IPME RAS, 2009. P. 112–117

[16] G. Fleisher Energetic method of wear definition / Investigations in tribotechnology. M.: Machine building information research institute, 1975. pp. 277–291

[17] I.V. Kragelsky, M.N. Dobychin, V.S. Kombalov Calculation fundamentals for friction and wear. M.: Mashinostroyeniye, 1977. – 526 p.

[18] I.D. Ibatullin Kinetics of fatigue failures. – Samara, State Technical University, 2008.– 387 p.

[19] S.E. Andreyev,V.A. Perov, V.V. Zverevich Crushing, grinding and screening of minerals. 3-d edition. M.: Nedra, 1980. – 415 p.

[20] Ore Processing Manual. V. 1 – M.: Nedra, 1972. – 447 p.

[21] Yu.A. Fadin.,O.V. Polevaya, I.M. Popov Sizes and shape of particles in dry friction of metals // Messages to JTP. 1994. v. 20, ed. 17. pp. 47–51.

[22] Yu.A. Fadin Kinetics of metal surfaces destruction in friction. Doctor's Thesis. L., 1997. 30 pp.

[23] I.I. Blekhman What can vibration do? On vibrational mechanics and technology. – M.: Nauka, 1998. 208 p.

[24] J.M. Blednova, N.A. Makhutov, M.I. Chaevsky Method of bolt connection manufacture / RF patent 2256108. – Published 10.07.2005.

*Iliya I. Blekhman, V.O., Bolshoy av., 61, Saint Petersburg, 199178, Russia*

# Is there a lower bound for solid volume fraction in random loose packing of noncohesive rigid spheres?

Antonio Castellanos
castella@us.es

**Abstract**

The packing obtained by pouring bearing balls in a container, and then by shaking it in order to get the maximal densification (once eliminated wall effects), has a solid packing fraction of $0.6366 \pm 0.0004$ [1]. This state has been named random close packing (RCP). Theoretical ideas as well as numerical simulations give a packing fraction near the value of 0.64. Much less well defined is what is named as random loose packing (RLP) that is obtained in experiments by gently pouring steel balls in a container without trying to maximize density. In this way experimenters [1] have found packing fractions as low as $\phi_{RLP} = 0.60$. This was an accepted value for RLP for noncohesive spheres until Onoga and Liniger [2] found a lower value by sedimentation of spheres in liquids with almost matched densities. They attained a lower limit given by $\phi_{RLP} = 0.55 \pm 0.006$. However, a criticism to this work is that in the limit of zero buoyancy we can not avoid the effect of attractive interparticle forces. Recently Farrel et al. [3] avoided the pitfall of the influence of interparticle attractive forces by sedimentation of frictional balls, with finite buoyancy forces. They adjusted the physical parameters of particles and liquids in order to ensure that the colliding velocity at contact is almost zero. For a coefficient of friction $\mu_s = 0.96 \pm 0.03$ they found a packing fraction below 0.54. Extrapolating their results they predict a packing fraction of 0.53 for a coefficient of friction $\mu_s = 1.2$. This value is below the theoretical minimum for frictional spheres given by $\phi_{RLP} = 4/(4 + 2\sqrt{3}) = 0.536$. We show in this work that unless we include rolling friction this is not possible. A simple estimation, based on isostaticity, show that for a disproportionate large value of rolling friction we could achieve densities much lower than 0.536, with a lower bound quite near to 0.15.

## 1 Introduction

A packing is a static set of particles in a containing space which do not overlap among themselves or with the space boundary. The packing obtained by pouring bearing balls in a container, and then by shaking it in order to get the maximal densification (once eliminated wall effects), has a solid packing fraction of $0.6366 \pm 0.0004$ [1]. This state has been named random close packing (RCP). Berryman [4] defined random close packing of geometrically perfect spheres as the one which has minimum packing fraction for which the median nearest-neighbor radius equals the diameter of the spheres, and he obtained a value of $\phi_{RCP} = 0.64 \pm 0.02$. Numerous computational schemes of random packing of frictionless spheres, though they do not give the same packing fractions, they all pack near the value of 0.64. The word random, implying maximum disorder, is an elusive concept difficult to define. Nevertheless, the random close packing of spheres in containers, when taking precautions to avoid cristallization zones and wall effects, have astonishing robust

properties. The discrepancy between the experiment and the theory and simulations is ascribed to the non ideality (finite elasticity, friction, viscoplasticity, plasticity) of real spheres in the experiments.

Much less well defined is the random loose packing (RLP) obtained in experiments by gently pouring steel balls in a container without trying to maximize density. In this way experimenters [1] have found packing fractions as low as $\phi_{RLP} = 0.60$. This was an accepted value for RLP until Onoga and Liniger [2] found a lower value by sedimentation of spheres in liquids with almost matched densities. They attained a lower limit given by $\phi_{RLP} = 0.55 \pm 0.006$. However, a criticism to this work, is that in the limit of zero buoyancy we can not avoid the effect of attractive interparticle forces. In fact, the granular cohesive Bond number, defined as the ratio of interpaticle force to particle weight, could be greater than one (if exactly effective gravity equals zero, the Bond number will be infinite, because Van der Waals forces are always present). Song et al. [5] gave a phase diagram for jammed frictional spheres in the space of "coordination number-packing fraction". They found the diagram based on a statistical formulation of granular materials due to Edward and Oakeshot [6] and on detailed numerical simulations. In this diagram all disordered packings lie within a triangle demarcated by the RCP line, RLP line and a line called as granular line characterized by a coordination number of 4. In this work the theoretical minimum packing fraction of RLP is given by $\phi_{RLP} = 4/(4 + 2\sqrt{3}) = 0.536$.

Recently Farrel et al. [3] avoided the pitfall of the influence of interparticle attractive forces by sedimentation of frictional balls, with finite buoyancy forces. They adjusted the physical parameters of particles and liquids in order to ensure that the colliding velocity at contact is zero. They argue that they have measured the real coefficient of friction $\mu_s$ between two spheres in the liquid, and they attain a packing fraction slightly below 0.54, which is very close the theoretical minimum given by Song et al. From his work it is implied that for a coefficient of friction of $\mu_s = 1.2$ the extrapolated packing fraction would be 0.53 below the theoretical limit.

We suggest that including rolling friction we could attain lower values of the packing fraction. For the majority of the materials this effect would be negligible as the coefficient of rolling friction is very small. Theoretically, however, it is easy to see that if both the coefficient of rolling and dry friction approach infinity the falling particle will stick to the touching particle in the sediment and the packing fraction should approach the packing fraction of random ballistic deposition without restructuring which is quite near to 0.15, [7], [8]. This value is impossible to achieve in real experiments as there are no particles with neither an infinite value of dry friction, nor of the rolling coefficient. However, a general conclusion is that loose random packing of real spheres can not be defined only in terms of geometry because it is a dynamical problem dependent on the physical assembling procedure of the packing. We can not exclude that the packing fraction of the random loose packing in experiments will continue to decrease in the future, but we can not predict a well defined experimental lower limit for these RLP packings.

## 2 Coordination number in packing of spheres

The network of contacts inside the packing determine their mechanical properties. It is well known that the number of neighbours in contact with a given grain has a statistical distribution. Its average, $Z$, is called the coordination number of the packing. This is the simplest key parameter characterizing the network of contacts. Experimentally, $Z$ for spheres was determined by Bernal and Mason [9], by coating a system of ball bearings with paint, draining the paint, letting it dry, and counting the number of paint spots per particle

when the system was disassembled. They obtained a coordination number close to 8.5. This technique was used by Donev et al [10] for measuring the contacts between candies as model of ellipsoids claiming an excellent agreements between simulations and its unique experimental point. However this technique is very time consuming and prone to errors as it is very difficult to distinguish between true and close (but not touching) contacts. Recently Brujić et al [11] used as a model of granular packing fluorescently labeled silicone oil droplets with Nile red dye, suspended in a solution of 1:1:05 water to glycerol volume ratio to ensure refractive index matching. By means of confocal microscopic they were able to measure the contacts between droplets, and obtained a coordination number of $Z = 6.08$ for the RCP of the droplets, despite the polydispersity of the packing.

Compared with the scarcity of experimental measurements there are a plethora of numerical simulations of the packing of granular media in which we can found the statistics of contacts between grains as a function of shape, hardness, friction, interparticle forces and external load. There is an interesting work by Silbert et al [12] which simulates the packing of frictionless and frictional spheres. In this work it is shown that the coordination number decreases as we increase dry friction from $Z = 6$ for frictionless spheres to $Z = 4$ for spheres with an infinite coefficient of Coulmb friction. In the next section we discuss the relevance of these numerical findings.

## 3 Isostatic packings

In the area of Structural Rigidity it is well known that in a system of rotatable rigid rods in equilibrium the number of equations is exactly equal to the number of unknown internal stresses. This property of the rigidity between rotatable rigid rods is exploited by Moukarzel [13] to introduce the concept of isostaticity in granular media (a detailed discussion of this concept may be seen in [14]). Consequently a packing is said to be isostatic when the number of interparticle contacts is exactly the minimum needed for the packing to be stable under small loads. If the particles are themselves rigid the number of independent equations for the forces and torques must be equal to the number of contacts in order to determine univocally the unknown interparticle forces at each contact. For a packing of $N$ rigid smooth spheres we have $3N$ equations for each grain to be at equilibrium, and an unknown normal interparticle force at each of the $NZ/2$ contacts. Therefore the coordination number for the packing to be isostatic must be $Z = 6$. For fairly enough hard particles we have the coordination number very close to 6 as have shown in the previous section, both by experiments and numerical simulations. However, for real smooth particles due to elastic deformation we may close contacts otherwise open, and the coordination number can be larger than six.

In the case of infinite coefficient of dry friction, the spheres will never slip and at each contact the friction force is unknown. Therefore the number of unknown forces would the number of contacts multiplied by 3 (in components: one normal force, plus two tangential forces in the plane perpendicular to the normal). The number of equations would be 3N for the forces and 3N for the torques. Thus for isostaticity we must have $3 \times NZ/2 = 6N$ which gives $Z = 4$ for the coordination number. For frictional spheres with a finite coefficient of friction there will be a fraction of the set of contacts that have yielded under Coulomb dry friction law (fully mobilized friction contacts). For these contacts the tangential forces are known. Therefore the total number of unknown tangential forces will depend on the coefficient of dry friction, and consequently the coordination number would vary from 6 to 4 as the coefficient of friction increases from zero to infinity. This is in agreement with the simulations [12] (see also [15]).

## 4 The role of rolling friction

If we include a finite coefficient of rolling friction, the packing density as well as the coordination number should both decrease. However, as the rolling friction, is much smaller than the coefficient of dry friction, the number of fully mobilized contacts under rolling friction would be the majority of contacts. The number of unknown rolling torques would therefore be small and as a consequence the coordination number would be quite near 4.

From a purely theoretical point of view we may introduce at hoc an infinite value for the coefficient of rolling friction. Under this assumption the number of unknown components of the rolling torque torque increases by two at each contact, since this torque lies in the plane perpendicular to the normal force. Therefore we should have now

$$5 \times \frac{NZ}{2} = 6N \tag{1}$$

which gives for the coordination number $Z = 2.4$. Such a low value of the coordination number is consistent with the coordination number of spheres deposited by ballistic aggregation with no restructuring (hit and stick). This same packing is obtained under the assumption of infinite attractive interparticle forces, since the spheres also hit and stick at the point of contact. In both cases we obtain the theoretical minimum density slightly below 0.15 as have been verified numerically [7] and experimentally [8].

## 5 Conclusion

The arguments presented in this paper are based on the isostaticity of packings. Real packings are made of material particles, and the forces and torques are always well defined when taking into account the deformations of the particles under the forces. Real packings do not require isostaticity for being marginally rigid. The deformations and forces will depend on the elastic constants, or viscoplasticity and/or plasticity at contacts. Assuming that the deformations are negligibly small we may arrive at isostaticity by quite different physical deformation processes. In particular for hard particles under elastic deformations we will be nearer to the isostatic packing the harder is the particle. The arguments presented here, though theoretical in nature, opens the door to packings with density below the theoretical limit of frictional particles.

## Acknowledgements

*This research has been supported by Spanish Government, project FIS2011-25161 and by Andalusian Government Ayuda a Grupos de Investigación FQM-253. I also acknowledge very fruitful discussions with Dr. Elena Grekova.*

## References

[1] GD Scott and DM Kilgour. The density of random close packing of spheres. *Journal of Physics D: Applied Physics*, 2:863, 1969.

[2] S. Torquato, T. M. Truskett, and P. G. Debenedetti. Is random close packing of spheres well defined? *Phys. Rev. Lett.*, 84:2064–2067, Mar 2000.

[3] G.R. Farrell, K.M. Martini, and N. Menon. Loose packings of frictional spheres. *Soft Matter*, 6(13):2925–2930, 2010.

[4] J.G. Berryman. Random close packing of hard spheres and disks. *Physical Review A*, 27(2):1053, 1983.

[5] C. Song, P. Wang, and H.A. Makse. A phase diagram for jammed matter. *Nature*, 453(7195):629–632, 2008.

[6] S.F. Edwards and RBS Oakeshott. Theory of powders. *Physica A: Statistical and Theoretical Physics*, 157(3):1080–1090, 1989.

[7] P.K. Watson, H. Mizes, A. Castellanos, and A. Pérez. The packing of fine, cohesive powders. In *Powders & Grains 97: Proceedings of the Third International Conference on Powders & Grains held in Durham, NC 18-23 May 1997*, pages 109–12, 1997.

[8] J. Blum and R. Schräpler. Structure and mechanical properties of high-porosity macroscopic agglomerates formed by random ballistic deposition. *Physical review letters*, 93(11):115503, 2004.

[9] JD Bernal and J. Mason. Packing of spheres: co-ordination of randomly packed spheres. *Nature*, 188(4754):910–911, 1960.

[10] A. Donev, I. Cisse, D. Sachs, E.A. Variano, F.H. Stillinger, R. Connelly, S. Torquato, and PM Chaikin. Improving the density of jammed disordered packings using ellipsoids. *Science*, 303(5660):990–993, 2004.

[11] J. Brujić, C. Song, P. Wang, C. Briscoe, G. Marty, and H.A. Makse. Measuring the coordination number and entropy of a 3d jammed emulsion packing by confocal microscopy. *Physical review letters*, 98(24):248001, 2007.

[12] L.E. Silbert, D. Ertaş, G.S. Grest, T.C. Halsey, and D. Levine. Geometry of frictionless and frictional sphere packings. *Physical Review E*, 65(3):031304, 2002.

[13] C.F. Moukarzel. Isostatic phase transition and instability in stiff granular materials. *Physical review letters*, 81(8):1634–1637, 1998.

[14] J.N. Roux. Geometric origin of mechanical properties of granular materials. *Physical Review E*, 61(6):6802, 2000.

[15] K. Shundyak, M. Van Hecke, and W. Van Saarloos. Force mobilization and generalized isostaticity in jammed packings of frictional grains. *Physical Review E*, 75(1):010301, 2007.

*Antonio Castellanos, Facultad de Física, Avda Reina mercedes s/n, 41012, Seville, Spain*

# A simple statement of the essential spectrum with some applications : thin shells, plates with sharp edges

Alain Campbell
bulygin_an@mail.ru

**Abstract**

We first recall some properties of classical and non classical vibrating problems in continuous media. If the classical properties of compactness are not satisfied, we can obtain an essential spectrum of the self-adjoint operator which defines the spectral problem. In these cases, for very small data, we can obtain a large response and so these sequences can be physically interpreted as some kind of resonance. This local phenomena are quick oscillations in some directions which are called weakness directions. We will see that the singularities will propagate along directions which are orthogonal to these weakness ones.

An example is given by the spectral problem of thin elastic shells in membrane approximation. We propose to determine this spectrum and the corresponding weakness directions in every point of the shell. For an anisotropic shell, we obtain exactly the relation between the elements of the essential spectrum and the components of the weakness direction by using the second fundamental form and the compliance coefficients. Then we study the particular case of homogeneous and isotropic shells. We obtain a new relation and it appears that the essential spectrum depends only on the quotient of the fundamental forms and on the Young modulus, but is independent of the Poisson coefficient. We note that a geometrical interpretation of the quotient of the fundamental forms is the normal curvature of the surface in the directions of propagation. Conversely,if a spectral value is given, then we can find the directions of propagation of singularities. Their number can be zero, two or four. We illustrate with some concrete examples. In the last part about shells, we study the problem of propagation and reflection of singularities for an isotropic cylindrical shell and we show that the equation of propagation does not depend on the Poisson coefficient.

Another example is given by the two dimensional models for thin plates with sharp edges. The spectrum will contain a non empty essential part if the edge is sharp enough. Let us consider some point $P$ near the edge of the plate. We define the thickness of the plate in this point, $h(P)$, and $d(P)$ the distance to the edge. These functions are very small and the degree of sharpness is given by $\alpha$ so that $h(P) = O(d(P)^\alpha)$. Let us consider the longitudinal oscillations of the plate ; It can be shown that the spectrum is discrete. If $\alpha < 1$ all eigenvalues are positive and if $\alpha ?1$ zero is a triple eigenvalue with rigid modes. For the transversal oscillations we have the same results only if $\alpha < 2$. But if $\alpha ?2$ the essential spectrum is not empty.

## 1 Introduction

### 1.1 Classical and non classical vibrating problems

The classical form of a vibrating problem of structures can be writen in the form

$$\rho \frac{d^2u}{dt^2} + Au = 0 \tag{1}$$

and a solution $u(x)e^{i\omega t}$ satisfies to a spectral problem

$$Au = \rho\omega^2 u = \lambda u \tag{2}$$

or in the variational form,

$$\forall v \in H,\ a(u,v) = \lambda(u,v) \tag{3}$$

where $H$ is a good Hilbert space and $\lambda$ the spectral parameter. In the classical case, $A$ is a selfadjoint operator and with a compact resolvent and there exists a sequence of eigenvalues

$$O < \lambda_0 I \lambda_1 I ... I \lambda_k I \longrightarrow +\infty \tag{4}$$

with orthogonal modes.

### 1.2 Essential spectrum

Let us recall that the resolvent set is defined by,

$$\rho(A) = \{\ \zeta\ /\ (A - \zeta Id)^{-1} \in \mathcal{L}(H)\ \} \tag{5}$$

Its complement, the spectrum $\Sigma(A)$, is constituted of isolated eigenvalues of finite multiplicity - for these $\zeta$, $(A-\zeta Id)^{-1}$ does not exist - and of other values for which $(A-\zeta Id)^{-1}$ exists but does not belong to $\mathcal{L}(H)$. They are eigenvalues of infinite multiplicity, accumulation points of eigenvalues and continuous spectrum.

The set of these $\zeta$ which are not isolated eigenvalues of finite multiplicity is the essential spectrum $\Sigma_{ess}(A)$. It can be characterized as the set of $\zeta$ for which there exists a sequence $(u_k)$ called Weyl's sequence so that,

$$\begin{aligned} ||\ u_k\ ||\ &= 1 \\ u_k\ &\longrightarrow 0\ \text{ in H weakly} \\ (A-\zeta Id)(u_k)\ &\longrightarrow 0\ \text{ in H strongly} \end{aligned} \tag{6}$$

For very small data, we can obtain a large response and so these sequences can be physically interpreted as some kind of resonance. This local phenomena are quick oscillations in some directions which are called weakness directions. We will see that the singularities will propagate along directions which are orthogonal to these weakness ones.

## 2 The case of shells in membrane approximation

### 2.1 Essential spectrum

We consider a thin shell with a middle surface $S$. This surface is described by the map,

$$y = (y^1, y^2) \in \Omega \to r(y^1, y^2) \in \mathbb{R}^3 \tag{7}$$

where $\Omega$ is a domain of the plane. Let $u$ be the displacement vector of the surface. We introduce the Hilbert space $H = (L(\Omega))^3$ and we denote by $(u,v)$ the scalar product. The displacement $u$ belongs to the subset $V_1 = H^1(\Omega) \times H^1(\Omega) \times H^2(\Omega)$ which can be modified to take boundary conditions in account. The variational form of the problem of vibrations is,

We search for $u \in V_1$ so that,

$$\forall v \in V_1,\ a_m(u,v) + \epsilon^2 a_f(u,v) = \lambda(u,v) \tag{8}$$

The bilinear forms $a_m$ and $a_f$ correspond respectively to the membrane problem and the flexion problem. They are continuous on $V_1$. This problem is classical with a selfadjoint operator and compact resolvent and so there exists a sequence of eigenvalues but if the relative thickness of the shell, $\epsilon$, is very small, then the membrane approximation is an appropriate representation. The formulation of this problem is different. In this case, $u$ belongs to the space $V = H^1(\Omega) \times H^1(\Omega) \times L^2(\Omega)$. The inclusion of $V$ in $H$ is dense and continuous but is not compact.

The problem is written as,

We search for $u \in V$ so that,

$$\forall v \in V, \quad a_m(u, v) = \lambda(u, v) \tag{9}$$

This spectral problem is an elliptic system with mixed order. The classical properties of compactness are not satisfied and the spectrum both contains a sequence of eigenvalues depending on the domain, and an essential spectrum.

We define the fundamental forms of the shell, $A(x^1, x^2)$ and $B(x^1, x^2)$.
The equations of the vibrating shell in the membrane approximation give an explicit spectral problem on the displacement $u$. There appears derivatives of second order in $u_1$ and $u_2$ and of first order in $u_3$. The classical properties of compactness are not satisfied and there exists an essential spectrum. We have weakness directions noted by $(\xi_1, \xi_2)$ and the orthogonal ones $(x_1, x_2)$ will be the directions of propagation of the singularities. The values of $\lambda$ and $(\xi_1, \xi_2)$ correspond to the non-ellipticity of the system in the Douglis and Nirenberg sense.

We can obtain the relation between $\lambda$ and $(\xi_1, \xi_2)$,

$$\lambda = \frac{[B(x_1, x_2)]^2}{s^{\alpha\beta\lambda\mu} x_\alpha x_\beta x_\lambda x_\mu} \tag{10}$$

where $s^{\alpha\beta\lambda\mu}$ are the coefficients of the compliance coefficients. If a point is given on $S$, then the spectral parameter $\lambda$ belongs to a segment. In the case of an isotropic shell, we obtain the following outstanding form,

$$\lambda = E\Big[ \frac{B(x_1, x_2)}{A(x_1, x_2)} \Big]^2 \tag{11}$$

and it appears that the essential spectrum depends only on the geometry and the Young modulus but is independent of the Poisson coefficient. A geometrical interpretation of the quotient of the fundamental forms is the normal curvature $k_x$ of the surface in direction $(x_1, x_2)$. The essential spectrum is then exactly the segment, $\Sigma_{ess} = [\, E.Inf k_x^2,\ E.Sup k_x^2 \,]$. So, in an elliptic point of $S$ we have two directions $(x_1, x_2)$ but in a hyperbolic point several cases are possible, four or two directions and sometimes double directions.

## 2.2 Propagation of singularities in a cylindrical thin shell

We consider the cylindrical shell defined by the map,

$$(y^1, y^2) \in [0,1] \times [0, 2\pi[ \longrightarrow (x^1 = Ry^1, x^2 = Rcosy^2, x^3 = Rsiny^2) \tag{12}$$

The essential spectrum is the segment $[0, \frac{E}{R^2}]$. Denoting by $\lambda$ a value in the essential spectrum and by $\theta$ the polar angle of the directions of propagation $\underline{x}$, we obtain

$$\lambda = \frac{E}{R^2}\Big[\frac{tan^2\theta}{1+tan^2\theta}\Big]^2 \tag{13}$$

For the vibrating shell in the membrane approximation, we obtain the following homogeneous spectral problem,

$$\left\{\begin{array}{rl} u_{1,11} + \frac{1-\nu}{2}u_{1,22} + \frac{1+\nu}{2}u_{2,12} - \nu R u_{3,1} & = -\frac{\lambda}{KR^2}u_1 \\ \frac{1+\nu}{2}u_{1,12} + \frac{1-\nu}{2}u_{2,11} + u_{2,22} - R u_{3,2} & = -\frac{\lambda}{KR^2}u_2 \\ \nu u_{1,1} + u_{2,2} - R u_3 & = -\frac{\lambda}{KR}u_3 \end{array}\right. \tag{14}$$

where $u^1$, $u^2$ and $u^3$ are the contravariant components of the displacement and $K = \frac{Eh}{(1-\nu^2)R^4}$.
To study the propagation of the singularities, we introduce the following right-hand side which represents a point normal force

$$\left\{\begin{array}{rl} u_{1,11} + \frac{1-\nu}{2}u_{1,22} + \frac{1+\nu}{2}u_{2,12} - \nu R u_{3,1} + \frac{\lambda}{KR^2}u_1 & = 0 \\ \frac{1+\nu}{2}u_{1,12} + \frac{1-\nu}{2}u_{2,11} + u_{2,22} - R u_{3,2} + \frac{\lambda}{KR^2}u_2 & = 0 \\ \nu u_{1,1} + u_{2,2} - R u_3 + \frac{\lambda}{KR}u_3 & = \frac{1}{KR}\delta(y^1)\delta(y^2) \end{array}\right. \tag{15}$$

and we suppose that $\lambda$ belongs to the essential spectrum but is not an eigenvalue. We search for asymptotic expansions of the displacements on the form,

$$\left\{\begin{array}{ll} u_\alpha(y^1, y^2) & = U^1_\alpha(y^1)\delta(y^2 - my^1) + U^2_\alpha(y^1)Y(y^2 - my^1) + ... \quad \alpha = 1,2 \\ u_3(y^1, y^2) & = U^1_3(y^1)\delta'(y^2 - my^1) + U^2_3(y^1)\delta(y^2 - my^1) + ... \end{array}\right. \tag{16}$$

where $m = tan\theta$ is the slope of the direction of propagation, and we substitute these expressions in the problem. By identifications of the leading terms, we then still obtain $\lambda = KR^2(1-\nu^2)\frac{m^4}{(1+m^2)^2} = \frac{Ehm^4}{R^2(1+m^2)^2}$. We note that it does not depend on the Poisson coefficient. It is easy to calculate $U^1_1(y^1)$ and $U^1_2(y^1)$ according to $U^1_3(y^1)$:

$$U^1_1(y^1) = -Rm\frac{\nu m^2 - 1}{(1+m^2)^2}U^1_3(y^1) \tag{17}$$

and

$$U^1_2(y^1) = R\frac{(\nu+2)m^2 + 1}{(1+m^2)^2}U^1_3(y^1) \tag{18}$$

By writing the identifications of the next order terms, we obtain a nonhomogeneous system and then we have to satisfy a compatibility condition. A straightforward computation gives the following compatibility condition,

$$\nu m R(\nu m^2 - 1)U^1_3\,'(y^1) + \frac{m}{2}\Big((\nu^2 + \nu - 4)m^2 + 3\nu - 1\Big)U^1_2\,'(y^1) +$$

$$\Big(\nu m^4 - \frac{(1+\nu)(2-\nu)}{2}m^2 + \frac{1-\nu}{2}\Big)U_1^1{}'(y^1) = -(m^2+1)^2\frac{1}{KR}\delta(y^1) \tag{19}$$

By replacing $U_2^1(y^1)$ and $U_1^1(y^1)$ by their values, we finally obtain,

$$U_3^1{}'(y^1) = \frac{R^3(1+m^2)^3}{4Ehm^3}\delta(y^1) \tag{20}$$

and we see that this equation does not depend on the Poisson coefficient.
The function $U_3^1$ which defines the propagation of the singularity is

$$U_3^1(y^1) = \frac{R^3(1+m^2)^3}{4Ehm^3}(Y(y^1)+C) \tag{21}$$

where $C$ is arbitrary. The propagation of singularities is characterized by $U_3^1$ and is along the characteristic straight line which cuts the edges of the domain in two points. So we will have two conditions to determine only one constant $C$. It shows that the singularity will not disappear by reaching a point $P$ on $\partial\Omega$. We will have a reflection on another characteristic the slope of which is $-tan\theta$.
The previous calculus are not valid if $m = tan\theta$ and then $\lambda$ are equal to zero. In that case which is the static case, the propagation of singularities is rather different and there is no reflection.
That study of the propagation of singularities has been done in a particular case of isotropic shell. The equations of vibration of a cylindrical shell have constant coefficients and then the propagations are along straight lines. The general case is more complicated:
The segments which constitute the essential spectrum could be different in every point of the surface $S$. The characteristic curves are some pieces of curves and the propagations along them would depend on the reached point. For example, it is conceivable that the value of the spectral parameter which is given, will be go out of the essential spectrum in some point and that the propagation will stop.
Moreover, if some propagation reaches a hyperbolic point at the edge of a shell with four directions of propagation, then we will have several possibilities for the reflection and we do not know what will happen.

# 3 Spectra of two-dimensional models of thin plates with sharp edges

Considering a plate clamped at the edge, the spectral problems of thin plates with uniform thickness is a classical problem, but if the edge is sharp enough, we have special properties. We only consider the case of homogeneous isotropic elastic material and we suppose that we have a geometrical symmetry of the thickness. But we can also extend some results with more general cases, where the interaction of deflection and longitudinal deformation occurs.
Let $\omega \subset \mathbb{R}^2$ be the longitudinal cross-section of a thin isotropic plate with variable thickness. The thickness function $h$ vanishes on the edge $\partial\omega$ while,

$$h(x) = n^\alpha(H(s) + \tilde{h}(x)), \quad x \in \ \omega \cap \mathcal{V}, \tag{22}$$

where $\alpha > 0$, $(n, s)$ is the system of local curvilinear coordinates in a neighborhood of the $\partial\omega$, $n$ is the orientated distance to $\partial\omega$, $n > 0$ inside $\omega$ and $s$ is the arc length along $\partial\omega$ and $H$ is a smooth positive function on $\partial\omega$ and $\tilde{h}$ is a smooth function which vanishes on $\partial\omega$.

### 3.1 Longitudinal oscillations of the plate

We work in a weighted Lebesgue space with a norm which depends on $\alpha$.
The spectral problem where $\mu$ is the spectral parameter can be reduced to the abstract equation

$$T_\sharp v = \tau v \quad \text{in } \mathfrak{h}_\sharp \tag{23}$$

where $\tau$ is the new spectral parameter

$$\tau = (1+\mu)^{-1} \tag{24}$$

The Hilbert space $\mathfrak{h}_\sharp$ has a specific scalar product and $T_\sharp$ is a positive and continuous, symmetric, therefore, self-adjoint operator, which inherits some properties of compactness. We obtain the following results,
For any $\alpha$, the spectrum of the problem is discrete and form the eigenvalue sequence

$$\mu_1 I \mu_2 I \mu_3 ... I \mu_p I ... \longrightarrow +\infty \tag{25}$$

(multiplicity is taken into account). In the case $\alpha < 1$ all eigenvalues are positive while, for $\alpha i 1$, we have $\mu_4 > 0$ and $\mu_1 = \mu_2 = \mu_3 = 0$ with the eigenspace of rigid modes.

### 3.2 Transversal oscillations of the plate

In this case, we have a spectral problem where $\lambda$ is the spectral parameter in some Hilbert space $\mathfrak{h}_3$.
We also reduce the problem to the abstract equation

$$T_3 v = \tau v \quad \text{in } \mathfrak{h}_3 \tag{26}$$

where $\tau$ is the new spectral parameter

$$\tau = (1+\mu)^{-1} \tag{27}$$

and we have the following results,
The spectrum of the problem is discrete if and only if $\alpha < 2$. The corresponding eigenvalue sequence

$$\lambda_1 I \lambda_2 I \lambda_3 ... I \lambda_p I ... \longrightarrow +\infty \tag{28}$$

is positive in the case $\alpha < 1$ but, for $\alpha \in [1, 2[$, we have $\lambda_4 > 0$ and $\lambda_1 = \lambda_2 = \lambda_3 = 0$ with the eigenspace of rigid modes.
Moreover, if $\alpha i 2$, the essential spectrum of the problem is not empty and it is possible to find a singular Weyl sequence for operator $T_3$ at the point $\tau = 1$.

## References

[1] A. Campbell. “A model problem for vibration of thin elastic shells. propagation and reflection of singularities”, C. R. Acad. Sci. Paris. t. 329. Série II b. p.1-5. 2001.

[2] G. Grubb and G. Geymonat. “The essential spectrum of elliptic systems of mixed orders”, Math. Annal. 227 p.247-276. 1977.

[3] P. Karamian, J. Sanchez-Hubert, E. Sanchez-Palencia. "Non-smoothness in the asymptotics of thin shells and propagation of singularities. Hyperbolic case", Int. J. Appl. Math. Comput. Sci. Vol. 12, No 1, p.81-90. 2002.

[4] J. Sanchez-Hubert and E. Sanchez-Palencia. "Vibration and coupling of continuous systems", Springer, Berlin, 1989.

[5] A. Campbell, S.A. Nazarov and G. Sweers. "Spectra of two-dimensional models for thin plates with sharp edges", SIAM J. Math. Anal. 42 (2010), pp. 3020-3044.

*Alain Campbell, Groupe de Mécanique, Modélisation, Mathématique et Numérique, Laboratoire de Mathématiques Nicolas Oresme, UMR 6139. BP 5186 Université de Caen, 14032 Caen Cedex. France*

# Three-dimensional unstable displacement of miscible viscous fluids from porous media

Vladislav Dushin Valeriy Nikitin Yuri Philippov Nickolay Smirnov
ebifsin1@mech.math.msu.su

**Abstract**

Present paper is aimed at investigating 3D instability effects in displacement of viscous fluid by a less viscous one from porous medium, and to determine characteristics of displacement quality. Many experimental studies of these were performed under microgravity conditions. The present paper summarizes results of 3-D numerical analysis. Fluids are assumed incompressible and miscible. Numerical simulations are used to study the sensitivity of the displacement process to variation of values of the main governing parameters. Comparison with results of two-dimensional simulations enabled us to investigate the effect of aspect ratio on instability growth in viscous fluids displacement. A 1D model with 2 fitting parameters is created in order to simulate behavior of the cross section averaged parameters of the flow.

Keywords: Displacement, porous, viscous, fluid, incompressible, miscible, instability.

## Introduction

The problem of frontal displacement of a more viscous fluid by a less viscous one is relevant to hydrocarbon recovery, which is performed by the flow of water or solutions under a pressure gradient displacing the high viscosity oil. Saffman – Taylor instability of the interface could result in formation of "fingers" of displacing fluid penetrating the bulk of the displaced one. The growth of fingers and their further coalescence could not be described by a linear analysis. Growth of fingers causes irregularity of the mixing zone thus affecting the displacement quality.

Similar models are applicable to description of liquid non-aqueous phase contaminants underground migration, their entrapment in the zones of inhomogeneity, and forecasting the results of remediation activities in the vicinity of waste storages and contaminated sites.

The problems of seepage flows were studied by many authors [1-12]. Investigating instability in miscible displacement differs greatly from that in immiscible fluids. The presence of a small parameter incorporating surface tension for immiscible fluids allows to determine theoretically the characteristic shape and width of viscous fingers [7, 8], while in miscible fluids theoretical analysis allows to forecast the shape of the tips, but does not allow to determine the width of fingers, which remains a free parameter [5, 6]. Numerical simulations of viscous fingering in miscible and immiscible displacement were carried out in [9, 10]. Those papers contain an extensive bibliography on the history of the research as well. Numerical simulations [11] made it possible to explain new experimental results on the pear-shape of fingers and periodical separation of their tip elements from the main body of displacing fluid. Those separated blobs of less viscous fluid move much faster than the mean flow of the displaced viscous fluid [12].

The results of numerical simulations allowed to introduce dimensionless parameters characterizing the quality of displacement and the mixing flux induced by instability [12]. In the paper [13] the asymptotic behavior of miscible displacements in porous media was studied in the two limits, where a permeability-modified aspect ratio, became large or small, respectively.

The influence of inhomogeneity of porous matrix on displacement instability was investigated [13-15]. The modified Hele-Shaw cell containing regular and randomized obstacles was used to model and study the effect of inhomogeneity on displacement instability [12, 14]. Results of numerical simulations as well as physical experiment showed that the presence of inhomogeneity of a definite length scale could stabilize unstable displacement and could destabilize a stable one [14].

Most of viscous fingering numerical simulations were performed for two-dimensional problems; one of the first classical publications was by Homsy [9, 16]. This work used the spectral methods approach. In reality displacement and induced instability have a three dimensional nature. Papers [17 – 22] investigate 2D and 3D miscible displacement of fluids with account for gravity using the spectral methods, as in earlier works by Homsy.

First attempts to perform comparative analysis for the instabilities arising in displacement from 3D cells of different aspect ratios were performed in [23]. Theoretical and experimental studies of entrapped closed domain of fluid were performed in [24].

The present paper is aimed at numerical investigation of incompressible miscible fluids displacement in 3D geometry porous medium and studying the displacement scenarios being functions of aspect ratios and other dimensionless governing parameters.

For practical applications, such as simulating hydrocarbons displacement from rock formations, often it is not important to have a detailed picture of viscous fingers development, rather then to have a quantitative estimate of the mixing flux induced due to displacement instability. Thus it is necessary to elaborate methods making it possible to simulate instability induced mixing within some integral approach, not sensitive to spatial resolution [25, 26]. A 1D model describing dynamic behavior of cross section averaged parameters is built with two fit parameters. Developing those model parameters for description of displacement quality and the mixing flux due to instability is also one of the goals of the present research.

## Mathematical model

The volume controlled displacement problem was regarded. Detailed problem statement is present in [25, 26]. The computational domain has dimensions $L \times H \times Z$, displacement is performed along $L$ direction through cross-section $H \times Z$.

To launch instability in theoretical investigations one should introduce it initially:

$$t = 0: \quad s = \begin{cases} 0, & x \geq x_0 \\ s_\xi \cdot \xi, & x < x_0 \end{cases} \tag{1}$$

Here, $\xi$ is a random field which magnitudes are distributed uniformly from 0 to 1, $s_\xi$ is the random field scaling factor and $x_0$ should be as close to zero as possible. At $x_0 \to 0$ or $s_\xi \to 0$ we get close to the physical problem statement: all the domain is filled with fluid to be displaced off.

The following set of dimensionless governing parameters which control the solution of 2D or 3D displacement problem is obtained: $M = \mu_2/\mu_1$ – viscosity ratio of the fluid being displaced to that of displacing one; $Pe_L = \frac{H}{D_L}$, $Pe_T = \frac{H}{D_T}$ – Peclet numbers; $A = H/L$, $a = Z/L$ – aspect ratios, $s_\xi$,$x_0$ – destabilising factors.

## Validation of the numerical scheme

Validation of numerical scheme was performed by qualitative comparing the numerical 2D results with experiments performed in Hele-Shaw cells [12] and with results of numerical calculations undertaken using different numerical schemes. The direct quantitative comparison of results obtained using random initial conditions (1) is not a fair choice to validate the results, because those conditions depend directly on the grid parameters in our simulations. Therefore, in order to validate the scheme, we used initial conditions independent of the mesh size and of the random seed. However, the initial saturation should be non-uniform in order to obtain the unstable displacement.

We used the following initial conditions instead of (1), in our verification study:

$$s = \left\{ \begin{array}{cc} 1 - 10x & x < 0.1 \\ 0, & \text{otherwise} \end{array} \right\} \cdot \cos^2(10y) \cos^2(10z)$$

One should notice that these conditions introduce harmonic variations into the initial saturation, which are expected to produce fingers.

The artificial diffusion used in TVD method in order to suppress non-physical oscillations of solutions in the regions of sharp gradients of parameters, depends directly on the average size of the mesh, and its coefficient and artificial Peclet number could be estimated as follows:

$$Pe_a^{-1}|v| = \frac{1}{2}|v|\Delta x$$

One should notice that the artificial Peclet number is not equivalent to an ordinary Peclet as if it is some effective value, because the dispersion with artificial Peclet is applied only in the regions of sharp saturation gradients, and not elsewhere. Normally, it influences only the slope inclination, but in case of unstable displacement, its presence could influence the fingers growth as well. Note, that when the flux is promoted to the $2^{nd}$ order of accuracy, it does not allow jumps to dissolve above some level, unlike a linear diffusive flux. Thus, the effect of artificial diffusion is limited and not equal to an effect of diffusion at some Peclet number.

Two series of investigations were processed in order to investigate the influence of the mesh size. First series used the grid $80 \times 80 \times 40$ cells, second $100 \times 100 \times 50$. All the other parameters were the same. Calculations were processed for high viscosity ratio, medium Peclet number and high secondary aspect ratio: $M = 1000$, $Pe = 1000$, $a = 0.5$. The initial conditions were (17), other features of the problem statement, as above. Parameters correspond to a highly unstable displacement case. The effective artificial Peclet was 160 and 200, respectively. Results on the fig. 1 show 3D patterns of displacement front obtained by time $t = 0.129$ for both mesh cases (due to different calculation time interval, difference in times exists and is lower than 0.001). The 3D displacement front is illustrated by a surface $s(x, y, z) = 0.25$; the left picture corresponds to a fine mesh, the right to a coarse one.

Results shown on the fig.1 illustrate qualitative similarity of the patterns; some details are slightly different however. Yet many small features (e.g. secondary fingers) are nearly the same. Symmetry is due to symmetry of the initial and boundary conditions. The main difference is the advanced fingers length; it is a direct influence of artificial diffusion.

The distributions of cross section mean saturation corresponding to cases shown on the fig. 1 is presented at the fig. 2. Left and right plots relate to coarse and fine meshes; time moment is the same. The fingers are advanced more for the case of the fine grid (lower

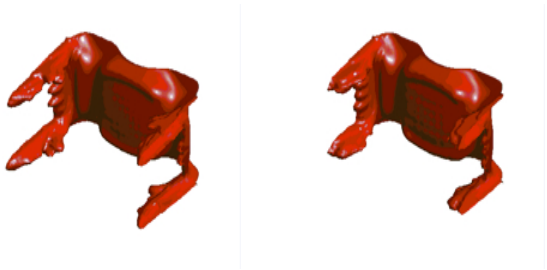

Figure 1: Unstable displacement front pattern shown by surface $s(x, y, z) = 0.25$ in space. Left plot corresponds to the fine mesh $100 \times 100 \times 50$, right to the coarse one $80 \times 80 \times 40$. Time moment is $t = 0.129$

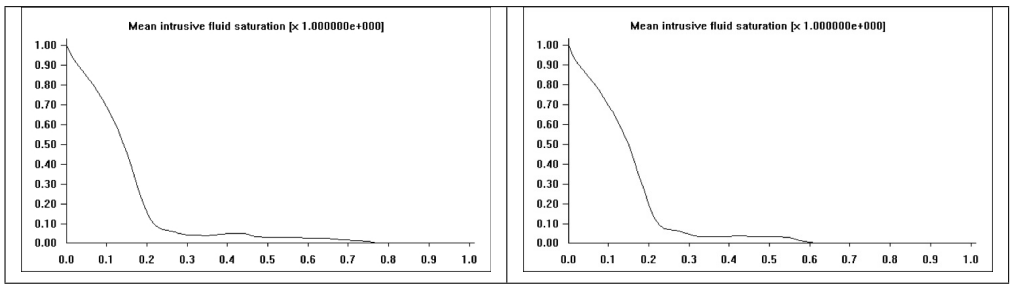


Figure 2: Mean saturation average distribution along the domain. Left plot corresponds to a coarse mesh $80 \times 80 \times 40$, right to a fine mesh $100 \times 100 \times 50$

artificial diffusion), but the overall difference of pictures is small: the error is within $3-5\%$ related to completely displaced state.

The results shown on the figs 1-2 show the expectable dependence of the flow patterns on the mesh size due to artificial diffusion effect. One of the remedies is using spectral methods instead of the TVD approach to the transport equation (2), which were applied to 2D and 3D displacement problems in [9], [16-22].

Thorough investigation of the error behavior due to artificial diffusion level is a subject of separate investigations; however, the error for Peclet numbers and viscosity ratios used in the present investigation is not high. We could mention however that the higher Peclet numbers bring to higher error for a fixed mesh. Probably, spectral methods with higher number of harmonics[16, 19] would be more effective for high Peclet numbers.

## Modeling integral parameters with 1D equation

The integral parameters of the flow can be estimated using a simple 1D one-equation model. This model simulates the dynamics of cross-section averaged saturation $\bar{s}$ (14). Such modeling was processed in [11], [12]; it was also proposed in [31].

If we average the dynamics of saturation equation in each cross-section determined by longitudinal coordinate $x$, we will obtain the following model for $\bar{s}$:

$$\frac{\partial \bar{s}}{\partial t} + \frac{\partial}{\partial x}(\bar{u} \cdot \bar{s}) + \frac{\partial}{\partial x}(\overline{\acute{u} \cdot \acute{s}}) = APe_L^{-1} \frac{\partial}{\partial x} \bar{u} \frac{\partial \bar{s}}{\partial x} \tag{2}$$

where $\bar{u}$ is the mean velocity in the cross-section and $\acute{u}$, $\acute{s}$ are deviations of the relative parameters from the cross-section means. The third term in the equation (2) is a subject of special modeling. Earlier [11], we have modeled it using convective (Buckley – Leverette)

and diffusive terms multiplied by model coefficients. It was shown however that this modeling cannot fit simultaneously both the long-run shape of the cumulative output curve and the breakthrough time. Then, introducing modifications into the convective term, modeling of the outflow for 2D case was processed [11] with much better fit.

We will model the additional convective term in (2) only with a convective component depending on averaged saturation, but using two fitting parameters. One can notice also that the dimensionless averaged velocity $\bar{u}$ is unity due to the constant rate case under investigation. We assume the following ad hoc dependence of the additional convective term $\overline{\acute{u}\acute{s}}$ on the mode parameters:

$$\overline{\acute{u}\acute{s}} = \alpha\bar{u} \cdot \bar{s}(1-\bar{s}) \left( \frac{\max\{M^\gamma - 1, 0\}}{1 + \bar{s}\max\{M^\gamma - 1, 0\}} \right) \tag{3}$$

The dependence (3) assumes that the additional flux takes place only when both fluids are present in the same cross section, that it cannot be opposite to average velocity, that its maximum is regulated by constants $\alpha$ and $\gamma$, which are to be modeled using comparison with multidimensional calculations.

Substituting (3) into (2) for $M > 1$, and taking into account that $\bar{u} = 1$, we will obtain:

$$\frac{\partial \bar{s}}{\partial t} + \frac{\partial}{\partial x}\left( (1-\alpha)\bar{s} + \alpha \frac{\bar{s}M^\gamma}{1 + \bar{s}(M^\gamma - 1)} \right) = APe_L^{-1} \frac{\partial^2 \bar{s}}{\partial x^2} \tag{4}$$

The initial and boundary conditions for (4) are obtained from (1) and look as follows:

$$\bar{s}(0,x) = \begin{cases} s_t(1 - x/x_0), & x < x_0 \\ 0, & \text{otherwise} \end{cases} \tag{5}$$

$$\bar{s}(t,0) = 1, \quad \partial\bar{s}/\partial x|_{x=1} = 0 \tag{6}$$

Note that there is no specific reason to introduce disturbance parameters into 1D modeling but they are used in (5) in order to fit the initial conditions of multidimensional modeling.

The outflow obtained by 1D modeling is determined by the convective term at $x = 1$ due to its definition (3), (4) is calculated as follows:

$$q(t) = \left( (1-\alpha)\bar{s} + \alpha \frac{\bar{s}M^\gamma}{1 + \bar{s}(M^\gamma - 1)} \right)_{x=1} \tag{7}$$

The breakthrough time obtained by 1D modeling is determined:

$$t_b = \min\left\{ t : q(t) > 0 \right\} \tag{8}$$

In order to calculate the fit parameters $\alpha$ and $\gamma$ depending on the governing parameters of the displacement process, we will use the following procedure.

- Fix the governing parameters.
- Process multidimensional modeling.
- Choose three time moments $t_k$, and obtain three profiles of cross section mean saturation $c_k(x) = c(t_k, x), \quad k = 1, 2, 3.$
- Obtain the outflow temporal profile $Q(t)$ and the breakthrough time $T_b$.

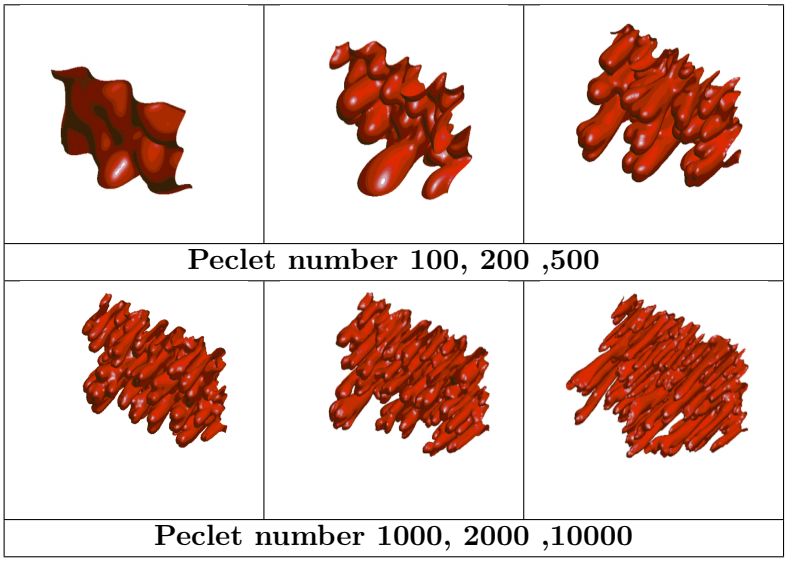


Figure 3: Flow patterns illustrated by displacing front surface $s(x, y, z) = 0.25$ for $M = 100, a = 0.5$ and various Peclet numbers

- For a given set of fitting parameters $\alpha, \gamma$ process 1D modeling.
- For the time moments $t_k$, obtain 3 profiles of the average saturation $\bar{s_k} = \bar{s}(t_k, x)$.
- Obtain the modeled outflow profile $q(t)$ and the breakthrough time $t_b$.
- Calculate the function to be minimized, which is chosen as follows:

$$\Psi = \frac{1}{3}\sum_{k=1}^{3}\left[\int_0^1 (\bar{s_k}(x) - c_k(x))^2 dx\right]^{1/2} + \left[\frac{1}{T}\int_0^T (q(t) - Q(t))^2 dt\right]^{1/2} + [T_b - t_b] \qquad (9)$$

Our goal is to find the parameters $\alpha$ and $\gamma$ which minimize the function $\Psi$. This function depends both on the governing parameters of the multidimensional model (parameters of the process) and on the fitting parameters $\alpha, \gamma$. Therefore, the fitting parameters minimizing $\Psi$ will depend on the governing parameters of the model.

## Results and discussions

Results for 3-D unstable displacement of viscous fluid from porous medium by a less viscous one are shown in Figs. 3-4. The Fig. 3 shows the influence of Peclet number. We fix the medium viscosity ratio ($M = 100$) and compare patterns of the front for different $Pe$ at $a = 0.5$. The Peclet numbers increase from left to right in each row; a wide range of Peclet numbers was investigated both lower and upper than the characteristic artificial Peclet number. Each plot corresponds to some characteristic time moment. Numerical investigations showed high irregularity of the displacing front; however, the fingers number naturally grows with the growth of the cross section area. For high $a$, development and splitting of the most advancing fingers looks similar; for low $a$, the front is bounded by the walls, and the fingers split in lower number of daughter structures. Therefore, the secondary aspect ratio is expected to influence the displacement features mostly when it is low.

Fig. 4 summarizes the flow patterns for 2D displacement simulations illustrating the saturation patterns for the displacing fluid. The flow patterns in each row are made for

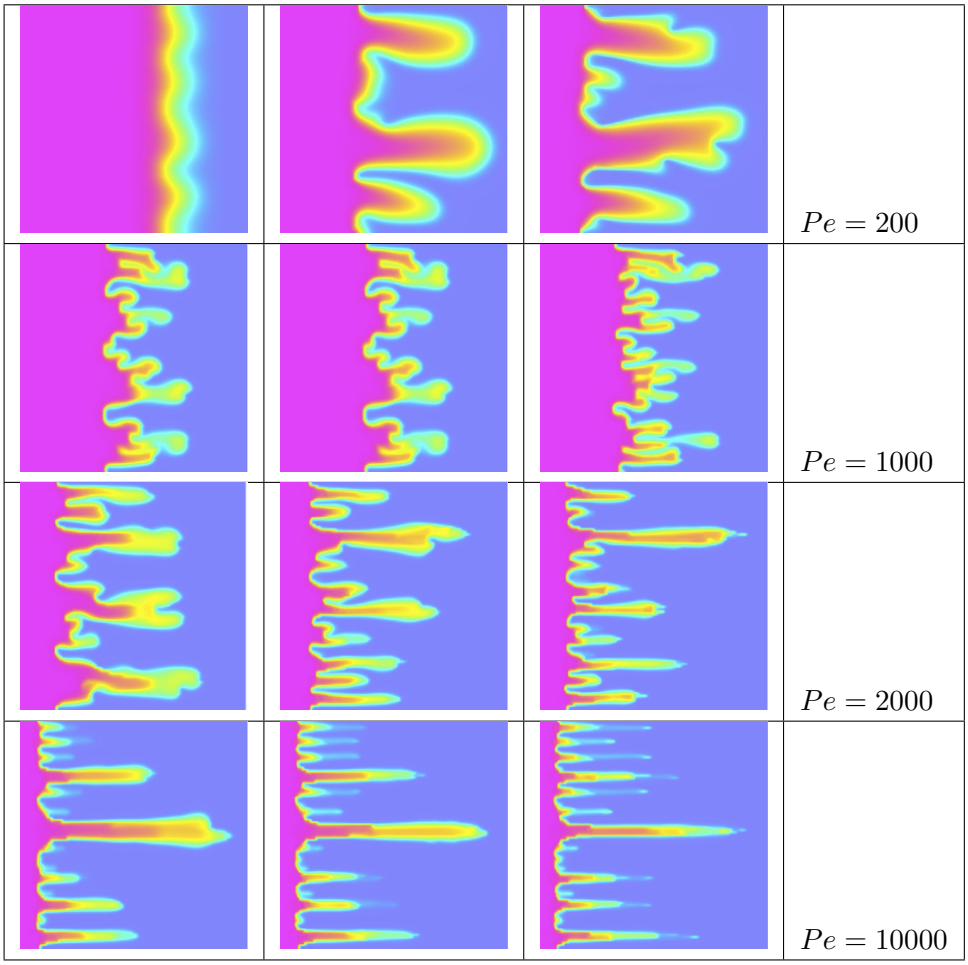


Figure 4: Saturation of the displacing fluid for 2D displacement process. Flow patterns for different Peclet numbers and viscosity

the same Peclet number and different viscosity ratio $M = 10, 100, 1000$ (from left to right). Fig. 4 shows the same tendencies of $M$ and $Pe$ influence on the displacement process as it was shown for 3D process on the figs. 2 and 4. However, two significant differences take place. First, the total number of fingers is very small compared with 3D displacement at high aspect ratio. Second, for high viscosity ratio and Peclet number, separation of tips of the fingers takes place instead of their split. We can not observe this separation on the displacement front patterns for 3D case because we monitor the surface of the displacement front there for $s = 0.25$ only, but the separated fingers have much less saturation.

## Results for the fitting parameters of 1D modeling

The fitting parameters of 1D modeling [12] $\alpha$ and $\gamma$ were obtained minimizing the function $\Psi$ (9) for each set of parameters $a, M, Pe$ for which multidimensional calculations were processed. The optimized values of $\alpha$ and $\gamma$ were obtained for each variant of the random seed, and then the average values and deviations of fit parameters were obtained as follows:

$$\alpha = \frac{1}{n}\sum_{k=1}^{n}\alpha_k \quad \gamma = \left(\prod_{k=1}^{n}\gamma_k\right)^{1/n}, d_\alpha = \max_k|\alpha_k - \alpha|, \quad d_\gamma = \max_k|\gamma_k - \gamma| \tag{10}$$

Here, $n$ is the number of variants, $d_\alpha$ and $d_\gamma$ are deviations. One could notice that, we used arithmetic averaging for $\alpha$ and geometry averaging for $\gamma$ due to their specific position in the formula (3) modeling the additional convective term. The results of fitting procedure show that the quality of fit is better for 3D case than for 2D, and for lower viscosity ratios rather than for higher ones. This phenomenon shows that our 1D modeling has its borders of applicability; expanding those borders may result in introducing an additional fit parameter, or some other features which are beyond the scope of the present study.

Results shows that change between the regular and irregular displacement modes does not influence parameter $\gamma$ so much as $\alpha$. Analysing the dependence of $\gamma$ on $Pe$ for different $M$, we noticed that it is good to assume independence of $\gamma$ on $M$ and linear dependence on $\ln Pe$. The dependence on the secondary aspect ratio was assumed as dependence via a complex $\beta = 2/(a + 1/a)$ because of the symmetry of physical solution at $a = 1$. The following interpolation was derived by least squares method:

$$\gamma = (0.0492 + 0.0348\beta) \cdot \ln Pe - (0.117 + 0.173\beta), \quad \beta = 2/(a + 1/a) \tag{11}$$

Fit parameters combination $G = \alpha\gamma$ dependence on Peclet number, viscosity ratio and secondary aspect ratio calculated by minimizing the function $\Psi$ for both regular and irregular displacement modes could be approximated by the following formula:

$$\begin{aligned} G(Pe, M, a) = \max\{&0.070 - 0.032 \ln M + 0.004 \ln^2 M, \\ &0.278 \cdot \ln(\ln Pe - (0.356 + 0.251 \ln M + 0.148\beta + 0.056\beta \ln M)) + \\ &(-0.444 + 0.050 \ln M - 0.047\beta + 0.019\beta \ln M)\} \end{aligned}$$

Changing two alternatives of the maximum operator in the above formula corresponds to change from regular to irregular mode of displacement.

## Conclusions

Multi-dimensional (2D and 3D) calculations of the displacement process were performed for a set of governing parameters (viscosity ratio, Peclet number and the secondary aspect ratio). The outflow of the displacing fluid versus time was obtained, together with profiles of the cross-section mean saturation of the displacing fluid.

Comparison of the integral parameters development showed that for the displacement percentage, the results for $a = 0.5$ differ significantly from the results for $a = 0.1$ (both cases) and the 2D case. The results for 2D modeling are close to the results of 3D at $a = 0.1$. However, the results for cumulative outflow of the displacing fluid differ insignificantly for all the cases investigated. The breakthrough of the displacing fluid takes place earlier for higher values of the "second" aspect ratio $a$; for 2D case the breakthrough time is the longest one. Thus flow instability and displacement front irregularity develop much faster in a 3D case then in a 2D one.

The multi-dimensional irregular displacement was modeled by 1D equation for the cross-section mean of the displacing fluid saturation. This model has 2 fitting parameters: $\alpha$ and $\gamma$, which still depend on the governing problem parameters, which testifies that the developed phenomenological model represents one possible approximation for the mixing flux, probably not the best one. However, the fitting parameters were found minimizing a functional depending on difference between profiles, 1D modeled and obtained from multi-dimensional calculations. The functional forms approximating dependence of fitting parameters on Peclet number, aspect and viscosity ratios were developed, making it possible to use the developed model for a rather wide range of governing parameters variation, which are suitable for practical applications.

It was obtained that 2D displacement integral parameters (such as the outflow of the displacing fluid) have much higher deviation than those parameters obtained in 3D modeling. This can be explained by much higher number of fingers in 3D cases of displacement reaching the outflow surface, and by the subsequent compensation of disturbances in the overall outflow.

Analysis of the fitting parameters of 1D modeling show that the "degree" parameter $\gamma$ depends mainly on Peclet number and aspect ratio, and not on the viscosity ratio. The dependence of a complex of those parameters: $G = \alpha\gamma$ on $Pe$ and $M$ is much clearer than the corresponding dependence of $\alpha$. This results in the development of rather simple interpolation formulae for $\gamma$ and $G$, which predict both dependence on Peclet number, viscosity ratio and secondary aspect ratio, and the conditions of change between regular and irregular modes of displacement.

Russian Foundation for Basic Research (12-08-00198) is acknowledged for financial support.

## References

[1] *Barenblatt G.I., Entov V.M., Ryzhik V.M.* Theory of fluids flows through natural rocks. Kluwer Academic Publishes - Dordrecht / Boston / London, 1990.

[2] *Nield D.A., Bejan A.* Convection in porous media. Springer-Verlag – New York / Berlin / Heidelberg / London, 1992.

[3] *Bear J., Bachmat Y.* Introduction to modelling of transport phenomena in porous media. Kluwer Academic Publishes - Dordrecht / Boston / London, 1990.

[4] *Kaviany M.* Principles of heat transfer in porous media. Dover Publications Inc. – New York, 1988.

[5] *Saffman, P.G., Taylor, G.J.* The penetration of a fluid into a porous medium of Hele-Show cell containing a more viscous fluid. Proc. R. Foc. Zond. 1958, A 245, 312.

[6] *Zhuravlev, P.* Zap Leningrad Com. Inst. 1956, 133, 54 (in Russian).

[7] *Meiburg, E. & Homsy, G.M.* Nonlinear unstable viscous fingers in Hele-Show flows. II. Numerical simulation. Phys. Fluids 1988, 31(3).

[8] *Tanveer, S.* Surprises in viscous fingering. J. Fluid Mech.,2000, vol. 409, p.273.

[9] *De Wit A., Homsy G.M.* Viscous fingering in periodically heterogeneous porous media. Part II. Numerical simulations. J. Chem. Phys. 1997. Vol. 107(22), 9619.

[10] *Guan X., Pitchumani R.* Viscous fingering in a Hele-Shaw cell with finite viscosity ratio and interfacial tension. ASME Journal of Fluids Engineering, 2003. Vol. 125, No. 2, pp. 354-364.

[11] *Smirnov N.N., Nikitin V.F., Ivashnyov O.E., Maximenko A., Thiercelin M., Vedernikov A., Scheid B., Legros J.C.* Microgravity investigations of instability and mixing flux in frontal displacement of fluids. Microgravity sci. technol. 2004, XV/3, pp. 3-28.

[12] *Smirnov N.N., Nikitin V.F., Maximenko A., Thiercelin M., Legros J.C.* Instability and mixing flux in frontal displacement of viscous fluids from porous media. Physics of Fluids, 2005, vol.17, 084102.

[13] *Z.M. Yang, Y.C. Yortsos, Dominique Salin.* Asymptotic regimes in unstable miscible displacements in random porous media. Advances in Water Resources, 2002, Vol. 25, issues 8-12, p. 885-898.

[14] *Smirnov N.N., J. C. Legros, V. F. Nikitin, E. Istasse, L. Schramm, F. Wassmuth, and D'Arcy Hart.* Filtration in Artificial Porous Media and Natural Sands under Microgravity Conditions. Microgravity sci. technol. 2003, XIV/2, pp. 3-28.

[15] *Brock D.C., Orr F.M.* Flow visualization of viscous fingering in heterogeneous porous media. SPE 22614, 1991.

[16] *Homsy G.M.* Viscous fingering in porous media. Ann. Rev. Fluid Mech., 1987, vol. 19, pp. 271-311.

[17] *Tchelepi H.A., Orr F.M. Jr., Rakotomalala N., Salin D., and Womeni R.* Dispersion, permeability heterogeneity and viscous fingering: Acoustic Experimental Observations and Particle-Tracking Simulations. Phys. Fluids A 5, 1993, No. 7, pp. 1558-1574.

[18] *Fayers J.F., Jouaux F., and Tchelepi H.A.* An improved macroscopic model for viscous fingering and its validation for 2D and 3D flows. I. Non-Gravity Flows. In Situ 18, 1994, No. 1, pp. 43-78.

[19] *Ruith M., Meiburg E.* Miscible rectilinear displacements with gravity override. Part 1. Homogeneous porous medium. Journal of Fluid Mechanics, 2000, 420, pp. 225-257

[20] *A. Riaz, E. Meiburg.* Three-dimensional miscible displacement simulations in homogeneous porous media with gravity override. Journal of Fluid Mechanics, 2003, 494, pp. 95-117.

[21] *Riaz A. Hesse M. Tchelepi H. Orr F.M.* Onset of convection in a gravitationally unstable diffusive boundary layer in porous media. Journal of Fluid Mechanics, 2006, 548, pp. 87-112.

[22] *Yortsos Y.C., Salin D.* On the selection principle for viscous fingering in porous media. Journal of Fluid Mechanics, 2006, v. 557, pp. 225-236.

[23] *Smirnov N.N., Nikitin V.F., Dushin V.R., Maximenko A., Thiercelin M., Legros J.C.* Instability in displacement of viscous fluids from porous specimens, Acta Astronautica, 2007, vol. 61, No 7-8, pp. 637-643.

[24] *Dushin V.R., Nikitin V.F., Vedernikov A.A., Scheid B., Legros J.C.* Instability of Seepage flows in porous media. Proc. 6th IASME/WSEAS International Conference on HEAT TRANSFER, THERMAL ENGINEERING And ENVIRONMENT. ISSN 1790-5095, Rhodes 2008, Part 1, pp. 37-42.

[25] *Dushin, V., Nikitin, V., Philippov, Y., Smirnov, N.* Two phase flows in porous media under microgravity conditions Microgravity Science and Technology 2008, vol. 20 (3-4), pp. 155-160.

[26] *Dushin, V.R., Nikitin, V.F., Legros J.C., Thiercelin M.,* Seepage Flows Instability in Porous Media. Acta Astronautica, 2009, vol. 64 (2-3), 295-312.

[27] *Yortsos Y.C., Zeybek M.* Dispersion driven instability in miscible displacement in porous media. Phys. Fluids, 1988, v. 31, pp. 3511.

[28] *Sorbie K.S., Zhang H.R., Tsibuklis N.B.* Linear viscous fingering: new experimental results, direct simulation and the evaluation of averaged models. Chemical Engineering Science, 1995, vol. 50, No. 4, pp. 601-616.

[29] *Smirnov N.N., Legros J.C., Nikitin V.F., Istasse E., Norkin A.V., Shevtsova V.M., Kudryavtseva O.V.* Capillary driven filtration in porous media. Microgravity Science and Technology, Hanser Publ., 1999, XII, pp. 23-35.

[30] *Smirnov N.N., Nikitin V.F., Norkin A.V., Kiselev A.B., Legros J.C., Istasse E.* Microgravity investigation of capillary forces in porous media. Space Forum 2000, 6(1-4), pp. 1-10.

[31] *Tardy Ph.* Viscous fingering in porous media. Towards 1D averaged models for fracture cleanup simulation. Proc. Moscow SMR Workshop, paper no. 403. April 2003.

*Vladislav Dushin, Valeriy Nikitin, Yuri Philippov, Nickolay Smirnov, Faculty of Mechanics and mathematics, Moscow M.V. Lomonosov State University, Leninskie (Vorobiovy) Gory 1, Moscow 119992, Russia, ebifsin1@mech.math.msu.su*
*Vladislav Dushin, Valeriy Nikitin, Nickolay Smirnov, Scientific Research Institute for System Analysis of the Russian Academy of Sciences, Moscow 117218, Russia*

# Mathematical model of micropolar anisotropic (orthotropic) multilayered thin plates

Anahit J. Farmanyan Samvel H. Sargsyan
afarmanyan@yahoo.com

**Abstract**

Micropolar theory of elasticity is a structural phenomenological model of rigid deformable bodies with strongly expressed internal structure [1]. From this point of view the construction of theories of micropolar anisotropic elastic multilayered thin bars, plates and shells is actual. In paper [2] general applied theories of micropolar elastic isotropic thin shells, plates and bars are constructed on the basis of mathematically confirmed hypotheses method.

In this paper this approach is developed and on the basis of accepted hypotheses for the whole package of multilayered plate general applied theory of micropolar orthotropic elastic multilayered thin plates of symmetric structure is constructed for plane stress state and bending.

## 1 Problem statement

A plate of constant thickness $2h$ composed of an odd number of homogeneous mic- ropolar orthotropic layers is considered. Layers which are symmetrically located with respect to the coordinate plane $\alpha_3 = 0$ have the same thickness and physical-mechanical properties. The coordinate plane $\alpha_3 = 0$ is the middle plane of the middle layer and the whole package of multilayered plate.

We start from the basic equations of the spatial static problem of linear micro- polar theory of elasticity for orthotropic body with free fields of displacements and rotations:

Equilibrium equations [3]:

$$\frac{1}{H_1H_2}\frac{\partial}{\partial\alpha_1}\left(H_2\sigma_{11}^i\right)+\frac{1}{H_1H_2}\frac{\partial}{\partial\alpha_2}\left(H_1\sigma_{21}^i\right)+\frac{\partial\sigma_{31}^i}{\partial\alpha_3}+\frac{1}{H_1H_2}\frac{\partial H_1}{\partial\alpha_2}\sigma_{12}^i-\frac{1}{H_1H_2}\frac{\partial H_2}{\partial\alpha_1}\sigma_{22}^i=0,$$

$$\frac{1}{H_1H_2}\frac{\partial}{\partial\alpha_1}\left(H_2\sigma_{12}^i\right)+\frac{1}{H_1H_2}\frac{\partial}{\partial\alpha_2}\left(H_1\sigma_{22}^i\right)+\frac{\partial\sigma_{32}^i}{\partial\alpha_3}+\frac{1}{H_1H_2}\frac{\partial H_2}{\partial\alpha_1}\sigma_{21}^i-\frac{1}{H_1H_2}\frac{\partial H_1}{\partial\alpha_2}\sigma_{11}^i=0,$$

$$\frac{1}{H_1H_2}\frac{\partial}{\partial\alpha_1}\left(H_2\sigma_{13}^i\right)+\frac{1}{H_1H_2}\frac{\partial}{\partial\alpha_2}\left(H_1\sigma_{23}^i\right)+\frac{\partial\sigma_{33}^i}{\partial\alpha_3}=0, \tag{1}$$

$$\frac{1}{H_1H_2}\frac{\partial}{\partial\alpha_1}\left(H_2\mu_{11}^i\right)+\frac{1}{H_1H_2}\frac{\partial}{\partial\alpha_2}\left(H_1\mu_{21}^i\right)+\frac{\partial\mu_{31}^i}{\partial\alpha_3}+\frac{1}{H_1H_2}\frac{\partial H_1}{\partial\alpha_2}\mu_{12}^i-$$
$$-\frac{1}{H_1H_2}\frac{\partial H_2}{\partial\alpha_1}\mu_{22}^i+\left(\sigma_{23}^i-\sigma_{32}^i\right)=0,$$

$$\frac{1}{H_1H_2}\frac{\partial}{\partial\alpha_1}\left(H_2\mu^i_{12}\right)+\frac{1}{H_1H_2}\frac{\partial}{\partial\alpha_2}\left(H_1\mu^i_{22}\right)+\frac{\partial\mu^i_{32}}{\partial\alpha_3}+\frac{1}{H_1H_2}\frac{\partial H_2}{\partial\alpha_1}\mu^i_{21}-$$
$$-\frac{1}{H_1H_2}\frac{\partial H_1}{\partial\alpha_2}\mu^i_{11}+\left(\sigma^i_{31}-\sigma^i_{13}\right)=0,$$

$$\frac{1}{H_1H_2}\frac{\partial}{\partial\alpha_1}\left(H_2\mu^i_{13}\right)+\frac{1}{H_1H_2}\frac{\partial}{\partial\alpha_2}\left(H_1\mu^i_{23}\right)+\frac{\partial\mu^i_{33}}{\partial\alpha_3}+\sigma^i_{12}-\sigma^i_{21}=0.$$

Here $H_1, H_2$ are Lame's coefficients in the curvilinear orthogonal system of coordinates; $\hat\sigma^i, \hat\mu^i$ are asymmetric tensors of force and moment stresses of the $i$ - th layer. Number of layers is equal to $2n+1$.

Physical relations [3]:

$$\gamma^i_{11}=a^i_{11}\sigma^i_{11}+a^i_{12}\sigma^i_{22}+a^i_{13}\sigma^i_{33},\ \gamma^i_{22}=a^i_{12}\sigma^i_{11}+a^i_{22}\sigma^i_{22}+a^i_{23}\sigma^i_{33},\ \gamma^i_{33}=a^i_{13}\sigma^i_{11}+a^i_{23}\sigma^i_{22}+a^i_{33}\sigma^i_{33},$$
$$\gamma^i_{12}=a^i_{77}\sigma^i_{12}+a^i_{78}\sigma^i_{21},\ a^i_{21}=a^i_{78}\sigma^i_{12}+a^i_{88}\sigma^i_{21},\ \gamma^i_{13}=a^i_{56}\sigma^i_{31}+a^i_{66}\sigma^i_{13},\ \gamma^i_{31}=\widetilde{a}^i_{55}\sigma^i_{31}+a^i_{56}\sigma^i_{13},$$
$$\gamma^i_{23}=a^i_{44}\sigma^i_{23}+a^i_{45}\sigma^i_{32},\ \ \gamma^i_{32}=a^i_{45}\sigma^i_{23}+a^i_{55}\sigma^i_{32}, \tag{2}$$
$$\chi^i_{11}=b^i_{11}\mu^i_{11}+b^i_{12}\mu^i_{22}+b^i_{13}\mu^i_{33},\ \chi^i_{22}=b^i_{12}\mu^i_{11}+b^i_{22}\mu^i_{22}+b^i_{23}\mu^i_{33},\ \chi^i_{33}=b^i_{13}\mu^i_{11}+b^i_{23}\mu^i_{22}+b^i_{33}\mu^i_{33},$$
$$\chi^i_{12}=b^i_{77}\mu^i_{12}+b^i_{78}\mu^i_{21},\ \chi^i_{21}=b^i_{78}\mu^i_{12}+b^i_{88}\mu^i_{21},\ \chi^i_{13}=b^i_{56}\mu^i_{31}+b^i_{66}\mu^i_{13},\ \chi^i_{31}=\widetilde{b}^i_{55}\mu^i_{31}+b^i_{56}\mu^i_{13},$$
$$\chi^i_{23}=b^i_{44}\mu^i_{23}+b^i_{45}\mu^i_{32},\ \ \chi^i_{32}=b^i_{45}\mu^i_{23}+b^i_{55}\mu^i_{32}.$$

Here $\hat\gamma^i, \hat\chi^i$ are asymmetric tensors of deformations and bending-torsions, $\hat a^i, \hat b^i$ are tensors of elastic constants for micropolar orthotropic material of the $i$ - th layer.

Geometric relations [3]:

$$\gamma^i_{11}=\frac{1}{H_1}\frac{\partial V^i_1}{\partial\alpha_1}+\frac{1}{H_1H_2}\frac{\partial H_1}{\partial\alpha_2}V^i_2,\ \ \gamma^i_{22}=\frac{1}{H_2}\frac{\partial V^i_2}{\partial\alpha_2}+\frac{1}{H_1H_2}\frac{\partial H_2}{\partial\alpha_1}V^i_1,\ \ \gamma^i_{33}=\frac{\partial V^i_3}{\partial\alpha_3},$$
$$\gamma^i_{12}=\frac{1}{H_1}\frac{\partial V^i_2}{\partial\alpha_1}-\frac{1}{H_1H_2}\frac{\partial H_1}{\partial\alpha_2}V^i_1-\omega^i_3,\ \ \gamma^i_{21}=\frac{1}{H_2}\frac{\partial V^i_1}{\partial\alpha_2}-\frac{1}{H_1H_2}\frac{\partial H_2}{\partial\alpha_1}V^i_2+\omega^i_3,$$
$$\gamma^i_{13}=\frac{1}{H_1}\frac{\partial V^i_3}{\partial\alpha_1}+\omega^i_2,\ \ \gamma^i_{31}=\frac{\partial V^i_1}{\partial\alpha_3}-\omega^i_2,\ \ \gamma^i_{23}=\frac{1}{H_2}\frac{\partial V^i_3}{\partial\alpha_2}-\omega^i_1,\ \ \gamma^i_{32}=\frac{\partial V^i_2}{\partial\alpha_3}+\omega^i_1,$$
$$\chi^i_{11}=\frac{1}{H_1}\frac{\partial\omega^i_1}{\partial\alpha_1}+\frac{1}{H_1H_2}\frac{\partial H_1}{\partial\alpha_2}\omega^i_2,\ \ \chi^i_{22}=\frac{1}{H_2}\frac{\partial\omega^i_2}{\partial\alpha_2}+\frac{1}{H_1H_2}\frac{\partial H_2}{\partial\alpha_1}\omega^i_1,\ \ \chi^i_{33}=\frac{\partial\omega^i_3}{\partial\alpha_3}, \tag{3}$$
$$\chi^i_{12}=\frac{1}{H_1}\frac{\partial\omega^i_2}{\partial\alpha_1}-\frac{1}{H_1H_2}\frac{\partial H_1}{\partial\alpha_2}\omega^i_1,\ \ \chi^i_{21}=\frac{1}{H_2}\frac{\partial\omega^i_1}{\partial\alpha_2}-\frac{1}{H_1H_2}\frac{\partial H_2}{\partial\alpha_1}\omega^i_2,$$
$$\chi^i_{13}=\frac{1}{H_1}\frac{\partial\omega^i_3}{\partial\alpha_1},\ \ \chi^i_{31}=\frac{\partial\omega^i_1}{\partial\alpha_3},\ \ \chi^i_{23}=\frac{1}{H_2}\frac{\partial\omega^i_3}{\partial\alpha_2},\ \ \chi^i_{32}=\frac{\partial\omega^i_2}{\partial\alpha_3}.$$

It is assumed that the layers of the plate are rigidly connected with each other and work together without slide. Conditions of conjugation of layers for displacements and rotations are written as follows:

$$V^i_1=V^{i+1}_1,\ \ V^i_2=V^{i+1}_2,\ \ V^i_3=V^{i+1}_3,\ \ \omega^i_1=\omega^{i+1}_1,\ \ \omega^i_2=\omega^{i+1}_2,\ \ \omega^i_3=\omega^{i+1}_3. \tag{4}$$

Conditions of the contact between the layers for force and moment stresses are written as follows:

$$\sigma^i_{31}=\sigma^{i+1}_{31},\ \ \sigma^i_{32}=\sigma^{i+1}_{32},\ \ \sigma^i_{33}=\sigma^{i+1}_{33},\ \ \mu^i_{31}=\mu^{i+1}_{31},\ \ \mu^i_{32}=\mu^{i+1}_{32},\ \ \mu^i_{33}=\mu^{i+1}_{33}. \tag{5}$$

It is assumed that the following conditions are satisfied on the planes $\alpha_3 = \pm h_n$ of the plate:

$$\sigma^n_{31}|_{\alpha_3=h_n} = q^+_1,\ \ \sigma^n_{32}|_{\alpha_3=h_n} = q^+_2,\ \ \sigma^n_{33}|_{\alpha_3=h_n} = q^+_3,\ \ \mu^n_{31}|_{\alpha_3=h_n} = m^+_1,\ \ \mu^n_{32}|_{\alpha_3=h_n} = m^+_2,$$

$$\mu^n_{33}|_{\alpha_3=h_n} = m^+_3,\ \ \sigma^{-n}_{31}\Big|_{\alpha_3=-h_n} = -q^-_1,\ \ \sigma^{-n}_{32}\Big|_{\alpha_3=-h_n} = q^{-n}_2,\ \ \sigma^{-n}_{33}\Big|_{\alpha_3=-h_n} = -q^-_3, \quad (6)$$

$$\mu^{-n}_{31}\Big|_{\alpha_3=-h_n} = m^-_1,\quad \mu^{-n}_{32}\Big|_{\alpha_3=-h_n} = -m^-_2,\quad \mu^{-n}_{33}\Big|_{\alpha_3=-h_n} = -m^+_3.$$

Following three types of boundary conditions are considered on the surface $\sum$ of the plate: 1) Force and moment stresses are given;2) points of the surface $\sum$ are fixed; 3) three-dimensional mixed boundary conditions of hinged support are given.

It is assumed that the thickness $2h$ of the plate is small compared with typical radii of curvature of the middle plane.

## 2 The construction of model of micropolar orthotropic elastic multilayered plate of symmetric structure

Considering that the method of hypotheses, along with extremely visibility, very quickly and relatively simply leads to final results for engineering practice, the model of micropolar orthotropic elastic multilayered plates will be constructed on the basis of this method. Following hypotheses are formulated for the construction of the mathematical model of micropolar orthotropic elastic multilayered plates composed of an odd number of layers, which are symmetrically located with respect to the middle plane (these are generalized hypotheses of single layered micropolar isotropic plates [2]:

1. During the deformation initially straight and normal to the middle plane of the plate fibers rotate freely at an angle as a whole rigid body, without changing their length and without remaining perpendicular to the deformed middle plane.

The formulated hypothesis is mathematically written as follows:

$$V^i_1 = u_1(\alpha_1,\alpha_2) + \alpha_3\Psi_1(\alpha_1,\alpha_2),\ V^i_2 = u_2(\alpha_1,\alpha_2) + \alpha_3\Psi_2(\alpha_1,\alpha_2),$$

$$V^i_3 = w(\alpha_1,\alpha_2). \quad (7)$$

$$\omega^i_1 = \Omega_1(\alpha_1,\alpha_2),\ \omega^i_2 = \Omega_2(\alpha_1,\alpha_2),\ \omega^i_3 = \omega_3(\alpha_1,\alpha_2) + \alpha_3\iota(\alpha_1,\alpha_2). \quad (8)$$

Thus, tangential displacements and normal rotation are changed by a linear law along the plate thickness. Bending and tangential rotations do not depend on coordinate $\alpha_3$.It should be noted that part (7) of the accepted hypothesis, in essence, is Timoshenko's hypothesis in the classical theory of shells and plates. Here, like in paper [2], hypothesis (9), (10) in full we shall call Timoshenko's generalized for micropolar case kinematic hypothesis.

2. In the generalized Hook's law (2) force stress $\sigma^i_{33}$ and moment stresses $\mu^i_{31}$, $\mu^i_{32}$ in each layer can be neglected respectively in relation to the force stresses $\sigma^i_{11}$, $\sigma^i_{22}$ and moment stresses $\mu^i_{13}$, $\mu^i_{23}$.

3. During the determination of the deformations, bending-torsions, force and moment stresses in each layer, first for the force stresses $\sigma^i_{31}$, $\sigma^i_{22}$ and moment stress $\mu^i_{33}$ we'll take:

$$\sigma^i_{31} = \overset{o^i}{\sigma}_{31}(\alpha_1,\alpha_2),\ \sigma^i_{32} = \overset{o^i}{\sigma}_{32}(\alpha_1,\alpha_2),\ \mu^i_{33} = \overset{o^i}{\mu}_{33}(\alpha_1,\alpha_2). \quad (9)$$

After determination of mentioned quantities, values of $\sigma^i_{31}$, $\sigma^i_{32}$ and $\mu^i_{33}$ in each layer will be finally defined by the addition to the correspondent values (9) summed up, obtained

by integration of the first, second and sixth equilibrium equations of (1), for which the condition will be required, that quantities, averaged along the layer's thickness, are equal to zero.

With the help of the accepted hypotheses displacements, rotations, deformations, bending-torsions, force and moment stresses will be determined and conditions (4), (5) will be satisfied. In order to bring the three-dimensional problem of the mic- ropolar theory of elasticity (1)-(6) to two-dimensional, instead of the components of the tensors of force and moment stresses statically equivalent to them integral characteristics-forces $T_{11}$, $T_{22}$, $S_{12}$, $S_{21}$, $N_{13}$, $N_{23}$, $N_{31}$, $N_{32}$, moments $L_{13}$, $L_{23}$, $M_{11}$, $M_{22}$, $H_{12}$, $H_{21}$, $L_{11}$, $L_{22}$, $L_{33}$, $L_{12}$, $L_{21}$ and hypermoments $\Lambda_{13}$, $\Lambda_{23}$ are introduced:

$$T_{11} = 2\left[\int_0^{h_1}\sigma_{11}^1 d\alpha_3 + \sum_{i=1}^{n}\int_{h_i}^{h_{i+1}}\sigma_{11}^{i+1}d\alpha_3\right],\ S_{12} = 2\left[\int_0^{h_1}\sigma_{12}^1 d\alpha_3 + \sum_{i=1}^{n}\int_{h_i-1}^{h_i}\sigma_{12}^{i}d\alpha_3\right],$$

$$L_{11} = 2\left[\int_0^{h_1}\mu_{11}^1 d\alpha_3 + \sum_{i=1}^{n}\int_{h_i-1}^{h_i}\mu_{11}^{i}d\alpha_3\right], L_{12} = 2\left[\int_0^{h_1}\mu_{12}^1 d\alpha_3 + \sum_{i=1}^{n}\int_{h_i-1}^{h_i}\mu_{12}^{i}d\alpha_3\right], \quad (10)$$

$$M_{11} = 2\left[\int_0^{h_1}\alpha_3\sigma_{11}^1 d\alpha_3 + \sum_{i=1}^{n}\int_{h_i-1}^{h_i}\alpha_3\sigma_{11}^{i}d\alpha_3\right], H_{12} = 2\left[\int_0^{h_1}\alpha_3\sigma_{12}^1 d\alpha_3 + \sum_{i=1}^{n}\int_{h_i-1}^{h_i}\alpha_3\sigma_{12}^{i}d\alpha_3\right],$$

$$N_{13} = 2\left[\int_0^{h_1}\sigma_{13}^1 d\alpha_3 + \sum_{i=1}^{n}\int_{h_i-1}^{h_i}\sigma_{13}^{i}d\alpha_3\right],\ \Lambda_{13} = 2\left[\int_0^{h_1}\alpha_3\mu_{13}^1 d\alpha_3 + \sum_{i=1}^{n}\int_{h_i-1}^{h_i}\alpha_3\mu_{13}^{i}d\alpha_3\right],$$

$$L_{13} = 2\left[\int_0^{h_1}\mu_{13}^1 d\alpha_3 + \sum_{i=1}^{n}\int_{h_i-1}^{h_i}\mu_{13}^{i}d\alpha_3\right], L_{33} = 2\left[\int_0^{h_1}\mu_{23}^1 d\alpha_3 + \sum_{i=1}^{n}\int_{h_i-1}^{h_i}\mu_{33}^{i}d\alpha_3\right]; (1 \leftrightarrow 2).$$

Here $\Delta h_{i+1} = h_{i+1} - h_i$ is the thickness of the $i$-th layer; $2h_1$-of the middle plane.

On the basis of the accepted hypotheses the basic system of equations of mic- ropolar orthotropic elastic multilayered thin plates with free fields of displacements and rotations will be split into two independent systems of equations (the system of plane stress state and the system of bending).

Equations of plane stress state of micropolar orthotropic elastic multilayered thin plates with symmetric structure:

Equilibrium equations:

$$\frac{1}{A_1}\frac{\partial T_{11}}{\partial \alpha_1} + \frac{1}{A_1A_2}\frac{\partial A_2}{\partial \alpha_1}(T_{11} - T_{22}) + \frac{1}{A_2}\frac{\partial S_{21}}{\partial \alpha_2} + \frac{1}{A_1A_2}\frac{\partial A_1}{\partial \alpha_2}(S_{21} + S_{12}) = -(q_1^+ + q_1^-),$$

$$\frac{1}{A_2}\frac{\partial T_{22}}{\partial \alpha_2} + \frac{1}{A_1A_2}\frac{\partial A_1}{\partial \alpha_2}(T_{22} - T_{11}) + \frac{1}{A_1}\frac{\partial S_{12}}{\partial \alpha_1} + \frac{1}{A_1A_2}\frac{\partial A_2}{\partial \alpha_1}(S_{12} + S_{21}) = -(q_2^+ + q_2^-), \quad (11)$$

$$\frac{1}{A_1}\frac{\partial L_{13}}{\partial \alpha_1} + \frac{1}{A_1A_2}\frac{\partial A_2}{\partial \alpha_1}L_{13} + \frac{1}{A_2}\frac{\partial L_{23}}{\partial \alpha_2} + \frac{1}{A_1A_2}\frac{\partial A_1}{\partial \alpha_2}L_{23} + S_{12} - S_{21} = -(m_3^+ + m_3^-).$$

Physical relations:

$$T_{11} = C_{11}\Gamma_{11} + C_{12}\Gamma_{22},\ T_{22} = C_{22}\Gamma_{22} + C_{12}\Gamma_{11},\ S_{12} = C_{88}\Gamma_{12} + C_{78}\Gamma_{21},$$

$$S_{21} = C_{77}\Gamma_{21} + C_{78}\Gamma_{12},\ L_{13} = d_{66}k_{13},\ L_{23} = d_{44}k_{23}, \tag{12}$$

where

$$C_{11} = 2\left[\Delta h_1 \frac{a_{22}^1}{a_{11}^1 a_{22}^1 - \left(a_{12}^1\right)^2} + \sum_{i=1}^{n} \Delta h_{i+1} \frac{a_{22}^{i+1}}{a_{11}^{i+1} a_{22}^{i+1} - \left(a_{12}^{i+1}\right)^2}\right], \quad \cdots$$

$$d_{66} = 2\left[\Delta h_1 \frac{1}{b_{66}^1} + \sum_{i=1}^{n} \Delta h_{i+1} \frac{1}{b_{66}^{i+1}}\right], \quad \cdots. \tag{13}$$

Geometric relations:

$$\Gamma_{11} = \frac{1}{A_1}\frac{\partial u_1}{\partial \alpha_1} + \frac{1}{A_1 A_2}\frac{\partial A_1}{\partial \alpha_2}u_2,\ \Gamma_{22} = \frac{1}{A_2}\frac{\partial u_2}{\partial \alpha_2} + \frac{1}{A_1 A_2}\frac{\partial A_2}{\partial \alpha_1}u_1,$$

$$\Gamma_{12} = \frac{1}{A_1}\frac{\partial u_2}{\partial \alpha_1} - \frac{1}{A_1 A_2}\frac{\partial A_1}{\partial \alpha_2}u_1 - \Omega_3,\ \Gamma_{21} = \frac{1}{A_2}\frac{\partial u_1}{\partial \alpha_2} - \frac{1}{A_1 A_2}\frac{\partial A_2}{\partial \alpha_1}u_2 + \Omega_3,$$

$$k_{13} = \frac{1}{A_1}\frac{\partial \Omega_3}{\partial \alpha_2},\ k_{23} = \frac{1}{A_1}\frac{\partial \Omega_3}{\partial \alpha_2}, \tag{14}$$

$$k_{11} = \frac{1}{A_1}\frac{\partial \Omega_1}{\partial \alpha_1} + \frac{1}{A_1 A_2}\frac{\partial A_1}{\partial \alpha_2}\Omega_2,\ k_{22} = \frac{1}{A_1}\frac{\partial \Omega_2}{\partial \alpha_2} + \frac{1}{A_1 A_2}\frac{\partial A_2}{\partial \alpha_2}\Omega_1,\ k_{33} = \iota.$$

“Softened" boundary conditions on the boundary contour of the middle plane of the plate are the followings:

$$T_{11} = T_{11}^* \text{ or } u_1 = u_1^*,\ S_{12} = S_{12}^* \text{ or } u_2 = u_2^*,\ L_{13} = L_{13}^* \text{ or } \kappa_{13} = \kappa_{13}^*. \tag{15}$$

Equations of bending of micropolar orthotropic elastic multilayered thin plates with symmetric structure:

Equilibrium equations:

$$\frac{1}{A_1}\frac{\partial N_{13}}{\partial \alpha_1} + \frac{1}{A_1 A_2}\frac{\partial A_{21}}{\partial \alpha_1}N_{13} + \frac{1}{A_2}\frac{\partial N_{23}}{\partial \alpha_2} - \frac{T_{11}}{R_1} - \frac{T_{22}}{R_2} = q_3^+ + q_3^-,$$

$$N_{31} - \frac{1}{A_1}\frac{\partial M_{11}}{\partial \alpha_1} + \frac{1}{A_1 A_2}\frac{\partial A_2}{\partial \alpha_1}(M_{22} - M_{11}) - \frac{1}{A_2}\frac{\partial H_{21}}{\partial \alpha_2} -$$
$$-\frac{1}{A_1 A_2}\frac{\partial A_1}{\partial \alpha_2}(H_{21} + H_{12}) = h(q_1^+ - q_1^-),$$

$$N_{32} - \frac{1}{A_2}\frac{\partial M_{22}}{\partial \alpha_2} + \frac{1}{A_1 A_2}\frac{\partial A_1}{\partial \alpha_2}(M_{11} - M_{22}) - \frac{1}{A_1}\frac{\partial H_{12}}{\partial \alpha_1} -$$
$$-\frac{1}{A_1 A_2}\frac{\partial A_2}{\partial \alpha_1}(H_{12} + H_{21}) = h(q_2^+ - q_2^-), \tag{16}$$

$$\frac{1}{A_1}\frac{\partial L_{11}}{\partial \alpha_1} + \frac{1}{A_1 A_2}\frac{\partial A_2}{\partial \alpha_1}(L_{11} - L_{22}) + \frac{1}{A_2}\frac{\partial L_{21}}{\partial \alpha_2} + \frac{1}{A_1 A_2}\frac{\partial H_1}{\partial \alpha_2}(L_{21} + L_{12}) +$$
$$+N_{23} - N_{32} = -(m_1^+ + m_1^-),$$

$$\frac{1}{A_2}\frac{\partial L_{22}}{\partial \alpha_2} + \frac{1}{A_1 A_2}\frac{\partial A_1}{\partial \alpha_2}(L_{22} - L_{11}) + \frac{1}{A_1}\frac{\partial L_{12}}{\partial \alpha_1} + \frac{1}{A_1 A_2}\frac{\partial A_2}{\partial \alpha_1}(L_{12} + L_{21}) +$$
$$+N_{31} - N_{13} = -(m_2^+ + m_2^-),$$

$$L_{33} - \frac{1}{A_1}\frac{\partial \Lambda_{13}}{\partial \alpha_1} - \frac{1}{A_1 A_2}\frac{\partial A_2}{\partial \alpha_1}\Lambda_{13} - \frac{1}{A_2}\frac{\partial \Lambda_{23}}{\partial \alpha_2} - \frac{1}{A_1 A_2}\frac{\partial A_1}{\partial \alpha_2}\Lambda_{23} + \\ + H_{12} - H_{21} = h(m_3^+ - m_3^-).$$

Physical relations:

$$M_{11} = D_{11}K_{11} + D_{12}K_{22},\ \ M_{22} = D_{22}K_{22} + D_{12}K_{11},$$

$$H_{12} = D_{88}K_{12} + D_{78}K_{21},\ \ H_{21} = D_{77}K_{21} + D_{78}K_{12},\ N_{13} = \widetilde{C}_{55}\Gamma_{13} + C_{56}\Gamma_{31},$$
$$N_{31} = C_{66}\Gamma_{31} + C_{56}\Gamma_{13},\ N_{23} = C_{55}\Gamma_{23} + C_{45}\Gamma_{32},\ \ N_{32} = C_{44}\Gamma_{32} + C_{45}\Gamma_{23}, \qquad (17)$$
$$L_{11} = d_{11}k_{11} + d_{12}k_{22} + d_{13}k_{33},\ \ L_{22} = d_{22}k_{22} + d_{21}k_{11} + d_{23}k_{33},$$
$$L_{33} = d_{33}k_{33} + d_{31}k_{11} + d_{32}k_{22},\ L_{12} = d_{88}k_{12} + d_{78}k_{21},\ L_{21} = d_{77}k_{21} + d_{78}k_{12},$$
$$\Lambda_{13} = \lambda_{66}l_{13},\ \ \Lambda_{23} = \lambda_{44}l_{23},$$

where

$$D_{11} = 2\left[\frac{h_i^3 - h_{i-1}^3}{3}\frac{a_{22}^1}{a_{11}^1 a_{22}^1 - \left(a_{12}^1\right)^2} + \sum_{i=1}^{n}\frac{h_i^3 - h_{i-1}^3}{3}\frac{a_{22}^{i+1}}{a_{11}^{i+1}a_{22}^{i+1} - \left(a_{12}^{i+1}\right)^2}\right], \quad \dots$$

$$C_{44} = 2\left[\Delta h_1\frac{a_{44}^1}{a_{44}^1 a_{55}^1 - \left(a_{45}^1\right)^2} + \sum_{i=1}^{n}\Delta h_{i+1}\frac{a_{44}^{i+1}}{a_{44}^{i+1}a_{55}^{i+1} - \left(a_{45}^{i+1}\right)^2}\right], \quad \dots$$

$$d_{11} = 2\left[\Delta h_1\frac{b_{22}^1 b_{33}^1 - \left(b_{23}^1\right)^2}{\Delta^i} + \sum_{i=1}^{n}\Delta h_{i+1}\frac{b_{22}^{i+1}b_{33}^{i+1} - \left(b_{23}^{i+1}\right)^2}{\Delta^{i+1}}\right], \quad \dots \qquad (18)$$

$$\lambda_{66} = 2\left[\frac{h_i^3 - h_{i-1}^3}{3}\frac{1}{b_{66}^1} + \sum_{i=1}^{n}\frac{h_i^3 - h_{i-1}^3}{3}\frac{1}{b_{66}^{i+1}}\right], \quad \dots.$$

Geometric relations:

$$K_{11} = \frac{1}{A_1}\frac{\partial \Psi_1}{\partial \alpha_1} + \frac{1}{A_1 A_2}\frac{\partial A_1}{\partial \alpha_2}\Psi_2,\ K_{22} = \frac{1}{A_2}\frac{\partial \Psi_2}{\partial \alpha_2} + \frac{1}{A_1 A_2}\frac{\partial A_2}{\partial \alpha_1}\Psi_1,$$
$$\Gamma_{23} = -\vartheta_2 - \Omega_1,\ \Gamma_{32} = \Psi_2 + \Omega_1,\ \Gamma_{13} = -\vartheta_1 + \Omega_2,\ \Gamma_{31} = \Psi_1 - \Omega_2,$$
$$\vartheta_2 = -\frac{1}{A_2}\frac{\partial w}{\partial \alpha_2} + \frac{u_2}{R_2},\ \vartheta_1 = -\frac{1}{A_1}\frac{\partial w}{\partial \alpha_1} + \frac{u_1}{R_1},$$
$$K_{12} = \frac{1}{A_1}\frac{\partial \Psi_2}{\partial \alpha_1} - \frac{1}{A_1 A_2}\frac{\partial A_1}{\partial \alpha_2}\Psi_1 - \iota,\ K_{21} = \frac{1}{A_2}\frac{\partial \Psi_1}{\partial \alpha_1} - \frac{1}{A_1 A_2}\frac{\partial A_1}{\partial \alpha_2}\Psi_2 + \iota, \qquad (19)$$
$$k_{12} = \frac{1}{A_1}\frac{\partial \Omega_2}{\partial \alpha_1} - \frac{1}{A_1 A_2}\frac{\partial A_1}{\partial \alpha_2}\Omega_1,\ k_{21} = \frac{1}{A_2}\frac{\partial \Omega_1}{\partial \alpha_2} - \frac{1}{A_1 A_2}\frac{\partial A_2}{\partial \alpha_1}\Omega_2,$$
$$l_{13} = \frac{1}{A_1}\frac{\partial \iota}{\partial \alpha_1},\ l_{23} = \frac{1}{A_2}\frac{\partial \iota}{\partial \alpha_2},$$
$$k_{11} = \frac{1}{A_1}\frac{\partial \Omega_1}{\partial \alpha_1} + \frac{1}{A_1 A_2}\frac{\partial A_1}{\partial \alpha_2}\Omega_2,\ k_{22} = \frac{1}{A_1}\frac{\partial \Omega_2}{\partial \alpha_2} + \frac{1}{A_1 A_2}\frac{\partial A_2}{\partial \alpha_2}\Omega_1,\ k_{33} = \iota.$$

"Softened" boundary conditions are the followings:

$$N_{13} = N_{13}^* \text{ or } w = w^*,\ M_{11} = M_{11}^* \text{ or } K_{11} = K_{11}^*,\ H_{12} = H_{12}^* \text{ or } K_{12} = K_{12}^*,$$

$$L_{11} = L_{11}^* \text{ or } \kappa_{11} = \kappa_{11}^*,\ L_{12} = L_{12}^* \text{ or } \kappa_{12} = \kappa_{12}^*,\ \Lambda_{13} = \Lambda_{13}^* \text{ or } l_{13} = l_{13}^*. \tag{20}$$

On the basis of the constructed models of plane stress state (11)-(15) and bending (16)-(20) concrete problems of statics, free and forced vibrations of multilayered micropolar orthotropic plates will be studied.

## References

[1] Ivanova E.A., Krivcov A.M., Morozov N.F. Obtaining of macroscopic relations of elasticity of complex crystal lattices with consideration of momental interactions at the micro level. Applied Mathematics and Mechanics. Vol.71. N4. P.595-615. 2007.

[2] Sargsyan S.H. General mathematical models of micropolar elastic thin plates. Izvestiya NAS Armenia. Mechanics. Vol.64. N1. P. 58-67. 2011.

[3] Iesen D. Torsion of anisotropic micropolar elastic cylinders. Z Angew. Math. Mech (ZAMM). Vol. 54. N12. P. 773-779. 1974.

*Anahit J. Farmanyan, Trdat Chartarapet, 7/1, ap.9, Gyumri, Armenia*
*Samvel H. Sargsyan, Sayat Nova 2, ap. 11, Gyumri, Armenia*

# Thorny path to fusion in plasma: confinement state as a waveleton

Antonina N. Fedorova Michael G. Zeitlin
anton@math.ipme.ru, zeitlin@math.ipme.ru

**Abstract**

A fast and efficient numerical-analytical approach is proposed for description of complex behaviour in non-equilibrium ensembles in the BBGKY framework. We construct the multiscale representation for hierarchy of partition functions by means of the variational approach and multiresolution decomposition. Numerical modeling shows the creation of various internal structures from fundamental localized (eigen)modes. These patterns determine the behaviour of plasma. The localized pattern (waveleton) is a model for energy confinement state (fusion) in plasma.

**"A magnetically confined plasma cannot be in thermodinamical equilibrium"**
Unknown author ... Folklore

## 1 Introduction.

It is well known that fusion problem in plasma physics could be solved neither experimentally nor theoretically during last fifty years. At the same time, during this long period other areas of physics and engineering demonstrated vast growth, on the level of both theoretical understanding and practical smart realizability. Because financing contributions in this area definitely exceeds that of almost all other areas of Physics, it seems that there are the serious obstacles which prevent real progress in the problem of real fusion as the main subject in the area [1,2]. Of course, it may be a result of some unknown no-go theorem(s) but it seems that the current theoretical level definitely demonstrates that not all possibilities, at least on the level of theoretical and matematical modeling, are exhausted. Surely, it is more than clear that perturbations, linearization, PIC or MC do not exhaust all instruments which we have at our hands on the route to theoretical understanding and predictions. Definitely, we need much more to have influence on almost free-of-theoretical-background work of experimentalists and engineers who contribute to ITER, NIF and other related top level projects. So, this paper and related one [3] can be considered as a small contribution to an attempt to avoid the existing obstacles appeared on the main roads of current plasma physics, especially along thorny path to solution of fusion problem. Definitely, the first thing which we need to change is a framework of generic mathematical methods which can help to improve the current state of the theory. Our postulates (conjectures) are as follows [4], [7]–[23]:

**A)** The fusion problem (at least at the first step) must be considered as a problem inside the (non) equilibrium ensemble in the full phase space. It means, at least, that:

**A1)** our dynamical variables are partitions (partition functions, hierarchy of N-points partition functions),

**A2)** it is impossible to fix a priori the concrete distribution function and postulate it (e.g. Maxwell-like or other concrete (gaussian-like or even not) distributions) but, on the contrary, the proper distrubution(s) must be the solutions of proper (stochastic) dynamical problem(s), e.g., it may be the well-known framework of BBGKY hierarchy of kinetic equations or something similar. So, the full set of dynamical variables must include partitions also.

**B)** Fusion state = (meta) stable state (with minimum entropy and zero measure) in the space of partitions on the whole phase space in which most of energy of the system is concentrated in the relatively small area (preferable with measure zero) of the whole domain of definition in the phase space during the time period which is enough to take reasonable part of it outside for possible usage. From the formal/mathematical point of view it means that:

**B1)** fusion state must be localized (first of all, in the phase space),

**B2)** we need a set of building blocks, localized basic states or eigenmodes which can provide

**B3)** the creation of localized pattern which can be considered as a possible model for plasma in a fusion state. Such pattern must be:

**B4)** (meta) stable and controllable, because of obvious reasons. So, the main courses are:

**C1)** to present smart localized building blocks which may be not only useful from point of view of analytical statements, such as the best possible localization, fast convergence, sparse operators representation, etc, but also exist as real physical fundamental modes,

**C2)** to construct various possible patterns with special attention to localized pattern which can be considered as a needful thing in analysis of fusion;

**C3)** after points C1 and C2 in ensemble (BBGKY) framework to consider some standard reductions to Vlasov-like and RMS-like equations (following the set-up from well-known results [2]) which may be useful also. These particular cases may be important as from physical point of view as some illustration of general consideration [3].

The lines above are motivated by our attempts to analyze the hidden internal contents of the phrase mentioned in the epigraph of this paper: "A magnetically confined plasma cannot be in thermodinamical equilibrium." Also, it should be noted that our results below can be applied to any scenario (fusion, ignition, etc): we describe pattern formation in arbitrary non-equilibrium ensembles.

## 2 Motivations

It is obvious that any reasonable set-up for analysis of fusion leads to very complex system and one hardly believes that such system can be analyzed by means of almost exhausted methods like perturbations, linearization, etc. At the same time, because such complex chaotic/stochastic dynamics is overcompleted by short- and long-living fluctuations, instabilities, etc one needs to find something more proper than usual plane waves or gaussians for modeling a complicated complex behaviour. For reminiscences we may consider simple standard soliton equations like KdV, KP or sine-Gordon ones. It is well-known that neither linearization, nor perturbations, nor plane-wave-like approximations are proper for the reasonable analysis of such equations in contrary to wave or other simple linear equations: it is impossible to approximate the spectrum of such models (solitons, breathers or finite-gap solutions) by means of linear Fourier harmonics because they are not proper modes in complex situation. Moreover, such linear methods are not adequate in more complicated situations which are very far even from the exactly integrable case (Liouvillean

tori). It would appear that as a first step in this direction is to find a reasonable extension of understanding of the non-equilibrium dynamics as a whole. One needs to sketch up the underlying ingredients of the theory (spaces of states, observables, measures, classes of smoothness, dynamical set-up, etc.) in an attempt to provide the maximally extendable but at the same time really calculable and realizable description of the complex dynamics inside hierarchies like BBKGY and their reductions. The general idea is rather simple: it is well known that the idea of "symmetry" is the key ingredient of any reasonable physical theory from classical (in)finite dimensional (integrable) Hamiltonian dynamics to different sub-planckian models based on strings. A starting point for us is a possible model for fundamental localized modes with the subsequent description of the whole zoo of possible realizable (controllable) states/patterns which may be useful from the point of view of experimentalists and engineers. The proper representation theory is well known as "local nonlinear harmonic analysis", in particular case of simple underlying symmetry-affine group-aka wavelet analysis. From our point of view the advantages of such approach are as follows:

**i)** natural realization of localized states in any proper functional realization of (functional) space of states,

**ii)** hidden symmetry of chosen realization of proper functional model provides the (whole) spectrum of possible states via the so-called multiresolution decomposition.

So, indeed, the hidden symmetry (non-abelian affine group in the simplest case) of the space of states via proper representation theory generates the physical spectrum and this procedure depends on the choice of the functional realization of the space of states. It explicitly demonstrates that the structure and properties of the functional realization of the space of states are the natural properties of physical world at the same level of importance as a particular choice of Hamiltonian, or the equation of motion, or the action principle (variational method). It should be noted that in such picture we can naturally include the effects of self-interaction on the way of construction and subsequent analysis of nonlinear models. So, our consideration will be in the framework of (Nonlinear) Pseudodifferential Dynamics ($\Psi DOD$). Existence of such internal multiscales with different dynamics at each scale and transitions, interactions, and intermittency between scales demonstrates that statistical mechanics in BBGKY form, despite its linear structure, is really a complicated problem from the mathematical point of view. It seems, that well-known underlying "stochastic" complexity is a result of transition by means of (still rather unclear) procedure of dynamical irreversible evolution or interscale redistribution from complexity related to individual classical dynamics to the rich pseudodifferential (more exactly, microlocal) structure on the non-equilibrium ensemble side. Anyway, the whole zoo of solutions consists of possible patterns, including very important ones from the point of view of underlying physics:

**iii)** chaotic states (definitely, non proper for modeling of fusion state but proper for pre- or post-fusion description) vs. localized modes (basis modes, eigenmodes) and fusion-like localized patterns constructed from them by means of proper representation of underlying hidden symmetry group. For practical reasons controllable patterns (with prescribed behaviour) are the most useful. We mention the so-called waveleton-like pattern which we consider as the most important one. It means:

**iv)** waveleton $\approx$ (meta)stable localized (controllable) pattern.

To summarize, the approach described below allows

**v)** to solve wide classes of general $\Psi DOD$ problems, including generic for us BBGKY hierarchy and its reductions, and

**vi)** to present the analytical/numerical realization for physically interesting patterns, like fusion states.

## 3 Set-up

Let us consider the following generic $\Psi DOD$ dynamical problem

$$L^j\{Op^i\}\Psi = 0, \tag{1}$$

described by a finite or infinite number of equations which include general classes of operators $Op^i$ such as differential, integral, pseudodifferential etc. Surely, all hierarchies and their reductions are inside this class. The main objects are:

**i)** (Hilbert) space of states, $H = \{\Psi\}$, with a proper functional realization, e.g.,: $L^2$, Sobolev, Schwartz, $C^0$, $C^k$, ... $C^\infty$, ...; definitely, $L^2(R^2)$, $L^2(S^2)$, $L^2(S^1 \times S^1)$, $L^2(S^1 \times S^1 \ltimes Z_n)$ are different objects proper for different physics inside. E.g., two last cases describe tokamak and stellarator, correspondingly. Of course, they are different spaces and generate different physics.

**ii)** Class of smoothness. The proper choice determines natural consideration of dynamics with/without Chaos/Fractality properties.

**iii)** Decompositions

$$\Psi \approx \sum_i a_i e^i \tag{2}$$

via high-localized bases (wavelet families, generic wavelet packets etc), frames, atomic decomposition (Fig. 1, 2) with the following main properties: (exp) control of convergence, maximal rate of convergence for any $\Psi$ in any $H$ [5], [6].

**iv)** Observables/Operators (ODO, PDO, $\Psi DO$ , SIO,..., Microlocal analysis of Kashiwara-Shapira (with change from functions to sheaves)) satisfy the main property - the matrix representation in localized bases

$$< \Psi|Op^i|\Psi > \tag{3}$$

is maximum sparse.

$$\begin{pmatrix} D_1 & 0 & 0 & \dots \\ 0 & D_2 & 0 & \dots \\ 0 & 0 & D_3 & \dots \\ \vdots & \vdots & \vdots & \ddots \end{pmatrix}, \qquad \text{where} \qquad D_i = \begin{pmatrix} A_i & B_i \\ C_i & 0 \end{pmatrix}.$$

Such almost diagonal structure is provided by the so-called Fast Wavelet Transform [5].

**v)** Measures: multifractal wavelet measures $\{\mu_i\}$ together with the class of smoothness are very important for analysis of complicated analytical behaviour [5].

**vi)** Variational/Projection methods, from Galerkin to Rabinowitz minimax, Floer (in symplectic case of Arnold-Weinstein curves with preservation of Poisson or symplectic structures). Main advantages are the reduction to algebraic systems, which provides a tool for the smart subsequent control of behaviour and control of convergence.

**vii)** Multiresolution or multiscale decomposition, MRA (or wavelet microscope) consists of the understanding and choosing of (internal) symmetry structure, e.g., affine group = {translations, dilations} or many others; construction of representation/action of this symmetry on $H = \{\Psi\}$. As a result of such hidden coherence together with using point vi) we'll have: **a).** Localized Bases, **b).** Exact Multiscale Decomposition with the best convergence properties and real evaluation of the rate of convergence via proper "multinorms".

Fig. 4 demonstrates MRA decomposition for the kick (Fig. 3).

**viii)** Effectiveness of proper numerics: CPU-time, HDD-space, minimal complexity of algorithms, and (Shannon) entropy of calculations are provided by points i)-vii) above.

Finally, such Variational-Multiscale approach based on points i)-viii) provides us with the full possible Zoo of Patterns: localized, chaotic, etc. In next Sections we will consider details for important case of kinetic equations.

## 4 Description

So, we will consider the application of our numerical/analytical technique based on local nonlinear harmonic analysis approach for the description of complex non-equilibrium behaviour of statistical ensembles, considered in the framework of the general BBGKY hierarchy of kinetic equations, including quantum counterpart, and their different truncations/reductions [7]–[23]. The main points of our ideology are described below. All these facts are well-known or mentioned above but it is preferable to bring it together to present our arguments in most clear form.

- Kinetic theory in nonequilibrium situation is an important part of general statistical physics related to phenomena which cannot be understood on the thermodynamical or fluid models level of description as well as on the level of numerical modeling based on consideration of "collection of particles" instead of "complex non-equilibrium ensembles of particles".
- We restrict ourselves to the rational/polynomial type of nonlinearities (with respect to the set of all dynamical variables, including partitions) that allows to use our results, based on the so called multiresolution framework and the variational formulation of initial nonlinear (pseudodifferential) problems.
- Our approach is based on the set of mathematical methods which give a possibility to work with well-localized bases in functional spaces and provide the maximum sparse forms for the general type of operators (differential, integral, pseudodifferential) in such bases.
- It provides the best possible rates of convergence and minimal complexity of algorithms inside and, as a result, saves CPU time and HDD space.
- In all cases below by the system under consideration we mean the full BBGKY hierarchy or some its cut-off or its various reductions. Our scheme of cut-off for the infinite system of

equations is based on some criterion of convergence of the full solution by means of some norm introduced in the proper functional space constructed by us.

• This criterion is based on a natural norm in the proper functional space, which takes into account (non-perturbatively) the underlying multiscale structure of complex statistical dynamics. According to our approach the choice of the underlying functional space is important to understand the corresponding complex dynamics.

• It is obvious that we need accurately to fix the space, where we construct the solutions, evaluate convergence, etc. and where the very complicated infinite set of operators, appeared in the BBGKY formulation, acts.

• We underline that many concrete features of the complex dynamics are related not only to the concrete form/class of operators/equations but depend also on the proper choice of function spaces, where operators act. It should be noted that the class of smoothness (related at least to the appearance of chaotic/fractal-like type of behaviour) of the proper functional space under consideration plays a key role in the following.

• At this stage our main goal is an attempt of classification and construction of a possible zoo of nontrivial (meta) stable states/patterns: high-localized (nonlinear) eigenmodes, complex (chaotic-like or entangled) patterns, localized (stable) patterns (waveletons). We will use it later for fusion description, modeling and control.

• Localized (meta)stable pattern (waveleton) is a good image for fusion state in plasma (energy confinement).

Our constructions can be applied to the following general individual (members of ensemble under consideration) Hamiltonians:

$$H_N = \sum_{i=1}^{N} \Big( \frac{p_i^2}{2m} + U_i(q) \Big) + \sum_{1 \le i \le j \le N} U_{ij}(q_i, q_j), \tag{4}$$

where the potentials $U_i(q) = U_i(q_1, \dots, q_N)$ and $U_{ij}(q_i, q_j)$ are restricted to rational functions on the coordinates. Let $L_s$ and $L_{ij}$ be the Liouvillean operators and

$$F_N(x_1, \dots, x_N; t) \tag{5}$$

be the hierarchy of $N$-particle distribution function, satisfying the standard BBGKY hierarchy ($\upsilon$ is the volume):

$$\frac{\partial F_s}{\partial t} + L_s F_s = \frac{1}{\upsilon} \int d\mu_{s+1} \sum_{i=1}^{s} L_{i,s+1} F_{s+1}. \tag{6}$$

Our key point is the proper nonperturbative generalization of the previous perturbative multiscale approaches (like Bogolubov/virial expansions). The infinite hierarchy of distribution functions is:

$$\begin{aligned} &F = \{F_0, F_1(x_1; t), \dots, F_N(x_1, \dots, x_N; t), \dots\}, \\ &F_p(x_1, \dots, x_p; t) \in H^p, \quad H^0 = R, \ H^p = L^2(R^{6p}), \\ &F \in H^\infty = H^0 \oplus H^1 \oplus \dots \oplus H^p \oplus \dots \end{aligned} \tag{7}$$

with the natural Fock space like norm (guaranteeing the positivity of the full measure):

$$(F, F) = F_0^2 + \sum_i \int F_i^2(x_1, \dots, x_i; t) \prod_{\ell=1}^{i} \mu_\ell. \tag{8}$$

• Multiresolution decomposition (filtration) naturally and efficiently introduces the infinite sequence (tower) of the underlying hidden scales, which is a sequence of increasing closed subspaces $V_j \in L^2(R)$:

$$...V_{-2} \subset V_{-1} \subset V_0 \subset V_1 \subset V_2 \subset ... \tag{9}$$

• Our variational approach reduces the initial problem to the problem of solution of functional equations at the first stage and some algebraic problems at the second one.

Let $L$ be an arbitrary (non)linear differential/integral operator with matrix dimension $d$ (finite or infinite), which acts on some set of functions from $L^2(\Omega^{\otimes^n})$: $\Psi \equiv \Psi(t, x_1, x_2, \dots) = \Big(\Psi^1(t, x_1, x_2, \dots), \dots, \Psi^d(t, x_1, x_2, \dots)\Big)$, $x_i \in \Omega \subset \mathbf{R}^6$, $n$ is the number of particles:

$$\begin{aligned} &L\Psi \equiv L(Q, t, x_i)\Psi(t, x_i) = 0, \\ &Q \equiv Q_{d_0,d_1,d_2,\dots}(t, x_1, x_2, \dots, \partial/\partial t, \partial/\partial x_1, \partial/\partial x_2, \dots, \int \mu_k) \\ &= \sum_{i_0,i_1,i_2,\dots=1}^{d_0,d_1,d_2,\dots} q_{i_0 i_1 i_2 \dots}(t, x_1, x_2, \dots)\Big(\frac{\partial}{\partial t}\Big)^{i_0}\Big(\frac{\partial}{\partial x_1}\Big)^{i_1}\Big(\frac{\partial}{\partial x_2}\Big)^{i_2} \dots \int \mu_k. \end{aligned} \tag{10}$$

Let us consider now the $N$ mode approximation for the solution as the following ansatz:

$$\Psi^N(t, x_1, x_2, \dots) = \sum_{i_0,i_1,i_2,\dots=1}^{N} a_{i_0 i_1 i_2 \dots} A_{i_0} \otimes B_{i_1} \otimes C_{i_2} \dots (t, x_1, x_2, \dots). \tag{11}$$

We shall determine the expansion coefficients from the following conditions:

$$\ell^N_{k_0,k_1,k_2,\dots} \equiv \int (L\Psi^N) A_{k_0}(t) B_{k_1}(x_1) C_{k_2}(x_2) \mathrm{d}t \mathrm{d}x_1 \mathrm{d}x_2 \cdots = 0. \tag{12}$$

As a result the solution has the following multiscale/multiresolution decomposition via nonlinear high-localized eigenmodes

$$\begin{aligned} &F(t, x_1, x_2, \dots) = \sum_{(i,j) \in Z^2} a_{ij} U^i \otimes V^j(t, x_1, x_2, \dots), \\ &V^j(t) = V_N^{j,slow}(t) + \sum_{l \geq N} V_l^j(\omega_l t),\ \omega_l \sim 2^l, \\ &U^i(x_s) = U_M^{i,slow}(x_s) + \sum_{m \geq M} U_m^i(k_m^s x_s),\ k_m^s \sim 2^m, \end{aligned} \tag{13}$$

These formulas give the expansion into a slow and fast oscillating parts. So, we may move from the coarse scales of resolution (coarse graining) to the finest ones for obtaining more detailed information about the dynamical process.

• In this way one obtains contributions to the full solution from each scale of resolution or each time/space scale or from each nonlinear eigenmode.

• It should be noted that such representations give the best possible localization properties in the corresponding (phase) space/time coordinates.

• Numerical calculations are based on compactly supported wavelets and related wavelet families and on evaluation of the accuracy on the level $N$ of the corresponding cut-off of the full system w.r.t. the norm (8):

$$\|F^{N+1} - F^N\| \leq \varepsilon \tag{14}$$

• Numerical modeling shows the creation of various internal structures from localized modes, which are related to (meta)stable or unstable type of behaviour and the corresponding patterns (waveletons) formation. Reduced algebraic structure provides the pure algebraic control of stability/unstability scenario.
• So, we considered the construction for controllable (meta) stable waveleton configuration representing a reasonable approximation for the possible realizable confinement state.

# 5 Conclusions

Let us summarize our main results:

### Physical Conjectures:

**P1** State of fusion (confinement of energy) in plasma physics may and need be considered from the point of view of non-equilibrium statistical physics. According to this BBGKY framework looks naturally as first iteration. Main dynamical variables are partitions.

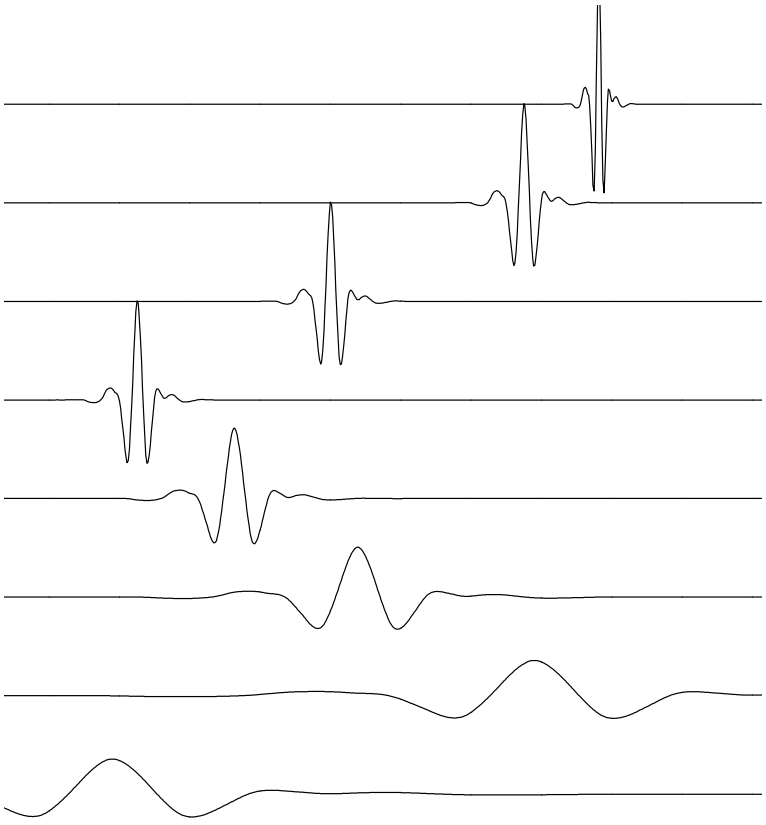

Figure 1: Localized Modes.

**P2** High localized nonlinear eigenmodes (Figs. 1, 2) are real physical modes important for fusion modeling. Intermode multiscale interactions create various patterns from these fundamental building blocks, and determine the behaviour of plasma (Fig. 5). High localized (meta) stable patterns (waveletons), considered as long-living fluctuations, are proper images for plasma in fusion state (Fig. 6).

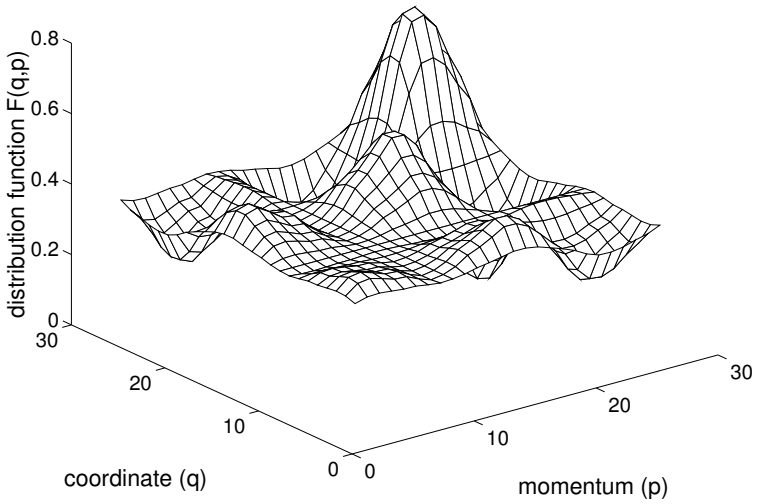


Figure 2: Two-dimensional Localized Mode Contribution to Distribution Function.

## Mathematical framework:

**M1** The problems under consideration, like BBGKY hierarchies (6) or their reductions from paper [3] are considered as $\Psi DO$ problems in the framework of proper family of methods unified by effective multiresolution approach or local nonlinear harmonic analysis on the orbits of representations of hidden underlying symmetry of properly chosen functional space.

**M2** Formulae (13) based on generalized dispersion relations (GDR) (12) provide exact multiscale representation for all dynamical variables (partitions, first of all) in the basis of high-localized nonlinear (eigen)modes. Numerical realizations in this framework are maximally effective from the point of view of complexity of all algorithms inside. GDR provide the way for the state control on the algbraic level.

**Realizability**

According to this approach, it is possible on formal level, in principle, to control ensemble behaviour and to realize the localization of energy (confinement state) inside the waveleton configurations created from a few fundamentals modes only during self-organization via possible (external) control (Fig. 7, 8).

**Open Questions**

**Q1** Definitely, all above is only very naive ensemble approach. Current level of non-equilibrium statistical physics provides us only by BBGKY generic framework. All related internal unsolved problems are well-known but we still have nothing better. At the same time possible Vlasov-like reductions or phenomenological models also look as very far from reasonable from the point of view of the fusion problem set-up.

**Q2** Considering for allusion successful areas of physics like superconductivity, for example, we may conclude that only microscopic BCS formulation provides the full explanation although Ginzburg-Landau (GL) phenomenological approach and even Froelich's and London's ones contributed to the general picture. Whether Vlasov equations are the analogue of GL ones and whether it is possible to construct microscopic model for plasma, these two important questions remain unanswered at present time.

**Q3** It may be natural also that approaches proposed in this paper and related ones are wrong because the proper and adequate framework for solution of fusion problem is re-

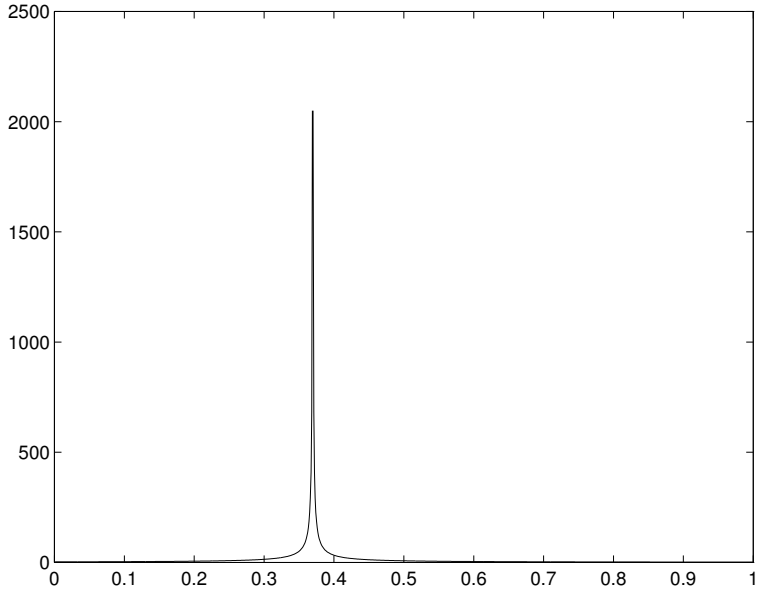


Figure 3: Kick.

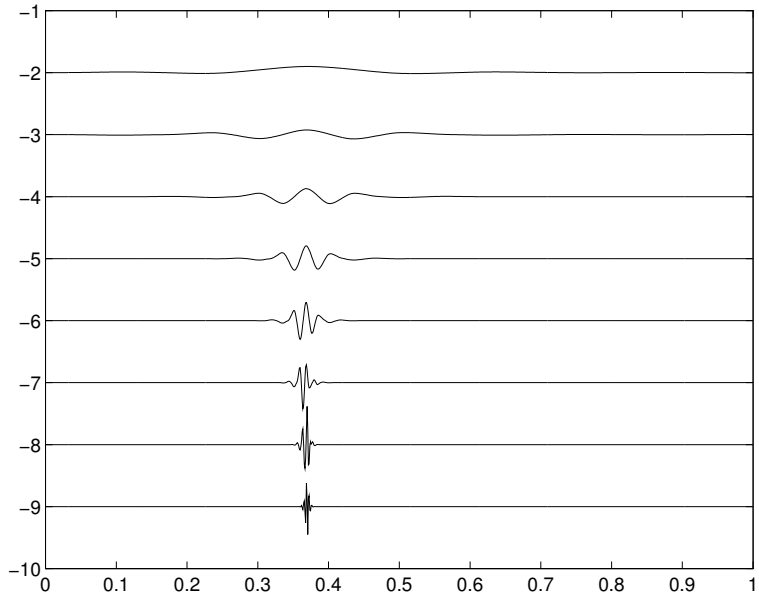


Figure 4: MRA for Kick.

lated to confinement of magnetic lines or loops (new physical dynamical variables instead of partitions) or fluxes instead of confinement of localized point modes (attribute of any local field theory) considered as new and really proper physical variables (magnetic reconnection problem can be considered in the same framework). Such an approach demands the topological background related to proper mathematical constructions. As allusion it is possible to consider, e.g., the description of (fractional) quantum Hall effect by means of Chern-Simons/anyon models which allow to describe the dynamics on (of) knots and braids analytically. Anyway, it is still possible to apply successfull methods from (M1) and (M2) here too. Other open possibility is related to taking into account internal quantum properties. From this point of view our approach is very useful because we unify quantum description and its classical counterpart in the general $\Psi DO$ framework [4]. We believe

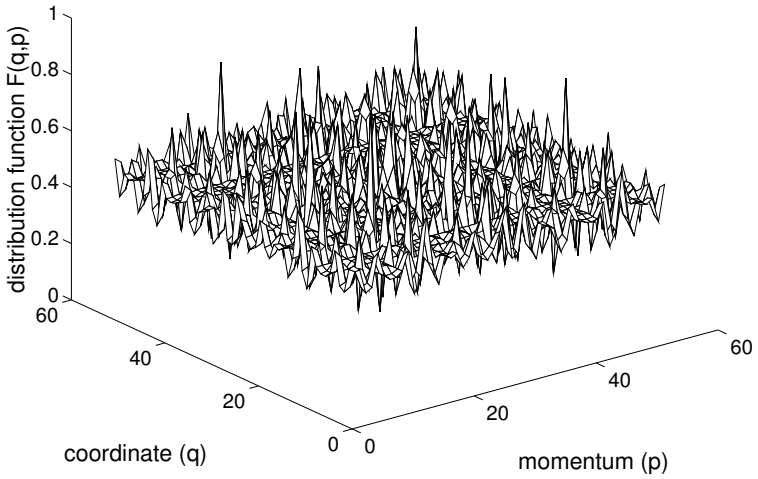


Figure 5: Trash: Chaotic Partition.

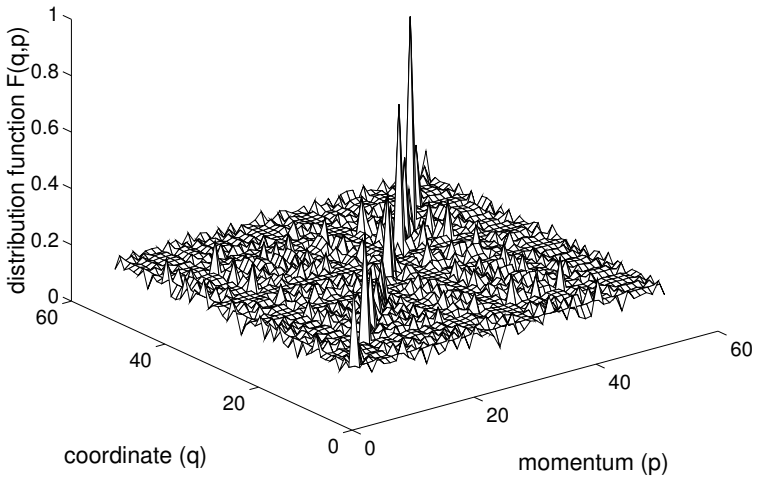


Figure 6: Goal: Localized Partition.

that the appearance of nontrivial localized (meta) stable patterns (Fig. 7, 8) observed by these methods is a general effect which present in the full BBGKY-hierarchy, due to its complicated intrinsic multiscale dynamics and it depends on neither the cut-off level nor the phenomenological-like hypothesis on correlators. So, representations for solutions like (13) and as a result the prediction of the existence of the (meta) stable localized patterns/states (waveletons) which can realize energy confinement (fusion) states in BBGKY-like systems are the main results of this approach. In addition, such an approach open the way to solve the control problem by means of reduction from initial (pseudodifferential) formulation to reduced set of algebraic one (12) and as a result to create and support the needed fusion state(s) after solution of proper control problem.

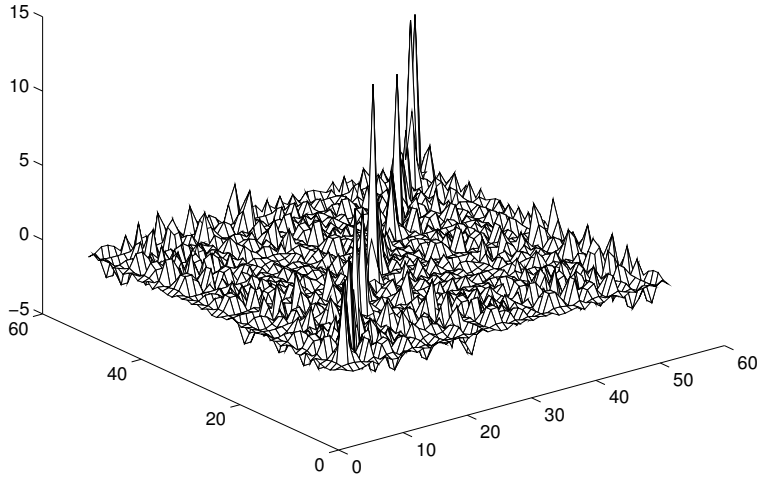


Figure 7: Fusion-like state: Confinement of Energy.

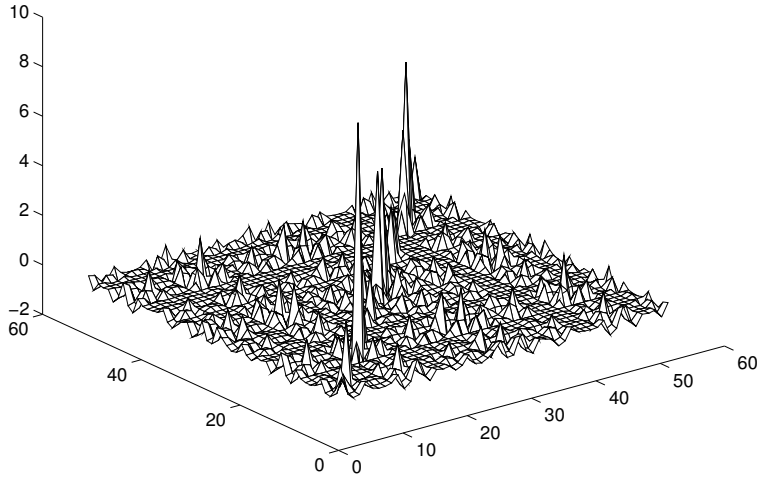


Figure 8: Fusion-like state: Waveleton Pattern.

## Acknowledgement

We are very grateful to National Science Foundation (NSF), Institute for Pure and Applied Mathematics (IPAM) at University of California, Los Angeles, where this work was partly done, for financial support and invitation to Program "Computational Methods in High Energy Density Plasmas". We would like to thank Organizers, Professors R. Caflisch (IPAM), C. Ratsch (IPAM), F. Graziani (LLNL), Ms. S. Beggs for permanent support and patience, Prof. T. Barth (NASA) for fruitful work in his Working Group and all participants for useful discussions in different areas of Plasma Physics.

## References


[1] *A. H. Boozer*, Rev. Mod. Phys., 76, 1071 (2004).

[2] *R. C. Davidson and H. Qin*, Physics of Intense Charged Particle Beams in High Energy Accelerators (World Scientific, Singapore, 2001); R. Balescu, Equilibrium and Nonequilibrium Statistical Mechanics, (Wiley, New York, 1975).

[3] *A. N. Fedorova and M. G. Zeitlin*, Multiscale Representation for Vlasov Equations, This Volume.

[4] *A. N. Fedorova and M. G. Zeitlin*, a list of papers/preprints (including links to arXiv) can be found on web sites below.

[5] Y. Meyer, Wavelets and Operators (Cambridge Univ. Press, 1990); G. Beylkin, R. Coifman, V. Rokhlin, Fast Wavelet transform and Numerical Algorithms, Comm. Pure Applid Math, 44, 141-183, 1991.

[6] F. Auger e.a., *Time-Frequency Toolbox* (CNRS, 1996); D. Donoho, *WaveLab* (Stanford, 2000).

[7] A.N. Fedorova and M.G. Zeitlin, Quasiclassical Calculations for Wigner Functions via Multiresolution, Localized Coherent Structures and Patterns Formation in Collective Models of Beam Motion, in *Quantum Aspects of Beam Physics*, Ed. P. Chen (World Scientific, Singapore, 2002) pp. 527–538, 539–550; arXiv: physics/0101006; physics/0101007.

[8] A.N. Fedorova and M.G. Zeitlin, BBGKY Dynamics: from Localization to Pattern Formation, in *Progress in Nonequilibrium Green's Functions II*, Ed. M. Bonitz, (World Scientific, 2003) pp. 481–492; arXiv: physics/0212066.

[9] A.N. Fedorova and M.G. Zeitlin, Pattern Formation in Wigner-like Equations via Multiresolution, in *Quantum Aspects of Beam Physics*, Eds. Pisin Chen, K. Reil (World Scientific, 2004) pp. 22-35; Preprint SLAC-R-630; arXiv: quant-ph/0306197.

[10] A.N. Fedorova and M.G. Zeitlin, Localization and pattern formation in Wigner representation via multiresolution, *Nuclear Inst. and Methods in Physics Research, A*, **502A/2-3**, pp. 657 - 659, 2003; arXiv: quant-ph/0212166.

[11] A.N. Fedorova and M.G. Zeitlin, Fast Calculations in Nonlinear Collective Models of Beam/Plasma Physics, *Nuclear Inst. and Methods in Physics Research, A*, **502/2-3**, pp. 660 - 662, 2003; arXiv: physics/0212115.

[12] A.N. Fedorova and M.G. Zeitlin, Classical and quantum ensembles via multiresolution: I-BBGKY hierarchy; Classical and quantum ensembles via multiresolution. II. Wigner ensembles; *Nucl. Instr. Methods Physics Res.*, **534A** (2004)309-313; 314-318; arXiv: quant-ph/0406009; quant-ph/0406010.

[13] A.N. Fedorova and M.G. Zeitlin, Localization and Pattern Formation in Quantum Physics. I. Phenomena of Localization, in *The Nature of Light: What is a Photon? SPIE*, vol.**5866**, pp. 245-256, 2005; arXiv: quant-ph/0505114;

[14] A.N. Fedorova and M.G. Zeitlin, Localization and Pattern Formation in Quantum Physics. II. Waveletons in Quantum Ensembles, in *The Nature of Light: What is a Photon?SPIE*, vol. **5866**, pp. 257-268, 2005; arXiv: quant-ph/0505115.

[15] A.N. Fedorova and M.G. Zeitlin, Pattern Formation in Quantum Ensembles, *Intl. J. Mod. Physics* **B20**(2006)1570-1592; arXiv: 0711.0724.

[16] A.N. Fedorova and M.G. Zeitlin, Patterns in Wigner-Weyl approach, Fusion modeling in plasma physics: Vlasov-like systems, *Proceedings in Applied Mathematics and Mechanics (PAMM)*, Volume **6**, Issue 1, p. 625, p. 627, Wiley InterScience, 2006; arXiv:1012.4971, arXiv:1012.4965.

[17] A.N. Fedorova and M.G. Zeitlin, Localization and Fusion Modeling in Plasma Physics. Part I: Math Framework for Non-Equilibrium Hierarchies, pp.61-86, in *Current Trends in International Fusion Research*, Ed. E. Panarella, R. Raman, National Research Council (NRC) Research Press, Ottawa, Ontario, Canada, 2009; arXiv: physics/0603167.

[18] A.N. Fedorova and M.G. Zeitlin, Localization and Fusion Modeling in Plasma Physics. Part II: Vlasov-like Systems. Important Reductions, pp.87-100, in *Current Trends in International Fusion Research*, Ed. E. Panarella, R. Raman, National Research Council (NRC) Research Press, Ottawa, Ontario, Canada, 2009; arXiv: physics/0603169.

[19] A.N. Fedorova and M.G. Zeitlin, Fusion State in Plasma as a Waveleton (Localized (Meta)-Stable Pattern), p. 272, in *AIP Conference Proceedings*, Volume **1154**, Issue 1, *Current Trends in International Fusion Research*, Ed. E. Panarella, R. Raman, AIP, 2009, doi:10.1063/1.3204585.

[20] A.N. Fedorova and M.G. Zeitlin, Exact Multiscale Representations for (Non)-Equilibrium Dynamics of Plasma, p.291, in *AIP Conference Proceedings*, Volume **1154**, Issue 1, *Current Trends in International Fusion Research*, Ed. E. Panarella, R. Raman, AIP, 2009, doi:10.1063/1.3204592.

[21] A.N. Fedorova and M.G. Zeitlin, Fusion Modeling in Vlasov-Like Models, *Journal Plasma Fusion Res. Series*, Vol. **8**, pp. 126-131, 2009.

[22] A.N. Fedorova and M.G. Zeitlin, Quantum points/patterns, Part 2: from quantum points to quantum patterns via multiresolution, SPIE, vol. 8121, 81210K (2011), doi:10.1117/12.893537; arXiv:1109.5042.

[23] A.N. Fedorova and M.G. Zeitlin, Quantum points/patterns, Part 1. From geometrical points to quantum points in sheaf framework , SPIE, vol. 8121, 81210J (2011), doi:10.1117/12.893502; arXiv:1109.5035.

*Antonina N. Fedorova, Michael G. Zeitlin*
*Mathematical Methods in Mechanics Group, IPME RAS, V.O. Bolshoj pr., 61, 199178, St. Petersburg, Russia*
*http://www.ipme.ru/zeitlin.html, http:/mp.ipme.ru/zeitlin.html*

# Multiscale representation for Vlasov equations

Antonina N. Fedorova Michael G. Zeitlin
anton@math.ipme.ru, zeitlin@math.ipme.ru

**Abstract**

We consider the applications of a numerical-analytical approach based on multiscale variational wavelet technique to the systems with collective type behaviour described by some forms of Vlasov-Poisson/Maxwell equations. We calculate the exact fast convergent representations for solutions in framework of multiresolution decompositions via high-localized nonlinear eigenmodes (wavelet-like base functions), which correspond to internal hidden symmetry of underlying functional spaces. It allows to control process of self-organization during evolution from chaos to localization on the pure algebraical level of generalized dispersion relations.

## 1 Introduction

In this paper we consider the applications of numerical-analytical approach based on multiscale variational wavelet technique to the systems with collective type behaviour described by some forms of Vlasov-Poisson/Maxwell equations [1], [2]. Such approach may be useful in all models in which it is possible and reasonable to reduce all complicated problems related with statistical distributions to the problems described by the systems of nonlinear ordinary/partial differential/integral equations with or without some (functional) constraints. In periodic accelerators and transport systems at the high beam currents and charge densities the effects of the intense self-fields, which are produced by the beam space charge and currents, determinine (possible) equilibrium states, stability and transport properties according to underlying nonlinear dynamics [2]. The dynamics of such space-charge dominated high brightness beam systems can provide the understanding of the instability phenomena such as emittance growth, mismatch, halo formation related to the complicated behaviour of underlying hidden nonlinear modes outside of perturbative tori-like KAM regions. Our analysis is based on the variational-wavelet approach [3], [4], [7]–[23], which allows us to consider polynomial and rational type of nonlinearities. In some sense our approach is direct generaliztion of traditional nonlinear $\delta F$ approach in which weighted Klimontovich representation

$$\delta f_j = a_j \sum_{i=1}^{N_j} w_{ji} \delta(x - x_{ji}) \delta(p - p_{ji}) \tag{1}$$

or self-similar decompostion [2] like

$$\delta n_j = b_j \sum_{i=1}^{N_j} w_{ji} s(x - x_{ji}), \tag{2}$$

where $s(x - x_{ji})$ is a shape function of distributing particles on the grids in configuration space, are replaced by powerful technique from local nonlinear harmonic analysis, based

on underlying symmetries of functional space such as affine or more general. The solution has the multiscale/multiresolution decomposition via nonlinear high-localized eigenmodes, which corresponds to the full multiresolution expansion in all underlying time/phase space scales. Starting from Vlasov-Poisson equations in part 2, we consider the approach based on multiscale variational-wavelet formulation in part 3. We give the explicit representation for all dynamical variables in the base of compactly supported wavelets or nonlinear eigenmodes. Our solutions are parametrized by solutions of a number of reduced algebraical problems one from which is nonlinear with the same degree of nonlinearity as initial problem and the others are the linear problems which correspond to the particular method of calculations inside concrete wavelet scheme. Because our approach started from variational formulation we can control evolution of instability on the pure algebraical level of reduced algebraical system of equations by means of generalized dispersion relations. It allows to control stability/unstability scenario of evolution in parameter space on pure algebraical level. In all these models numerical modeling demonstrates the appearance of coherent high-localized structures and as a result we may control process of localized pattern formation or self- organization of the (meta)stable long-living fluctuations (waveletons) from standard chaotic- like behaviour.

## 2 Vlasov-Poisson equations

Analysis based on the non-linear Vlasov equations leads to more clear understanding of collective effects and nonlinear beam dynamics of high intensity beam propagation in periodic-focusing and uniform-focusing transport systems. We consider the following form of equations (refs. [1], [2] for setup and designation):

$$\Big\{\frac{\partial}{\partial s}+p_x\frac{\partial}{\partial x}+p_y\frac{\partial}{\partial y}-\Big[k_x(s)x+\frac{\partial\psi}{\partial x}\Big]\frac{\partial}{\partial p_x}-$$
$$\Big[k_y(s)y+\frac{\partial\psi}{\partial y}\Big]\frac{\partial}{\partial p_y}\Big\}f_b(x,y,p_x,p_y,s)=0, \tag{3}$$
$$\Big(\frac{\partial^2}{\partial x^2}+\frac{\partial^2}{\partial y^2}\Big)\psi=-\frac{2\pi K_b}{N_b}\int \mathrm{d}p_x\mathrm{d}p_y f_b, \tag{4}$$
$$\int \mathrm{d}x\mathrm{d}y\mathrm{d}p_x\mathrm{d}p_y f_b=N_b \tag{5}$$

The corresponding Hamiltonian for transverse single-particle motion is given by

$$H(x,y,p_x,p_y,s)=\frac{1}{2}(p_x^2+p_y^2)+\frac{1}{2}[k_x(s)x^2 \tag{6}$$
$$+k_y(s)y^2]+H_1(x,y,p_x,p_y,s)+\psi(x,y,s),$$

where $H_1$ is nonlinear (polynomial/rational) part of the full Hamiltonian and corresponding characteristic equations are:

$$\frac{\mathrm{d}^2x}{\mathrm{d}s^2}+k_x(s)x+\frac{\partial}{\partial x}\psi(x,y,s) = 0 \tag{7}$$
$$\frac{\mathrm{d}^2y}{\mathrm{d}s^2}+k_y(s)y+\frac{\partial}{\partial y}\psi(x,y,s) = 0 \tag{8}$$

## 3 Multiscale representations

We obtain our multiscale/multiresolution representations for solutions of equations (3)-(8) via variational-wavelet approach. We decompose the solutions as

$$f_b(s,x,y,p_x,p_y) = \sum_{i=i_c}^{\infty} \oplus \delta^i f(s,x,y,p_x,p_y) \tag{9}$$

$$\psi(s,x,y) = \sum_{j=j_c}^{\infty} \oplus \delta^j \psi(s,x,y) \tag{10}$$

$$x(s) = \sum_{k=k_c}^{\infty} \oplus \delta^k x(s), \quad y(s) = \sum_{\ell=\ell_c}^{\infty} \oplus \delta^\ell y(s) \tag{11}$$

where set $(i_c, j_c, k_c, \ell_c)$ corresponds to the coarsest level of resolution (coarse graining) $c$ in the full multiresolution decomposition [5], [6]:

$$V_c \subset V_{c+1} \subset V_{c+2} \subset \dots \tag{12}$$

Introducing detail space $W_j$ as the orthonormal complement of $V_j$ with respect to $V_{j+1}$ : $V_{j+1} = V_j \bigoplus W_j$, we have for $f$, $\psi$, $x$, $y \subset L^2(\mathbf{R})$ from decompositions (9)-(11) the full fine-grained representation:

$$L^2(\mathbf{R}) = \overline{V_c \bigoplus_{j=c}^{\infty} W_j}, \tag{13}$$

In some sense (9)-(11) can be considered as generalization of the old $\delta F$ approach [1], [2].

Let $L$ be an arbitrary (non) linear differential/integral operator with matrix dimension $d$, which acts on some set of functions $\Psi \equiv \Psi(s,x) = \Big(\Psi^1(s,x), \dots, \Psi^d(s,x)\Big)$, $s, x \in \Omega \subset \mathbf{R}^{n+1}$ from $L^2(\Omega)$:

$$L\Psi \equiv L(R(s,x),s,x)\Psi(s,x) = 0, \tag{14}$$

($x$ are the generalized space coordinates or phase space coordinates, $s$ is "time" coordinate). After some anzatzes [4] the main reduced problem may be formulated as the system of ordinary differential equations

$$\begin{aligned} &Q_i(f)\frac{\mathrm{d}f_i}{\mathrm{d}s} = P_i(f,s), \quad f = (f_1, ..., f_n), \\ &i = 1, \dots, n, \quad \max_i deg\ P_i = p, \quad \max_i deg\ Q_i = q \end{aligned} \tag{15}$$

or a set of such systems corresponding to each independent coordinate in phase space. They have the fixed initial (or boundary) conditions $f_i(0)$, where $P_i, Q_i$ are not more than polynomial functions of dynamical variables $f_j$ and have arbitrary dependence on time. As result we have the following reduced algebraical system of equations, the Generalized Dispersion Relations (GDR), on the set of unknown coefficients $\lambda_i^k$ of localized eigenmode expansion (formula (17) below):

$$L(Q_{ij}, \lambda, \alpha_I) = M(P_{ij}, \lambda, \beta_J), \tag{16}$$

where operators L and M are algebraization of RHS and LHS of initial problem (15) and $\lambda$ are unknowns of reduced system of algebraical equations (RSAE) (16). After solution of

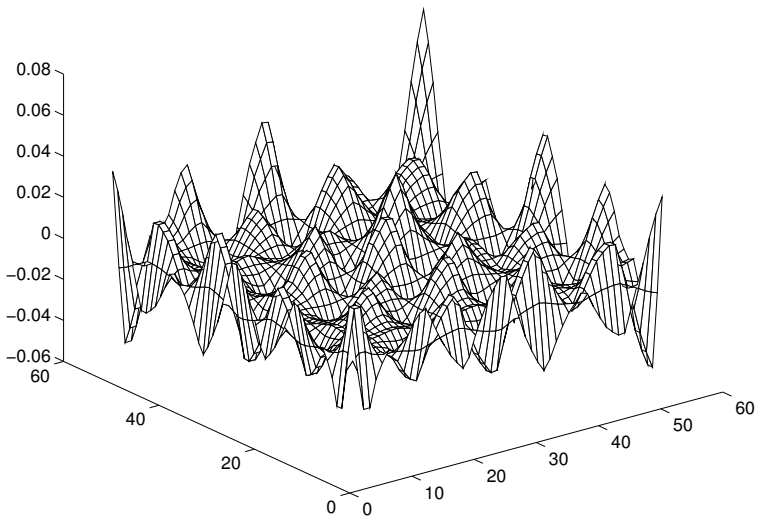


Figure 1: New Localized Modes

GDR, RSAE (16), we determine the coefficients of wavelet expansion and therefore obtain the solution of our initial problem. It should be noted that if we consider only truncated expansion with N terms then we have from (16) the system of $N \times n$ algebraical equations with degree $\ell = max\{p, q\}$ and the degree of this algebraical system coincides with degree of initial differential system. So, we have the solution of the initial nonlinear (rational) problem in the form

$$f_i(s) = f_i(0) + \sum_{k=1}^{N} \lambda_i^k f_k(s), \tag{17}$$

where coefficients $\lambda_i^k$ are the roots of the corresponding reduced algebraical (polynomial) problem, GDR (16). Consequently, we have a parametrization of solution of initial problem by the solution of reduced algebraical problem (16). The obtained solutions are given in the form (17), where $f_k(t)$ are basis functions obtained via multiresolution expansions (9)-(11), (13) and represented by some compactly supported wavelets. As a result, the solution of equations (3)-(8) has the following multiscale/multiresolution decomposition via nonlinear high-localized eigenmodes, which corresponds to the full multiresolution expansion in all underlying scales (13) starting from coarsest one (polynomial tensor bases and proper norms are considered in [4]; $\mathbf{x} = (x, y, p_x, p_y)$):

$$\begin{aligned}
\Psi(s, \mathbf{x}) &= \sum_{(i,j)\in Z^2} a_{ij} \mathbf{U}^i \otimes V^j(s, \mathbf{x}), \\
V^j(s) &= V_N^{j,slow}(s) + \sum_{l \geq N} V_l^j(\omega_l s), \quad \omega_l \sim 2^l \\
\mathbf{U}^i(\mathbf{x}) &= \mathbf{U}_M^{i,slow}(\mathbf{x}) + \sum_{m \geq M} \mathbf{U}_m^i(k_m \mathbf{x}), \quad k_m \sim 2^m,
\end{aligned} \tag{18}$$

Decomposition (18) gives us expansion into the slow part $\Psi_{N,M}^{slow}$ and fast oscillating parts for arbitrary N, M. So, we may move from coarse scales of resolution to the finest one for obtaining more detailed information about our dynamical process. The first terms

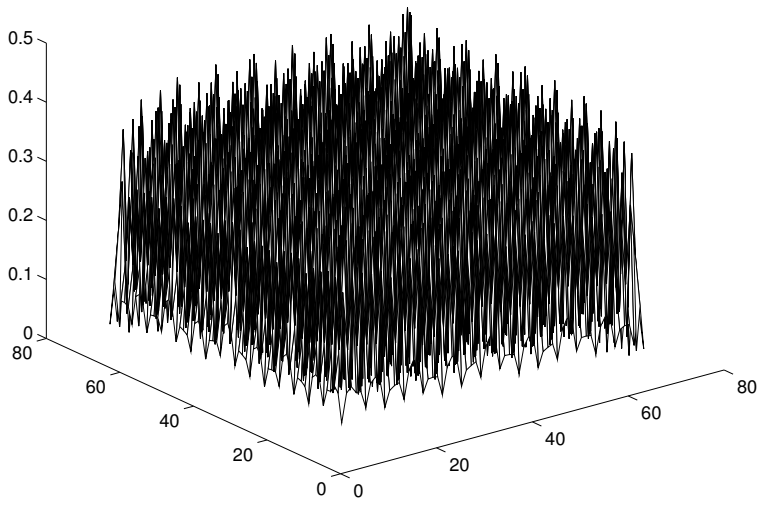


Figure 2: Chaotic-like Pattern

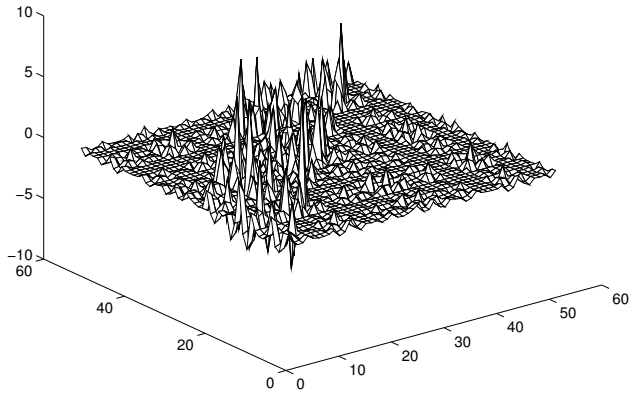


Figure 3: On the Route to Self-organization: From Chaos to Localization

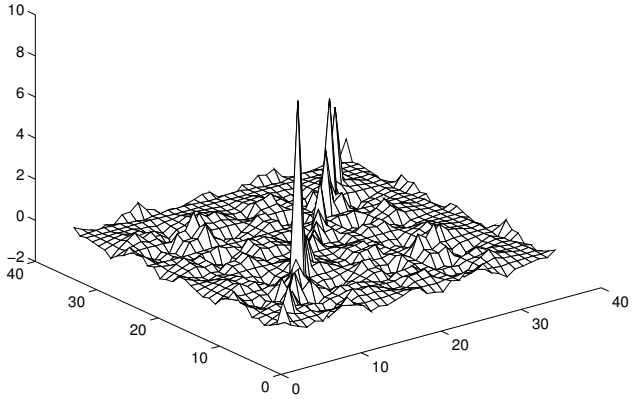


Figure 4: Localized Pattern: Waveleton

in the RHS of formulas (18) correspond on the global level of function space decomposition to resolution space and the second ones to detail space. It should be noted that such representations give the best possible localization properties in the corresponding (phase)space/time coordinates. In contrast with different approaches formulas (18) do not use perturbation technique or linearization procedures. So, by using wavelet bases with their good (phase) space/time localization properties we can describe high-localized (coherent) structures in spatially-extended stochastic systems with collective behaviour. Modelling demonstrates the appearance of (meta)stable localized pattern formation from high-localized coherent base structures or chaotic behaviour [3]. On Fig. 1 we present contribution to the full expansion from the coarsest level of resolution (base fundamental localized non-linear eigenmodes) of decomposition (18). Figs. 2-4 show the representation for the controllable (via GDR (16)) process of self-organization during the evolution of pattern formation: from chaotic-like pattern (Fig. 2) via partly localized pattern (Fig. 3) to our main goal, localized pattern or waveleton (Fig. 4). It is a universal model for long-living (meta)stable state/fluctuation useful in many applications, in both beam physics and plasma physics. GDR (16) provide a way for state control on the algebraic level. According to this approach, it is possible on the formal level, in principle, to control ensemble behaviour and to realize the localization of energy (confinement state) inside waveleton configurations created from a few fundamental physical modes only. Definitely, it is a good pre-image for fusion modeling in plasma.

## Acknowledgement

We are very grateful to National Science Foundation (NSF), Institute for Pure and Applied Mathematics (IPAM) at University of California, Los Angeles, where this work was partly done, for financial support and invitation to Program "Computational Methods in High Energy Density Plasmas". We would like to thank Organizers, Professors R. Caflisch (IPAM), C. Ratsch (IPAM), F. Graziani (LLNL), Ms. S. Beggs for permanent support and patience, Prof. T. Barth (NASA) for fruitful work in his Working Group and all participants for useful discussions in different areas of Plasma Physics.

## References

[1] *A. H. Boozer*, Rev. Mod. Phys., 76, 1071 (2004).

[2] *R. C. Davidson and H. Qin*, Physics of Intense Charged Particle Beams in High Energy Accelerators (World Scientific, Singapore, 2001); R.C. Davidson, e.a., Phys. Rev., ST AB, 4, 104401, 2001; Phys. Rev., ST AB, 3, 084401, 2000; R. Balescu, Equilibrium and Nonequilibrium Statistical Mechanics, (Wiley, New York, 1975).

[3] *A. N. Fedorova and M. G. Zeitlin*, Thorny Path to Fusion in Plasma: Confinement State as a Waveleton, This Volume.

[4] *A. N. Fedorova and M. G. Zeitlin*, a list of papers/preprints (including links to arXiv) can be found on web sites below.

[5] Y. Meyer, Wavelets and Operators (Cambridge Univ. Press, 1990); G. Beylkin, R. Coifman, V. Rokhlin, Fast Wavelet transform and Numerical Algorithms, Comm. Pure Applid Math, 44, 141-183, 1991.

[6] F. Auger e.a., *Time-Frequency Toolbox* (CNRS, 1996); D. Donoho, *WaveLab* (Stanford, 2000).

[7] A.N. Fedorova and M.G. Zeitlin, Quasiclassical Calculations for Wigner Functions via Multiresolution, Localized Coherent Structures and Patterns Formation in Collective Models of Beam Motion, in *Quantum Aspects of Beam Physics*, Ed. P. Chen (World Scientific, Singapore, 2002) pp. 527–538, 539–550; arXiv: physics/0101006; physics/0101007.

[8] A.N. Fedorova and M.G. Zeitlin, BBGKY Dynamics: from Localization to Pattern Formation, in *Progress in Nonequilibrium Green's Functions II*, Ed. M. Bonitz, (World Scientific, 2003) pp. 481–492; arXiv: physics/0212066.

[9] A.N. Fedorova and M.G. Zeitlin, Pattern Formation in Wigner-like Equations via Multiresolution, in *Quantum Aspects of Beam Physics*, Eds. Pisin Chen, K. Reil (World Scientific, 2004) pp. 22-35; Preprint SLAC-R-630; arXiv: quant-ph/0306197.

[10] A.N. Fedorova and M.G. Zeitlin, Localization and pattern formation in Wigner representation via multiresolution, *Nuclear Inst. and Methods in Physics Research, A*, **502A/2-3**, pp. 657 - 659, 2003; arXiv: quant-ph/0212166.

[11] A.N. Fedorova and M.G. Zeitlin, Fast Calculations in Nonlinear Collective Models of Beam/Plasma Physics, *Nuclear Inst. and Methods in Physics Research, A*, **502/2-3**, pp. 660 - 662, 2003; arXiv: physics/0212115.

[12] A.N. Fedorova and M.G. Zeitlin, Classical and quantum ensembles via multiresolution: I-BBGKY hierarchy; Classical and quantum ensembles via multiresolution. II. Wigner ensembles; *Nucl. Instr. Methods Physics Res.*, **534A** (2004)309-313; 314-318; arXiv: quant-ph/0406009; quant-ph/0406010.

[13] A.N. Fedorova and M.G. Zeitlin, Localization and Pattern Formation in Quantum Physics. I. Phenomena of Localization, in *The Nature of Light: What is a Photon? SPIE*, vol.**5866**, pp. 245-256, 2005; arXiv: quant-ph/0505114;

[14] A.N. Fedorova and M.G. Zeitlin, Localization and Pattern Formation in Quantum Physics. II. Waveletons in Quantum Ensembles, in *The Nature of Light: What is a Photon?SPIE*, vol. **5866**, pp. 257-268, 2005; arXiv: quant-ph/0505115.

[15] A.N. Fedorova and M.G. Zeitlin, Pattern Formation in Quantum Ensembles, *Intl. J. Mod. Physics* **B20**(2006)1570-1592; arXiv: 0711.0724.

[16] A.N. Fedorova and M.G. Zeitlin, Patterns in Wigner-Weyl approach, Fusion modeling in plasma physics: Vlasov-like systems, *Proceedings in Applied Mathematics and Mechanics (PAMM)*, Volume **6**, Issue 1, p. 625, p. 627, Wiley InterScience, 2006; arXiv:1012.4971, arXiv:1012.4965.

[17] A.N. Fedorova and M.G. Zeitlin, Localization and Fusion Modeling in Plasma Physics. Part I: Math Framework for Non-Equilibrium Hierarchies, pp.61-86, in *Current Trends in International Fusion Research*, Ed. E. Panarella, R. Raman, National Research Council (NRC) Research Press, Ottawa, Ontario, Canada, 2009; arXiv: physics/0603167.

[18] A.N. Fedorova and M.G. Zeitlin, Localization and Fusion Modeling in Plasma Physics. Part II: Vlasov-like Systems. Important Reductions, pp.87-100, in *Current Trends in International Fusion Research*, Ed. E. Panarella, R. Raman, National Research Council (NRC) Research Press, Ottawa, Ontario, Canada, 2009; arXiv: physics/0603169.

[19] A.N. Fedorova and M.G. Zeitlin, Fusion State in Plasma as a Waveleton (Localized (Meta)-Stable Pattern), p. 272, in *AIP Conference Proceedings*, Volume **1154**, Issue 1, *Current Trends in International Fusion Research*, Ed. E. Panarella, R. Raman, AIP, 2009, doi:10.1063/1.3204585.

[20] A.N. Fedorova and M.G. Zeitlin, Exact Multiscale Representations for (Non)-Equilibrium Dynamics of Plasma, p.291, in *AIP Conference Proceedings*, Volume **1154**, Issue 1, *Current Trends in International Fusion Research*, Ed. E. Panarella, R. Raman, AIP, 2009, doi:10.1063/1.3204592.

[21] A.N. Fedorova and M.G. Zeitlin, Fusion Modeling in Vlasov-Like Models, *Journal Plasma Fusion Res. Series*, Vol. **8**, pp. 126-131, 2009.

[22] A.N. Fedorova and M.G. Zeitlin, Quantum points/patterns, Part 2: from quantum points to quantum patterns via multiresolution, SPIE, vol. 8121, 81210K (2011), doi:10.1117/12.893537; arXiv:1109.5042.

[23] A.N. Fedorova and M.G. Zeitlin, Quantum points/patterns, Part 1. From geometrical points to quantum points in sheaf framework , SPIE, vol. 8121, 81210J (2011), doi:10.1117/12.893502; arXiv:1109.5035.

*Antonina N. Fedorova, Michael G. Zeitlin*
*Mathematical Methods in Mechanics Group, IPME RAS, V.O. Bolshoj pr., 61, 199178, St. Petersburg, Russia*
*http://www.ipme.ru/zeitlin.html, http:/mp.ipme.ru/zeitlin.html*

# Simulation of thermal fields in permafrost around engineering constructions in presence of seasonal cooling devices

Mikhail Yu. Filimonov Natalia A. Vaganova
fmy@imm.uran.ru

**Abstract**

A new mathematical model of heat distribution in permafrost soils is considered taking into account different climatic and physical factors. The first group of factors includes consideration of solar radiation, seasonal changes of air temperature, leading to periodic thawing (freezing) of soil, and possible snow layers. The second group of factors is the heterogeneity of the soil (not only in horizontal layers), the presence of a number of piles, or foundation structures, seasonal cooling devices. Seasonal cooling devices (SCDs) are vapor–fluid devices consisting of a hermetically sealed and seasoned with coolant, metal pipe with diameter 57 mm, length up to 10 meters or more, consisting of aerial parts (condenser fins) up to 2.5 meters and the underground part. These devices operate without external power sources only by the laws of physics. Taking into account these factors leads to the solution of three-dimensional quasilinear heat distribution equation (quasi-linear equation due to the dependence of the thermophysical parameters on temperature) of the Stefan problem in a rectangular parallelepiped, but also with a nonlinear boundary condition at the soil surface associated with solar radiation. It is assumed that the side faces of the computational domain are insulated and are chosen sufficiently far from the location of engineering structures, and a computational grid of large dimension to be used, with adaptation to the heat(cold) sources. Computational codes is designed for numerical simulation of thermal fields in permafrost and melted soil, taking into account thermal diffusion properties of the soil and heat exchange between the soil and air, including also due to heat loss by radiation. The presentation is devoted to the results of numerical simulations carried out for the project work in several oil and gas fields in Russia, located in the permafrost zone.

## Introduction

Permafrost takes place about 25 % of the total land area of the globe [1] (mainly in Alaska, the northern territories of Canada, Russia, China, highland areas) and is closely related with external influences. The main characteristics of permafrost, which are usually taken into account are the type of distribution (continuous, intermittent, island), the type of cryogenic structure (massive, layered, mesh) and the degree of iciness. Soils, which compose permafrost, have different physical and chemical properties that are nonuniform and nonisotropic. In summer, because of the positive air temperatures and solar radiation, there is a seasonal thawing of the upper soil layer, and in winter, the reverse process is observed. It was noted that in the northern high latitudes, the average temperature has increased more rapidly than the global mean temperature [2], which could affect on permafrost.

In developing the oil and gas fields in a permafrost zone an important objective is to reduce the influence of different heat sources (construction and production wells, for

example) on permafrost. The problem of reducing the intensity of the thermal interaction on permafrost is of particular importance for solving problems energy saving, environmental protection, safety, cost savings and improve operational reliability of wells. In the design one should provide both insulation of production wells, and construction of platforms on which these wells located. In Russia, permafrost occupies a total area of 10 million km$^2$, up to 65 % of the territory. Age of permafrost corresponds to Pliocene (1.8-2.4 Ma). These areas are extremely important for Russian economy, as here there are produced about 93 % of Russian natural gas and 75 % of oil, which in monetary terms, provides up to 70 % of exports. It had been thought that the average thickness of permafrost in these areas ranges from 10 to 800 m, however, in the northwestern part of Yakutia it has been found by drilling that a depth of permafrost is 1400 m. There are number of papers devoted to the problem of permafrost thawing in Russia, for example, [3, 4].

Extraction and transportation of oil and gas also has a significant effect on permafrost, as heat flux from the heated oil in wells and pipelines leading to permafrost thawing. Note that more than 75 % of all Russian buildings and structures in the permafrost zone are constructed and operated on the base of principle of conservation of frozen soil foundation. Therefore the problem of reducing the intensity of thermal interaction in the "heat source–permafrost" zones is of particular importance for solving problems of energy saving, environmental protection, safety, cost savings and improve the reliability of various engineering structures.

In the papers [5, 6] we consider permafrost thawing in the system "well-permafrost", in [7] for an underground pipeline the thermal fields are calculated with taking into account water filtration in the soil, but without taking into account the possible phase transition.

## 1 Mathematical model of heat distribution in a heat source–permafrost system

First let consider heat exchange on a flat ground surface directly illuminated by the sun. Let the initial time be $t_0 = 0$, and the ground is a box $\Omega$ and has a temperature $T_0(x, y, z)$. The computational domain is a three-dimensional box, where $x$ and $y$ axes are parallel to the ground surface and the $z$ axis is directed downward. We assume that the size of the region $\Omega$ is defined by positive numbers $L_x$, $L_y$, $L_z$: $-L_x \le x \le L_x$, $-Ly \le y \le L_y$, $-L_z \le z \le 0$. To simulate the propagation of heat in this volume the following mathematical model is suggested. Let $T = T(t, x, y, z)$ be soil temperature at the point $(x, y, z)$ at the time moment $t$. The main heat flow associated with climatic factors on the surface $z = 0$ is shown in Figure 1.

$T_{air} = T_{air}(t)$ denotes the temperature in the surface layer of air, which varies from time to time in accordance with the annual cycle of temperature; $\sigma = 5,67 \cdot 10^{-}8\ Wt/(m^2K^4)$ is Stefan-Boltzmann constant; $b = b(t, x, y)$ is heat transfer coefficient; $\varepsilon = \varepsilon(t, x, y)$ is the coefficient of emissivity. The coefficients of heat transfer and emissivity depend on the type and condition of the soil surface. Total solar radiation $q(t)$ is the sum of direct solar radiation and diffuse radiation. Soil is absorbed only part of the total radiation which equals to $\alpha q(t)$, where $\alpha = \alpha(t, x, y)$ is the part of energy that is formed to heat the soil, which in general depends on atmospheric conditions, angle of incidence of solar radiation, i.e. latitude and time. $\Omega$ can include a number of engineering structures (e.g., layers of riprap on the surface of the ground, piles). Suppose that in $\Omega$ there are $n$ objects that are heat sources (foundations, producing insulated wells, pipelines) and cold sources (SCDs). We denote the surface of these objects by $\Omega_i = \Omega_i(x, y, z)$, $i = 1, ..., n$ (Fig.1). To account the heat from each of the $\Omega_i$ the equation of the contact (diffusion) heat conductivity with

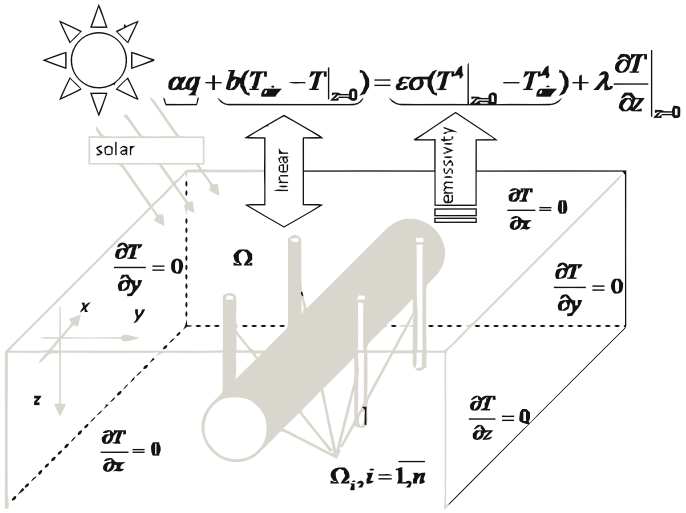


Figure 1: The main heat flows and boundary conditions.

inhomogeneous coefficients is used as a basic mathematical model with including localized heat of phase transition — an approach to solve the problem of Stefan type, without the explicit separation of the phase transition [8, 9]. The heat of phase transformation is introduced with using Dirac $\delta$-function as a concentrated heat of phase transition in the specific heat ratio. The obtained discontinuous function then "shared" with respect to temperature, and does not depend on the number of measurements, phases, and fronts. Thus, the modeling of thawing in the soil is reduced to the solution in $\Omega$ of the equation following heat equation [8]:

$$\rho\big(c_\nu(T) + k\delta(T - T^*)\big)\frac{\partial T}{\partial t} = \operatorname{div}\left(\lambda(T)\operatorname{grad}T\right), \tag{1}$$

where $\rho$ is density $[kg/m^3]$, $T^*$ is temperature of phase transition $[K]$,

$$c_\nu(T) = \begin{cases} c_1(x,y,z), & T < T^*, \\ c_2(x,y,z), & T > T^*, \end{cases} \text{ is specific heat [J/kg K]},$$

$$\lambda(T) = \begin{cases} \lambda_1(x,y,z), & T < T^*, \\ \lambda_2(x,y,z), & T > T^*, \end{cases} \text{ is thermal conductivity coefficient [Wt/m K ]},$$

$k = k(x,y,z)$ is specific heat of phase transition, $\delta$ is the Dirac delta function.

Thus, it is necessary to solve equation (1) in the area $\Omega$ with initial condition

$$T(0,x,y,z) = T_0(x,y,z). \tag{2}$$

and boundary conditions

$$\alpha q + b(T_{air} - T_{z=0}) = \varepsilon\sigma(T^4_{z=0} - T^4_{air}) + \lambda\frac{\partial T}{\partial z}, \tag{3}$$

$$T\Big|_{\Omega_i} = T_i(t), i = 1,\dots,n, \tag{4}$$

$$\frac{\partial T}{\partial x}\Big|_{x=\pm L_x} = \frac{\partial T}{\partial y}\Big|_{y=\pm L_y} = \frac{\partial T}{\partial z}\Big|_{z=\pm L_z} = 0. \tag{5}$$

Condition (2) determines the initial distribution of soil temperature at the time moment from which we plan to start the numerical calculation. Condition (3) is obtained from the balance the heat fluxes at the ground surface $z = 0$. Conditions (4) appear in the case if in the ground there are different objects, which temperature is different from the surrounding soil. For SCDs the temperature $T_i(t)$ is determined by the temperature of air $T_{air}$. It is assumed that SCDs work effectively when $T_{air} < -10°C$. Conditions (5) are necessary to carry out numerical calculations in the given area. Note that the lower boundary ($z = -L_z$) of the computational domain instead of the zero heat flux is more correct to set the geothermal flux. However, due to the smallness of the geothermal flow in this area for the proposed model we use (5).

Thus, the simulation of heat transfer in three-dimensional domain with the phase transition is reduced to solving the initial-boundary value problem (1)–(5). In contrast to the known results on the calculations of permafrost defrosting, in this mathematical model includes not only geometric and thermal insulation characteristics of engineering structures around the well but also various options for thermal insulating the outer surface of the well.

It should be noted that the size of the computational domain $\Omega$ $(L_x, L_y, L_z)$ is chosen so that the effect of lateral boundaries in the numerical calculations has no significant effect on the temperature distribution around the objects, bounded by surfaces $\Omega_i$.

To compute heat distribution by equations (1)–(5) in a three-dimensional domain a finite-difference method with splitting by spatial variables is used. Computations are carried out on orthogonal grid, uniform or adapted by layers and to the well. The basic heat equation is approximated by an economical implicit finite-difference pattern in each of spatial dimensions. System of linear difference equations has a three-diagonal form and may be solved by a sweep method. On surface $z = 0$, there is an algebraic equation of fourth degree, which is solved by Newton's method. The solvability of implicit difference equations that approximate the problem (1)-(5) is proved in [10].

## 2 Numerical results

Let consider seasonal thawing (freezing) of the upper layer of the soil. The mathematical model takes into account two basic factors: monthly dependent changes of solar energy reaching surface of the soil and changes of air temperature. Figure 2 shows the averages of intensity of sunlight and air temperature for the considered region.

To prevent permafrost thawing and soil temperature stabilization SCDs are used. Let consider the process of functioning of the SCD during one year. The computational domain is a cube with sides equal to 50 meters. As a basic soil we will use a loam with parameters shown in Table 1. The background temperature of permafrost is -1.5°C, except for the layer of seasonal thawing (freezing) of soil. Figure 3a shows the temperature profiles near the surface in March, June, September, and December — the natural annual cycle of temperature fluctuations in the uniform soil.

Further, we will consider two SCDs with diameter 5.7 cm, depth 12 m are in the center of the computational domain at a distance of 1.2m. In Figure 3b the temperature profiles are shown on March, June, September, and December, produced by two SCDs in uniform soil. The profiles are shown for the line between of two SCDs at the distance of 60 cm.

In Figure 4 on the ground there are a layer of water with depth of 20 cm. Figure 4a shows temperature without SCDs, Figure 4b — with two SCDs.

The structure of the ground in Figure 5 is more complex. There are 4 layers: peat is from 0 to 0.5 m., clay is from 1 m. to 1.5 m. and loam is from 0.5 m. to 1 m. and from

Table 1.

| **Parameter** | **x** | **y** | **z** |
|---|---|---|---|
| Size of area, m | 50 | 50 | 50 |
| Number of points | 151 | 151 | 101 |
| soil(loam) | | frozen | melted |
| Heat conductivity | $Wt/mK$ | 1.93 | 1.57 |
| Volumetric heat | $J/(m^3K)$ | $2.15 \cdot 10^6$ | $3.49 \cdot 10^6$ |
| Volumetric heat of phase transition | $J/m^3$ | $1.415 \cdot 10^5$ | |
| water/ice | | frozen | melted |
| Heat conductivity | $Wt/mK$ | 2.26 | 0.56 |
| Volumetric heat | $J/(m^3K)$ | $1.99 \cdot 10^6$ | $4.2 \cdot 10^6$ |
| Volumetric heat of phase transition | $J/m^3$ | $3.35 \cdot 10^8$ | |
| peat | | frozen | melted |
| Heat conductivity | $Wt/mK$ | 1.34 | 0.81 |
| Volumetric heat | $J/(m^3K)$ | $2.31 \cdot 10^6$ | $4.00 \cdot 10^6$ |
| Volumetric heat of phase transition | $J/m^3$ | $3.015 \cdot 10^8$ | |
| clay | | frozen | melted |
| Heat conductivity | $Wt/mK$ | 1.90 | 0.90 |
| Volumetric heat | $J/(m^3K)$ | $1.70 \cdot 10^6$ | $2.30 \cdot 10^6$ |
| Volumetric heat of phase transition | $J/m^3$ | $1.6 \cdot 10^8$ | |

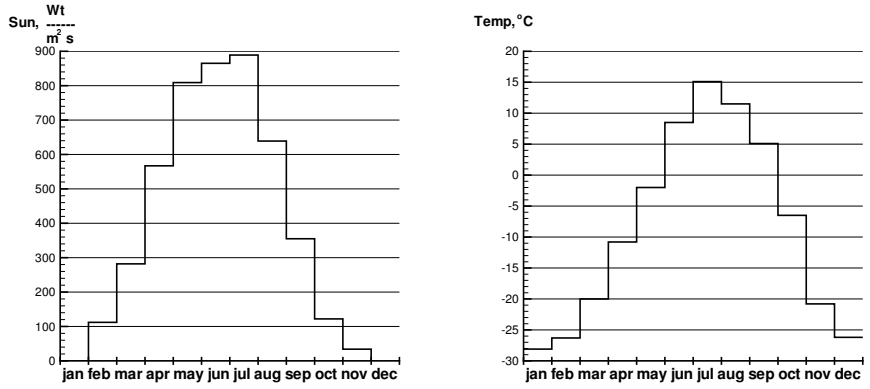


(a) (b)

Figure 2: Intensity of sunlight (a) and average month temperature (b).

1.5 m. and deeper. Also there is an ice lens of an elliptical shape with the values of the semiaxes by x,y, and z are 2.5 m., 2.5 m., and 0.25 m. The center of the lens is in the center of computational domain at the deph of 1.25 m.

The presented profiles show that the temperature field formed by SCDs depends on the structure of the soil. In particular, better insulation of the upper surface in summer offers the best safety of the "cold", delivered to the lower layers of soil by SCDs in winter.

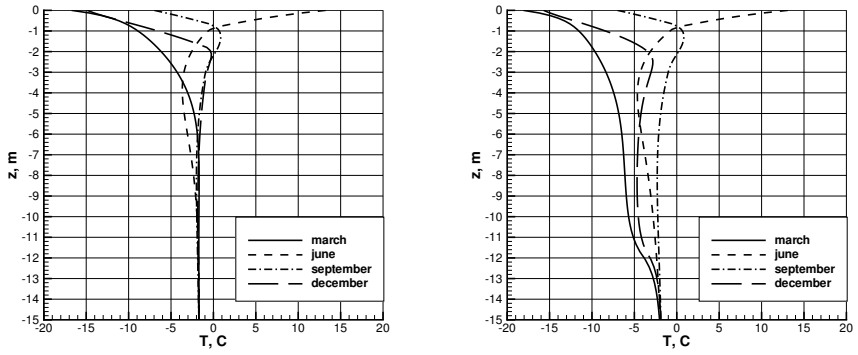


(a) (b)

Figure 3: Temperature in an uniform soil (a) and with 2 SCDs (b).

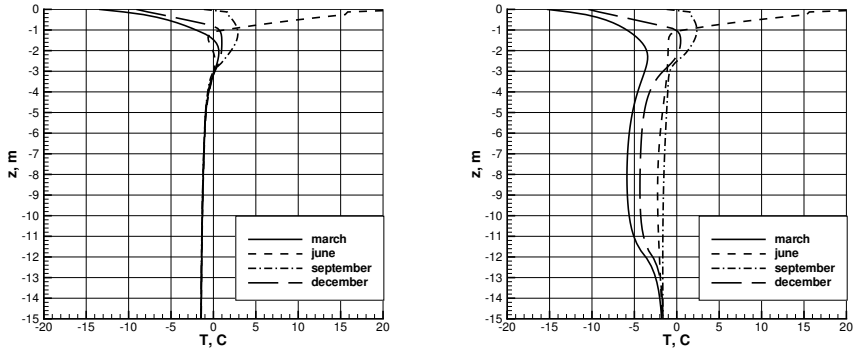


(a) (b)

Figure 4: Temperature in soil with a water layer without of SCDs (a) and with two SCDs (b).

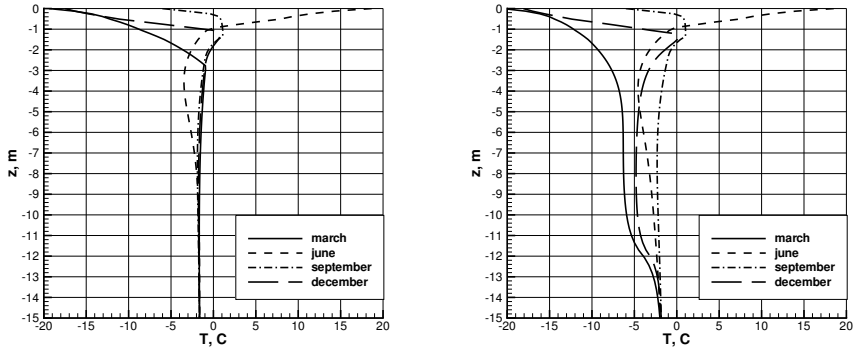


(a) (b)

Figure 5: Temperature in soil with an ice lens (a) and with two SCDs (b).

## 3 Thermal fields around an engeneering constructions

Consider the process of SCDs operation in the presence of a heat source. Let in the center of the computational domain be located a cylindrical container with diameter of 10 meters, a depth of 5 m, with 20 cm concrete walls. In the container $10°C$ constant temperature is kept. Further, the following figures show the temperature field near the considered area after 3 years (in the ground there is a stabilization of the temperature field): Figure 6a

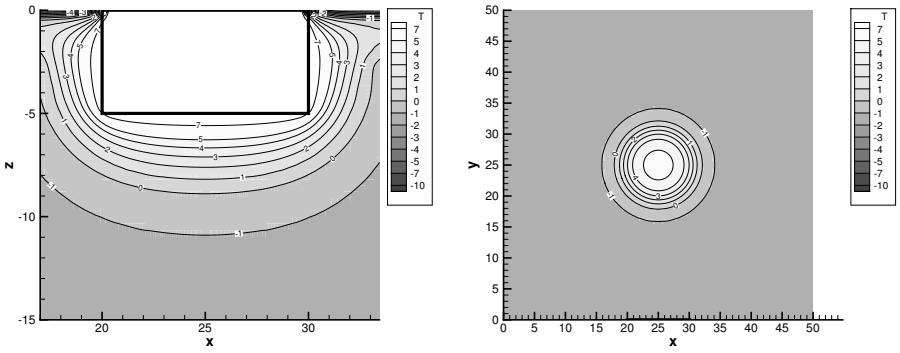


(a) (b)

Figure 6: Temperature near container a in an uniform soil in $(x, z)$ (a) and at the depth of $z = 6m$. (b), in September.

are shown in the plane (x,z) along the axis of symmetry, Figures 6b, 7, and 8 — in the plane (x,y) at the depth of 6 m from the surface (1 m from the bottom of the container). Comparison of Figures 6b, 7b, and 8b illustrates the efficiency of SCDs operating: the radius of thawing is restrained, even under the floor of the container.

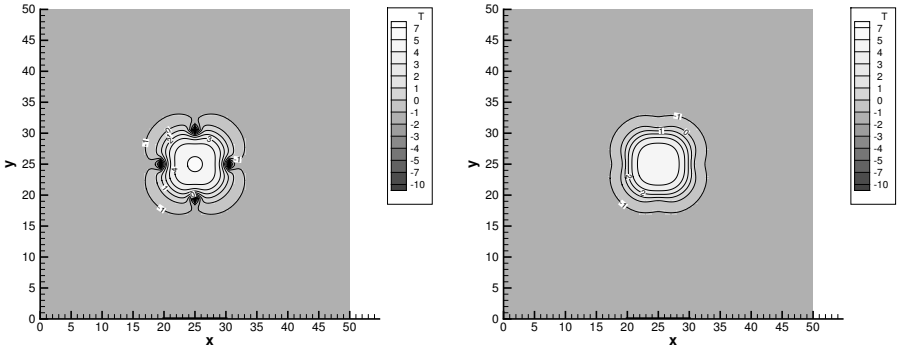


(a) (b)

Figure 7: Temperature at the depth of $z = 6m$. with 4 SCDs in March (a) and in September (b).

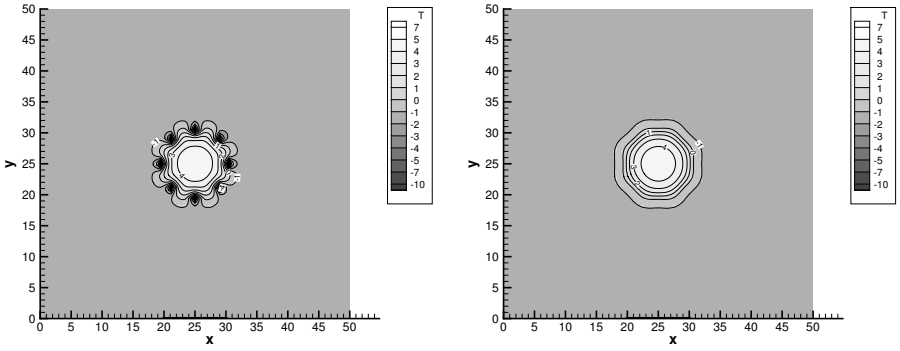


(a) (b)

Figure 8: Temperature at the depth of $z = 6m$. with 4 SCDs in March (a) and in September (b).

Thus, the software product developed on the basis of the model (1)–(5) makes it possible to carry out a series of numerical experiments and make predictions about long-term dynamics of permafrost thawing, including the presence of various engineering structures, including the seasonal cooling devices. Monthly changes of air temperature and solar radiation, soil heterogeneity in 3D areas are taken into account in mathematical model as well as of geophysical features of the simulated region. The results of numerical simulations allow to evaluate the effectiveness of SCDs work for thermal stabilization of soil, to determine the required number and its optimal location on a given surface.

## Acknowledgements

*This work is partially supported by Russian Foundation for Basic Research – URAL 10–08–96014 and Program of Presidium of RAS 12–P–1–1009.*

## References

[1] T. Zhang, R. G. Barry, K. Knowles, J. A. Heginbottom, J. Brown. Statistics and characteristics of permafrost and ground ice distribution in the Northern Hemisphere. Polar Geography. **23**, 2, 1999.

[2] O. Anisimov, B. Fitzharris, J. O. Hagan, R. Jeffries, H. Marchant, F. E. Nelson, T. Prowse, D. G. Vaughan. Polar regions (Arctic and Antarctic). Climate Change: Impacts, Adaptation, and Vulnerability, The Contribution of Working Group II of the Intergovernmental Panel on Climate Change, Third Assessment Review, Cambridge, U.K., Cambridge University Press, 2001.

[3] A. V. Pavlov. Permafrost and climate change in the northem Russia: observations, prognosis. Izvestiya RAN. Seriya geograficheskaya, 6, 2003.

[4] A .A. Vasiliev, D. S. Drozdov, N. G. Moskalenko. Permafrost temperature dynamics of west siberia in context of climate changes. Earth cryosphere, **12**, 2, 2008.

[5] M. Yu. Filimonov, A. G. Kravets, N. A. Vaganova. Simulation of thermal interaction in a zone of extractive well in permafrost. Proc. of APM-2010, 2010.

[6] M. Yu. Filimonov, N. A. Vaganova. Permafrost defrosting as a result of extractive wells operating. Proc. of APM-2011, 2011.

[7] V. V. Bashurov, N. A. Vaganova, M. Y. Filimonov. Numerical simulation of thermal conductivity processes with fluid filtration in soil. Computational technologies, **16**, 4, 2011.

[8] A. A. Samarsky, B .D. Moiseenko. ZhVMiMF, **5**, 5 1965.

[9] A. A. Samarsky, P .N. Vabishchevich. Computational Heat Transfer. M.: Editorial URSS, 2003.

[10] N. A. Vaganova. Existence of a solution of an initial-boundary value difference problem for a linear heat equation with a nonlinear boundary condition. Proceedings of the Steklov Institute of Mathematics, **261**, 1, 2008.

*Mikhail Yu. Filimonov*
*Institute of Mathematics and Mechanics UrB RAS, S. Kovalevskaya str. 16, Ekaterinburg, 620990, Russia*

# Modeling of contact interaction between atomic force microscope probe and an elastic brittle damage material

Oleg K. Garishin Sergey N. Lebedev
gar@icmm.ru

**Abstract**

Atomic force microscope (AFM) can be used to obtain information not only about the topology of the internal structure of the material, but also on its local physical properties. The corresponding theoretical models must be used for correct decoding of the experimental results. Modeling the contact interaction of AFM probe with the elastic brittle specimen is presented in this paper.

At this stage of the research it was considered that the mechanical behavior of a model sample is described by Neo-Hookean elastic potential. Mechanical strength of the reaction to the probe indentation was determined from the solution of the corresponding contact boundary problem. The required solution sought numerically - the finite element method (in nonlinear elastic axisymmetric formulation) was applied used. As a result, we obtained dependencies of the mechanical response force on the depth of indentation, specimen elastic modulus and geometric characteristics of the probe: the radius of the top and cone angle.

Processes of AFM probe cyclic indentation into fragile medium damaged by deformation were numerically investigated using this approach. AFM probe pressed repeatedly in the same place on the sample surface, that improves the accuracy of measurements. Theoretical modeling is to aid in its adequate decryption.

As a result, the dependencies of reaction force on the probe depth of penetration and the size of the hole formed after the previous contact. Probe indentation into the surface with the existing microwells, which simulated caries damaged tooth is also modeled.

Atomic force microscopy (AFM) is one of the most promising research tools for nanoscale materials level. They can be used to obtain information not only about the topology of the internal structure of the material, but also on its local physical properties [1, 2, 3, 4]. You can get unique information about the mechanical properties of materials at the nanoscopic level, exploring the process of introducing the probe into the specimen: the emergence of dislocations, the occurrence of shear instability, phase transitions and many other phenomena that are inaccessible to the previously known techniques [5]. The corresponding theoretical models (which contain additional knowledge about the subject of study) must be used for the correct interpretation of the experimental results [6, 7, 8]. One such approach modeling the contact interaction between the AFM probe and the sample surface is presented in this paper.

Design model scheme consists of a specimen with a flat surface (investigated material) and an indenter (AFM probe) in the form of a cone with a rounded apex (Fig. 1). The surface may contain different types of wells.

It is considered that the probe is absolutely rigid, and mechanical behavior of a model sample can be described by the Neo-Hookean elastic potential. The mechanical force of the reaction to the probe indentation is determined from the solution of the corresponding

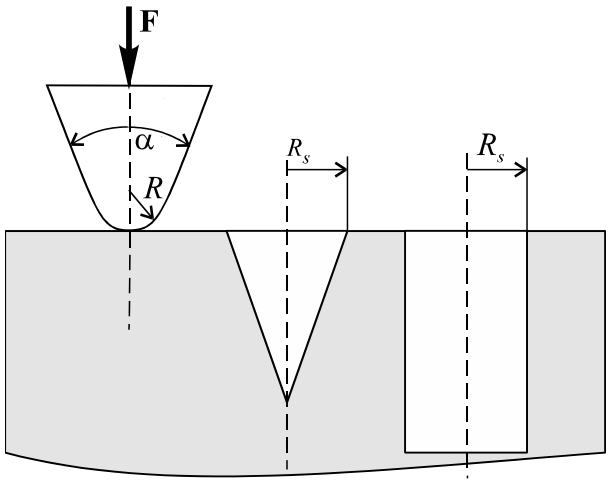


Figure 1: Design scheme of contact interaction of the AFM probe with the specimen

contact boundary-value problem. The required solution sought numerically - using the finite element method (in the nonlinear elastic axisymmetric formulation). As a result, we obtain the dependence of the elastic reaction force on mechanical properties of the specimen material and geometric characteristics of a probe tip radius $R$ and the cone angle $\alpha$.

Comparison of the nonlinear solution (in the case of finite nonlinear elastic deformation) with the known problem of the Hertz contact of two linear-elastic spheres under small deformations was carried out using this model [9]. At present this solution is widely used in practice for the first assessment calculations. It is a standard set of software most of the AFM. Hertz's formula for the case when one of the spheres has an infinitely large radius (i.e. contact with the half-plane) and the second is absolutely rigid has the following form

$$F_{Hertz} = \frac{4E_s R^{1/2}}{3(1-\nu_s^2)} u^{3/2} \tag{1}$$

where $E_s$ — the initial Young's modulus of the specimen, $\nu_s$ — Poisson's ratio (all hereinafter: the index "$s$" means that the parameter refers to the sample). For the case of nonlinear elastic contact problem similar dependence has the form

$$F = 8.6 C_s R^2 \left(\frac{u}{R}\right)^{1.3} \tag{2}$$

where $C_s$ — Neo-Hookean elastic constant. For an incompressible medium $\nu_s = 0.5$, then $C_s$ corresponds to the initial Young's modulus as $E_s = 6C_s$. Fig. 2 shows the dependence of reaction force $F$, acting on the tip on the depth of its penetration into the material $u$, calculated from Hertz formula and numerically (Neo-Hooke). The graphs show that the divergence of Hertz formula and non-linear elastic solution starts at $u/R > 0.4$ (and non-linear elastic solution gives higher values of force). For smaller values it is quite possible to use Hertz formula.

Different types of probes are used, depending on the mechanical properties of tested on the ACM materials. In the study of elastomers and soft thermoplastics probes with a smaller cone are usually used, for relatively hard samples, respectively, more "blunt"

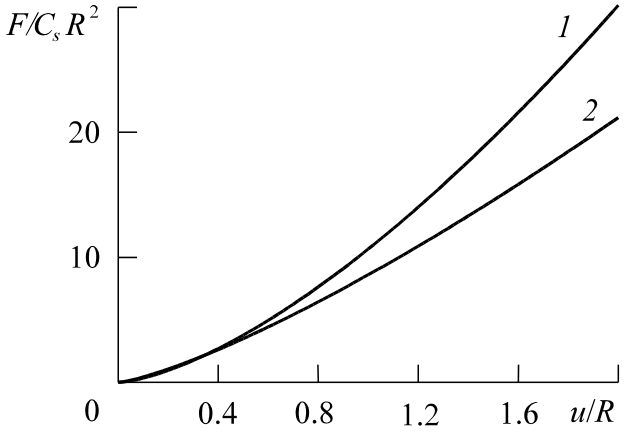


Figure 2: Dependences of reaction force $F$, acting on the tip, on the depth of its penetration into the material $u$. 1 — Hertz formula, 2 — numerical nonlinear elastic solution (Neo-Hooke)

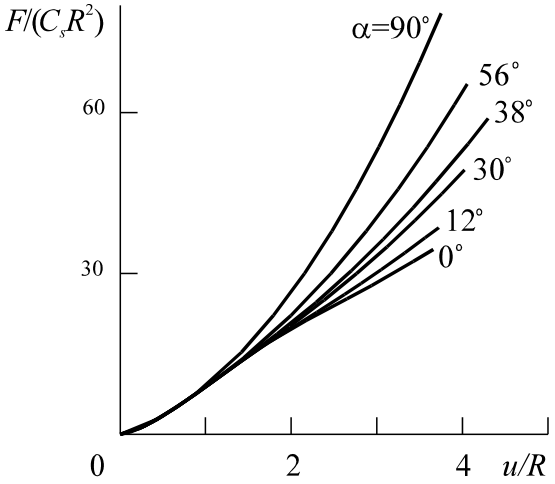


Figure 3: Dependence of reaction force $F$ on AFM probe penetration depth into the specimen $u$ and cone angle $\alpha$

(and stronger) indenters are chosen. In determining the dependence of $F$ on $\alpha$ values of the arguments ranged from 0 (cylindrical probe with a rounded apex of radius $R$) to 90° (Fig. 3).

Calculations show that the angle of the probe cone begins to significantly affect the reaction force when the depth of penetration of the probe into the specimen reaches values of $3 - 4R$, that is, this factor should be necessarily taken into account in describing large deformation in the contact zone. Thus, when the indentation of the probe to a depth of $4R$, $F(\alpha = 90°)$ more than twice the $F(\alpha = 0°)$.

The problem of repeated indentation of a hard "blunt" AFM probe (($\alpha = 90°$) in a brittle breaking in the process of deformation elastic material has been solved using this approach. The corresponding model studies carried out.

Repeated indentation of the AFM probe into the same place of damageable elastic brittle surface was modeled, and after each contact in the sample had ever increasing hole depth $\delta$. Hole is a result of brittle fracture of the material during the probe indentation, that is, changing the geometry the specimen surface happens but without residual plastic

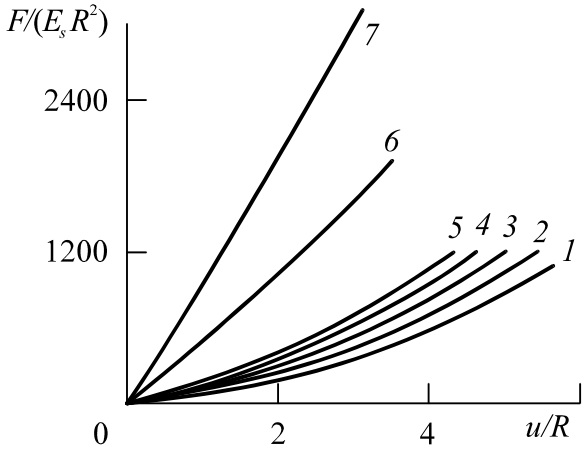


Figure 4: Dependence of reaction force $F$ on AFM probe on the depth of its indentation $u$ into brittle sample and depth of the hole $\delta$: 1 — $\delta/R = 0$, 2 — 0.5, 3 — 1, 4 — 1.5, 5 — 2, 6 — 5, 7 — 10

stresses. Such processes are characteristic, for example, for AFM studies of tooth enamel. The enamel can have different mechanical properties of its thickness(a variety of injuries can be on the surface, the surface can be covered with a thin coating of another material, etc.). Repeated indentation into the same place of tooth enamel can help to gather the necessary information about its true mechanical properties, and mathematical simulation of this process should help in deciphering the data adequately.

As a result, dependences of the reaction forces on depth of probe indentation and the magnitude of the hole formed after the previous contacts were built (Fig. 4). The movement of the probe into the material after the occurrence of contact between it and the bottom of the hole was taken as $u$. It was established, the deeper the hole, the greater the effort required for its further growth. At very large depths (curves 6 and 7) dependence of $F$ on $u$ were practically linear, and they were lying significantly higher than the other curves.

The surface of a tooth can not always be regarded as flat and smooth. Therefore, the task of impressing a hard indenter into conical and cylindrical holes in brittle elastic surface has been solved (see Fig. 1). These grooves simulated caries microdamages in tooth enamel. Dependences of the force pressing the AFM probe $F$ on the depth of penetration of $u$ into a conical cavity with radius $R_s$, when the indenter has the form of a cone ($\alpha = 90°$) with rounded apex radius $R$ are shown in Fig. 5. Angle of the cone-shaped hole $\alpha_s$ was 70° (solid lines) and 90°90 (dashed lines). Variants when the probe tip radius was equal to the radius of the hole, or exceeded it in 1.5, 2, 3 and 4 times were calculated. The calculations show that the value of $F$ is weakly dependent on the relation between $R$ and $R_s$. The graphs are the limiting curves for the cases of $R/R_s = 4$ and $R/Rs = 1$. Rest dependencies lay between them. For wells with a gently sloping sides ($\alpha = 90°$) curves were slightly higher (but insignificant).

Also, a similar problem on a conical indentation of the AFM probe in a cylindrical cavity of radius $R_s$ (the limiting case of "degeneracy" cone-shaped hole in the cylinder) for different values of probe cone angle $\alpha$ has been solved. $\alpha$ was taken to be 40°, 60°, and 90°. The results are shown in Fig. 6. The curves corresponding to $\alpha = 90°$, also lay close to those shown in Fig. 5, so a form of wells not very effect on strength of the reaction (for the considered range of $\alpha_s$ values). A different situation is observed for the parameter $\alpha$. As can be seen from the graphs in Fig. 6 the reaction force of the probe indentation into the cavity depends strongly on the "sharpness" of the cone. The larger $\alpha$, the harder it is

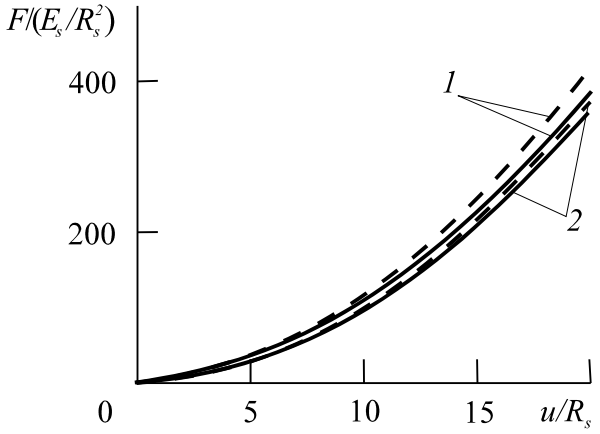


Figure 5: Indentation the conical probe (full cone angle $\alpha = 90°$) with rounded apex of radius R in a conical cavity. Solid lines — $\alpha_s = 70°$. Dashed lines — $\alpha_s = 90°$. 1 — $R/R_s = 4$, 2 — $R/R_s = 1$

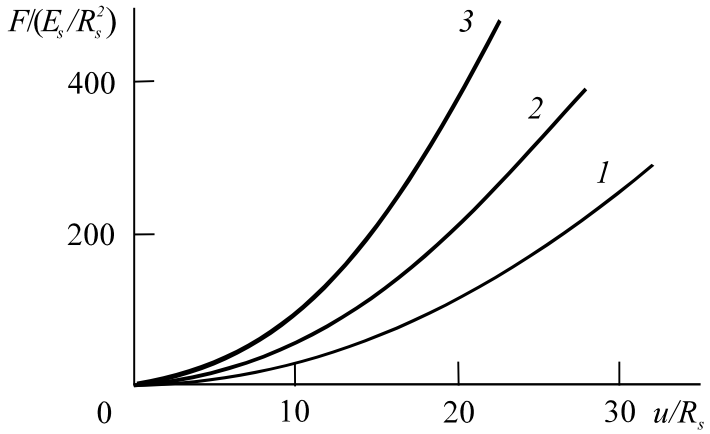


Figure 6: The indentation of a conical probe in a cylindrical cavity of radius $R_s$. 1 — $\alpha = 40°$, 2 — 60°, 3 — 90°

to enter the probe into the hole on the sample surface.

## Acknowledgements

*This work is executed at a financial support of the Russian fund of basic researches and the Ministry of the industry of innovations and a science of the Perm (Grants 11-08-96001-r urals a, 11-08-96018-r urals a), the Grant of the state support of leading scientific schools NSh-5389.2012.1.*

## References

[1] Bhushan B. Nanotribology and nanomechanics. Springer, (2005), 1148 p.

[2] Schuh C.A. Nanoindentation studies of materials // Materials Today, (2007). V. 9, N 5, P. 32–40.y nano-composites and the effective clay particle // Polymer, (2004), V. 45, P. 487–506.

[3] Giessib F.J. AFM's path to atomic resolution // Materials Today, (2005), V. 8, N 5, P. 32–41.

[4] Butt H-J., Capella B., Kappl V. Force measurements with atomic force microscope: Technique, interpretation and applications // Surface Science reports, (2005), V. 59, P. 1–150.

[5] Fischer-Cripps A.C. Nanoindentation. Springer, (2002), 217 p.

[6] Vanlandingham M.R., McKnicht S.H., Palmese G.R., Eduljee R.F., Gillepie J.W., McCulough Jr.R.L. Relating elastic modulus to indentation response using atomic force microscopy // Journal of Materials Science Letters, (1997), V. 16, P. 117–119.

[7] Dao M., Chollacoop N., Van Vliet K.J., Venkatesh T.A., Suresh S. Computational modeling of the forward and reverse problems in instrumented indentation // Acta Mater., (2001), V. 49, N 19, P. 3899–3918.

[8] Oliver W.C. An improved technique for determining hardness and elastic modulus using load and displacement sensing indentation experiments // J. Mater. Sci., (1992), V. 7, N 6, 1564–1583.

[9] Timoshenko S.P. The theory of elasticity. M.: Nauka, (1975), 576 p. (in Russian).

*Oleg K. Garishin, Institute of Continuous Media Mechanics, Perm, Russia*
*Sergey N. Lebedev, Institute of Continuous Media Mechanics, Perm, Russia*

# Research of interrelation between polyolefine/clay nanocomposites structure and their mechanical properties

O. K. Garishin A. S. Korlyakov V. V. Shadrin
korlaykov@icmm.ru

**Abstract**

The object of this study are polyolefin polymers and nanocomposites with a group of silicate filler on them. These materials have a complex hierarchical structure. First, the polyolefins are themselves part of crystallizing materials. That is, they are structurally heterogeneous at the nano and micro levels: lamellae (thickness of about 5-10 nm) and spherulitic formation (from 0.1 to 1000 microns)[1, 2]. The second type of structural heterogeneity introduces a filler. In the investigated materials as used in this layered clay minerals (smectite). Filler particles have the form of ultra-thin flakes of thickness of several nanometers and a typical diameter of tens of nanometers to 1 micron. Were carried out experimental investigations of the elastic, viscous and plastic properties of nanocomposites with a polyethylene matrix and the filler of layered silicate nanoparticles. For samples with varying degrees of filling of the dependencies between the stresses and deformations under cyclic loading with increasing amplitude and relaxation after a stop at the loading and unloading, as well as the corresponding relaxation curves. Tests were conducted on the waste before the procedure, allowing for an experiment to obtain all necessary for further theoretical modeling of the data on the elasto-visco-plastic behavior Using the experimental data has been built structurally phenomenological elasto-visco-plastic finite-deformable model of a heterogeneous environment. At the same time used the differential approach to the construction of constitutive equations based on the interpretation of the mechanical behavior of materials with the help of symbolic schemes.

## Tested materials and experiments

In Fig. 1 shows the results of the cyclic deformation of polyethylene mark "PE-107-02K" with increasing amplitude in the mode: stretching → stress relaxation for 10 minutes → decrease in strain to zero tensile force → stress relaxation for 10 minutes → next cycle of deformation. This mode allows you to separate viscoelastic and elastoplastic behavior of the sample in one experiment and learn them yourself. The rate of deformation of in tension and compression of the sample was 1 $min^{-1}$. Extension was carried out before such time as the sample does not begin to take shape "plastic collar".

## Model of the mechanical behavior of nanocomposites

The mechanical behavior of nanocomposites is described by the model schematically represented in Fig. 2, where each point corresponds to a particular set of constitutive equations. The first branch (the elastic-plastic) models the behavior of the agglomerates of crystallites are more stringent (and nanofiller particles), their displacement and destruction during the deformation. The second (visco-elastic) describes the flow of the amorphous polymer

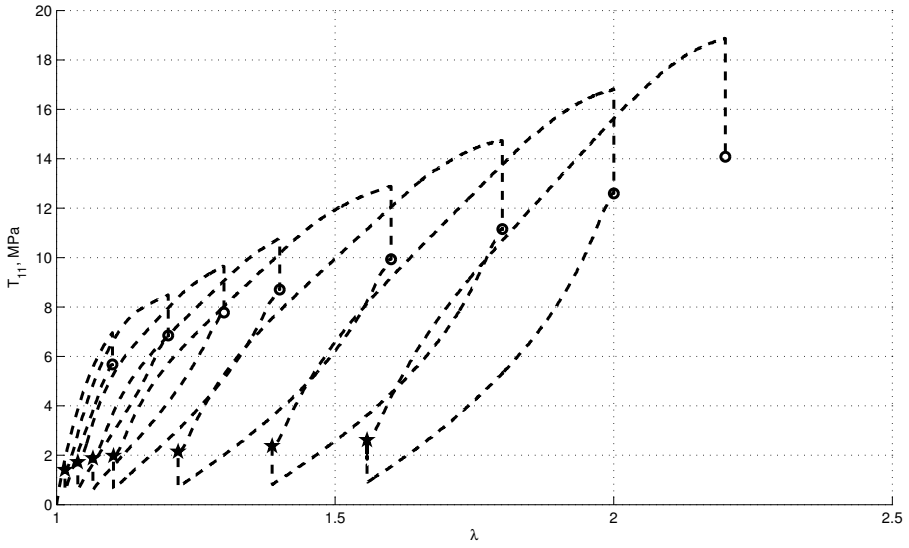


Figure 1: The scheme of cyclic loading of the sample. Circles - the end of stress relaxation at the maximum strain in this cycle, stars - the end of the relaxation after removal of the load on a given cycle.

between the lamellae inside the crystallites and in the space around the crystallites and particles. As shown by certain experiments, these processes are practically independent, that was the rationale for the choice of the scheme. The scheme shows how the tensor nonlinear equations are combined into the system of equations used to calculate the complex viscoelastic behavior of the medium deformed in an arbitrary way. The algorithm for constructing constitutive equations consisting of separate groups of equations (elastic, viscous, plastic) is described in detail in work [3]. The model uses the approach that is based on additive decomposition of the deformation-rate tensor of the medium into the deformation-rate tensors of the scheme elements [4]. The internal scheme points are required to meet the condition of correlation of the Cauchy stress tensors [3]. The scheme for the mechanical behavior of the material involves elastic, viscous and plastic elements that correspond to the folowing equations.

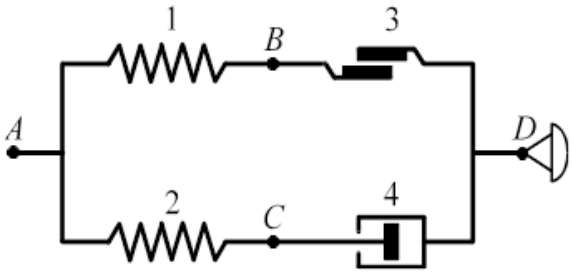


Figure 2: Schematic of the model of the mechanical behavior of nanocomposites.

The material is assumed to be incompressible. The deviator of the Cauchy stress tensor

of the elastic element is calculated from the equations of the theory of elasticity

$$\operatorname{dev}\mathbf{T}_i = \operatorname{dev}\left(\rho\sum_{k=1}^{3}\lambda_k^{(i)}\frac{\partial f}{\partial\lambda_k^{(i)}}\,\mathbf{n}_k^{(i)}\otimes\mathbf{n}_k^{(i)}\right),$$

in which the mass density of the medium free energy $f$ depends on the extension ratios of elastic elements.

$$f = w_n = C_i(\lambda_1^N + \lambda_2^N + \lambda_3^N - 3) = C_i(tr(\mathbf{V}^N) - 3)$$

where $\lambda_1^{(i)}$, $\lambda_2^{(i)}$, $\lambda_3^{(i)}$ and $\mathbf{n}_1^{(i)}$, $\mathbf{n}_2^{(i)}$, $\mathbf{n}_3^{(i)}$ — are the extension ratios and eigenvectors of the stretch tensor $\mathbf{V}_i$ of the i-th elastic element . Time variations in the tensor $\mathbf{V}_i$ are calculated by the evolution equation.

$$\frac{2}{\nu_i}\,\mathbf{Y}_i{}^{0.5}\,\mathbf{D}_i\mathbf{Y}_i{}^{0.5} = \dot{\mathbf{Y}}_i - \mathbf{Y}_i\,\mathbf{W}_{\mathbf{R}}^{\mathrm{T}} - \mathbf{W}_{\mathbf{R}}\,\mathbf{Y}_i, \qquad \mathbf{W}_{\mathbf{R}} = \dot{\mathbf{R}}\,\mathbf{R}^{\mathrm{T}}.$$

The formula uses the following notations:

$$\mathbf{Y}_i = \mathbf{V}_i{}^{\frac{2}{\nu_m}}, \qquad \nu_m > 0,$$

where $\mathbf{R}$ — is the rotation tensor in the polar decomposition $\mathbf{F} = \mathbf{VR}$ of the strain gradient of the medium $\mathbf{F}$ into the left stretch tensor $\mathbf{V}$ and the rotation $\mathbf{R}$; $\nu_m$ is the ratio of the m-th transmission element, which is connected on the left to the elastic element under consideration. The rate of work done in the i-th elastic element is determined by the formula

$$\mathbf{T}_i\cdot\mathbf{D}_i = \rho\sum_{k=1}^{3}\frac{\partial f}{\partial\lambda_k^{(i)}}\,\dot{\lambda}_k^{(i)} - \frac{\rho\,\dot{\nu}_m}{\nu_m}\sum_{k=1}^{3}\frac{\partial f}{\partial\lambda_k^{(i)}}\,\lambda_k^{(i)}\ln(\lambda_k^{(i)}).$$

The deviator of the Cauchy stress tensor $\mathbf{T}_j$ of the viscous element is calculated from the equations of the theory of nonlinear viscous fluid using the appropriate strain rate tensor $\mathbf{D}_j$ :

$$\operatorname{dev}\mathbf{T}_j = 2\,\eta_j\,\mathbf{D}_j,$$

For the n-th plastic element, the Cauchy stress tensor deviator is determined by the equations of the theory of plastic flow

$$\mathbf{D}_n = \sqrt{\frac{\mathbf{D}_n\cdot\mathbf{D}_n}{\operatorname{dev}\mathbf{T}_n\cdot\operatorname{dev}\mathbf{T}_n}}\,\operatorname{dev}\mathbf{T}_n,$$

To complete the system of equations, the proportional relation between the strain rate tensors of the plastic element $\mathbf{D}_n$ and that of the material is used $\mathbf{D}$.

$$\sqrt{\mathbf{D}_n\cdot\mathbf{D}_n} = \kappa_n\sqrt{\mathbf{D}\cdot\mathbf{D}},$$

where the term $\kappa_n$ is the non-negative function obtained from the relation

$$\kappa_n = \begin{cases} 0, & \text{when } \Phi_n(\mathbf{T},...) < g_n, \\ \zeta_n(g_n), & \text{when } \Phi_n(\mathbf{T},...) = g_n. \end{cases}$$

The flow function $\Phi_n$ that is used to formulate the criterion for the development of plastic deformations in the medium is the function of the Cauchy stress tensor $\mathbf{T}$ of the

medium. The plastic deformation of the medium takes place only in the case when the flow function $\Phi_n$ reaches its maximum value over the entire history of the medium development.

$$g_n = \max \Phi_n.$$

To describe the nonlinear visco-elastic-plastic behavior of the environment with the help of this model, you need to know four of dependence, which can be obtained from the experimental data for uniaxial cyclic loading with increasing sample at each cycle, the maximum strain (Fig. 1). This $C_1(g)$, $C_2(g)$, $\kappa(g)$ and $\eta(g)$, where $g = g_3 = \max \Phi_3(\mathrm{V})$.

## Results

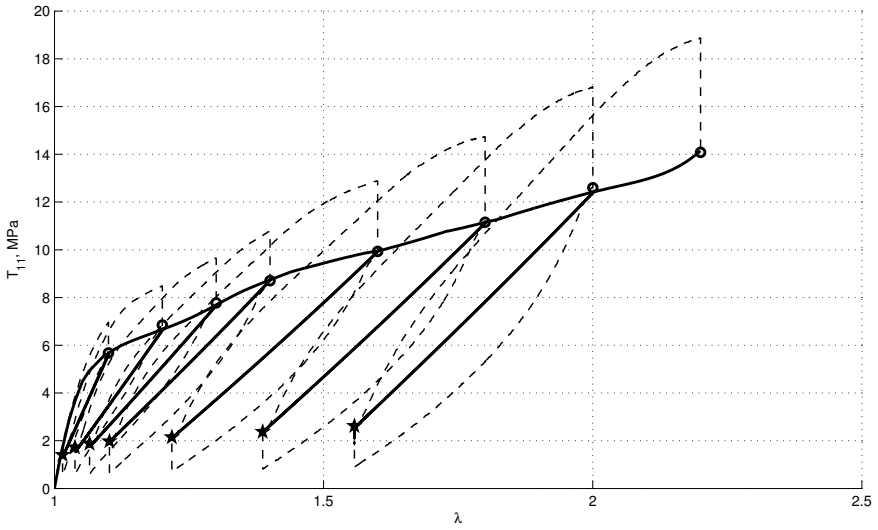


Figure 3: Scheme of the equilibrium cycle loading (excluding the viscous properties of the medium).

Calculating dependencies carried out in two stages. In the first phase were determined $C_1(g)$ and $\kappa(g)$. At the same time believed that the medium is elastic-plastic, ie, considered the equilibrium loading of the material (so slow that the relaxation processes associated with the viscous flow of the medium can be ignored) (Fig. 3). In this case the elastic stiffness of the elastic element number 1 for the maximum in a given cycle of deformation can be determined from the unloading curve through the points marked with ∘ (the end of the relaxation after the load) and * (end of relaxation after unloading), as this process was considered a purely elastic. Doing it this way: There are two points ∘ and *. Through them it is necessary to carry out the purely elastic curve of uniaxial tension (compression):

$$\sigma(C_1, \lambda_e) = \sigma^0 \lambda_e$$

where $\lambda_e$ - the multiplicity of elastic elongation of the sample, $\lambda$ - complete (ie, taking into account the multiplicity of plastic elongation $\lambda_p$). You must solve a system of two nonlinear equations with two unknowns: $C_1$ and $\lambda_p$.

Contact the plastic and elastic deformation viewed as relations between $\lambda_e$ $\lambda_p$, and because of the multiplicative decomposition of the Lie:

$$\lambda = \lambda_e \times \lambda_p$$

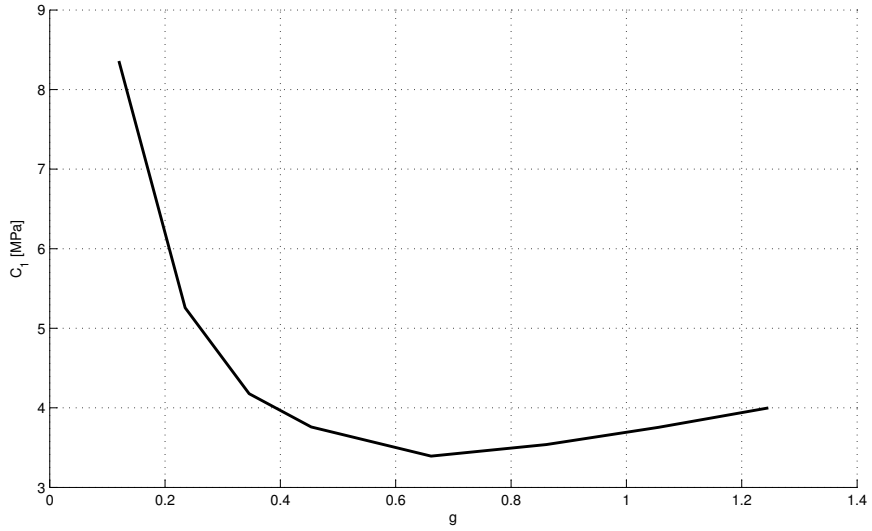


Figure 4: The dependence of the elastic stiffness of the element number 1 on the parameter $g$.

Substituting in the desired elastic equation (uniaxial loading) will have the form:

$$\begin{cases} \sigma\mid_0 = NC_1[(\lambda_o/\lambda_p)^N - (\lambda_o/\lambda_p)^{-N/2}] \\ \sigma\mid_* = NC_1[(\lambda_*/\lambda_p)^N - (\lambda_*/\lambda_p)^{-N/2}] \end{cases}$$

write the functional $\Psi(C_1,\, \lambda_p)$ and minimize it:

$$\Psi(C_1, \lambda_p) = \\ = \{\sigma\mid_0 - NC_1[(\lambda_o/\lambda_p)^N - (\lambda_o/\lambda_p)^{-N/2}]\}^2 + \{\sigma\mid_* - NC_1[(\lambda_*/\lambda_p)^N - (\lambda_*/\lambda_p)^{-N/2}]\}^2.$$

The values $C_1$, $\lambda_p$, the corresponding $\Psi(C_1,\, \lambda_p) = 0$, are the required quantities.

The dependence of the plastic parameter $\kappa$ on q were selected from the incremental elastic-plastic solutions of the model problem (excluding at this stage, the viscous component of the model) so as to maximize overlap with the experiment. In this case it means that the calculated curve corresponding to an increase in the load must pass through the "circles" and the handling of dependence - through the "circles" and "stars" (see Fig. 3, 4). Seeking $\kappa$ dependence on $g$ is shown in Fig. 5.

It was believed that the parameter $C_2$ is responsible for the elastic properties of the amorphous phase of the polymer, which does not undergo structural changes during deformation of the medium.

Therefore, the model $C_2$ was considered constant.

By setting different values for the constants $C_2$ and choosing the appropriate form of the curve $\eta(g)$ was found optimal in terms of coincidence of calculation and the experimental value of $C_2$ is approximately 10 MPa. For the Neo-Hooke, this corresponds to the initial Young's modulus $E_0 = 60$ MPa, which agrees well with known data on polyethylene.

In Fig. 6 shows the final calculated curves and the experiment.

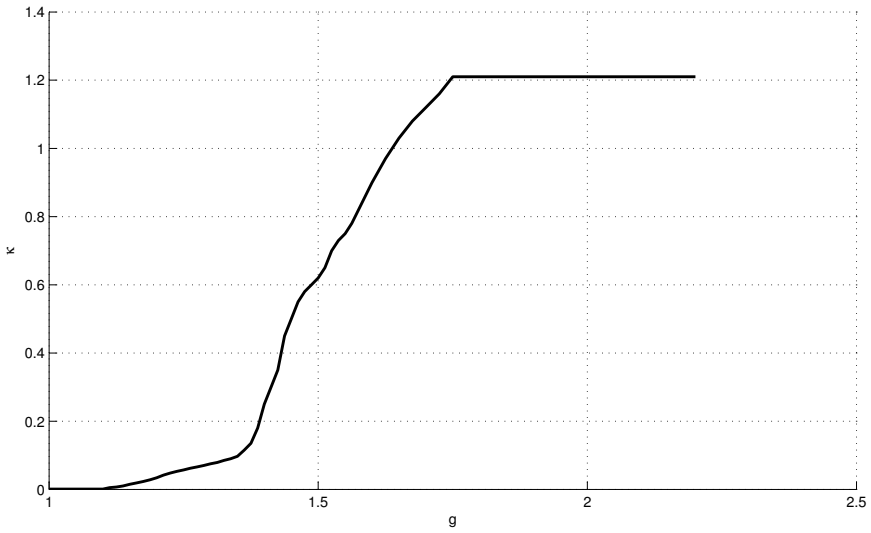


Figure 5: The dependence of the plastic parameter $\kappa$ on $g$.

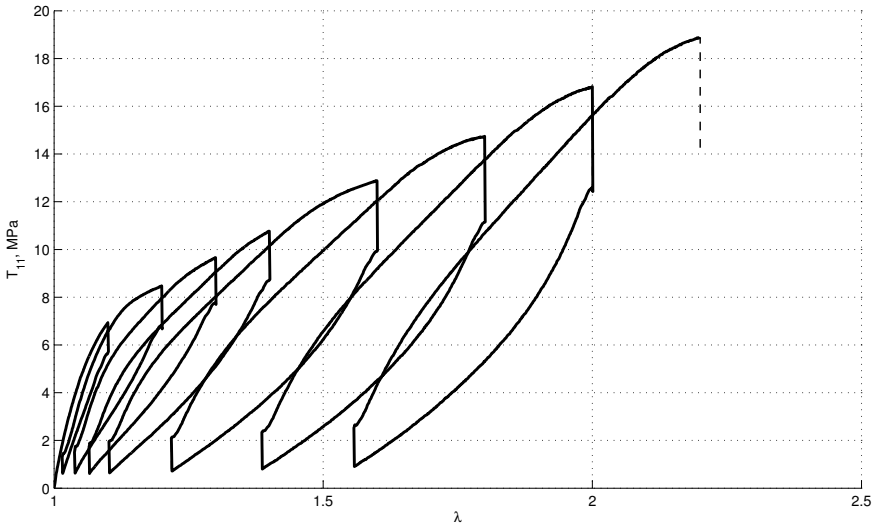


Figure 6: Curves of cyclic elasto-visco-plastic loading of polyethylene. Dashed line - experiment, solid - the calculation.

## Conclusion

As can be seen from the last graph, the model allowed to describe accurately the actual cyclic loading of polyethylene with an increasing strain on each cycle.

## Acknowledgements

*This work is executed at a financial support of the Russian fund (Grant 12-03-00694 a and The Research Program of UB RAS, SB RAS and FEB RAS 12-C-1-1015).*

## References

[1] Fengge G. Clay/polymer composites: the story. Materials Today. - 2004. - N 11. - P. 50-55.

[2] Sheng N., Boyce M.C., Parks D.M., Rutledge G.C., Abes J.I., Cohen R.E. Multiscale micromechanical modeling of polymer/clay nano-composites and the effective clay particle // Polymer. - 2004. - V. 45. - P. 487-506.

[3] Svistkov A. L., Lauke B., Heinrich G. Modeling of viscoelastic properties and softening of rubber materials // Proceedings of 5th European conference "Constitutive models for rubbers" Paris, 2007. P. 113-118.

[4] Palmov V. A. Comparison of different approaches in viscoelastoplasticity for large strain // ZAMM. 2000. V. 80. P. 801-806.

*Garishin O.K., Korlyakov A.S., Shadrin V.V. Institute of continuous media mechanics UB RAS, Perm, Russia*

# Influence of purity degree on the evolution the mechanical properties of aluminium commercial

A. Hakem Y. Bouafia
a_hakem1951@yahoo.fr

**Abstract**

The influence of the purity degree of the commercial aluminium on the mechanical properties: elastic stress, tensile strength, Brinell hardness, resilience and elongation at break was investigated. It was found that the first three resistance characteristics decrease with the growth of the purity of the material chosen to the detriment of two ductility characteristics that rise to the three states considered: crude of casting noted: $F$, Annealed noted: $O$, hardened noted : $H1/4$. Furthermore, it is important to note that the hardened and the annealed lead respectively to a considerable hardening and a considerable softening. This hardening and this softening of the material in question can be respectively associated with the increase in dislocation density and immigration impurity elements of dislocations.

**Keywords:** Purity, aluminum, properties, mechanical, hardness.
**Themes:** Mechanical and civil engineering applications.

## 1 Introduction

The natural aluminum does not exist. Indeed, although equal to 8% of elements on earth, man invented by extracting it from bauxite. The discovery of aluminum material with outstanding features: light weight, ductility, mechanical strength and weather, fastness, good thermal and electrical conductivities. These properties have quickly made aluminum one of the most magical materials used in the production of consumer goods of high and very high series with a tendency to consolidate its position as second only to steel. Extracted for the first time in the laboratory in 1825 and operated only industrially since 1880 after the discovery of electrolysis, aluminum has become in a century for its strength and lightness in in a wide range of applications on land, sea and air. This material has no harmful influence on environment both in production and in its recovery to its recyclability.

Aluminium and its alloys, and therefore will have a positive impact on quality of life for all of us.

Historically, the study of physical, chemical and mechanical in general especially the aluminum business and raises many questions of scientific interest and technological importance which did not leave indifferent to many researchers, since the use of this material is widely used in industry and in practice. It easily lends itself to shaping the cold plastic deformation (drawing, spinning, bending, cutting and boiler). He demonstrated excellent performance in a humid atmosphere and ocean.

Since the commercial aluminum enters the composition of many achievements and industrial applications, which are subject to various mechanical stresses, and in order to achieve a reliable product that must meet the proper functioning of the system to which

it belongs, the properties this material mechanical saw multitudes of investigations and attracted the attention of many researchers. It was shown that the purity of the commercial aluminum significantly influences its mech anical properties.

In the literature, it was shown that the value of the yield strength of pure polycrystalline aluminum is about 4 times lower than that of the commercial aluminum.

Many authors have studied the mechanical properties of commercial aluminum with a purity of at least 99%. They lead to the following results: in the annealed condition, the majority of the mechanical properties are low, but they can be improved by cold working: for example, in the annealed condition hardened state, the yield increased from 28 to 125 MPa and the tensile strength varies from 70 to 130 MPa.

However, the results obtained by different authors are often conflicting and tight, if not contradictory.

Our job is to contribute to the effect of purity on the mechanical strength, Brinell hardness and resilience of the aluminum used in several commercial industrial achievements.

## 2 Material studied

The materials used are provided by the national ELECTRO - INDUSTRIES. There are three types of aluminum commercial purity (Al-99, 0%, Al-99, 5% Al-99, 8%) who were selected to carry out this study.

## 3 Elaboration of the alloy studied

### 3.1 Casting:

The melting of the metal is in a gas oven production will switch from front to back, with a graphite crucible with a capacity 350Kg load is composed approximately $\approx 100\%$ of aluminum ingots new commercial dimensions standardized composition and specified characteristics, delivered by the French company Pechiney. Once the mass has become liquid full at about 700° C. The liquid mass is then subjected to degassing treatment and coverage in the oven.

Then the metal is poured, or in a warm pocket of 50Kg prepared for this purpose for sand casting and series, or in a holding furnace of 150kg set properly for the unit shell mold preheated and that we proceed carefully prepared refining operations. Parts can be cast into the shell, respectively single metal or sand molds prepared for it, so the reference specimens are known as a crude of casting noting: F. To seek to increase over the characteristics of resistance to the state F, the two materials different degrees of purity will be subject to specific treatments of annealed and the hardened.

### 3.2 MOLDING:

**METAL SHELL:** In this mode of molding, the mold consists of two steel slabs (5% chromium), which is responsible for maintaining the footprints. These steel slabs, separated by a parting line, may be prepared and heated to a temperature $(200 \div 300)°$ C. After molding, the specimens cast metal shell by gravitation will be divided into three lots, each consisting of five identical tensile specimens , five specimens of resilience and a sample for the micrographic observation considering three states: a crude of casting notes: F, annealing noted: O and hardened noted: $H1/4$.

### 3.3 TREATMENTS OF:

- Annealing: heating and dissolved with homogenization at 540° C for 10 h followed by cooling in the oven,
- Hardening: deformation of 25% in 3 passes with a six-cylinder mill.

Once processing is done, the material will be tested in quasi-static uniaxial tensile loads and low speeds, Brinell hardness and quasi dynamic resilience to quantify the different characteristics of resistance and ductility needed for different calculations which we need the design engineer at the department. The microstructure complement the study to fully identify the material.

## 4 EXPERIMENTAL PROCEDURE:

To determine the behavior of the material meet the different demands it may encounter during use, these solicitations are reproduced using static or dynamic tests, usually performed on standard specimens to determine the characteristics encrypted material. Four techniques are used, namely: the pull to identify the various constraints, the Brinell hardness HB for the stress field, Kcv resilience tells us about the mode of fracture, fragility and the impact resistance and metallography to identify structures. We will describe in more detail and present in the main mechanical characteristics of the material being obtained in this study.

## 5 RESULTS OBTAINED AND DISCUSSION

The average values of mechanical strength, impact strength and hardness of the three states of the aluminum commercial are those given by averaging five identical specimens for each of the respective cases and are represented by the figures of 1 to 5 mentioned below.

### 5.1 Influence of purity degree on the evolution the caracteristics of resistance of the three states of the commercial aluminum

**DISCUSSION:** For the three states considered in choosing commercial aluminum, we followed the evolution of variations of the three main features of resistance: average stress of elasticity noted $< \sigma e >$, maximum average stress noted $< \sigma m >$ and Brinell hardness average noted $< HB >$ depending in the purity of the material studied.

Figures 1, 2 and 3 show that the average curves of the three mechanical characteristics of resistance of the three states considered to decrease with the growth of the purity at the expense of ductility, however, the speed of decrease varies differently depending on the mechanical characteristic and the state considered.

We also note that the average curves of the three characteristics of resistance of the hardened state are located too far above those of the annealed condition, which are themselves just above those of the as-cast state.

### 5.2 Influence of purity degree on the evolution the caracteristics of ductility of the three states of the commercial aluminum

**DISCUSSION:** The same for the three states considered in choosing commercial aluminum, we have also followed the evolution of variations of two main features of ductility:

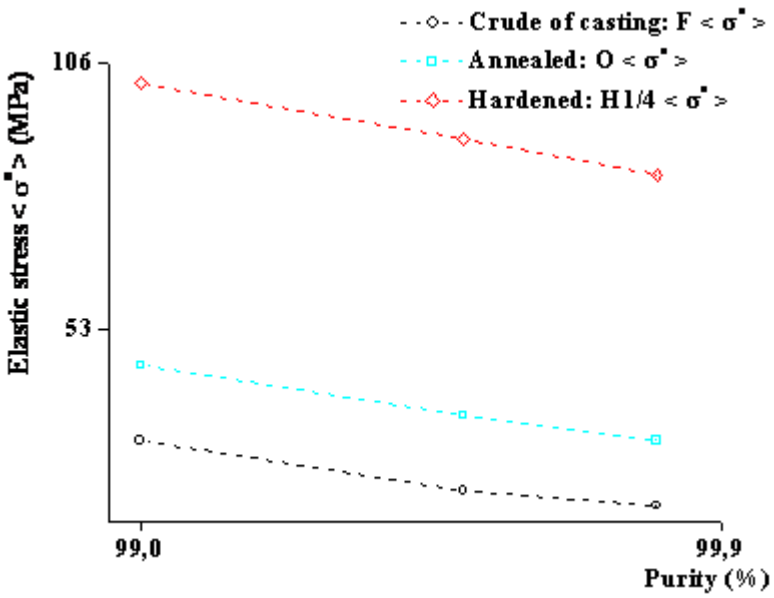


Figure 1: Group of graphs (average stress of elasticity – purity degree) of comparison in averaging a series of five identical specimens of the aluminum commercial of the three states: crude of casting noted: F, annealing noted: O and hardened noted: $H1/4$.

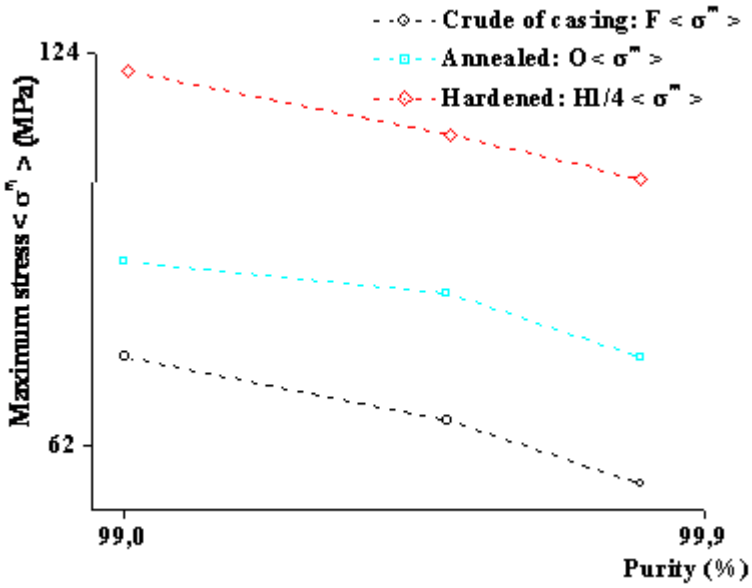


Figure 2: Group of graphs (maximum average stress – purity degree) of comparison in averaging a series of five identical specimens of the aluminum commercial of the three states: crude of casting noted: F, annealing noted: O and hardened noted: $H1/4$.

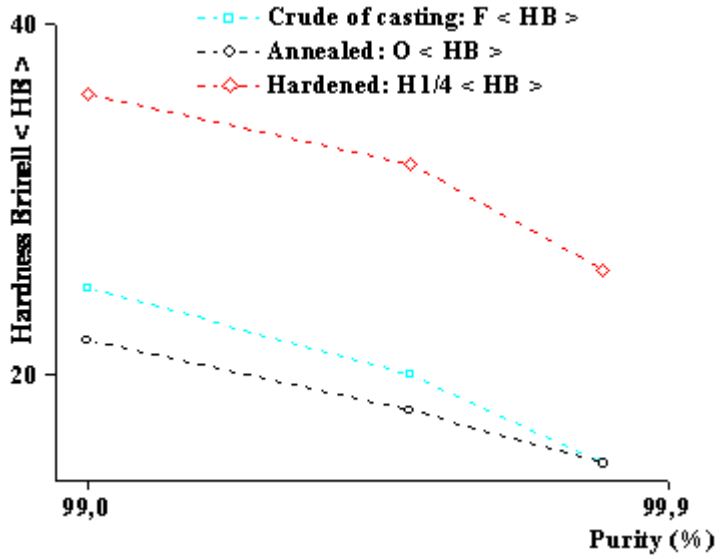


Figure 3: Group of graphs (hardness Brinell HB average – purity degree) of comparison in averaging a series of five identical specimens of the aluminum commercial of the three states: crude of casting noted: F, annealing noted: O and hardened noted: $H1/4$.

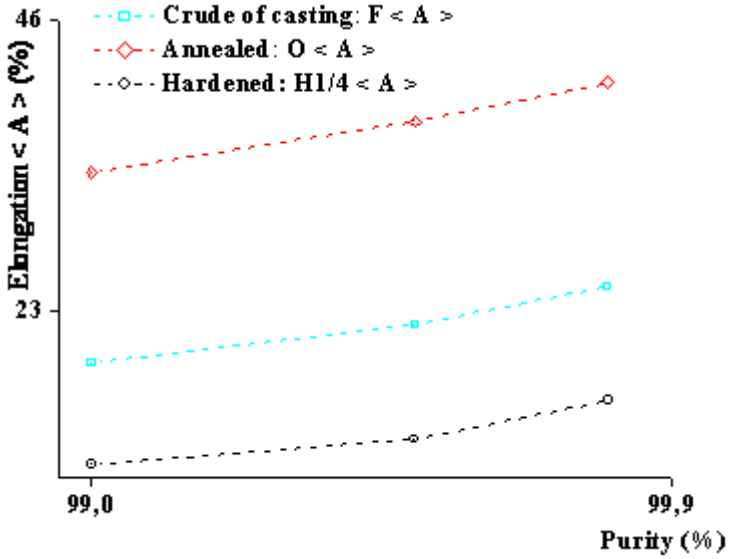


Figure 4: Group of graphs (average elongation A% – purity degree) of comparison in averaging a series of five identical specimens of the aluminum commercial of the three states: crude of casting noted: F, annealing noted: O and hardened noted: $H1/4$.

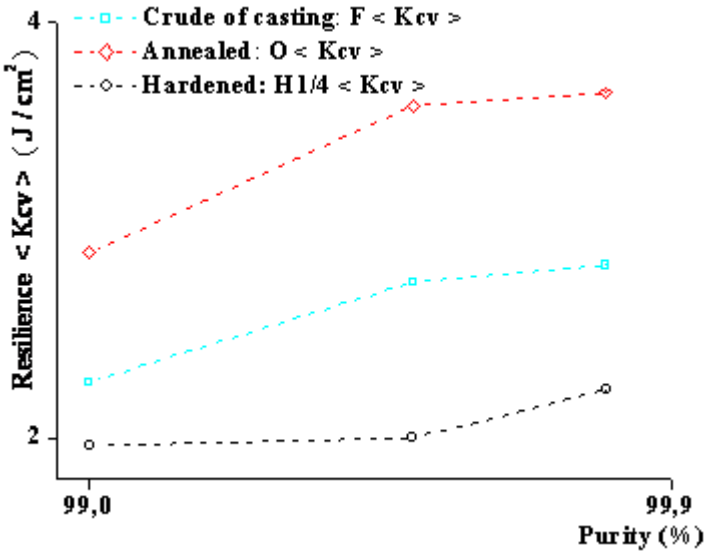


Figure 5: Group of graphs (average resilience Kcv – purity degree) of comparison in averaging a series of five identical specimens of the aluminum commercial of the three states: crude of casting noted: F, annealing noted: O and hardened noted: $H1/4$.

average resilience designated < Kcv > and average elongation designated < A% > depending on the purity of the material studied.

Figures 4 and 5 show that the average curves of the two mechanical characteristics of ductility of the three states considered to grow with the growth of the purity at the expense of resistance characteristics , however, the growth speed varies differently depending on the mechanical characteristic and the state considered.

We also note that the average curves of the two characteristics of ductility of the annealed state are located too far above those of the as-cast state, which are themselves just above those of the hardened state.

**CONCLUSION:** In this study the mechanical properties of tensile, Brinell hardness and resilience of the aluminum commercial, we have shown that the strain hardening delays the onset of the movement of dislocations, but accelerates the process of rupture and also leads to a considerable hardening and a drop of plasticity simultaneously. In the annealed condition, the material hardens, but the hardening is lower to that of the material in the hardened state. In addition, during this annealing is a great plasticity of the material. The poor mechanical properties of the material in the as-cast state be associated with the presence of heterogeneities. The increase in purity leads to softening of the material.

## References

[1] Lakhtine. Metallography and heat treatment of metals, Third Edition Mir, 1982.

[2] Solidifications characteristics of aluminum alloys: Volume 2: Foundry alloys, Amer Foundry society, 1993.

[3] Ahmed HAKEM, Y. BOUAFIA, A. SALHI, influence of industrial processes of molding and time of maturation on the characteristics of resistance of ductility and struc-

tural alloy hypoeutectic AlSi7Mg, Summer School in Advanced Problems in Mechanics APM 2010, July 1 - 5 2010, St. Petersburg, Russia.

[4] Ahmed HAKEM, A. BENMEDJBER, A.SALHI, Y.BOUAFIA, influence of the addition of Mg, the mode of elaboration and the time of maturation on the mechanical and structural properties of the alloy eutectic 44000 unstandardized, APM 2011 Advanced Problems in Mechanics Russia, St. Petersburg July 1 - 5, 2011 International Summer School-Conference.

[5] L. Bäckerud, Solidification characteristics of aluminum alloy, Oslo, Norway: Skanaluminium,Universitetsforlaget AS, 1986-1996.

[6] Ahmed Hakem, Y. Bouafia, A. Salhi Influence of User Development and Aging on Mechanical Characteristics and microstructure of the alloy foundry AlSi10Mg, ACMA, 2010, 12-14 May 2010, Marrakech, Marocco.

[7] Ahmed Hakem, Y. Bouafia, S. Naïli, A. Bouhaci, Development of industrial aluminum alloys foundry AlSi7Mg, AlSi10Mg and AlSi13Mg, International Symposium - Characterization and Modeling of Materials and Structures 16, 17 and18 November, 2008 - University Mouloud Mammeri Tizi-Ouzou, Algeria.

[8] Ahmed Hakem, memory magister, Microstructure and Mechanical Properties of Alloy hypoeutectic AlSi7Mg, 2005, Department of Engineering - Mechanical Engineering, Faculty of Engineering Building, University Mouloud Mammeri Tizi – Ouzou . Algeria.

[9] M. Colombia and Coll, Industrial Materials: Metal Materials, p.867, Dunod, Paris (2000).

[10] Jean-Paul Baillon, Jean-Marie Dorlot, Materials, p.729, 3rd edition, Ecole Polytechnique de Montreal, Montreal (2000).

[11] 1.Jean Baralis Gerard Maeder, Handbook of Metallurgy: (Preparation, structure, properties, normalization), p.232, 1ereédition, AFNOR-Nathan, Paris (1997).

*Ahmed HAKEM, Y. BOUAFIA, Laboratory LaMoMS, Mouloud MAMMERI university of Tizi-Ouzou Hasnaoua II, 15000 Algeria*

# Linking microscopic reversibility to macroscopic irreversibility, emphasizing the role of deterministic thermostats and simple examples, at and away from equilibrium

Wm. G. Hoover Carol G. Hoover
hooverwilliam@yahoo.com

**Abstract**

Molecular Dynamics and Statistical Mechanics make possible a particle-based understanding of Thermodynamics and Hydrodynamics, including the fascinating Loschmidt contradiction between time-reversible atomistic mechanics and the time-irreversible thermodynamic dissipation incorporated into macroscopic fluid and solid mechanics.

## 1 Introduction

Among the many problem areas in mechanics the study of instabilities and irreversible processes seem particularly interesting. Engineering mechanics exists as a discipline because failures of structures cost so many lives. The analysis of local Lyapunov instability gives a means for localizing and predicting catastrophic failures so that there is a decidedly practical engineering aspect of this fascinating scientific research area.

The goal we pursue here is to develop models that help us to understand. It is profoundly interesting that the small scale microscopic models of material behavior (ordinary Newtonian mechanics) are time-reversible while the macroscopic models of the same thing (finite-element and finite-difference fluid mechanics and solid mechanics) are irreversible. The tools from nonlinear dynamics and chaos are useful in analyzing these two kinds of description.

Here we describe the basic building blocks for particle simulation and point out the ways that these time-reversible simulations already lead to time-irreversible behavior. Most of the examples treated here are also described in our three books on computational statistical mechanics, smooth-particle applied mechanics, and time reversibility, computer simulation, algorithms, and chaos[1, 2, 3].

## 2 Algorithm for Conservative Particle Mechanics

No special tricks are necessary to get started with particle-based simulations. Microscopic mechanics can provide us with accurate particle trajectories $\{ q(t) \}$ . All we need to do is to integrate Newton's ordinary differential equations of motion ,

$$\{ m\ddot{q} = F(q) = -\nabla\Phi \} .$$

Here $\Phi$ is the potential energy, a function of the coordinates $\{\ q\ \}$ . Alternatively, we can obtain an equivalent coordinate-momentum description $\{\ q(t), p(t)\ \}$ by integrating Hamilton's first-order ordinary differential equations:

$$\{\ \dot{q} = +(\partial\mathcal{H}/\partial p)\ ;\ \dot{p} = -(\partial\mathcal{H}/\partial q)\ \}\ .$$

Both these approaches are time-reversible. That is, a movie of the motion, played backwards, satisfies exactly the *same* equations (with the values of $q$ and $p$ in reversed order and with the sign of $p$ changed also). A movie is an excellent analog of numerical simulation. Both the simulation and the movie are sets of discrete records of coordinates at discrete values of the time, separated by the "timestep" $\Delta t$ . In addition to the basic algorithm keep in mind that three crucial questions remain to be answered: [1] what are the initial conditions, [2] what are the boundary conditions, and (most important of all) [3] what is the problem to be solved?

Macroscopic continuum mechanics is based on the three conservation laws for mass, momentum, and energy:

$$\dot{\rho} = -\rho\nabla\cdot u\ ;\ \rho\dot{u} = -\nabla\cdot P\ ;\ \rho\dot{e} = -\nabla u : P - \nabla\cdot Q\ .$$

Here $\rho$ is density, $u$ is velocity, $e$ is energy per unit mass, $P$ is the pressure tensor (force per unit area, necessarily a symmetric second-rank tensor), and $Q$ is the heat flux vector (energy flow per unit area). All these variables are continuous functions of space and time. Both $P$ and $Q$ , as well as $\dot{\rho}$ , $\dot{u}$ , and $\dot{e}$ , are defined in the *comoving* frame, a coordinate frame moving with the local velocity $u(r,t)$ . Finite-difference approximations to the gradients on the righthand sides of the three continuum equations, evaluated at a discrete set of spatial mesh points, reduce the partial differential equations to ordinary ones, which can then be solved with Runge-Kutta integration. Again, the hard part of the problem is the same: what to do and how to implement the initial and boundary conditions.

Different materials can be described by different types of constitutive relations (elastic, plastic, viscous, ...) giving $P$ and $Q$ in terms of the basic $\{\ \rho, u, e\ \}$ set, together with their time derivatives and spatial gradients. Time-reversed movies of solved macroscopic problems look "funny" and make no sense. This is because the underlying phenomenological constitutive relations are typically irreversible. The simplest most familiar irreversible examples are Newtonian viscosity and Fourier heat conduction:

$$P = [\ P_{\rm eq} - \lambda\nabla\cdot u\ ]I + \eta[\ \nabla u + \nabla u^t\ ]\ ;\ Q = -\kappa\nabla T\ .$$

In the symmetrized velocity gradient $\nabla u^t$ is the transpose of $\nabla u$ . $I$ is the unit tensor. A boxed conducting fluid, with that fluid initially in motion, (a Rayleigh-Bénard flow, for instance, but with the box suddenly insulated and with the accelerating gravitational field suddenly switched off) described with a shear viscosity $\eta$ and a heat conductivity $\kappa$ eventually comes to an isothermal state of rest. Evidently the reversed movie of this decay makes no sense and would correspond to an illegal "something from nothing" contradicting the Second Law of Thermodynamics. Of course, with the right initial conditions and the right boundary conditions, one can indeed observe tornadoes! For an $L \times L$ (two-dimensional) system, with kinematic viscosity and thermal diffusivity of order $D$ the initial gradients decay exponentially, $\simeq e^{-Dt/L^2}$ . The reversed movie, with its exponential growth, $\simeq e^{+Dt/L^2}$ , is simply wrong.

In applications of mechanics to simulation we strongly recommend the use of the fourth-order Runge-Kutta integrator because it is easy to use and to modify for the treatment of

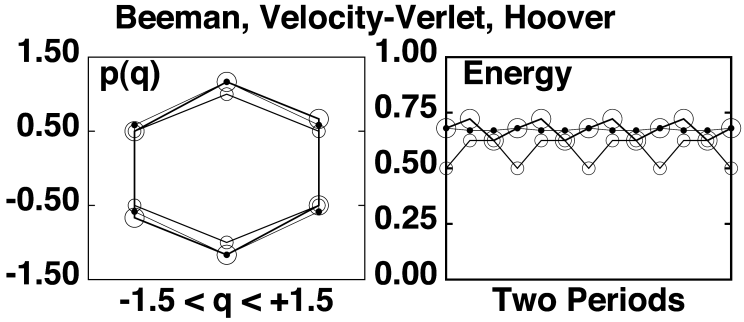


Figure 1: The Beeman and Velocity-Verlet approximations to the harmonic oscillator momentum are compared with the more nearly accurate formula given in the text (at the left). The corresponding total energies are shown at the right over two oscillations with $\Delta t = 1$ . The approximation mentioned in the text is the best of the three and corresponds to the smallest dots.

open systems interacting with their environments. If the focus is on the time-reversibility of conservative Newtonian systems it is useful to consider a very simple, yet rigorously time-reversible, integrator discovered by Levesque and Verlet[4]. In order better to understand the coexistence of the reversible microscopic and irreversible macroscopic views we adopt Levesque and Verlet's "bit-reversible" algorithm. This approach generates a numerical trajectory in an *integer* coordinate space, by rounding off the acceleration terms:

$$\{\ q_{n+1} - 2q_n + q_{n-1} = [\ (F(q_n)(\Delta t)^2\ ]_{\text{integer}}\ \}\ .$$

The subscripts indicate the time, in units of the (integer) timestep $\Delta t$ . The initial conditions to start this algorithm are the coordinates at two successive times.

A simple illustration of the algorithm follows a harmonic oscillator trajectory, using unit mass, force constant, and timestep $\Delta t$:

$$q_+ - 2q_0 + q_- = -q_0 \longrightarrow q_+ \equiv q_0 - q_-\ .$$

The solution of repeating coordinates $\{\ +1, +1, 0, -1, -1, 0, \ldots\ \}$ , is typical, and illustrates the fact that no matter what the initial conditions, the solution is both periodic (for chaotic problems, the length of the period is of order the square root of the number of states) and reversible. The algorithm is a faithful analog of classical deterministic time-reversible mechanics. If momenta are desired they too can be approximated accurately from the coordinate values:

$$p_0 \equiv \left[\frac{4}{3}\right] \frac{(q_+ - q_-)}{2\Delta t} - \left[\frac{1}{3}\right] \frac{(q_{++} - q_{--})}{4\Delta t}\ .$$

Figure 1 compares the energy calculated with these momenta with calculations based on the Beeman and velocity-Verlet algorithms. Our formulation (small dots in the Figure) is clearly an improvement. It is evident that a promising research area lies in the development of higher-order bit-reversible algorithms combining coordinates, velocities, and accelerations from more than three successive times.

## 3 Irreversibility from Time-Reversible Motion Equations?

Is there any chance of detecting *irreversibility* with such a time-reversible algorithm? Oddly enough, there is! It is based on the analysis of Lyapunov instability, looking in the *neigh-*

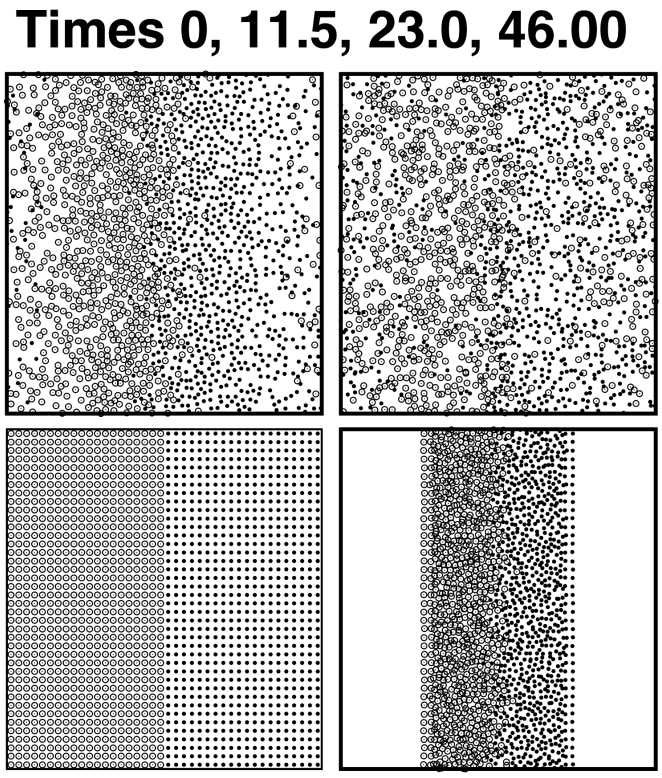


Figure 2: Snapshots from the twofold compression of a $40 \times 40$ cold crystal with unit density and with the pair potential $\phi = (1 - r^2)^4$ . Initially half the particles move to the right and half to the left, at speed 0.875 . The second snapshot, time = 11.5, and located at bottom right, corresponds to the maximum twofold compression. Such "irreversible" motions can be reversed precisely, for as long as desired, with the Levesque-Verlet bit-reversible integration algorithm.

*borhood* of the trajectory, not just at the trajectory itself. Such a nonlocal analysis necessarily depends upon the imagination and the information contributed by an observer of the motion. Let us take an example, a *maximally irreversible* situation described by time-reversible, even bit-reversible, Newtonian mechanics. Consider the pair of shock-waves launched by the collision of two mirror-image fluid samples. See Figure 2 for four snapshots of such a problem. *Initially* the velocities are $\pm u$ . *Eventually* the periodic $L \times L$ system shows no more systematic motion – the initial kinetic energy has been completely converted to internal energy (heat):

$$(u^2/2) \to e \ .$$

Just as before, any portion of the developing trajectory can be reversed precisely and exactly despite the Lyapunov instability (exponential growth of perturbations) of the dynamics.

There is a vast literature[5, 6, 7, 8, 9] on the quantification of Lyapunov instability, the exponentially sensitive deformation of comoving hypervolumes in $q$ space, $p$ space, or $\{ q, p, \}$ phase space. For $N$ particles in two dimensions the $4N$-dimensional phase-space motion defines $4N$ local Lyapunov exponents. The fact that these "local" exponents

depend upon the chosen coordinate system can be viewed as a disadvantage or as an opportunity. Again, there are many promising research problems suggested by this observation. Optimizing the analysis is certainly a useful and stimulating activity.

The largest Lyapunov exponent – we will call it $\lambda_1(t)$ – associated with the motion can be found by following two nearby trajectories in time. The primary or "reference" trajectory can be generated with bit-reversible dynamics, so that it is possible to extend it as far as desired into the future or the past[7]. The dynamics of a nearby "satellite" trajectory is restricted by constraining the satellite trajectory to stay within a fixed distance of the reference trajectory. The satellite dynamics can readily be generated with Runge-Kutta integration, rescaling the separation between the two trajectories at the end of each time step. The local Lyapunov exponent is:

$$\lambda_1(t) \equiv \left[\frac{1}{\Delta t}\right] \ln\left[\frac{(\Delta r)_{\text{before}}}{(\Delta r)_{\text{after}}}\right] \ ; \ \Delta r \equiv |r_{\text{satellite}} - r_{\text{reference}}| \ .$$

Although the motion equations are perfectly reversible for both the reference and the satellite, the reversed satellite trajectory turns out to be totally unlike the forward one, *if* the system is a nonequilibrium system. Both the local Lyapunov exponent associated with the instability and the identities of those particles making above-average contributions to the offset vector separating the trajectories , $\Delta r \equiv r_{\text{satellite}} - r_{\text{reference}}$, are qualitatively different. In a typical shockwave simulation of the type shown in Figure 2 the number of these more-heavily-weighted particles is about twice as great in the reversed motion as in the forward one.

This is an extremely interesting result. No doubt it suggests various "Arrows of Time" which can be constructed based on the structure of nearby trajectories (which react to the past, not the future). A study of irreversible flows from this standpoint should shed light on the reversibility paradox for simple Newtonian and Hamiltonian systems.

# 4 Irreversibility for Time-Reversible "Open" Systems

In order to control nonequilibrium states, in particular nonequilibrium *steady* states, it is necessary to do work and/or to exchange heat, with the system of interest. The dynamics becomes a little more complicated due to these interactions, but the interpretation compensates by becoming simpler. Here we take up the description of "open systems".

## 4.1 Microscopic Pressure, Heat Flux, and Temperature

"Open" systems have mechanical and/or thermal connections to their environment, opening up the possibility of simulating processes including thermodynamic work and the flow of heat. Analysis of these systems requires microscopic analogs for all the continuum variables. Density, velocity, and energy are the simplest of these. We adopt the smooth-particle averaging method discovered by Lucy and Monaghan in 1977[10, 11]:

$$\rho(r,t) \equiv \sum_i m_i w(r - r_i) \ ; \ \rho(r,t)u(r,t) \equiv \sum_i m_i v_i w(r - r_i) \ ; \ \rho(r,t)e(r,t) \equiv \sum_i m_i e_i w(r - r_i) \ .$$

The particle energies $\{ \ e_i \ \}$ are necessarily defined in the comoving frame, which moves with velocity $u(r,t)$ . A useful weight function, with a range $h$ which can be optimized, is Lucy's, here normalized for two space dimensions:

$$w(r) = (5/\pi h^2)(1 + 3z)(1 - z)^3 \ z \equiv |r|/h \ .$$

This weight-function approach guarantees the continuity of the first and second spatial derivatives of the field variables and lends itself to optimization studies.

In addition to the basic mass, momentum, and energy, several other variables need to be considered in order to compare microscopic and macroscopic simulations. Unlike their continuum cousins, the pressure tensor and the heat flux vector from molecular dynamics are respectively even and odd functions of the time:

$$PV = \sum_{\text{pairs}} (rF)_{ij} + \sum_i (pp/m)_i \ ; \ QV = \sum_{\text{pairs}} r_{ij}[\ F_{ij} \cdot (p_i + p_j)/2\ ] + \sum_i (ep/m)_i \ .$$

Here $r_{ij} \equiv r_i - r_j$ and $F_{ij}$ is the force on Particle $i$ due to its interaction with Particle $j$. The individual particle energies $\{\ e_i\ \}$ include half of each particle's pair interactions with its neighbors.

Temperature needs a definition too. The usual equilibrium definition, based on entropy, is useless away from equilibrium where entropy has no consistent definition[1, 2]. *At* equilibrium *Temperature* can be defined in many ways, all based on Gibbs' statistical mechanics or Maxwell and Boltzmann's kinetic theory. The even moments of the velocity distribution are examples. In addition to these there are also configurational definitions. The simplest "configurational temperature" is based on an identity from Landau and Lifshitz' text[12, 13]:

$$kT = \frac{\langle\ (\nabla \mathcal{H})^2\ \rangle}{\langle\ \nabla^2 \mathcal{H}\ \rangle} \ .$$

This definition follows from an integration by parts in Gibbs' canonical ensemble. If the differentiation indicated by $\nabla$ is carried out in momentum space the Landau-Lifshitz formula gives the usual kinetic-theory definition of temperature , $mkT_{xx} = \langle\ p_x^2\ \rangle$ . If instead the gradient is carried out in coordinate space the "configurational temperature" depends on the first and second derivatives of the potential function governing the motion:

$$kT_{\text{configurational}} \equiv \langle\ F^2\ \rangle / \langle\ \nabla^2 \Phi\ \rangle \ .$$

One-body or many-body configurational temperatures, either scalar or tensor, can be defined in this way. But an evaluation of them for the shockwave problem reveals divergences. Typically particle values of $\nabla^2\Phi$ frequently alternate between positive or negative values, so that the corresponding configurational temperatures frequently diverge! Configurational temperature also has unphysical undesirable contributions arising from rotation whenever Coriolis' or centrifugal forces are significant.

The simplest definition for temperature is the kinetic second-moment one. It is based on a mechanical model of a working ideal-gas thermometer. In that instance a relatively heavy mass-$M$ "system atom" interacts with a collection of light-weight mass-$m$ "ideal-gas thermometer" particles characterized by an unchanging equilibrium Maxwell-Boltzmann distribution with temperature $T$ . Kinetic theory shows that the averaged effect of such collisions causes the system-atom velocity to decay while its mean-squared velocity approaches the equilibrium value for the temperature $T$:

$$\langle\ \dot{v}_x\ \rangle \propto -(v_x/\tau) \ ; \ \langle\ \dot{v}_x v_x\ \rangle \propto [\ (kT_{xx}/m) - v_x^2\ ]/\tau \ ; \ [\ \text{for } m << M\ ] \ .$$

Accordingly, we adopt the kinetic definition of temperature in what follows. With temperature defined we can proceed to devise "thermostats" able to control it.

### 4.2 Time-Reversible Deterministic Thermostats

The first of the deterministic mechanical thermostats was Woodcock's isokinetic thermostat[14], implemented by rescaling the velocities at the end of each timestep. Much later it was discovered[15, 16] that a continuous time-reversible version of this thermostat could be implemented with a *time-reversible* friction coefficient $\zeta$:

$$\dot{p} = F(q) - \zeta p \ ; \ \zeta = \sum (F \cdot p) / \sum (p^2/m) \to (d/dt) \sum (p^2/m) \equiv 0 \ .$$

This "isokinetic" thermostat can be applied to one or many particles and to one or many space directions.

An illustrative application is the "Galton Board"[1, 2, 15], in which a single particle is accelerated through a lattice of scatterers but constrained to move at constant speed. Overall, the potential energy drops. Because the mean value of the friction coefficient is necessarily positive, the phase-space probability density collapses onto a multifractal strange attractor, quantifying the rarity of nonequilibrium phase-space states. This approach to temperature control is often termed the "Gaussian" thermostat because Gauss' Principle (of Least Constraint) gives this thermostat when applied to the problem of constraining the kinetic energy[16]. Reference 15 is a detailed discussion of the model (summarized in References 1 and 2). This work clearly shows the fractal nature of the phase space (with vanishing phase volume) that results when the dynamics is thermostated. Fancier thermostats, based on statistical mechanics, can be found.

In 1984 Shuichi Nosé discovered a precursor of the best of them, a thermostat[17] with a more elaborate basis in Lagrangian and Hamiltonian mechanics, but somewhat disfigured by a novel "time-scaling variable" $s \equiv dt_{\rm old}/dt_{\rm new}$ . His thermostat imposed Gibbs' canonical phase space distribution at equilibrium rather than the less-usual isokinetic one. A simplification of his equation of motion, without the useless time-scaling, likewise contained a friction coefficient, which itself obeyed an evolution equation depending upon *past* values of the kinetic energy:

$$\{ \ \dot{p} = F(q) - \zeta p \ \} \ ; \ \dot{\zeta} = [ \ (T(\{p\})/T_0) - 1 \ ]/\tau^2 \ [ \ \text{Nosé} - \text{Hoover} \ ] \ .$$

The relaxation time $\tau$ is a free parameter determining the time required for the thermostat forces $\{-\zeta p\}$ to bring the kinetic temperature $T(\{p\})$ to the desired thermostat temperature $T_0$ . Just as in the isokinetic case the nonequilibrium averaged friction coefficient for this "Nosé-Hoover" mechanics is positive, leading once again to multifractal phase space distributions away from equilibrium. There is an extensive somewhat mathematical literature having to do with picking the "right" relaxation time or the "right" thermostat.

The Gaussian and Nosé-Hoover thermostats are particularly useful for controlling nonequilibrium problems, such as shear flows and heat flows, and the Rayleigh-Bénard problem combining them. The definition of temperature depends upon the definition of the local velocity $u(r,t)$ . A straightforward definition of velocity, which nicely satisfies the continuity equation exactly[3], can be based on smooth-particle weighting functions:

$$u(r,t) \equiv \sum_i v_i w(|r - r_i|) / \sum_i w(|r - r_i|) \ .$$

The Gauss, Nosé, and Nosé-Hoover thermostats can *all* be related to Hamiltonian mechanics. Dettmann, together with Morriss, carried out much of this work, with later contributions by Bond, Laird, and Leimkuhler, and then by Campisi, Hänggi, Talkner, and Zhan[18, 19, 20, 21]. All of them helped to clarify the connections of time-reversible thermostats with standard Hamiltonian mechanics. This work leads to the conclusion

that *many* different thermostats can be used at equilibrium but that some of them fail in nonequilibrium situations, even in situations close to equilibrium. Just as in real life the failures, rather than the successes, are the more newsworthy subjects. Let us turn to some examples.

### 4.3 Thermostat Failures – Oscillators, Heat Conduction, and the $\phi^4$ Model

A very stimulating "log-thermostat" has just been described by Campisi, Hänggi, Talkner, and Zhan[21]. They pointed out that the microcanonical (constant energy) ensemble distribution for a logarithmic potential generates (at least formally) the Maxwell-Boltzmann velocity distribution:

$$\phi \equiv kT \ln q \rightarrow \int_0^{+\infty} dq \delta[\ 2H_0 - kT \ln q^2 - (p^2/m)\ ] \propto \exp[\ (H_0/kT) - (p^2/2mkT)\ ]$$

Because the dynamics of this thermostat is unstable, there being nothing to keep $q$ away from the origin, in applications they recommend using $kT \ln(q^2+\delta^2)$ , where $\delta$ is sufficiently small.

Our effort to use this thermostat for a nonequilibrium heat flow problem failed. Connecting a cold and a hot log-thermostat to opposite ends of a two-particle $\phi^4$ chain gave different temperatures at the two ends, but *no heat flux at all.* The problem is that the Hamiltonian log-thermostat is unable to replicate the phase-space contraction associated with dissipative systems. There are some other examples of such failures. Leete and Hoover's Hamiltonian[22, 23] ,

$$\mathcal{H}_{\rm HL} = \sqrt{4K(p)K_0} + \Phi(q) - K_0 \ ,$$

keeps the kinetic energy, $\sum(m\dot{q}^2/2)$ constant, equal to $K_0$ . The *configurational* temperature can alternatively be kept constant using a special Hamiltonian. In both these cases a cold and a hot thermostated region, in contact with Newtonian regions, gives *no heat flux at all* despite huge temperature differences. The lesson is that Hamiltonian mechanics is not able to describe dissipation properly.

## 5 Thermostat Successes" Oscillators and Complex Systems

A "good" thermostat should, for instance, be able to provide good solutions of the Rayleigh-Bénard problem, heat transfer through a compressible fluid in a gravitational field. It should also be useful in treating small-scale "toy problems". The simplest thermostat test problems are [1] a harmonic oscillator[24] with a coordinate-dependent temperature:

$$T(q) = 1 + \epsilon \tanh(q) \ ;$$

and [2] the flow of heat through a $\phi^4$ chain of particles:

$$\mathcal{H} \equiv \sum_i [\ (p_i^2/2m) + (\delta x_i^4/4)\ ] + \sum_{i<j} \phi_{ij} \ ,$$

where $\phi$ is a nearest-neighbor Hooke's-Law potential and where the first few and last few particles in the chain are thermostated with a Gaussian or Nosé-Hoover or another thermostat. This model is a specially good one to study because it is known to satisfy

Fourier's law, even in one dimension. A comparison of seven different thermostat methods showed that the $\phi^4$ problem is well-posed and relatively easy to solve[25].

Some Hamiltonian-based thermostats are ineffective for nonequilibrium problems[21, 22, 23] and it is useful to understand why. At equilibrium a given temperature and volume imply corresponding values of the kinetic and potential energies. This is also true for particular states away from equilibrium, even where there is no longer a unique equation-of-state relation. Using a Hamiltonian thermostat away from equilibrium one can independently specify the kinetic energy *and* the potential energy or the temperature *and* the energy. This additional freedom contradicts the notion of thermodynamic state and can lead to very strange results[23]. Constraining the configurational temperature or using a version of Hamiltonian mechanics to constrain the kinetic energy discovered by Hoover and Leete provide temperature profiles that make no sense. The log-thermostat is another demonstration that Hamiltonian mechanics is a poor choice for thermostats. This paradoxical situation is the symptom of two incompatible requirements on the dynamics: [1] Liouville's Theorem requires that the phase-space motion be incompressible; [2] Heat flow consistent with the Second Law of Thermodynamics requires that the phase volume decrease to zero.

Several of the thermostats have no problem with generating heat flows and solve the problem of decreasing phase volume by generating strange attractors in the phase space. Let us consider what might appear to be the simplest of these problems, the Nosé-Hoover oscillator[24] with a temperature gradient[1]:

$$\dot{q} = p \ ; \ \dot{p} = -q - \zeta p \ ; \ \dot{\zeta} = p^2 - T(q) \ ; \ T(q) = 1 + \epsilon \tanh(q) \ ; \ 0 < \epsilon < 1 \ .$$

For $\epsilon > 0.4$ the motion is a one-dimensional limit cycle with $\langle \ \zeta \ \rangle$ positive. The mean value of the friction coefficient $\zeta$ in the range $(0.44 < \epsilon < 1.0)$ increases from about 0.15 to 1.35 . Figure 3 shows the gradual expansion of the hysteretic limit cycle as the maximum temperature gradient is increased from 0.44 to 1.00 .

Figures 4 and 5 show a bit of the complexity associated with smaller values of the temperature gradient. Using an initial momentum of unity gives more regular attractors, of the type shown to the left. On the other hand, much higher initial momenta give chaotic distributions like those shown to the right. This complexity is no doubt related to that seen without any temperature gradient at all[24]. In that latter case the phase-space distribution is divided into an *infinite* number of coexisting distributions, whose union is Gibbs' canonical distribution ,

$$f_{\rm Gibbs} = e^{-[ \ q^2 + p^2 + \zeta^2 \ ]/2} \ .$$

The Figures show projections of a strange attractor that forms with $\epsilon = 0.40$ . The Lyapunov spectrum in this case is nearly symmetric, so that it is difficult to compute an accurate information dimension of the attractor.

Fortunately, the complex dynamics of the thermostated oscillator can be greatly simplified by adding another control variable, a friction coefficient controlling the fourth velocity moment[26]:

$$\{ \ \dot{q} = p \ ; \ \dot{p} = -q - \zeta p - \xi p^3 \ ; \dot{\zeta} = p^2 - T(q) \ ; \ \dot{\xi} = p^4 - 3p^2 T(q) \ ; \ T(q) = 1 + \epsilon \tanh(q) \ \} \ .$$

At equilibrium the extra control variable allows the oscillator to sample the complete canonical distribution. This works at nonequilibrium too. Figure 6 compares the distributions of the two friction coefficients $(\zeta, \xi)$ for $\epsilon$ equal to 0.5 and 1.0 . Even in the latter case the chaos induced by the two coefficients is enough to prevent collapse of the dynamics onto a limit cycle. Although counterintuitive, it appears to be true that a four-dimensional attractor is actually much *simpler* than its three-dimensional counterpart.

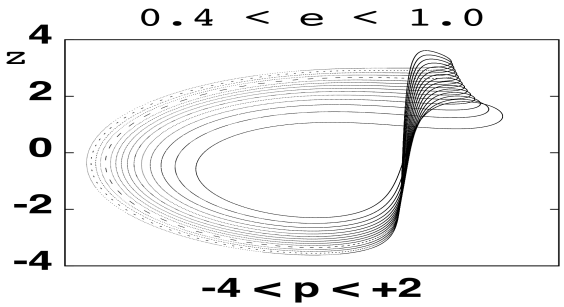


Figure 3: $\zeta(p)$ is plotted for fifteen equally-spaced values ($\epsilon = 0.44$ to 1.00) of the maximum temperature gradient for the $(q, p, \zeta)$ nonequilibrium Nosé-Hoover oscillator. All these data correspond to fully-converged limit cycles.

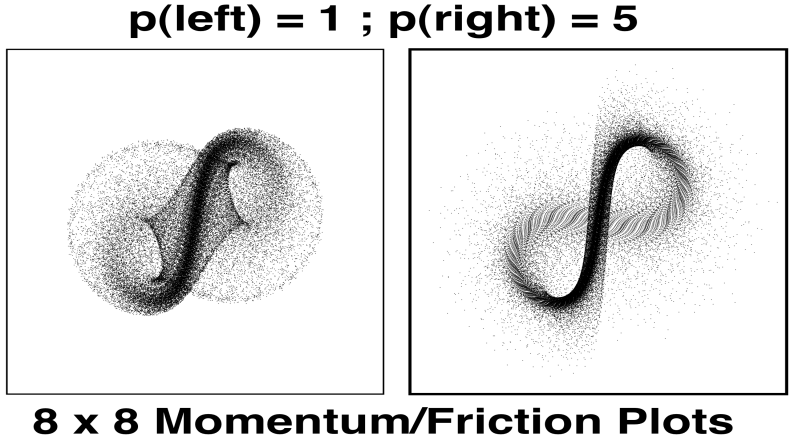


Figure 4: $\zeta(p)$ for the nonequilibrium Nosé-Hoover oscillator ($\epsilon = 0.4$) is plotted between the limits $\pm 4$ for two different initial conditions. For $p = 5$ the Lyapunov exponents are roughly $\pm 0.0025$ and 0. For $p = 1$ the exponents are much larger in magnitude, $\pm 0.0085$ and 0.

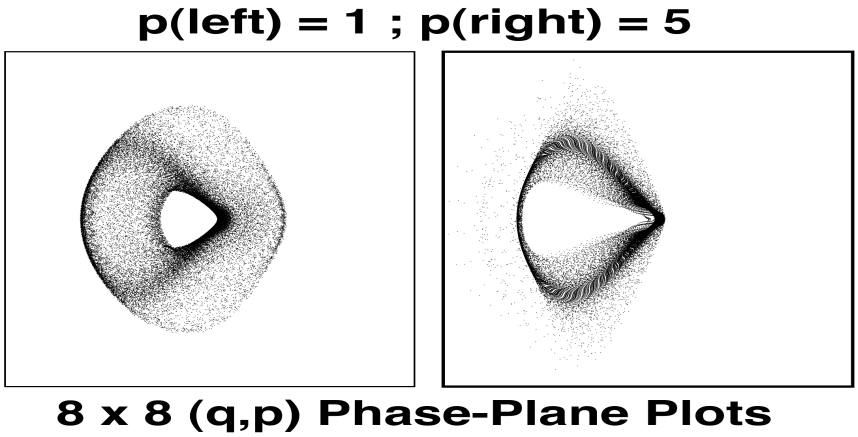


Figure 5: $p(q)$ is plotted between the limits $\pm 4$ for the two different initial conditions of Figure 4 . Note the preference of the oscillator for the lower-temperature states to the left of the origin.

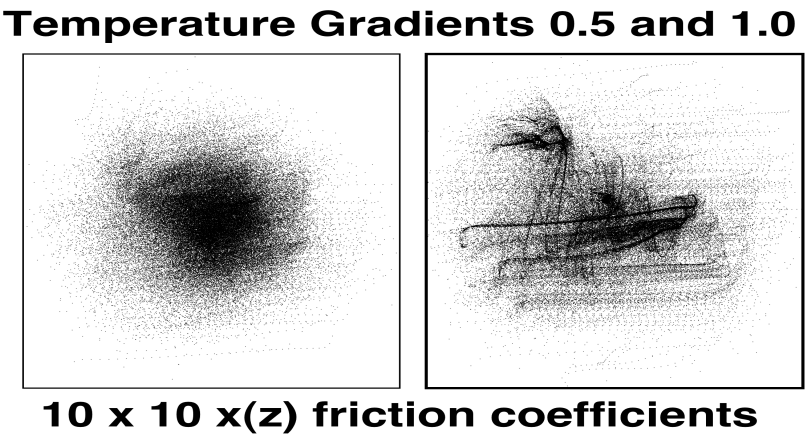


Figure 6: Friction coefficient distribution $\xi(\zeta)$ for two values of the maximum temperature gradient, 0.5 and 1.0 . This doubly-thermostated oscillator covers the complete canonical distribution in the equilibrium case. Here there is no dependence of the attractor on the initial value of the momentum. 100,000 points are printed taken from the last half of a 200 million timestep run. The timestep $\Delta t$ is 0.0002 .

### 5.1 Larger Systems and Thermodynamics

Larger systems fit the pattern to which the small systems hint. The phase-space distribution shrinks to a strange attractor. In a system with several thermostated degrees of freedom Liouville's Theorem gives the details of the shrinkage[1, 15, 26]:

$$(d \ln f/dt) \equiv -(\dot{\otimes}/\otimes) = \sum \zeta \equiv \exp[\ (\dot{S}/k)\ ]\ .$$

Here $\dot{S}$ is the external entropy production, the heat extracted from the controlled system by the thermostats, divided by the thermostat temperature. $\otimes$ is a small comoving phase volume. $\otimes$ has three possible evolutions: it can expand; it can shrink; or it can remain the same. The last possibility is the equilibrium one, with no net heat transfer to the outside world. The first possibility (expansion) is ruled out for steady states, as a continually expanding phase volume implies catastrophic instability. Only the possibility of continual shrinkage, dissipation, is left. The accessible phase-space states for a nonequilibrium steady state continually decrease in number as the volume shrinks (exponentially fast) toward zero. The deterministic time-reversible thermostats make possible a simple geometric interpretation of the Second Law of Thermodynamics. Nonequilibrium steady states necessarily collapse to a zero-volume strange attractor. Thus nonequilibrium states are vanishingly rare. Any attempt to reverse the (time-reversible) dynamics would lead to divergence, with a positive Lyapunov sum, and a violation of the Second Law. What happens in fact is that, when reversed, the dynamics soon breaks its time symmetry and seeks out again the attractor. Time-reversible thermostats have deepened our understanding of the Second Law[1, 27].

## 6 Summary

The paradoxical reversibility properties of Newtonian and Hamiltonian mechanics can be modeled with bit-reversible algorithms. Such algorithms don't exist in cases where the phase volume changes, where the mechanics is thermostated. In the latter case Lyapunov

instability seeks out the unstable strange attractor, more stable still than is its repeller twin, leading to a simple geometric understanding of the Second Law of Thermodynamics for open systems.

The symmetry breaking revealed by strong shockwaves suggests that a deepened understanding of isolated systems can come from study of the local Lyapunov spectrum. Both of these problem areas, nonequilibrium conservative systems and nonequilibrium open systems, suggest many interesting research opportunities for the future.

## 7 Acknowledgment

This work represents a continuing effort which has been stimulated by many colleagues. Most recently, we thank Francesco Ginelli and Massimo Cencini for inviting our contribution to a special issue of the Journal of Physics A (Mathematical and Theoretical), Lyapunov Analysis from Dynamical Systems Theory to Applications. Anton Krivtsov and Vitaly Kuzkin encouraged our participation in this meeting. We are also specially grateful to Michele Campisi and his colleagues and coworkers for many stimulating emails which helped us to identify some of the many interesting problem areas presented here.

## References

[1] Wm. G. Hoover and C. G. Hoover, *Time Reversibility, Computer Simulation, Algorithms, and Chaos* (World Scientific, Singapore, Second Edition, 2012).

[2] Wm. G. Hoover, *Computational Statistical Mechanics* (Elsevier, Amsterdam, 1991, and available free at http://www.williamhoover.info).

[3] Wm. G. Hoover *Smooth Particle Applied Mechanics: the State of the Art* (World Scientific, Singapore, 2006).

[4] D. Levesque and L. Verlet, "Molecular Dynamics and Time Reversibility", Journal of Statistical Physics **72**, 519-537 (1993).

[5] F. Ginelli, P. Poggi, A. Turchi, H. Chaté, R. Livi, and A. Politi, "Characterizing Dynamics with Covariant Lyapunov Vectors", Physical Review Letters **99**, 130601 (2007).

[6] C. L. Wolfe and R. M. Samelson, "An Efficient Method for Recovering Lyapunov Vectors from Singular Vectors", Tellus **59A**, 355-366 (2007).

[7] M. Romero-Bastida, D. Pázo, J. M. López, and M. A. Rodriguez, "Structure of Characteristic Lyapunov Vectors in Anharmonic Hamiltonian Lattices", Physical Review E **82**, 036205 (2010).

[8] J. D. Farmer, E. Ott, and J. A. Yorke, "The Dimension of Chaotic Attractors", Physica **7D**, 153-180 (1983).

[9] S. D. Stoddard and J. Ford, "Numerical Experiments on the Stochastic Behavior of a Lennard-Jones Gas System", Physical Review A **8**, 1504-1512 (1973).

[10] L. B. Lucy, "A Numerical Approach to the Testing of the Fission Hypothesis", The Astronomical Journal **82**, 1013-1024 (1977).

[11] R. A. Gingold and J. J. Monaghan, "Smoothed Particle Hydrodynamics: Theory and Application to Nonspherical Stars", Monthly Notices of the Royal Astronomical Society **181**, 375-398 (1977).

[12] L. D. Landau and E. M. Lifshitz, *Statistical Physics*, equation 33.14 (McGraw-Hill, New Jersey, 1958).

[13] C. Braga and K. P. Travis, "A Configurational Temperature Nosé-Hoover Thermostat", Journal of Chemical Physics **123**, 134101 (2005).

[14] L. V. Woodcock, "Isothermal Molecular Dynamics Calculations for Liquid Salts", Chemical Physics Letters **10**, 257-261 (1971).

[15] B. Moran, Wm. G. Hoover, and S. Bestiale, "Diffusion in a Periodic Lorentz Gas", Journal of Statistical Physics **48**, 709-726 (1987).

[16] D. J. Evans, W. G. Hoover, B. H. Failor, B. Moran, and A. J. C. Ladd, "Nonequilibrium Molecular Dynamics *via* Gauss' Principle of Least Constraint", Physical Review A **28**, 1016-1021 (1983).

[17] S. Nosé, "Constant Temperature Molecular Dynamics Methods", Progress of Theoretical Physics Supplement **103**, 1-46, (1991).

[18] Wm. G. Hoover, "Mécanique de Nonéquilibre à la Californienne", Physica A **240**, 1-11 (1997).

[19] C. P. Dettmann and G. P. Morriss, "Hamiltonian Reformulation and Pairing of Lyapunov Exponents for Nosé-Hoover Dynamics"вЂќ, Physical Review E **55**, 3693-3696 (1997).

[20] S. D. Bond, B. J. Leimkuhler, and B. B. Laird, "The Nosé-Poincaré Method for Constant Temperature Molecular Dynamics", Journal of Computational Physics **151**, 114-134 (1999).

[21] M. Campisi, F. Zhan, P. Talkner, and P. Hänggi, "Logarithmic Oscillators: Ideal Hamiltonian Thermostats", ar$\chi$iv 1203.5968 and 1204.0312 "Reply to W. G. Hoover" (2012) .

[22] T. M. Leete, "The Hamiltonian Dynamics of Constrained Lagrangian Systems" [ M. S. Thesis, West Virginia University, 1979 ].

[23] Wm. G. Hoover and C. G. Hoover, "Hamiltonian Dynamics of Thermostated Systems: Two-Temperature Heat-Conducting $\phi^4$ Chains", Journal of Chemical Physics **126**, 164113 (2007).

[24] H. A. Posch, Wm. G. Hoover, and F. J. Vesely, "Canonical Dynamics of the Nosé Oscillator: Stability, Order, and Chaos", Physical Review A**33**, 4253-4265 (1986).

[25] Wm. G. Hoover, K. Aoki, C. G. Hoover, and S. V. De Groot, "Time-Reversible Deterministic Thermostats", Physica D **187**, 253-267 (2004).

[26] Wm. G. Hoover, C. G. Hoover, H. A. Posch, and J. A. Codelli, "The Second Law of Thermodynamics and Multifractal Distribution Functions: Bin Counting, Pair Correlations, and the Kaplan-Yorke Conjecture", Communications in Nonlinear Science and Numerical Simulation **12**, 214-231 (2007).

[27] B. L. Holian, Wm. G. Hoover, and H. A. Posch, "Resolution of Loschmidt's Paradox: the Origin of Irreversible Behavior in Reversible Atomistic Dynamics", Physical Review Letters **59**, 10-13 (1987).

*Ruby Valley Research Institute, Highway Contract 60, Box 601, Ruby Valley, Nevada 89833*

# Microscopic and macroscopic Rayleigh-Bénard flows: continuum and particle simulations, turbulence, fluctuations, time reversibility, and Lyapunov instability

Wm. G. Hoover hooverwilliam@yahoo.com
Carol G. Hoover hoover1carol@yahoo.com

**Abstract**

We discuss the irreversibility, nonlocality, and fluctuations, as well as the Lyapunov and hydrodynamic instabilities characterizing atomistic, smooth-particle, and finite-difference solutions of the two-dimensional Rayleigh-Bénard problem. To speed up the numerical analysis we control the time-dependence of the Rayleigh number, $\mathcal{R}(t)$ , so as to include many distinct flow morphologies in a single simulation. The relatively simple nature of these computational algorithms and the richness of the results they can yield make such studies and their interpretation particularly well suited to graduate-level research.

Keywords: Rayleigh-Bénard flows, macroscopic flows, microscopic flows, Lyapunov instability, chaos.

## 1 Introduction

"Understanding Turbulence" is an enduring catch phrase and has been a potential funding source since the early days of computers. There is no shortage of reviews ranging from short sketches[1, 2, 3] to scholarly studies[4, 5, 6]. The vast research literature takes in earth, air, fire, and water as well as the weather, the sun, aircraft design, and small-box chaos. Spectra and power-law relations abound. Mostly the working fluid is incompressible and often its motion is described as a superposition of modes or vortices. Two- and three-dimensional turbulence behave differently, with the flow of energy away from or toward smaller length scales in these two cases[4]. "Enstrophy", the squared vorticity [ squared rotation rate ], is "conserved" in two-dimensional incompressible flow[4].

Despite all this information there appears to be more to learn. How many vortices should we expect to see? What is the Lyapunov spectrum like? How localized are the vectors corresponding to the exponents? The simple nature of the underlying model, a conducting viscous fluid, the complexity of the flows that result, and the multitude of computational schemes, all provide opportunities for imaginative approaches and analyses. We recommend their study and describe our own explorations of what seems to us the simplest problem involving turbulence, Rayleigh-Bénard flow[1, 2, 3, 4, 5, 6, 7, 8, 9, 10, 11].

The classical Rayleigh-Bénard problem describes the convective behavior of a compressible, heat conducting, viscous fluid in the presence of gravity and a temperature gradient. Here we suppose that the fluid is confined by a stationary square $L \times L$ box with fixed boundary temperatures. Despite these simplest possible of boundary conditions, even in two space dimensions this problem provides interesting *internal* flows of mass, momentum, and energy. The heat driving these flows enters and exits along the boundaries. Most of

it comes in at the bottom and flows out at the top. There are two competing mechanisms for the heat flow from bottom to top. The simpler of the two is conduction, described by Fourier's law, $Q = -\kappa \nabla T$ . But *mechanical* ( or "convective" ) heat flow is possible too and comes to dominate conduction as the flow begins to move, and continues to grow as the flow eventually becomes turbulent.

Thermal expansion near the bottom of the box provides the buoyancy necessary to carry the hot fluid upward. Cooling and compression near the top encourages downward flow. These vertical driving forces due to temperature and gravity are balanced by the dissipative effects of heat conduction and viscosity which lead to macroscopic entropy production. The dimensionless ratios of these effects, the Rayleigh Number $\mathcal{R}$ and, to a lesser extent, the Prandtl Number $\mathcal{P}$ [ which we set equal to unity in our work here ] :

$$\mathcal{R} \equiv g(\partial \ln V/\partial T)_P \Delta T L^3/(\nu D) \; ; \; \mathcal{P} = (\nu/D) \; ,$$

control the overall flow. The Nusselt number $\mathcal{N}$ completes the list of dimensionless flow variables. It is an observable rather than an input. $\mathcal{N}$ is simply the ratio of the ( time-averaged, if necessary ) vertical heat flux to the prediction of Fourier's law :

$$\mathcal{N} = -(LQ_y/\kappa \Delta T) \; .$$

With our thermostated sidewalls the definition of the Nusselt Number is somewhat arbitrary. *Entropy production* is a more appropriate measure of our flows' separation from equilibrium, though we will not discuss those interesting results here for lack of space.

The convective flow patterns characterizing Rayleigh-Bénard flow can be stationary, periodic in time, or chaotic. It is often possible to observe qualitatively different solutions – different numbers of convective rolls for instance – for the *same* external boundary conditions[11]. And at very "high" Rayleigh numbers [ on the order of a half million or more ], chaotic flows *never repeat*. Chaotic solutions describe at least two distinct regimes of turbulence[1, 2], called "soft" and "hard", and distinguished by the form of their fluctuations, Gaussian or exponential respectively[1, 4, 5]. The time scales associated with eddy rotation vary from seconds in the laboratory to æons inside the earth and sun. The richness of Rayleigh-Bénard flow patterns, even or especially in two dimensions, together with their illustration of the fundamentals of fluid mechanics, instability theory, nonlinear dynamics, and irreversible thermodynamics, makes these problems an ideal introduction to the use of numerical methods in computational fluid dynamics[2, 8, 9].

We choose to study here the simplest possible constitutive model, an ideal gas ,

$$PV = NkT = E = Nme \longrightarrow (\partial \ln V/\partial T)_P = (1/T) \; ; \; (S/k) = \int_0^L \int_0^L \rho \ln(T/\rho) dx dy \; .$$

For simplicity we set Boltzmann's constant $k$, the particle mass $m$, and the overall mass density $\rho$ equal to unity. We choose the hot and cold temperatures equal to 1.5 and 0.5 so that $\Delta T \simeq T$. Finally, we choose the gravitational constant $g$ so as to give a constant-density solution of the equation of motion in the quiescent purely conducting case :

$$-(dP/dy) = \rho g = -\rho(kdT/dy) \rightarrow \{ \; g = (k\Delta T/mL) \equiv (1/L) \; \rightarrow \rho \simeq 1 \; , \text{ a constant } \} \; .$$

With these simplifications a square [ $N \equiv L \times L$ ]-cell system with a Rayleigh number $\mathcal{R}$ and a Prandtl Number $\mathcal{P}$ is achieved by choosing the two constitutive properties, kinematic viscosity $\nu$ and thermal diffusivity $D$ , to satisfy the two definitions :

$$(\nu/D) \equiv \mathcal{P} \; ; \; \mathcal{R} \equiv (L/\nu)(L/D) \; .$$

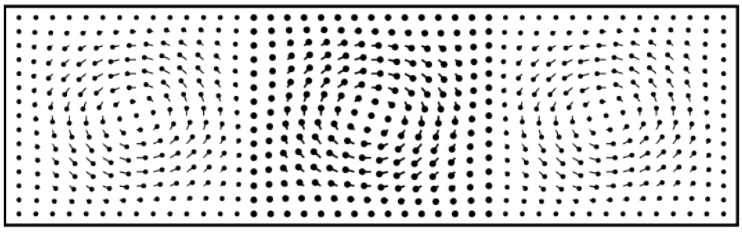


Figure 1: An $L \times L$ square with an idealized roll using the "stick" boundary condition [ zero velocity at the wall ] : $u_x \propto +\sin(y)\cos(x/2)$ ; $u_y \propto -\sin(x)\cos(y/2)$ ; $-\pi \leq x, y \leq +\pi$ , is shown at the center. These data are also reflected, both to the right and to the left, to make an array with three rolls. This illustrates a handy initialization technique to use in the search for stable multiroll solutions.

Unlike experimentalists we computational scientists are not limited to physical materials, dimensions, or boundary conditions. We have the undoubted luxury that our transport coefficients ( as well as the gravitational acceleration and even the box size ) can *all* be time dependent if we like. In the simulations reported here we typically use time-dependent transport coefficients, chosen so that the Rayleigh number increases or decreases [ to check for hysteresis ] linearly with time. In this way a whole *range* of Rayleigh numbers, with varying roll numbers, kinetic energies, and Lyapunov exponents ( *if* the increase is carried out sufficiently slowly ), can all be obtained with a single simulation.

For sufficiently large values of the Rayleigh number ( 4960 or more for the static fixed-temperature boundary conditions used here[7] ) one or more viscous conducting rolls form and evolve with time. With the convective heat flow directed upward, and on the average balanced by the gravitational forces acting downward, either stationary, periodic, or chaotic flows can be achieved. Figure 1 shows how a simple single vortex can be used to construct initial conditions with one or more vortices.

Since the 1980s nominally steady-state solutions for such flows have been computed with three distinct methods: microscopic molecular dynamics together with particle-based and grid-based macroscopic simulation methods[8, 9, 10, 11]. The Smooth-*Particle* Applied Mechanics Method ( SPAM ) offers a welcome bridge between the microscopic and macroscopic approaches[8]. In SPAM the dynamics of macroscopic particles is governed by motion equations including the macroscopic *irreversible* constitutive laws. But the form of those laws mimics that of the microscopic motion equations. In both cases the accelerations are based on summed-up contributions from neighboring pairs of particles. SPAM calculations can also be thought of as a finite-difference algorithm on an irregular grid.

The resulting macroscopic flow patterns exhibit interesting solution changes as the Rayleigh number increases above the critical value of 4960 . The *positions* of the rolls' centers can exhibit both periodic and chaotic motion. Lyapunov exponents characterize the growth of the instabilities leading to chaotic motion[4, 7]. For continuum simulations with thousands of degrees of freedom the simplest calculation of the instabilities involves only the largest exponent. There is evidence that the "spectrum" of Lyapunov exponents is roughly linear [ and with a negative sum, due to the dissipative nature of continuum

flows ][4].

It turns out that the relative stability of particular flows depends upon the initial conditions. No known variational principle ( like maximum entropy, or minimum entropy production ) predicts *which* of the several flows is stable[11]. The various "principles" based on energy or entropy can be evaluated for these simulations. Intercomparisons of the three simulation methods can shed light on the dissipation described by the Second Law of Thermodynamics and the differing time reversibilities of the microscopic and macroscopic techniques.

In Section II we summarize the continuum physics of fluid flow problems: mass, momentum, and energy conservation are always required. Shear flows and heat flows can result. In Section III we outline three numerical solution techniques and display some typical results. In Section IV we present our conclusions and suggest research directions useful for students.

## 2 Continuum Mechanics and Rayleigh-Bénard Flow

A physical description of any continuum flow necessarily obeys the conservation laws for mass, momentum, and energy :

$$\dot{\rho} = -\rho \nabla \cdot u \ ; \ \rho \dot{u} = -\nabla \cdot P + \rho g \ ; \ \rho \dot{e} = -\nabla u : P - \nabla \cdot Q \ .$$

The simplest *derivation* of these three laws uses an *Eulerian* coordinate system fixed in space. The summed-up fluxes of each conserved quantity through the surfaces of each of the $L^2$ computational cells, plus the internal gravitational contributions give the time rates of change in the cells. In the Rayleigh-Bénard problem the boundary source terms introduce and extract energy at the bottom, along the sides, and at the top, while the gravitational momentum density source $\rho g$ acts throughout the volume . The fluid's constitutive properties – the pressure tensor $P$ and the heat flux vector $Q$ – are computed from the local state variables $\{ \rho, u, e \}$ and their gradients. $P$ and $Q$ are the momentum and energy fluxes in a coordinate system "comoving" with the local velocity $u(r,t)$ .

It is easy to solve the continuum flow laws by converting them to sets of ordinary differential equations. These latter equations incorporate the linear phenomenological constitutive relations pioneered by Newton and Fourier, expressing pressure in terms of the symmetrized velocity gradient, and the heat flux vector in terms of the temperature gradient :

$$P = (P_{\rm eq} - \lambda \nabla \cdot u) I - \eta [ \ \nabla u + \nabla u^t \ ] \ ; \ Q = -\kappa \nabla T \ .$$

$\kappa$ is the thermal conductivity. We set the bulk viscosity equal to zero ( appropriate for an ideal gas ) by setting $\lambda + \eta = 0$ so that the pressure tensor has the following form :

$$P_{xx} = P_{\rm eq} - \eta [ \ (\partial u_x / \partial x) - (\partial u_y / \partial y) \ ] \ ;$$

$$P_{yy} = P_{\rm eq} - \eta [ \ (\partial u_y / \partial y) - (\partial u_x / \partial x) \ ] \ ;$$

$$P_{xy} = -\eta [ \ (\partial u_y / \partial x) + (\partial u_x / \partial y) \ ] \ .$$

With these constitutive relations specified we have a well-posed continuum problem ready to solve.

Figure 2 shows observed stationary roll patterns typical of a Rayleigh-Bénard flow with a gravitational force acting in the negative y direction and a temperature gradient resulting in heat convection in the positive $y$ direction. The temperature and velocity are fixed on the horizontal and vertical boundaries, just as in the idealized one- and three-roll flows of

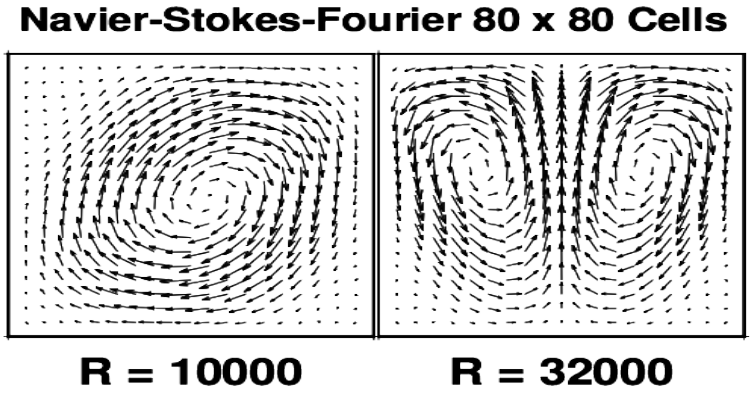


Figure 2: Stationary roll patterns observed at Rayleigh Numbers of 10,000 and 32,000 with a Prandtl number of unity. The velocities are taken from Eulerian grid-based solutions of the conservation laws with linear Newton-Fourier constitutive relations.

Figure 1 . Higher values of the Rayleigh number result in solutions that form with three or more rolls, periodic roll motions, and finally chaotic motions. See References 6 and 7 .

Figure 3 shows four typical *chaotic* Rayleigh-Bénard velocity plots. The Rayleigh Number here is 800 000 . A mesh of $160 \times 160$ cells and $161 \times 161$ nodes was used.

# 3 Numerical Methods for Rayleigh-Bénard Flows

## 3.1 Particle Methods: Nonequilibrium Molecular Dynamics and SPAM

**Nonequilibrium molecular dynamics** is a straightforward but limited method for studying Rayleigh-Bénard flows. Though the method is both simple and fundamental, atomistic particle studies have several disadvantages : first, the *equation of state* can't be specified in advance ( only the interatomic force law is given in molecular dynamics ) ; second, the *number of degrees of freedom* required to simulate convective rolls is either thousands ( in two dimensions[9] ) or millions ( in three dimensions[10] ) ; third, the *time step* in molecular dynamics simulations is a fraction of the collision time rather than the considerably larger time [ $dt = (dx/c)$ , where $c$ is the sound velocity ] given by the continuum Courant condition. Finally, even with these large particle numbers and small time steps, the *fluctuations* in the atomistic simulations are so large that snapshots of nominally steady flows show large deviations from time averages.

Mareschal and Rapaport and their coworkers[9, 10] have studied two- and three-dimensional molecular dynamics systems, relatively large at the time they were carried out ( with 5000 and 3,507,170 particles respectively ). In both these cases time averages were required. The simulations did confirm that these *time averages* of the atomistic flows closely matched the corresponding stationary continuum simulations. We have carried out a few corroborating simulations. In these we used thermostated boundaries composed of particles tethered to fixed lattice sites. Rather than obeying conservative Newtonian mechanics, where the bottom row of "hot" and top row of "cold" boundary particles separately follow *thermostated* equations of motion with their temperatures controlled by the

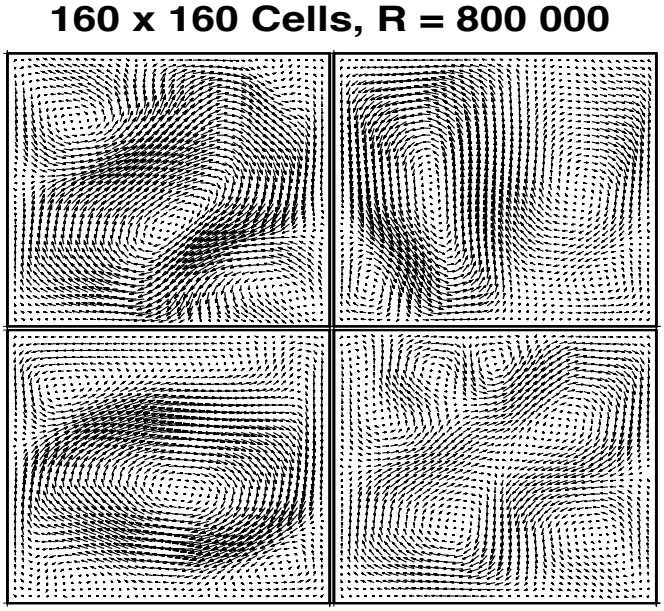


Figure 3: Four snapshots of a turbulent flow computed with 160 × 160 computational cells.

Nosé-Hoover friction coefficients[7] ( $\zeta_{\rm hot}, \zeta_{\rm cold}$ ) :

$$\{\ \ddot{r} = (F(\{\ r\ \})/m) - \zeta_{\rm hot}\dot{r}\ \}_{\rm hot}\ ;\ \{\ \ddot{r} = (F(\{\ r\ \})/m) - \zeta_{\rm cold}\dot{r}\ \}_{\rm cold}\ .$$

Particle escapes can be prevented by using a strong repulsive boundary potential to reflect any particle venturing "outside" the box. Figure 4 compares a time-averaged exposure of a typical molecular dynamics run with 23,700 particles to the final snapshot from the same simulation.

**Smooth Particle Applied Mechanics** (SPAM[8]) is a *macroscopic* particle alternative to molecular dynamics. SPAM simulations are based on the continuum constitutive relations rather than atomistic interatomic forces. Hundreds of particles, rather than thousands, can generate rolls, the timestep is much larger, and individual snapshots do reproduce the stable roll structures quite well. SPAM defines local continuum averages by combining contributions from a few dozen nearby particles. *All* of these continuum properties, $\{\ \rho, u, e, P, Q,\ \ldots\ \}$ are *local averages* from sums using a weight function like Lucy's, which is shown in Figure 5 :

$$w(r < h) = (5/\pi h^2)(1 + 3z)(1 - z)^3\ ;\ z \equiv (r/h)\ .$$

Averages computed using this twice-differentiable weight function have two continuous spatial derivatives, enough for representing the righthand sides of the diffusive continuum equations with continuous functions.

Consider the simplest application of SPAM averaging, the *definitions* of the local densities and velocities in terms of smooth-particle weighted sums :

$$\rho(r) \equiv m \sum_i w(r - r_i)\ ;\ \rho(r)u(r) \equiv m \sum_i w(r - r_i)v_i\ .$$

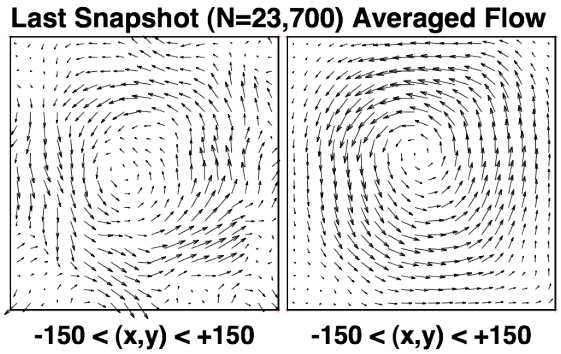


Figure 4: Simulation of Rayleigh-Bénard flow with molecular dynamics. A snapshot, using smooth-particle averages of the particle velocities, is at the left. Averages appear at the right.

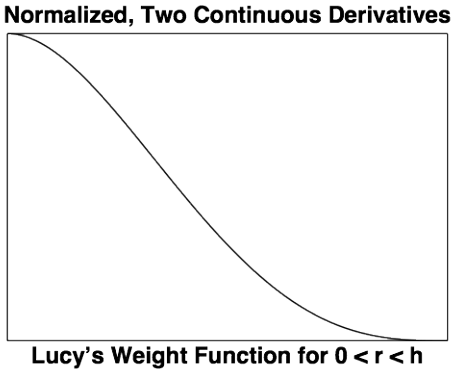


Figure 5: Lucy's weight function, normalized for two dimensions, $\int_0^h 2\pi r w(r<h)dr \equiv 1$ .

These definitions satisfy the continuum continuity equation exactly! The variation of the density at a fixed location $r$ can be evaluated by the chain rule :

$$(\partial\rho/\partial t)_r = m\sum_i w' v_i \cdot (r_i - r)/|r - r_i| \ .$$

Then notice that the gradient with respect to $r$ of the product $(\rho u)$ includes exactly the same terms, but with the opposite signs :

$$\nabla_r \cdot (\rho u) = m\sum_i w' v_i \cdot (r - r_i)/|r - r_i| \ .$$

Thus *the SPAM version of the continuity equation* ,

$$(\partial\rho/\partial t) \equiv -\nabla\cdot(\rho u) \longleftrightarrow \dot\rho = -\rho\nabla\cdot u \ ,$$

*is an identity*, independent of the form or range $h$ of the weight function $w(r<h)$ . This is not entirely a surprise as there is no ambiguity in the locations of the particles' masses and momenta.

The pressure and energy are more complicated. The smooth-particle equation of motion[8] is antisymmetric in the particle indices. Thus that motion equation ,

$$\dot{v}_i \equiv -m \sum_j [\ (P/\rho^2)_i + (P/\rho^2)_j\ ] \cdot \nabla_i w(r_i - r_j)\ ;$$

conserves *linear* momentum ( but *not* angular momentum ) exactly. Notice that whenever the pressure varies slowly in space the weight function plays the role of a repulsive potential with the strength of the interparticle "forces" proportional to the local pressure.

The *gradients* in SPAM are evaluated by taking derivatives of the corresponding sums. The temperature gradient, for example, is :

$$(\nabla T)_i \equiv m \sum_j (T_j - T_i) w'_{ij} [\ (r_j - r_i)/(|r_{ij}|\rho_{ij})\ ]\ ;\ \rho_{ij} \equiv \sqrt{\rho_i \rho_j}\ \text{or}\ (\rho_i + \rho_j)/2\ .$$

Notice that two neighboring particles make no contribution to the temperature gradient if their temperatures match. With the gradients defined the pressure tensor and heat flux vectors can be evaluated for all the particles and used to advance the particle properties to the next time step :

$$\{\ \dot{r}, \dot{v}, \dot{e}\ \} \longrightarrow \{\ r, v, e\ \}$$

In all, the SPAM method averages involve about two dozen distinct particle properties. This computational effort is compensated by SPAM's longer length and time scales.

In addition to providing an alternative approach to solving the continuum equations the SPAM averaging technique can be used to average molecular dynamics properties such as $P$ and $Q$. This approach is particularly valuable in shockwaves ( see Chapter 6 of Reference 7 ), where constitutive properties change on an atomistic distance scale. It would be interesting to compare the two sides of the continuum energy and motion equations and to use this comparison to optimize the choice of the weight function's range $h$ .

The molecular dynamics results differ qualitatively from continuum results in their time symmetry, so that averaging offers a way of reducing this conflict. Time-dependent solutions offer a specially flexible technique for bringing the two approaches into better agreement. The weight functions also offer a way of carrying out the coarse graining which could be used to reduce the conflict between the microscopic and macroscopic forms of mechanics.

### 3.2 Eulerian Finite-Difference Method[9]

Straightforward centered-difference approximations to the continuum equations provide a useful approach to the Rayleigh-Bénard problem. Mareschal and his coworkers pointed out that an efficient numerical method can be based on square cells or zones, with the velocities and energies defined at the nodes and the densities defined in the cells. A small $10 \times 10$ cell program written in this way would solve $3 \times 11 \times 11 + 10 \times 10 = 463$ ordinary differential equations. The solution procedure follows a seven-step plan: [1] use linear interpolation and extrapolation near the boundaries to find the complete set of 484 nodal variables and 400 cell variables; [2] use centered differences to find $\nabla v$ and $\nabla T$ ; [3] use these gradients to obtain $P$ and $Q$ ; [4] evaluate $\nabla v : P$ and $\nabla \cdot Q$ ; [5] evaluate $(\partial \rho/\partial t)$ from the neighboring nodal values ; [6] evaluate $(\partial u/\partial t)$ from the pressure gradients and $(\partial e/\partial t)$ by summing the convective contributions and the work and heat; [7] use fourth-order Runge-Kutta integration to advance the 463 dependent variables to the next time step.

The Rayleigh-Bénard solutions – simple rolls[11], periodic solutions, or chaos – can be observed in either two dimensions, where there are plenty of puzzles to solve, or three. Because simulation and visualization are simpler in two dimensions, while the challenges to understanding remain severe, we choose two dimensions. The critical Rayleigh Number of about 5000 corresponds to an eddy width which can easily be resolved with $8 \times 8$ cells and a one-roll Reynolds number of order unity.

The Rayleigh number varies as $L^4$. Doubling the sidelength $L \to 2L$ with $g$ and the transport coefficients fixed changes $\mathcal{R} : 5000 \to 80000$ and increases the number of rolls to four. Desktop or laptop machines are quite capable of simulations with $\mathcal{R} = 1\ 000\ 000$ , for which this simple-minded reasoning could lead us to expect about $(1000000/5000)^{1/4} \simeq 14$ rolls. In fact this doesn't happen. See Figure 7 below. In two dimensions the energy flow is *toward*, rather than away from, large rolls. For $\mathcal{R} = 800K$ [ $K$ indicates thousands ] and a $160 \times 160$ mesh one finds occcasional deep minima in the time-dependent kinetic energy. These minima correspond to only two large rolls, as in the simple solutions without chaos, with $\mathcal{R} \simeq 10K$ . In three dimensions the chaotic flow is qualitatively different, and more complicated. Instead of whirling vortices one finds plumes ascending and descending, with mushroom shaped heads for large Prandtl numbers ( glycerin ) where viscosity dominates conductivity[1].

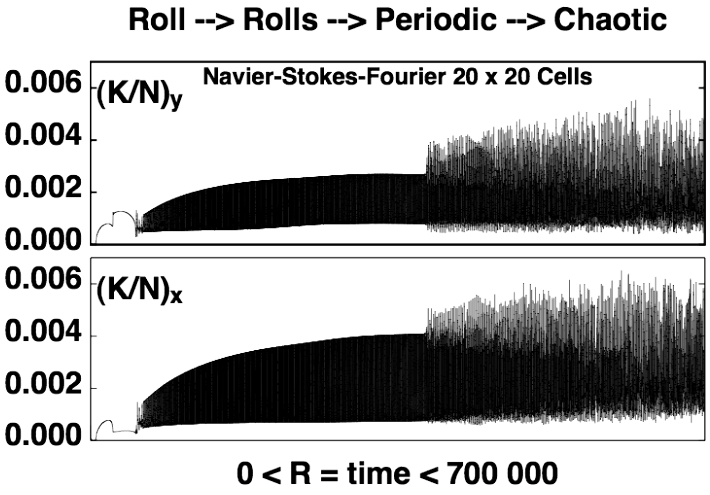


Figure 6: Kinetic energy per cell (vertical at top and horizontal at bottom) from a simulation with $\mathcal{R} = t$. Notice, at the extreme left of the two plots, the reduction in the horizontal kinetic energy at the transition from one roll to two ( $\mathcal{R} \simeq 25K$ ) .

Figure 6 shows the variation of the kinetic energy per cell with the Rayleigh Number, where $\mathcal{R} = t \leq 700K$. The transitions go from one roll to two, and from two rolls to a time-periodic arrangement with perhaps four, which in turn gives rise to chaos. Our simple centered-finite-difference fixed-timestep code "blew up" at Rayleigh numbers of

$$\{\ 715K,\ 810K,\ 840K,\ 860K,\ 905K,\ 940K\ \} \text{ for } L = \{\ 16,\ 24,\ 32,\ 48,\ 64,\ 96\ \} .$$

Figure 6 suggests that chaos sets in around $\mathcal{R} = 385K$ and gradually increases in strength until the algorithm becomes unstable for the chosen mesh.

The motion responds relatively quickly to perturbations. To demonstrate this we show in Figure 7 six snapshots from a $24 \times 24$ simulation with *all* of the flow velocities *instantaneously* reversed from forward to backward at time 0, where the forward chaotic flow has three distinct rolls. By a time of 500 (a few dozen sound traversal times) the flow is back

to normal, again with three rolls. But in the transformational process of discarding the time-reversed morphology the stabilizing flow acquires as many as seven rolls, in accord with the estimate that roughly $8 \times 8$ cells required to resolve a roll. The quick reduction in roll number as steady chaos is regained is again a symptom of the flow of energy from smaller to larger rolls in two dimensions.

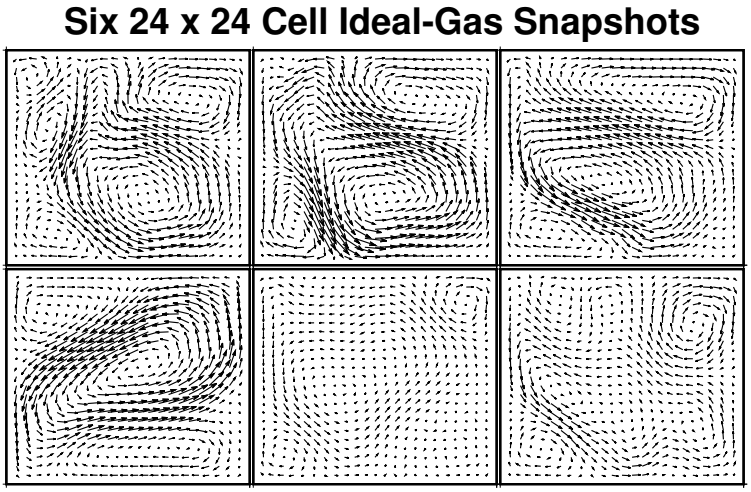


Figure 7: Snapshots at time 0, 100, 200, (bottom row, left to right) and 300, 400, 500 (top row, left to right) starting with an instantaneously reversed chaotic flow with $\mathcal{R} = 800\ 000$ .

Although there is no difficulty in simulating the motion on larger meshes even the modest 576-cell simulation of Figure 7 provides an excellent characterization of chaos. Characterizing chaos quantitatively entails evaluating Lyapunov exponents, the tendency of nearby trajectories to separate farther or to approach one another. The separation of a satellite trajectory from its reference has four component types :

$$\delta \equiv (\ \{\delta\rho\}, \{\delta u_x\}, \{\delta u_y\}, \{\delta e\}\ ) \ .$$

Keeping the separation constant by rescaling at every timestep gives the local exponent ,

$$\lambda_i(t) = \ln(|\ \delta_{\text{before}}\ |/|\ \delta_{\text{after}}\ |)/dt \ .$$

In atomistic simulations it is well known that the largest Lyapunov exponent can be measured in configuration, momentum, or phase space, with identical longtime averages[12]. In continuum simulations one would expect that the density, velocity, or energy subspaces could be used in this same way. By choosing particular mass, length, and time units any one of the three subspaces could be made to dominate the local Lyapunov exponent.

Figure 8 shows the exponential separation of a satellite trajectory from its reference trajectory, without rescaling, as measured in the density, velocity, energy, and complete state spaces of the flow. The similarity of the four curves is so complete that we don't attempt to label them separatedly in the figure. Evidently, despite the changing morphology of the chaotic vortices, the underlying chaos ( at a Rayleigh Number of $800K$ ) is quite steady. The research literature indicates that the Lyapunov spectrum in such

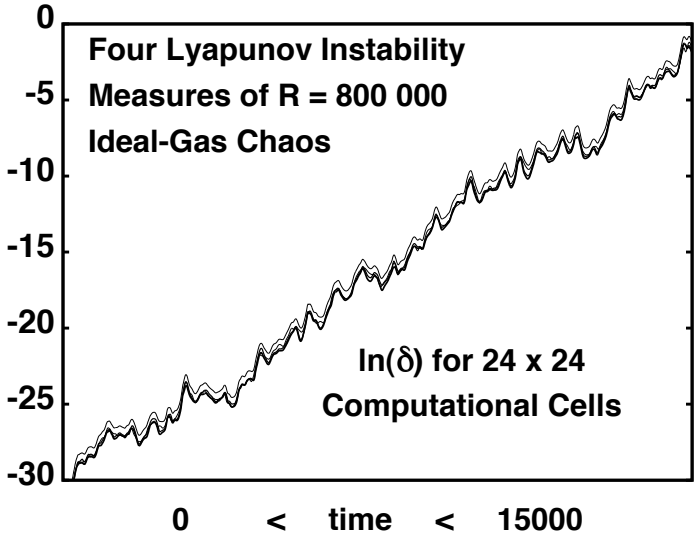


Figure 8: Separation between two strongly chaotic simulations. The fourth-order Runge-Kutta timestep is 0.05. Although four different sets of data (for $\rho$, $u$, $e$ subspaces as well as the complete space) are shown, here, the local Lyapunov exponents are scarcely distinguishable from one another.

two-dimensional flows is roughly linear, and corresponds to a strange attractor with only a few degrees of freedom, no doubt corresponding to the number of observed vortices.

The low dimensionality of two-dimensional turbulent chaos results from the tremendous dissipation inherent in the Navier-Stokes-Newton-Fourier model. If we evaluate the three "phase-space derivatives" which contribute to the continuum analog of Liouville's particle Theorem :

$$(\partial\dot{\rho}/\partial\rho) \; ; \; (\partial\dot{u}/\partial u) \; ; \; (\partial\dot{e}/\partial e) \; ,$$

[ here the dots are time derivatives *at fixed cells or nodes* ] the velocity and energy derivatives give $-4(\eta/\rho)/(dx)^2$ and $-4\kappa/(dx)^2$ respectively while the density derivative vanishes. In the end only a few degrees of freedom exhibit chaos.

## 4 Conclusions and Suggestions for Research

Continuum mechanics can be studied with finite-difference ordinary differential equations, or with particle differential equations, resembling those used in molecular dynamics. The finite-difference approach is certainly the most efficient of these possibilities. The Rayleigh-Bénard problems exhibit a variety of flows, with interesting results at the level of a few hundred compuational cells. The relative stability of the flows and the characterization of the chaos are both interesting research areas. With the limited dimensionality of the chaotic flows' attractors estimating only a few Lyapunov exponents suffice to characterize Rayleigh-Bénard chaos. The loci of Lyapunov vectors' instability is yet another source of fascinating questions and answers.

Though we have no space to discuss them here the useful smooth-particle technique for bridging together the particle and continuum methods suggests a variety of problems designed to reduce the discrepancies between the three types of numerical algorithm.

## 5 Acknowledgments

We first learned about the Rayleigh-Bénard problem through a lecture by Jerry Gollub at Sitges some 25 years ago. That talk led to Ph D projects for Oyeon Kum and Vic Castillo at the University of California's Davis/Livermore Campus' "Teller Tech". Their work continues to provide us with inspiration. We thank Denis Rapaport for helpful emails and Anton Krivtsov and Vitaly Kuzkin for encouraging our preparation of this lecture.

## References

[1] L. P. Kadanoff, "Turbulent Heat Flow: Structures and Scaling", Physics Today 34-39 (August 2001).

[2] N. T. Ouellette, "Turbulence in Two Dimensions", Physics Today 68-69 (May 2012).

[3] G. E. Karniadakis and S. A. Orszag, "Nodes, Modes, and Flow Codes", Physics Today 34-42 (March 1993).

[4] A. E. Deane and L. Sirovich, "A Computational Study of Rayleigh-Bénard Convection. Part 1. Rayleigh-Number Scaling [ and ] Part 2. Dimension Considerations", Journal of Fluid Mechanics **222**, 231-250 [ and ] 251-265 (1991).

[5] R. H. Kraichnan and D. Montgomery, "Two-Dimensional Turbulence", Reports on Progress in Physics **43**, 547-619 (1980).

[6] A. V. Getling, *Rayleigh-Bénard Convection – Structures and Dynamics.* (World Scientific, Singapore, 1998).

[7] Wm. G. Hoover and Carol G. Hoover, *Time Reversibility, Computer Simulation, Algorithms, and Chaos* (Second Edition, World Scientific, Singapore, 2012) .

[8] Wm. G. Hoover, *Smooth Particle Applied Mechanics: the State of the Art*, World Scientific, Singapore, 2006) .

[9] A. Puhl, M. M. Mansour, and M. Mareschal, "Quantitative Comparison of Molecular Dynamics with Hydrodynamics in Rayleigh-Bénard Convection", Physical Review A **40**, 1999-2012 (1989).

[10] D. C. Rapaport, "Hexagonal Convection Patterns in Atomistically Simulated Fluids", Physical Review E **73**, 025301R (2006).

[11] V. M. Castillo, Wm. G. Hoover, and C. G. Hoover, "Coexisting Attractors in Compressible Rayleigh-Bénard Flow", Physical Review E **55**, 5546-5550 (1997).

[12] S. D. Stoddard and J. Ford, "Numerical Experiments on the Stochastic Behavior of a Lennard-Jones Gas System", Physical Review A **8**, 1504-1512 (1973).

*Wm. G. Hoover and Carol G. Hoover*
*Ruby Valley Research Institute*
*Highway Contract 60, Box 601*
*Ruby Valley, Nevada 89833*

# Motion of the rigid body consisting of two disks

Mikhail O. Itskovich Alexander S. Kuleshov
kuleshov@mech.math.msu.su

**Abstract**

We present a kinematic analysis and dynamic simulation motion of a rigid body consisting of two equal elliptical disks whose symmetry planes are at right angle. The no-slip constraints of the body are integrable since the system is essentially holonomic. Trajectories of the ground contact points are found. All equilibrium positions of the body on the plane are found and their stability analysis is performed.

## 1 Introduction

Let us consider the rigid body of the following form: it comprises of two symmetric laminae whose planes of symmetry make a right angle between each other. The laminae are connected along the common axis of symmetry. When this body moves along the fixed horizontal plane it touches the plane in two points (Fig. 1).

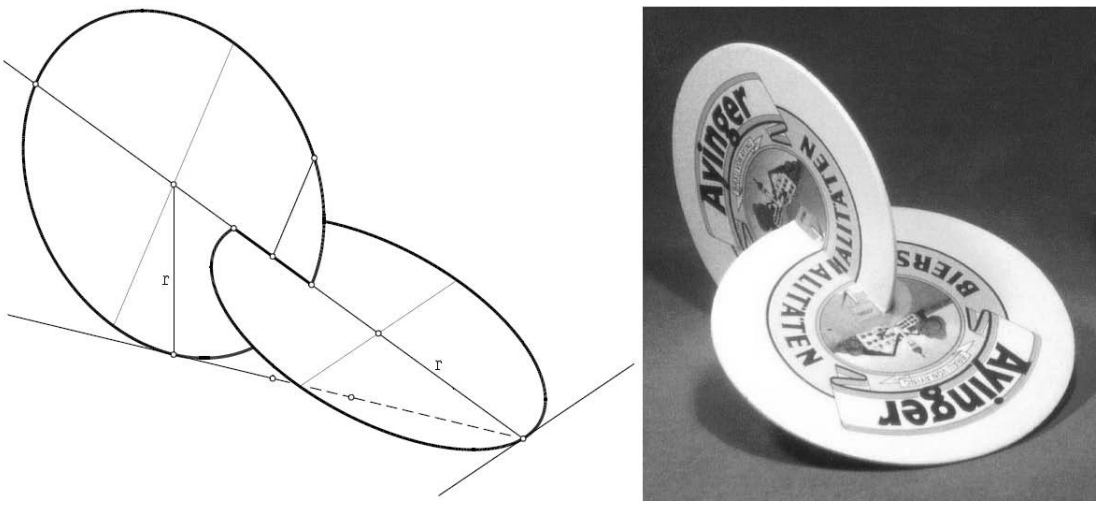


Figure 1: The Two-Circle-Roller and the Oloid.

The most known bodies of such a form are the Two-Circle-Roller [1, 2] and the Oloid [3, 4, 5]. The Two-Circle-Roller consists of two interlocked circular disks with the distance between their centers is $r\sqrt{2}$, where $r$ is a common radius of the disks (Fig. 1). The Oloid is similar to Two-Circle-Roller: it consists of two interlocked circular disks but the distance between their centers equals to their radius $r$. For both of these bodies their motion on the fixed horizontal plane is studied in details [1]-[5]. However it is interesting to investigate the motion of the rigid body whose form differs from Two-Circle-Roller and Oloid.

The theory proposed in [4, 5] allows to investigate the motion of the rigid body when this body comprises of two symmetric laminae of the arbitrary form. In this paper we study

the motion of the rigid body consisting of two interlocked elliptical disks whose planes of symmetry make a right angle between each other. The distance between their centers can be arbitrary value. Trajectories of the ground contact points are found. The equilibria of the body on the plane are found and their stability conditions are obtained.

## 2 Problem Formulation

Let two identical elliptical disks with semi-axes $a$ and $b$, $(a > b)$ in perpendicular planes be given such that the distance between their centers $C_1$ and $C_2$ equals $2\Delta$ and $\Delta < a$. Suppose that these elliptical disks are connected along their major axis of symmetry (Fig. 2). According to the theory discussed in [4, 5] let us introduce the moving coordinate frame $Gx_1x_2x_3$. The origin of this frame will be at the midpoint $G$ of $C_1C_2$ (i.e. $G$ is the center of mass of the system). The $Gx_3$ - axis is perpendicular to the plane $\Pi_1$ of the first disk, $Gx_1$ - axis is perpendicular to the plane $\Pi_2$ of the second disk and $Gx_2$ axis is directed along the common axis of symmetry of two elliptical disks. The unit vectors of this coordinate system will be $\boldsymbol{e}_1$, $\boldsymbol{e}_2$, $\boldsymbol{e}_3$.

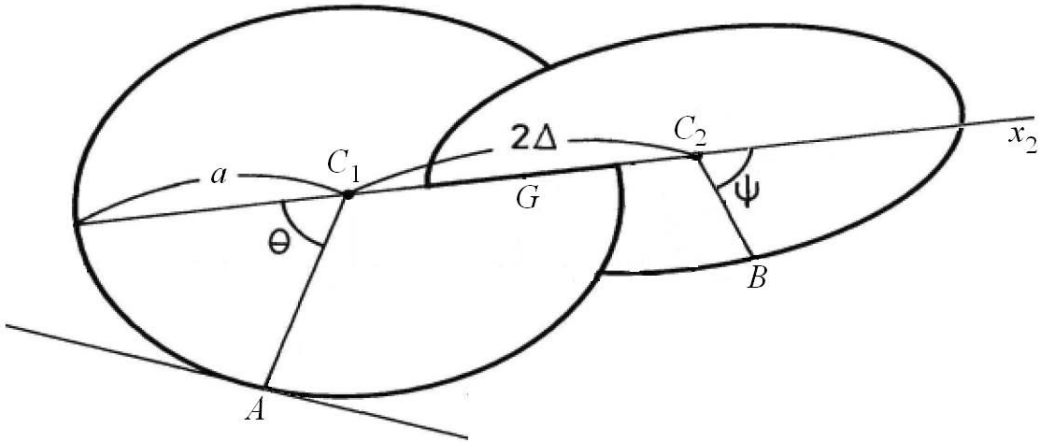


Figure 2: Rigid body consisting of two elliptical disks.

We will parametrize the first disk by the angle $\theta$ between the negative direction of $Gx_2$ axis and the direction to the point of contact $A$. Then the parametric equations for the bound of the first disk in terms of $\theta$ have the following form:

$$x_1 = \frac{ab\sin\theta}{\sqrt{a^2\sin^2\theta + b^2\cos^2\theta}}, \quad x_2 = -\frac{ab\cos\theta}{\sqrt{a^2\sin^2\theta + b^2\cos^2\theta}}.$$

It is necessary to note that the natural arc-length parameter $s$ is connected with the variable $\theta$ by the formula:

$$\frac{ds}{d\theta} = \frac{ab\sqrt{a^4\sin^2\theta + b^4\cos^2\theta}}{\left(a^2\sin^2\theta + b^2\cos^2\theta\right)^{\frac{3}{2}}}. \tag{1}$$

Let us introduce also the angle $\psi$ for the parametrization of the second disk: let $\psi$ be the angle between the positive direction of $Gx_2$ axis and the direction to the point of contact $B$. The parametric equations for the bound of the second disk have the form:

$$x_2 = \frac{ab\cos\psi}{\sqrt{a^2\sin^2\psi + b^2\cos^2\psi}}, \quad x_3 = -\frac{ab\sin\psi}{\sqrt{a^2\sin^2\psi + b^2\cos^2\psi}}.$$

The radius - vector of the point $A$ can be written as follows:

$$\overrightarrow{GA} = \boldsymbol{r}_1 = \frac{ab\sin\theta}{\sqrt{a^2\sin^2\theta + b^2\cos^2\theta}}e_1 - \left(\Delta + \frac{ab\cos\theta}{\sqrt{a^2\sin^2\theta + b^2\cos^2\theta}}\right)\boldsymbol{e}_2.$$

The radius-vector of the point $B$ has the form:

$$\overrightarrow{GB} = \boldsymbol{r}_2 = \left(\Delta + \frac{ab\cos\psi}{\sqrt{a^2\sin^2\psi + b^2\cos^2\psi}}\right)\boldsymbol{e}_2 - \frac{ab\sin\psi}{\sqrt{a^2\sin^2\psi + b^2\cos^2\psi}}\boldsymbol{e}_3.$$

When the considered rigid body rolls on a fixed horizontal plane the three vectors $\boldsymbol{r}_2 - \boldsymbol{r}_1$, $(\boldsymbol{r}_1)'_\theta$ and $(\boldsymbol{r}_2)'_\psi$ are always in this plane. We can write this condition as follows:

$$< \boldsymbol{r}_2 - \boldsymbol{r}_1,\, (\boldsymbol{r}_1)'_\theta,\, (\boldsymbol{r}_2)'_\psi >= 0,$$

where $< \cdot, \cdot, \cdot >$ is a triple scalar product of these vectors. From this condition we can find the following connection between $\theta$ and $\psi$:

$$\cos\psi = -\frac{a^2\cos\theta}{\sqrt{a^4 + 4ab\Delta\cos\theta\sqrt{a^2\sin^2\theta + b^2\cos^2\theta} + 4b^2\Delta^2\cos^2\theta}}$$

and obtain the radius – vector $\overrightarrow{GB} = \boldsymbol{r}_2$ in the $\theta$ – parametrization:

$$\begin{aligned}\boldsymbol{r}_2 = &\left(\Delta - \frac{a^2 b\cos\theta}{a\sqrt{a^2\sin^2\theta + b^2\cos^2\theta} + 2b\Delta\cos\theta}\right)\boldsymbol{e}_2 - \\ &- \frac{b\sqrt{a^4\sin^2\theta + 4ab\Delta\cos\theta\sqrt{a^2\sin^2\theta + b^2\cos^2\theta} + 4b^2\Delta^2\cos^2\theta}}{a\sqrt{a^2\sin^2\theta + b^2\cos^2\theta} + 2b\Delta\cos\theta}\boldsymbol{e}_3.\end{aligned} \tag{2}$$

Expression (2) for the radius - vector $\boldsymbol{r}_2$ should make a sense therefore we should have

$$a^2\sin^2\theta + 4pb\cos\theta\sqrt{a^2\sin^2\theta + b^2\cos^2\theta} + 4p^2b^2\cos^2\theta \geq 0.$$

This means that $\cos\theta$ should satisfy to inequality:

$$\cos\theta > -\frac{a^2}{\sqrt{a^4 + 4a\Delta b^2 + 4\Delta^2 b^2}}.$$

Therefore we have the following restrictions for the variables $\theta$ and $\psi$:

$$-\arccos\left(-\frac{a^2}{\sqrt{a^4+4a\Delta b^2+4\Delta^2 b^2}}\right) < \theta < \arccos\left(-\frac{a^2}{\sqrt{a^4+4a\Delta b^2+4\Delta^2 b^2}}\right),$$

$$-\arccos\left(-\frac{a^2}{\sqrt{a^4+4a\Delta b^2+4\Delta^2 b^2}}\right) < \psi < \arccos\left(-\frac{a^2}{\sqrt{a^4+4a\Delta b^2+4\Delta^2 b^2}}\right),$$

## 3 Trajectories of the points of contact.

Let us derive now equation for the fixed plane in the $Gx_1x_2x_3$ coordinate system. This equation can be derived from the condition that points $A$, $B$ and the tangent vector to the first disk at $A$ are in the fixed plane. Therefore, after some simplifications we get:

$$-a^2\sin\theta X + b^2\cos\theta Y + b\left(a\sqrt{a^2\sin^2\theta + b^2\cos^2\theta} + b\Delta\cos\theta\right) +$$

$$+Z\sqrt{a^4\sin^2\theta + 4ab\Delta\cos\theta\sqrt{a^2\sin^2\theta + b^2\cos^2\theta} + 4b^2\Delta^2\cos^2\theta} = 0.$$

The unit vector

$$\boldsymbol{n} = -\frac{a^2\sin\theta}{\sqrt{2a^4\sin^2\theta + b^4\cos^2\theta + 4ab\Delta\cos\theta\sqrt{a^2\sin^2\theta + b^2\cos^2\theta} + 4b^2\Delta^2\cos^2\theta}}\boldsymbol{e}_1 +$$

$$+\frac{b^2\cos\theta}{\sqrt{2a^4\sin^2\theta + b^4\cos^2\theta + 4ab\Delta\cos\theta\sqrt{a^2\sin^2\theta + b^2\cos^2\theta} + 4b^2\Delta^2\cos^2\theta}}\boldsymbol{e}_2 +$$

$$+\frac{\sqrt{a^4\sin^2\theta + 4ab\Delta\cos\theta\sqrt{a^2\sin^2\theta + b^2\cos^2\theta} + 4b^2\Delta^2\cos^2\theta}}{\sqrt{2a^4\sin^2\theta + b^4\cos^2\theta + 4ab\Delta\cos\theta\sqrt{a^2\sin^2\theta + b^2\cos^2\theta} + 4b^2\Delta^2\cos^2\theta}}\boldsymbol{e}_3$$

is the normal vector to this plane. Therefore the angle between the plane of the first disk and the fixed plane is determined by the formula:

$$\begin{aligned}\cos\varphi &= (\boldsymbol{n}\cdot\boldsymbol{e}_3) = \\ &= \frac{\sqrt{a^4\sin^2\theta + 4ab\Delta\cos\theta\sqrt{a^2\sin^2\theta + b^2\cos^2\theta} + 4b^2\Delta^2\cos^2\theta}}{\sqrt{2a^4\sin^2\theta + b^4\cos^2\theta + 4ab\Delta\cos\theta\sqrt{a^2\sin^2\theta + b^2\cos^2\theta} + 4b^2\Delta^2\cos^2\theta}}.\end{aligned}$$

The curvature of the bounding ellips of the first disk is:

$$k = \frac{ab\left(a^2\sin^2\theta + b^2\cos^2\theta\right)^{\frac{3}{2}}}{\left(a^4\sin^2\theta + b^4\cos^2\theta\right)^{\frac{3}{2}}}.$$

This curvature is connected with the curvature of the trajectory of the ground contact point of the first disk by the the following equation [4, 5]:

$$K = k\cos\varphi.$$

Having the expression for $K$ we can easily find the parametric equations of the trajectory of point $A$ on the fixed plane. For this purpose we introduce the fixed coordinate system $OXYZ$. The origin $O$ of this system coincides with the point of contact of the first disk with the plane at $\theta = 0$. The $OX$ - axis is tangent to the first disk at $\theta = 0$, the $OZ$ - axis is directed upwards. The $OY$ - axis forms the right triple with the $OX$ and $OZ$ axes. Let $\alpha$ be the angle between the tangent vector to the trajectory of the point $A$ and the $OX$-axis. Then the functions $X_A = X_A(\theta)$, $Y_A = Y_A(\theta)$ which give the parametric

representation of this trajectory in terms of the variable $\theta$ can be determined as a solution of the following system of differential equations [4, 5]:

$$\frac{dX_A}{d\theta} = \frac{ds}{d\theta}\cos\alpha, \quad \frac{dY_A}{d\theta} = \frac{ds}{d\theta}\sin\alpha, \quad \frac{d\alpha}{d\theta} = K(\theta)\frac{ds}{d\theta}. \tag{3}$$

Taking into account equation (1) we can rewrite equations (3) in the form:

$$\frac{dX_A}{d\theta} = \frac{ab\sqrt{a^4\sin^2\theta + b^4\cos^2\theta}}{\left(a^2\sin^2\theta + b^2\cos^2\theta\right)^{\frac{3}{2}}}\cos\alpha, \tag{4}$$

$$\frac{dY_A}{d\theta} = \frac{ab\sqrt{a^4\sin^2\theta + b^4\cos^2\theta}}{\left(a^2\sin^2\theta + b^2\cos^2\theta\right)^{\frac{3}{2}}}\sin\alpha, \tag{5}$$

$$\begin{aligned}\frac{d\alpha}{d\theta} = {} & \frac{a^2b^2}{\left(a^4\sin^2\theta + b^4\cos^2\theta\right)}\times \\ & \times\frac{\sqrt{a^4\sin^2\theta + 4ab\Delta\cos\theta\sqrt{a^2\sin^2\theta + b^2\cos^2\theta} + 4b^2\Delta^2\cos^2\theta}}{\sqrt{2a^4\sin^2\theta + b^4\cos^2\theta + 4ab\Delta\cos\theta\sqrt{a^2\sin^2\theta + b^2\cos^2\theta} + 4b^2\Delta^2\cos^2\theta}}.\end{aligned} \tag{6}$$

Equations (4)-(6) are very complicated. In general case it is impossible to find the explicit form of expressions for $X_A$, $Y_A$ and $\alpha$. Therefore we integrate these equations numerically for various values of parameters $a$, $b$ and $\Delta$. The similar equations can be derived for the trajectory of the point $B$. Fig 3-4. shows the trajectories of points $A$ and $B$ on the fixed plane. The bottom curve is the trajectory of point $A$ and the upper curve is a trajectory of point $B$.

Note that the system (4)-(6) can be solved for the particular values of parameters. For the Oloid ($a = b$, $\Delta = a/2$) this system is solved in terms of elementary functions [4, 5]. For the Two-Circle-Roller ($a = b$, $\Delta = a/\sqrt{2}$) it is solved with the help of elliptic integrals of the third kind [2].

## 4 Equilibria of the body and their stability

Having expressions for the vector $\overrightarrow{GA} = \boldsymbol{r}_1$ and the normal vector to the fixed plane $\boldsymbol{n}$, we can easily find expression for the potential energy of the rigid body consisting of two elliptical disks:

$$\begin{aligned} V &= Mgz_G = -Mg\left(\overrightarrow{GA}\cdot\boldsymbol{n}\right) = \\ &= \frac{Mgb\left(\Delta b\cos\theta + a\sqrt{a^2\sin^2\theta + b^2\cos^2\theta}\right)}{\sqrt{2a^4\sin^2\theta + b^4\cos^2\theta + 4ab\Delta\cos\theta\sqrt{a^2\sin^2\theta + b^2\cos^2\theta} + 4b^2\Delta^2\cos^2\theta}}.\end{aligned}$$

Critical points of the potential energy correspond to the equilibria of the system. The derivative of the potential energy has the form:

$$\begin{aligned} V'_\theta &= \frac{Mga^3b^3\sin\theta\cos\theta}{\sqrt{a^2\sin^2\theta + b^2\cos^2\theta}}\times \\ &\times \frac{\left(b^2 - 2a^2 + 2\Delta^2\right)}{\left(2a^4\sin^2\theta + b^4\cos^2\theta + 4ab\Delta\cos\theta\sqrt{a^2\sin^2\theta + b^2\cos^2\theta} + 4b^2\Delta^2\cos^2\theta\right)^{\frac{3}{2}}}.\end{aligned}$$

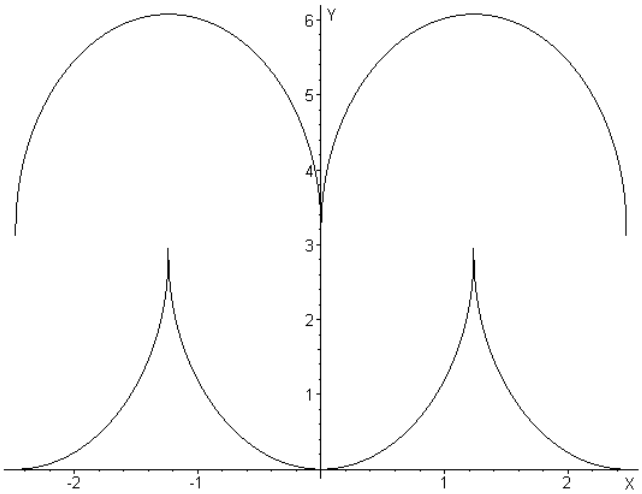


Figure 3: Trajectories of the ground contact points $A$ (bottom curve) and $B$ (upper curve). The values of parameters are: $a = 2$, $\Delta = 1$, $b = 1$.

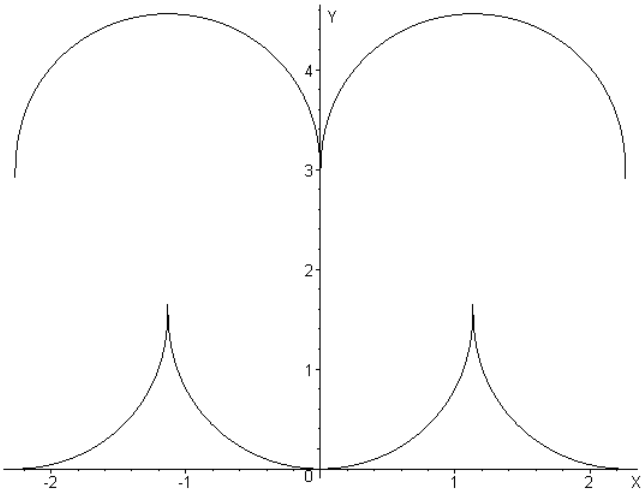


Figure 4: Trajectories of the ground contact points $A$ (bottom curve) and $B$ (upper curve). The values of parameters are: $a = \frac{\sqrt{3}}{\sqrt{2}}$, $\Delta = 1$, $b = 1$.

Thus the rigid body consisting of two elliptical disks has two equilibria: $\theta = 0$ and $\theta = \pi/2$. The sign of the second derivative of $V$, calculating at the corresponding equilibrium gives the conditions of stability of this equilibrium. Therefore for the equilibrium $\theta = 0$ we have

$$V''\Big|_{\theta=0} = \frac{Mga^3\left(b^2 - 2a^2 + 2\Delta^2\right)}{b\left(b^2 + 4a\Delta + 4\Delta^2\right)^{\frac{3}{2}}}.$$

This means that the equilibrium $\theta = 0$ is stable when $b^2 - 2a^2 + 2\Delta^2 > 0$ and unstable when $b^2 - 2a^2 + 2\Delta^2 < 0$. Similarly for the equilibrium $\theta = \pi/2$ we have

$$V''\Big|_{\theta=\pi/2} = -\frac{\sqrt{2}Mgb^3\left(b^2 - 2a^2 + 2\Delta^2\right)}{4a^4} > 0.$$

and the equilibrium $\theta = \pi/2$ is stable when $b^2 - 2a^2 + 2\Delta^2 < 0$ and unstable when $b^2 - 2a^2 + 2\Delta^2 > 0$.

The case when $b^2 - 2a^2 + 2\Delta^2 = 0$ or

$$\Delta = \sqrt{a^2 - \frac{b^2}{2}}$$

corresponds to neutral equilibrium. In this case the potential energy of the body is constant: the center of mass of the body moves at a constant height.

For the first author (Alexander S. Kuleshov) this work was supported financially by the Russian Foundation for Basic Research (grant no. 11-01-00322)

## References

[1] Stewart A.T. (1966) Two circle roller. *American Journal of Physics*, **34** (2): 166 — 167.

[2] Ira H. (2011) The Development of the Two Circle Roller in a Numerical Way.

*http://ilabo.bufsiz.jp/Development/2c-english.pdf*

[3] Dirnbök H., Stachel H. (1997) The Development of the Oloid. *J. Geometry Graphics* **1**:105-118.

[4] Kuleshov A.S., Hubbard M., Peterson D.L., Gede G. (2011) On the motion of the Oloid toy. *Proceedings of XXXIX International Summer School-Conference APM 2011.* Saint Petersburg: IPME. 275–282.

[5] Kuleshov A.S., Hubbard M., Peterson D.L., Gede G. (2011) Motion of the Oloid toy // *Proceedings of the 7th European Nonlinear Dynamics Conference (ENOC 2011)* Eds: D. Bernardini, G. Rega and F. Romeo.
*http://w3.uniroma1.it/dsg/enoc2011/proceedings/pdf/kuleshov_et_al_6pages.pdf*

*Mikhail O. Itskovich, Department of Mechanics and Mathematics, Moscow State University, Moscow, Russia*
*Alexander S. Kuleshov, Department of Mechanics and Mathematics, Moscow State University, Moscow, Russia*

# Several ways to automatically estimate optimal technological parameters of vibrational screening devices

K. S. Ivanov
ivanov.k.s@gmail.com

**Abstract**

A great variety of computer analysis methods developed last years has shown their potency in a number of problems. These methods such as swarm intelligence systems, evolutionary algorithms etc could be used in any field where it is necessary to deal with large amount of data. When working with a number of problems that preclude full analytical studies, it became possible to solve extremum problems using this methods joined with numerical models. The scope of such paired application of computer models and numerical optimization techniques is constantly expanding, encompassing a variety of practical areas: from economics to engineering.

This article presents an example of such methods application in the technical field. The methods were used for making a preliminary estimation of optimal technical parameters of vibrational screening devices. Basic data were obtained using original high performance algorithm of vibrational screening modeling and experiments.

## 1 Introduction

When mastered by the research community, new scientific and methodological knowledge not only widens the range of approaches available for solving practical problems, but also changes the view of the objects studied [1]. In this way, development of computer simulation methods had fundamentally changed new equipment creation processes. However, the influence of such changes became widespread only quarter of a century after the laying of foundations and making up of basic principles behind the currently most common approaches. This trend is clearly evident in the development of all areas of technical knowledge, including the mining industry. The history of vibrational screening application for separating granular materials extends back over three centuries and covers numerous practical areas of human activity: from ore dressing to such sophisticated industries as pharmacology. And yet, unified engineering approaches for calculating respective equipment did not appear until the seventies of the previous century. At that time, a unified approach could not be developed as it was conceptually impossible to consider material at the level of individual particles due to their large numbers. The behavior of granular medium under vibration depends upon specific features of interaction between its particles, as well as between the particles and machinery structural parts, force fields and the environment. In this regard, high significance is attached to dry friction forces and impacts. That is, at the particle level, the system is essentially discontinuous, and small parameter modifications may lead to radical changes in behavior of the material under examination. For this reason, classical approaches considered granular materials as continuous media, were based on task-specific phenomenology, and, therefore, had very limited applicability.

## 2 Background in mining industry

Universal molecular dynamics and discrete element methods (DEM) that appeared in the seventies of the twentieth century were not widespread until the mid-nineties. This was due to the fact that, at that time, the scientific community had not yet sufficiently mastered computational approaches to solving practical problems, as well as to the unavailability of appropriate computing resources. By now, these two obstacles have been overcome almost completely, although the high resource intensity of methods applied for analyzing granular media at the particle level and, as a result, the high time requirements of respective simulation processes should be emphasized. In a general sense, it should be noted that development of computer simulation methods not only changed the approach to calculations of parts and machinery, but also cleared the way for radically new design and construction techniques. In particular, when working with a number of models that preclude full analytical studies, it became possible to solve extremum problems using, for example, such methods as stochastic optimization. The scope of such paired application of computer models and numerical optimization techniques is constantly expanding, encompassing a variety of practical areas: from economics to engineering [2]. Numerical optimization techniques imply relatively frequent computations of objective function values depending on the resulting parameters of the model used and, therefore, naturally require high simulation rates. This, of course, limits applicability of the above-mentioned universal granular media examination methods due to their high resource intensity. With a view to solve several problems, not excluding this one, a simplified method was developed for quick numerical simulation of vibrational screening [3].

## 3 The simplified model of vibrational screening process and its application for optimal design of screening devices

The proposed vibration screening simulation method is based upon generalization of classical approaches, as described in [4]. Granular material is represented in the form of a cellular continuous medium hosting the processes of segregation, mixing, sieving and vibrational displacement. A separate model is used for each process which makes the general calculation scheme highly flexible and easily adaptable to new conditions. For example, the original computational scheme [3] using ideas from [5] allowed improving simulation of the granular medium particles passage through sieve apertures; moreover, a separate program was drawn up for vibrational displacement studies [6]. The diagram for material representation on the screen surface is shown in Fig. 1.

This model has very low resource intensity and, despite its simplicity, is sufficiently accurate. Its applicability has been tested through a series of experiments. Comparative field experiment and model application results are shown in the following table (Fig. 2).

A program for automatic estimation of optimal vibrational screen parameters based on joint use of simulation approaches and particle swarm optimization [7] was presented in [8]. This program requires considerably less time, as compared even to a single detailed DEM-based simulation. At the same time, with allowable value ranges specified, it enables conducting a series of simulations and making up of a preliminary, but quite accurate assessment of such optimal screen parameters as linear dimensions, aperture diameters, useful screen area, its inclination angle and vibration parameters (i.e. the parameters determining vibrational displacement velocities), as well as screen feed and other parameters. An example of program application results is shown in Fig. 3.

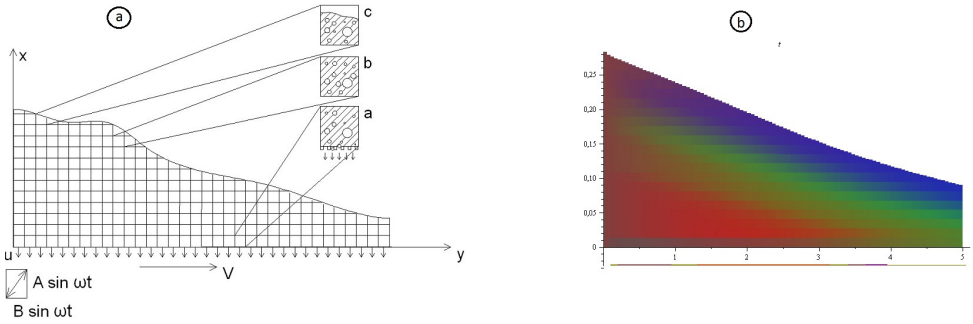


Figure 1: Material layer lateral section on the screen: a) the scheme of the section as it is processed by the program, b) simulation visualisation

| | granulation mm | % | production level m. tons/h | openings mm | extraction in-situ | comp |
|---|---|---|---|---|---|---|
| 1 | -0,071+0 | 1,5283 | 1,7250 | 0,3150 | 0,8889 | 0,9479 |
| | -0,18+0,071 | 11,9831 | | | 0,8657 | 0,9352 |
| | -0,315+0,18 | 8,5949 | | | 0,6129 | 0,6788 |
| | -0,63+0,315 | 17,0231 | | | 0,0000 | 0,0000 |
| | +0,63 | 62,3989 | | | 0,0000 | 0,0000 |
| | | | | | | |
| 2 | -0,071+0 | 2,5017 | 0,4637 | 0,3150 | 0,9730 | 0,9606 |
| | -0,18+0,071 | 12,6385 | | | 0,9898 | 0,9581 |
| | -0,315+0,18 | 10,7355 | | | 0,8475 | 0,9109 |
| | -0,63+0,315 | 11,9395 | | | 0,0000 | 0,0000 |
| | +0,63 | 64,6865 | | | 0,0000 | 0,0000 |
| | | | | | | |
| 3 | -0,071+0 | 1,2957 | 0,5604 | 0,3150 | 1,0000 | 0,9622 |
| | -0,18+0,071 | 11,7853 | | | 0,9886 | 0,9592 |
| | -0,315+0,18 | 9,0126 | | | 0,7500 | 0,8984 |
| | -0,63+0,315 | 16,4013 | | | 0,0000 | 0,0000 |
| | +0,63 | 62,8007 | | | 0,0000 | 0,0000 |
| | | | | | | |
| 4 | -0,071+0 | 2,5819 | 1,0336 | 0,3150 | 0,9412 | 0,9574 |
| | -0,18+0,071 | 12,6417 | | | 0,9663 | 0,9511 |
| | -0,315+0,18 | 11,9143 | | | 0,7857 | 0,8083 |
| | -0,63+0,315 | 13,0111 | | | 0,0000 | 0,0000 |
| | +0,63 | 62,4329 | | | 0,0000 | 0,0000 |

Figure 2: Experimental validation of the model

## 4 Prospects of the development of the approach

The prospects of these approaches to designing vibration equipment are covered in [9]. However, it is worth adding that the software system described is constantly improving. Besides the extensive upgrading opportunities of the basic screening model itself, as mentioned above, the program may easily use other numerical optimization approaches. For

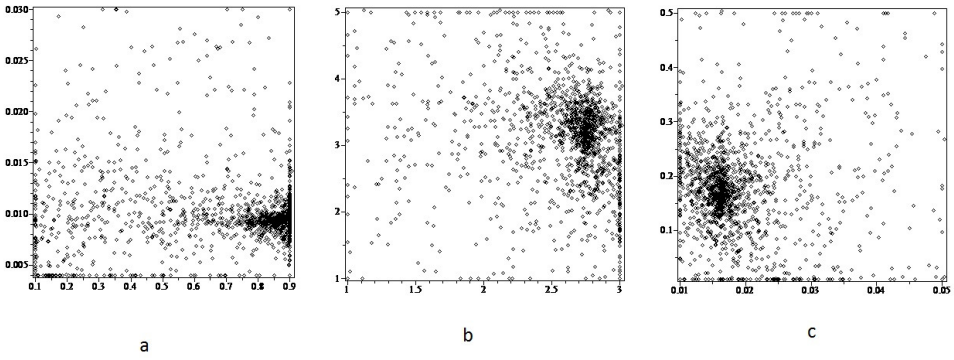


Figure 3: PSO and the vibrational screening model joined application results: crowded areas contain optimal parameters values a) useful screen area and screen openings diameter, b) length and width of the sieve, c) vibrational displacement rate and initial thickness of the material layer

example, a version of the program was implemented, based on the differential evolution method. The process of selecting optimal parameters may also be accelerated through reductions in the number of simulations carried out by storing intermediate results obtained in previous versions of the program. It may also be positively affected by reducing the initial search area through the use of the available statistics and data mining methods. Consequently, the software described allows conventionally dividing the optimal vibrating screen design process into three phases. The first phase implies shaping of a search area using alleged material characteristics and acceptable ranges of process parameters, as set by the designer, using statistics data. The second phase uses numerical optimization and the simplified screening model for preliminary estimations of equipment optimal parameters. And the third phase includes direct equipment development by the designer, using field experiments and more accurate methods, such as, for example, DEM. This structure ensures early elimination of numerous incorrect technical solutions under minimum time requirements and, all other things being equal, enables paying more attention to equipment fine-tuning and improvement.

## Acknowledgements

*The work is carried out with financial support of Russian Foundation for Basic Research, Grant 12-08-01102*

## References

[1] J. Greenwood. The Third Industrial Revolution: Technology, Productivity and Income Inequality, AEI Studies on Understanding Inequality, Washington, DC. The AEI Press. 1999

[2] T-H. Kim, I. Maruta, T. Sugie. A simple and efficient constrained particle swarm optimization and its application to engineering design problems, Journal of Mechanical Engineering Science, 2010, vol 224, No C2, pp. 389–400

[3] Ivanov K.S. Modeling and optimization of vibrational screening process //Proceedings of the XXXIX International Summer School Conference APM 2011. – St. Petersburg (Repino), July 1-5, 2011. PP. 213–218.

[4] Vaisberg L.A., Rubisov D.G. Vibrational screening of granular materials (in Russian). Mekhanobr, 1994, 47 p.

[5] Pelevin A.E. Probability of particles passing through the sieve openings and separation process in vibrational screening devices (in Russian) // Izvestiya vuzov. Mining Journal. 2011. N 1. pp. 119–129

[6] Blekhman I.I., Ivanov K.S. On a vibroimpact system in which chaos is caused by the rare attractor packing. Proceedings of the 2-nd international symposium RA'11. Riga-Jurmala, Latvia, RTU 2011. pp. 65–69

[7] Kennedy J., Eberhart R. Particle Swarm Optimization. Proceedings of IEEE International Conference on Neural Networks. IV, 1995, pp. 1942–1948

[8] Ivanov K.S. Optimization of Vibrational Screening Process //Proc. Vibration Problems ICOVP 2011, Technical University of Liberec. 2011, PP. 174-179

[9] Ivanov K.S. Prospects of stochastic optimization methods application in vibrational machinery development. (in Russian) V int. sc. conf. "Innovative development and demand for science in present-day Kazakhstan", V 4. The Foundation of the First President of the Republic of Kazakhstan. 2011. pp. 70–73

*Kirill S. Ivanov, V.O., Bolshoy av., 61, Saint Petersburg, 199178, Russia*

# Bounded positional control of mechanical system under uncertainties

Victoriya F. Ivanova
ivano-va@ipmnet.ru

**Abstract**

The method of constructing a limited positional control of a multidimensional mechanical system is offered. The movement of the dynamic system with viscous friction, potential forces, an uncertain limited influence (interference) is considered in a bounded phase area. The built algorithm guarantees the coming of the system into the phase zero in a finite (not fixed) time at any admissible interference and any initial state from the particular bounded region of a phase space. The assumed restrictions on system and movement parameters may be weaker, than the corresponding restrictions in the other methods of solving the similar tasks, because inertia terms, viscous friction and a part of potential forces aren't included in an interference and aren't compensated by a control in the presented research. This may help to reduce demanded modules of control components or to expand an acceptable area of movement. The given way of solving may be useful, for example, to control of a space design or a manipulation robot with viscous friction in hinges.

The offered method is based on the use of the function similar to Lyapunov function and on the system decomposition. In particular, the indicated function helps to find the multitude of admissible initial phase values. The numerical example of control constructing is considered.

## 1 Problem formulation

The dynamic system movement, which is described by Lagrange equations

$$M(q)\ddot{q} + B\dot{q} = U(q,\dot{q}) + Q_*(q,\dot{q}) + Q, \;\; t \geq 0, \; (q,\dot{q}) \in \Omega, \; (q_0,\dot{q}_0) \in \Omega_0, \tag{1}$$

is considered, where $q$ – $n$-dimensional vector of generalized coordinates, $\Omega$ – a given bounded phase movement area, $\Omega_0$ – an unknown region of admissible initial values; $M(q)$ – a known mass matrix, $M^T = M > 0$ (symmetric), functions $M(q)$, $M^{-1}(q)$ satisfy Lipschitz condition in $\Omega$; $B \neq 0$ – a known constant matrix, $B^T = B \geq 0$; $U(q,\dot{q})$ – a positional control,

$$|U_i\,| \leq U_{0i} = const, \quad i = \overline{1,n}, \tag{2}$$

$U_{0i}$ – preassigned constants; $Q = Q(t,q,\dot{q})$ – an uncertain interference,

$$|Q_i(t)|\;|_\Omega \leq Q_{0i} = const = Q_{0i}(\Omega), \;\; (q,\dot{q}) \in \Omega, \;\; t \geq 0, \;\; i = \overline{1,n}, \tag{3}$$

where $Q(t) = Q(\,t,\; q(t),\; \dot{q}(t))$; $Q_*(q,\dot{q})$ – a known continuous function.

It's required to choose the positional algorithm $U(q,\dot{q})$ (2), which leads the system (1) into the phase origin $O$ in a finite (not fixed) time at any interference realization $Q(t)$ (3), and also to find some corresponding area $\Omega_0$ . The methods for the similar tasks were proposed in [1]–[4]. The presented work generalizes the results of the author [5] on the case of a degenerate matrix of viscous friction.

## 2 Control choice and the arrival into phase zero

Let's compensate (annul) a part of the terms $Q_*(q,\dot q)$ in (1) by means of some positional control $U^*(q,\dot q)$.

Designations $U^+(q,\dot q)=U-U^*$, $m=rank\ B\le n$, $E_{n\,m}=diag\ \{\ E_m\ ,\ 0\}$ – $(n\times n)$ matrix, where $E_m$ – the identity $(m\times m)$ matrix.

After the nondegenerate substitution

$$q=P\ z,\quad det\ P\ne 0,\quad P=const,\quad P^TB\ P=E_{n\,m}\ , \tag{4}$$

the equation (1) is multiplied at the left by the matrix $P^{-1}M^{-1}(q)$, the sum

$$U(q,\dot q)=U^*+U^+, \tag{5}$$

$$U^*(q,\dot q)=-Q_*-M\ P\ A\ P^{-1}q,\quad A=const=diag\ge 0, \tag{6}$$

is put into (1), where $A$ – any expediently chosen matrix – the free parameter of the control constructing procedure. The result is

$$\ddot z+D_+(t)\ E_{n\,m}\ \dot z+Az=w(z,\dot z)+\zeta(t,z,\dot z),\ (z,\dot z)\in\Omega_Z\ ,\ (z_0\ ,\dot z_0\ )\in\Omega_{Z0}, \tag{7}$$

where $D_+(t)=D_+^T=P^{-1}M^{-1}(q(t))\ P^{-1T}>0$; $\Omega_Z\ ,\Omega_{Z0}$ – the images of $\Omega,\Omega_0$ ;

$$w(z,\dot z)=P^{-1}M^{-1}U^+, \tag{8}$$

$$\zeta(t)=\zeta(\ t,\ z(t),\ \dot z(t))=P^{-1}M^{-1}Q \tag{9}$$

– the positional control and the uncertain interference.

Designations

$$U_{0i}^*=\sup_{\Omega}\ |U_i^*(q,\dot q)|,\ \ U_{0i}^+=U_{0i}-U_{0i}^*\ ,\ \ V_{0i}^+=\sup_{\Omega}\ |U_i^+(q,\dot q)|,\ \ i=\overline{1,n}. \tag{10}$$

Let the inequalities $U_{0i}^+>0,\ \ i=\overline{1,n},$ are true. According to (2), it needs to subject the sought control $U^+$ to the limitation

$$V_{0i}^+\le U_{0i}^+\ ,\quad i=\overline{1,n}. \tag{11}$$

The following relations are gotten from (3), (9)

$$|\zeta_i(t)|\ |_{\Omega_Z}\le\zeta_{0i}=\zeta_{0i}(\Omega)=const,\quad t\ge 0,\quad i=\overline{1,n}, \tag{12}$$

$$\zeta_{0i}(\Omega)=\sup_{\Omega}\ \sum_{j=1}^{n}\ |(\ P^{-1}M^{-1})_{ij}\ |\ Q_{0j}\ ,\quad i=\overline{1,n}. \tag{13}$$

Let's select the sought control $w$ in the kind

$$w_i=w_i(z_i\ ,\dot z_i\ ),\quad |w_i\ |\le w_{0i}=const,\quad i=\overline{1,n}, \tag{14}$$

$$\zeta_{0i}<w_{0i},\quad i=\overline{1,n}. \tag{15}$$

According to (8), (11), it needs to subject the sizes $w_{0i}$ to the restriction

$$\sup_{\Omega}\ \sum_{j=1}^{n}\ |(\ P\ M\ )_{ij}\ |\ w_{0j}\le U_{0i}^+\ ,\quad i=\overline{1,n}. \tag{16}$$

Let the system of the relations (15), (16), (13) has a solution $(w_{0i}\ ,\ \ i=\overline{1,n})$, and let any such solution is fixed.

The block form of (7) is

$$\ddot{x}+D(t)\ \dot{x}+\Lambda x=u(x,\dot{x})+\varepsilon(t,z,\dot{z}),\ \ (x,\dot{x})\in\Omega_X\ ,\ \ (x_0\ ,\dot{x}_0\ )\in\Omega_{X0}\ , \tag{17}$$

$$\ddot{y}+D_1(t)\ \dot{x}+Hy=h(y,\dot{y})+\xi(t,z,\dot{z}), \tag{18}$$

where $x$ – $m$-dimensional vector, $(x,y)=z,\ \ (u,h)=w,\ \ (\varepsilon,\xi)=\zeta;\ \ D(t)=D^T=D(\ z(t))>0,$ as a diagonal block of the matrix $D_+\ ;\ \ \Omega_X$ – a real movement area in the subspace $\{(x,\dot{x})\};\ \ \Omega_{X0}$ – a projection of the region $\Omega_{Z0}$ on $\{(x,\dot{x})\}$.

Designations $u_{0i}=w_{0i}\ ,\ \ \varepsilon_{0i}=\zeta_{0i}\ ,\ \ i=\overline{1,m};\ \ h_{0i}=w_{0\ m+i}\ ,\ \ i=\overline{1,\ n-m};\ \ \Delta w_{0i}=w_{0i}-\zeta_{0i}\ ,\ \ \Delta u_{0i}=u_{0i}-\varepsilon_{0i}\ ;\ \ \rho_i(z_i\ )=-sign\ z_i\ \sqrt{2\ \Delta w_{0i}\ |z_i\ |};\ \ \rho_i$ – the corresponding curve $\dot{z}_i=\rho_i(z_i\ )$ on the phase plane $O\ z_i\ \dot{z}_i$ too;

$$g_i=\{-1,\ \dot{z}_i>\rho_i(z_i\ );\ \ 1,\ \dot{z}_i<\rho_i(z_i\ );\ \ sign\ z_i\ ,\ \dot{z}_i=\rho_i(z_i\ )\},\ \ s_i=sign\ \dot{z}_i\ . \tag{19}$$

Let's choose the relay control $w=(u,h)$ (14), (15) in the kind

$$u_i=u_i(x_i\ ,\dot{x}_i\ )=\Delta u_{0i}\ g_i(x_i\ ,\dot{x}_i\ )-\varepsilon_{0i}\ s_i(\dot{x}_i\ ),\quad i=\overline{1,m}, \tag{20}$$

$$h_i=h_i(y_i\ ,\dot{y}_i\ )=h_{0i}\ g_{m+i}(y_i\ ,\dot{y}_i\ ),\quad i=\overline{1,\ n-m}. \tag{21}$$

It's disregarded a control delay in the paper. Therefore it's accepted that all values $|g_i\ |\le 1,\ \ |s_i\ |\le 1$ are possible on the switches lines in sliding regimes.

Let's introduce the continuous functions

$$S_i(x_i\ ,\dot{x}_i\ )=(1/2)\dot{x}_i^2+(1/2)\Lambda_i x_i^2+\Delta u_{0i}\ |x_i\ |,\ \ S(x,\dot{x})=\sum_{i=1}^{m}S_i(x_i\ ,\dot{x}_i\ ), \tag{22}$$

$S>0$ out of the point $x=\dot{x}=0,\ \ S\to\infty$ at $|x|+\ |\dot{x}|\to\infty$.

If all derivatives $\dot{S}_i(t)$ in accordance with (17), (20) exists,

$$\dot{S}_i(t)=\dot{x}_i\ \Delta u_{0i}\ (g_i+sign\ x_i\ )+\dot{x}_i\ (\varepsilon_i-\varepsilon_{0i}\ s_i\ )-\dot{x}_i\ \sum_{j=1}^{m}D_{ij}\ \dot{x}_j\ ,$$

$$\dot{S}(t)=\sum_{i=1}^{m}|\dot{x}_i\ |\ \Big\{sign\ \dot{x}_i\ \ \big[\Delta u_{0i}(g_i+sign\ x_i\ )+\varepsilon_i-\varepsilon_{0i}\ s_i\ \big]\Big\}-(D\dot{x}\cdot\dot{x}). \tag{23}$$

The functions in the curly brackets (23) are nonpositive (15), (19). Therefore

$$\limsup_{\Delta t\to 0}\ \frac{\Delta S}{\Delta t}\le-(\ D\ \dot{x}\ \cdot\ \dot{x})\le 0,\quad t\ge 0, \tag{24}$$

where $\Delta S=S(t+\Delta t)-\ S(t)$, $\limsup$ – limit superior, on any trajectory (17)–(21), (12) in every moment $t\ge 0$, in particular, for sliding regimes of control switches. So, the function $S(t)$ doesn't increase on any curve (17)–(21), (12).

This permits to select the set $\Omega_{Z0}$ (7) in the kind

$$\Omega_{Z0}=\overline{\Phi}\ \subseteq\ \Omega_Z\ ,\quad \Phi=\ \cup\ \{\ (\ z(t),\ \dot{z}(t)),\ \ t\ge 0\ \}, \tag{25}$$

where $\overline{\Phi}$ – the closure of the set $\Phi$, $\Phi$ – the union of all trajectories $(z,\dot{z})$ at any realizations (12) with any beginnings from the multitude

$$\big\{\ (\ (x_0\ ,\dot{x}_0\ )\in\Omega_{X0}\ ,\quad y_0=\dot{y}_0=0\ )\ \big\}\ , \tag{26}$$

$\Omega_{X0}$ (17), in turn, is chosen in the kind

$$\Omega_{X0} = \Omega_X = \{\ S(x, \dot{x}) \le S_* = const\ \}. \tag{27}$$

Such set $\Omega_{Z0} \subseteq \Omega_Z$ exists, because the real area of the movement (17)–(21), (12) tightens into the point $O$ at $S_* \to 0$ (27) [1]–[4] and coincides with $\Omega_{Z0}$ at enough small values $S_*$ in accordance with constructing.

So, any trajectory with a beginning in $\Omega_{Z0} = \overline{\Phi} \subseteq \Omega_Z$ can't go from $\Omega_{Z0}$.

It follows from (24) that

$$S(t) \le S(\tau) - \int_\tau^t (\ D\ \dot{x}\ \cdot\ \dot{x})\ |_s\ ds, \quad 0 \le \tau \le t. \tag{28}$$

According to (17)–(21) the accelerations are bounded in the bounded region (25)–(27), therefore according to the properties of the functions $M^{-1}(q)$, $D_+(q)$ (7), $D(q)$ in the area $\Omega$ the function $(\ D(t)\ \dot{x}(t)\ \cdot\ \dot{x}(t))$ in (28) satisfies Lipschitz condition in $t$ on the interval $t \ge 0$. The equality

$$\lim_{t\,\to\,\infty} (\ D\ \dot{x}\ \cdot\ \dot{x}) = 0 \tag{29}$$

is true on an fixed trajectory, because in the opposing case the untrue conclusion $\{\ S(t) < 0,\ \exists\ t > 0\ \}$ follows from (28) and the Lipschitz property in (28) [5].

The inequality $|D\ \dot{x}\ |^2 \le d_*(\ D\ \dot{x}\ \cdot\ \dot{x})$ is true for any matrix $D = D^T \ge 0$, where $d_*$ – an maximal characteristic root of $D$; the matrix $D(q)$ (17) is bounded in norm on the set $\Omega$. Therefore the following relation is the consequence from (29)

$$\lim_{t\,\to\,\infty}\ D(t)\ \dot{x}(t) = 0. \tag{30}$$

The equality (30) permits to decompose [4] the subsystem (17), (20) after an enough big time into the one-dimensional independent equations

$$\ddot{x}_i + \Lambda_i x_i = u_i + \varepsilon_i + \delta_i\ ,\ \ |\delta_i| \le \delta_0 = const,\ t \ge t_* = const \ge 0,\ i = \overline{1, m}, \tag{31}$$

where $\delta_i$ – the friction terms as an additional uncertain interference, $\delta_0$ – any unlimitedly small number; moment $t_*$ depends on a trajectory and $\delta_0$.

Let's enter the additional restriction on the system and movement parameters

$$\varepsilon_{0i} < u_{0i}\ /3, \quad i = \overline{1, m}, \tag{32}$$

i.e. let the relations system (15), (16), (32), (13) has a solution $(w_{0i}\ ,\ i = \overline{1, n})$, and let any such solution is fixed. The inequalities (32) guarantee that there aren't rest points distinct from the point $O$ in the system at any interference realization (12). This follows directly from the equalities (17)–(21).

Designations $a_i = u_{0i} - 3\ \varepsilon_{0i} > 0$ (32),

$$a = \min_i\ a_i\ > 0, \quad i = \overline{1, m}. \tag{33}$$

Let's fix any trajectory (17)–(21) with a beginning in the region $\Omega_{Z0}$ (25)–(27). Let's choose the moment $t_*$ (31) in accordance with the condition

$$|\delta_i(t)\ | \le a/4, \quad t \ge t_*(\delta_0 = a/4), \quad i = \overline{1, m}. \tag{34}$$

Then the trajectory (31)–(34) comes into the point $x = \dot{x} = 0$ in a finite time $\Delta T$ [1]–[4]. The friction disappears in (18) at $t \ge t_* + \Delta T$, consequently, the trajectory $(y, \dot{y})$ arrives into the point $O$ in a finite time too [1]–[4].

The formula of the corresponding positional control $U$ (1), (2)

$$U(q, \dot{q}) = -Q_* - M\ P\ A\ P^{-1}q + U^+, \quad U^+(q, \dot{q}) = M\ P\ w(\ P^{-1}q,\ P^{-1}\dot{q}\ ), \tag{35}$$

is gotten from (4)–(6),(8), where $w$ – the relay algorithm (20),(21), (15),(16),(32).

## 3 Example of constructing the solution

The horizontal movement of a two-link manipulation robot is considered. The design parameters and the limits on the controlling moments coincide with the data in the example from [2], but the viscous friction in both hinges and the external uncertain limited interference are added into the system. Unlike Sect. 1,2, here the admissible region $\Omega$ is an unknown sought set $\Omega = \Omega_0$ (25)–(27), (4).

It's accepted that external interference limits $Q_{0i}$ (3) don't depend on $\Omega$.

Designations $G = \Omega_0 \cap \{\dot{q} = 0\}$, $C_2$ – the mass centre of the second link; $O_1$ , $O_2$ – the vertical axes of hinges, and the points of these axes in the horizontal plane with $C_2$ ; $m_1$ , $m_2$ – masses of links; $I_1$ , $I_2$ – the inertia moments of links relating to the axes $O_1$ , $O_2$ correspondingly; $l_1 = |O_1\ O_2\ |$, $l_2 = |O_2\ C_2\ |$; $q = (q_1\ , q_2\ )$ – relative angles of the links rotation [2]; $K_1$ , $K_2$ – the controlling moments in the hinges $O_1$ , $O_2$ , satisfying the restriction $|K_i\ | \le K_{0i} = const$, $i = \overline{1,2}$ .

The purpose of a calculation is to provide the comparatively simple form and maximal sizes of the set $G$, and to find the corresponding control, which leads the system into the point $O$ in a finite time.

After the transition to the nondimensional time $t' = K_{02}^{1/2}(m_2\ l_1\ l_2\ )^{-1/2}\ t$ and multiplying by $K_{02}^{-1}$ the movement equations are nondimensionalized. They have the kind (1)–(3), where a point above a function means $d/dt'$ ;

$$Q_* = (\ Q_{*1}\ , Q_{*2}\ ), \quad Q_{*1} = (\ 2\ \dot{q}_1\ \dot{q}_2 + \dot{q}_2^2\ )\ \sin q_2\ , \quad Q_{*2} = -\dot{q}_1^2\ \sin q_2 \tag{36}$$

– the terms, quadratically depending on velocities;

$$B = diag\ \{b_1\ ,\ b_2\ \} = const > 0; \tag{37}$$

$U_i = K_i\ /K_{02}$ , $U_{0i} = K_{0i}\ /K_{02}$ , $i = \overline{1,2}$. It follows from (37), (17), (18) that

$$n = m = 2, \quad x = z, \quad u = w, \quad \varepsilon = \zeta, \quad \Lambda = A, \quad \Omega_X = \Omega_Z = \Omega_{X0}\ . \tag{38}$$

Let's enter the data $m_2 = 10\ kg$, $l_1 = 1\ m$, $l_2 = 0.5\ m$, $I_1 = I_2 = 3.33\ kg \cdot m^2$, $K_{01} = 2.9\ N \cdot m$, $K_{02} = 1\ N \cdot m$, where $m = metre$, $N = Newton$ [2]; $Q_{01} = 3 \cdot 10^{-2}$, $Q_{02} = 5.5 \cdot 10^{-4}$;

$$b_1 = b_{1C}\ b, \quad b_2 = b_{2C}\ b, \quad b_{1C} = 0.5, \quad b_{2C} = 1, \quad b = const > 0, \tag{39}$$

where $b$ – a coefficient, which won't affect the calculation results.

In accordance with (4), (37), (38) the coordinates transformation are

$$x = \Theta^T P_0^{-1} q, \quad P_0 = diag\ \{b_1^{-1/2}\ ,\ b_2^{-1/2}\ \}, \quad \Theta_{11} = \Theta_{22} = \cos\vartheta,$$
$$\Theta_{21} = -\Theta_{12} = \sin\vartheta, \quad \vartheta = const, \quad -\pi/2 < \vartheta \le \pi/2, \tag{40}$$

where $\vartheta$ – the free procedure parameter. It doesn't need to consider the other matrixes $\Theta = \Theta^{-1T}$, because this doesn't affect the constructing results.

Let's demand the set $G$ to be a maximal in area rectangle in the kind

$$G = \left\{\ |q_i\ | \le q_{*i} = const, \ \ i = \overline{1,2}\ \right\}, \tag{41}$$

$$q_{*1}\ q_{*2} \to \max \tag{42}$$

at the restrictions (16), (32). The boundary equation for the region $\Omega_0$ (22), (27), (40) shows that the kind (41) is equivalent to the condition

$$\Delta u_{01} = \Delta u_{02}\ , \quad \vartheta \in\ \{\ \pm\pi/4\ \}, \quad \Lambda = 0. \tag{43}$$

Let's put (43) into (27) and do the substitution of the parameter $S_* = s_*\sqrt{b}\ \Delta u_{01}$ . The results are the families of the regions

$$\Omega(\ \Delta u_{01}\ , s_*\ ) = \left\{ (1/2)(b_1\dot{q}_1^2 + b_2\dot{q}_2^2) + \sqrt{2}\Delta u_{01} \max\left( |q_1|\sqrt{b_1}\ , |q_2|\sqrt{b_2} \right) \le s_*\sqrt{b}\Delta u_{01} \right\}, \tag{44}$$

$$G(s_*\ ) = \left\{ \sqrt{2}\ \max\left( |q_1\ |\sqrt{b_{1C}}\ ,\ \ |q_2\ |\sqrt{b_{2C}}\ \right) \le s_* \right\}. \tag{45}$$

Therefore the criteria (42) at the restrictions (16), (32) takes on the form

$$s_*\ \to\ \max. \tag{46}$$

Designations $\varepsilon_M = \max_i\ \varepsilon_{0i}\ ,\ \ u_M = \max_i\ u_{0i}\ ,\ \ i = \overline{1,m}.$

It was accepted that the limits $Q_{0i}$ don't depend on $\Omega$, therefore in accordance with (6), (8), (10), (13), (32), (33), (40), (43) it may consider the dependences

$$\varepsilon_{0i}(\ \Theta, G\ ) = \varepsilon_{0i}(\vartheta, s_*\ ), \quad \Delta u_{01}(a, \vartheta, s_*\ ) = 2\ \varepsilon_M(\vartheta, s_*\ ) + a,$$
$$u_{0i}(a, \vartheta, s_*\ ) = \varepsilon_{0i} + \Delta u_{01}\ ,\ \ V_{0i}^+(w_0\ , \Theta, G\ ) = V_{0i}^+(a, \vartheta, s_*\ ),\ \ U_{0i}^*(a, \vartheta, s_*\ ). \tag{47}$$

Let's fix any parameters $(a, \vartheta)$. Let the following inequalities are true

$$V_{0i}^+(a, \vartheta, s_* = 0) < U_{0i}\ , \quad i = \overline{1,2}. \tag{48}$$

The functions (47) have the certain properties of monotone change in $a$ and in $s_*$ , which follow from (36), (43)–(45). According to these properties, the conditions (16), (32), (48) and the relations $U_{0i}^*(a, \vartheta, s_* = 0) = 0$ (36), the equation

$$\min_i\ \left\{ U_{0i} - V_{0i}^+(a, \vartheta, s_*\ ) - U_{0i}^*(a, \vartheta, s_*\ )\ \right\} = 0 \tag{49}$$

has the unique root $s_* = s_*^0(a, \vartheta) > 0,$ which is the maximal admissible value $s_*$ at given $(a, \vartheta)$. Besides, the function $s_*^0(a, \vartheta)$ strongly monotonely decreases in $a$.

Therefore in accordance with the criteria (46) let's fix some enough small value $a = a_0$ as a primary constant of the constructing procedure. The characteristic time of the dynamic process $t_{CH}$ must be not very large. This limits $a_0$ from below, because $t_{CH} \to \infty$ at $a_0 \to 0$ (17)–(21), (32), (33).

Designation $s_*^M = s_*^M(a_0\ ) = \max_\vartheta\ s_*^0(a_0\ , \vartheta)$.

If the parameter $a_0$ is small compared with the value $u_M$ , it may say about the quasi-optimal set $G(s_*^M\ )$ (41), (42), (45).

Thus, it needs to do the following procedure.

1. To value the supposed sizes of the function $\varepsilon_M$ (47). This function doesn't depend on $s_*$ and $\vartheta$ (43), because the corresponding maximum on $G$ from two values $\varepsilon_{0i}$ (13) is achieved in the point $O$ in the given example.

2. To choose the parameter

$$a = a_0 = a_C\sqrt{b}, \quad a_C = 10^{-2} \tag{50}$$

(or some other acceptable enough small constant $a_C$ ), where $b$ – the coefficient from (39). The relation $a_0\ /u_M = a_0\ /(3\ \varepsilon_M + a_0\ ) = 5 \cdot 10^{-2}$ doesn't depend on $b$ at $a_C = const$ (13), (40), (50).

3. To fix any value $\vartheta$ (43).

4. To find in steps the functions (47) (except $U_{0i}^{*}$) and the family (44). The factors $b$ in (44) cancel on (13), (40), (50).

5. To find the functions $U_{0i}^{*}$ (47).

6. To check the condition (48) and to solve the equation (49). The gotten root

$$s_{*}^{0} = s_{*}^{M} = s_{*}^{M}(a_C = 10^{-2}) = 2.13$$

doesn't depend on $\vartheta$ (43) thanks to the relation $b_1 < b_2$ (39).

7. To get the quasi-optimal rectangle $G$ by means of (41), (45). The result is

$$q_{*1} = q_{*1}^{M} = s_{*}^{M} / \sqrt{2\, b_{1C}} = 2.13\ rad,\ \ q_{*2} = q_{*2}^{M} = s_{*}^{M} / \sqrt{2\, b_{2C}} = 1.50\ rad.$$

8. To find the area (44) at $s_{*} = s_{*}^{M}$.

9. To get the corresponding control algorithm $U$ (35), (40), (43).

So, the reverse task was demonstrated with help of the example. Unlike Sect. 1,2, the control parameters $\Delta w_{0i}$ aren't free in Sect. 3, are subjected to the choice of an possibly less constant $a_C$ (50). It was shown that the found quasi-maximal (in some sense) acceptable movement area $\Omega = \Omega_0$ and corresponding quasi-optimal control $U(q, \dot{q})$ don't depend on the norm $||B||$ (39)). This follows from the accepted parameters connection (50) and the other procedure formulas.

The presented method of leading the dynamic system into the point $O$ is useful, if the matrix $D(t)$ (17) is nondiagonal, $m \geq 2$. If $D(t)$ is diagonal, the ways [1]–[4] should be implemented for positional control constructing.

## References

[1] Chernousko F.L. Decomposition and synthesis of control in dynamical systems. Soviet J. of Computer and Systems Sciences **29(5)**, p. 126–144, 1991.

[2] Chernousko F.L., Ananievski I.M., Reshmin S.A. Control of Nonlinear Dynamical Systems. Methods and Applications. Springer-Verlag, Berlin, Heidelberg, 2008.

[3] Krasovskii N.N. Game-theoretic Problems on the Encounter of Motions. Nauka, Moscow, 1970 (in Russian).

[4] Pyatnitskiy Ye.S. A decoupling principle in control of mechanical systems. Reports of the Russian Academy of Sciences **300(2)**, p. 300–303, 1988 (in Russian).

[5] Sokolov B.N. Constrained positional control of a mechanical system near an equilibrium. Mechanics of Solids. A J. of Russian Academy of Sciences **41(4)**, p. 83–86, 2006.

*Victoriya F. Ivanova, Prospekt Vernadskogo 101, bld.1, Moscow, Russia*

# Evaluation of temporal derivative for propagating front of hydraulic fracture

David Jaworski Alexander Linkov Liliana Rybarska-Rusinek
djaworski@stud.prz.edu.pl

**Abstract**

The work concerns with the problem of hydraulic fracture propagating in time. Then in the hypersingular equation, connecting the net-pressure with the fracture opening, the integrand and limits of integration depend on the parameter (time). The rate of the pressure change, being of practical significance, we derive a rule for evaluation of the time derivative of a hypersingular integral with respect to a parameter. We present (i) the new concept of the complex variable hypersingular (CVH) integral with the density and limits of integration depending on a parameter, (ii) the theorem, which gives the rule for differentiation of the integral with respect to the parameter, (iii) application of the derived rule to the particular case when the fracture propagates under constant net-pressure.

## 1 Introduction

Using complex variable (CV) singular and hypersingular integral equations has proved to be an efficient means for solving various problems of fluid and solid mechanics. In particular, they are applied when studying hydraulic fractures (e.g. [1], [2], [3]). To the date, the theory of the CV singular [4] and hypersingular [5] integrals refers to problems, in which the boundary of a surface is fixed. Meanwhile, in problems of hydraulic fractures the boundary of the fracture propagates in time. Therefore, when considering hydraulic fractures, we need to extend the theory and to obtain a rule, which allows one to perform the differentiation of the CV singular and hypersingular integrals with respect to a parameter (time) when the density and/or contour depend on the parameter.

The main result of the paper is expressed by the proved theorem, which states that under physically sound assumptions, the usual rule of differentiation of a proper integral with respect to a parameter stays true for CVH integrals of arbitrary order. The paper contains also needed prerequisites and illustration of the derived rule by the example of the hydraulic fracture, propagating at early stage after initiation, when the net-pressure is actually constant along the fracture surface.

## 2 Problem formulation

A mathematical formulation of the problem of hydraulic fracture includes (i) fluid, (ii) solid, and (iii) fracture mechanics equations (see, e.g. [1], [2]). In this paper we focus on the second group as that, which defines the dependence between the net-pressure $p$ and the fracture opening $w$. In the simplest case of a 2D problem for a straight crack, propagating

along the $x$-axis, the dependence is given by the classical equation [6]:

$$p(x) = -\frac{E}{4\pi(1-\nu^2)} \int\limits_a^b \frac{\partial w(\tau)}{\partial \tau} \frac{d\tau}{\tau - x}, \ a \le x \le b, \tag{1}$$

where $E$ is the elasticity modulus, $\nu$ is the Poisson's ratio of the rock mass, $a$ and $b$ are points corresponding to the edges of the fracture; the integral on the r.h.s. is assumed as the singular (principle value) integral. The equation (1) contains the spatial derivative of the opening rather than the opening itself what is inconvenient in practical calculations. Thus it is reasonable to re-write (1) in the hypersingular form:

$$p(\alpha, x) = -\frac{E}{4\pi(1-\nu^2)} \int\limits_{a(\alpha)}^{b(\alpha)} \frac{w(\alpha, \tau) d\tau}{(\tau - x)^2}, \tag{2}$$

where we have also taken into account that for a propagating fracture, its edges $a$, $b$, the opening $w$ and the net-pressure $p$ are functions of the time. Thus, equation (2) defines the change of the net-pressure in time as a hypersingular integral with the density and limits depending on a parameter $\alpha$. The latter, in the considered problem, is the time. The rate of the pressure change $\partial p(\alpha, x)/\partial \alpha$ is a characteristic strongly dependent on the fluid injection regime. Its evaluation is also of need for numerical modeling of hydraulic fractures. Therefore, it is reasonable to obtain a rule for evaluation of the derivative of the hypersingular integral in (2) with respect to the parameter $\alpha$. To get such a rule, we employ and extend the general theory of CV hypersingular integrals, presented in [5].

## 3 Theorem on the derivative with respect to parameter

Let $ab$ be an open curve (arc) in the complex plane $z = x + iy$ ($i = \sqrt{-1}$). The equation of the arc is $\tau(\gamma) = x(\gamma) + iy(\gamma)$, where $\gamma$ is a real parameter such that its value $\gamma_a$ corresponds to start point $a$, while the value $\gamma_b$ corresponds to end point $b$: $a = x(\gamma_a) + iy(\gamma_a)$, $b = x(\gamma_b) + iy(\gamma_b)$. The arc is smooth in the sense explained in [4]. In further discussion, the positions of the edges $a$ and $b$ may change depending on a real parameter $\alpha$. Thus $\gamma_a = \gamma_a(\alpha)$, $\gamma_b = \gamma_b(\alpha)$, $a = a(\alpha)$, $b = b(\alpha)$. We assume that the functions $\gamma_a(\alpha)$, $\gamma_b = \gamma_b(\alpha)$ have Holder continuous derivatives.

Consider a hypersingular integral of order $k$

$$I_k(\alpha, t) = \int\limits_{a(\alpha)}^{b(\alpha)} \frac{g(\alpha, \tau)}{(\tau - t)^k} d\tau \tag{3}$$

with the density $g(\alpha, \tau)$ depending on the parameter $\alpha$. We assume that the density has Holder continuous $k-th$ derivative $\frac{\partial^k g(\alpha,\tau)}{\partial \tau^k}$ with respect to $\tau$ for each $\alpha$ and it also has Holder continuous derivative $\frac{\partial g(\alpha,\tau)}{\partial \alpha}$ with respect to $\alpha$ for each $\tau \in ab$. For any fixed $\alpha$ and $t \in ab$, the integral (3) is defined in accordance with the general theory [5]. Consequently, for a fixed $\alpha$, the following formulae, used below, are true.

(i) Extended Newton-Leibnitz formula:

$$\int_{a(\alpha)}^{b(\alpha)} \frac{g(\alpha, \tau)}{(\tau - t)^k} d\tau = J_g(\alpha, b) - J_g(\alpha, a) + \frac{i\pi}{k!} g_t^{(k-1)}(\alpha, t), \tag{4}$$

where $J_g(\alpha,\tau)$ is an antiderivative of the integrand $\frac{g(\alpha,\tau)}{(\tau-t)^k}$, that is

$$\frac{\partial J_g(\alpha,c)}{\partial c}=\frac{g(\alpha,c)}{(c-t)^k}. \tag{5}$$

(ii) The third regularization formula for $k\geq 2$:

$$\frac{d}{dt}\int\limits_{a(\alpha)}^{b(\alpha)}\frac{g(\alpha,\tau)}{(\tau-t)^{k-1}}d\tau=(k-1)\int\limits_{a(\alpha)}^{b(\alpha)}\frac{g(\alpha,\tau)}{(\tau-t)^k}d\tau. \tag{6}$$

By differentiating (5) with respect to $\alpha$ and changing the order of derivatives with respect to $\alpha$ and $c$, what is justified under accepted assumptions, we obtain:

$$\frac{\partial}{\partial c}\left(\frac{\partial J_g(\alpha,c)}{\partial\alpha}\right)=\frac{\frac{\partial g(\alpha,c)}{\partial\alpha}}{(c-t)^k}. \tag{7}$$

Equation (7) means that $\frac{\partial J_g(\alpha,c)}{\partial\alpha}$ is an antiderivative of the function $\frac{\partial g(\alpha,c)/\partial\alpha}{(c-t)^k}$. Then using this function and its antiderivative in the extended Newton-Leibnitz formula (4), we obtain:

$$\int_{a(\alpha)}^{b(\alpha)}\frac{\frac{\partial g(\alpha,\tau)}{\partial\alpha}}{(\tau-t)^k}d\tau=\frac{\partial J_g}{\partial\alpha}(\alpha,b)-\frac{\partial J_g}{\partial\alpha}(\alpha,a)+\frac{i\pi}{k!}\frac{\partial g_t^{(k-1)}}{\partial\alpha}(\alpha,t). \tag{8}$$

On the other hand, the results of differentiation of the both parts of (4) with respect to $\alpha$ may be written as

$$\frac{\partial}{\partial\alpha}\int_{a(\alpha)}^{b(\alpha)}\frac{g(\alpha,\tau)}{(\tau-t)^k}d\tau=\frac{\partial J_g}{\partial\alpha}(\alpha,b)-\frac{\partial J_g}{\partial\alpha}(\alpha,a)+\frac{i\pi}{k!}\frac{\partial g_t^{(k-1)}}{\partial\alpha}(\alpha,t)+$$
$$+\frac{\partial J_g}{\partial b}\frac{db}{d\alpha}-\frac{\partial J_g}{\partial a}\frac{da}{d\alpha}. \tag{9}$$

Noting that the sum of the first three terms on the r.h.s. of (9) is given by the integral in (8), equation (9) becomes:

$$\frac{\partial}{\partial\alpha}\int_{a(\alpha)}^{b(\alpha)}\frac{g(\alpha,\tau)}{(\tau-t)^k}d\tau=\int_{a(\alpha)}^{b(\alpha)}\frac{\partial g(\alpha,\tau)}{\partial\alpha}\frac{d\tau}{(\tau-t)^k}+\frac{g(\alpha,b)}{(b-t)^k}\frac{db}{d\alpha}-\frac{g(\alpha,a)}{(a-t)^k}\frac{da}{d\alpha}. \tag{10}$$

Equation (10) shows that the classical rule for differentiation of a proper integral with respect to a parameter holds for a CV hypersingular integral of an arbitrary order, as well. Thus, we have proved the theorem.

**Theorem 1** (Differentiation of a CVHI with respect to a parameter)**.** *For a smooth arc $a,b$ with $a(\alpha)$ and $b(\alpha)$ being Holder continuous in a parameter $\alpha$ and for a density $g(\alpha,\tau)$ having $k-1-th$ Holder continuous derivative with respect to $\tau$ and Holder continuous derivative with respect to $\alpha$, the derivative of a hypersingular integral $I_k(\alpha,t)$ with respect to the parameter $\alpha$ has the form (10) similar to the common rule for proper integrals.*

In the problem of hydraulic fracturing, $k=2$, $\alpha$ has the meaning of the time, the integral on the l.h.s. of (10) is proportional to the net-pressure, the density $g(\alpha,\tau)$ is the fracture opening and the derivatives $db/d\alpha$ and $da/d\alpha$ express the speeds, with which the fracture front propagates. According to (10), the inflence of the speeds on the rate of the pressure change strongly depends on the values $g(\alpha,a)$ and $g(\alpha,b)$ of the opening at the points of the front $a$ and $b$. Usually, near a point $c$ of the front, the opening tends to zero as $(c-\tau)^\gamma$, where $\gamma>0$. Hence, we need to extend the theorem to the case when near an edge point $c$ ($c=a$ or $c=b$) the density is of the form $g(\alpha,\tau)=(c-\tau)^\gamma g_\gamma(\alpha,\tau)$.

## 4 Extension to densities with derivatives having power-type singularity at arc tips

Consider a density of the form $g(\alpha,\tau)=(c-\tau)^{\gamma}g_{\gamma}(\alpha,\tau)$. For generality, we assume that $\gamma$ is a complex number with $Re\gamma>0$. Note that if $j-1<Re\gamma<j$, where $j$ is non-negative integer, then the derivatives $\partial^j g(\alpha,\tau)/\partial\tau^j$ and $\partial^j g(c,\tau)/\partial\tau^{j-1}\partial c$ are singular at the point $\tau=c$, tending to infinity as $1/(c-\tau)^{j-Re\gamma}$. As the definitions of the hypersingular integral and the theorem of the previous section employ assumptions on the derivatives, there is need in further agreements on the behaviour of the density. We shall assume that $k-2<Re\gamma<k-1$ and call $g(\alpha,\tau)=(c-\tau)^{\gamma}g_{\gamma}(\alpha,\tau)$ the density of class $H_*^k$. For $k=1$, the class $H_*^k$ coincides with the class $H_*$, defined and studied in [4].

For the density of class $H_*^k$, we may represent the CVHI (3) as the sum of three integrals

$$\int\limits_{a(\alpha)}^{b(\alpha)}\frac{g(\alpha,\tau)}{(\tau-t)^k}d\tau=\int\limits_{a_1(\alpha)}^{b_1(\alpha)}\frac{g(\alpha,\tau)}{(\tau-t)^k}d\tau+\int\limits_{a(\alpha)}^{a_1(\alpha)}\frac{g(\alpha,\tau)}{(\tau-t)^k}d\tau+\int\limits_{b_1(\alpha)}^{b(\alpha)}\frac{g(\alpha,\tau)}{(\tau-t)^k}d\tau, \tag{11}$$

where $a_1(\alpha)$ is an arbitrary point between $a(\alpha)$ and $t$, while $b_1(\alpha)$ is an arbitrary point between $t$ and $b(\alpha)$. The first of them does not contain the edges as points of integration; hence the general theory and the theorem are applicable to it. Two remaining integrals are usual improper integrals because the point $t$ does not belong to their intervals of integration; their partial derivatives with respect to $\alpha$ may be evaluated in a common way because, under the assumptions, the partial derivative $\partial g(c,\tau)/\partial c$ is integrable. This implies the extension of the theorem.

Extended theorem: *for a density of class $H_*^k$, the theorem holds for points within an open arc $ab$.*

We shall not dwell on the limit values of the derivative $\partial I_k/\partial\alpha$, when $t\to c$ ($c=a$ or $c=b$). They require involved calculations and will be discussed in a paper in preparation.

For $k\geq 2$, we have $Re\gamma>0$. Consequently, the density is zero at the edge points: $g(\alpha,c)=0$. Hence, in this case, the differentiation formula (10) means that it is possible to differentiate under the integral sign:

$$\frac{\partial}{\partial\alpha}\int_{a(\alpha)}^{b(\alpha)}\frac{g(\alpha,\tau)}{(\tau-t)^k}d\tau=\int_{a(\alpha)}^{b(\alpha)}\frac{\partial g(\alpha,\tau)}{\partial\alpha}\frac{d\tau}{(\tau-t)^k}. \tag{12}$$

This result is of special significance for hydraulic fractures, because the opening is zero at the fracture front. In view of the regularization formula (6), used in the form similar to (11), equation (12) may be written as

$$\frac{\partial}{\partial\alpha}\int_{a(\alpha)}^{b(\alpha)}\frac{g(\alpha,\tau)}{(\tau-t)^k}d\tau=\frac{1}{k-1}\frac{\partial}{\partial t}\int_{a(\alpha)}^{b(\alpha)}\frac{\partial g(\alpha,\tau)}{\partial\alpha}\frac{d\tau}{(\tau-t)^{k-1}}. \tag{13}$$

In the next section, we shall check this formula by separate evaluation its left and right hand side for a particular case of the hydraulic fracture propagation.

## 5 Example

At an early stage of the hydraulic fracturing, the fracture propagates in the toughness dominated regime, when the influence of viscosity is negligible and the net-pressure is actually constant along the fracture: $p=p(\alpha)$,$\partial p/\partial x=0$ (recall that in the considered

problem, parameter $\alpha$ is the time, $x$ is the spatial coordinate). Then for plain-strain conditions, the opening $w$ in (1) is given by the well-known formula (e.g. [6]):

$$w(\alpha,\tau)=\frac{4(1-\nu^2)}{E}p(\alpha)\sqrt{[\tau-a(\alpha)][b(\alpha)-\tau]},$$

where we have taken into account that $p$, $a$ and $b$ may change in time depending on the injection regime and local changes of fracture toughness. The equation (2) becomes:

$$p(\alpha)=-\frac{1}{\pi}\int\limits_{a(\alpha)}^{b(\alpha)}\frac{g(\alpha,\tau)d\tau}{(\tau-x)^2}, \tag{14}$$

with $g(\alpha,\tau)=p(\alpha)\sqrt{[\tau-a(\alpha)][b(\alpha)-\tau]}$. For the derivative $\partial p/\partial\alpha=dp/d\alpha$, it yields

$$\frac{dp}{d\alpha}=-\frac{1}{\pi}\frac{\partial}{\partial\alpha}\int\limits_{a(\alpha)}^{b(\alpha)}\frac{g(\alpha,\tau)d\tau}{(\tau-x)^2}. \tag{15}$$

We want to evaluate the r.h.s. of (15) by employing the derived formula (13) and to compare the result with the l.h.s. of (15). To this end, the next two identities, easily following from the general theory [4], [6] for $x\in ab$, are used:

$$\int\limits_a^b\frac{\sqrt{(\tau-a)(b-\tau)}d\tau}{(\tau-x)^2}=-\pi,\quad \int\limits_a^b\frac{d\tau}{\sqrt{(\tau-a)(b-\tau)}(\tau-x)}=0. \tag{16}$$

The first of them, actually gives (14) for the considered $g(\alpha,\tau)$.

With $g(\alpha,\tau)=p(\alpha)\sqrt{[\tau-a(\alpha)][b(\alpha)-\tau]}$, $t=x$ and $k=2$, the differentiation rule (13) yields:

$$\frac{\partial}{\partial\alpha}\int_{a(\alpha)}^{b(\alpha)}\frac{p(\alpha)\sqrt{[\tau-a(\alpha)][b(\alpha)-\tau]}}{(\tau-x)^2}d\tau=$$

$$=\frac{dp(\alpha)}{d\alpha}\int_{a(\alpha)}^{b(\alpha)}\frac{\sqrt{[\tau-a(\alpha)][b(\alpha)-\tau]}d\tau}{(\tau-x)^2}+p(\alpha)\frac{1}{2}\frac{\partial}{\partial x}\int\limits_a^b\frac{(\tau-a)db/d\alpha-(b-\tau)da/d\alpha}{\sqrt{(\tau-a)(b-\tau)}(\tau-x)}d\tau.$$

By using (16) and taking into account that $a$ and $b$ depend only on the time $\alpha$, we have

$$\frac{\partial}{\partial\alpha}\int_{a(\alpha)}^{b(\alpha)}\frac{p(\alpha)\sqrt{[\tau-a(\alpha)][b(\alpha)-\tau]}}{(\tau-x)^2}d\tau=$$

$$=-\pi\frac{dp(\alpha)}{d\alpha}+p(\alpha)\frac{1}{2}\left(\frac{db}{d\alpha}+\frac{da}{d\alpha}\right)\frac{\partial}{\partial x}\int\limits_a^b\frac{\tau}{\sqrt{(\tau-a)(b-\tau)}(\tau-x)}d\tau.$$

Writing $\tau=(\tau-x)+x$, the last integral is represented by the sum

$$\int\limits_a^b\frac{\tau}{\sqrt{(\tau-a)(b-\tau)}(\tau-x)}d\tau=\int\limits_a^b\frac{d\tau}{\sqrt{(\tau-a)(b-\tau)}}+x\int\limits_a^b\frac{d\tau}{\sqrt{(\tau-a)(b-\tau)}(\tau-x)}.$$

The first term of the sum does not depend on $x$, while the second term is zero by the second of (16). Finally, we obtain:

$$\frac{\partial}{\partial\alpha}\int_{a(\alpha)}^{b(\alpha)}\frac{p(\alpha)\sqrt{[\tau-a(\alpha)][b(\alpha)-\tau]}}{(\tau-x)^2}d\tau=-\pi\frac{dp(\alpha)}{d\alpha},$$

what actually coincides with (15).

## 6 Acknowledgment

*The first and the second of the authors (D. J. and A. L.) gratefully acknowledge the support of the European Research Agency (FP7-PEOPLE-2009-IAPP Marie Curie IAPP transfer of knowledge programme, Project Reference # 251475). The third auther (L. R.-R.) appreciates the support of the Polish Ministry of Science and Higher Education (Scientific Project N N519 440739 for 2010- 2012).*

## References

[1] Spence D. A., Sharp P. W. Self-similar solutions for elastohydrodynamic cavity flow. Proc. Roy. Soc. London, Series A, 1985, 400, 289-313.

[2] Adachi J. I., Detournay E., Self-similar solution of plane-strain fracture driven by a power-law liquid. Int. J. Numer. Anal. Meth. Geomech., 2002, 26, 579-604.

[3] Linkov A. M. On efficient simulation of hydraulic fracturing in terms of particle velocity. Int. J. Eng. Sci., 2012, 52, 77-88.

[4] Muskhelishvili N. Singular Interal Equations. Groningen, Noordhoff, 1953.

[5] Linkov A. M. Boundary Integral Equations in Elasticity Theory. Dordrecht, Kluwer Academic Publishers, 2002.

[6] Muskhelishvili N. Some Basic Problems of the Mathematical Theory of Elasticity. Groningen, Noordhoff, 1975.

*Dawid Jaworski, Alexander M. Linkov, Liliana Rybarska-Rusinek, Rzeszow University of Technology, Powstancow Warszawy 12, 35-959 Rzeszow, Poland.*

# Problems due to faulty design in welded steel structures in cranes

Samir Khoshaba Walter Heinrich
Samir.Khoshaba@lnu.se, walter.heinrich@inspecta.com

**Abstract**

This paper deals with fundamental problems related to welded steel structures in cranes, and it is based on many years' experience of crane inspections and condition monitoring in Sweden. In general, failures in steel structures and machines occur due to faulty designs, poor material quality, bad manufacturing processes, handling faults, and a defective maintenance. Only the problems related to Faulty machine design are treated here. Welded joints, in particular, are very sensitive to fatigue loads, corrosion, low welding quality or a combination of these situations. Old cranes were designed according to standards with a limited fatigue analysis, which resulted in weak welded joints. Fortunately, newer standards include more detailed and precise calculation processes that usually lead to better results. Nowadays there exists a wide series of new high tensile weldable steels; however, although they show very high static yields and ultimate strength, the fatigue strength (endurance limit) is very far from 100% in relation with the static strength. One of the biggest difficulties for designers is placing the welds on suitable places, i.e. on places with low stress. These stresses, however, can be relieved by a heat treatment directly applied after welding, but this technique is expensive and difficult to accomplish. Multiple examples of crane failures and failure analysis are presented along the text. Some of them were discovered during the inspections and therefore fatalities were avoided; other failures, unfortunately, led to catastrophic crashes and death accidents.

## 1 Introduction

Cranes exist in an enormous variety of forms – each tailored to a specific use. Sometimes sizes range from the smallest jib cranes, used inside workshops, to the tallest tower cranes, used for constructing high buildings. We can even find large floating cranes generally used to build oil rigs and salvage sunken ships. Hence cranes are used in many different environments and are subjected to different loads. So, for example, a crane used in an industrial workshop where the ambient temperature is constant around the year will necessarily suffer less and last longer than a harbor crane working in a corrosive environment with changing temperatures, and, above the lifting loads, is subjected to wind, snow, and ice loads.

Since cranes are normally used for lifting loads, they must be light-weighted in order to maximize their load capacity at the same time that a reduction of weight results in material savings and a reduction of cost. For this purpose, carrying beams consist of steel bars and plates where welded joints make an important contribution to the strength and life length of cranes. The crane frames and other mechanical parts related to them are subjected to variable loads and must be dimensioned for fatigue failures. The welding technology of today provides an excellent joining capacity for the flexible fabrication of different machine parts and structures; however, welded joints may represent the weakest

part of structures when improperly done. Modern advances in welding techniques and equipment have provided engineers with a range of attractive choices for fastening, as an alternative to bolts or rivets for fabricating parts. Furthermore, machine elements can often be manufactured at lower cost by welding than by casting or forging [1]. Figure 1 shows three examples of machine parts fabricated by welding. The majority of industrial welding is done by fusion, with the joining pieces melting at their common surfaces. The quality and strength of welded joints depends on the design, dimensioning, and manufacturing processes. Weak designs, wrong dimensioning, residual stresses in the joints or metallurgical changes in the base material will decrease the life of crane structures and may eventually lead to catastrophic failures involving severe injuries and even death. The right design of welded joints requires taking multiple aspects into consideration, such as the manner of loading the joints, the materials involved in the weld, and the geometry of each joint itself [2].

An incorrect material selection may result in brittle material as well as welding problems such as cracking. Welding procedures have to be correctly formulated and approved to avoid imperfections. Supervision needs to be implemented to insure that the quality specified in current standards will be achieved. To assure fabrication with effective welding, workshop managers need to be aware of the source of potential troubles and introduce appropriate quality procedures[3]. Since heat is used in welding operations, certain metallurgical changes take place in the parents (base) metals around the vicinity of the weld. When the reliability of the components is high, a testing program should be established to learn what changes or additions to the operations are necessary to ensure the best quality [4]. Breakdowns of welded structures are usually the consequence of fatigue loading. Fatigue fractures are commonly initiated in the region close to the weld toe but can also begin in the weld root and from discontinuities inside the weld [5]. In general, failures in steel structures and machines occur due to faulty designs, poor material quality, bad manufacturing processes, handling faults, and a defective maintenance. These different reasons for failure in cranes and lifting machines are discussed below, and the conclusions drawn from this analysis are based on a long experience over many decades of inspection of such devices and machines.

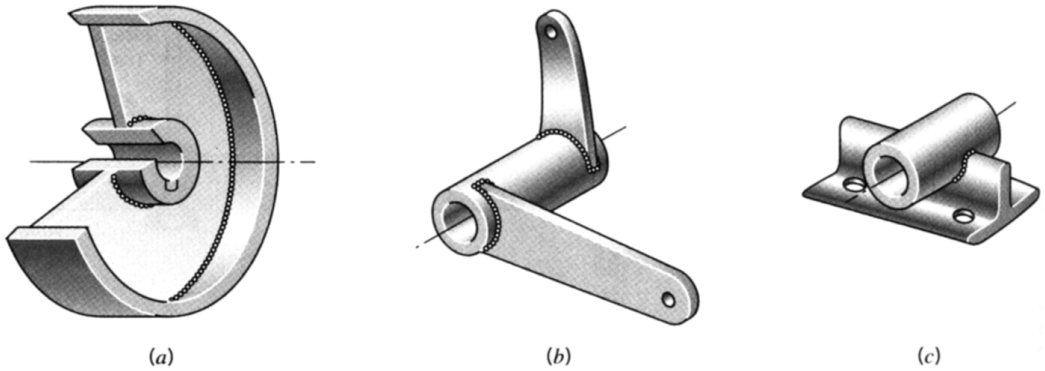


Figure 1: Examples of machine parts fabricated by welding

## 2 Problems due to Faulty Designs and Poor Material Quality

In mechanical engineering, the design stage is probably the most important stage for the life length of machine components. Piece dimensioning and design, material selection, manufacturing methods, quality control, safety, ergonomics, etc. will be decided in this

stage. Also, the budget assigned to the project and its economical limitations are typically fixed under or before this stage, and must be taken into consideration. Gurney [6] stated that in the design of a component or structure the designer has to satisfy three conditions:

1. It must be able to perform its specified functions as efficiently as possible.
2. It must be capable of being fabricated economically.
3. It must be capable of providing an adequate service life.

As a direct result of the first and second of these conditions the modern trends in engineering design are to reduce factors of safety to a bare minimum, in order to reduce weights and costs, and to increase the speed of operations of machines and production processes, in order to make the most efficient use of the invested capital. Unfortunately both these trends tend to work against the designer in his efforts to obtain an adequate service life, particularly in cases where fatigue failure is likely to occur. Perhaps it is therefore not so surprising that it has been estimated that 90% of the failures which occur in engineering components can be attributed to fatigue [6]. A great number of evidences from machine inspections show that Gurney's statement is very true.

The strength of welded joints depends on many factors that must be properly controlled in order to obtain high quality welds. The heat of welding may cause metallurgical changes in the parent (base) metal in the vicinity of the weld. Residual stresses may be introduced through thermal gradients, which cause differential expansion and contraction patterns, the influence of clamping forces, and the changes in yield strength with temperature. Residual stress and wrapping problems are most pronounced when welding pieces of varying thickness and irregular shape, although these problems can be avoided by heating the parts to a uniform temperature before welding, following detailed "good-welding practice" for the application involved, giving the weldment a low-temperature stress-relieving anneal after welding, and shot-peening the weld area after cooling [2]. Some advantages of welded joints over threaded fasteners are that they are inexpensive and there is no danger of the joint loosening. Some disadvantages of welded joints over threaded fasteners are that they produce residual stresses; they distort the shape of the piece, metallurgical changes occur, and disassembly is usually a hard problem [7]. This statement fits very well with the experiences learned from inspecting cranes.

The essential points made by the authors in this article are the following:

1. Residual stress distortions can give tolerance failures in general purpose steel structures. Gearboxes with bad tolerances, due to welding problems like wrapping, when connected to motors and rope drums can result in dangerous failures and crashes. Figure 2 shows a gearbox case where the gear flank is loaded only on one side due to an incorrect shaft parallelism, what eventually resulted in pitting defects.

2. Residual stresses can also lead to stress relaxation and deformations, directly after welding or later in service, due to external loads. In general, steel structure tolerances are regulated in standards such as European Standards EN 1090-2 [8].

3. The residual stresses should be added to the load stresses in the fatigue-based calculation of total life time. This is a very common problem, especially for very high tensile steels, and its importance must be highlighted.

4. In the case of welded joints, the term "High quality" should be changed to "Right quality" in order to take economical considerations into account.

It is very important to pay extra attention to the dimensioning procedure of welded structures subjected to variable loads. Most of the cranes included in this research are quite old, and they were designed according to old standards. The handbook "Design with Weldox and Hardox" [9] which is based on the 1970's Swedish Standard for steel structures StBK-N2 greatly differs from current fatigue-based procedures for the estimations of

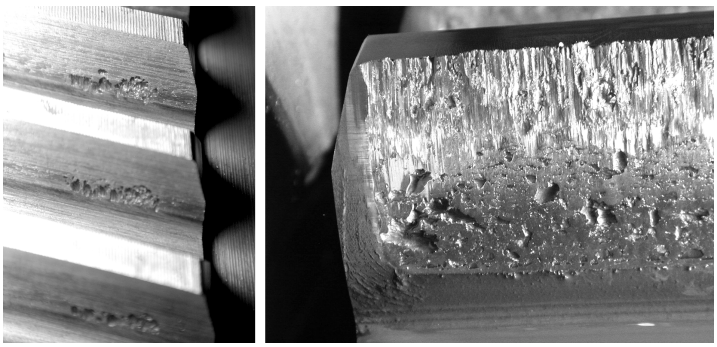

Figure 2: Pitting failure on one side of the gear due to the lack of parallelism of the shaft supports of a gearbox housing

allowable stresses, traditionally based on static models. The static strength for a Weldox 960, for example, is 960 MPa, and if we use the recommended safety factor of 1.5 the final allowable static yield strength is reduced to 640 MPa. On the other hand, the fatigue strength (endurance limit) for fully reversed loading using a probability of failure QB $< 10^{-5}$ (according to StBK-N2) with a fatigue stress concentration factor Kx = 5 (fillet welds in weld class WB), for infinite life (N = 2 x $10^6$), the resulting allowable fatigue strength is less than 39 MPa. As this comparison proves, the fatigue strength of 39 MPa is only 6 % of the initial static strength of 640 MPa. For $10^3$ cycles, which can be considered as a static load, the allowable fatigue strength is reduced to 491 MPa. It is worth mentioning that the standard StBK-N2 has been replaced by Euro Code 3 [10], which should give about the same result.

The following set of photos illustrates a variety of failure modes found in welded joints taken during the inspection of cranes. These problems were found to be more common than expected.

Figure 3 represents two images of a mobile crane boom. These photos clearly show the cracks initiated in fillet welds (between the boom and a secondary plate), and how they evolved through the weld material.

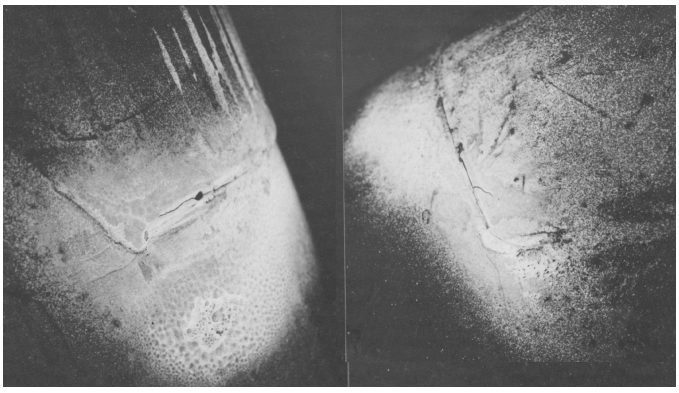

Figure 3: Cracks in fillet welds

Figure 4a shows the in-site inspection of a mobile crane boom. Figure 4b provides a close up of the crane boom welded with tubes used for protecting electrical cables. These tubes are fixed to the boom with a small weld. This arrangement produced an extra stress concentration in the weld, which initiated a crack on the boom at the area with the highest tension stress.

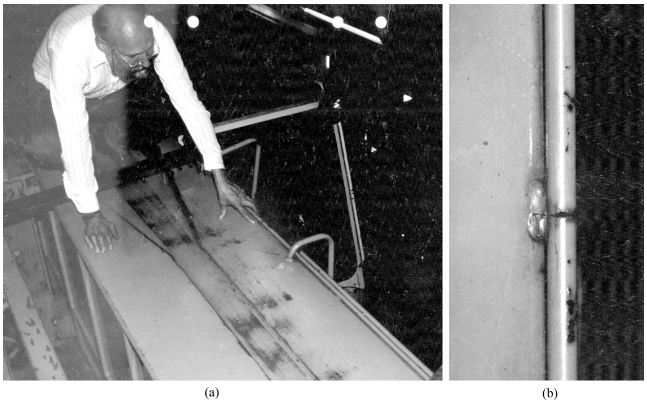


Figure 4: Inspection of a mobile crane (a) and crack in the weld joint (b)

Figure 5 provides typical examples of welded parts on booms. Figures 5a and 5c show a device for guiding steel ropes on the boom, which tends to be on the upper side of the boom. As seen in the schematic, the device is welded on the part of the boom with the highest tension stresses. It would be more effective to place the joints close to the neutral plane of the beam. Figure 5b depicts two L-shaped profiles introduced for reducing the clearance between telescoping booms at their most extended position. In this case, the welds are also placed on a high-stress area.

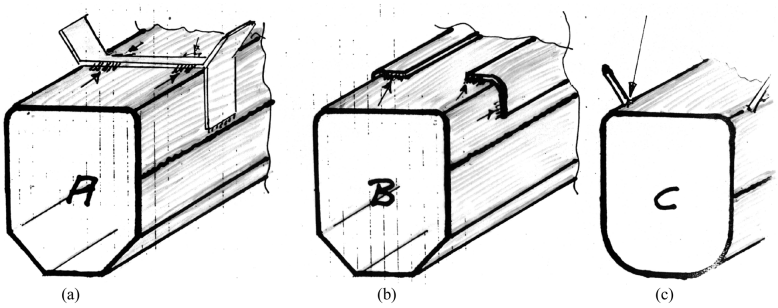


Figure 5: Examples of welded parts on booms

The summation of the different types of stress actuating on a beam must be calculated for the sections of the highest stress in order to calculate the total maximum stress. Figure 6 shows a diagram of how this addition can be carried out.

Figure 7a evidences how residual stresses can deform the upper flange of the head beam of an overhead traveling crane. Figure 7b is a close up of the crack of figure 7a, where it is shown that the crack goes through the whole flange used to support the crane rail. Similar problems have been reported in the crane runways, which imply that cracks may appear in both fillet welds and flanges. The round profile portrayed in the image is a backing support for the weld.

## 3 Conclusions

As shown along the text, the life of cranes is affected by many factors, from the dimensioning and design stage to crane handling and inspection. It is crucial to investigate type and magnitude of the loads affecting each part of the weld before conducting fatigue calculations. The quality of the material must match the minimum requirements set for a

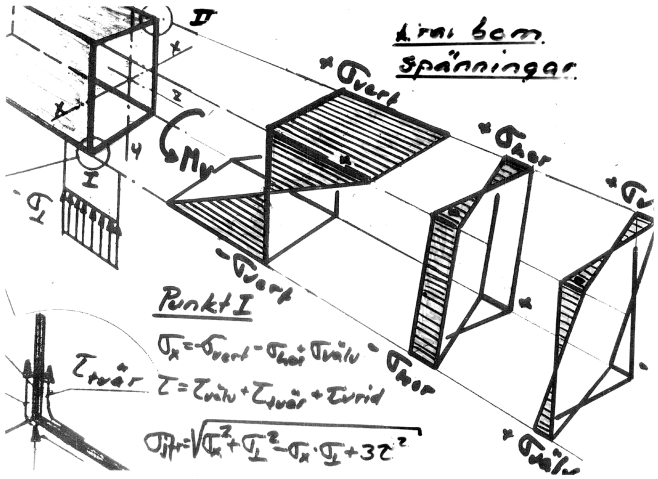


Figure 6: Calculation of stresses in beams

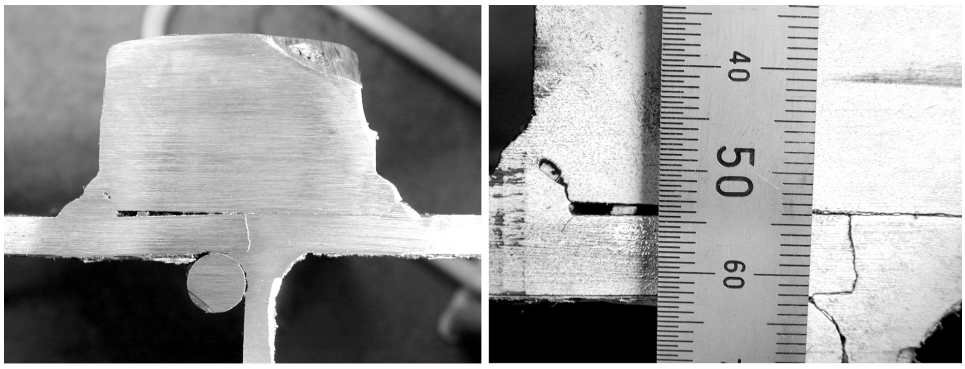


(a) (b)

Figure 7: Deformations and cracks provoked by residual stresses

reliable design. Although the negative effect of corrosion has not been covered in this work, it is important to keep in mind its consequences, as corrosion turns the ductile material into brittle, and destroying the material from the surface. As a matter of fact, welds are particularly sensitive to corrosion, especially when combined with fatigue loading; therefore, crane structures must be coated with paint or other protecting chemicals. Sometimes, a disadvantageous design induces water and dirt to come inside unprotected beams and structures. This detrimental situation facilitates corrosion in hidden spots not easy to detect with visual inspection. Failures in crane structures may lead to extremely dangerous situations for people in or around the cranes, and it normally leads to massive economical losses. Therefore, at the challenging dichotomy faced by the designer between cost and quality, the quality, the safety, and the future failure consequences of the crane must be given clear priority.

## Acknowledgements

*The authors of this article are very grateful to:*

- *Mr. Kjell Andersson from Inspecta Sweden AB, who provided the photos shown in figures 7a and 7b.*
- *Dr. Francisco Rovira M6s, from the University of Valencia for reviewing the text of*

*this article.*

## References

[1] Juvinall R. C. and Marshek, K. M., Fundamentals of Machine Component Design (2012). John Wiley & Sons.

[2] Mott, R. L., Machine Elements in Mechanical Design (2004). Pearson Prentice Hall.

[3] European Standard EN 729-1:1994.

[4] Shigley, J. E. and Mischke, C. R., Mechanical Engineering Design (2001). McGraw-hill International Edition, Singapore.

[5] Bergdahl, S., An Examination of Welded Joints Regarding Weld Geometry, Weld Discontinuities and the Effect of Shot Peening (2006). http://www.uppsatser.se/uppsats/14a7e51908/

[6] Gurney, T. R., Fatigue of welded structures (1979). Cambridge University Press.

[7] Hamrock, B. J., Jacobson, B., and Schmid, S. R., Fundamentals of Machine Elements (1999). McGraw-Hill, USA.

[8] European Standard EN 1090-2:2008 + A1: 2011

[9] SSAB, Design with Weldox and Hardox (1991). Цхелцsund. Sweden.

[10] Euro Code 3 EN 1993-1-9:2005.

*Samir Khoshaba, Linnaeus University, Vдxjц, 351 95, Sweden*
*Walter Heinrich, Inspecta Crane Technology, Norrgatan 15, Vдxjц, 352 31, Sweden*

# The Chandler wobble is a phantom

Dmitry G. Kiryan Georges V. Kiryan
diki.ipme@gmail.com

**Abstract**

In this paper we have proved that the assertion on the existence of residual motion of the Earth rotation axis within the Earth is a result of erroneous interpretation of the zenith distance (angle) measurements with instruments using as a reference the plumb-in line or artificial horizon. The functional relationship between the plumb-in line deviation and Moon's perigee position has been established for an arbitrary point on the rotating Earth surface. This relationship manifests itself as variations in the gravitational acceleration vector direction and magnitude at the observation point or, in other words, as periodical deviations of the plumb-in line (point normal). The results of our work show that it is necessary to revise some postulates of metrology, gravimetry, astronomy, geophysics and satellite navigation.

## 1 Sources of the problem

Based on observations of "variations of latitudes" from 1726 to 1890, the then astronomic community put forward a hypothesis that the latitude variation results from the rotating Earth wobbling on its rotation axis. In 1892, Chandler[1] combined the latitude variation observations collected by 17 observatories during the period from 1837 to 1891 in a united time series, processed them, and revealed that latitude variations obey a characteristic periodicity of 410–440 days [1]. The Chandler's discovery and the "variation of latidude" hypothesis did not get the necessary and sufficient experimental confirmation at that time; however, at the turn of 19th century they allowed the scientific community to come up with the following hypothesis: the Earth's rotation axis executes within the Earth residual motion with the characteristic "Chandler period". At the end of the 20th century, leading European and USA experts in the theory of the Earth's polar (rotation axis) motion and the Earth's rotation theory had to state in the paper devoted to the Chandler's discovery centenary [2] the absolute absence of results of this phenomenon investigation.

## 2 Problem definition

The fact that the period close to the Chandler's period manifests[2] itself in variations in the gravitational acceleration on the Earth's surface leads to an assumption that Chandler's wobble in astrometry results from instability of the gravitational field at the point where the zenith distance is measured[3]. Let us consider the problem of gravitational field instability caused by the Moon as a problem of the Earth's and Moon's gravitational forces effect on

[1] Seth Carlo Chandler, Jr. (1846–1913)

[2] This paper does not consider results of spectral analysis of time series reflecting variations in the ocean level, atmospheric pressure and Earth gravitational acceleration.

[3] The angle between the direction to the celestial body and zenith.

a point mass located at point **A** on the Earth surface (Fig. 1). We will use an orthogonal frame of reference **A***xyz* with the origin at point **A**. Assume that it is oriented so that the **A***xy* plane is tangent to the Earth surface at point **A**, while the **A***z* axis is directed away from the Earth.

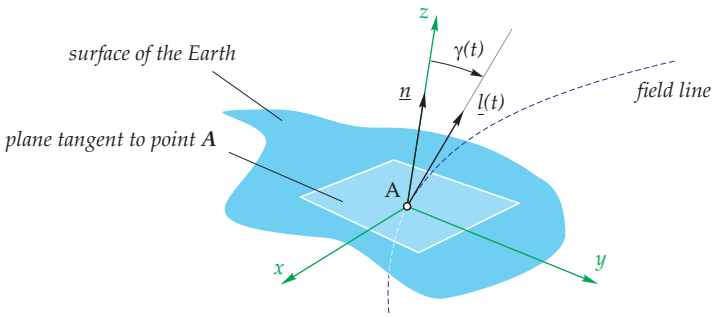


Figure 1: Angle of the gravitational field line departure at point **A**

Define the force acting on the point mass at point **A** as a function of gradient of the Earth–Moon system gravitational field potential $\mathbf{U}(t)$:

$$\underline{f}(t) = -\nabla \mathbf{U}(t) \; . \tag{1}$$

Force $\underline{f}(t)$ that is tangent to the line of force is just that defines *the plumb-in line*. Variations in the force $\underline{f}(t)$ direction in the **A***xyz* frame of reference will be followed up through vector $\underline{l}(t)$ by calculating angle $\gamma(t)$ between the fixed unit vector $\underline{n}$ (**A***z* axis ort) and vector $\underline{l}(t)$ by using the cosine law:

$$\gamma(t) = acos\big(\, \underline{n} \cdot \underline{l}(t) \,\big) \; , \quad where \quad \underline{l}(t) = -\frac{\underline{f}(t)}{|\underline{f}(t)|} \; , \quad |\underline{l}(t)| = 1 \; . \tag{2}$$

We do not take into account other evidently existing physical phenomena since they are not critical in the problem defined here. I.e., we make the problem maximally simple in order to reveal the process essence without diverting our attention to secondary factors that, however, can play a significant role under other conditions.

## 3 Observer

Let us consider two fixed orthogonal frames of reference $\mathbf{O}x^e y^e z^e$ and $\mathbf{O}x'y'z'$ with the common origin at point **O** (Fig. 2). Plane $\mathbf{O}x^e y^e$ belongs to the ecliptic, while plane $\mathbf{O}x'y'$ coincides with the Earth equator plane. Assume that the Earth is an ellipsoid of revolution. $\mathbf{O}z'$ is the axis of the Earth self-rotation and maximum inertia moment. $\mathbf{O}z'$ forms angle $\varepsilon$ with the $\mathbf{O}z^e$ axis. Axes $\mathbf{O}x'$ and $\mathbf{O}x^e$ are of the same direction and are parallel to the vernal equinox line $\Upsilon$.

The point **A** coordinates on the Earth surface are given by the latitude and longitude. Latitude $\varphi_A$ is the angle between plane $\mathbf{O}x'y'$ (equator) and direction to point **A**. Longitude $\lambda_A$ is defined as an angle in the $\mathbf{O}x'y'$ plane between the zero meridian and point **A** meridian. The zero meridian and point **A** rotate in block about axis $\mathbf{O}z'$. Designate the distance between the Earth mass center **O** and point **A** as $R_A$. This distance is a function of latitude and parameters of the Earth's ellipsoid of revolution:

$$R_A = R_A(\varphi_A, e_{terra}, a_{terra}) \; . \tag{3}$$

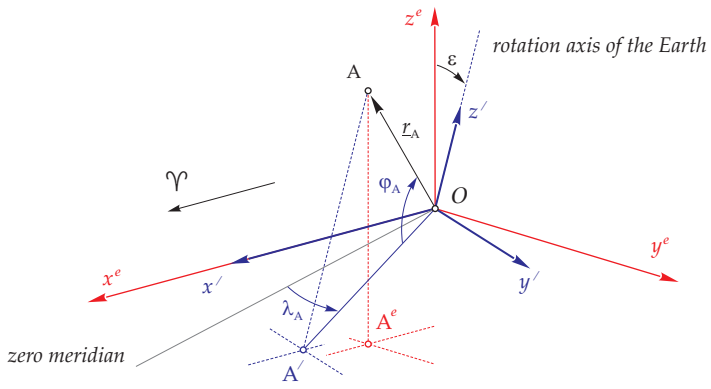


Figure 2: Observer **A** on the Earth surface.

In the fixed frame of reference $\mathbf{O}x^e y^e z^e$ (Fig. 3), point **A** can be defined via the position vector:

$$\underline{r}_A(t) = R_A \cdot \mathbf{P}_x(\varepsilon) \cdot \mathbf{P}_z(\lambda(t)) \cdot \begin{pmatrix} \cos\varphi_A \cos\lambda_A \\ \cos\varphi_A \sin\lambda_A \\ \sin\varphi_A \end{pmatrix} , \quad |\underline{r}_A(t)| = R_A , \tag{4}$$

where $\mathbf{P}_x$, $\mathbf{P}_z$ are the Earth rotation matrices[4]; $\mathbf{A}^e$ is the point **A** projection to the ecliptic plane $\mathbf{O}x^e y^e$; $\lambda(t)$ is the angle in the ecliptic plane $\mathbf{O}x^e y^e$ between axis $\mathbf{O}x^e$ and line passing through points **O** and $\mathbf{A}^e$. Let us define angle $\lambda(t)$ via the Sun longitude $\lambda_{sun}$ for the appropriate epoch [3] and time moment selected for detecting the physical phenomenon under study, e.g., when the event referred to as "local midnight" takes place at point **A**:

$$\lambda(t) = \lambda_{sun}(t) - \pi . \tag{5}$$

Notice that the conventional *solar day* (the time interval between the Sun transits) is in fact formed by summing two angular velocities: that of the Earth self rotation and that of additional rotation caused by the Earth annual revolution about the Sun:

$$\omega(t) = \omega_{terra}(t) + \omega_{year}(t) , \tag{6}$$

here $\omega_{terra}(t)$ is the Earth self rotation angular velocity (the Earth makes a turn around its axis with respect to stars during the time equal to $\approx 23^h 56^m 04^s$); $\omega_{year}(t)$ is the

[4]Let position vector $\underline{r}$ define the point $M$ location in the $\mathbf{O}xyz$ frame of reference; then, if we consider point $M$ in a new frame of reference $\mathbf{O}x'y'z'$ obtained by a series of counterclockwise turns by appropriate angles, its coordinates will be different. Matrices of rotation by angle $\xi$ about axes $\mathbf{O}x$, $\mathbf{O}y$, $\mathbf{O}z$ are given below. The counterclockwise rotation is assumed to be positive.

$$\underline{r}' = \mathbf{P}_x(\xi)\underline{r} , \quad \mathbf{P}_x(\xi) = \begin{pmatrix} 1 & 0 & 0 \\ 0 & \cos(\xi) & -\sin(\xi) \\ 0 & \sin(\xi) & \cos(\xi) \end{pmatrix} , \quad \underline{r} = \mathbf{P}_x^{-1}(\xi)\underline{r}'$$

$$\underline{r}' = \mathbf{P}_y(\xi)\underline{r} , \quad \mathbf{P}_y(\xi) = \begin{pmatrix} \cos(\xi) & 0 & -\sin(\xi) \\ 0 & 1 & 0 \\ \sin(\xi) & 0 & \cos(\xi) \end{pmatrix} , \quad \underline{r} = \mathbf{P}_y^{-1}(\xi)\underline{r}'$$

$$\underline{r}' = \mathbf{P}_z(\xi)\underline{r} , \quad \mathbf{P}_z(\xi) = \begin{pmatrix} \cos(\xi) & \sin(\xi) & 0 \\ -\sin(\xi) & \cos(\xi) & 0 \\ 0 & 0 & 1 \end{pmatrix} , \quad \underline{r} = \mathbf{P}_z^{-1}(\xi)\underline{r}'$$

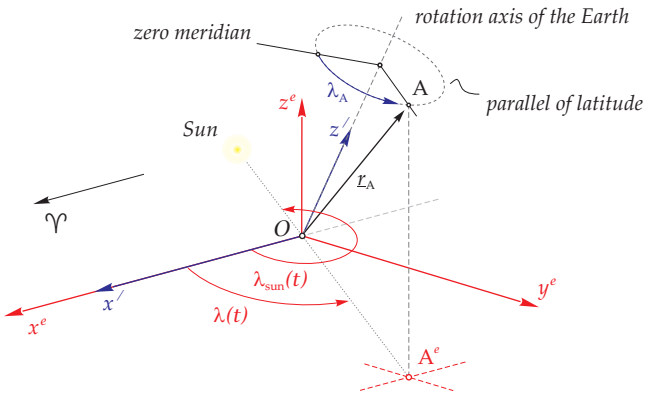


Figure 3: "Local midnight" at point **A**.

additional angular rotation velocity ensuring the usual apparent alternation of sunsets and dawns, namely, the solar day. Since the measurement is performed only once a day, we can neglect the "fast" component of the Earth daily rotation $\omega_{terra}$; after that, the Earth rotation speed will be represented only by the additional angular velocity $\omega_{year}(t)$. This additional angular velocity is the time derivative of the Sun longitude $\lambda_{sun}(t)$, thus (6) gets the following form:

$$\omega(t) = \omega_{year}(t) = \frac{\mathrm{d}\lambda_{sun}(t)}{\mathrm{d}t}\ , \quad where \quad \frac{2\pi}{\omega_{year}(t)} \approx 365\ day \tag{7}$$

This means that we assume the Earth to move round the Sun in the space facing it always with the same side. Accordingly, the Observer staying at any point chosen on the Earth surface will always retain his position with respect to the direction to the Sun.

## 4 Moon

The Moon's orbit is a complex open spatial curve. The Moon motion is considered with respect to fixed point **O** coinciding with the Earth mass center (Fig. 4). The Moon location in the $\mathbf{O}x^e y^e z^e$ frame of reference is set by a combination of 6 cyclically variable orbit components [4].

$$\underline{r}_{lune}(t) = \underline{r}_{lune}\big(\, i(t), \psi(t), \varphi(t), e(t), a(t), t_*(t) \,\big)\ , \tag{8}$$

where $i(t)$ is the orbit tilt angle defined as the angle of intersection between the ecliptic plane $\mathbf{O}x^e y^e$ and the Moon's trajectory plane; $\psi(t)$ is the node line longitude (the inter-plane intersection line); the nodes are counted from the $\mathbf{O}x^e$ axis that is parallel to the vernal equinox line $\Upsilon$ at any moment of the Earth motion (point **O**) about the Sun; $\varphi(t)$ is the angle between the nodal line and line of apsides; the Moon's trajectory ellipticity is defined by eccentricity $e(t)$ and semimajor axis $a(t)$; $t_*$ is the time moment when the Moon passes through the perigee point.

For instance, relations for $\psi(t)$ and $\varphi(t)$ taken from paper [4] for the 1900 epoch look like:

$$\begin{aligned} \psi(t) &= 259^\circ\, 10'\, 59''\!,77 - 1934^\circ\, 08'\, 31''\!,23 \cdot \tau + 07''\!,48 \cdot \tau^2 + 0''\!,0080 \cdot \tau^3\ , \\ \varphi(t) &= 75^\circ\, 08'\, 46''\!,61 + 6003^\circ\, 10'\, 33''\!,75 \cdot \tau - 44''\!,65 \cdot \tau^2 - 0''\!,0530 \cdot \tau^3\ , \\ \tau(t) &= (2415020 - t)/36525\ , \end{aligned} \tag{9}$$

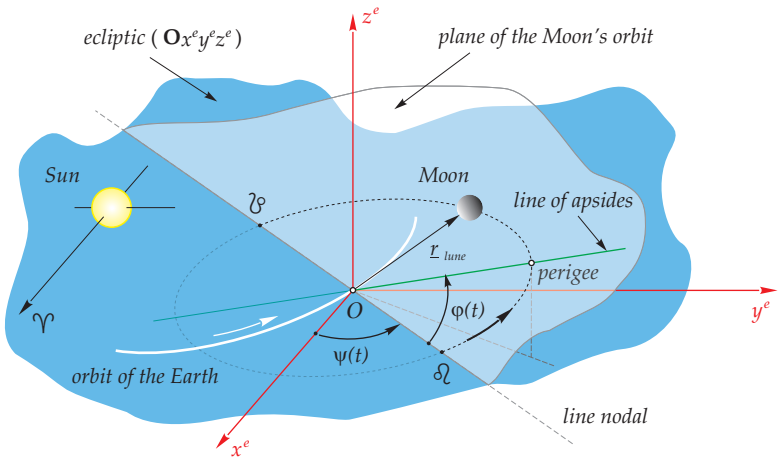


Figure 4: Moon's orbit components.

where $\tau(t)$ is the time expressed in Julian centuries as a function of the Julian date $t$. Derivatives of these functions give us the periods of rotation of the nodal line and line of apsides, respectively:

$$T_\psi = \frac{2\pi}{\mathrm{d}\psi/\mathrm{d}t} \approx -18.6\ year\ , \qquad T_\varphi = \frac{2\pi}{\mathrm{d}\varphi/\mathrm{d}t} \approx 6\ year \tag{10}$$

Therefore, according to the angular velocity sum rule, rotation period of the perigee involved in these two rotations about point **O** in the $\mathbf{O}x^e y^e z^e$ frame of reference is

$$T_{perigee} = \frac{T_\psi \cdot T_\varphi}{T_\psi + T_\varphi} \approx 8.8\ year. \tag{11}$$

**Moon's perigee mass.** Let us find out how the Moon's perigee displacement affects the direction and magnitude of gravitational acceleration at point **A** on the Earth's surface. Substitute the Moon's gravitational effect on the Earth with the equivalent gravitational effect of a certain body located in the Moon's perigee. Derive this body mass from the Moon's gravitational effect on the fixed Earth (point **O**) during one cycle $T_{lune} \approx 28\ days$. Due to the axial symmetry and non-zero eccentricity, the resulting force of the gravitational nature will be directed towards the perigee (Fig. 5).

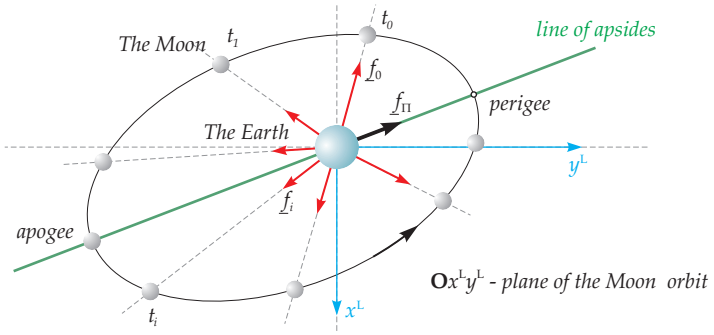


Figure 5: Force $\underline{f}_\Pi$ is the Moon's gravitational impact on the Earth for the period of its revolution about the Earth by the Keplerian orbit.

The force module $|\underline{f}_\Pi|$ is the integral of the Moon's gravitational impact on the Earth

over the time interval equal to the period of the Moon revolution about the Earth:

$$|\underline{f}_{\Pi}| = \frac{1}{2\pi}\mathbf{G}M^*_{terra}M_{lune}\int\limits_0^{2\pi}\frac{\cos\alpha}{r(\alpha)^2}\ \mathrm{d}\alpha\ , \quad M^*_{terra} = M_{terra} + M_{lune}\ , \tag{12}$$

where

$$r(\alpha) = \frac{p}{1+e\cos\alpha}\ , \quad p = a(1-e^2)\ , \quad \alpha = \frac{2\pi}{T_{lune}}\,t\ . \tag{13}$$

Here $r(\alpha)$ is the Moon's focal radius as a function of angle $\alpha$ counted counterclockwise from the direction to the perigee; $p$ is the focal parameter; $e$ is the eccentricity; $a$ is the semimajor axis. Integrating (12), we obtain:

$$|\underline{f}_{\Pi}| = \mathbf{G}M^*_{terra}M_{lune}\frac{e}{p^2}\ . \tag{14}$$

Now, knowing force module $|\underline{f}_{\Pi}|$, we can write a relation for a certain mass ensuring the necessary gravitational effect. Hereinafter we will refer to this mass as the *Moon's perigee mass*. Let us derive the desired mass from the two-body gravitational interaction law:

$$m_{\Pi} = \frac{|\underline{f}_{\Pi}|}{\mathbf{G}M^*_{terra}}\Pi^2_{lune}\ , \quad \Pi_{lune} = \frac{p}{1+e}\ , \tag{15}$$

here $\Pi_{lune}$ is the distance between the ellipse focus (point $\mathbf{O}$) and the perigee. Substituting (14) into (15), we obtain the expression for the perigee mass:

$$m_{\Pi}(e) = M_{lune}\frac{e}{(1+e)^2}\ , \quad m_{\Pi}(e)\Big|_{e=0} = 0\ . \tag{16}$$

Thus, the Moon's perigee mass is defined as a function of the Moon's Keplerian orbit eccentricity. As mentioned above, the Moon's orbit components are of the cyclic character; therefore, we can assume in the first approximation that eccentricity $e(t)$ is a harmonic function with the period equal to the time of the perigee revolution about the Earth center [4]:

$$e(t) = \overline{e} + \frac{1}{2}\big(e_{max} - e_{min}\big)\sin\left(\frac{2\pi}{T_{perigee}}t\right)\ , \quad \overline{e} = const\ . \tag{17}$$

Introduction of dummy perigee mass $m_{\Pi}(e)$ allowed us to exclude the "fast" Moon motion component and consider only the Moon's perigee motion. The perigee mass position in the fixed frame of reference $\mathbf{O}x^ey^ez^e$ is determined by position vector:

$$\underline{r}_{\Pi}(t) = \overbrace{\Pi_{lune}\big(e,a\big)}^{a(1-e)}\cdot\mathbf{P}_z\big(\psi(t)\big)\cdot\mathbf{P}_x\big(i(t)\big)\cdot\mathbf{P}_z\big(\varphi(t)\big)\cdot\underline{e}_1 \tag{18}$$

## 5 Plumb-in line and Moon's perigee

Let us reveal how angle $\gamma(t)$ depends on the mutual arrangement of the Moon's perigee $\mathbf{\Pi}$ and Observer $\mathbf{A}$ on the rotating Earth surface (Fig. 6).

In the $\mathbf{O}x^ey^ez^e$ frame of reference, point $\mathbf{A}$ (Observer) and point $\mathbf{\Pi}$ (Moon's perigee mass) rotate along their trajectories about point $\mathbf{O}$ (the Earth's mass center) in the same

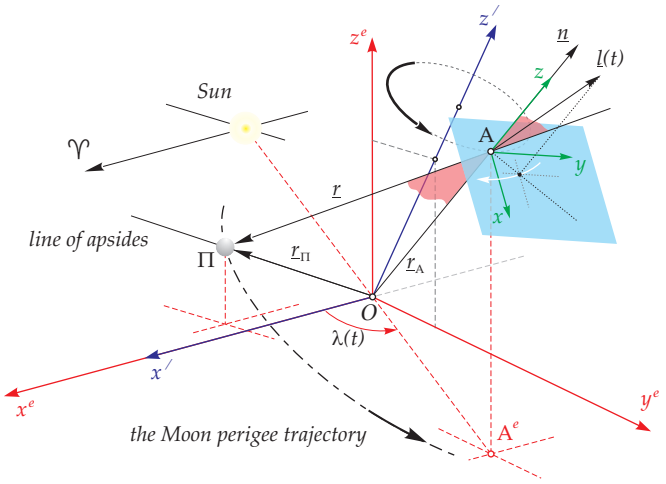


Figure 6: The Moon's perigee **Π** and Observer **A** in the fixed frame of reference $\mathbf{O}x^e y^e z^e$.

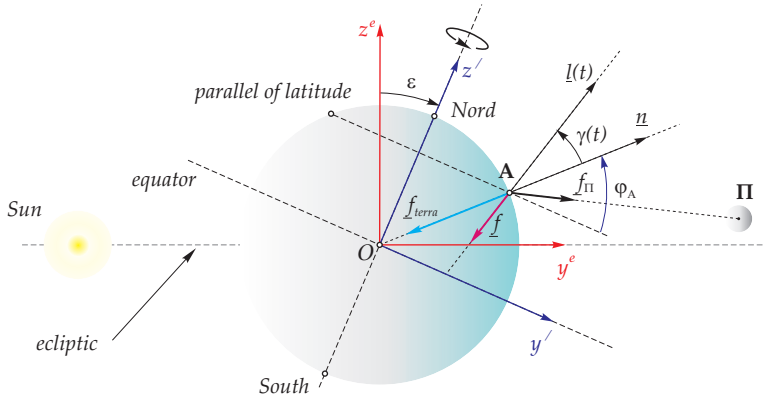


Figure 7: Forces acting on the point mass at point **A** at the moment when the Sun, Earth and Moon's perigee are in $\mathbf{O}y^e z^e$.

direction (counterclockwise) but with different angular velocities. Point mass $m_A = 1$ at point **A** (Fig. 7) is subject to two gravitational forces (from the Earth and Moon's perigee mass).

$$\underline{f}_{terra}(t) = \mathbf{G}\, m_A M_{terra}\, \frac{\underline{r}_A}{|\underline{r}_A|^3}\,, \quad \underline{f}_{\Pi}(t) = \mathbf{G}\, m_A m_{\Pi}\, \frac{\underline{r}_{\Pi} - \underline{r}_A}{|\underline{r}_{\Pi} - \underline{r}_A|^3}\,, \tag{19}$$

here $\underline{r}_{\Pi}(t)$, $\underline{r}_A(t)$ are the Moon's perigee (18) and observer's (4) position vectors, respectively. Designate as $\underline{f}(t)$ the sum of forces acting at point **A**:

$$\underline{f}(t) = \underline{f}_{terra}(t) + \underline{f}_{\Pi}(t)\,, \tag{20}$$

in this case, force $\underline{f}(t)$ in the mobile frame of reference $\mathbf{A}xyz$ is

$$\underline{f}_A(t) = \mathbf{P}_A(t)\cdot\underline{f}(t)\,, \quad |\underline{f}_A(t)| = |\underline{f}(t)|\,, \tag{21}$$

where

$$\mathbf{P}_A(t) = \mathbf{P}_x\left(-\varepsilon\right)\cdot\mathbf{P}_z\left(\lambda(t)\right)\cdot\mathbf{P}_y\left(\frac{\pi}{2} - \varphi_A\right)\,. \tag{22}$$

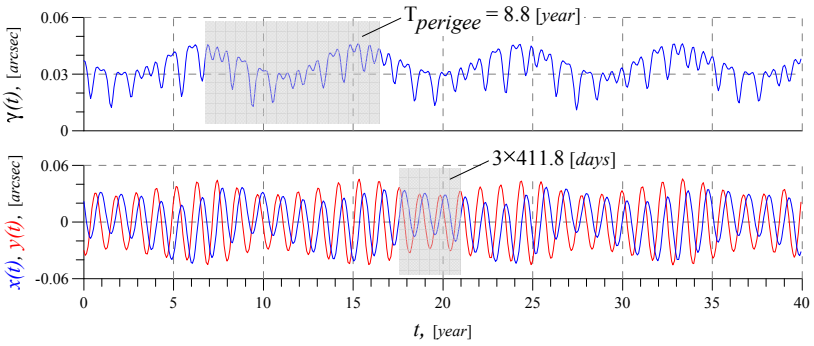


Figure 8: Angle $\gamma(t)$ as a function of the Moon's perigee motion.

Computations showed that the vector $\underline{l}(t)$ apex in the $\mathbf{A}xyz$ frame of reference (Fig. 6) moves cyclically counterclockwise about normal $\underline{n}$ with the period of $T_{cycle} \approx 411.8$ days. Figs. 8 and 9 illustrate this process graphically.

Period $T_{cycle} \approx 411.8$ *days* in the $\mathbf{A}xyz$ rotating frame of reference is a result of summing two rotations: the Observer's (point $\mathbf{A}$) rotation about axis $\mathbf{O}z'$ with a period equal to that of the Earth revolution about the Sun and Moon's perigee rotation about the Earth's center. The long-period ($\approx$ 8.8 year) component of the observed process (Fig. 8) is determined only by cyclic variations in the Moon's elliptic trajectory eccentricity and semimajor axis.

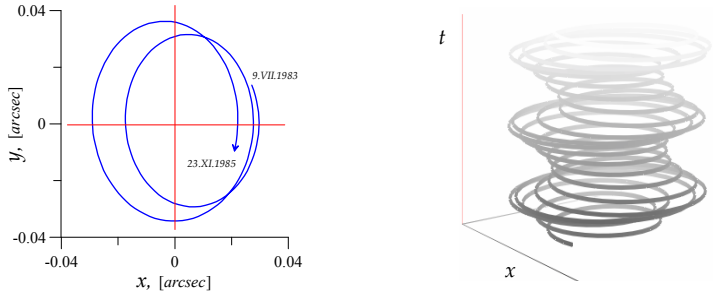


Figure 9: A fragment of the vector $\underline{l}(t)$ apex trajectory projection on plane $\mathbf{A}xy$ and its time scan.

Some difference in the amplitudes is inevitable since the data acquisition and processing techniques used in astrometry are based on the following postulate: *variations in the point latitude are caused by motion of the Earth instant rotation axis (Chandler wobble) in the absolute absence of external forces.* Actually, each latitude measurement with classical astrometric instruments occurs in the gravitational field that varies continuously due to the Earth's self-rotation and motion relatively to the Sun, Moon and planets. Naturally, continuous and non-random variations in the gravitational pattern at the observation point on the Earth change the spatial attitude of the plumb-in line (or artificial horizon) [5, 6]. This means that it is impermissible to combine in one time series observations obtained with different instruments under different gravitational conditions.

The physical process suggested here is the only one that explains the field line spatial variations with the period of about $\approx 411.8$ day. Numerical modelling of the process fit well the results of long-term observations of variations in the Earth gravitational field $\Delta\mathbf{g}$ performed at the *Bad Homburg* and *Boulder* stations (Fig. 10).

The *Johannesburg* and *Brussels* observations of the "variation of latitude" $\Delta\varphi(t)$ (Fig. 11) also confirm our version of the Chandler wobble nature and the actual absence of the Chandler's residual motion of the Earth instant rotation axis within the Earth. It

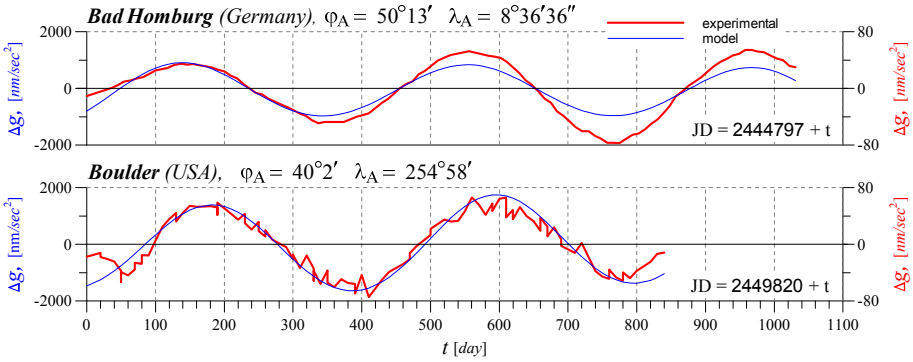


Figure 10: Comparison of the computed and actual variations in gravitational acceleration $\Delta\mathbf{g}$ at stations *Bad Homburg* [7] and *Boulder* [8].

should be emphasized that the observed "variation of latitudes" (more exactly, the variation in the field line deviation angle) and the gravitational acceleration variation have the same period and are strictly antiphased.

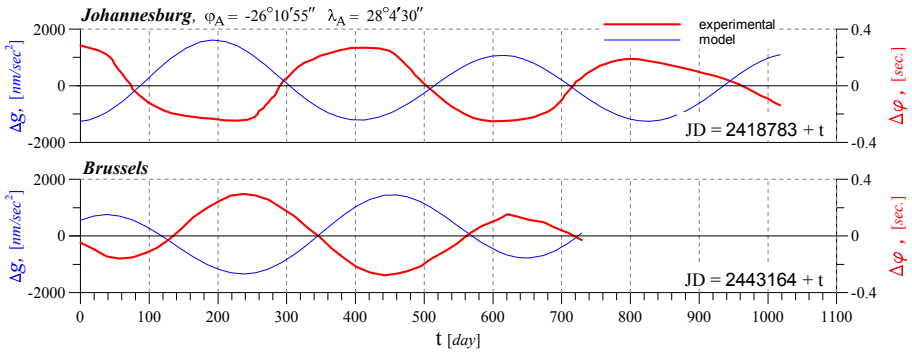


Figure 11: Comparison of variations in the gravitational acceleration and "variation of latitudes" at stations *Johannesburg* [9] and *Brussels* [10].

The existence of the Chandler wobble (with the approximately ≈411-day period) has been confirmed by analyzing cycle duration (Fig. 12) of the so called residual (or "Chandler") motion of the Earth rotation axis based on the `IERS` data[5].

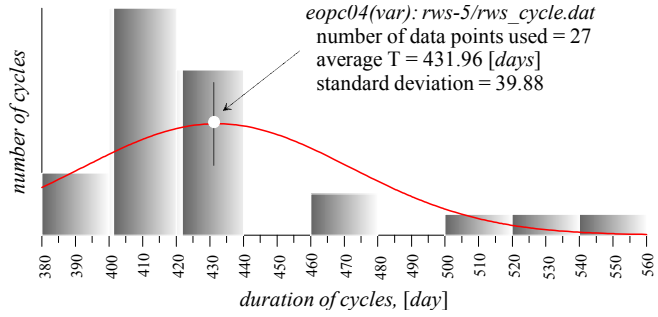


Figure 12: Distribution of the hodograph cycles duration [11].

Among the entire totality of periods revealed, only the ≈411-day period reflects the really existing process, i.e., is of the natural origin. Other periods, including the statistical

[5] `http://hpiers.obspm.fr/eop-pc/`

pseudo-period of ≈432 days, do not reflect actual phenomena but result from drawbacks of the experimental technique used in observation.

Fig. 13 illustrates the Moon influence on the variation in the spatial attitude of the Earth–Moon system gravitational field line and, hence, in deviation of tangent vector $\underline{l}(t)$.

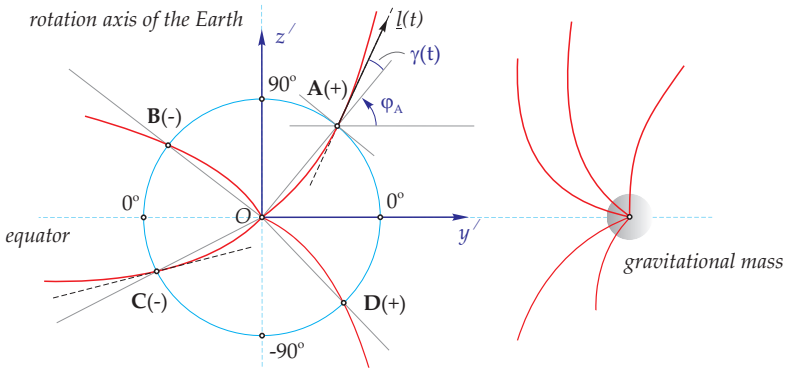


Figure 13: Plumb-in line $\underline{l}(t)$ deviation at different Earth surface points as a function of an external gravitating mass.

When the external gravitating mass approaches, an imaginary effect of the latitude increase takes place at points **A** and **D**, while latitudes at points **C** and **B** seem to decrease. Therefore, when the star zenith distances are observed simultaneously at one and the same meridian but on different sides of the equatorial zone, the plumb-in line $\underline{l}(t)$ deviations shall be in-phase.

Applying the resonance method of analyzing irregular time series [12] to perennial observations of the Earth gravitational field variations obtained in the scope of the `OHPDMC`[6], we confirmed the existence of the gravitational field perturbations with the characteristic period of about ≈411 days. Let us refer to this period according to its historical proper name *Chandler's*; here we should add that Chandler wobble can be detected in every gravitation-based process observed on the Earth surface. Magnitudes of such "Chandler wobbles" will always depend on the actual parameters of the earth Observer motion with respect to the Moon's perigee.

## 6 Conclusions

- In this paper we state that such a theoretically revealed phenomenon as Chandler wobble [7] (residual motion of the Earth rotation axis within the Earth) does not exist in reality. The observed variations in the star zenith distance measurements are caused by variations in the plumb-in line that is used as a measuring instrument reference. The plumb-in line (gravitational acceleration vector) deflections occur due to the gravitating bodies surrounding the Earth, e.g., the Moon.

- Wrong interpretation of the zenith distance variations shown by astrometric instruments required for corrections *for the pole displacement* and *for irregularity of the Earth rotation* that are not only useless but, moreover, deform the verity. These

[6] `http://ohp-ju.eri.u-tokyo.ac.jp/`

[7] Let us refer to the 411-day period according to its historical proper name *Chandler's*; note that Chandler's period can be detected in gravitation-based processes observed on the Earth surface. Magnitudes of such period of Chandler will always depend on actual parameters of the earth Observer–Moon mutual motion.

corrections distort the Universal Time system, navigation systems (GPS, GLONASS, etc.), results of geodesic, metrological and physical measurements, etc.

## References


[1] Chandler, S. C. *New study of the polar motion for the interval, 1890–1901*, Astronomical Journal. 1902. June. Vol. 22., Pp. 145–148.

[2] Runcorn, S. K., Wilkins, G. A., Groten, E. et al., *The excitation of the Chandler wobble*. Surveys in Geophysics. 1987. September. Vol. 9. Pp. 419–449.

[3] *Астрономический ежегодник СССР на 1991 год*, Институт теоретической астрономии АН СССР. Ленинград: «НАУКА», 1989. т.70 ("USSR astronomical yearbook, 1991", vol. 70, Institute for Theoretical Astronomy AS USSR)

[4] Куликов, К. А., Гуревич, В. Б. *Основы лунной астрометрии*. Москва: «НАУКА», 1972 (Kulikov, K. A., Gurevitch, V. B. "Principles of Lunar astrometry")

[5] Кирьян, Г. В. Авторское свидетельство No 1718632. *Искусственный горизонт.* — 1988, приоритет от 20 октября (Kiryan, G. V. et al., Author's Certificate No 1718632. "Artificial horizon", Priority of October 20, 1988)

[6] Кирьян, Д. Г. и др. Авторское свидетельство No 1831137. *Вакуумная камера телескопа.* — 1988, приоритет от 20 октября (Kiryan, D. G. et al., Author's Certificate No 1831137. "Telescope vacuum chamber", Priority of October 20, 1988)

[7] Schneider, M. *Earth Rotation — Research Group for Space Geodesy.* — 1998. January.

[8] van Dam, T. M., Francis, O. *Two years of continuous measurements of tidal and nontidal variations of gravity in Boulder, Colorado*. Geophysical Research Letters — 1998. Vol. 25. Pp. 393–396.

[9] Филиппов, А. Е. *Сравнение Пулковских и Йоханнесбургских наблюдений широты.* Издательство Академии наук Украинской ССР, 1956. VI (Filippov, A. E. "Comparative analysis of Pulkovo and Johannesburg latitude observations". vol. 6. Ukraine Academy of Sciences)

[10] Подобед, В. В., Нестеров, В. В. *Общая астрометрия.* Москва: «НАУКА», 1982 (Podobed, V. V., Nesterov, V. V. "General astrometry")

[11] Кирьян, Г. В., Кирьян, Д. Г. *Движение центра массы Земли. Физические основы.* Санкт-Петербург: СПбГПУ, 2003. Монография. (Kiryan, G. V., Kiryan, D. G. "Basic physics of the Eart mass center motion". Monograph.)

[12] Кирьян, Д. Г., Кирьян, Г. В. *Резонансный метод в исследовании временных рядов* // Механика и процессы управления. Санкт-Петербург, СПбГТУ, 1997 No 467. УДК52+55. (Kiryan, D. G., Kiryan, G. V. "Resonance method in analyzing time series". In Mechanics and control processes, vol. 467, SPbGTU, Saint Petersburg)


*Dmitry G. Kiryan, Institute of Problems of Mechanical Engineering of RAS*
*61 Bolshoy Prospect V.O., 199178, Saint Petersburg, Russia*

# Acoustic estimation of substance capacity into cylindrical container

Vitaly Kolykhalin
cap-07@mail.ru

**Abstract**

The acoustic measurement of liquid and solid substance capacity in cylindrical motor transport tanks are considered. The knock acoustic source of sound pressure is installed on the outside cylindrical container. The relative sound pressure levels of "free" air volumes into tank are corresponded of different substance capacity into cylindrical container and controlled by a microphone. The knock spectrums and sound level meter signals considerably differed from each other in low frequency band are analyzed.

## 1 Introduction

The volume of black oil transportation on highways of the Russian Federation has considerably increased therefore a process of loading and the unloading of motor tanks should be accelerated for exception of stoppage. The automatic remote control of oil product quantity in a motor transport during loading and unloading is very important especially at night. It will be noted that the hardware has been developed with relative acoustic measurements of oil products mass with consideration for "free" air volume by sound pressure measurement with compensation for influence of variable external and internal technological conditions [1]. The knock acoustic source is installed on the outside cylindrical container. The relative level of sound pressure of oil volumes is registered by the microphone fixed inside of air phase of tank and the sound level meter installed with computer in the driver's cab (Fig.1). The microphone Mk, the sound level meter Sm, the computer PC, knock acoustic source S and cylindrical motor tank Mt are shown on Fig.1.

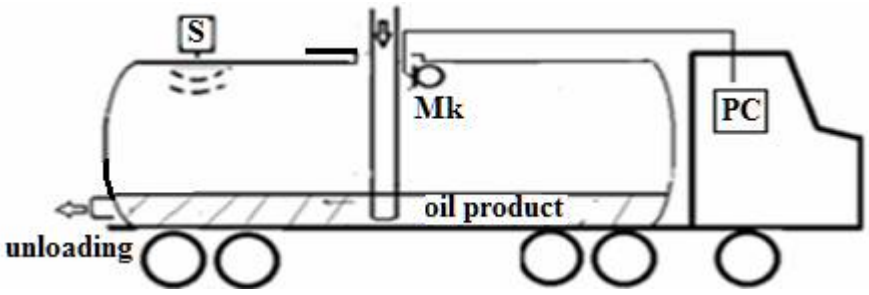


Figure 1: The measuring installation of the motor tank: Mk is the microphone, S is the knock acoustic source and PC is the computer

The eigen frequencies into cylindrical tank air space are excited by oscillation of the metallic tank border when the knock acoustic source S at regular intervals is switched on.

The complication of acoustic field measuring finds out so encompass factor for analysis as acoustic oscillation in a fluid, acoustic oscillation of air, oscillation of a cylindrical metallic border witch is installed on a foundation with damping elements of construction and having an open sight hole .

Uniquely to solve the problem in view of these factors is very hard. There is a problem to select of a physical analog to describe those regularities quantitatively. The mane purpose of the work is to describe on the relative spectrum method using data witch was obtained experimentally.

## 2 Measuring spectrum of levels of sound pressures

### 2.1 The sound source is located in the outside cylindrical container

The level of pressure Po is measured in the frequency band 63. . . 10000 Hz in the empty tank and the level of pressure Pi is measured in the frequency band 63. . . 10000 Hz in the partially filled tank (Fig.1). The attitude of pressure levels Po/Pi are disposed on the ordinate axis and the substance capacities Vm are shown on the abscissa axis (Fig.2).

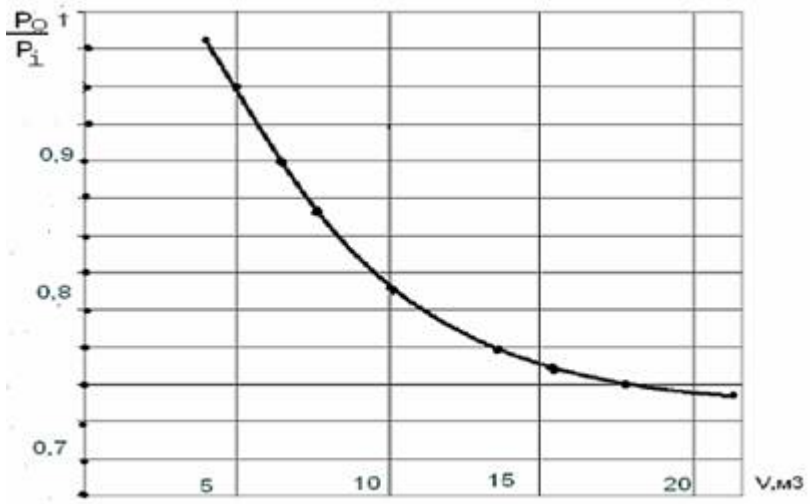


Figure 2: The diagram shows the dependence of the comparative pressure Po/Pi from the substance capacity Vm for the motor tank

### 2.2 The harmonic sound source is located into the cylindrical container

There is second method of acoustic measurement liquid ore solid substance capacity in the cylindrical motor transport tank when the tank is transported to the place of discharge by a car and installed stationary on surface for same time (Fig.3). It is appropriate to use the harmonic sound source and locates it into the cylindrical container. The graph of attitude pressure levels Po/Pi and capacity of black oil Vm for case which shown on Fig.3 is similar to Fig.2. Thus there are some channels of scattering the sound energy: the damping properties of the black oil surface, the exit of the energy through the open tank hole, the energy of scattering through the metallic border.

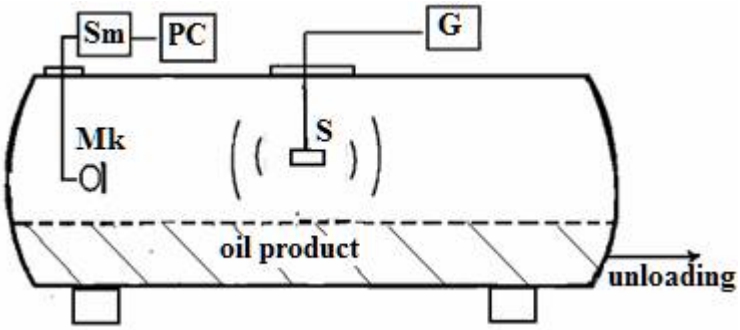


Figure 3: The measuring installation of the cylindrical container: Sm is the sound level meter, Mk is the microphone, S is the loud-speaker, G is the harmonic oscillator and PC is the computer

### 2.3 Approximate model of the harmonic sound source

The solution of the problem with a point source located in the point (r, $\phi$, z) can be obtained in case of boundary conditions

$$U_n|_G = \left.\frac{\partial P}{\partial n}\right|_G \cdot \frac{1}{\rho\omega^2} = 0 \tag{1}$$

If the located point source is switched on at time t=0 than the solution of the time-dependent problem has view:

$$\left(\Delta - \frac{1}{c^2}\frac{\partial^2}{\partial t^2}\right)\tilde{P}(r,\varphi,z,t) = F_0\delta(\bar{X}_c - \bar{X}_{ict})f(t) \quad , \tag{2}$$

where $\bar{X}_i, \bar{X}_c$are coordinates of the source signal and microphone, $\Delta$ is Laplas' operator, Fo is a coefficient, f(t) is the source function, c is sound speed.

The equation (2) can be solved by Laplas' method and the acoustic pressure into the cylindrical container is represented in the form

$$P_{\bar{m}}(t) = \frac{F_0\delta(\bar{X}_c - \bar{X}_{ist.})}{2\pi_j}\int_{A-j\infty}^{A+j\infty}\frac{e^{pt}\hat{F}(p)dp}{p^2+\omega_{\bar{n}}^2} \tag{3}$$

where $\omega$ are eigen frequencies, $\delta$ is Dirac' function.

## 3 Conclusions

The constructed analytical solution of the problem is correct for the whole interval of frequencies. But the most interesting experimental results in the area of medium frequencies acoustical waves were fixed.

## References

[1] V.M. Kolykhalin. Different methods of acoustical diagnostics of solid rest of oil product in tank wagons, Conference "ELPIT-2005" (Russian Academy of Science, Samara, 2005), pp.97-101.

[2] Morse P.M. Vibration and Sound. – New York, 1948.

[3] L.F. Lependin Acoustics. -.M.: High School, 1978.

*Vitaly Kolykhalin, St. Petersburg State University of Cinematography and Television, St. Petersburg, Russia*

# On the influence of inverse wave on local energy fluxes in waveguide stimulated by the point source

Daniil P. Kouzov Natalya A. Mirolubova
EDK291179@yandex.ru

**Abstract**

Through the example of elastic band it is shown that inverse wave can essentially change the character of the energy flux behavior. The "laminar" energy flux at the frequencies below the frequencies of existence of inverse wave is changed to the "turbulent" one at the frequencies this wave exists.

## 1 Introduction

It is well known that in thin layers and plates there are special type of waves that have a phase and group velocity directed into opposite sides. In the isotropic plates that are described in this article only longitudinal inverse waves can exist.

Energy is one of the important physical values that describe processes of propagation of waves. The group velocity corresponds to the energy transfer. Some unusual phenomenon in the energy flux behavior could be observed if inverse wave exists. Article [1] is one of the works where the energy fluxes are considered in the cases of medium with inverse waves. This article is devoted to general energy flux of the transversal waves in a piezocrystal.

It seems that the first investigation of local energy fluxes (the energy flux dependence on the cross-section) in normal wave in thin elastic plates was carried out in [2]. In this work the phenomenon of the energy flux opposite direction of the normal waves was found. It was noted that the same phenomenon usually takes place for inverse waves, but sometimes it can take place for the usual wave, too. In article [3] it was shown that in cases when normal waves propagate in the composed construction the opposite transfer of the general energy fluxes can take place in the different elements of construction.

The aim of the article is to study the energy flux structure. These fluxes are induced by the point force source. The consideration has been carried out on a simple elastic model where inverse waves can exist. This is an infinite plate of constant width (elastic band).

This work continues the investigation of the local energy flux in a thin elastic plate which was started in article [2].

## 2 The problem statement

Let us consider an elastic band (a plate with fixed width $2a$ and small thickness $h$). The edges of the band are supposed to be free. The co-ordinate axes are directed by the following way: axis $y$ – along the band ($-\infty < y < \infty$), axis $x$ – orthogonally to axis $y$ ($-a < x < a$).

The point force source is applied to the origin. It is polarized along the axis $x$. There are longitudinal and shear vibrations in the band which are stimulated by the point force

source. All vibration processes are supposed to be harmonic. We will omit the factor $e^{-i\omega t}$, which determines the dependence of time. The vibration equations and boundary conditions of the problem have the following form

$$\begin{aligned} &\frac{1}{1-\sigma^2}\frac{\partial^2 u}{\partial x^2}+\frac{1}{2(1+\sigma)}\frac{\partial^2 u}{\partial y^2}+\frac{1}{1-\sigma}\frac{\partial^2 v}{\partial x\partial y}+\frac{\rho\omega^2}{E}u=\frac{F}{E}\delta(x)\delta(y)\\ &\frac{1}{1-\sigma^2}\frac{\partial^2 v}{\partial y^2}+\frac{1}{2(1+\sigma)}\frac{\partial^2 v}{\partial x^2}+\frac{1}{1-\sigma}\frac{\partial^2 u}{\partial x\partial y}+\frac{\rho\omega^2}{E}v=0 \end{aligned} \tag{1}$$

$$\left(\frac{\partial u}{\partial x}+\sigma\frac{\partial v}{\partial y}\right)\Bigg|_{x=\pm a}=0,\ \left(\frac{\partial u}{\partial y}+\frac{\partial v}{\partial x}\right)\Bigg|_{x=\pm a}=0, \tag{2}$$

where $u$ and $v$ are shear and longitudinal displacements correspondingly, $\rho$ is the density of material, $E$ is the Young's modulus, $\sigma$ is the Poisson ratio, $F$ is the external force. Equations (1) are well known equations of Fylon of the thin plates theory. Boundary conditions (2) describe the absence of the normal and tangential forces on the free edges.

## 3 Solution of the problem

The process of finding solution of the problem is traditional. After using the Fourier transformation by variable $y$ we get the integral representation of solution. For getting the distribution in normal waves we use the theorem of residue. The result is that

$$u=2\pi i\sum_n \operatorname{Res}\frac{\Delta_1(x,\mu)}{\Delta(\mu)}e^{i\mu y},\ v=2\pi i\sum_n \operatorname{Res}\frac{\Delta_2(x,\mu)}{\Delta(\mu)}e^{i\mu y}. \tag{3}$$

Here

$$\begin{aligned} \Delta(\mu)&=dq\sin\lambda_1 a\cos\lambda_2 a+pf\sin\lambda_2 a\cos\lambda_1 a,\\ k_2\Delta_1(x,\mu)&=\{\ \lambda_1\lambda_2\left(dq\cos\lambda_1 a\cos\lambda_2 a-pf\sin\lambda_1 a\sin\lambda_2 a\right)-\lambda_1\mu qf\cos\lambda_1 x-\\ &\quad-\mu^2\left(dq\sin\lambda_1 a\sin\lambda_2 a-pf\cos\lambda_1 a\cos\lambda_2 a\right)-\lambda_2\mu dp\cos\lambda_2 x+\\ &\quad+\lambda_1\lambda_2\sin\lambda_1|x|\Delta(\mu)+\mu^2\sin\lambda_2|x|\Delta(\mu)\ \}\,,\\ k_2\Delta_2(x,\mu)&=\{\ \mu\lambda_2\left(dq\cos\lambda_1 a\cos\lambda_2 a-pf\sin\lambda_1 a\sin\lambda_2 a\right)+\mu^2 qf\sin\lambda_1 x+\\ &\quad+\mu\lambda_2\left(dq\sin\lambda_1 a\sin\lambda_2 a-pf\cos\lambda_1 a\cos\lambda_2 a\right)-\lambda_2^2 dp\sin\lambda_2 x-\\ &\quad-\mu\lambda_2\operatorname{sign}x\cos\lambda_1 x\Delta(\mu)+\lambda_2\mu\operatorname{sign}x\cos\lambda_2 x\Delta(\mu)\ \}\,, \end{aligned}$$

where

$$d=\lambda_1^2-\sigma\mu^2,\ p=2\lambda_1\mu,\ f=\lambda_2\mu(\sigma-1),q=\lambda_2^2-\mu^2,$$

$\mu$ is the dual variable to ordinate $y$ by Fourier transformation. If we put the denominator $\Delta(\mu)$ equal to zero we will get the well known dispersion equation for the wave numbers of asymmetrical normal waves in this waveguide.

It is impossible to find analytical solution to this transcendental dispersion equation. Therefore all next calculations will be carried out numerically with fixed geometrical dimensions and physical parameters. These calculations and experimental measurements for different mechanical parameters were carried out by many authors. We use following values of parameters. The width of the band $a$ was taken to be 0.5 m, thickness $h=0.01$ m, the material was taken to be steel with material's density $\rho=7800$ kg/m$^3$, Young's modulus $E=2.6\cdot 10^{11}$ N/m$^2$, and Poisson ratio $\sigma=0.3$.

Note that only waves that are damped from the source and waves with group velocity directed from the source exist in the band. Thus, getting the normal-mode expansion of forced field one should pay attention to the group velocity, but not to the phase one.

## 4 The energy flux density

Analytical representation for energy flux density is that

$$\Pi = \frac{\omega E h}{2(1-\sigma^2)} \operatorname{Im}\left[\frac{1-\sigma}{2}\left(\frac{\partial u}{\partial y}+\frac{\partial v}{\partial x}\right)\overline{u}+\left(\frac{\partial v}{\partial y}+\frac{\partial u}{\partial x}\right)\overline{v}\right]\mathbf{j}+ \\ + \frac{\omega E h}{2(1-\sigma^2)} \operatorname{Im}\left[\frac{1-\sigma}{2}\left(\frac{\partial u}{\partial y}+\frac{\partial v}{\partial x}\right)\overline{v}+\left(\frac{\partial u}{\partial y}+\frac{\partial v}{\partial x}\right)\overline{u}\right]\mathbf{i}. \tag{4}$$

We will calculate the energy flux density at two neighboring frequencies $f = 4700$ Hz and $f = 4710$ Hz. The corresponding vector fields are presented in fig. 1 – 4. The abscissa axis is directed orthogonal to the band. The ordinate axis is directed longitudinal to the band. The source of the vibration is situated in the origin. The arrows show the direction of the energy flux density.

Fig. 1 describes a case when inverse wave doesn't exist ($f = 4700$ Hz). We can see that the flux of energy is "laminar" in the whole. There are two small zones of "turbulence" that can be interpreted as the "presage" of the future "turbulence". Fig. 2 shows the near-source region in the larger scale. Fig. 3 and 4 describe a case when inverse wave exists ($f = 4710$ Hz). The flux of energy on the fig. 3 is irregular and forms many vortexes. One part of the band near the source is shown in fig. 4 in the magnified scale. There are two symmetrical vortexes in fig. 4.

Thus, vector fields on fig. 1, 2 and 3, 4 are essentially different.

## 5 Conclusions

The appearance of inverse waves leads to essential change in the energy flux density behavior. The presence of energy transfer into the opposite direction generates numerous vortexes along the whole waveguide.

So, we may conclude that in elastic waveguide at the frequencies, when inverse waves exist, the transformation of energy transfer takes place. We have obtained this result in the case of a simple model (thin elastic band), but the same effects can be found in different types of waveguide with more complicated structure. If inverse waves exist the same phenomenon can take place in waveguide with a different physical nature also.

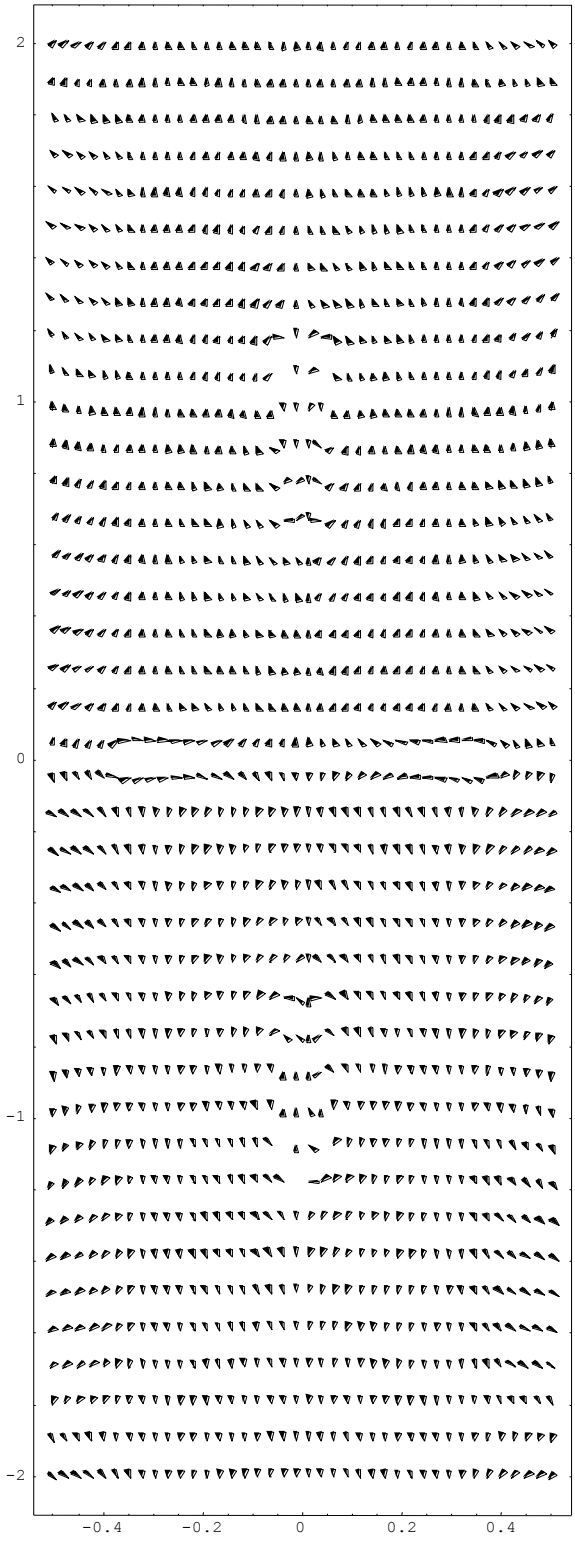


Figure 1: Vector fields of energy flux density without inverse wave in spectrum (frequency 4700 Hz)

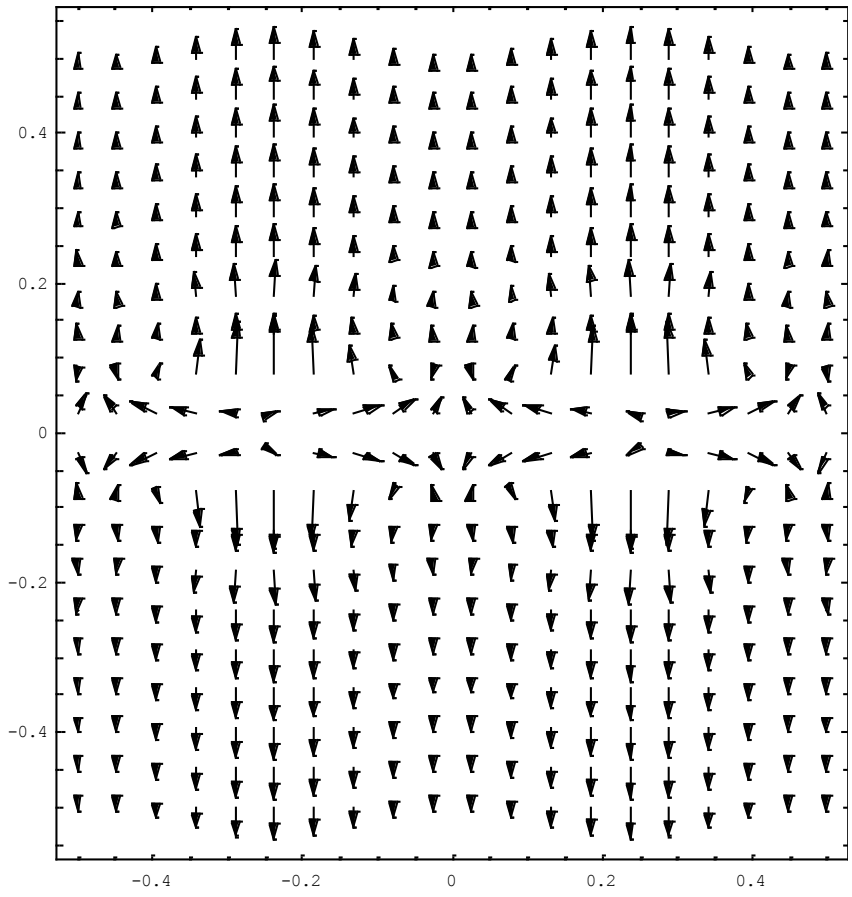


Figure 2: Vector fields of energy flux density near the source of field in a magnified scale(frequency 4700 Hz)

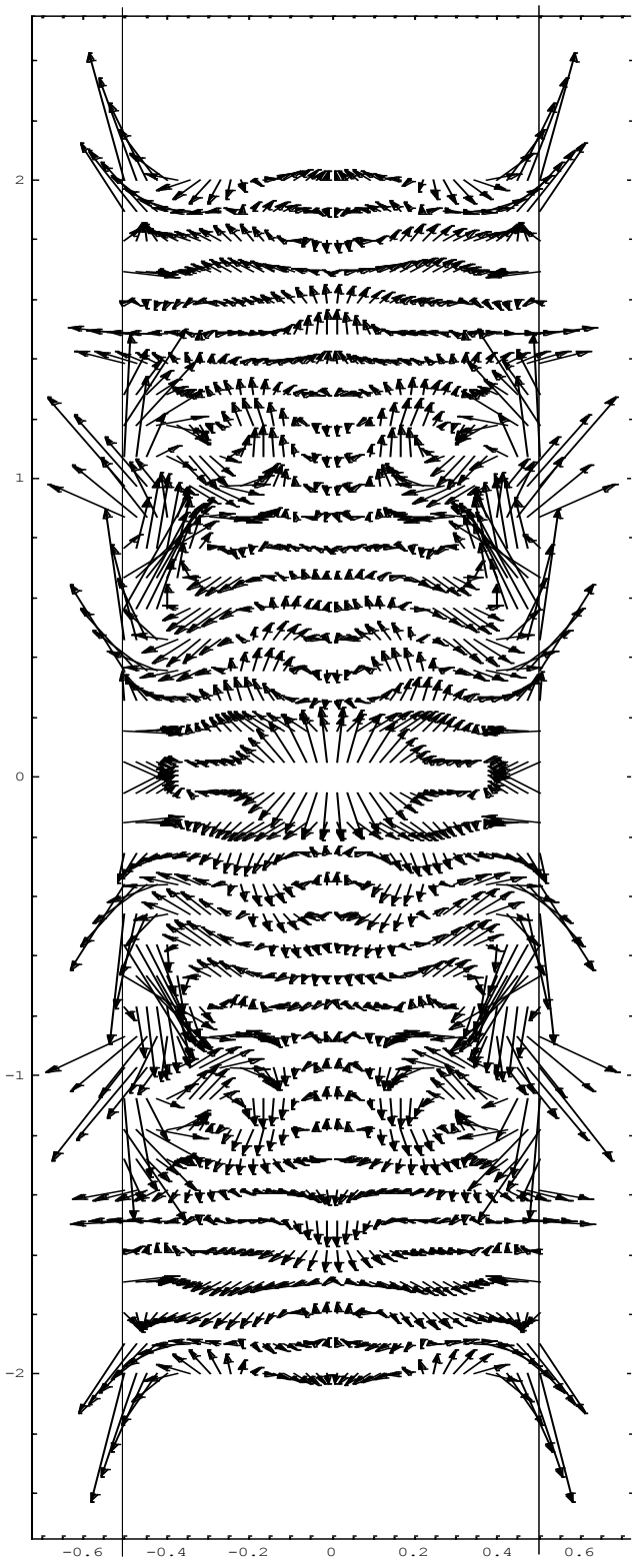


Figure 3: Vector fields of energy flux density after appearance of inverse wave in spectrum (frequency 4710 Hz)

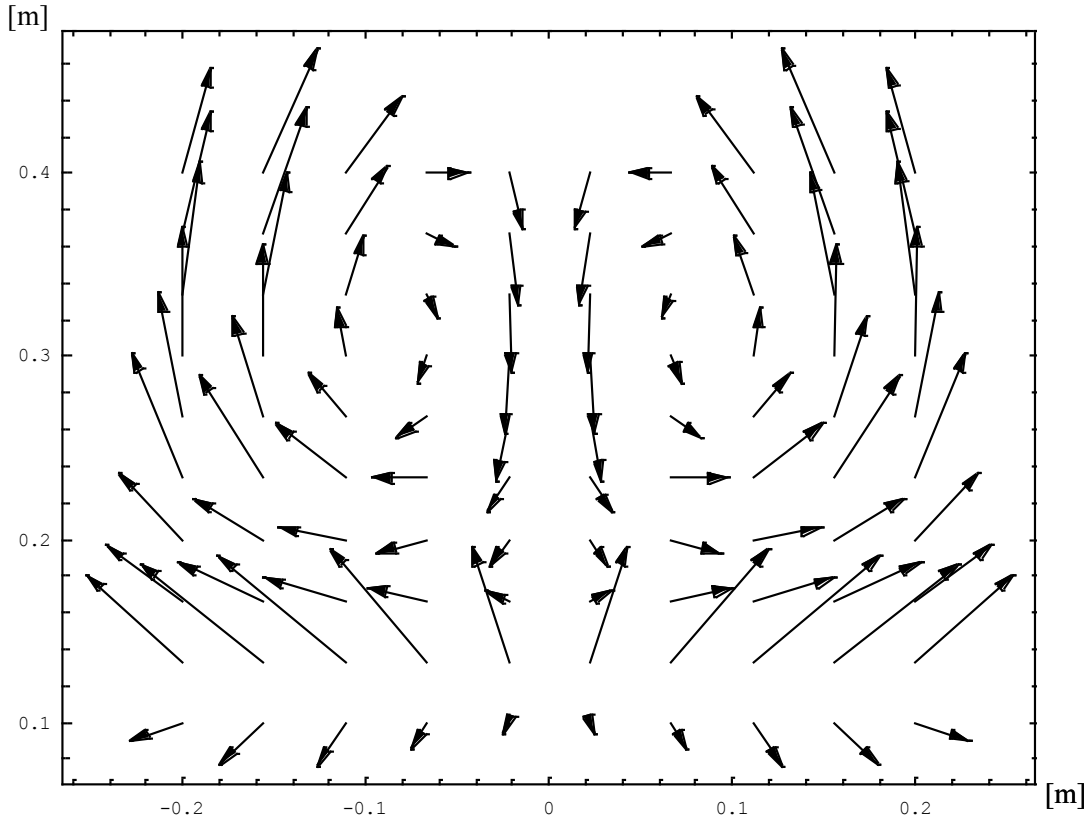


Figure 4: Double vortex of energy flux in a magnified scale (frequency 4710 Hz)

## References

[1] I. Ya. Kucherov, E. V. Malyarenko, Energy Flows of Direct and Inverse Normal Transverse Acoustic Waves in Piezoelectric Plates, Acoustical Physics, Vol. 44, No. 4, 1998, p. 420.

[2] V. A. Veshev, D. P. Kouzov, N. A. Mirolubova, On opposite directions of the energy's flux of normal wave propagation in thin-wall waveguide, Proc. of the XXIV Summer School "Nonlinear oscillations in mechanical systems", IPME RAS, 1997, p. 71 – 78.

[3] V. A. Veshev, D. P. Kouzov, N. A. Mirolubova, Energy Fluxes and Dispersion of Flexural Normal Waves in a Cross-Shaped Beam, Acoustical Physics, Vol. 45, No. 3, 1999, p. 289.

*Daniil P. Kouzov, IPME RAS, St. Petersburg, Russia*

# Influence of vibration on the dynamics of a light spherical body in rotating cavity with liquid

Nikolay V. Kozlov
kozlovn@pspu.ru

Stanislav V. Subbotin
subbozza@mail.ru

**Abstract**

An experimental study is carried of the dynamics of the light spherical body placed in the rotating liquid-filled cavity. The containers used are of cylindrical and spherical shape. The rotation axis is oriented horizontally. The rotation speed is sufficiently high, so that under the action of the centrifugal force the free light body occupies a position near the cavity axis. The system is subject to the translational vibrations, perpendicular to the rotation axis.

In the absence of vibrations, the sphere rotates slower than the cavity (in the laboratory frame). The influence of vibrations is manifested in the resonant excitation of the differential rotation of the sphere. It occurs at coincidence of the inertial oscillations frequency of the sphere and the vibration frequency. Depending on the vibration parameters, the intensive outstripping or lagging rotation of the sphere is excited. The resonant areas position is determined by the ratio of the vibration frequency to the cavity rotation speed $n \equiv \Omega_{vib}/\Omega_{rot}$. Depending on $\Omega_{rot}$, the sphere occupies different steady positions, displacing along the rotation axis. Different steady positions of the sphere are matched by different velocities of its rotation.

It is found that in the liquid contained between the sphere and the cavity end-walls a shear flow appears in the form of the Taylor – Proudman column. At relatively fast differential rotation of the sphere (outstripping or lagging) the column boundary becomes unstable, giving rise to a two-dimensional wave propagating in the azimuthal direction. The wave length decreases with the decrease of the differential rotation speed of the sphere.

## 1 Introduction

Problems of vibrational hydrodynamics at rotation are actual as they consider the phenomena widely spread in nature and engineering.

If a solid is placed in the liquid-filled rotating cavity, its rotation speed being different from that of the cavity, then in the liquid the shear flow is generated in the form of a column extended along the axis. It is called the "Taylor – Proudman column", its boundary is formed by the shear layer. The fluid particles do not cross the column boundary, as a result it rotates practically as an organic whole with the speed different from that of the surrounding liquid [1].

An important feature of the rotating hydrodynamic systems is their elastic properties determined by the action of the inertia forces on the liquid particles. A remarkable example are the inertial waves propagating on the interface of two centrifuged immiscible liquids of different density (the light liquid forms a cylindrical column in the centre) in consequence of the action of an external periodic force [2].

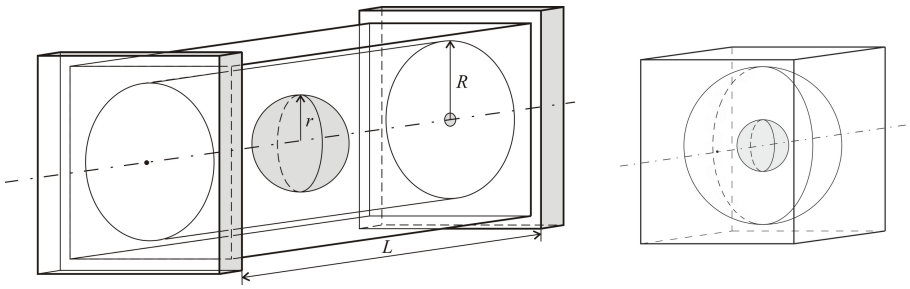


Figure 1: The scheme of the cavities of the cylindrical and spherical shape

In case when a light solid body is placed in the liquid, under the action of the centrifugal force of inertia it occupies the steady position on the cavity axis. An external periodic force, for example due to the transversal vibrations, induces the circular body oscillations. This leads to its differential rotation excitation [3]. In consequence, the liquid Taylor – Proudman column is formed as a geometric continuation of the solid. When the body is considerably shorter than the cavity, in which it is situated, then the liquid column dynamics cannot be neglected. This case is studied in the present work on the light sphere example.

## 2 Experimental setup and techniques

The experimental setup consists of the cavity in which the light body of the spherical shape is placed. The cavity is filled with liquid (aqueous solutions of glycerin with the kinematic viscosity $\nu = 1 - 10$ cSt) and fixed on the platform of the electrodynamic vibrator, which produces translational vibrations normal to the rotation axis. In experiments the cavities made of plexiglass are used, one has the cylindrical shape (the sizes of cavity: $R = 26.0$ mm, $L = 62.0 - 72.0$ mm) and the other is spherical ($R = 44.5$ mm) (fig. 1). Radius of the sphere $r = 17.7$ mm, average density $\rho_s = 0.17$ g/cm$^3$.

In the work the spherical body dynamics is studied depending on the cavity rotation speed $\Omega_{rot}$ in the absence of vibrations and at the vibration action. The velocity of rotation is always high and the sphere occupies the steady position near the rotation axis under the action of the centrifugal forces. In the experiments the sphere rotation speed $\Omega_s$ in the laboratory frame and the distances $x_1$ and $x_2$ from the sphere boundaries to the cavity end-faces are measured. Observations are carried out in the stroboscopic illumination. The rotation speed of the cavity and of the body is measured with the strobotachometer with accuracy 0.06 rad/s. The body position in the cavity is found using the photo registration method. The obtained data is used to calculate the relative rotation speed of the sphere $\Delta\Omega = \Omega_{rot} - \Omega_s$ and its position relative to the end-faces of the cavity $x = (x_2 - x_1)/(x_2 + x_1)$.

The cavity rotation speed varies in the interval $\Omega_{rot} = 50 - 300$ rad/s and is set with the accuracy of 0.06 rad/s. Frequency and amplitude of vibrations vary in the intervals $f_{vib} = 20 - 45Hz$, $b_{vib} = 0.1 - 0.5$ mm.

## 3 Experimental results

In the absence of rotation the light sphere is situated at the cavity boundary in its upper part. With the increase of the cavity rotation speed $\Omega_{rot}$ the sphere is entrained by the fluid (in the rotation direction), and on reaching some critical value $\Omega_{rot}$ it occupies the steady position on the cavity axis. In the absence of vibrations the sphere in such state always

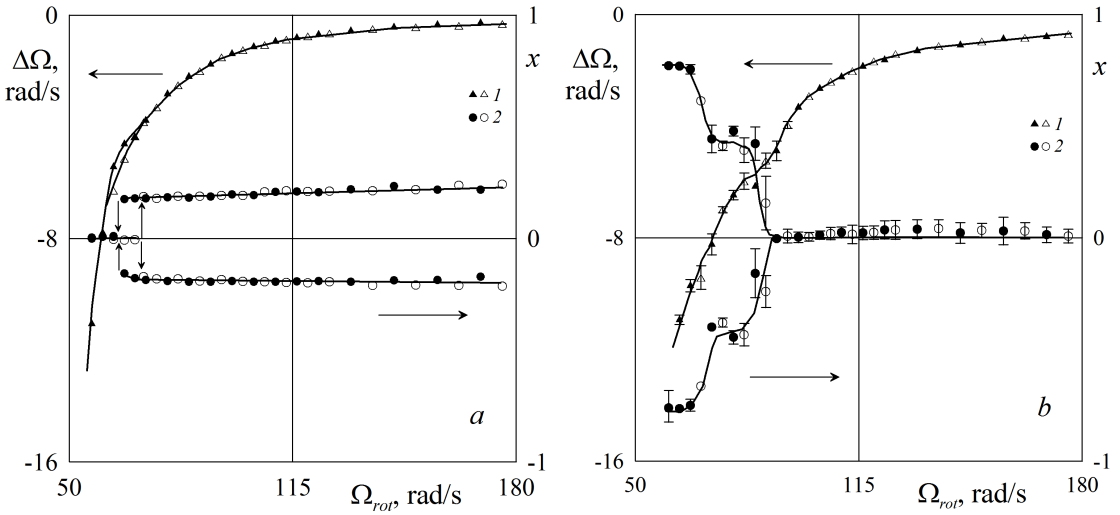


Figure 2: The relative rotation velocity $\Delta\Omega$ (*1*) and the sphere position $x$ (*2*) vs. the cavity rotation speed ($a$ – cylindrical cavity, $b$ – spherical) for $\nu = 5.0$ cSt; here and further light symbols signify the increase of $\Omega_{rot}$, dark – decrease

rotates slower that the cavity, thus $\Delta\Omega < 0$. Such behaviour of the sphere is characteristic for both, cylindrical and spherical cavities (fig. 2, *a*, *b*, points *1*). In process of the $\Omega_{rot}$ magnification the body lagging intensity gradually decreases. It occurs until rotation of the whole system does not become almost solid-state. The experimental points obtained at the decrease of $\Omega_{rot}$ coincide with the points obtained at its increase. However, on reaching the critical value, at which the sphere transition to the rotation axis occurred, there is no collapse (the transition from the axis to the exterior boundary of the rotating cavity) observed.

Besides the differential rotation speed of the sphere, at the changing of $\Omega_{rot}$ there is the changing of the sphere position on the rotation axis relative to the cavity end-walls, characterized by the dimensionless coordinates (fig. 2, *a*, *b*, points *2*). In the cavity of the cylindrical shape ($L = 72.0$ mm) with increase of the velocity $\Omega_{rot}$ the sphere position in the center becomes unstable, and the sphere displaces along the rotation axis to one of the end-faces. The new position of the sphere on the axis is stationary. The shift can occur both to the right and to the left. It does not depend on the direction of the cavity rotation. The relative velocity of the body rotation also does not depend on which end-wall it will be moved to.

In the cavity of the spherical shape (fig. 2, *b*, points *2*), the dependence of the sphere position dynamics on $\Omega_{rot}$ is opposite. Under the influence of the centrifugal forces at the rotation velocity increase, the sphere transfers to the rotation axis, but not in the cavity center, and to one of its poles. At the further increase of $\Omega_{rot}$ the sphere gradually drifts towards the cavity center, this displacement going in steps. When shifting the sphere to the right or left, the curves of dependence $x(\Omega_{rot})$ are mirror-symmetrical, so it is the pitchfork bifurcation.

The change of the fluid viscosity leads only to the change of the thresholds of loss of stability of the sphere symmetrical position, its dynamics does not change qualitatively [4].

The behaviour of the sphere at vibrations significantly changes only in the resonance areas when the frequency of vibration action coincides with the eigenfrequency of inertial oscillations of the sphere. In the region $\Omega_{rot} < \Omega_{vib}$ ($\Omega_{vib} = 2\pi f_{vib}$) the excitation of intensive outstripping rotation of the sphere is observed, which does not exist without

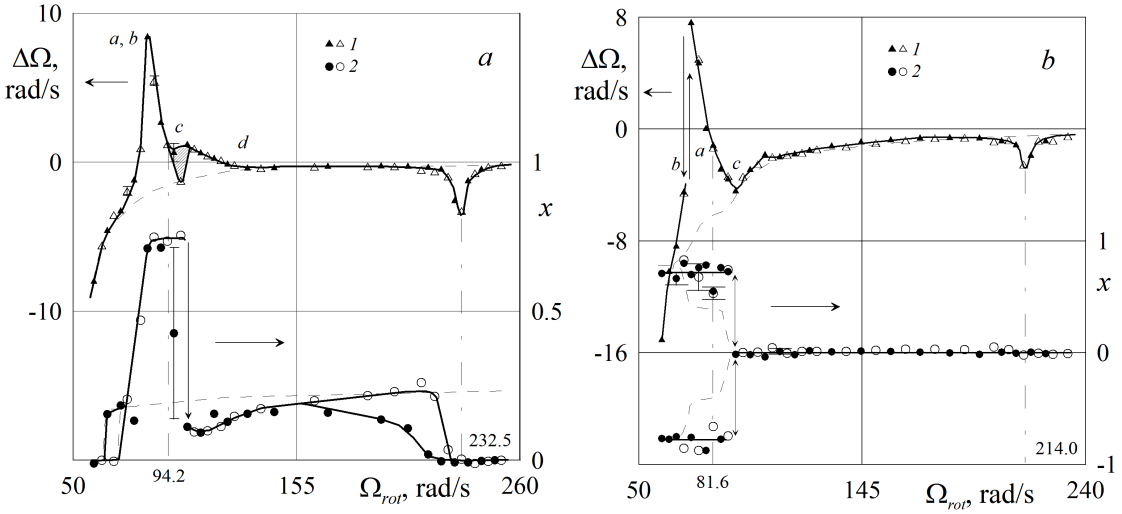


Figure 3: The velocity $\Delta\Omega$ (*1*) and the sphere position $x$ (*2*) vs. the velocity $\Omega_{rot}$ of the cylindrical cavity (*a*) and spherical one (*b*); $f_{vib}$= 30 Hz, $b_{vib}$= 0.27 mm, $\nu$ = 5.0 cSt; dashed lines – the experiment in the absence of vibration

vibrations (fig. 3, *a*, *b*, points *1*). In the area where the vibration frequency is less than the cyclic frequency of the cavity rotation ($\Omega_{rot} > \Omega_{vib}$), the intensive lagging differential rotation is raised ($\Delta\Omega < 0$). Intensive rotation in resonance areas is accompanied by high-amplitude oscillations of the sphere of circular polarisation with the frequency of driving force $\Omega_{vib}$. Out of the resonance areas the velocity of the sphere rotation at vibrations is not different from the one in their absence.

At slow increase of the cavity rotation speed the outstripping rotation excitation (threshold *a*) can occur smoothly (fig. 3, *a*) or abruptly (fig. 3, *b*) depending on the parameters of vibrations. The finite-amplitude transitions are conventionally shown by vertical arrows. At the subsequent increase of $\Omega_{rot}$ the relative velocity starts to decrease sharply. In the cylindrical cavity the rate of the outstripping motion decrease diminishes in the threshold way in the point *c*, then the vibrational outstripping motion is maintained up to the point *d*, where the vibrational curve crosses the gravitational one. In the cavity of the spherical shape the threshold *d* is absent, the intensive outstripping motion stops in the point *c*. At the decrease of the cavity rotation speed (dark points on fig. 3) the measured data coincide with the results obtained at the increase of $\Omega_{rot}$. The breakdown of the outstripping rotation occurs abruptly in the point *b*.

Simultaneously with velocity the sphere position changes in the resonance areas (fig. 3, *a*, *b*, points *2*) outside of which it practically coincides with the off-vibration case. In the outstripping motion area the sphere shifts to one of the end faces. The maximum displacement is observed in the point *c*, where the intensive outstripping motion is excited. The position of the sphere in the cavity center ($x = 0$) is stable in the area of the resonant lagging rotation.

Dot-dashed lines in fig. 3 show the position of the resonance frequency on the axis $\Omega_{rot}$. In cavities of various geometry they differ at the same vibration parameters. In the spherical cavity the resonance frequencies have smaller values $\Omega^{+}_{rot}$= 81.6 rad/s and $\Omega^{-}_{rot}$ = 214.0 rad/s, for the cylindrical cavity – $\Omega^{+}_{rot}$= 94.2 rad/s and $\Omega^{-}_{rot}$ = 232.5 rad/s.

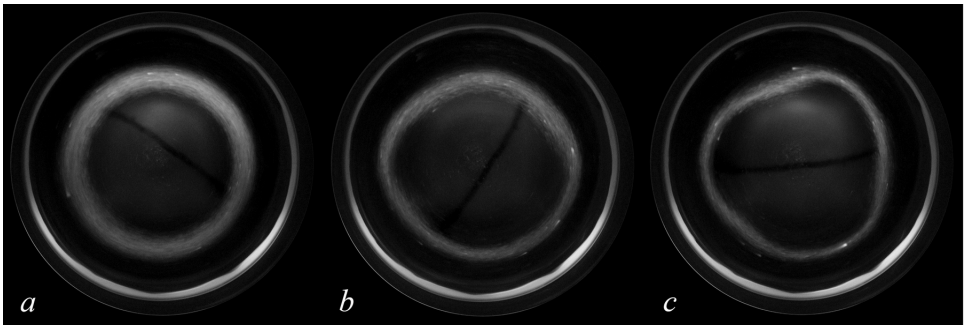


Figure 4: Photos of the Stewartson shear layer in traversal section in the absence of vibrations; $\Omega_{rot} = 100.5$ ($a$) and 75.5 rad/s ($b$, $c$), $\nu = 6.7$ cSt, $L = 62.0$ mm

## 4 Flow structures

At differential rotation of the sphere, in the fluid volume between the sphere and the cavity end-faces the Stewartson shear layer extended along the rotation axis is formed, delimiting the Taylor – Proudman column. On fig. 4 the flow patterns in the cylindrical cavity in the absence of vibrations are presented. In the centre the sphere is visible, around which white light-scattering particles trace the column boundary.

At slow relative rotation of the sphere the column has the shape of the circular cylinder (fig. 4, $a$), its traversal size coincides with diameter of the body. With magnification of the difference of velocities between the sphere and the cavity the column boundary becomes instable and takes the form of the polyhedral prism ($b$). Angular velocity of rotation of the prism (wave phase velocity) in the laboratory frame is less than the velocity of the sphere rotation. With growth of intensity of the differential rotation of the body the length of the azimuthal wave propagating on the liquid column boundary, is incremented ($c$), the number of bounds of the prism decreases. In the experiments, the patterns with the wave numbers $m = 3 - 6$ are observed. In the spherical fluid shell the similar geostrophic flow in the form of the Taylor – Proudman column is raised.

## 5 Analysis

In the absence of vibrations, the sphere dynamics is governed by the dimensionless gravitational acceleration $\Gamma = 2g/(\Omega_{rot}^2 d)$, where $g$ is the gravitational acceleration, $d$ – the sphere diameter. With the increase of the cavity rotation speed the sphere rotation intensity decreases, the experimental points displace towards lower $|\Delta\Omega|/\Omega_{rot}$ when the $\Gamma$ value is decreased (fig. 5). On the graph one can see that the cavity geometry influences only the differential rotation intensity. The relative speed of the sphere varies according to the law $|\Delta\Omega|/\Omega_{rot} \sim \Gamma^2$. This result slightly differs from the one in case of the cylindrical body, where $|\Delta\Omega|/\Omega_{rot} \sim \Gamma^{1.75}$ [5].

The azimuthal wave, propagating on the Taylor – Proudman column boundary (fig. 4), is due to the Stewartson shear layer instability [6, 7]. In difference from the cited works, in our research the sphere is free, and its differential rotation relative to the cavity is not set, but generated by the body circular oscillations under the action of the gravity field and thus entirely determined by the dimensionless frequency $\omega = \Omega_{rot} d^2/\nu$, i.e. the cavity rotation speed.

The dependence of the dimensionless phase velocity of the azimuthal wave propagation on the Stewartson layer boundary on the sphere differential rotation speed is shown on fig. 6. Here $\Delta\Omega_w$ is calculated relative to the cavity: $\Delta\Omega_w = \Omega_w - \Omega_{rot}$. The decrease of the

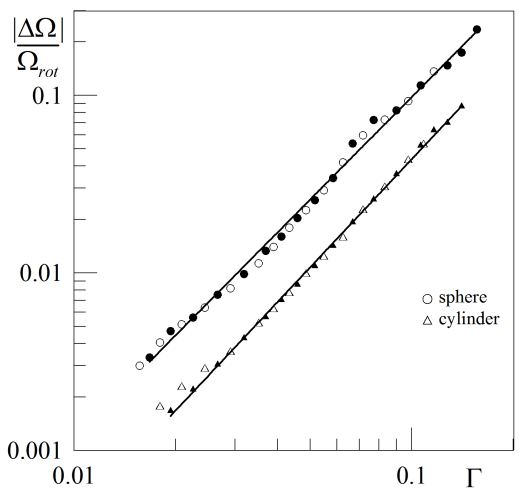


Figure 5: Dependence of the dimensionless rotation speed of the sphere on the dimensionless acceleration Γ, $\nu$ =5 cSt

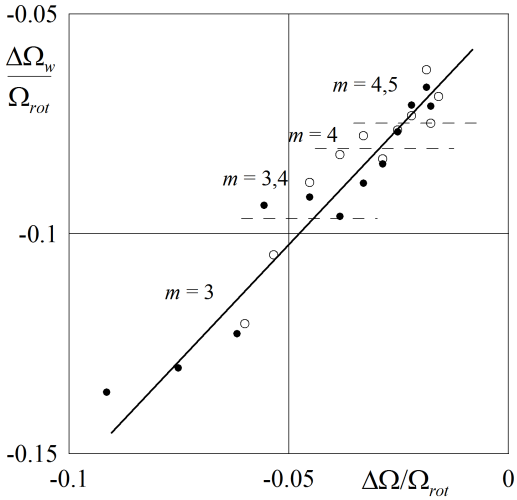


Figure 6: The dimensionless wave velocity vs. the relative rotation speed of the sphere, $\nu$ =6.7 cSt

sphere rotation intensity leads to the wave phase velocity increase and the consequent wave pattern change, at the same time the wave length decreases. Thus, at centrifugation the triangular column is formed ($m = 3$), with the cavity rotation speed increase the transition to the state with wave number $m = 4$ is observed, etc. The axisymmetric flow, when the column has the circular cylinder shape (fig. 4, *a*), is observed at $|\Delta\Omega|/\Omega_{rot} < 0.016$. The boundaries of the column transformation are shown on fig. 6 with the dashed lines.

Comparison of the experimental results with the theoretical ones [7] for the negative differential rotation of the sphere in the spherical liquid layer shows their satisfactory agreement.

The dynamics of the intensive vibrational rotation of the sphere is determined by the dimensionless vibration frequency $n \equiv \Omega_{vib}/\Omega_{rot}$ (fig. 7). The curves obtained for the vibrations of different frequency and equal amplitude are in good agreement on the chosen plane of dimensionless parameters. As in the cylindrical cavity (fig. 7, *a*), as in the spherical one (*b*), the values of $n$ are equal for the resonant areas of both, outstripping and lagging motion. This is true for both the differential rotation speed and the sphere position on the axis. The most pronounced sphere displacement from the cavity centre along the rotation axis is shown by the slash-dotted lines. It is remarkable that this one coincides with the transition *c*, in which the intensive outstripping rotation is excited. The areas of the resonant excitation of the inertial body oscillations (and its intensive differential rotation) in different cavities are only slightly different in the dimensionless vibration frequency. Partially this difference may be due to the different values of the relative body radius $r/R$ [8]. There are no qualitative changes in the sphere dynamics observed as the cavity geometry is changed. The existence of the areas of the intensive lagging and outstripping motion is explained by the coincidence of the vibration frequency with one of the two eigenfrequencies of the sphere inertial oscillations. As a result, the resonant growth of its oscillations amplitude occurs. This leads to the average force generation in the viscous boundary layer on the solid surface of the light body [3], which in its turn excites the body differential rotation.

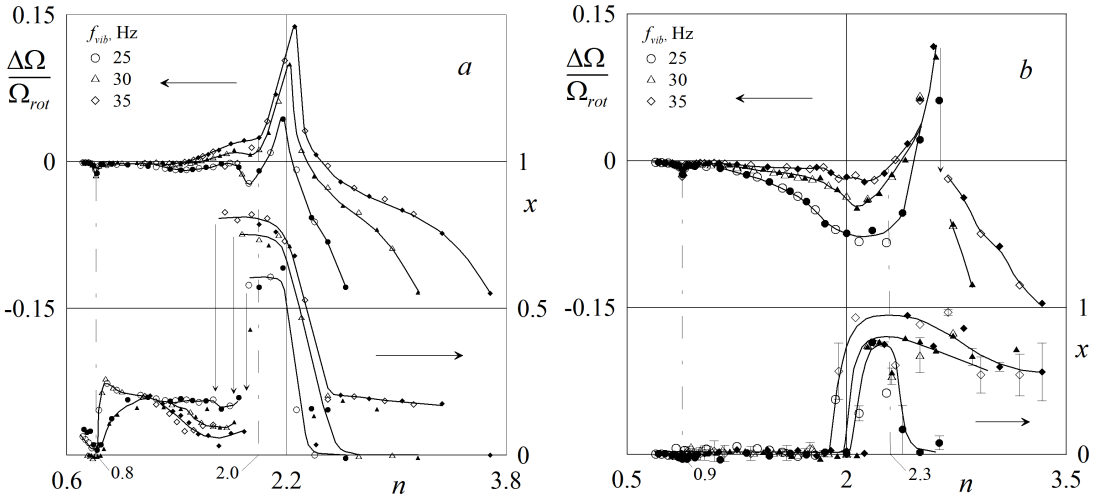


Figure 7: The dimensionless speed of the sphere differential rotation and its position on the axis vs. the dimensionless vibration frequency for the cylindrical cavity ($a$) and the spherical one ($b$); $f_{vib} = 30$ Hz, $b_{vib} = 0.27$ mm, $\nu = 5.0$ cSt

## 6 Conclusion

Was experimentally studied the vibrational dynamics of the light spherical body in the liquid-filled cavity (of cylindrical and spherical shape), rotating around the horizontal axis, at vibrations normal to the rotation axis. The excitation of the intensive differential rotation of the sphere (outstripping or lagging) in the resonant areas, which are determined by the dimensionless vibration frequency $n \equiv \Omega_{vib}/\Omega_{rot}$. The outstripping rotation is excited at $n > 1$, the lagging one – at $n < 1$.

The loss of stability of the sphere position in the cavity centre relative to the end-walls is found. The maximal sphere displacement from the centre is observed at the frequency of excitation of the outstripping rotation. On the contrary, at the intensive lagging vibrational rotation the position of the sphere in the centre becomes stable.

Is found the wave instability on the boundary of the liquid column, which is formed by the Stewartson shear layer.

## Acknowledgements

*The research was supported by RFBR (grant 09-01-00665a)*

## References

[1] Greenspan H.P. The theory of rotating fluids. Cambridge: University Press, 1968.

[2] Kozlov N., Salnikova A., Stambouli M. Vibrational dynamics of two immiscible liquids under rotation // 61st International Astronautical Congress 2010. 2010. V. 4. P. 2886-2892.

[3] Kozlov V.G., Kozlov N.V. Vibrational Dynamics of a Light Body in a Liquid-Filled Rotating Cylinder // Fluid Dynamics. 2008. Vol. 43. No 1. P. 9–19.

[4] Kozlov N.V., Subbotin S.V. Average dynamics of the light sphere in rotating horizontal cavity // Convective Flows... Vol. 5 / Perm: PSPU, 2011. P. 101–117. (*in Russian*)

[5] Kozlov N.V. On the theory of the vibrational hydrodynamic top // Convective Flows. . . Vol. 5 / Perm: PSPU, 2011. P. 93–100. (*in Russian*)

[6] Hide R., Titman C. W. Detached shear layers in a rotating fluid // J. Fluid Mech. 1967. V. 29. P. 39–60.

[7] Schaeffer N., Cardin P. Quasi-geostrophic model of the instabilities of the Stewartson layer in flat and depth varying containers // Phys. Fluids. 2005. V. 17. P. 104111.

[8] Phillips O.M. Centrifugal waves // J. Fluid Mech. 1960. V. 7. P. 340–352.

*Kozlov N.V., Perm State Pedagogical University, Perm, Russia*
*Subbotin S.V., Perm State Pedagogical University, Perm, Russia*

# Numerical modeling of hydraulic fractures: State of art and new results

Alexander Linkov
linkoval@prz.edu.pl

**Abstract**

Hydraulic fracturing is one of the most efficient methods to increase production of oil, gas and heat from underground reservoirs. Its numerical modeling has been the subject of numerous publications. The paper briefly summarizes their results and presents recent findings, which notably improve numerical modeling. The conclusions are drawn on new options and further work for enhancing numerical modeling of hydraulic fractures.

## 1 Introduction

Hydraulic fracturing is a technique used extensively to increase the surface to or from which a fluid flows in a rock mass. Beginning with the papers [1], [2], [3], [4], [5], [6], [7], numerous studies have been published on the theory and numerical simulation of hydraulic fracturing (see, e. g., the papers [8], [9], [10], [11], [12], [13], [14], [15], [16], [17] and detailed reviews in many of them). They have provided knowledge on the asymptotics of the solution, possibility to neglect the lag between the liquid front and the fracture contour and on the typical regimes. The knowledge was incorporated in the computational codes for practical applications (e.g. [11], [14]). Still, there is the need "to dramatically speed up" simulators [14].

The goal cannot be reached without clear understanding of underlying computational difficulties which strongly influence the accuracy and stability of numerical results and robustness of procedures. The recent studies of the author [18], [19], [20], [21], tended to address this challenge, have disclosed hidden features of the problem important for numerical modeling. They have led to the modified formulation of the problem, which opens new options for improving simulators.

The paper aims to (i) clearly explain the conventional formulation, (ii) present the recent findings, summarized in the modified formulation, (iii) demonstrate the advantages of the latter, and (iv) make conclusions on the further work.

## 2 Conventional formulation

A mathematical formulation of the problem includes (i) fluid, (ii) solid, and (iii) fracture mechanics equations. Their conventional forms are as follows.

*Fluid equations.* They include the equation of the mass conservation and the Poiseuille type eq1uation for flow in a narrow channel. For incompressible fluid, the mass conservation means the volume conservation:

$$\frac{\partial w}{\partial t} + div\mathbf{q} + q_l = 0, \tag{1}$$

where $w(\mathbf{x},t)$ is the channel width (fracture opening), $\mathbf{q}(\mathbf{x},t)$ is the flux vector through the fracture height, $q_l(\mathbf{x},t)$ is the intensity of distributed sources (usually this term accounts for leak-off and assumed positive), $\mathbf{x}$ denotes the vector of the position of a point on the surface of the flow, $t$ is the time. The flux and divergence are defined in the tangent plane to the surface of the flow.

The Poiseuille type equation is of the form

$$\mathbf{q} = -D(w,p)gradp, \tag{2}$$

where $p(\mathbf{x},t)$ is the net-pressure, $D$ is a function or operator, such that $D(0,p)gradp = 0$. Gradient is also defined in the tangent plane.

Substitution of (2) into (1) yields the lubrication (Reynolds) equation:

$$\frac{\partial w}{\partial t} - div(D(w,p)gradp) + q_l = 0. \tag{3}$$

An initial spatial distribution $w_0(\mathbf{x})$ of the opening is defined at start time $t_0$:

$$w(\mathbf{x},t_0) = w_0(\mathbf{x}). \tag{4}$$

The spatial operator in (3), being elliptic of the second order, it requires only one boundary condition (BC) at the fluid contour $L_f$. When neglecting the lag between the fluid front $L_f$ and the fracture contour $L_c$, it may be the condition of the prescribed normal component $q_n$ of the flux:

$$q_n(\mathbf{x}) = q_0(\mathbf{x}), \quad \mathbf{x} \in L_f, \tag{5}$$

where $q_0(\mathbf{x})$ is a known function at $L_f$; at the points of the fluid injection it is defined by the injection regime; at the points of fluid front, coinciding with the fracture contour, we have $w = 0$ and equation (2) implies $q_0(\mathbf{x}) = 0$.

*Solid mechanics equations* define a dependence of the opening on the net-pressure caused by deformation of rock:

$$Aw = p, \tag{6}$$

with the condition of zero opening at points of the fracture contour $\mathbf{x}_c$:

$$w(\mathbf{x}_c) = 0. \tag{7}$$

Commonly, the operator $A$ in (6) is obtained by using the theory of linear elasticity. As mentioned, when neglecting the lag, the condition of zero opening (7) replaces the condition of zero flux on the front. Henceforth, we shall consider this case and write $\mathbf{x}_c = \mathbf{x}_*$ with the star marking that a quantity refers to the fluid front.

*Fracture mechanics equations* define the critical state and the perspective direction of the fracture propagation. In the commonly considered case of the tensile mode of fracture, these are:

$$K_I(\mathbf{x}_c) = K_{IC}, \qquad K_{II}(\mathbf{x}_c) = 0, \tag{8}$$

where $K_I$ is the tensile stress intensity factor (SIF), $K_{IC}$ is its critical value, $K_{II}$ is the shear SIF.

The problem consists in solving the PDE (3) together with the elasticity equation (6) under the initial condition (4), boundary conditions (5), (7) and the fracture conditions (8). The global mass balance is usually employed to follow the fluid front propagation (e.g. [7], [9], [11], [14]).

## 3 Fluid particle velocity. Speed equation

The equations of the conventional formulation do not contain the average velocity of fluid particles in a narrow channel. Rather it employs the flux $\mathbf{q}$. The latter, by definition, is the particle velocity averaged across the opening and multiplied by the opening

$$\mathbf{q}(\mathbf{x}) = \mathbf{v}(\mathbf{x})w(\mathbf{x}). \tag{9}$$

Meanwhile, the particle velocity is the primary quantity used when deriving the mass conservation equation and the Poiseuille type equation. It and its averaged (across opening) value are significant from the physical and computational points of view. Of special importance is that the limit value of the average particle velocity at the fluid front $v_{n*}$ represents the speed of the front propagation $V_*$ [18]:

$$V_* = \frac{dx_{n*}}{dt} = v_{n*}(\mathbf{x}_*). \tag{10}$$

Herein, $x_{n*}$ is the normal component of point $\mathbf{x}_*$ on the front. It is assumed that sucking or evaporation through the front is negligible.

In view of (9), the speed equation (10) may be written as

$$V_* = \frac{q_{n*}}{w_*}. \tag{11}$$

For the flux, defined by the Poiseuille type dependence (2), it specifies the *speed equation (SE) for a flow of incompressible fluid in a narrow channel* [18]-[21]:

$$V_* = \frac{dx_{n*}}{dt} = -\frac{1}{w_*(x_*)} D(w,p) \frac{\partial p}{\partial n}_{x=x_*}. \tag{12}$$

Thus we have the *local* condition (12) at points of the propagating fluid front. This allows one to trace the propagation by well-developed methods of the theory of propagating interfaces (see, e. g. [22]). In contrast, the conventional formulation employs the *global* mass balance (e.g. [7], [9], [11], [14]), which is a *single* equation. The latter is sufficient when considering 1-D problems with one point of the front to be traced. However, in the general case of 2D fracture, it is preferable to employ the SE, which is formulated at *each* of many traced points of the fluid front. This gives the first evidence that using the particle velocity is beneficial from the computational point of view.

The next evidence follows from the definition of the flux (9). In view of (2) it implies:

$$\mathbf{v} = \frac{\mathbf{q}}{w} = -\frac{1}{w} D(w,p) grad p. \tag{13}$$

From (10) and (13) we see that even when $w_*(x_*) = 0$ and $q_{n*} = 0$, the limit of the ratio $\mathbf{q}/w$ should be finite to exclude the front propagation with infinite velocity. Thus near the front, where both the flux and the opening rapidly decrease, their ratio, representing the particle velocity, does not change thus fast being finite and non-zero. Moreover, the particle velocity is non-zero in the entire flow region except for flows with stagnation points. From (13), it can be also seen that the particle velocity is notably smoother function than the pressure. Therefore, the particle velocity is a better choice as an unknown function in the lubrication equation than the flux or the pressure. We conclude that *it is reasonable to employ the particle velocity* for numerical modeling of hydraulic fracture propagation. Below it will be shown that the equality of the particle velocity at the front to the propagation speed (10), provides additional computational advantages.

# 4 Clear evidence that BVP is ill-posed

## 4.1 Nordgren problem

The SE (12) is additional to a prescribed boundary condition at the points of the fluid front. For zero lag, this leads to difficulties common to over-determined problems when solving the boundary value problem (BVP) numerically for a fixed position of the front on an iteration. To disclose the difficulties and to find a means to overcome them, we study the Nordgren problem [6].

The Nordgren model considers a straight fracture of the height $h$ propagating along the $x$-axis under plain-strain conditions. Then the net-pressure in equation (6) is proportional to the opening: $p = k_e w$, where $k_e = (2/\pi h)E/(1-\nu^2)$, $E$ is the Young's modulus, $\nu$ is the Poisson's ratio of rock mass. The fluid is assumed Newtonian and consequently the operator $D$ in (2) is the multiplier $D(w,p) = k_l w^3$, where in the case of an elliptic cross section considered by Nordgren $k_l = 1/(\pi^2\mu)$, $\mu$ is the dynamic viscosity.

For simplicity, we neglect leak-off and use the dimensionless variables: $x_d = x/x_n$, $x_{*d} = x_*/x_n$, $w_d = w/w_n$, $y_d = y/y_n$, $v_d = v/v_n$, $p_d = p/p_n$, $q_d = q/q_n$, $q_{0d} = q_0/q_n$, where $x_n = (k_l k_e/4)^{1/5} q_n^{3/5} t_n^{4/5}$, $w_n = q_n t_n/x_n$, $y_n = w_n^3$, $v_n = x_n/t_n$, $p_n = k_r w_n/4$, $q_n$, and $t_n$ are *normalizing* length, opening, cubed opening, particle velocity, flux and time, respectively. The normalizing quantities $q_n$, $t_n$ may be chosen as convenient. From this point on, we omit the subscript $d$ at the normalized variables and consider only dimensionless values. The PDE (3) becomes

$$\frac{\partial w}{\partial t} - \frac{\partial^2 w^4}{\partial x^2} = 0. \tag{14}$$

The initial condition (4) in the 1-D case reads

$$w(x, t_0) = w_0(x), \tag{15}$$

with $w_0(x) = 0$ ahead of the fluid front $x_*$. The BC (5) of the prescribed influx $q_0$ at the inlet $x = 0$ and the BC (7) of zero opening at the front $x = x_*$ are, respectively,

$$-\frac{\partial w^4}{\partial x}_{x=0} = q_0, \tag{16}$$

$$w(x_*, t) = 0. \tag{17}$$

The SE (12) is not used in the conventional formulation. In the dimensionless variables it reads:

$$V_* = \frac{dx_*}{dt} = -\frac{4}{3}\frac{\partial w^3}{\partial x}_{x=x_*(t)}. \tag{18}$$

We see that the PDE (14) is of *second order* in the spatial variable $x$, while there are *three* rather than two *boundary conditions* (16)-(18) for any fixed position of the front $x_*$. It can be shown (see subsection (4.3)) that under the BC (17), in limit $x \to x_*$, the PDE (14) turns into the SE (18). Thus one may expect difficulties when trying to solve the problem (14)-(17) numerically under fixed $x_*$ at each iteration within a time step. Further discussion confirms this suggestion.

### 4.2 Straightforward solving BVP for starting PDE

Nordgren [6] used straightforward numerical integration of the problem (14)-(17). This author applied Crank-Nicolson finite difference scheme to approximate the PDE (14) and to meet the BC (16), (17). The SE (18) was not mentioned. The paper [6] does not contain details of calculations on the initialization, the time step, the number of nodes in spatial discretization, the number of iterations, stability of numerical results and expected accuracy. To obtain knowledge on these issues, we also solved the BVP (14)-(17) in a straightforward way by using the Crank-Nicolson scheme. The results are as follows [19].

Actually performing 20 iterations to account for the non-linear term $w^4$ is sufficient to reproduce four digits of the fracture opening, except for a close vicinity of the liquid front. (Increasing the number to 100 iterations does not improve the solution for all tested time and spatial steps.). For various time steps ($\Delta t = 10^{-2}$, $10^{-3}$, $10^{-4}$) and different spatial steps ($10^{-2}$, $10^{-3}$, $10^{-4}$) taken in various combinations, the results are stable along the main part of the interval $[0, x_*(t)]$. However, *the results always deteriorate and they are unreliable in a close vicinity of the front* ($1 - x/x_* < 0.001$). The results coincide with those given in the paper [6] to the accuracy of two significant digits accepted in this work. In all the calculations, *by no means could we have a reliable third digit* not only near the front but in the entire flow region. Fine spatial meshes did not improve the accuracy as compared with a rough mesh having the step 0.01. Moreover, using very fine spatial meshes with the step less than $10^{-5}$ led to complete deterioration of the solution in the entire flow region.

The numerical results clearly show that the BVP with a fixed position of the front at an iteration cannot be solved accurately without regularization. The *problem appears ill-posed* in the Hadamard sense [23].

### 4.3 Straightforward solving BVP for ODE of self-similar formulation

To further clarify the essence of the difficulties, we employ the fact that the Nordgren problem does not include characteristic geometrical and time parameters. Consequently, its self-similar formulation becomes available [6], [7]. For the constant influx $q_0$, the self-similar variables are: the self-similar coordinate $\xi = xt^{-4/5}$, the self-similar opening $\psi(\xi)$, the self-similar particle velocity $v_\psi(\xi) = -\frac{4}{3}\frac{d\psi^3}{d\xi}$ and the self-similar fracture length $\xi_* = x_* t^{-4/5}$. They define the physical quantities as the functions with separated temporal $t^\beta$ and spatial $\varsigma = x/x_* = \xi/\xi_*$ variables: $w(t,x) = t^{1/5}\psi(\xi)$, $v(t,x) = t^{-1/5}v_\psi(\xi)$, $x_* = \xi_* t^{4/5}$. The self-similar front speed is $V_{\psi *} = 0.8\xi_*$; the physical speed is $V_* = \frac{dx_*}{dt} = 0.8\xi_* t^{-1/5}$.

In terms of the self similar quantities, the PDE (14) becomes the ODE:

$$y\frac{d^2y}{d\xi^2} + \frac{1}{3}\left(\frac{dy}{d\xi} + 0.6\xi\right)\frac{dy}{d\xi} - \frac{3}{20}y = 0, \tag{19}$$

where $y(\xi) = \psi^3(\xi)$. The BC (16) and (17) become, respectively,

$$\sqrt[3]{y(0)}\frac{dy}{d\xi}_{\xi=0} = -\frac{3}{4}q_0, \tag{20}$$

$$y(\xi_*) = 0. \tag{21}$$

The SE (18) in the self-similar form reads:

$$\frac{dy}{d\xi}_{\xi=\xi_*} = -0.6\xi_*. \tag{22}$$

In limit $\xi \to \xi_*$, for a solution, satisfying the BC (21), the ODE (19) turns into the SE (22). Hence, for the ODE (19), at the point $\xi_*$, we have imposed not only the BC (21) for unknown function $y$, but also the BC (22) for its derivative $dy/d\xi$. The problem appears ill-posed. The following discussion makes it obvious.

Re-write the ODE (19) as

$$\frac{d^2y}{d\xi^2} + a(y, dy/d\xi, \xi)\frac{dy}{d\xi} - \frac{3}{20} = 0, \tag{23}$$

where $a(y, dy/d\xi, \xi) = (dy/d\xi + 0.6\xi)/(3y)$. The equations (21), (22) imply that the factor $a$ in (23) is finite at the fluid front.

It is easy to check by direct substitution that if $y_1(\xi_1)$ is the solution of the problem (19)-(21) for $q_0 = q_{01}$ with $\xi_* = \xi_{*1}$, then $y_2(\xi_2) = y_1(\xi_2\sqrt{k})/k$ is the solution of the problem ()-() for $q_{02} = k^{-5/6}q_{01}$ with $\xi_{*2} = \xi_{*1}/\sqrt{k}$; herein, $k$ is an arbitrary positive number. This implies that $C_* = q_0^{0.6}/\xi_*$ and $C_0 = y(0)/\xi_*^2$ are constants independent on the prescribed influx $q_0$. As $\xi_* = q_0^{0.6}/C_*$, it is a matter of convenience to prescribe $q_0$ or $\xi_*$. A particular value of $q_0$ or $\xi_*$ may be also taken as convenient. Indeed, with the solution $y_1(\xi_1)$ for $q_0 = q_{01}$, we find the solution for any $q_0$: $y(\xi) = y_1(\xi\sqrt{k})/k$, where $k = (q_{01}/q_0)^{6/5}$, $\xi = \xi_1/\sqrt{k}$ ($\xi_* = \xi_{*1}/\sqrt{k}$ ).

Let us fix $\xi_*$. According to (21), (22), at the point $\xi_*$, we have prescribed both the function $y$ and its derivative $dy/d\xi$. Thus, for the ODE of the second order (19) we have a Cauchy (initial value) problem. Its solution defines $y(0)$, $\frac{dy}{d\xi}_{\xi=0}$ and consequently the flux $q_0$ at $\xi = 0$. Hence, even a small error when prescribing $q_0$ in (20), excludes the existence of the solution of the BV problem (19)-(21). Therefore, by Hadamard definition [23], the BV problem (19)-(21) is ill-posed. It cannot be solved without a proper regularization [24].

Direct computations confirm that it is impossible to accurately solve the BVP (23), (20), (21). We performed hundreds of numerical experiments with various numbers of nodal points and iterations and different values of the prescribed influx $q_{01}$ at the inlet. Finite difference approximations of second order for $d^2y/d\xi^2$ and $dy/d\xi$ were combined with iterations for the non-linear term $a(y, dy/d\xi, \xi)$. Up to 100 000 nodal points and up to 1500 iterations were used in attempts to reach the accuracy of three correct digits, at least. The attempts failed: by no means could we have more than two correct digits in the entire flow region. Moreover, the results always strongly deteriorate near the fluid front. The numerical results clearly demonstrate that the BV problem (19)-(21) is ill-posed. It cannot be solved accurately without regularization.

# 5 e-regularization

## 5.1 e-regularization for self-similar formulation

A regularization method is suggested by the conditions (21), (22). Indeed, we may use them together to get the approximate equation $y \approx 0.6\xi_*(\xi_* - \xi)$ near the front. Hence, instead of prescribing the BC (21) at the fluid front $\xi = \xi_*$, where it is implicitly complemented by the SE (22), we may impose the boundary condition, which combines (21) and (22) at a point $\xi_\varepsilon = \xi_*(1 - \varepsilon)$ at a small relative distance $\varepsilon = 1 - \xi_\varepsilon/\xi_*$ from the front:

$$y(\xi_\varepsilon) = 0.6\xi_*^2(1 - \varepsilon). \tag{24}$$

The BV problem (19), (20), (24) is well-posed and it may be solved by finite differences. Numerical implementation of this approach shows that with $\varepsilon = 10^{-3}$, $10^{-4}$, the results for the step $\Delta\zeta = \Delta\xi/\xi_* = 10^{-3}$, $10^{-4}$, $10^{-5}$, $10^{-6}$ coincide with those of the benchmark

solution [19]. The time expense is fractions of a second. The results are stable if $\varepsilon$ and $\Delta\zeta$ are not simultaneously too small (both $\varepsilon$ and $\Delta\zeta$ are greater than $10^{-5}$).

The essence of the suggested regularization consists in using the SE together with a prescribed BC to formulate a BC at a small distance behind the liquid front rather than on the front itself. Besides, the SE is also imposed at the point $\xi_\varepsilon$; it is used for iterations. We call such an approach e-regularization.

### 5.2 e-regularization for starting PDE

Extension of e-regularization to solve the starting PDE (14) requires using the BC (17) on the front combined with the SE (18) to impose a BC at a small relative distance from the front. Introduce the relative distance $\eta = (x_* - x))/x_*$ from the front. The relative distance from the inlet is $\varsigma = 1 - \eta = x/x_*$. When using the variable $\varsigma$, the PDE (14) becomes:

$$\frac{d^2Y}{d\xi^2} + A(Y, \partial Y/\partial\varsigma, \varsigma)\frac{dY}{d\varsigma} - B(Y, x_*)\frac{\partial Y}{\partial t} = 0, \tag{25}$$

where $Y(\varsigma, t) = w^3(\varsigma x_*(t), t)$, $A(Y, dY/d\varsigma, \varsigma) = (\partial Y/\partial\varsigma + 0.75 x_* V_* \varsigma)/(3Y)$, $B(Y, x_*) = x_*^2/(4Y)$. The BC (16), (17) in the new variables read:

$$\frac{\sqrt[3]{Y(0)}}{x_*}\frac{\partial Y}{\partial\varsigma}_{\varsigma=0} = -\frac{3}{4}q_0, \tag{26}$$

$$Y(\varsigma, t)_{\varsigma=1} = 0. \tag{27}$$

The SE (18) takes the form:

$$\frac{\partial Y}{\partial\varsigma}_{\varsigma=1} = -0.75 x_* V_*. \tag{28}$$

Note that in view of the conditions (27) and (28), the factor $A(Y, dY/d\varsigma, \varsigma)$ and the term $B(Y, x_*)\partial Y/\partial t$ are finite at the fluid front $\varsigma = 1$. Note also that under the BC (27), in limit $\varsigma \to 1$, the PDE (25) turns into the SE (28). In terms of the starting problem, this means that under the BC (17), in limit $x \to x_*$, the PDE (14) turns into the SE (18).

The regularization of the problem (25)-(27) follows the line used for the self-similar formulation. The BC (27) is combined with the SE (28) to obtain the approximate equation near the liquid front:

$$Y(\varsigma, t) \approx 0.75 x_*(t) V_*(t)(1 - \varsigma). \tag{29}$$

Thus we may impose the BC at a small relative distance $\varepsilon$ from the front by taking equality sign in (29):

$$Y(\varsigma_\varepsilon, t) = 0.75 x_*(t) V_*(t)\varepsilon, \tag{30}$$

where $\varsigma_\varepsilon = 1 - \varepsilon$. In contrast with the problem (25)-(27), the problem (25), (26), (30) does not involve an additional BC. We may expect that it is well-posed and provides the needed regularization. Extensive numerical tests confirm the expectation [19]. We solved the problem (25), (26), (30) by using the Crank-Nicolson scheme and iterations for non-linear multipliers $A(Y, dY/d\varsigma, \varsigma)$ and $B(Y, x_*)$ at a time step. The velocity was also iterated by imposing the SE at the point $\varsigma_\varepsilon = 1 - \varepsilon$. We could see that with $\varepsilon = 0.0001$, $\Delta\varsigma = 0.01$, and fifty iterations of the non-linear terms at a time step, the relative error of the fracture

length $x_*$ and the front speed $x_*$ was less than 0.03% at each of 20000 time steps. Moreover, starting from the relatively small time $t = 0.01$, we could reach the time $t = 36128$ without loss of accuracy. There were no signs of instability or deterioration of the opening near the front in these and many other specially designed experiments. Therefore, e-regularization is quite efficient.

### 5.3 e-regularization in general case

According to the rationale presented in the preceding subsections, it appears that the strategy of using e-regularization when tracing 2-D hydrofracture propagation is as follows. At each point of the liquid front, an exact boundary condition is changed to an approximate equality at a small distance $r_\varepsilon$ behind the front. This approximate equality is obtained by combining the boundary condition at the fluid front, particular for a considered problem, with the SE, which is quite general. In practical calculations, the distance (absolute $r_\varepsilon$ or relative $\varepsilon$) is taken small enough to use the equality sign in the derived approximate condition. This gives us the *e-regularized boundary condition* near the front. The SE is also assumed to be met at the distance $r_\varepsilon$ with an accepted accuracy. This gives us the *e-regularized speed equation.* The e-regularized boundary condition allows one to avoid unfavorable computational effects; the e-regularized SE serves to find the front propagation.

In this way, in general, the speed equation (12) is combined with a condition on the fluid front to obtain the e-regularized boundary condition [19], [20]:

$$\int_{p_*}^{p_\varepsilon} \frac{1}{w} D(w,p)dp = V_* r_\varepsilon, \tag{31}$$

where $p_*$ is the pressure at the front, $p_\varepsilon = p(r_\varepsilon)$ is the pressure at the distance $r_\varepsilon$ from the front.

The e-regularized form of the SE (12) is:

$$V_*(t) = \frac{dx_{n*}}{dt} = -\frac{1}{w} D(w,p) \frac{\partial p}{\partial n}_{r_\varepsilon}. \tag{32}$$

For the Nordgren problem, in the normalized variableswe have $p = 4w$, $p_* = 4w(x_*) = 0$, $D(w,p) = w^3$, $r_\varepsilon = \varepsilon x_*$; then, since $Y = w^3$ and $\partial/\partial n = -\frac{1}{x_*}\partial/\partial\varsigma$, the regularized BC (31) and the regularized SE (32) reduce to (30) and $\partial Y/\partial\varsigma_{\varsigma=\varsigma_\varepsilon} = -0.75 x_* V_*$, respectively.

## 6 Choice of proper variables

In Section 2, it has been shown that the *particle velocity* is a better choice as an unknown function in the lubrication equation than the flux or the pressure. A proper choice of the *spatial variables* near the liquid front is suggested by e-regularization and by the asymptotic behavior of the opening near the liquid front. Recall that the e-regularized equations (31) and (32) actually employ the system moving with the front. Thus it is reasonable to re-write the lubrication equation (3) in this system. In it, the $r$-axis is directed opposite to the front velocity, while the other axis is tangent to the front. Then equation (3) becomes [19]:

$$\frac{\partial \ln w}{\partial t} = \frac{\partial v_n}{\partial r} + (v_n - V_*)\frac{\partial \ln w}{\partial r} - \frac{1}{w} q_l, \tag{33}$$

where using $\ln w$ serves to account for an arbitrary power asymptotic behavior of the opening $w(r,t) = C(t)r^\alpha + O(r^\delta)$ near the front ($\alpha \geq 0$, $\delta > \alpha$). The value of the exponent

$\alpha$ is known in a number of important particular cases, $\delta = 1 + \alpha$ when the leak off is neglected (see, e.g. [7], [8], [9], [15]).

When the opening has the power asymptotic near the front with $\alpha > 0$, it yields singular behavior of the spatial derivatives $\partial w/\partial r$, $\partial^2 w/\partial r^2$ at the front, and this complicates numerical solution of a problem. Therefore, *it is reasonable, in addition to the particle velocity, to use the variable* $Y = w^{1/\alpha}$, which is linear near the front. In terms of the variables $Y$, $v_n$ and $r$, the lubrication equation (3) near the liquid front becomes

$$\frac{\partial Y}{\partial t} = \frac{Y}{\alpha}\frac{\partial v_n}{\partial r} + (v_n - V_*)\frac{\partial Y}{\partial r} - \frac{Y^{1-\alpha}}{\alpha} q_l. \tag{34}$$

The initial condition (4), boundary condition (5) and the SE (12) are easily re-written in these variables.

In 1-D cases, the PDE (34) is applicable to the entire fluid. In these cases, there is the only spatial coordinate $x$ and it is reasonable to normalize $x$ or, what is actually equivalent, $r$ by the distance $x_*(t)$ from the inlet to the front. Then in terms of $\varsigma = x/x_* = 1 - r/x_*$, the lubrication equation (34) in 1-D cases reads:

$$\frac{\partial Y}{\partial t} = \frac{1}{x_*}\left[(\varsigma V_* - v)\frac{\partial Y}{\partial \varsigma} - \frac{Y}{\alpha}\frac{\partial v}{\partial \varsigma}\right] - \frac{Y^{1-\alpha}}{\alpha} q_l, \tag{35}$$

where we have omitted the subscript $n$ in the notation of the particle velocity. Note that when $q_l$ near the front decreases faster than $w = Y^\alpha$, we may divide (35) by $Y$, obtaining the equation

$$\frac{1}{Y}\frac{\partial Y}{\partial t} = \frac{\varsigma V_* - v}{x_* Y}\frac{\partial Y}{\partial \varsigma} - \frac{1}{\alpha x_*}\frac{\partial v}{\partial \varsigma} - \frac{1}{\alpha Y^\alpha} q_l, \tag{36}$$

where under the assumed asymptotics of $q_l$, the term $(\partial Y/\partial t)/Y$, the factor $(\varsigma V_* - v)/(x_* Y)$ and the derivative $\partial v/\partial \varsigma$ are finite, while the term $q_l/(\alpha Y^\alpha)$ tends to zero at the liquid front.

# 7 Modified formulation. Computational and analytical advantages

## 7.1 Modified formulation

Employing the suggested variables and e-regularization results in the modified formulation of the hydraulic fracture problem. In contrast with the conventional formulation it uses [18]-[21]:

1. the particle velocity, as a variable smooth near the liquid front, instead of the pressure;

2. the opening taken in a degree, defined by its asymptotic behavior at the liquid front, instead of the opening itself;

3. the speed equation at each point of the front to trace the fracture propagation by the well-developed methods [22], instead of the commonly employed single equation of the global mass balance; the speed equation also presents the basis for proper regularization;

4. e-regularization, that is imposing the boundary condition and the speed equation at a small distance from the front rather than on the front itself, to exclude deterioration of the solution near the front caused by the fact [18],[19] that the BVP is ill-posed for a fixed position of the front when neglecting the lag;

5. the spatial coordinates moving with the front and evaluation of the temporal derivative under fixed values of these coordinates;

6. reformulation of the common system of equations and boundary conditions in terms of the suggested variables complemented, when appropriate, with e-regularization.

### 7.2 Advantages of modified formulation

The *computational advantages* of using the modified formulation have been explained in the course of the exposition. There are also *analytical advantages*, which appear due to smoothness of the new variables (particle velocity and $Y = w^{1/\alpha}$) near the fluid front. In 1-D cases, they allow one to obtain analytical solutions of problems, like those by Nordgren [6], Spence & Sharp [7], which otherwise require involved calculations. The analytical solutions of these problems may be found in the paper [21]. Further obvious applications of the analytical approach may include accounting for leak-off, when the latter is prescribed in separated temporal and spatial variables with a specially chosen temporal part and with the spatial part having the same asymptotic near the fluid front as the opening. Analogous axisymmetric problems may be solved in this way, as well.

## 8 Conclusions on further work

Further work on enhancing numerical modeling of hydraulic fractures may employ new facilities suggested by the modified formulation of the problem. Some of them have been mentioned above.

1. Since the SE is formulated at each point of the front, it notably extends options for tracing the fracture propagation as compared with the traditional approach employing the single equation of the global mass balance. The SE opens the possibility to use the well-developed numerical methods of the theory of propagating interfaces [22]. In particular, level set methods and fast marching methods become of use.

2. New efficient iterative schemes may employ the particle velocity as an unknown function, which is notably smoother than commonly employed net-pressure. What also looks beneficial, only the *first* spatial derivatives of the particle velocity enter the modified lubrication equation. The same refers to using the opening at the degree defined by its asymptotic behavior near the front.

3. Employing e-regularization provides an opportunity for examining and improving the accuracy of existing commercial codes serving for modeling hydraulic fractures.

4. For an area sufficiently close to the front, where the solution changes faster than at the remaining part of a fracture, the PDE (34) and the SE (12), after spatial discretization, suggest efficient integration in time of a non-linear system of ODE under initial (Cauchy) conditions by using multi-stage methods like the Runge-Kutta methods.

5. Obtaining analytical solutions accounting for leak-off in 1-D plain-strain and axisymmetric problems. Using these solutions for accurate description of the boundary layer effects caused by the existence of the lag between the fluid front and the fracture contour.

6. Working out improved while simple models and numerical schemes for accounting for the proppant movement.

Perhaps, execution of these works may facilitate progress in solving even more difficult and important problems of hydraulic fracturing concerning with strong inhomogenuity of rocks and presence of multiple contacts and natural cracks, which may serve as channels for fluid flow. Still the greatest challenge is to comprehend and to properly model hydraulic fractures in low permiable shales.

### Acknowledgments

This research has been supported by FP7 Marie Curie IAPP project (PIAP-GA-2009-251475).

## References

[1] Khristianovic S. A., Zheltov Y. P. Formation of vertical fractures by means of highly viscous liquid. In: Proc. 4-th World Petroleum Congress, Rome, 1955, 579-586.

[2] Carter E. Optimum fluid characteristics for fracture extension. In: Howard G., Fast C. (eds.) Drilling and Production Practices, American Petroleum Institute, 1957, 261–270.

[3] Perkins T. K., Kern L. R. Widths of hydraulic fractures. J. Pet. Tech., 1961, 13 (9), 937-949.

[4] Geertsma J., de Klerk F. A rapid method of predicting width and extent of hydraulically induced fractures. J. Pet. Tech., 1969, 21, 1571-1581.

[5] Haward G. C., Fast C. R. Hydraulic fracturing. Monograph series, v. 2, Richardson, Soc. Petroleum Eng., 1970.

[6] Nordgren R. P. Propagation of a vertical hydraulic fracture. SPE J., 1972, 12 (8), 306-314.

[7] Spence D. A., Sharp P. W. Self-similar solution for elastodynamic cavity flow. Proc. Roy. Soc. London, Ser A, 1985, 400, 289-313.

[8] Desroches J., Detournay E. et al. The crack tip region in hydraulic fracturing. Proc. Roy. Soc. Lond. Ser. A, 1994, 447, 39-48.

[9] Adachi J. I., Detournay E. Self-similar solution of plane-strain fracture driven by a power-law fluid. Int. J. Numer. Anal. Meth. Geomech., 2002, 26, 579-604.

[10] Savitski A., Detournay E. Propagation of a fluid driven penny-shaped fracture in an impermeable rock: asymptotic solutions. Int. J. Solids Struct., 2002, 39, 6311-6337.

[11] Jamamoto K., Shimamoto T., Sukemura S. Multi fracture propagation model for a three-dimensional hydraulic fracture simulator. Int. J. Geomech., ASCE, 2004 (1), 46-57.

[12] Garagash D. I. Propagation of a plane-strain hydraulic fracture with a fluid lag: Early time solution. Int. J. Solids Struct., 2006, 43, 5811-5835.

[13] Mitchell S. L., Kuske R., Peirce A. An asymptotic framework for finite hydraulic fractures including leakoff. SIAM J. Appl. Math., 2007, 67(2), 364–386.

[14] Adachi J., Siebrits E. et al. Computer simulatiion of hydraulic fractures. Int. J. Rock Mech. Min. Sci., 2007, 44, 739-757.

[15] Kovalyshen Y., Detournay E. A reexamination of the classical PKN model of hydraulic fracture, Transp. Porous Med., 2009, 81, 317-339..

[16] Hu J., Garagash D. I. Plane-strain propagation of a fluid-driven crack in a permeable rock with fracture toughness. J. Eng. Mech., ASCE, 2010, 136 (9), 1152-1166.

[17] Garagash D. I., Detournay E., Adachi J. I. Multiscale tip asymptotics in hydraulic fracture with leak-off. J. Fluid Mech., 2011, 669, 260-297.

[18] Linkov A. M. Speed equation and its application for solving ill-posed problems of hydraulic fracturing. ISSM 1028-3358, Doklady Physics, 2011, 56 (8), 436-438. Pleiades Publishing, Ltd. 2011.

[19] Linkov A. M. Use of a speed equation for numerical simulation of hydraulic fractures. Available at: http://arxiv.org/abs/1108.6146. Date: Wed, 31 Aug 2011 07:47:52 GMT (726kb). Cite as: *arXiv*: 1108.6146v1 [physics.flu-dyn].

[20] Linkov A. M. On numerical simulation of hydraulic fracturing. Proc. XXXVIII Summer School-Conference, "Advanced Problems in Mechanics-2011", Repino, St. Petersburg, July 1-5, 2011, 291-296.

[21] Linkov A. M. On efficient simulation of hydfraulic fracturing in terms of particle velocity. Int. J. Eng. Sci., 2012, 52, 77-88.

[22] Sethian J. A. Level set methods and fast marching methods. Cambridge, Cambridge University Press, 1998.

[23] Hadamard J. Sur les problemes aux derivees partielles et leur signification physique. Princeton University Press, 1902, 49-52.

[24] Tychonoff A. N. Solution of incorrectly formulated problems and the regularization method. Soviet Mathematics, 1963, 4, 1035-1038.

*Alexander M. Linkov, Rzeszow University of Technology, Powstancow Warszawy 12, 35-959 Rzeszow, Poland.*

# Software development rapid synthesis of nonlinear robust adaptive control systems of complex dynamic objects

Evgene V. Lubimov Alexander A. Dyda
berms@mail.ru

**Abstract**

The paper deals with the problem computer-aided design of nonlinear control systems. It is proposed to pass from the problem of synthesis of nonlinear control systems related to various theoretical complexities of the problem of parameterization and reduction of the mathematical model of control object to the required form. The developed software achieves the synthesis of control laws in symbolic form, and sends for further analysis, simulation in Matlab. The methods of synthesis used the method of exact linearization via nonlinear feedback, adaptive, robust algorithms based on Lyapunov functions and direct compensation scheme.

## 1 Introduction

Modern controlled objects are characterized by a high degree of complexity to the factors which are multi-dimensionality, nonlinearity, uncertainty, mathematical models and, etc. Software computational tools can to accelerate synthesis control system and to reduce the volume of routine work of designer. For today the majority modern research on the synthesis and design of automatic control laws is carried out using mathematical packages and specialized programming languages. With increasing dimension of problems, even the use of software computational tools does not reduce difficulty the synthesis and simulation, the developer substantially limits the possibilities computer-aided design [1]

The obvious solution specific problem is a decrease impact by designer on the process of building control laws, by applying a formal analytical method. These methods allow by mathematical model of control object, recorded in analytical or symbolic form, obtain the control law in the analytical or symbolic form too. Ideal variant is a situation where the synthesis of control laws in symbolic form is fully automatic.

The paper considers a variant of algorithm is fully automatic synthesis. Use two contour control system, based on the method of feedback linearization [1,5], adaptive synthesis algorithms based on Lyapunov functions and the scheme direct compensation [6,3]. Not looking some restrictions of the proposed approach, greater value is the speed construction of a workable control laws which insure the motion control object along the required trajectory.

Important to note that the strategy of synthesis of control systems, as a rule, is in a preliminary study of the control object. At this stage is performed the numerical simulation of the motion along the desired trajectories. The developed software complex gives the designer a tool to quickly go from a mathematical model to the simulated results. In the next stage designer can start to the synthesis higher quality control laws in manual or automatic modes, based on radically different methods of synthesis, or by optimizing the algorithm which is automatically synthesized at the before stage.

## 2 Description of software

The developed software package has a modular, linear principle. Stage of the synthesis is carried out with the use of library functions that are implemented in the language of Maple. Stage modeling is performed in Matlab, a numerical experimental doing on basis of generated during the synthesis of Matlab's files containing the model and control laws.

Working with the software on the synthesis stage is to write a program in Maple, using the developed functions.The initial data for the synthesis of a mathematical model of control object, which is written in an analytical, symbolic form. After entering the model, the designer run a series of function to perform. The structure of the software complex with a sequence of functions of run is shown in Figure 1.

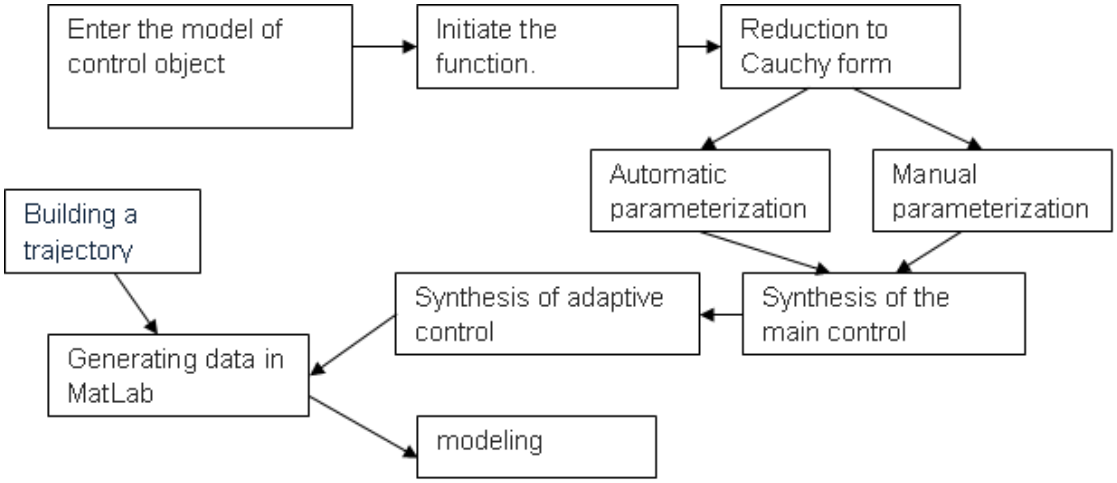


Figure 1: The functional structure of the software system.

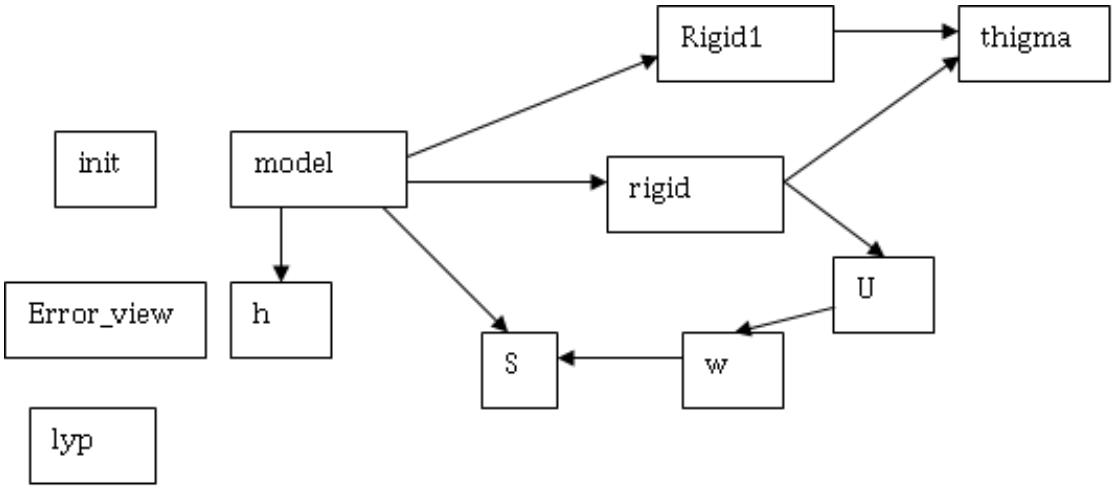


Figure 2: Scheme function calls Matlab-files.

The final stage of using of the Maple is the generation of the system files for simulate closed control system in the environment of MatLab (Fig. 2). Simulation in Matlab is by running the file "model" or by constructing block model in the environment Simulink.

The major file is “rigid1” or “rigid”, which are inserted into the standard solver of ordinary differential equations (ODE) as the called functions calculating of the next step.

The proposed scheme generation matlab-file is more flexible. In fact, the researcher immediately after synthesis system receives all the graphs of the simulated signals the control system. It may itself configure the Matlab simulation environment, depending on the desired results. Among the important configurable selected parameters: a method of solving an ODE step solving - greatly determine the speed and precision of simulation.

## 3 Algorithms for the main and adaptive control contour

In this paper used the strategy of direct adaptive control - direct compensation scheme, and a group gradient algorithm, called adaptive algorithms with Lyapunov functions [6]. The model of uncertain dynamic control object is represented by the following equation:

$$\dot{x} = f(x) + g(x)(u + \omega(x,t)^T\theta(x,u,t)) + \delta(t), \tag{1}$$

where $\dot{x} = (x_1, ...x_n)^T$, $u = (u_1, ...u_m)^T$ are the state and control vectors, respectively, $\omega(x,t)$ - matrix (regressor) of dimension $(n \times q)$, $\theta(x,u,t) = (\theta_1, ...\theta_q)^T$ - vector of uncertainty parameters, $\delta(t) = (\delta_1, ...\delta_n)^T$ - vector of unmeasured external disturbances. Feature of the model (1) is that all the uncertainty of the object control, including parametric, signaling, structural uncertainty is concentrated in the vector $\theta$ In accordance with the principle of direct compensation form the control law as:

$$u = U_0 - \omega(x,t)^T\hat{\theta}, \tag{2}$$

$$\hat{\theta} = \Theta(x, \hat{\theta}, t), \tag{3}$$

where $\hat{\theta}$ - estimate vector undefined parameters, If found by the regulator (3) estimate of the vector equal to actual value $\hat{\theta} = \theta$ , then the law (2) provides the full compensation of the disturbing influence of uncertainty $\theta$ (without $\delta$ ) and model (1) can be written as:

$$\dot{x} = f(x) + g(x)U_0, \tag{4}$$

Regulator (2), (3) can be designed with adaptive, adaptive-robust and robust nonlinear control laws:

$$\hat{\theta} = \hat{\theta}_S + \hat{\theta}_I, \tag{5}$$

$$\dot{\hat{\theta}}_S = \mu\omega\frac{\partial V}{x}(x)g(x), \tag{6}$$

$$\dot{\hat{\theta}}_I = \gamma\omega\frac{\partial V}{x}(x)g(x) - \sigma\hat{\theta}_I, \tag{7}$$

where $\mu > 0$, $\gamma > 0$ and $\theta >$) - constant, $V(x)$ - a Lyapunov function that guarantees the stability of the model (4), (5) - nonlinear robust control, (6) - adaptive and robust control. Synthesis of the main control $U_0$ is using the method of feedback linearization is described in details [1,4]:

$$U_0 = \frac{1}{L_g L_f^{r-1} h}(-L_f^r + \tilde{u}), \tag{8}$$

where $r$ - vector relative degree, $h(x)$ - additional output of the system (1).Going to the synthesis of an additional control $\tilde{u}$, we use the method of inverse dynamics problems [5], we write the control as follows:

$$\tilde{u} = (y^*)^r + k_r e_y^{r-1} + ... + k_1 e_y, \tag{9}$$

$$e_y = y^* - h(x), \tag{10}$$

where $y^*$ - required trajectory. Control (7), (8) provide a tracking the output $y \to y^*$. If $h(x) = x$ , then the problem is solved by tracking the state vector $x \to x^*$ or the problem of stabilizing $x \to 0$.

## 4 Final comments

Practical results using of the software show the effectiveness the approach proposed rapid synthesis of control systems. Testing was carried out on systems of various degrees of complexity and uncertainty of the mathematical model of the object controls, in particular, examined three-tier manipulators, mobile underwater vehicles, 3-phase motors with a maximum size of the ODE to 30.

Speed of symbolic synthesis is almost independent of the complexity of the mathematical model and is less than 1 minute. Speed of simulation depends on the chosen parameters of ODE solver, can be varied from minutes to hours depending on the complexity of the problem. During symbolic synthesis can be run special procedures of optimization of computational complexity of control laws which essentially accelerate the phase of the simulation.

From the standpoint of the quality of the obtained control laws, the use of 2 independent circuits requires careful selection of the coefficients of the laws (5) (6). During numerical experiments to ensure an acceptable amplitude and frequency of the control laws signal applied strategy to gradually tuning of the coefficients. In general, the simulation results show the stability of the synthesized control system obtained control laws can be immediately applied in practice in the implementation of control systems.

## References

[1] B.R. Andrievsky, A. L. Fradkov Elements of mathematical modeling in software environments Matlab and Scilab. St. Petersburg. Science, 2001.

[2] H. Nijmeijer, A. Van der Schaft Nonlinear Adaptive Feedback Linearization of Systems. New York: Springer-Verlag, 1990.

[3] P.V. Kokotovic, placeI. Kanellakopoulos, A.S. Morse Adaptive Feedback Linearization of Nonlinear Systems. Foundation of Adaptive Control. Berlin: Springer-Verlag, 1991.

[4] A. A. Dyda, S. Di Gennaro Adaptive trajectory control for underwater robot. Proc. OCEANS-94 Osates, Brest, 1994.

[5] D. P. Kim The theory of automatic control. V.2. Multi-dimensional, nonlinear, optimal and adaptive systems. Moscow, Phismathlit, 2004.

[6] I. V. Miroshnik, V. O. Nikiforov, A. L. Fradkov Nonlinear and adaptive control of complex dynamic systems. St. Petersburg. Science, 2000.

[7] A. Isidori Nonlinear Control Systems. Berlin: Springer-Verlag, 1995.

*Evgene V. Lyubimov, Vladivostok, Russia*
*Alexander A. Dyda, Vladivostok, Russia*

# Thermal stresses in a layered cylinder are the result of the process cooling and consolidation of the melt during the formation individual layers

Olga N. Lyubimova Konstantin N. Pestov
berms@mail.ru

**Abstract**

The formation of thermoelastic stresses review in a layered cylinder with a view of phase transitions in separate layers. We formulate an evolutionary boundary value problem in the quasistatic approximation of the kinetics of crystallization and changes in temperature. Numerical solutions were obtained for three-layer cylinder in the case of crystallization of one or two layers.

Modern industrial development is directly linked to the widespread introduction of new materials, among them a special place is given layered composite materials (LCM). Engineering processes for some of layered composite materials, such as bimetals or materials on base glass and metal [1] include the temperature conditions under which in the materials are possible phase transitions of first order. As a result, during the production of level of technological stresses caused by from thermal stresses and crystallization stresses may exceed the ultimate strength of a composite material that gives rise to defects. Therefore, the development and improvement of methods for studying the kinetics of formation of stresses, taking into account the phase transitions are modern problems in the mechanics of deformable solids.

The main results of studies of domestic scientists of phase transitions in the framework of continuum mechanics in recent years are reflected in the works [2-5]. In this paper we consider the problem of determining the stress-deformation condition (SDC) at the last stage of formation LCM - cooling, during which the possible consolidation of the individual layers. Numerically solved the problems for of crystallization from the liquid phase of the inner layer or two outer layers for LCM cylindrical form which made of three different materials.

Mathematical model of this problem can be written using methods mechanics of growing coats (bodies) [6], where of crystallized material is represented as growing out from the liquid phase. Model is carried out under the following assumptions: the contribution of the dissipative stresses is insignificant and does not have effect on heat transfer and course processes of phase transformations; rheological processes are absent, it means maintaining the elasticity of the solid and liquid phase, a quasistatic equilibrium of the liquid phase.

These assumptions make it possible to divide the problem into two independent:

- the problem of determining the temperature fields and the movement of frontier the phase transition of first order, if any are possible in the material, the numerical method for solving this problem is proposed in [7];
- boundary value problem of determining the SDC for a layered material with thermal and structural homogeneities.

One of ways constructs a boundary value problem with moving boundary; it constructs equations of continuum mechanics and the boundary conditions in the velocities. Then mathematical model will represent the system of equations for the unknowns $\dot{\sigma_{ij}}$, $\dot{\varepsilon_{ij}}$, $\dot{u_i}$ containing for each layer: the equilibrium equation, the equation of state (like the Duhamel-Neumann relations), the conditions of Cauchy, boundary conditions on the outer surface of the LCM, conditions of pairing for different materials and equation at the phase interface. In fact, the model will differ from the classical model of the mechanics of growing bodies [6], only the last equation, so we stop for consider in detail this condition. We define the conditions a complete mechanical at the boundary of the growing body (growing body will be solid phase) and liquid phase. This condition of continuity vectors of the displacement and the stress.

$$[u_i]\Big|_{\Gamma^*_{kl}} = 0 \tag{1}$$

$$[\sigma_{ij} n_j]\Big|_{\Gamma^*_{kl}} = 0 \tag{2}$$

here $n_j$ are the direction cosines of the outward normal to the $\Gamma^*_{kl}$ phase interface in the $k$ layer from the solution of the problem is known function of the temperature surface phase transition boundary $(\Phi(M,t) = 0)$ for each point in time.

As for the layered materials in the case of crystallization of the inner layers have to take into account the pressure arising from side the liquid phase, the stress of the liquid phase is determined from the equation of state

$$\sigma_{ij} n_j\Big|_{\Gamma^*_{kl}+0} = n_j \int_0^{t^*} 3K(\dot{\varepsilon} - \beta\dot{T})\delta_{ij} dt = n_i \int_0^{t^*} 3K(\dot{\varepsilon} - \beta\dot{T}) dt,$$

where $\dot{\varepsilon} = \dot{\varepsilon_{ii}}$, $t^*(M)$ is time of accession element to a growing body and also it's the time the birth of element of the point $M(x_1, x_2, x_3)$ . Unknown vector of external forces determined by the pressure of the fluid on boundary of growing the solid phase.

At the same time, to the deformation element, acquired in a liquid state, we add the structural deformation associated with the change of aggregation state of the element and the elastic deformation as resulting from the pressure of the liquid phase

$$\varepsilon^*_{ij} = \varepsilon_{ij}(t^* - 0) + \varepsilon^s_{ij} + \varepsilon^e_{ij}$$

where $\varepsilon^s_{ij}$– structural deformations, $\varepsilon^e_{ij}$– elastic deformations, $\varepsilon_{ij}(t^* - 0)$–initial of deformations of the solid phase will define as follows

$$\varepsilon_{ij}(t^* - 0) = \int_0^{t^*} \dot{\varepsilon_{ij}} dt.$$

Structural deformations appear at the time of accession in the arisen solid phase, it can be explained the change of aggregation state. If the arisen solid phase has got isotropic nature, then the correct formula

$$\varepsilon^s_{ij} = \frac{\delta_{ij}}{3}\Big(\frac{\rho^+}{\rho^-} - 1\Big),$$

where $\rho^+$, $\rho^-$– density of liquid and solid phases, respectively.

The stresses in the accession element will be consisting from stresses accumulated in the liquid phase and some stresses as result of deformation as part of a growing body:

$$\sigma^*_{ij} = \int_0^{t^*} \dot{\sigma_{ij}} dt + \Delta\sigma_{ij}.$$

It is obvious, the value of the additional stresses and strains are related by Hooke's law:

$$\Delta\sigma_{ij} = E_{ijkl}\varepsilon^{e}_{kl}.$$

In order to write the junction conditions of the liquid and solid phases in the rates of stresses and displacements, we differentiate with respect to time of (1) and (2), we obtain

$$\frac{d}{dt}\Big[u_i(x_1,x_2,x_3,t)\Big]\Big|_{\Gamma^*_{kl}} = \Big[\frac{\partial}{\partial t}u_i(x_1,x_2,x_3,t) + \frac{\partial}{\partial x_j}u_i(x_1,x_2,x_3,t)\frac{dx_j}{dt}\Big]\Big|_{\Gamma^*_{kl}}. \tag{3}$$

It is obvious that $\left(\frac{dx_1}{dt}, \frac{dx_2}{dt}, \frac{dx_3}{dt}\right)$ are the components of the velocity vector $\underline{\vartheta}(t)$, if we take into account that the boundary of the phase transition is moving on normal vector, then the speed of moving boundary we will define by the following expression

$$\underline{\vartheta}(t) = -\frac{\partial\Phi}{\partial t}\frac{\underline{grad}\Phi}{|\underline{grad}\Phi|^2},$$

and condition (3) takes the form

$$\Big[\frac{\partial u_i}{\partial t}\Big]\Big|_{\Gamma^*_{kl}} = -\vartheta_m\Big[\frac{\partial u_i}{\partial x_m}\Big]\Big|_{\Gamma^*_{kl}}. \tag{4}$$

Similarly, differentiating with respect to time, the condition (2) and taking into account

$$\frac{d}{dt}\Big([\sigma_{ij}]n_j\Big|_{\Gamma^*_{kl}}\Big) = \Big(\frac{\partial([\sigma_{ij}]n_j)}{\partial t} + \vartheta_m\frac{\partial([\sigma_{ij}]n_j)}{\partial x_m}\Big)\Big|_{\Gamma^*_{kl}},$$

we get

$$\Big(\frac{\partial[\sigma_{ij}]}{\partial t}n_j + \frac{\partial n_j}{\partial t}[\sigma_{ij}] + \vartheta_m\frac{\partial[\sigma_{ij}]}{\partial x_m}n_j + \vartheta_m\frac{\partial n_j}{\partial x_m}[\sigma_{ij}]\Big)\Big|_{\Gamma^*_{kl}} = 0. \tag{5}$$

For the components of the normal vector we have the following equality

$$n_j = \frac{\partial\Phi}{\partial x_j}\Big(\frac{\partial\Phi}{\partial x_m}\frac{\partial\Phi}{\partial x_m}\Big)^{-\frac{1}{2}}.$$

If we differentiate to time this, we obtain the connection between of components the velocity of normal and the equation of surface

$$\frac{\partial n_j}{\partial t} = \Big(\frac{\partial^2\Phi}{\partial t\partial x_j}\Big)\cdot\frac{1}{|\underline{\nabla}\Phi|} + \frac{|\vartheta|}{|\underline{\nabla}\Phi|}n_j.$$

Conditions (4) - (5) close the boundary value problem of elasticity theory for a layered material with consolidating the layers.

Using the proposed model was obtained by numerical solution of the problem of determining the thermal stresses in the process of formation:

(1) layered rod, glass-aluminum-steel, aggregation state changes in the middle layer for the elastic approximation (Fig. 1 a), b), c));

(2) three-layer cylindrical shell of aluminum -glass-aluminum, aggregation state changes in outer layers for the elastic approximation (Fig. 1 d), e), f)).

Fig . 1 (a) shows the position boundary of the phase transition in time. Fig. 1 (b) shows the plots of stress intensity from time in the middle layer at the border contacts, it shows that the interval of time, when the layer is crystallized, the stress intensity grows much faster, that may be explained the existence structural deformation during crystallization. Fig. 1 (c) shows the plots of stress intensity of upper graph and stresses lower graph from the radial coordinate at the finite of moment time. Similar graphs were made and show on Fig. 1 (d), (e), (f). But on some initial moment of time two boundaries of the phase transition are in the presence of, this is reflected in the graph Fig. 1 (d).

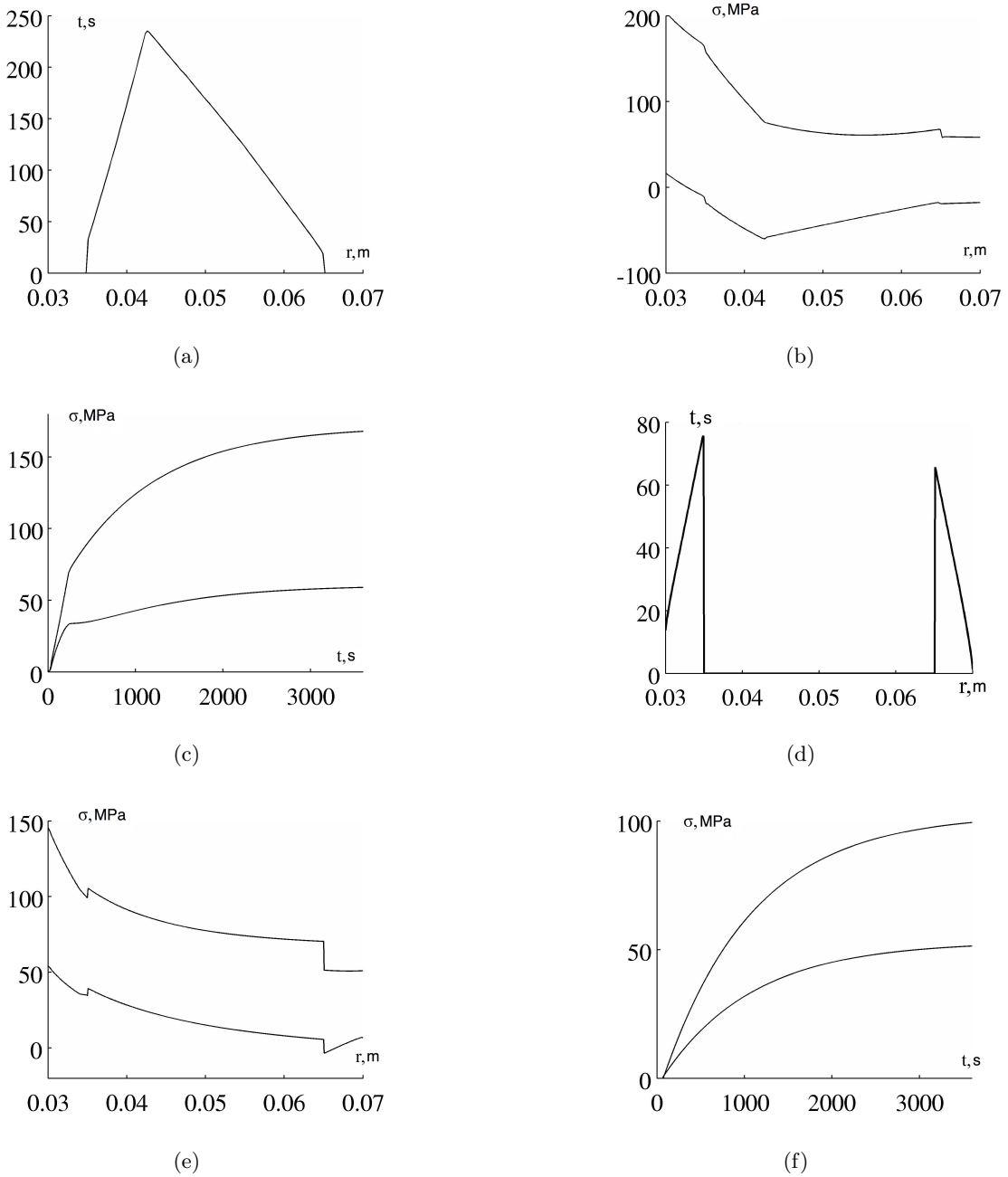


(a) (b) (c) (d) (e) (f)

Figure 1: The results of numerical solution for composites glass-aluminum-steel and aluminum-glass-aluminum in the elastic approximation

The results are qualitatively consistent about mechanical representations of the deformation process, taking into account the crystallization.

## References

[1] Patent No 2428389 RF, MPK C03C 27/02. Method of making steklometallokompozita / Gridasova E. L., Lyubimova O.N., Pestov K.N., Kayak G. L.- No 2009149794; Zayav. 31.12.2009; Opubl. 10.09.2011, Bul. No 25.- 6 p.

[2] Eremeev V.A., Zubov L.M. Uslovia fazovogo ravnovesia v nelineyno-uprugix sredax s mikrostrukturoy // Doklad AN. - 1992. - T. 322. - No 6. - T. 1052-1056

[3] Kondaurov V.I., Fortov V.E. Osnovi termomexaniki kondensirovanix sred - M.: MFTI, 2002. - 336 p.

[4] Grinfeld M.A. Metodi mexaniki sploshnix sred v teory fazovix prevrasheniy. - M.: Nauka, 1990. - 312 p.

[5] Morozov N.F., Freidin A.B. Zoni fazovix perexodov i fazovie prevrasheniy uprugix tel pri razlichnix vidax napryagenogo sostoyaniya //Tr. matem. in-ta im. V.A. Steclova - 1998. - T. 223. - No 2. - P. 220-232.

[6] Aratynyan N.X., Manshirov A. V., Naumov V.E. Kontaktnie zadachi mexaniki rastushix tel. M.: Nauka, 1991.-176 p.

[7] Lyubimova O. N., Pestov K.N., Gridasova E.A. Numerical solution of problem fusion penetration metal, when glass welds metal by diffusion welding // Proceedings of international summer smhool “Advanced Problems in Mechanics”.-St. Petersburg: IPME - 2010. - P. 419-425.

*Olga N. Lyubimova, Vladivostok, Russia*
*Konstantin N. Pestov, Vladivostok, Russia*

# Quasi-particles associated with surface acoustic wave (SAW) modes

Gérard A. Maugin Martine Rousseau
gerard.maugin@upmc.fr

**Abstract**

Following along the line of recent works, the present paper introduces the notion of quasi-particles that are associated with surface acoustic waves (essentially Rayleigh and shear horizontal waves) of different types via canonical conservation laws. The emphasis is placed on original cases and on various type of perturbations. The established wave-quasi-particle dualism is illustrated in the transmission-reflection problem at interfaces.

## 1 Introduction

In recent works (see [1], [2], [3], [4]), influenced by the theories of phonons in solid state physics and of solitons in mathematical physics, we have expanded a theory of *quasi-particles* that are associated with surface acoustic wave (SAW) modes. These particles we nicknamed "grains of SAWs" [5]. This association akin to a dualism is obtained, once we know the continuum solution of the SAW problem, by exploiting the so-called canonical equations of conservation of wave momentum and energy — see [6] for this general concept. These equations are obtained by any means (e.g., application of Noether's invariance theorem [7] in the case of nondissipative systems for which we know the Lagrangian; or direct manipulation of the standard balance laws in the presence of dissipation). Special attention was paid to SAWs of the Rayleigh type or, when they exist, pure shear-h! orizontal (SH) waves, e.g., on account of some piezoelectric coupling (so-called Bleustein-Gulyaev SAWs [8]) or when the boundary is a material surface endowed with its own mechanical properties (elasticity and inertia; case of so-called Murdoch SAWs [9]). Perturbations by various means may be considered (dispersion, viscosity in the substrate [4], nonlinearity of the substrate [3]).

In each case, the applied methodology consists in evaluating the expression of the "mass" and the accompanying "kinetic energy" of the associated quasi-particle. This is done by integrating the local conservation laws of wave momentum (cf. Brenig [10] for this notion) over a material volume that is representative of the studied wave motion. In propagation space this amounts to an average over one wavelength. Then one has to substitute for the known analytical wave solution in the resulting equations. For linear waves and also a weakly nonlinear perturbation [3] the obtained motion of the associated quasi-particle is Newtonian and inertial. In the presence of dissipation the motion naturally becomes non-inertial with an effect of friction [4]. The accompanying point-wise energy equation is Leibnizian (strict conservation of kinetic energy or *vis viva*) or with a source term corresponding to the power expended by a friction ! force.

The aim of this contribution is to present in one place but in a condensed manner most of the relevant results exhibiting well an existing wave-quasi-particle dualism that offers

an alternate view of elastic wave problems, in particular in crucial reflection-transmission problems as useful in non-destructive evaluation (NDE) techniques.

## 2 The notions of conservation law, wave momentum and quasi-particle

Although not sufficiently emphasized in most works by engineers, there exists a fundamental difference between *field equations* that govern individual degrees of freedom of a physical system and *conservation laws* that pertain to the whole considered system. This difference was first made clear by Emmy Noether in her celebrated theorem of 1918, probably the most fruitful theorem of mathematical physics of the 20th century [7]. For example, referring to continuum solid mechanics in small strains the *field equation* (so-called balance of -physical- linear momentum) reads in Cartesian index notation in the absence of body force and for a volume element

$$\frac{\partial}{\partial t}(\rho_0\,\dot{u}_i) - \frac{\partial}{\partial x_j}\sigma_{ji} = 0, \tag{1}$$

where $\rho_0$ is the matter density at the reference configuration, $u_i$ denotes the three components of the displacement, $\dot{u}_i$ denotes the corresponding velocity, and $\sigma_{ji}$ stands for the symmetric Cauchy stress. This applies to elasticity, anelasticity, isotropic and anisotropic bodies, in the presence or absence of material inhomogeneities. Equation (1) pertains to *the* displacement component $u_i$. In contrast, the local balance of energy governs *all* degrees of freedom simultaneously and reads in the absence of external source of energy

$$\frac{\partial}{\partial t}\left(\frac{1}{2}\,\rho_0\,\dot{\mathbf{u}}^2 + E\right) - \frac{\partial}{\partial x_j}(\sigma_{ji}\,\dot{u}_i - Q_j) = 0, \tag{2}$$

where $E$ is the internal energy per unit volume and $Q_j$ denotes the components of the (in)flux of heat. Equation (2) in fact is *a true conservation law* for the considered thermomechanical physical system. It reflects its invariance under time translations. It is not the only conservation law as we should in parallel consider the invariance under spatial parametrization (material coordinates). The resulting equation is called the conservation of material (or pseudo-) momentum and generally reads [6]

$$\frac{\partial}{\partial t}P_i - \frac{\partial}{\partial x_j}b_{ji} = f_i^S, \tag{3}$$

where

$$P_i = -\rho_0\,\dot{u}_j\,u_{j,i}, \quad b_{ji} = -\left(\frac{1}{2}\,\rho_0\,\dot{\mathbf{u}}^2 - W\right)\delta_{ji} - \sigma_{j,k}\,u_{k,i}. \tag{4}$$

Here $b_{ji}$ is referred to as the Eshelby (material) stress, $W = E - \theta\,S$, is the free energy density, $S$ is the entropy density, $\theta$ is the thermodynamical temperature, and the "force" source term $f_i^S$ accounts for effects of true material inhomogeneities, thermal and anelastic effects, if any, all in the form of "*forces of inhomogeneity*" [6]. Equation (2) can also be re-written as [6]

$$\frac{\partial}{\partial t}(S\,\theta) + \frac{\partial}{\partial x_i}Q_i = h^S, \tag{5}$$

where the heat source term $h^S$ also accounts for thermal and anelastic effects. For a perfectly homogeneous (but possibly anisotropic) purely elastic body $f_i^S$ vanishes identically

and (3) becomes a *strict* (covariant) *conservation law* reflecting an invariance under translation of material coordinates. This case follows from the application of Noether' theorem relating to the invariance under material space parametrization. Otherwise, equations (3) and (5) are deduced from the standard equations (1) and (2) through manipulations. If equations (1) is traditionally used to solve static and dynamic (wave) problems on account of prescribed boundary and initial conditions, the additional equation (3) must be exploited in a second step, such as in a post-processing procedure. The book [6] is devoted to such applications in fracture, shock waves, phase transitions, nonlinear waves and numerical schemes. In the present setting we propose to exploit equation (3) with a view to associating a quasi-particle vision to linear wave processes of a certain type (e.g., acoustic surface waves propagating on the top of a substrate once the analytical wavelike solution is known). In particular, an interesting quantity here is the so-called quasi-particle (wave) momentum obtained by evaluating the average of $P_i$ over a volume element most representative of the studied wave process, i.e., symbolically

$$P_i^{QP} = < P_i > . \tag{6}$$

Then equation (3) will yield the "equation of motion" of the associated quasi-particle by integration over this volume. The same procedure is applied to the energy equation. The effective "mass" of the quasi-particle is evaluated in the procedure. For lack of space we shall not give details of computations that can be cumbersome in spite of their straightforwardness.

## 3 Rayleigh surface waves

### A. Standard Rayleigh SAWs

In this case, $x_1$ being in the propagation direction and $x_2$ in the depth direction, both equation (1) and the homogeneous form of equation (3) valid in the substrate (half space) $x_2 > 0$ are complemented by boundary conditions at $x_2 = 0$ (free boundary) and limit conditions at $x_2 \to \infty$ (vanishing of the amplitude). This standard Rayleigh SAW in a linear homogeneous isotropic substrate concerns an elastic displacement polarized parallel to the $(x_1, x_2)$ sagittal plane $\Pi_S$. The Rayleigh solution is well known [11]. Its "dispersion" relation reads

$$D(c_R; c_T, c_L) \equiv 4\sqrt{1-(c_R/c_T)^2}\,\sqrt{1-(c_R/c_L)^2} - \big(2-(c_R/c_T)^2\big)^2 = 0, \tag{7}$$

where longitudinal and transverse wave speeds are given by

$$c_L = \sqrt{\frac{\lambda+2\,\mu}{\rho_0}}, \quad c_T = \sqrt{\frac{\mu}{\rho_0}}, \tag{8}$$

in terms of Lamé's coefficients $\lambda$ and $\mu$. The above sketched out procedure with wave-representative volume element $\Omega = [x_{10}, x_{10}+\lambda^w] \times [0, +\infty) \times [0, 1]$ — where $\lambda^w$ is one wave length chosen at any place $x_{10} = (x_1)_0$ along the path of the wave — is shown to yield a *Newton-like* point-particle equation of motion in the $x_1$ direction as

$$\frac{\mathrm{d}}{\mathrm{d}t}(M_R\, c_R) = 0 \tag{9}$$

where $c_R$ is the solution of (7) and the "mass" is given by an expression

$$M_R = \rho_0\, \pi\, f(k_R, \alpha_L, \alpha_T)\, U^2, \tag{10}$$

where $f$ is a complicated expression in terms of the Rayleigh wave number $k_R$ and the depth attenuation coefficients of the longitudinal ($\alpha_L$) and transverse ($\alpha_T$) components [2]. The mass $M_R$ depends on all characteristic parameters of the SAW. What is important here is the fact that this mass is proportional to the square of the amplitude of the wave hence to its energy. This is an essential property of all quasi-particles exhibited in this contribution. With some more work it can be shown that the volume integral of the energy equation proves that the kinetic energy of the point-like quasi-particle is constant:

$$E = \frac{1}{2}\, M_R\, c_R^2 = const., \tag{11}$$

so that the motion is not only Newtonian but also Leibnizian.

### B. Perburbed Rayleigh SAWs

Several cases of perturbation of the above reported ideal case have been studied. The simplest case is that of a perturbation by a *surface energy* distributed on the limiting surface $x_2 = 0$ [2]. The pathological case where the elastic medium at $x_2 = 0$ is in contact with a low-density inviscid fluid medium which occupies the half-space $x_2 < 0$ is also of interest. The Rayleigh wave associated with the semi-infinite elastic medium is then perturbed by the existence of the fluid and it becomes a *leaky* Rayleigh wave. This is examined in Ref. [2] yielding a nonsensical situation that can only be solved by the theory of *bounded beams* in the framework of wave theory (cf. [12]). The question of how to remedy this deficiency in the quasi-particle framework is unsettled.

## 4 SH and Bleustein-Gulyaev (BG) waves

### 4.1 Standard BG SAWs

Shear-horizontal (SH) SAWs are in principle much simpler than Rayleigh SAWS because they involve only *one* displacement component $u_3$ orthogonal to the sagittal plane $\Pi_S$, but they exist only in specific conditions usually related to a perturbation of some kind of the boundary conditions at the surface of the substrate (see, e.g., [13]). Such conditions are obtained by coupling with electric properties in piezoelectric materials of 6mm symmetry axis orthogonal to $\Pi_S$ (see Chapter 4 in [8]). These SAWs were discovered by Bleustein and Gulyaev in 1968. Their associated quasi-particles and their perturbations are particularly easy to study in the present framework although coupling with quasi-electrostatics for dielectrics is necessary. Equation (1) is replaced by the system

$$\frac{\partial}{\partial t}(\rho_0\, \dot{u}_i) - \frac{\partial}{\partial x_j}\sigma_{ji} = 0, \quad \frac{\partial}{\partial x_i} D_i = 0, \tag{12}$$

with constitutive equations

$$\sigma = -\frac{\partial L}{\partial \mathbf{e}} = \frac{\partial W}{\partial \mathbf{e}}, \quad \mathbf{D} = \frac{\partial L}{\partial \mathbf{E}} = \varepsilon_0\, \mathbf{E} + \mathbf{P}, \quad \mathbf{P} = -\frac{\partial W}{\partial \mathbf{E}}, \tag{13}$$

where

$$L = \frac{1}{2}\, \rho_0\, \mathbf{v}^2 + \frac{1}{2}\, \varepsilon_0\, \mathbf{E}^2 - W(\mathbf{e}, \mathbf{E}), \tag{14}$$

and

$$W(\mathbf{e}, \mathbf{E}) = \frac{1}{2}\, C_{ijkl}\, e_{ij}\, e_{kl} - e_{qij}\, E_q\, e_{ij} - \frac{1}{2}\, \chi_{ij}\, E_i\, E_j. \tag{15}$$

Here $\mathbf{D}$ is the electric displacement, $\mathbf{e}$ is the small strain, $\mathbf{E}$ is the electric field and, $L$ is a Lagrangian density. The three terms in (15) stand for elasticity, piezoelectricity and electric polarization properties *per se*. For the sake of example the field equations (12) are complemented by boundary conditions at the limiting plane $x_2 = 0$ (mechanically free but electrically grounded boundary)

$$n_j\,\sigma_{ji} = 0, \quad \phi = \phi_0 = 0, \quad n_j\,D_j = w, \tag{16}$$

where $\phi$ is the electric potential (such that $E_i = -\partial\phi/\partial x_i$) and $w$ is an eventual surface charge density.

The energy equation is now given by

$$\frac{\partial}{\partial t}\left(\frac{1}{2}\,\rho_0\,v^2 + W - \frac{1}{2}\,\varepsilon_0\,\mathbf{E}^2\right) - \frac{\partial}{\partial x_j}\left(\sigma_{ji}\,\frac{\partial u_i}{\partial t} + D_j\,\frac{\partial\phi}{\partial t}\right) = 0. \tag{17}$$

It is shown [1] that equations (3)–(4) are replaced by

$$\frac{\partial}{\partial t}P_i - \frac{\partial}{\partial x_j}b_{ji} = 0, \tag{18}$$

and

$$P_i = -\rho_0\,\dot{u}_j\,u_{j,i}, \;\; b_{ji} = -\left(\frac{1}{2}\,\rho_0\,\dot{\mathbf{u}}^2 - W + \frac{1}{2}\,\varepsilon_0\,\mathbf{E}^2\right)\,\delta_{ji} - \sigma_{j,k}\,u_{k,i} - D_j\,\phi_i. \tag{19}$$

The standard solution of the BG surface wave is now well known via the introduction of an effective electric potential that accounts for the electromechanical coupling (cf. [8], Chapter 4). The corresponding point thermo-mechanics of the associated quasi-particle is obtained in the Newtonian-Leibnizian following form form [1]:

$$\frac{\mathrm{d}}{\mathrm{d}t}P_{BG} = 0, \quad \frac{\mathrm{d}}{\mathrm{d}t}K_{BG} = 0, \tag{20}$$

wherein

$$P_{BG} := M_{BG}\,c_{BG}, \quad K_{BG} = \frac{1}{2}\,M_{BG}\,c_{BG}^2, \quad M_{BG} = \frac{\rho_0\,\pi\,U^2}{2\,\overline{K}^2}, \tag{21}$$

with

$$\bar{c}_T^2 = \bar{c}_{44}/\rho_0, \;\; \bar{c}_{44} = c_{44}\,(1+K^2), \;\; K^2 = e_{15}^2/\varepsilon_{11}\,c_{44}, \;\; \overline{K}^2 = K^2/(1+K^2), \tag{22}$$

corresponding to the "dispersion" relation

$$D(\omega, k_1) := \omega^2 - c_{BG}^2\,k_1^2, \quad c_{BG} = \omega/k_{BG} = \sqrt{(\bar{c}_{44}/\rho_0)\,(1-\overline{K}^4)}. \tag{23}$$

In these equations, $c_{44}$, $e_{15}$ and $\varepsilon_{11} = \varepsilon_0 + \chi_{11}$ are the only surviving material coefficients of the general anisotropic expression (20) for the considered symmetry. The results (20)–(21) are particularly simple with a momentum $P_{BG}$ in the $x_1$ propagation direction, a mass $M_{BG}$ that is naturally quadratic in the wave amplitude, and a quasi-particle kinetic energy $K_{BG}$ that appears purely kinetic (via the mass $M_{BG}$) although originating in the continuum framework from kinetic, elastic, piezoelectric and electrostatic energies altogether. The BG solution (wavelike or particle-like) does not exist when the electromechanical coupling factor $K$ vanishes. It is the relative simplicity of the obtained solution that made the authors envisage several types of perturbations.

### 4.2 Bleustein-Gulyaev SAWs perturbed by a weak elastic nonlinearity

We contemplate the case where the volume energy (15) is augmented by a non-quadratic elastic term to be treated further as a perturbation. This was recently treated in Ref.[3]. For the considered BG configuration, the pure elastic contribution in (15) is now written as

$$W^{elas} = \frac{1}{2}\, c_{44}\, \Phi + \frac{1}{4}\, \beta\, c_{44}\, \Phi^2 + h.o.t, \tag{24}$$

where $h.o.t$ means higher order terms that are to be neglected and $\beta$ is the small elastic nonlinearity coefficient, and $\Phi = (u_{3,1})^2 + (u_{3,2})^2$. The elastic energy now is a quartic, what means that the system becomes a generator of *third harmonic*. It is shown that the problem for $x_2 > 0$ is reduced to the system

$$\bar{c}_{44}\, \nabla^2 u_3 + \beta\, \bar{c}_{44}\, [(\Phi\, u_{3,1})_{,1} + (\Phi\, u_{3,2})_{,2}] = \rho_0\, \ddot{u}_3, \quad \nabla^2 \psi = 0, \tag{25}$$

where $\nabla^2$ is the two-dimensional Laplacian in the $(x_1, x_2)$ plane and $\Psi$ is the same effective electric potential as in the above recalled linear BG case. The boundary conditions at $x_2 = 0$ are formally unchanged compared to the linear case. The general form of equations (12) and (17)–(19) is unchanged but for the elastic nonlinearity. But the propagating wave solution now involves first and third harmonics of the basic frequency $\omega$. For instance, the $u_3$ has the form

$$\begin{aligned} u_3 = {} & U\, \exp(-\alpha\, x_2)\, \cos(k\, x_1 - \omega\, t) \\ & + \beta\, U^3\, \exp(-3\, \alpha\, x_2)\, \cos(3\, (k\, x_1 - \omega\, t)) + \mathcal{O}(\beta^2), \end{aligned} \tag{26}$$

where $\alpha$ (a part of the solution) measures the exponential decrease of the amplitude with depth in the substrate. The amplitude-dependent "dispersion" relation at order $\beta$ now reads:

$$D(\omega, k, \alpha) := \omega^2 - \frac{\bar{c}_{44}}{\rho_0} \left[ (k^2 - \alpha^2) - \frac{\beta}{4}\, U^2\, \mathrm{e}^{-2\, \alpha\, x_2}\, (9\, \alpha^4 - 3\, k^4 + 2\, k^2\, \alpha^2) \right] = 0. \tag{27}$$

In the treatment of the associated quasi-particle, the relevant representative domain of integration of the conservation equation is given by $\Omega = [0, \lambda_S] \times [0, +\infty) \times [0, 1]$, where $\lambda_S = 2\, \pi / k_S$ is the wavelength of the first harmonic component *as altered by the nonlinearity*. On account of the smallness of $\beta$ it can be proved [3] that the following Newton and Leibniz equations of motion and energy are obtained (the system still is non dissipative involving no source terms in its quasi-particle solution):

$$\frac{\mathrm{d}}{\mathrm{d}t}(M_{BGNL}\, c_{BGNL}) = 0, \quad \frac{\mathrm{d}}{\mathrm{d}t} \left( \frac{1}{2}\, M_{BGNL}\, c_{BGNL}^2 \right) = 0, \tag{28}$$

with, at order $\beta$,

$$M_{BGNL} = M_{BG} \left[ 1 - \frac{\beta}{4}\, (3\, \overline{K}^4 - 1)\, k_{BG}^2\, U^2 \right], \tag{29}$$

$$\lambda_S = \frac{2\, \pi}{k_0} \left[ 1 - \beta\, \frac{\bar{k}_S}{k_0} \right] = \lambda_{BG} \left[ 1 - \beta\, \frac{\bar{k}_S}{k_{BG}} \right], \tag{30}$$

$$c_{BGNL} = c_S = \frac{\omega}{k_S} = c_{BG} \left[ 1 - \beta\, \frac{\bar{k}_S}{k_{BG}} \right]. \tag{31}$$

It is observed that the wave number correction $\bar{k}_S$ is negative, and both the mass and the kinetic energy of the quasi-particle are increased compared to those of the linear case. Note that the two equations (28) are proved independently of one another, all quantities labelled BG relating to the linear case.

### 4.3 Bleustein-Gulyaev SAWs perturbed by a weak viscosity of the elastic substrate

This case is treated in detail in Ref. [4] to which the reader is referred. Both equations (17) and (18) acquire source terms in their right-hand sides. This is treated in the case of a wavelike solution perturbed by an added small viscosity of the substrate. The latter was obtained in Ref. [14] to which we refer the reader. The quasi-particle motion becomes non-inertial with a source term due to a friction. Simultaneoulsy, the associated kinetic energy is no longer conserved. This case is distinctly remarkable in that the "mass" becomes a function of time and the associated quasi-particle momentum is no longer strictly parallel to the plane boundary: at order $\varepsilon$, the motion of our quasi-particle has become two-dimensional in the sagittal place.

## 5 Other case: Murdoch SAWs

The reader may be deceived by the fact that we did not treat the case of Love SAWs (pure SH SAWs existing as a result of the superimposition of a "slow" elastic layer of finite thickness on top of the linear elastic substrate). The reason is due to the difficulty of carrying the required analysis to its end. Fortunately, another model that also involves a unique SH displacement is the one introduced by Murdoch [9]. This model is particularly interesting because (i) of its purely mechanical nature, (ii) of its relative simplicity with a *dispersive monomode* of propagation only (thus much simpler than the *dispersive multimode* Love SAWs that need the consideration of a superimposed layer of small but finite thickness), and (iii) it lends itself to remarkably simple computations. It may be said that it also corresponds to the *very thin plate limit* considered by Tiersten and co-workers [15]–[16] in thei! r study of signal-processing devices (wavelength of signal much larger than the thickness of the superimposed layer). The basic field equations are

$$\rho_0 \frac{\partial^2 u_i}{\partial t^2} = \frac{\partial}{\partial x_j}\sigma_{ji} \qquad \text{for } x_2 > 0; \tag{32}$$

$$\hat{\rho}_0 \frac{\partial^2 \hat{u}_i}{\partial t^2} = \frac{\partial}{\partial \hat{x}_j}\hat{\sigma}_{ji} - n_j\, \sigma^+_{ji} \qquad \text{at } x_2 = 0. \tag{33}$$

Region $x_2 < 0$ is considered a vacuum. Here superimposed carets refer to quantities related to the surface of unit outward oriented normal $n_j$. Thus $\hat{\sigma}_{ji}$ is a surface stress while $\sigma^+_{ji} = \lim \sigma_{ji}$, $x_2 \to 0^+$ is the three-dimensional stress from the body. Mass density $\hat{\rho}_0$ is per unit surface, so that the limiting surface is endowed both with inertia and elasticity; it is a "*material*" surface. System (32)–(33) admits a pure SH SAW solution. We note

$$c_T^2 = \frac{\mu}{\rho_0}, \quad \hat{c}_T^2 = \frac{\hat{\mu}}{\hat{\rho}_0}, \quad k_a^2 = \frac{\mu}{\hat{\mu}}. \tag{34}$$

The resulting SH SAW solution $u_3$ of (32)–(33) has a (true) dispersion relation given by

$$D(\omega, k_1) := \omega^2 - c_T^2\left(k_1^2 - \frac{1}{k_a^2}\left(\frac{\omega^2}{\hat{c}_T^2} - k_1^2\right)^2\right) = 0, \tag{35}$$

and the solution exists only for phase velocities $c$ such that $\hat{c}_T < c = c_M < c_T$. It is shown [17] that the canonical conservation laws of wave momentum and energy are obtained by combining those associated with the surface motion at $x_2 = 0$ with the volume

ones integrated over the depth in the substrate. The final result is a quasi-particle with Newtonian-Leibnizian properties, i.e,

$$\frac{\mathrm{d}}{\mathrm{d}t}(M_M\, c_M) = 0, \quad \frac{\mathrm{d}}{\mathrm{d}t}\left(\frac{1}{2}\, M_M\, c_M^2\right) = 0 \tag{36}$$

with mass given by [17]

$$M_M = \left(\hat{\rho}_0 + \frac{\rho_0}{2\,\alpha}\right) U^2\, \pi\, k_M, \quad k_M = k_1 = \frac{2\,\pi}{\alpha_M}, \tag{37}$$

$\alpha$ being the attenuation coefficient in depth such that

$$\alpha = \left(\frac{c^2}{\hat{c}_T^2} - 1\right) \frac{k_1^2}{k_a}, \tag{38}$$

hence a function of the wavelength. This provides an original example of quasi-particle associated with a *dispersive* SAW.

# 6 An example of practical problem: transmission and reflection

## 6.1 Perfect interface between two solids

For the sake of simplicity we discard the attenuation in depth of the wave and thus consider a propagating SH face wave. Propagation from left (medium 1) to right (medium 2) is described by the following equations in 1D linear elasticity:

$$\frac{\partial p}{\partial t} - \frac{\partial \sigma}{\partial x} = 0, \quad p = \rho\, \frac{\partial u}{\partial t}, \quad \sigma = \mu\, \frac{\partial u}{\partial x} \tag{39}$$

in media 1 and 2, and matching conditions at $x = 0$

$$u_1 = u_2, \quad \mu_1\, u_{1,x} = \mu_2\, u_{2,x}. \tag{40}$$

In each medium, the "dispersion" relation reads

$$D(\omega, k) = \omega^2 - c^2\, k^2 = 0, \quad c = (\mu/\rho)^{1/2}. \tag{41}$$

The general solution in media 1 and 2 is written

$$u_1 = u_I + u_R, \quad u_2 = u_T \tag{42}$$

with

$$u_1 = U\, \cos(k_1\, x - \omega\, t) + R_0\, U\, \cos(k_1\, x + \omega\, t), \;\; u_2 = T_0\, U\, \cos(k_2\, x - \omega\, t), \tag{43}$$

where subscripts $I$, $R$ and $T$ refer to the incident, reflected and transmitted signals, respectively. The conservation of energy flux stands in the well known form

$$F_0 = 1 - R_0^2 - (z_2/z_1)\, T_0^2 \equiv 0. \tag{44}$$

where $R_0$ and $T_0$ are the reflection and transmission coefficients such that ($z_\alpha = \rho_\alpha\, c_\alpha$, $\alpha = 1, 2$, are impedances)

$$R_0 = \frac{z_1 - z_2}{z_1 + z_2}, \quad T_0 = \frac{2\, z_1}{z_1 + z_2}. \tag{45}$$

In the associated quasi-particle picture the local conservation laws of wave momentum and energy read in each medium

$$\frac{\partial H}{\partial t} - \frac{\partial Q}{\partial x} = 0, \quad \frac{\partial P}{\partial t} - \frac{\partial b}{\partial x} = 0, \tag{46}$$

where the energy or Hamiltonian per unit volume $H$, the energy flux $Q$, the wave momentum $P$ and the (here reduced to a scalar) Eshelby stress $b$ are defined by (see [6] for the canonical definitions in three dimensions)

$$H = E + W = \frac{1}{2}\,\rho\, u_{,t}^2 + \frac{1}{2}\,\rho\, u_{,x}^2, \quad Q = \sigma\, u_t = \mu\, u_{,x}\, u_{,t} \tag{47}$$

$$P = -\rho\, u_{,t}\, u_{,x}, \quad b = -(L + \sigma\, u_{,x}), \quad L = H - \sigma\, u_{,x}. \tag{48}$$

With the perfect interface at $x = 0$, we can associate one quasi-particle with each wave component of the problem. With an obvious notation we have the following "masses":

$$M_I = \rho_1\, k_1\, \pi\, U^2, \quad M_R = \rho_1\, k_1\, \pi\, R_0^2\, U^2, \quad M_T = \rho_2\, k_2\, \pi\, T_0^2\, U^2. \tag{49}$$

The corresponding averaged wave momenta are given by

$$\overline{P}_I \equiv < P_I > = \rho_1\, \omega\, \pi\, U^2 \tag{50}$$

$$\overline{P}_R \equiv < P_R > = -\rho_1\, \omega\, \pi\, R_0^2\, U^2, \quad \overline{P}_T \equiv < P_T > = \rho_2\, \omega\, \pi\, T_0^2\, U^2 \tag{51}$$

where we account for the fact that the averaged wave momentum $\overline{P}_R$ is oriented towards negative $x'$s. We note $\Delta M$, $\Delta\overline{P}$, and $\Delta\overline{H}$ the possible misfits in mass, momentum and kinetic quasi-particle kinetic energy defined by

$$\Delta M := M_R + M_T - M_I, \tag{52}$$

$$\Delta\overline{P} = |\overline{P}_R| + |\overline{P}_T| - |\overline{P}_I|, \tag{53}$$

$$\Delta\overline{H} = \overline{H}_R + \overline{H}_T - \overline{H}_I, \tag{54}$$

where the symbolism $|\ldots|$ refers to the absolute value of its enclosure. That is, we are comparing the strengths of the momenta and, therefore, we are not effecting a vectorial balance. We say that a quantity is conserved during the transmission-reflection problem if the corresponding misfit vanishes. It is shown that

$$\Delta\overline{H} = \left(\frac{1}{2}\, z_1\, \omega\, \pi\, U^2\right) F_0, \tag{55}$$

where $F_0$ has been defined in (44). But the latter vanishes. Accordingly, $\Delta\overline{H} \equiv 0$: *kinetic energy is conserved* in the transmission-reflection problem seen as a quasi-particle process that may be qualified of Leibnizian (conservation of *vis-viva*). But "mass" and momentum are not generally conserved in the present problem as it is immediately shown that [18]

$$\Delta M = \rho_2\, k_2\, \pi\, T_0^2\, U^2 \left(\frac{c_1^2 - c_2^2}{c_1^2}\right), \tag{56}$$

$$\Delta\overline{P} = \left(\frac{c_1\, c_2}{c_1 + c_2}\right) \Delta M, \tag{57}$$

so that $\Delta\overline{P}$ and $\Delta M$ always are in the same sign. In particular, $\Delta M > 0$ if $c_1 > c_2$ and $\Delta M < 0$ if $c_1 < c_2$; $\Delta M = 0$ if and only if $c_1 = c_2$.

### 6.2 Imperfect interface with possible delamination

In the case of an *imperfect interface with possible delamination* where the matching conditions (45) are replaced by the conditions (known as Jones' conditions [19])

$$\sigma_1 = \sigma_2 \equiv K\,[u], \tag{58}$$

where $K$ is a positive (spring) coefficient characterizing the degree of delamination and the symbol [..] means the jump of its enclosure, i.e., $[u] = u_2 - u_1$ at $x = 0$. We must look for *complex* solutions of the type $u = A\,\exp(i\,(k\,x - \omega\,t))$. Conditions (58) yield the following equation that replaces (44) — now $|R|$ and $|T|$ are the moduli of complex reflection and transmission coefficients:

$$F_K = 1 - |R|^2 - (z_2/z_1)\,|T|^2 \equiv 0. \tag{59}$$

It is shown that [18]

$$F_K = F_0 \left( 1 - \frac{z_1^2\, z_2^2}{z_1^2\, z_2^2 + (K/\omega)^2\,(z_1 + z_2)^2} \right). \tag{60}$$

The solution of this imperfect interface case is characterized by the parameter $K/\omega$ which shows the role played by the frequency $\omega$. The limit case $K \to \infty$ corresponds to the *perfect interface* for which (44) holds true. The limit case $K \to 0$ corresponds to *full delamination* (no more transmission and complete reflection: $T = 0$, $R = 1$).

In the *associated quasi-particle picture*, there is no need to redo the computations. It suffices to replace the transmission and reflection coefficients of the perfect case by the moduli of the new complex coefficients. Thus (55) is replaced by

$$\Delta\overline{H} = \left( \frac{1}{2}\, z_1\, \omega\, \pi\, U^2 \right) F_K. \tag{61}$$

But this also vanishes by virtue of (59). Similarly, (56) holds with $T_0^2$ replaced by $|T|^2$ while (57) remains unchanged, noting that the coefficient $c_1\, c_2/(c_1 + c_2)$ does not depend on $K$. In the case when $K \neq 0$ but media 2 and 1 are identical, the presence of the $K$ spring distribution can simulate a homogeneous surface of damage. In this case, both $\Delta M$ and $\Delta\overline{P}$ vanish so that $K$ is no longer involved. The dependence on $K$ shows only through the value of any of $M_R$, $M_T$, $\overline{P}_R$ and $\overline{P}_T$.

### 6.3 Case of a sandwiched slab and a multi-layered interface

In the case where an elastic slab (medium 2) of thickness $d$ is sandwiched between two media of elastic type 1, the propagation considered is from left to right with reflection coefficient $R$ in the left medium 1 and transmission coefficient $T$ in the right medium 1. We assume that $d \gg \lambda_2$, where $\lambda_2$ is the (elastic wave) characteristic wavelength of medium 2, so that the association of quasi-particle properties makes sense in the slab. We need not reconsider the wavelike solution. It suffices to apply the results of the foregoing paragraphs to the two interfaces at $x = 0$ (transition $1 \to 2$) and at $x = d$ (transition $2 \to 1$). Just as before $M_I$, $M_R$, $M_T$, $\overline{P}_1$, $\overline{P}_R$ and $\overline{P}_T$ are masses and momenta granted to the quasi-particles in left and right regions 1. We obviously have (compare (54))

$$M_I \propto U^2, \quad M_R \propto |R|\,U^2, \quad M_T \propto |T|\,U^2, \quad |R|^2 + |T|^2 = 1. \tag{62}$$

In an obvious notation we note

$$\Delta M_{11} = (M_R + M_T) - M_I = 0, \tag{63}$$

and

$$\Delta \overline{P}_{11} = \left(|\overline{P}_R| + |\overline{P}_T|\right) - |\overline{P}_I| \equiv 0. \tag{64}$$

Within the slab we distinguish between the particle momentum $\overline{P}^+$ with mass $M^+$ associated with the right motion and particle momentum $\overline{P}^-$ with mass $M^-$ associated with the left motion.

Thus for the interface $x = 0$ we can write

$$\Delta M_{1\to 2} := (M^+ + M^- + M_R) - M_I = (M^+ + M^-) - M_T \neq 0, \tag{65}$$

and

$$\Delta \overline{P}_{1\to 2} = \left(|\overline{P}^+| + |\overline{P}^-| + |\overline{P}_R|\right) - |\overline{P}_I| = \left(|\overline{P}^+| + |\overline{P}^-|\right) - \overline{P}_T \neq 0, \tag{66}$$

while for the interface $x = d$ we have similarly

$$\Delta M_{2\to 1} = M_T - (M^+ + M^-) = -\Delta M_{1\to 2} \neq 0, \tag{67}$$

and

$$\Delta \overline{P}_{2\to 1} = |\overline{P}_T| - \left(|\overline{P}^+| + |\overline{P}^-|\right) = -\Delta \overline{P}_{1\to 2} \neq 0. \tag{68}$$

Note that, logically,

$$\left(|\overline{P}^+| + |\overline{P}^-|\right) = \Delta \overline{P}_{1\to 2} + |\overline{P}_T| \tag{69}$$

while, obviously,

$$R \equiv R_{1\to 2\to 1}, \quad T = T_{1\to 2\to 1}. \tag{70}$$

These two coefficients can be computed in terms of the mechanical properties of media 1 and 2.

### Case of a sandwiched multi-layered structure

With a careful bookkeeping, the formalism and "algebra" just introduced can be applied to the more complicated case where the sandwiched slab is made of a number $n - 1$ of perfectly elastic layers (each with its own elastic properties) numbered $i = 2, \ldots, n$, in perfect contact (cf. [18]).

## 7 Conclusive remarks

The wealth of treated cases shows that the association of the waves of interest and the notion of quasi-particle is not a difficult matter but is limited by the analytical difficulties met in solving the wavelike continuum problem.

## References

[1] Maugin, G. A., Rousseau, M. Bleustein-Galyaev SAW and its associated quasi-particle, Int. J. Engn. Sci., **8**, 1462–1469 (2010)

[2] Rousseau, M., Maugin, G. A. Rayleigh surface waves and their canonically associated quasi-particles, Proc. Royal Soc. Lond., A**467**, 495–507 (2011).

[3] Rousseau, M., Maugin, G. A. Quasi-particles associated with Bleustein-Gulyaev SAWs: perturbations by elastic nonlinearities, Int. J. Non-linear Mechanics, **47**, 67–71 (2012).

[4] Rousseau, M., Maugin, G. A. Influence of viscosity on the motion of quasi-particles associated with surface acoustic waves, Int. J. Engng. Sci., **50**, 10–21 (2012).

[5] Maugin, G. A., Rousseau, M. Grains of SAWs: Associating quasi-particles to surface acoustic waves, Int. J. Engng. Sci., (special issue in honour of V. L. Berdichevsky). Accepted for publication, 2011; to be published in 2012.

[6] Maugin, G. A. Configurational forces: thermodynamics, physics, mathematics and numerics, CRC/Chapman/Taylor and Francis, Boca Raton/New York, USA (2011).

[7] Neuenschwander, D. E. Emmy Noether's wonderful theorem, Johns Hopkins University Press, Baltimore (2011).

[8] Maugin, G. A. Continum mechanics of electromagnetic solids, North-Holland, Amsterdam (1988) [in Russian, Mir, Moscow, 1991].

[9] Murdoch, A. I. The propagation of surface waves in bodies with material boundaries. J. Mech. Phys. Solids, **24**, 137–146 (1976).

[10] Brenig, W. Bessitzen Schallwellen einen Impulz, Zeit. Phys., **143**, 168–172 (1955).

[11] Achenbach, J. D. Wave propagation in elastic solids, North-Holland, Amsterdam (1975).

[12] Bertoni, H. L., Tamir, T. Unified theory of Rayleigh-angle phenomena for acoustic beams at liquid-solid interfaces, Appl. Phys. A. Materials Science & Processing, **2**/4, 157–172 (1973).

[13] Maugin, G. A. Shear horizontal surface acoustic waves on solids. In: Recent developments in surface acoustic waves. Eds D. F. Parker, G. A. Maugin, pp. 158–172, Springer, Berlin (1987).

[14] Rousseau, M., Maugin, G. A. Bleustein-Gulyaev SAWs with low losses: Approximate direct solution, J. Electromagnetic Analysis and Applications, **3**, 122–127 (2011).

[15] Tiersten, H.F. Elastic surface waves guided by thin films, J. Applied Physics, **40**, 770–789 (1969).

[16] Tiersten, H. F., Sinha, B. K., Meeker, T. R. Intrinsic stress in thin films deposited on anisotropic substrates and its influence on the natural frequencies of piezoelectric resonators, J. Applied Physics, **52**, 5614–5624 (1981).

[17] Rousseau, M., Maugin, G. A. Quasi-particle aspects of Murdoch surface acoustic waves, Quart. J. Mech. Applied Math., submitted Sept. 2011.

[18] Rousseau, M, Maugin, G. A. Wave-quasi-particle dualism in the transmission-reflection problem for elastic waves (in progress 2011–2012).

[19] Jones, J. P., Whittier, J. S. Waves at a flexibly bonded interface, J. Appl. Mech. (ASME), **34**/4, 905–908 (1967).

*Gérard A. Maugin, UPMC Univ Paris 06, UMR 7190, CNRS, Institut Jean Le Rond d'Alembert, Case 162, 4 place Jussieu, 75252 Paris Cedex 05, France*
*Martine Rousseau, UPMC Univ Paris 06, UMR 7190, CNRS, Institut Jean Le Rond d'Alembert, Case 162, 4 place Jussieu, 75252 Paris Cedex 05, France*

# Influence of scale effects on local stiffness of filled elastomers in structural modeling

Ilya A. Morozov Bernd Lauke
ilya.morozov@gmail.com

**Abstract**

A realistic model of spatial arrangement of fillers in rubber is developed. Structural parameters of the model as the distribution of filler size, characteristics of secondary clusters and the presence of large bulk particles (micropellets) are taken from AFM-scans of carbon black filled rubber vulcanizates. A descriptor of filler distribution in the matrix - inhomogeneity index is suggested. The analysis of stiffness and inhomogeneity index of synthesized 3D-structures allowed to judge the reliability of different simplifications, as fillers of the same size or random filler arrangement and the absence of micropellets in structural modelling. Investigation of stiffness versus the size of modelled volumes showed large deviations of measured values at small scale of observation ($\approx 1\mu m$).

## 1 Introduction

The addition of active fillers (carbon black, silanized silica) to a rubber matrix leads to significant reinforcement of composites. This reinforcement is manifested as an increase in the toughness, durability of elastomers and, consequently to a longer service life, whereas their elasticity and ability to multiple reversible deformations caused by stretching remain unchanged. This is mainly due to strong interphase physicochemical interactions proceeding in the composite. Filled elastomers are heterogeneous materials and have a microstructure consisting of spatially connected clusters. A continuous filler network formed in the material by the branches of fractal clusters even at a relatively low filler volume fraction of $\approx 12\%$.

To predict the macroscopic response of such composites under external loading, the model should reflect in full measure the peculiarities of the microstructure of materials and demonstrate the interactions between neighbor components. The high processing capabilities of modern computers make it possible to directly model a representative volume of the filler network and then to apply some external loading. A starting point for such simulations must be information about filler geometry and arrangement in the polymer matrix. The new methods of analysis of AFM-images of filled rubbers developed recently [1] allowed us to determine the filler geometry and parameters of secondary clusters. This paper focuses on a method for computer synthesis of spatial filler networks. Input parameters for the model are taken from the structural analysis of AFM-images of filled rubbers.

To investigate the changes of stiffness, such variables as filler fraction, size of representative volume, presence or absence of single large inclusions, random or cluster filler arrangement, and filler size (filler particles are equal in size, or particles sizes are distributed in a log-normal fashion) are taken into account. Much attention is paid to the estimation

of a minimal reliable size of the structure (mesoscale) to ensure that consideration is given to a typical representative volume element.

## 2 Experiments and data analysis

In order to obtain input parameters for the model, carbon black filled styrene-butadiene vulcanizate samples were examined. The content of carbon black of 10, 30 and 50 phr (i.e., grams of carbon black per 100 grams of polymer) corresponds to the volume fractions of 0.04, 0.13 and 0.21, respectively.

Experiments were carried out on an atomic force microscope Bruker Icon. The surfaces of fresh cuts of filled polymer samples were examined. To perform statistical data analysis, a few high-quality scans were acquired for each material and further analyzed using our algorithms developed in Matlab. Example of microstructure image and processing results are presented in Fig. 1.

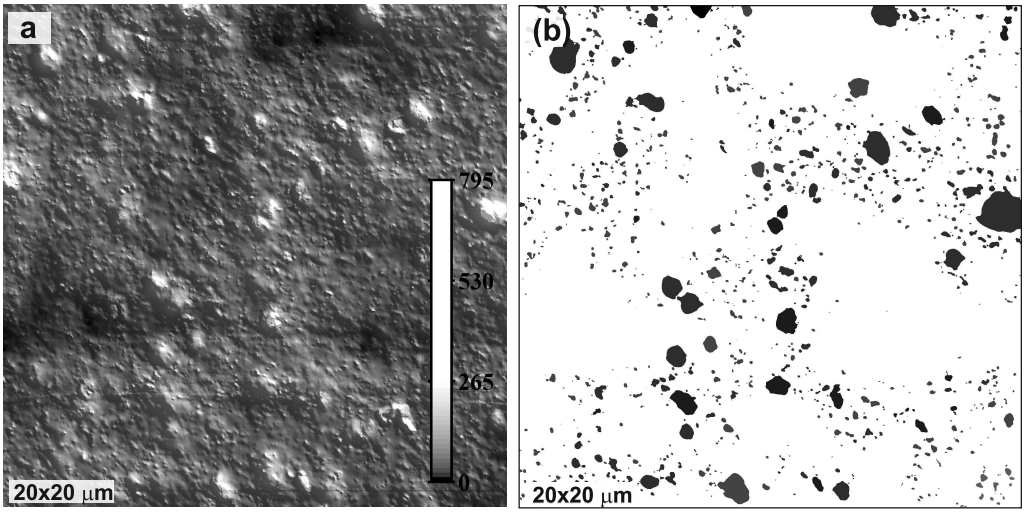


Figure 1: AFM-image of the surface of SBR/50 (a) and the result of image segmentation (b)

The algorithm of image segmentetion involves two steps. 1): Find any local maxima of the surface under study (vertices of future segments). 2): Examine the contour lines around the obtained maxima and determine the boundaries of segments. Hence, the continuous relief is divided into separate field of segments.

Examination of the sizes and shapes of segments allowed us to define two types of inclusions in the polymer: 1) micropellets - for segments of size $\geq$ 300 nm and compactness $\geq$ 0.85. 2) filler aggregates - for the rest of segments. The fraction of micropellets is calculated as the ratio of the total area of the bases of micropellets to the total area of filler fragments. The results show that the fraction of micropellets decreases with increasing filler concentration: 41, 23 and 1.1% for SBR/10, 30 and 50 phr respectively. The average size of such structures is 555, 457, 354 nm. The aggregate size distributions in the materials under study can be fairly well approximated by the log-normal probability distribution density law with known parameters.

The segmented surfaces are not homogeneous. It is seen that these surfaces have the high filler concentration regions connected by branches, i.e., the visible parts of spatial secondary structures (agglomerates). The number of primary structures (aggregates), $N$, is related to the size of agglomerates, $R$ by the fractal distribution law as $N = \mu R^D$,

where $\mu$ is the constant, and $D$ is the fractal dimension. The algorithms for image analysis developed previously [1] allowed us to calculate the fractal dimensions of the secondary structures of filler aggregates in the materials under study: 1.78 for SBR/30 and 2.02 for SBR/50. The number of secondary structures per $1\mu m^2$ of image is 0.06 and 0.11 respectively (name this parameter $\alpha$).

To quantify the filler distribution (non-spherical objects of different sizes) in the observed areas, the heterogeneity index, $J$, is introduced. This value indicates the minimum size of the window, where the filler arrangement is assumed to be homogeneous and can be calculated as: the $m$ squares of size $s^2$ are randomly chosen in the examined image, and $J(s)$ is defined as

$$J(s) = (min(A_i/s^2) + max(A_i/s^2))/(2\varphi^*)$$

where $A_i$ is the area occupied by filler segments in the $i$-th square; $\varphi^*$ - total fraction of area occupied by segments in the analyzed image. The number of squares, $m$, is obtained using the following equation: $m = 0.1exp(-7s/L)$. The closer the value of $J(s)$ to unity, the more homogeneous the distribution of the filler throughout the material will be at this scale. With decreasing $s$, the window starts to get the areas of both the high and low filler concentration. The value of $s^*$, from which $J(s)$ substantially deviates from unity, can be regarded as a critical scale (mesoscopic scale); for any scale $s \geq s^*$, the filler distribution can be considered as homogeneous. For the examined materials $s^*$ is 13, 8 and 5 $\mu m$.

## 3 Structural model of filled rubber

The structure is modeled by a cube of side-length $H$. The cube is filled with spheres representing micropellets or aggregates. The side $H$ is related to the mesoscopic scale as $H = 1.5s^*$. To avoid boundary effects, the cube of a greater volume was constructed, and all the statistics were calculated in its central part with side-length $s^*$. The sizes of spheres-micropellets were generated using uniform random distribution until the given fraction of micropellets was reached. After that, they were arbitrarily placed in inside the volume $H^3$. The aggregates were generated using the lognormal distribution of sizes until the total filler fraction was obtained. To construct the spatial network of secondary structures, the cores of agglomerates were randomly placed in the volume. The number of cores is related to the parameter $\alpha$ as $(\alpha H^2 + 1)^3$. The fractal agglomerates of dimension $D$ grew sequentially around the cores until all the spheres were placed in the volume. The algorithm to connect the $i$-th sphere and the $k$-agglomerate is as follows.

Let $R_k$ be the size of the $k$-th agglomerate. The initial $R_k$ is equal to the radius of agglomerate core. The numbers of spheres belonging to this agglomerate and located at a distance $\leq R_k \pm R_\delta$ from its core are collected into an array $\{a\}$, where $R_\delta$ is supposed to be the average diameter of aggregates. An arbitrary value $a_j$ is taken from the array $\{a\}$. Next, a series of trials are made to place the $i$-th sphere near the $a_j$-th sphere avoiding the intersections of the $i$-th sphere and the existing structures. To do this, the coordinates of the $i$-th sphere are set using the randomly chosen spherical angles with respect to the $a_j$-th sphere. If all the trials fail, then the next arbitrary sphere with the number from the array $\{a\}$ is taken (previous $a_j$-s are not considered). If all the elements from the array $\{a\}$ are checked and the $i$-th sphere is not yet connected with the $k$-th agglomerate this means that the $k$-th agglomerate has reached its maximum size. In this case, further growth of this agglomerate is stopped, and the $i$-th sphere is placed into the arbitrary unoccupied region of the volume and becomes the core of a new agglomerate. In the case of successful dislocation of the $i$-th sphere in the $k$-th agglomerate, the analysis of the

fractal dependence between the existing number of spheres $N_k$ and its size is performed. if $N_k > R_k^D$ then the agglomerate size increases: $R_k = R_k + R_\delta$.

After all of this is over, the next $i+1$ sphere-aggregate is connected with the $k+1$ agglomerate (or the first agglomerate, if the last has been reached), until all the spheres are placed inside the volume.

As regards the minimum distance between the aggregates (spheres) in the model, it is impossible to extract it from the AFM-images because of the limitations associated with the AFM-tip dimensions (10 nm). However, according to the dielectric spectroscopy measurements [2], the minimal distance between the carbon black aggregates is ranging between 2 and 5 nm.

## 4 Results and discussion

Apart from the structures synthesized using all the above mentioned parameters (case I), the simplified realizations of these structures are constructed: case II - without micropellets; case III - without micropellets and with spheres of equal size; case IV - without micropellets, with spheres of equal size and with random filler arrangement in the matrix. Since the size $s^*$ is quite high, the constructed volumes look like black cubes. For better representation, only the "cuts" of the obtained materials - the spheres, whose z-coordinates are within 500 nm from the centre of the volume - are shown in Fig. 2.

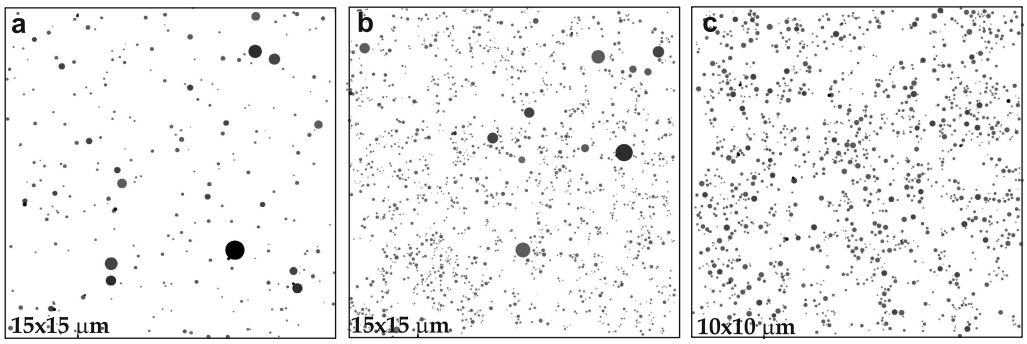


Figure 2: 'Cuts' of the obtained structures - SBR/10 (a), SBR/30 (b), SBR/50 (c).

For comparison of the synthesized structures with their simplified versions from the viewpoint of their mechanical stiffness and the development of the continuous filler-network, the gap $l_{gap}$ between the closest spheres comprising the sample chain from top to bottom was measured. That is, the first sphere at the top is arbitrarily selected, the closest sphere that lies lower is found, the in-between gap is measured, the next lower sphere closest to the second is found, and so on until the bottom is reached. The condition 'the closest sphere that lies lower' means that the $z_i$-coordinate of the centre of the $i$-th sphere which is closest to the $k$-th sphere must lie lower than the point $z_k - R_k$.

In the case of small extension applied to the modelled volume, the mechanical response of the domain in the gap between the adjacent spheres can be described as the stiffness, $G$, of an elastic rod. This type of modelling [3] provides the following relationship between the gap size and stiffness:

$$G = E_m R_{min}^2 (25 + 4\psi) ln(1+\psi) (\delta / R_{min})^{0.15 ln(\delta/R_{min}) - 0.2 ln(0.5+\psi)}$$

where $E_m$ is the elastic modulus of the material in the gap; $\delta$ is the gap between the spheres with radii $R_{max}$ and $R_{min}$, calculated in the same way as $l_{gap}$; $\psi = R_{max}/R_{min}$

The values of the gap between the spheres and the average force $F_z$ ($F_z = G_u$) in the chain going from top to bottom are summarized (for extension $u = 1$ nm and modulus $E_m$ 1 MPa) in Table 1. The table does not include any data for the materials with 10 phr because at low filler concentration no branchy structures of agglomerates appear.

| | SBR/30 | | | | SBR/50 | | | |
|---|---|---|---|---|---|---|---|---|
| | I | II | III | IV | I | II | III | IV |
| gap $l_g$, nm | 29.8 | 27.3 | 19.3 | 42.2 | 22.1 | 22.6 | 13.6 | 13.4 |
| Fz, kN | 77 | 75 | 42 | 23 | 75 | 76 | 30 | 16.1 |

Table 3: Comparison of different realizations of the structure

I - 'actual' structure; II - without micropellets; III - without micropellets, spheres of equal size; IV - without micropellets, spheres of equal size, random filler distribution.

As shown in Table, in all cases there are differences between the 'actual' and simplified structures: a) the absence of micropellets (large-size inclusions) results in a minor decrease in the gap, and thus the stiffness of the system changes; b) the spheres of equal size provide a significant (20-30%) decrease in the gap size, as well as in the stiffness; c). Random filler distribution causes a three-fold reduction in stiffness and a slight increase in the gap size (significant for SBR/30).

Index of inhomogeneity $J_3$ for the spatial structures could be calculated by simply changing areas to volumes in eq. (1). However, this drastically increases the calculation time. Thus, $J_3(s)$ was approximated with average value in the cross-sections of the 'sample'. Results are shown in Fig. 3.

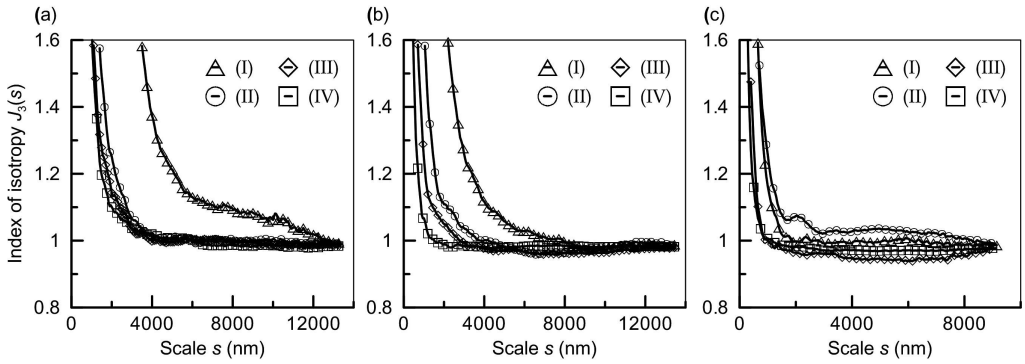


Figure 3: Heterogeneity index for different realizations of spatial structures: (a) - SBR/10, (b) - SBR/30, (c) - SBR/50.

The value of the scale factor, s, at which J(s) falls to almost unity, gives the minimum size at which the material can be considered as a homogeneous one. Absence of micropellets (II), usage of spheres of same size (III) and random filler distribution (IV) decrease the inhomogeneities of filler distribution, especially for the materials with 10 and 30 phr (Fig. 3). The results clearly show that the presence of large inclusions in the material sufficiently changes the homogeneity of the composite. At the same time, the presence of micropellets changes only slightly the stiffness and gap size of volumes filled with spheres (See Table). Thus, if one intends to use such systems to model the mechanical response of filled rubbers, the micropellets can be neglected, but the other structural properties should be taken into account. For case (I), the mesoscale is equal to 2000 nm for SBR/50, 6000 nm for SBR/30 and 11000 nm for SBR/10, respectively. For case (II), the mesoscale is equal to 2000 nm SBR/50, 3500 nm for SBR/30 and 4000 nm SBR/10, respectively.

Consider how the choice of a representative size of the volume influences the stiffness of the 'sample'. To this end, a number of volumes with a variable side length, $s$, were cut arbitrarily from different places of large structures, and the average value of $F_z$ and the standard deviation were computed (Fig. 4).

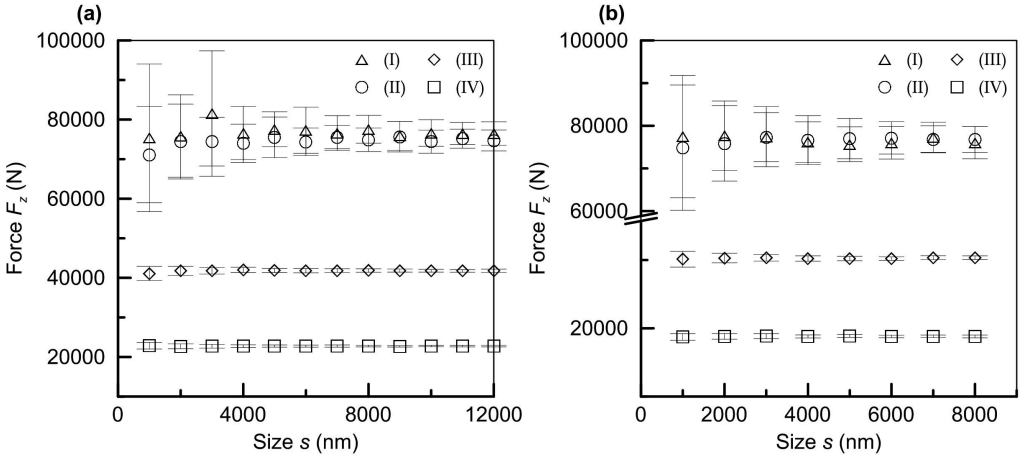


Figure 4: Tensile force of the "sample" versus its size for SBR/30 (a) and SBR/50 (b).

The vertical bars in Figure 4 mark standard deviation. It is shown that the significant variation of stiffness (force) is observed for small representative volumes (Fig. 4a). This fact once again points out that the structural-mechanical investigation of such structures based on the relatively small volumes can lead to essential disagreement with the bulk properties. It is clearly shown that the standard deviation approaches some asymptotic value as the variable side length, $s$, increases. These values of s are in agreement with study when $J(s)$ goes down to unity (see Fig. 3). The absence of micropellets (case II) and other simplifications of the model also decrease the deviation and reduce the path to asymptote.

# 5 Conclusion

An algorithm has been developed to construct the spatial structures reflecting the peculiarities of the actual microstructure of filled polymers. The following structural properties have been considered: the arrangement of filler particles in secondary structures (agglomerates), the minimum representative size of the modelled volume, the lognormal aggregate size distribution, and the presence of large particles. These input parameters of the model were determined in the structural analysis of the AFM-images of the materials under study. To evaluate the size of filler dispersion inhomogeneity, a new characteristic - the heterogeneity index - was introduced. To find the input parameters for the model, the structural analysis of styrene-butadiene carbon black filled vulcanizates with 10, 30 and 50 mass parts of filler was performed. The simulation results reveal that the presence of micropellets increases the scale of inhomogeneity of filler dispersion, but changes the stiffness of the materials only slightly. It is shown that the use of 'fillers' of equal size increases the homogeneity of the structure but decreases its stiffness. All the observed effects are more pronounced at low and moderate filler concentrations. The approach and results presented here will be used further in structural-mechanical modelling of filled elastomers.

## Acknowledgements

*The work was supported by the grant of the President of the Russian Federation (MK-3914.2011.8) and the RFBR-grant (11-08-00178-a).*

## References

[1] Morozov I.A., Lauke B., Heinrich G. A New approach to quantitative microstructural investigation of carbon black filled rubbers by AFM // Rubber chemistry and technology. 2012. (in print).

[2] J. G. Meier, M. Kluppel. Carbon Black Networking in Elastomers Monitored by Dynamic Mechanical and Dielectric Spectroscopy // Macromolecular materials and engineering. 2008. V. 293. P. 12-38.

[3] Moshev V.V., Garishin O.K. Physical discretization approach to evaluation of elastic moduli of highly filled granular composites // International Journal of Solids and Structures. 1993. V. 30. No. 17. P. 2347-2355.

*Ilya A. Morozov, str. Koroleva 1,Perm, Russia*
*Bernd Lauke, Hohe str. 6, Dresden, Germany*

# MAC model for the linear elasticity theory

Igor Neygebauer
newigor52r@yahoo.com

**Abstract**

The point boundary conditions in the models of continuum mechanics do not usually create the solutions which could be obtained in the models of particles interactions. For example that occurs in the linear and in nonlinear theory of elasticity and in fluid mechanics. The corresponding MAC (method of additional conditions) models were suggested using the MAC Green's functions and the principle of superposition. One example of these models was presented at the Conference APM 2011. The differential MAC models are considered in this paper. The method introducing these models is based on the changing of the classical differential equations using an experiment. The experiment consists in the particular test problem in the classical theory there the solution is not well from the physical point of view. Then the physically acceptable solution is taken to put it into the stated problem. Some terms in the equations are excluded or added to include the test solution into the MAC model. The classical membrane problem is considered and the differential MAC model for membrane is introduced. This problem could be considered as a test problem to create the MAC models for the elastic plate, elasticity, hydrodynamics, heat conduction equation, Maxwell's equations, Schroedinger equation and Klein-Gordon equation. The differential MAC models are very convenient to consider them using the methods developed in the classical theories. The application of the trigonometric series is considered as an example.
KEY WORDS: Continuum Mechanics, Differential MAC Model.

## 1 Introduction

An elastic body with the given displacement of its one point create the infinite stresses acting near that point in the body [1], [2], [3], [4]. Then the elasticity theory should use the stress-strain relations for infinite stresses. The experiment with the tension of a rod is an important tool to obtain the real stress-strain relations for an elastic body. And that experiments do not show the existance of such relations for infinite stresses. It means that we cannot apply the traditional elasticity theory to the case of point boundary conditions. For example if the force is applied to some point of the linear elastic body then the infinite displacements are at that point and the condition of finite displacement at that point could not be fulfilled. We suggest to use the differential MAC models of elasticity to analyze the elastic problems not only with point boundary conditions but also in traditional distributed boundary conditions in form of displacements or stresses. The strength criteria could be used in the form which includes the strains but not stresses. The models which used the membrane equation could be found in many problems of continuum mechanics. That equation and particular problem for them will be considered first of all and the differential MAC models for membrane will be introduced. Then these MAC models could be used to create the MAC models for other theories of continuum mechanics.

The membrane equation was considered in [6] where an integro-differential MAC model for membrane was introduced. The differential MAC models for membrane are considered in this paper.

## 2 Statement of the membrane problem

Let us consider an elastic membrane. The equation of motion of the membrane is given in [7] or in [8]:

$$T_0\left(\frac{\partial^2 u}{\partial x^2}+\frac{\partial^2 u}{\partial y^2}\right)=\rho\frac{\partial^2 u}{\partial t^2}+q(x,y,t), \tag{1}$$

where the membrane lies in the plane $(x,y)$ in its natural state, $T_0$ is its tension per a unit of length, $u(x,y,t)$ is the transversal displacement of the point $(x,y)$ of the initially plane membrane, $\rho$ is the density of mass per unit area, $t$ is time, $q(x,y,t)$ is the density of the transversal body forces per unit area.
We can write the equation (1) in the form

$$c^2\left(\frac{\partial^2 u}{\partial x^2}+\frac{\partial^2 u}{\partial y^2}\right)=\frac{\partial^2 u}{\partial t^2}+p(x,y,t), \tag{2}$$

where

$$c^2=\frac{T_0}{\rho},\ p(x,y,t)=\frac{q(x,y,t)}{\rho}. \tag{3}$$

The correspondent initial and boundary conditions should be added to the equation (2) to obtain the unique solution of the problem.
Consider the steady state problem for the membrane without any given distributed forces $q=0$. Then the function $u(x,y)$ does not depend on time $t$ and the equation (2) becomes

$$\frac{\partial^2 u}{\partial x^2}+\frac{\partial^2 u}{\partial y^2}=0. \tag{4}$$

the membrane could be considered bounded or unbounded with Dirichlet's or Neumann's boundary conditions.

## 3 Differential MAC models for membrane

### 3.1 Model 1

Let us consider one particular problem for a circular elastic membrane with the fixed boundary conditions on the circle and with the nonzero finite displacement at the center of the membrane. We know that the solution of that problem does not correspond to the results of the simple experiment with the real membrane [6]. Let us take the experimental solution and substitute it into the membrane equation (4). Then we will transform the classical equation of membrane to the form which includes the experimental function as a solution of the new equation.
Let us take the membrane equation (4) in polar coordinates:

$$\frac{\partial^2 u}{\partial r^2}+\frac{1}{r}\frac{\partial u}{\partial r}+\frac{1}{r^2}\frac{\partial^2 u}{\partial \varphi^2}=0, \tag{5}$$

where $r, \varphi$ are the polar coordinates. Let the membrane occupies the circle $0 \leq r \leq R < \infty$, where $R$ is the radius of a circle.
The boundary conditions are supposed to be

$$u(0) = u_0, u(R) = 0. \tag{6}$$

We accept the experimental solution as

$$u = u_0 \left(1 - \frac{r}{R}\right). \tag{7}$$

The solution (7) is taken from the reality and it is just a function representing the experimental results obtained in experiments with the circular membranes.
Then substituting the function (7) into the equation (5) we obtain the nonzero term

$$\frac{1}{r}\frac{\partial u}{\partial r}, \tag{8}$$

which will be excluded from the equation (5). If we accept the equation (5) where the second term is excluded for all possible membrane solutions then we obtain the differential MAC model 1 for the steady state membrane problem in the following form

$$\frac{\partial^2 u}{\partial r^2} + \frac{1}{r^2}\frac{\partial^2 u}{\partial \varphi^2} = 0. \tag{9}$$

The equation (9) in Cartesian coordinates will take the form

$$\frac{\partial^2 u}{\partial x^2} + \frac{\partial^2 u}{\partial y^2} - \frac{x}{x^2+y^2}\frac{\partial u}{\partial x} - \frac{y}{x^2+y^2}\frac{\partial u}{\partial y} = 0. \tag{10}$$

The MAC model 1 corresponding to the equation (2) has the equation

$$c^2\left(\frac{\partial^2 u}{\partial x^2} + \frac{\partial^2 u}{\partial y^2} - \frac{x}{x^2+y^2}\frac{\partial u}{\partial x} - \frac{y}{x^2+y^2}\frac{\partial u}{\partial y}\right) = \frac{\partial^2 u}{\partial t^2} + p(x, y, t). \tag{11}$$

The equation (11) could be written in polar coordinates

$$c^2\left(\frac{\partial^2 u}{\partial r^2} + \frac{1}{r^2}\frac{\partial^2 u}{\partial \varphi^2}\right) = \frac{\partial^2 u}{\partial t^2} + \widetilde{p}(r, \varphi, t), \tag{12}$$

where $\widetilde{p}(r, \varphi, t) = p(x, y, t)$. The boundary and initial conditions should be added to the equation (11) or (12) to obtain an unique solution of the membrane problem. The methods to obtain the solutions of the presented equations could be taken for example in [9].

## 3.2 Comparison of classical and MAC solutions for circular membrane

### 3.2.1 Problem 1

Consider a circular membrane under constant pressure $-p$ in classical case. Then the stated problem is

$$\frac{d^2 u}{dr^2} + \frac{1}{r}\frac{du}{dr} = -p,\ u(R) = 0. \tag{13}$$

The solution of the problem (13) is

$$u(r) = \frac{p}{4}(R^2 - r^2). \tag{14}$$

The differential MAC model 1 for membrane is

$$\frac{d^2u}{dr^2} = -p,\ \frac{dU}{dr}(0) = 0,\ u(R) = 0. \tag{15}$$

The solution of the problem (15) is

$$u(r) = \frac{p}{2}(R^2 - r^2). \tag{16}$$

Then we see that the value $u(0) = \frac{pR^2}{2}$ in MAC model is two times more as in the classical case.

### 3.2.2 Problem 2

Let us add the following condition to the above Problem 1:

$$u(0) = 0. \tag{17}$$

Then the solution in classical case does not exist at all. But the MAC solution exists and is as follows

$$u(r) = \frac{pr}{2}(R - r). \tag{18}$$

### 3.2.3 Problem 3

Let us consider now the free symmetric harmonic vibrations of a circular membrane. The stated problem in classical case is

$$\frac{d^2U}{dr^2} + \frac{1}{r}\frac{dU}{dr} + \frac{\omega^2}{c^2}U = 0,\ \frac{dU}{dr}(0) = 0,\ U(R) = 0, \tag{19}$$

where $U(r)$ is the form of membrane corresponding to the eigenfrequency $\omega$. The eigenfrequences of the problem (19) satisfy the equation

$$J_0\left(\frac{\omega R}{c}\right) = 0, \tag{20}$$

where $J_0(r)$ is the Bessel function of the first kind and of order zero.
The corresponding problem for MAC model 1 is in this case:

$$\frac{d^2U}{dr^2} + \frac{\omega^2}{c^2}U = 0,\ \frac{dU}{dr}(0) = 0,\ U(R) = 0, \tag{21}$$

Solving the problem (21) we obtain the following eigenfrequences:

$$\omega_n = \frac{\pi c}{R}(0.5 + n),\ n = 0, 1, 2, \ldots. \tag{22}$$

### 3.2.4 Problem 4

Let us replace the second condition in the classical and in the MAC models of membrane in the Problem 3 through $U(0) = 0$. The eigenfrequences in classical model do not exist at all. And the MAC model gives

$$\omega_n = \frac{\pi c}{R} n,\ n = 1, 2, \ldots. \tag{23}$$

## 3.3 MAC solution for rectangular membrane

The trigonometric series could be useful to consider the membrane problems for rectangular membrane like in classical case.
Consider the following problem for a rectangular membrane using the differential MAC model 1:

$$c^2 \left( \frac{\partial^2 u}{\partial x^2} + \frac{\partial^2 u}{\partial y^2} - \frac{x}{x^2+y^2}\frac{\partial u}{\partial x} - \frac{y}{x^2+y^2}\frac{\partial u}{\partial y} \right) = p, \tag{24}$$

where $p$ is a constant, $-a \le x \le a$, $-b \le y \le b$ nd the boundary conditions are: $u(-a, y) = u(a, y) = u(x, -b) = u(x, b) = 0$.
Multiplying the equation (24) by $x^2 + y^2$ the solution of the problem could be written in the form

$$u(x, y) = \sum_{n=1}^{\infty} \sum_{m=1}^{\infty} a_{nm} \cos \frac{\pi x(2n-1)}{2a} \cos \frac{\pi y(2n-1)}{2b}, \tag{25}$$

where

$$a_{nm} = \frac{p^2}{c^2} \frac{(-1)^{n+m} 192 a^2 b^2 (a^2+b^2)}{\pi^2 (2n-1)(2m-1)\{12a^2b^2 - \pi^2(a^2+b^2[b^2(2n-1)^2 + a^2(2m-1)^2]\}} \tag{26}$$

for $n, m = 1, 2, \ldots$.

## 3.4 Model 2

The experimental solution of the real membrane test problem could be taken in more general form:

$$u(r) = u_0 \left( 1 - \left( \frac{r}{R} \right)^{\alpha} \right), \tag{27}$$

where $\alpha$ is an experimental constant. We may change the classical membrane equation for this symmetric problem to the following one:

$$\frac{\partial^2 u}{\partial r^2} + \frac{1-\alpha}{r} \frac{\partial u}{\partial r} = 0. \tag{28}$$

The solution (27) satisfies the equation (28) exactly. It is not an unique equation which includes the function (27) into its set of solutions. For example the following equations are satisfied using the solution (27):

$$\frac{\partial^2 u}{\partial r^2} + \frac{1}{r} \frac{\partial u}{\partial r} + \alpha^2 \frac{1-u}{r^2} = 0 \tag{29}$$

or

$$\frac{\partial^2 u}{\partial r^2} + \frac{\alpha^2 - \alpha}{r^2}(1 - u) = 0. \tag{30}$$

We take the equation (28) to create the MAC model 2. Then the equation for the steady state membrane problem will be

$$\frac{\partial^2 u}{\partial r^2} + \frac{1 - \alpha}{r}\frac{\partial u}{\partial r} + \frac{1}{r^2}\frac{\partial^2 u}{\partial \varphi^2} = 0. \tag{31}$$

The differential MAC model 2 for membrane in polar coordinates therefore is

$$c^2\left(\frac{\partial^2 u}{\partial r^2} + \frac{1 - \alpha}{r}\frac{\partial u}{\partial r} + \frac{1}{r^2}\frac{\partial^2 u}{\partial \varphi^2}\right) = \frac{\partial^2 u}{\partial t^2} + p(r, \varphi, t). \tag{32}$$

The equations (31) and (32) in polar coordinates are

$$\frac{\partial^2 u}{\partial x^2} + \frac{\partial^2 u}{\partial y^2} - \frac{\alpha x}{x^2 + y^2}\frac{\partial u}{\partial x} - \frac{\alpha y}{x^2 + y^2}\frac{\partial u}{\partial y} = 0, \tag{33}$$

$$c^2\left(\frac{\partial^2 u}{\partial x^2} + \frac{\partial^2 u}{\partial y^2} - \frac{\alpha x}{x^2 + y^2}\frac{\partial u}{\partial x} - \frac{\alpha y}{x^2 + y^2}\frac{\partial u}{\partial y}\right) = \frac{\partial^2 u}{\partial t^2} + p(x, y, t). \tag{34}$$

### 3.5 Model 3

The MAC model 1 was created for a bounded membrane. If we consider the unbounded membrane then the experimental solution (7) will not satisfy both boundary conditions: at the origin and at the infinity. We can consider the following virtual experimental solution in this case

$$u = u_0 \exp(-\beta r), \tag{35}$$

where $\beta > 0$.
The function (35) may satisfy the following differential equation

$$\frac{d^2 u}{dr^2} + \beta\frac{du}{dr} = 0 \tag{36}$$

or

$$\frac{d^2 u}{dr^2} - \beta^2 u = 0. \tag{37}$$

The additional experiments with membrane should be used to choose the equation (36) or (37). If we choose the equation (36) then the corresponding membrane equation for MAC model 3 will take the form

$$c^2\left(\frac{\partial^2 u}{\partial r^2} + \beta\frac{\partial u}{\partial r} + \frac{1}{r^2}\frac{\partial^2 u}{\partial \varphi^2}\right) = \frac{\partial^2 u}{\partial t^2} + p(r, \varphi, t). \tag{38}$$

We have considered some differential MAC models without changing the order of the partial differential equation of membrane. But it is possible to consider the MAC models introducing the differential equation of higher order as the classical one. It is not considered in this paper.

## 4 Differential MAC model for elasticity

Let us consider the following particular problem of the linear isotropic elasticity [5]. An elastic body occupies the unbounded cylinder $0 \leq r \leq R$, where $R$ is the finite radius of the cylinder. Let the displacement field of the body is in cylindrical coordinates $r, \varphi, z$:

$$u_r = u_r(r, \varphi),\ u_\varphi = u_{r,\varphi},\ u_z = u_z(r). \tag{39}$$

Then the component $u_z$ satisfies the equation

$$\frac{\partial^2 u_z}{\partial r^2} + \frac{1}{r}\frac{\partial u_z}{\partial r} = 0. \tag{40}$$

Let us apply the boundary conditions $u_z(0) = u_0 \neq 0$, $u_z(R) = 0$. Then we have the same mathematical problem as for the membrane problem where the MAC model 1 was created. Using the obtained MAC model 1 for membrane we may introduce the MAC model 1 for elasticity equations. The differential MAC model 1 equations for the linear isotropic elasticity in Cartesian coordinates are

$$(\lambda+\mu)\frac{\partial e}{\partial x} + \mu\left(\frac{\partial^2 u_x}{\partial x^2} + \frac{\partial^2 u_x}{\partial y^2} + \frac{\partial^2 u_x}{\partial z^2} - \frac{y}{y^2+z^2}\frac{\partial u_x}{\partial y} - \frac{z}{y^2+z^2}\frac{\partial u_x}{\partial z}\right) + \rho_0 B_x = \rho_0 \frac{\partial^2 u_x}{\partial t^2}, \tag{41}$$

$$(\lambda+\mu)\frac{\partial e}{\partial y} + \mu\left(\frac{\partial^2 u_y}{\partial x^2} + \frac{\partial^2 u_y}{\partial y^2} + \frac{\partial^2 u_y}{\partial z^2} - \frac{x}{x^2+z^2}\frac{\partial u_y}{\partial x} - \frac{z}{x^2+z^2}\frac{\partial u_y}{\partial z}\right) + \rho_0 B_y = \rho_0 \frac{\partial^2 u_y}{\partial t^2}, \tag{42}$$

$$(\lambda+\mu)\frac{\partial e}{\partial z} + \mu\left(\frac{\partial^2 u_z}{\partial x^2} + \frac{\partial^2 u_z}{\partial y^2} + \frac{\partial^2 u_z}{\partial z^2} - \frac{x}{x^2+y^2}\frac{\partial u_z}{\partial x} - \frac{y}{x^2+y^2}\frac{\partial u_z}{\partial y}\right) + \rho_0 B_z = \rho_0 \frac{\partial^2 u_z}{\partial t^2}, \tag{43}$$

where

$$e = \frac{\partial u_x}{\partial x} + \frac{\partial u_y}{\partial y} + \frac{\partial u_z}{\partial z}. \tag{44}$$

Other MAC models for elasticity could be easily obtained too.

## 5 Conclusion

The differential MAC models of many physical theories may be created in similar way replacing the Laplace operator through the given differential operators in MAC models for membrane. Examples of the theories which could give the differential MAC models are hydrodynamics, Maxwell's equations, Schroedinger equation, Klein- Gordon equation, heat conduction equation.

## References

[1] S. Antman, *Nonlinear Problems of Elasticity*, Springer, 2005, pp. 1-844.

[2] P.G. Ciarlet, *Mathematical Elasticity. Vol.1 Three-dimensional Elasticity*, NH, 1988, pp. 1-492.

[3] R.B. Hetnarski, M.R. Eslami, *Thermal stresses-advanced theory and applications*, Springer, 2009, pp. 1-559.

[4] O. Coussy, *Mechanics and Physics of Porous Solids*, John Wiley and Sons, Ltd, 2010, pp. 1-281.

[5] S.P. Timoshenko, J.N. Goodier, *Theory of Elasticity*, 1951, pp. 1-519.

[6] I. Neygebauer, MAC-solution for a rectangular membrane, *Journal of Concrete and Applicable Mathematics*, Vol.8, No.2, 2010, pp. 344-352.

[7] P. Villaggio, *Mathematical models for elastic structures*, Cambridge University Press, 1997.

[8] A.P.S. Selvadurai, *Partial differential equations in mechanics*, Springer, 2010.

[9] A.D. Polyanin, *Handbook of linear partial differential equations for engineers and scientists*, Chapman&Hall/CRC Press, 2002.

*Igor Neygebauer, Department of Mathematics and Statistics, University of Dodoma, Tanzania, PO Box 259*

# Combustion onset in non-uniform dispersed mixtures

V. F. Nikitin V. R. Dushin N. N. Smirnov
ebifsun1@mech.math.msu.su

**Abstract**

The paper presents the results of theoretical investigations of combustion and detonation initiation in heterogeneous polydispersed mixtures. The problems of fuel droplets atomization, evaporation and combustion being the key factors for ignition delays and shock waves attenuation evaluation in heterogeneous mixtures and the non-equilibrium effects in droplets atomization and phase transitions were taken into account. The effects of droplets size non-uniformity and spatial distribution non-uniformity on mixture ignition and flame acceleration were investigated for strong and mild initiation of detonation: by a shock wave and spark ignition followed by deflagration to detonation transition (DDT).

Keywords: spray, detonation, combustion, onset, droplet.

## Introduction

Most of rocket and aviation engines have pulverized in air fuels combustion serving the base of their working cycle. Thus combustible mixtures formation and deflagration or detonation initiation in poly-dispersed fuel – air mixtures are the key aspects providing different limitations for operation of those engines. Onset of detonation being very dangerous for conventional engines could, however, serve the basis for creating new generation of engines - pulse detonating engines (PDE). Dispersed mixtures having been formed by different pulverizers could not be spatially uniform. However, in most experimental and theoretical investigations the ignition characteristics of uniformly distributed in space mixtures were studied. To achieve uniform droplet distribution and to avoid gravitational separation of the mixture having been formed investigations under microgravity conditions are performed [1]. The goal of the present research was, however, to investigate sensitivity of detonation onset to mixture parameters non-uniformity (spatial non-uniformity of dispersed phase, size distribution function, etc.) for both strong and mild initiation. Special attention was paid to peculiarities of droplet interaction with a high enthalpy flow.

## Mathematical model for polydispersed mixture combustion

The mathematical models for simulating turbulent chemically reacting flows in heterogeneous mixtures were described in details in [2 - 4]. Combustion processes in heterogeneous mixtures differ greatly from that in homogeneous mixtures, because they are governed not only by chemistry but also by physical processes of combustible mixture formation, such as droplet atomization [3, 4], evaporation and diffusive mixing of fuel vapor with an oxidant.

The model applies both deterministic methods of continuous mechanics of multiphase flows to determine the mean values of parameters of the gaseous phase and stochastic methods to describe the evolution of polydispersed particles in it and fluctuations of parameters. Thus the influence of chaotic pulsations on the rate of energy release and mean values of

flow parameters can be estimated. The transport of kinetic energy of turbulent pulsations at the same time obeys the deterministic laws being the macroscopic characteristic.

The motion of polydispersed droplets (particles) is modeled making use of a stochastic approach. A group of representative model particles is distinguished each of them representing a number of real particles. Motion of these particles is simulated directly taking into account the influence of the mean stream of gas and pulsations of parameters in gas phase [2, 3], as well as evaporation and atomization. Thus a great amount of real particles (liquid droplets) was modeled by an ensemble of model particles. Each model particle was characterized by a vector of values, representing its location, velocity, mass, number of real particles represented by the given model one and other properties. The number of model particles was 25000 each representing up to hundred thousand real particles (depending on mass fraction of fuel). The number of cells was of the order of thousand. Thus the minimal average number of model particles per a grid node was provided guaranteeing sufficient accuracy of fluxes between phases evaluation.

The momentum equation for a single droplet motion in the gas flow has the following form [2, 3]

$$m\frac{d\underline{u}}{dt} = m\underline{g} - \phi\cdot\nabla p + \underline{f}_d, \quad \frac{d\underline{r}}{dt} = \underline{u}, \quad \underline{f}_d = \frac{C_d}{2}\rho_g\frac{\pi d^2}{4}\left(\underline{v}-\underline{u}\right)\left|\underline{v}-\underline{u}\right|, \tag{1}$$

the drag coefficient being the function of Reynolds number

$$C_d = \left(\frac{24}{Re} + \frac{4,4}{\sqrt{Re}} + 0,42\right)\beta\cdot K, \quad Re = \frac{\rho\left|\underline{v}-\underline{u}\right|d}{\mu},$$

$$\beta = \sqrt{\frac{\rho}{\rho_s}\left(2-\frac{\rho}{\rho_s}\right)} \quad K = \left(\frac{T}{T_s}\right)^{4/5}$$

$$\frac{\rho_s}{\rho} = \begin{cases} \left(1+\frac{\gamma-1}{2}M^2\right)^{1/(\gamma-1)}, & M<1 \\ \frac{(\gamma+1)M^2}{(\gamma-1)M^2+2}\left(1+\frac{\gamma-1}{2}\frac{(\gamma-1)M^2+2}{2\gamma M^2-(\gamma-1)}\right)^{1/(\gamma-1)}, & M\geq 1 \end{cases} \tag{2}$$

The energy equation for a droplet has the following form [2]

$$m\frac{de}{dt} = q + Q_s, \text{where} \quad e = c_{vs}T_s + h_f^0 \quad Q_s = \frac{dm}{dt}h_L \tag{3}$$

where $h_L$ is the latent heat of evaporation, $Q_s$ - the energy of phase transitions. Heat flux to a single droplet from the surrounding gas flow is determined as follows [7]:

$$q = \begin{cases} \pi d\lambda\cdot Nu\cdot(T-T_s), & Re<1000, \\ \pi d^2\rho|\underline{v}-\underline{u}|\cdot St\cdot(H_r-H_w), & Re\geq 1000, \end{cases}$$
$$Nu = 2+0.16\cdot Re^{2/3}\cdot Pr^{1/3}, \quad St = \frac{C_d}{2}Pr^{-2/3} \tag{4}$$

The non-equilibrium evaporation model is used to determine the evaporation rate [3]

$$\dot{m} = \pi d\cdot\rho D\cdot Nu\cdot\log\left(\frac{1-Y_e}{1-Y_w}\right) \quad Y_w = \frac{W_N P_0}{W_p}\exp\left[\frac{H_b}{R}\left(\frac{1}{T_b(P_0)}-\frac{1}{T_s}\right)\right] - \dot{m}\frac{\sqrt{2\pi RT_s}}{\pi\delta_e p d^2} \tag{5}$$

The dynamic interaction of liquid droplets with the gaseous flow could bring to instability of the interface in the shear flow and atomization of droplets. The criterion for liquid droplets

instability is that of the critical Weber number [5]: $We = \frac{\rho v_{rel}^2 d}{\sigma}$, where $\sigma$ is the surface tension at the interface, $v_{rel}$ is relative velocity of a droplet versus gas. On exceeding the critical value of the Weber number droplets break up due to vibrational instability takes place. On essentially surpassing the critical Weber number other mechanisms start playing essential roles in the break up process that brings to formation of fine mist [3, 5, 7]. These main characteristics of the atomization process could be taken into account by the following approximate formula [3] determining mean diameters of droplets $d_a$ originating in atomization of initial droplets (diameter $d$):

$$d_a = \begin{cases} d = \left(\frac{6\alpha_2}{\pi n}\right)^{1/3}, & We < We_* \\ \frac{dWe_*}{We}, & We_* \le We \le We_{**} \\ d_*, & We > We_{**} \end{cases} \quad We_* = 12(1 + Lp^{-0.8}), We_{**} = 350 \quad (6)$$

where $n$ is the number of droplets per volume unit, $\alpha_2$ – volumetric fraction of the droplet phase, $We_*$ - the critical Weber number, $Lp = \frac{d\rho_c\sigma}{\mu_c^2}$ - the Laplace number, $\rho_c$, $\mu_c$ - liquid density and viscosity.

To determine the mean diameter of droplets $d_*$ after the breakup of a type of an explosion ($We > We_{**}$) one needs to evaluate the part of the accumulated by a droplet energy spent for the breakup. The assumption, that the breakup energy was spent for the formation of new free surface makes it possible to evaluate the number $N$ and the mean diameter $d_*$ of the formed droplets:

$$N = \left(1 + \frac{E_*}{\sigma\pi d^2}\right)^3 \quad d_* = \frac{d}{1 + \frac{E_*}{\sigma\pi d^2}} \quad E_* = A_{drag} - \sum_{i=1}^{N_*} \frac{m_i v_{i*}^2}{2} \quad (7)$$

Where the breakup energy is evaluated as the difference between the work of the drag forces separating small droplets from the initial one, and the kinetic energy of fragments' scattering. Thus main assumption of the model is the following: work of drag forces in separating pieces of droplets is spent for additional free surface formation and relative kinetic energy of fragments.

Assuming that the initial droplet is split into $N_*$ equal droplets ($N_* = \frac{d^3}{d_*^3}$) having equal velocities of radial expansion of the cloud $v_*$ and the separation of droplets takes place after the droplet is moved away at a distance $\sim d_*$, one obtains the following formulas:

$$A_{drag} = \frac{1}{8} N_* \rho C_d v_{rel}^2 \pi d_*^2 d_* \quad d_* = \frac{d}{1 + \frac{1}{4}\left(\frac{1}{2} C_d \rho v_{rel}^2 - \frac{1}{3}\rho_c v_*^2\right)\frac{d}{\sigma}} \quad (8)$$

The mean velocity of the cloud expansion $v_*$ could be evaluated based on the condition of matching the two formulas for $d_a$ at $We = We_{**}$. The reason to perform that matching is that both formulas for breakup regimes were obtained from experiments, thus, indirectly the expansion of the cloud of droplets after the breakup should have been taken into account. On the other hand, the dependence of characteristic droplets diameters on the Weber number should be continuous. In modeling droplets breakup in a gas flow the inertia of the process should be taken into account. Fragmentation does not take place instantaneously: it needs time for small droplets to separate from the initial one, i. e. it needs a definite time for the liquid bridges between the droplets to be established, elongated and broken [3]. Then, finally the first order estimates give the following formula:

$$d_* = \frac{dWe_*}{\frac{1}{8}C_d(We - We_{**})We_* + We_{**}} \quad t_* = \frac{d}{v_{rel}} \frac{We_*}{We} \left(1 + \frac{3}{8} C_d \frac{\rho}{\rho_c}\left(1 - \frac{4}{C_d We_*}\right)\right) \quad (9)$$

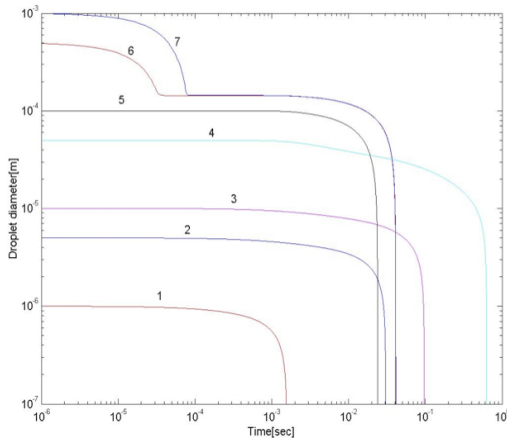


Figure 1: Droplet diameter variation versus time for droplets of different initial diameters. $V_0 = 50m/s$, taking into account atomization.

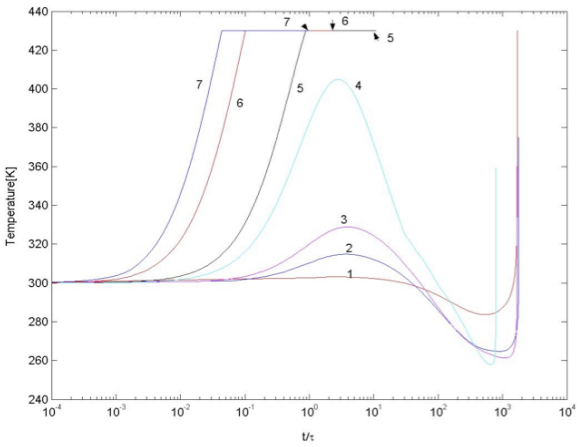


Figure 2: Mean droplet temperature variation versus dimensionless time for droplets of different diameters. $V_0 = 50m/s$, taking into account atomization.

Coalescence of droplets due to collisions is neglected. This assumption is valid for rarefied mixtures. In present simulations we'll study mixtures, wherein volume fraction of fluid is $10^{-3}$, which provides the probability of collision $10^{-6}$.

**Numerical investigation of gas-droplet interaction in streaming flows**

In order to evaluate the influence of different factors on the rate of droplet evaporation and mixture formation in heterogeneous detonation, let us investigate the problem of droplet interaction with the streaming gas flow taking into account mechanical drag, atomization of droplets, non-equilibrium heat and mass transfer. A series of model problems was regarded, in which gas flow and droplet initially had different relative velocities and temperatures, and then relaxation took place. Those model problems are similar to that encountered in shock wave initiation of detonation in combustible dispersed fuel-air mixtures. The two-phase flow becomes strongly non-equilibrium behind the shock wave, because due to mechanical inertia droplets keep their speed practically constant and gas accelerates on passing the shock wave. Besides, due to thermal inertia, temperature inside droplets practically does not change, while gas temperature increases instantaneously behind the shock wave. Due to that reason gas temperature in all the numerical experiments was assumed to be higher than the boiling temperature for liquid droplets.

The thermophysical properties for gas and droplets were assumed similar for all numerical experiments: ambient pressure $p = 1.013bar$, temperature $T = 1000K$, gaseous phase – air, liquid – n-decane ($C_{10}H_{22}$ ). Initial droplet temperature was assumed to be $T = 300K$.

The relaxation processes for droplets of different diameters were regarded. Numbered lines on the successive figures correspond to the following initial diameters of droplets: 1 – 1 $\mu m$; 2 – 5$\mu m$; 3 – 10 $\mu m$; 4 – 50 $\mu m$; 5 – 100 $\mu m$; 6 – 500 $\mu m$; 7 – 1000 $\mu m$.

Figs. 1-2 illustrate parameters of droplets variation in the process of mechanical and thermal relaxation for the set of numerical experiments assuming initial velocity difference to be equal to 50 m/s. Fig. 1 illustrates droplet diameter variation due to evaporation. Large droplets undergo atomization until their diameter gets smaller. That is the reason for the 6-th and 7-th curves in Fig. 1 to converge into one, because atomization terminates

on reaching by all droplets one and the same diameter. It is seen from the figure that evaporation time increases with the increase of initial droplet diameter, but the increase does not take place monotonically: the increase of life time (curves 1, 2, 3, 4) changes for a decrease (curves 4, 5) and then comes back to an increase (curves 5, 6, 7). That testifies the effect of manifestation of different mechanisms depending on the characteristic size of droplets.

One could distinguish the characteristic deceleration time $\tau$ (velocity decreases $e$ times) for each droplet. This time depends on droplet initial mass $m_0$, relative gas velocity $v_0$ and drag $f_d$.

$$\tau = \frac{v_0}{a_0} \quad \text{where} \quad a_0 = \frac{f_d(t=0)}{m_0} \tag{10}$$

The time being normalized to this value, and droplet diameter being normalized to its initial value allow us to obtain the dependences for a droplet temperature versus normalized time, which is present in Fig. 2. The dynamics of droplet heating is the following. For small droplets (curves 1, 2, 3, 4) in the very beginning the temperature increases due to external heating. On rapid decrease of droplet relative velocity evaporation in the stream of gas brings to a decrease of temperature. Then on decreasing droplet radius heat fluxes growth brings to an increase of temperature until the droplet disappears. The first increase of temperature is higher for larger droplets, which relative velocity decreases much slower than for small droplets. Very large droplets follow different scenario. The first increase of their temperature goes as high as up to the critical value. Then evaporation takes place at a critical temperature very rapidly. Arrows with numbers in Fig. 2 indicate the end of droplet life time. That is the reason for a larger droplet (curves 5 in Figs. 1 and 2) to have a shorter life time.

## Non-uniform sprays combustion

Numerical investigations of detonation initiation in dispersed hydrocarbon fuel - air mixtures after mild ignition via DDT and by shock waves of different intensities were performed in tubes of cylindrical geometry. The flow was assumed to have the following initial turbulence characteristics: energy $k = 0.1 J/kg$, the mixing length $l = 0.01m$, mean velocity $u = 0$, initial temperature 300 K. The number of model particles used in calculations was 25000. Validation of numerical scheme was performed based on comparing the obtained results of numerical simulations for the detonation wave velocities in dispersed mixtures with available experimental data. Fig. 6a illustrates detonation velocities in hydrocarbon-oxygen two-phase mixtures developed in numerical simulations and in experiments [8-10]. Liquid n-decane ($C_{10}H_{22}$) fuel was used. Fig. 6b illustrates turbulent flame propagation velocities versus velocity pulsation in gaseous mixtures of $CH_3OH, O_2$and $N_2$. (Curves – experiments [11], dots – numerical computations). Satisfactory coincidence of theoretical and experimental data could serve a macroscopical validation for the developed model.

To simulate hydrocarbons the following parameters were taken: $\rho = 850 kg/m^3$; $\Delta H = 43 MJ/kg$; $h_L = 200 kJ/kg$; $W = 140 kg/kmol$. The reduced kinetic model is provided in [7]. The share of water in hydrocarbon decomposition was assumed to be $\zeta = 0.2$.

Initiation of combustion by a shock wave was studied in a tube 0.5 m long and 0.05m diameter. The aerosol occupied the cylindrical coaxial zone beginning from 0.1 m along the axis its diameter being equal to 0.015 m. The mean droplets diameter was assumed $100\mu m$, minimal diameter - $10\mu m$, maximal- $200\mu m$. The droplets size distribution function was assumed to be a triangular one. The initial droplets density was varied from 5 to $20 kg/m^3$. The results of simulations (Figs. 3 and 4) show that for different fuel concentration and

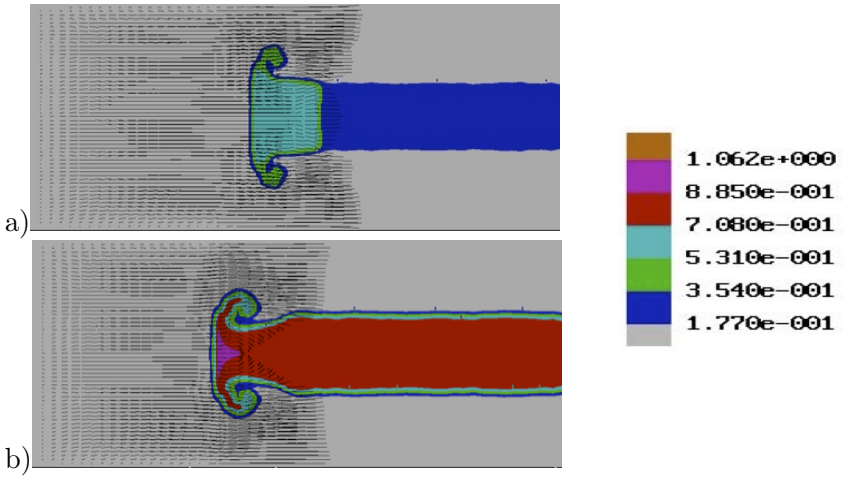


Figure 3: Hydrocarbon concentration for shock wave propagation in dispersed mixture (a - initial fuel density 5 kg/m$^3$; b - initial fuel density $20kg/m^3$).

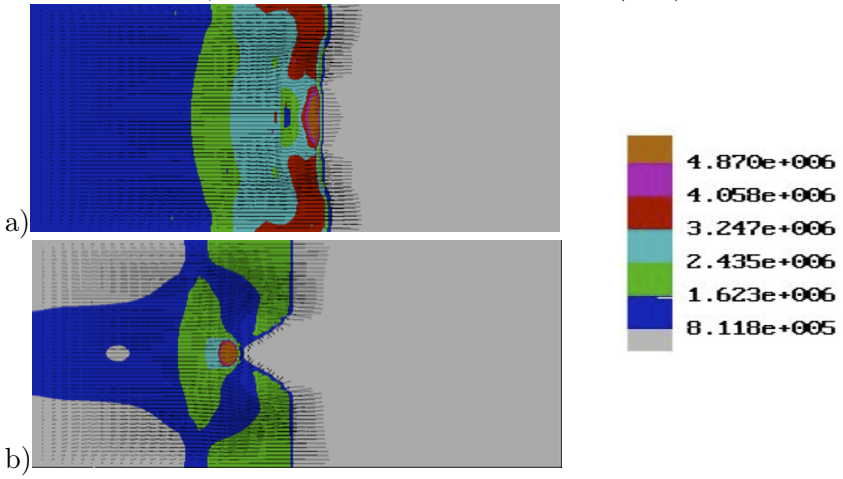


Figure 4: Pressure maps (Pa) for shock wave propagation in dispersed mixture (a - initial fuel density $5kg/m^3$; b - initial fuel density $20kg/m^3$).

intensity of shock wave initiation different scenarios of the process are possible. There could be formed a combustion wave lagging behind attenuating shock. There could be onset of detonation, or galloping detonation in the dispersed layer. For high average density of fuel droplets within the layer combustion does not take place inside layer, where pressure is maximal, however high speed detonation type process onset on the periphery is observed supported by the piston effect due to induced vapor combustion in the zones within the concentration limits.

Mild ignition and detonation onset via DDT was simulated in a tube, which diameter was 20 mm, the tube length was 2 m (Fig. 5), the mean droplet diameter was assumed $50\mu m$, minimal diameter - $10\mu m$, maximal - $100\mu m$. The droplet size distribution function was assumed to be a triangular one. The mixture filled the whole tube, initial droplet volume concentration being equal $\alpha = 0.001$.

Numerical modeling of two phase mixture ignition and combustion was carried out to understand better the deflagration to detonation transition (DDT) processes. Submicron particles did not play any role in the present study, as their lifetime was negligibly small being below the limit of accuracy of numeric scheme. The size of droplets accounted by the


Figure 5: Computational domain for DDT simulations.

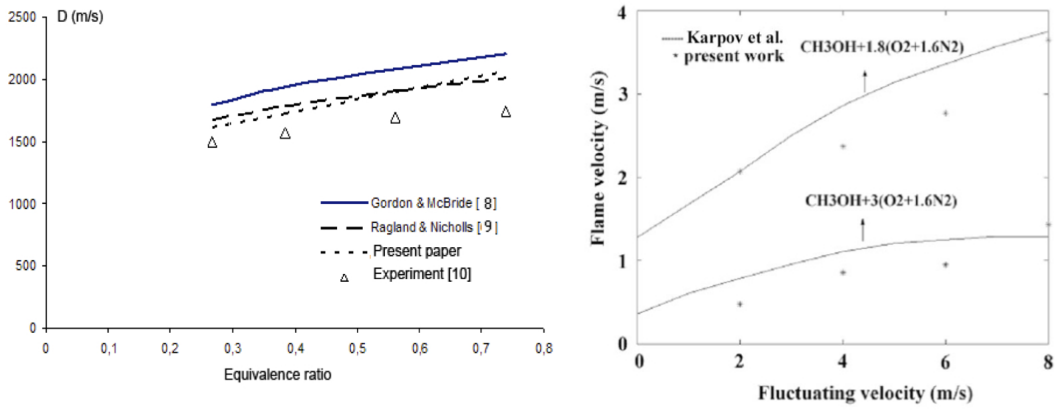


Figure 6: Detonation velocities in n-decane ($C_{10}H_{22}$)-oxygen two-phase mixture (a) and turbulent flame velocity in one-phase (b) mixture developed in numerical simulations and in physical experiments.

model is the one larger then minimal size evaporating within one time step. Reaction rate of smaller (submicron) particles cannot influence simulations, as the total energy release of their burning out is distributed within the computational cell within one time step. The effect of droplet size distribution function on the DDT process was investigated in [4]. Here we'll study the effect of droplet spatial distribution on the onset of detonation. As it was shown in [2] droplet spatial non-uniformity promotes ignition and combustion onset. In particular, the presence of concentration gradient in droplet spatial distribution lowers the minimal ignition concentration in the zone of energy release. The successive results illustrate the combustion zone averaged axial velocity variation versus time and tube length for different spatial distributions of droplets.

For one and the same fuel content ($\bar{\rho} = 0.8\text{kg/m}^3$) and similar droplet size distribution function the spatial non-uniformity along the longitudinal co-ordinate was investigated. The values of other ignition characteristics were also similar: $T_0 = 300K, p_0 = 1bar, k_0 = 0.1j/kg, E_{ign} = 3.5j, t_{ign} = 100\mu s$ Fig. 7 presents the comparison of results obtained for homogeneous (a) and non-homogeneous (b) spatial distribution of droplets. In case (b) mean fuel concentration is decreasing along x-axis.

For the case (a) the turbulent flame propagation in the mixture is very non-monotonic. Velocity first stays at the level of 200 m/s, then it increases up to 700 m/s, again decreases to 600 m/s then increases to 1100 m/s and decreases to 500 m/s again, and then increases up to 1800 m/s and decreases to an average self-sustaining velocity of 1600 m/s with periodical oscillations near that value. It is seen, that in the beginning some galloping combustion mode is established, which turns to be unstable with increasing amplitude of

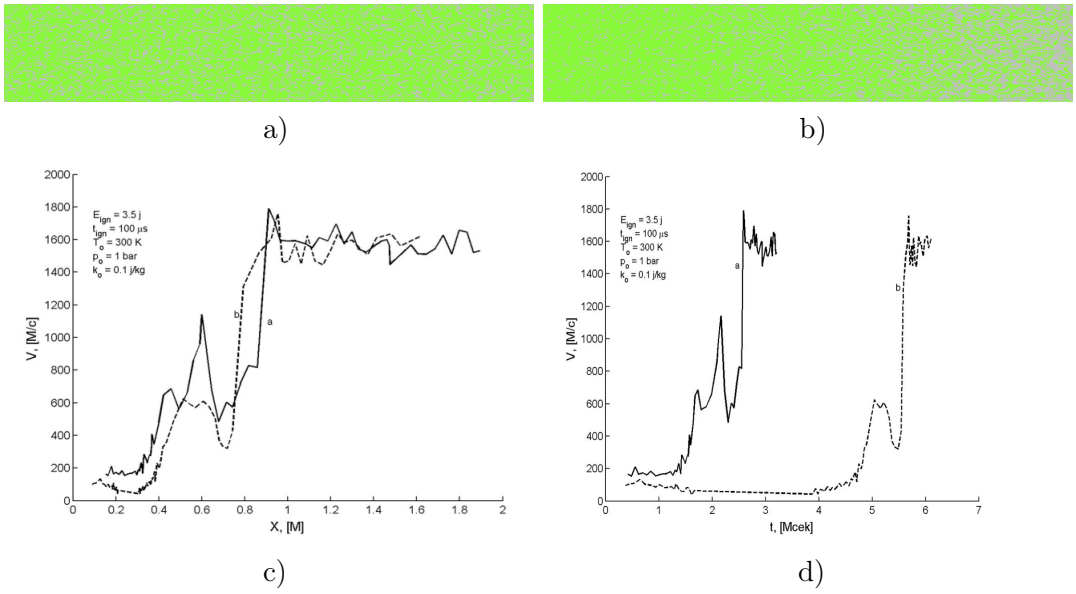


Figure 7: The effect of spatial non-uniformity of mean droplet concentration distribution (a – uniform, b – non-uniform) on the onset of detonation in polydispersed mixtures. Velocity versus axial coordinate (c) and versus time (d) diagrams.

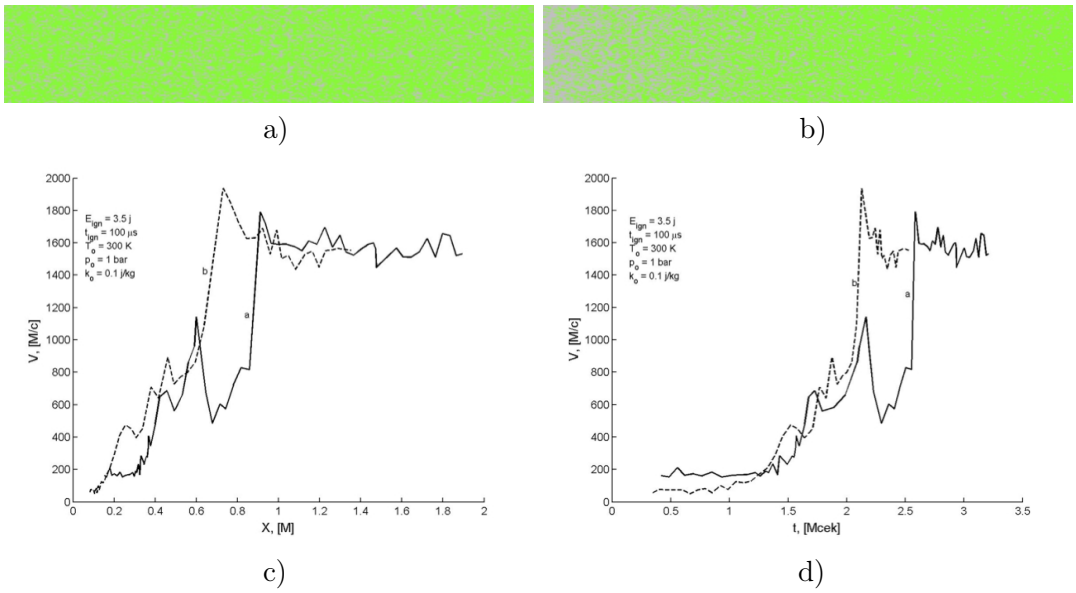


Figure 8: The effect of increasing along the axis mean droplet concentration (a – uniform, b – non-uniform) on the onset of detonation in polydispersed mixtures. Velocity versus axial coordinate (c) and versus time (d) diagrams.

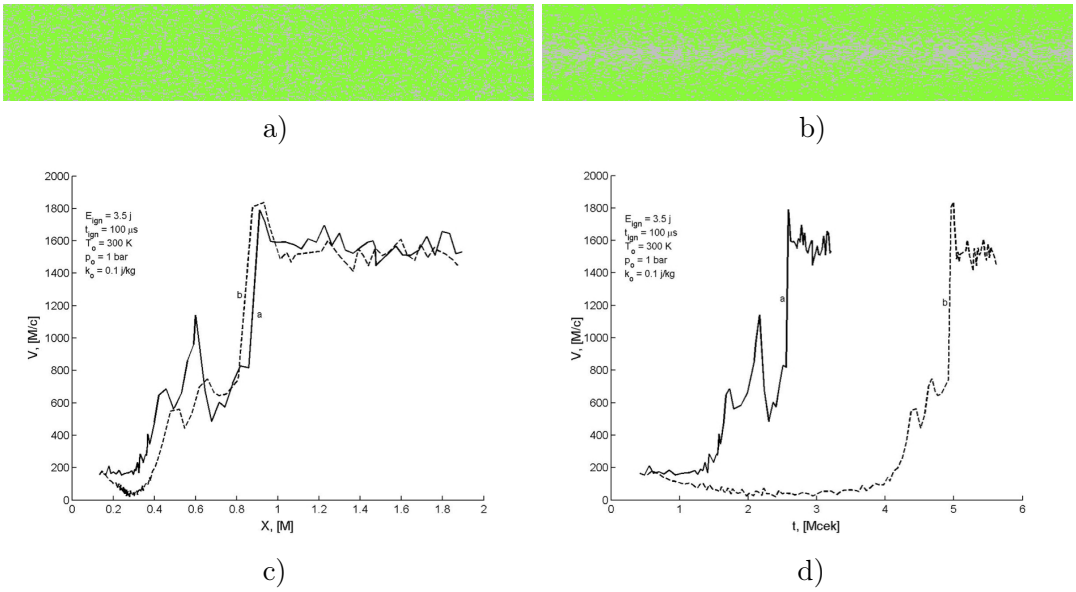


Figure 9: The effect of spatial non-uniformity of mean droplet concentration distribution in radial direction (a – uniform, b – minimum on the axis) on the onset of detonation in polydispersed mixtures. Velocity versus axial coordinate (c) and versus time (d) diagrams.

oscillations until finally an overdriven regime is formed, after which mean velocity cannot go down below the self-sustaining one. Detonation in poly-dispersed fuel-air mixture is named a self-sustaining propagation of shock induced ignition. Comparison with cellular gaseous detonation does not seem legible, because cellular structure is an attribute of gaseous detonation, but by no means its definition.

Results of numerical simulations show that pre-detonation length remains practically the same for different spatial distribution of condensed matter (Figure 7 c). It seems to be even a little shorter for the case of the increased fuel concentration in the beginning of the tube. While velocity versus time diagrams show essential increase of pre-detonation time. This effect is due to a serious decrease of flame propagation velocity in the ignition section (50 – 100 m/s), which takes place because of the increased heat losses to heat the increased mass of droplets.

Figs. 8-9 illustrate DDT process after ignition in the non-uniform mixture with increasing along the axis mean fuel content (Fig. 8), decreasing in the radial direction (minimal in the center – Fig. 9). Comparison of results shows, that for the increasing fuel concentration along the axis pre-detonation length and time practically do not depend on such type of non-uniformity, while for radial non-uniformity pre-detonation time grows due to initial decrease of mean axial flame propagation velocity. When fuel concentration is maximal in the ignition zone more time is needed to heat all the droplets, which increases ignition delay, when fuel concentration is minimal in the ignition zone at the axis, propagation velocity is limited by lean conditions, which brings to ignition delay due to the increase of evaporation time to guarantee the necessary vapor concentration.

The results of simulations based on the developed model show that the zone of increased density of droplets behind shock waves appear, which was first discovered numerically by Korobeinikov [6] and named the $\rho$-layer. Later, the formation of $\rho$-layers in dusty gases was confirmed experimentally. The present results show that for liquid droplets $\rho$-layers are formed as well behind shock waves despite droplets atomization. After ignition of dispersed mixture either turbulent combustion wave is formed lagging behind the atten-

uating shock wave, or a self-sustaining detonation wave. The spatial non-uniformity of droplet distribution in the radial direction for this type of initiation also inhibits the onset of detonation.

### Conclusions

Investigating the behavior of individual droplets in a heated air flow allowed distinguishing two scenarios for droplet heating and evaporation. Small droplets undergo successively heating, then cooling due to heat losses for evaporation, and then rapid heating till the end of their life time. Larger droplets could directly be heated up to a critical temperature and then evaporate rapidly. Atomization of droplets interferes heating and evaporation scenario.

Investigating droplet cloud strong ignition by a shock wave showed that increase of droplet concentration above definite value inhibits the onset of detonation in dispersed mixtures and gives birth to a detonation mode typical for non-premixed systems, when chemical reaction takes place only in a thin border layer of the cloud from thus supporting the shock wave in pure gas propagation.

The onset of detonation in case of a mild ignition of dispersed mixtures at ambient pressures and temperatures comes via galloping combustion mode with increasing amplitude finally bringing to an overdriven detonation regime, which then evolves into a self-sustaining one. Generally speaking, convective combustion in dispersed mixture could lead either to a galloping mode, or to onset of detonation. For large droplets and small ignition energy only galloping combustion modes could be attained.

Non-uniform spatial distribution of droplets has a strong influence on predetonation time (in most cases time is increasing) and much smaller effect on predetonation length. Different types of spatial non-uniformity inhibit deflagration to detonation transition, or direct initiation of detonation, while in case of turbulent flame initiation by spark ignition spatial non-uniformity could serve a promoting factor [2].

### Acknowledgments

Russian Foundation for Basic Research (Projects 11-03-00213 and 12-08-00804), is acknowledged for financial support.

## References

[1] N.N. Smirnov, Pushkin V.N., Dushin V.R., Kulchitskiy A.V. Microgravity investigation of laminar flame propagation in monodisperse gas-droplet mixtures. Acta Astronautica, 2007, vol. 61, 626-636.

[2] N.N. Smirnov, V.F. Nikitin, J.C. Legros, Ignition and combustion of turbulized dust – air mixtures. *Combust. Flame*, **123,** (1/2), (2000), 46 – 67.

[3] N.N. Smirnov, V.F. Nikitin, A.V. Kulchitskiy, J.C. Legros, V.M. Shevtsova. Detonation Initiation in Pulse Detonating Devices, In G.D.Roy, P.J.Strikowski (Eds.) *Proc. Thirteenth ONR Propulsion meeting,* Univ. of Minnesota, Minneapolis, 2000, p. 213-232.

[4] N.N. Smirnov, Nikitin V.F. Khadem J. Aliari Shourekhdeli Sh. Onset of Detonation in Polydispersed Fuel-Air Mixtures. Proceedings of the Combustion Institute. 2006, vol. 31, pp. 832-841.

[5] B.J. Azzopardi, G.F. Hewitt, Maximum drop sizes in gas-liquid flows. *Multiphase Sci.&Tech.*, 9, (1997), 109-204.

[6] V.P. Korobeinikov, On arising in dusty gas of zones with high concentration of particles. *Archivum Combustionis,* 9, (1/4), (1989), 149-152.

[7] V.B. Betelin, Smirnov N.N., Nikitin V.F., Dushin V.R., Kushnirenko A.G., Nerchenko V.A., Evaporation and ignition of droplets in combustion chambers modeling and simulation, Acta Astronautica (2012), vol. 70, 23-35.

[8] Gordon S. and McBride B. Computer program for calculation of complex chemical equilibrium compositions, rocket performance, Incident and Reflected shocks, and Chapman-Jouguet detonation. *NASA sp-273,* 1971.

[9] K.W.Ragland, E.K.Dabora and J.A.Nicholls Observed structure of spray detonations. *Physics of fluids,* Vol. 11, 1968.

[10] M.J.Tang, J.A.Nicholls, M.Sichel and Z.C.Lin, The direct initiation of detonation in decane-air and decane-oxygen sprays. *Gas dynamics laboratories, report No.* UM-018404-1, October 1983.

[11] V.P. Karpov, Politenkova G.G., Severin E.S., Turbulent burning of alcohol. *Combustion, Explosion, Shock waves,* 22, N 4: 12-14, 1986.

*V. F. Nikitin, V. R. Dushin, N. N. Smirnov, Moscow Lomonosov State University, Moscow 119992, Russia, Scientific Research Institute for System Analysis of the Russian Academy of Sciences, Moscow 117218, Russia*

# Numerical research of problems with variable interface

Anastasia Mikhailovna Onishkova
aonishkova@gmail.com

**Abstract**

A numerical algorithm for solving certain problems in mathematical physics (one- and two-dimensional), are to determine the minimum of a quadratic functional defined in a region containing the previously unknown surfaces. The latter is determined from the minimal functional with unknown functions. We consider the problem for a plane area. Two-dimensional problem is solved by the method of grids. Interface position is defined from a minimum condition. The presented new algorithm uses various methods to search minimum, in particular, genetic algorithms are implemented.

Keywords: algorithm, functional, at least, genetic algorithm, grid, function, area, interface

## 1 Introduction

Mathematical models of many physical processes and the phenomena lead to the boundary-value problems of mathematical physics containing in advance unknown surfaces, subject to determination during the problem solution. An example of such problem is the model of melting of ice - the so-called Stefan's problem. Since Gibbs works, for the solving of problems with unknown interfaces the variation methods are widely used. The idea of the solution of such problem consists of in determination of the extremal or stationary points of corresponding functional. A feature of this class of problems is that the variation should be viewed not only the unknown function, but also the position of an unknown interface. Thus, the mathematical challenge is to find such

$$u^*, \tilde{A} : I\left(u^*, \tilde{A}^*\right) = \min_{\underline{u} \in H, \Gamma} I(\underline{u}, \Gamma),$$

where $u$ is some of the functions of a certain space $H$, and $\Gamma$ is the position of an unknown interface.

The mathematical theory of this class of problems in a certain degree of development [8]. However, the numerical study of such problems are encountered considerable difficulties. In this paper, we propose a numerical algorithm for solving problems with unknown interfaces.The idea of the method is as follows.

Assume that we know any provision of $\tilde{\Gamma}$. Then, solving the problem of finding u $\min_u I(u, \tilde{\Gamma})$, can be found $\tilde{u}$ corresponding to the $\tilde{\Gamma}$. Substituting $\tilde{u}$ in $I$, we obtain a functional that depends only on $\Gamma$:

$$\tilde{I}(\Gamma) = I(\tilde{u}(\Gamma), \Gamma).$$

Steps of the algorithm can be roughly summarized as follows:

1. Set the initial position of the border: $\Gamma_0$.

2. A decision is determined $\underline{u}_0$.
3. Calculate $I_0 = I(u_0, \Gamma_0)$.
4. $\Gamma_n$−shall be verified the following approximation.
5. Find a solution $u_n : \min_u I(u, \Gamma_n)$.
6. Calculate $I_n = I(u_n, \Gamma_n$.
7. Check the condition of convergence.

The key questions are:

a) Choice of the next iteration $\Gamma$;

b) Choice of conditions for convergence of the minimization of the sequence $I_n$.

## 2 Problem Statement

In the rectangular area, where given an equation $k \pm \Delta u = f$, where $\Delta = \frac{\partial^2}{\partial x^2} + \frac{\partial^2}{\partial y^2}$ and Dirichlet boundary conditions, it is necessary to determine the position of the unknown interface $\Gamma$, which are given matching conditions$k_+ \frac{\partial up}{\partial n} = k_- \frac{\partial um}{\partial n}$.

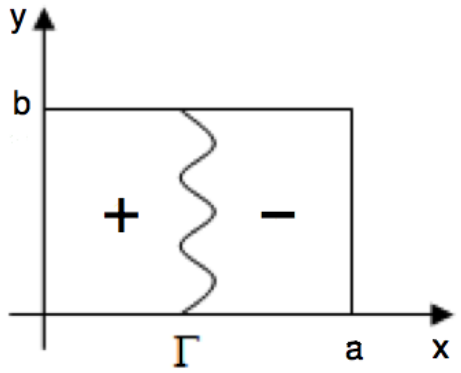


Figure 1: Formulating the problem

Interface $\Gamma$ is found by minimizing a functional

$$I = \frac{1}{2} \int\limits_{v_+} k_+ \nabla u^2 dV_+ + \frac{1}{2} \int\limits_{v_-} k_- \nabla u^2 dV_- - \int\limits_{v_+ \cup v_-} f u dV$$

## 3 Genetic algorithm

Note that the result we solve the problem of minimum of several variables. For two-dimensional problem the number of variables is twice the number of nodes used to approximate the unknown boundary. Therefore, it is essential to the issue of choosing a method of finding the minimum. Promising class of algorithms are the so-called genetic algorithms.What is a genetic algorithm?Genetic algorithm - a method for solving optimization problems based on natural selection, just as it is in the process of biological evolution. In the genetic algorithm is repeated modification of a family of individual decisions. At each step in the genetic algorithm were selected randomly chosen subjects from the resulting current solution, called the parent and which is used to generate the next generation

child. Through successive generations of selection is "evolution" toward an optimal solution.Genetic algorithm (GA) can be viewed as a type of random search, which is based on mechanisms that resemble natural selection and reproduction.

Unlike existing techniques, the GA starts with a random set of initial solutions, called population. Each element of the population is called a chromosome and represents a solution to a first approximation. Chromosome is a string of characters of some nature, not necessarily binary. Chromosomes evolve through many iterations, called generation (or generations). During each iteration of the chromosome is evaluated using some fitness function. To create the next generation of new chromosomes, called offspring, are formed either by crossover of two chromosomes - the parents of the current population, either by random changes (mutations) in one chromosome. New population is formed by (a) selection according to the match function of some parents and offspring and (b) removal of remaining in order to maintain a constant population size.

Chromosomes with higher fitness function are more likely to be selected (to survive). After several iterations, the algorithm converges to the best chromosome, which is either optimal or near-optimal solution.

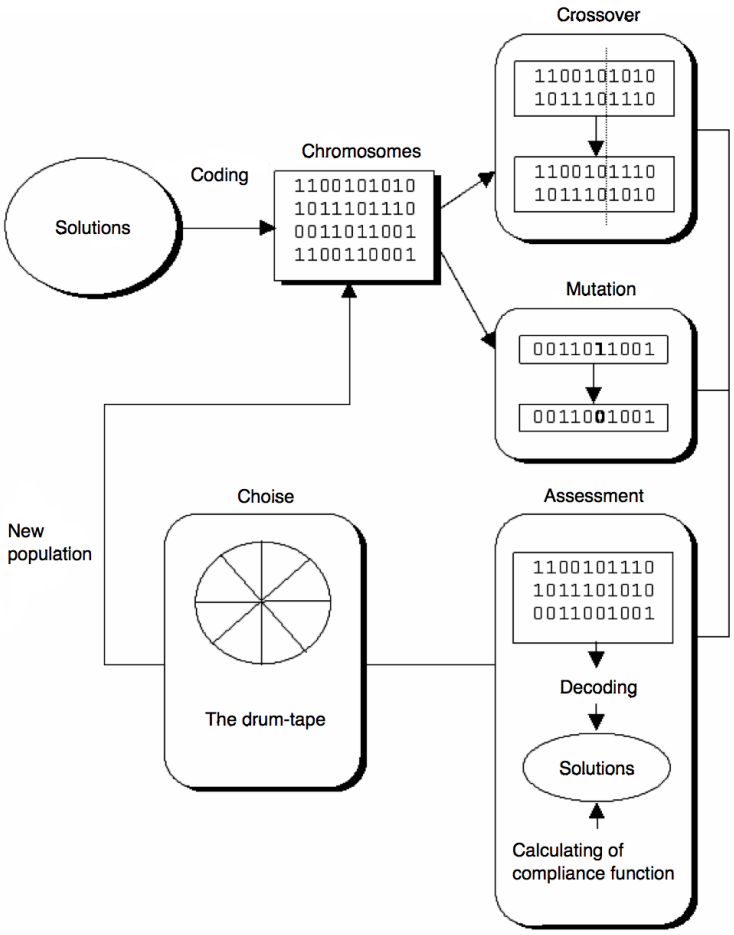


Figure 2: Generalized structure of the genetic algorithm.

Thus, two kinds of operations:

1. Genetic operations: crossover and mutation;
2. Evolutionary operation: a choice.

Genetic operations resemble the process of gene inheritance when creating a new offspring in each generation. Evolutionary operation, making the transition from one population to the next, like the process of Darwinian evolution.

There are two major advantages of genetic algorithms using optimization techniques to the classic:

1. GA has no significant mathematical requirements for the types of objective functions and constraints. The researcher should not simplify the object model, losing its adequacy, and seeking the possibility of using artificially available mathematical methods. It can be done a variety of target functions and constraints (linear and nonlinear) defined on discrete, continuous and mixed universal sets.
2. When using the classic turn-based methodology of global optimum may be found only when the problem has the property of convexity. At the same time the evolutionary operations of genetic algorithms make it possible to effectively seek out the global optimum.

# 4 Algorithm for solving

1. Set $a$, $b$, $h$, $k_+$, $k_-$ and the type of interface (until I considered only the case of straight boundaries).
2. Building a mesh: $n_a$ is number of points on $[0, a]$; $n_b$ is number of points on $[0, b]$; $x_i = (i-1) * h, i = 1...n_a$; $y_j = (j-1) * h, j = 1...n_b$.
3. In arrays $x_G$, $y_G$ put the mesh nodes, through which the border. $x_G$ stores the $x$ coordinate interface and $y_G$ is coordinate y.
4. Plotted on a grid and the resulting interface.
5. Obtain sets $V_+$ and $V_-$. $V_+$ will be stored in an array $xVP$ - sites of x and $yVP$ are nodes on y; $V_-$ will be stored in an array $xVM$ - sites of $x$, and $yVM$ - sites in $y$.
6. Determine the location of the interface, to remember the coordinates of the interface in arrays $gNy$ and $gNx$.
7. Assign the interface unknown constant $a$, the array of unknowns.
8. Looking $up$, a solution to the $V_+$:
   (a) Write the boundary conditions $up(:, 1) = 0$, $up(1, :) = 0$, $up(n_b, :) = 0$.
   (b) Compute $f(x, y)$ at grid points on the $V_+ - f_{ij}$.
   (c) For internal nodes equates using difference $formulami.Uravnenie\ k_+\delta up = f(x, y)$ takes the form $up_{i+1j} - 2up_{ij} + up_{i-1j} + up_{ij+1} - 2up_{ij} + up_{ij-1} - f_{ij}h^2/k_+ = 0$.
9. Solve the resulting system of equations.
10. Obtain the solution $up$, which depends on a, where $a = up(gNy(i), gNx(i))$.
11. Recall condition. If we assume that the boundary - a straight line, then the normal $n = [h\ 0]$. If we denote the set of nodes $V - um$, then we can write the expression for the gradients of the normal (written for the nodes within the mesh)
    $grup = [(up(gNy(i), gNx(i)) - up(gNy(i), gNx(i) - 1))/(h)(up(gNy(i), gNx(i)) - up(gNy(i) - 1, gNx(i)))/(h)]$

    $grum = [(um(gNy(i), gNx(i) + 1) - um(gNy(i), gNx(i)))/(h)(um(gNy(i) + 1, gNx(i)) - um(gNy(i), gNx(i)))/(h)]$

    The difference equation for the condition has the form

$$kp * (n(1) * grup(1) + n(2) * grup(2)) - km * (n(1) * grum(1) + n(2) * grum(2)) = 0.$$

Because $n = [h\ 0]$, we have

$$kp * (up(gNy(i), gNx(i)) - up(gNy(i), gNx(i) - 1)) - km * (um(gNy(i),$$
$$gNx(i) + 1) - um(gNy(i), gNx(i))) = 0.$$

For convenience $gNy(i) = i$, $gNx(i) = j$. Obtain

$$kp * up(i, j) - kp * up(i, j - 1) - km * um(i, j + 1) + km * um(i, j) = 0.$$

It is known that

$$up(i, j) = um(i, j). Then kp*up(i, j)-kp*up(i, j-1)-km*um(i, j+1)+km*up(i, j) = 0$$
$$(kp + km) * up(i, j) - kp * up(i, j - 1) - km * um(i, j + 1) = 0$$
$$um(i, j + 1) = ((kp + km) * up(i, j) - kp * up(i, j - 1))/km.$$

It turns out that we have expressed through the nodes set up $V_-$, are in the column that follows the border (marked with blue dots).

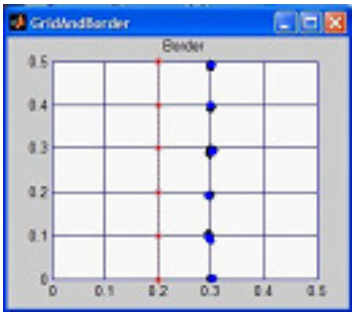


Figure 3: The column that follows the border

For the remaining nodes $um$:

(a) Write the boundary conditions $um(:, n_a) = 0$, $um(1, :) = 0$, $um(n_b, :) = 0$.

(b) For internal nodes equates using difference formulas. Equation $k_-\delta um = f(x, y)$ takes the form $um_{i+1j} - 2um_{ij} + um_{i-1j} + um_{ij+1} - 2um_{ij} + um_{ij-1} - f_{ij}h^2/k_- = 0$

(c) Compute $f(x, y)$ at grid $V_- - f_{ij}$.

12. Obtain a solution $um$, that depends on $a = up(gNy(i), gNx(i))$.

13. Searching of the functional

Term becomes

1. Term $\frac{1}{2}\int_{V_+} k_+ \nabla u^2 dV_+$ becomes

$$\frac{1}{2}\sum_m\sum_n\int_{x_n}^{x_{n+1}}\int_{y_m}^{y_{m+1}}\left(ux^2 + uy^2\right)dxdy =$$
$$= \frac{1}{2}\sum_m\sum_n\left(ux^2 + uy^2\right)(x_{n+1} - x_n)(y_{m+1} - y_m) = sp$$

There are

$$x_n, y_m \in V_+, ux = \frac{\partial u}{\partial x} = \frac{u_m^n - u_m^{n-1}}{h}, uy = \frac{\partial u}{\partial y} = \frac{u_m^n - u_{m-1}^n}{h}, \nabla u^2 = ux^2 + uy^2.$$

2. Term $\frac{1}{2}\int_{V_-} k_- \nabla u^2 dV_-$ becomes

$$\frac{1}{2}\sum_m \sum_n \int_{x_n}^{x_{n+1}} \int_{y_m}^{y_{m+1}} \left(ux^2 + uy^2\right) dxdy = \\ = \frac{1}{2}\sum_m \sum_n \left(ux^2 + uy^2\right)(x_{n+1} - x_n)(y_{m+1} - y_m) = sm$$

   There are $x_n, y_m \in V_-$.

3. Term $\frac{1}{2}\int_{V_+ \bigcup V_-} fudV$ becomes $so = sop + som$, where

$$sop = \frac{1}{2}\sum_i \sum_j f_{ij} up_{ij} \left(x_{j+1} - x_j\right)\left(y_{i+1} - y_i\right), x_j, y_i \in V_+$$
$$som = \frac{1}{2}\sum_k \sum_l f_{kl} um_{kl} \left(x_{k+1} - x_k\right)\left(y_{l+1} - y_l\right), x_k, y_l \in V_-/\Gamma.$$

4. Functional I = sp + sm-so. This functionality is expressed through up (i, j), because um was also expressed by up (i, j). The condition that the derivatives on the boundary with coefficients kp and km is also taken into account.

5. Run for the functional genetic algorithm.

## 5 Test cases

As a test case the results of solving several model problems.

*Example 1*

We consider the solution of the model problem for elliptic equations

$$\frac{\partial^2 u}{\partial x^2} + \frac{\partial^2 u}{\partial y^2} = -2y + 2y^2 - 2x + 2x^2$$

In the rectangle centered at the origin, unit height and width equal to one. On the sides of the rectangle placed homogeneous Dirichlet conditions. Exact solution is known

$$u(x, y) = xy - x^2 y - y^2 x + x^2 y^2.$$

Decision on the interface (i = 1) 0.03197Exact solution minFI = 0.0333.Thus, the error can also be considered good.Now take a step less than h = 0.1, thus the number of nodes increases.

*Example 2*

We consider the solution of the model problem for elliptic equations [21]

$$\frac{\partial^2 u}{\partial x^2} + \frac{\partial^2 u}{\partial y^2} = -5\pi \sin \pi x \cdot \sin 2\pi y$$

In the rectangle centered at the origin, unit height and width equal to two. On the sides of the rectangle placed homogeneous Dirichlet conditions. Exact solution is known.

$$u(x, y) = \sin \pi x \cdot \sin 2\pi y.$$

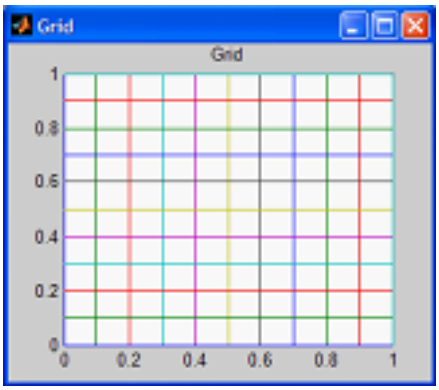


Figure 4: The grid

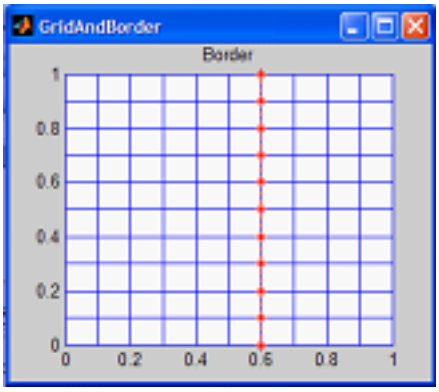


Figure 5: The border

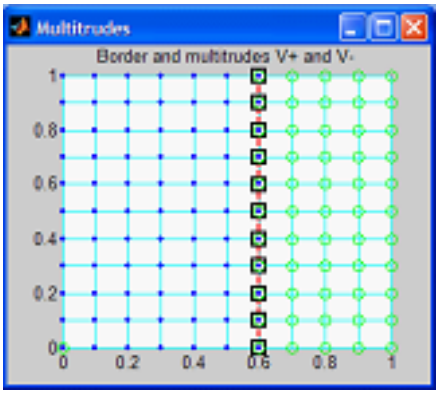


Figure 6: The multitudes

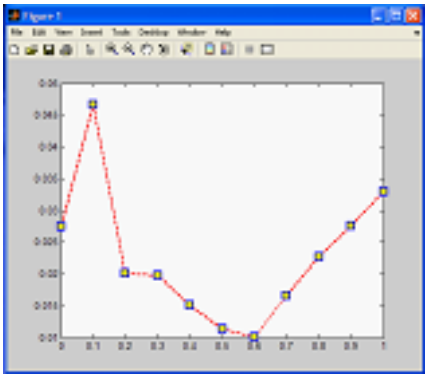

Figure 7: The functional

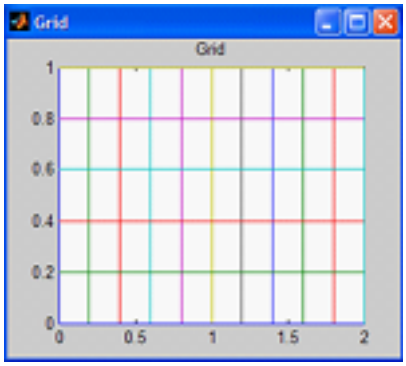


Figure 8: The grid

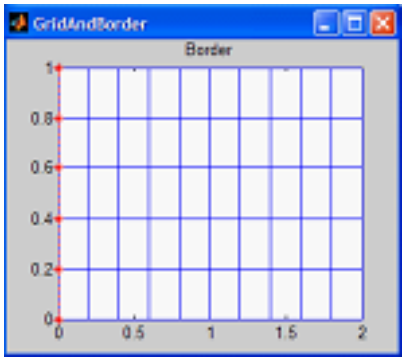


Figure 9: The border

## 6 Conclusions

For two-dimensional problems with free (pre-unknown) boundary developed numerical algorithm for finding its position, which is determined from the minimality of the corresponding functional.

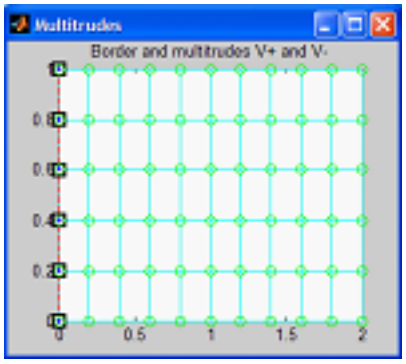


Figure 10: The multitudes

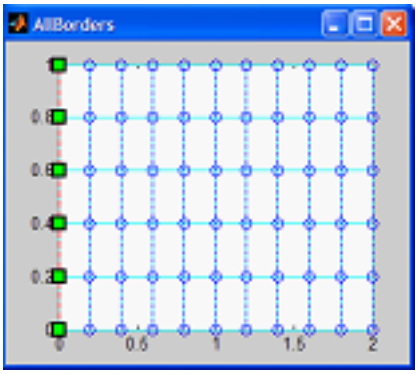


Figure 11: The multitudes

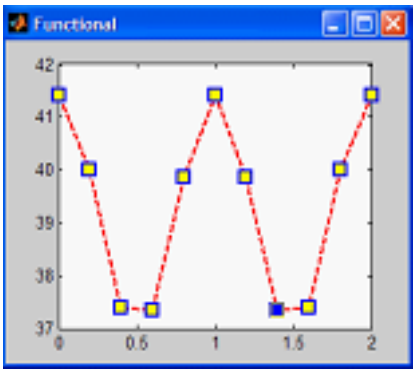


Figure 12: The functional

## References

[1] V.A.Likhachev, S.L.Kuz'min, Z.P.Kamentseva The shape memory effect. -L.: Leningrad State University, 1987.

[2] Materials with Shape Memory, ed. V.A.Likhachev. - Spb.: Univ NIIH St. Petersburg State University, 1998.

[3] Gibbs, J.W. Scientific Papers. V. 1. Thermodynamics. N.Y. etc. Dover,1906.

[4] Greenfield, M.A. On the conditions of thermodynamic equilibrium phase of nonlinear elastic material, Dokl. Akad. 1980. T.251. No 4. S.824-827.

[5] James, R.D. Finite deformation by mechanical twinning // Arch. Rat. Mech. Anal. 1981. V. 77. P. 143-177.

[6] Greenfield, M.A. Of continuum mechanics in the theory of phase transitions. - Moscow: Nauka, 1990. 312s.

[7] N.F.Morozov, I.R.Nazyrov, A.B.Freidin. One-dimensional problem of phase transformation of the elastic ball, "Dokl. RAN. 1996. T.346, nïS 2. S. 188-191.

[8] V.G.Osmolovskii. Variational problem on phase transitions in continuum mechanics. - SPb: Izd-vo SPb un-ta, 2000, 262s.

[9] Lodiz R., Parker R. The growth of single crystals. - Moscow: Mir, 1974. 540s.

[10] Love, B.J. Theory of crystallization in large volumes. - Moscow: Nauka. 1980. 512s.

[11] Bhattacharya, K., Kohn, R.V.//Arch. Rational Mech. Anal. 1997. 139, 99-180.

[12] Mielke, A., Theil, F., Levitas, V.I.// Arch. Rational Mech. Anal. 2002, 162, 137-177.

[13] N.S. Bakhvalov. Numerical methods. -M.: Nauka, 1985.

[14] N.N.Kalitkin. Numerical methods. -M.: Nauka, 1978.

[15] N.S.Bakhvalov, N.P.Zhidkov, G.M.Kobelkov. Numerical methods. -M.: Nauka, 1987.

[16] Zenkovskaya, S.M., Morshneva, I.V., Tsyvenkova, O.A. Methodical instructions to the workshop on the course "Numerical methods". Methods for solving Cauchy problems and boundary problems. Rostov-na-Donu: RGU UPL, 2001.

[17] G.E.Forsythe, M.A.Malcolm, K.Mouler. Computer Methods for Mathematical Computations. -M.: Mir, 1980.

[18] Dyakonov, V.P. Maple7: a training course. -St.: Peter, 2002.

[19] Savotchenko, S.E., Kuzmicheva, T.G. Methods of solving mathematical problems in Maple: Textbook. - Belgorod: Izd. Belaudit, 2001.

[20] Konushenko, V.V. Matlab. Getting Started with Matlab.

[21] Anoufriev, I.E., Smirnov, A.B., Smirnova, E.N. MATLAB7. - St.: ed. BHV-Petersburg, 2005.

*Onishkova Anastasia Mikhailovna, 344079, Rostov-on-Don, 63, 4, Russia*

# On stability of double-layer hollow cylinder under axial shrinking

A. V. Popov
a_v_popov@mail.ru

**Abstract**

The problem is to study the equilibrium stability of double-layer hollow cylinder within framework of nonlinear elasticiy. The cylinder consists of two parts inserted one into another and is exposed to axial shrinking. Each part is a hollow cylinder and the outer radius of inner one is larger then the inner radius of outer one in undeformed state. Thus, the cylinder being studied is composed of two initially strained layers and has internal stress, which exists even without external loads. The question is to determine how this internal stress influences on the stability of given body. The model of nonlinearly elastic isotropic incompressible material is used for solving the problem. The equations for neutral balance, linearised boundary conditions and conditions at the border of two layers are derived. The subcritical state solution is obtained from the exact solution of nonlinear Lame's problem for double-layer hollow cylinder. The problem of stability yields homogenius boundary-value problem for ODE-system. The numerical solution of system obtained allows answering the question of internal stress influence on the critical values of axial shrinking force.

## 1 Statement of the Problem

The problem of equilibrium stability of compound isotropic non-linearly elastic cylinder under axial shrinking is studied. Formation of the cylinder occurs as follows.

A hollow cylinder with inner radius $a_1$ and outer radius $b_1$ is posted in the other hollow cylinder with inner radius $a_2$ and outer radius $b_2$ in such a way, that $b_1 > a_2$, see Fig. 1. By the end faces of given compound cylinder a shrinking load is applied and yields the resultant force $P$, that coincides with the axis of the cylinder. Let $r_1$ be the radial coordinate within the first cylinder, $r_2$ be the radial coordinate within the outer cylinder. Obviously, $a_1 \leqslant r_1 \leqslant b_1$ and $a_2 \leqslant r_2 \leqslant b_2$.

## 2 Subcritical State

Both parts of compound cylinder are supposed to be incompressible isotropic non-linearly elastic bodies. Their deformation is described by the following coordinate transformation:

$$R_k = R_k(r_k), \quad \Phi = \varphi, \quad Z = \lambda z \ ; \quad k = 1, 2.$$

Here $r_k, \varphi, z$ and $R_k, \Phi, Z$ are cylindrical coordinates of undeformed and deformed state, respectively; $\lambda$ is elongation ratio. Deformation gradient tensor which corresponds to that transformations:

$$\mathbf{C}_k = R_k'(r_k)\mathbf{e}_r\mathbf{e}_r + \frac{R_k(r_k)}{r_k}\mathbf{e}_\varphi\mathbf{e}_\varphi + \lambda\mathbf{e}_z\mathbf{e}_z \ ; \quad k = 1, 2.$$

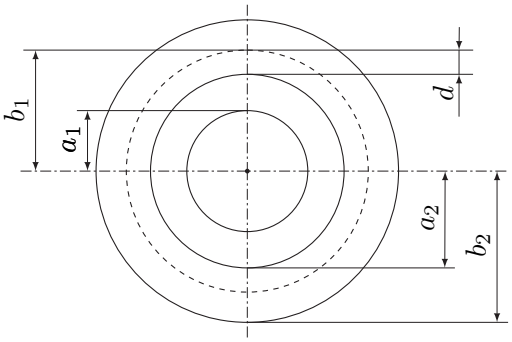


Figure 1: Cross-section of two parts of the compound cylinder before deformation.

Using the incompressibility condition $\det \mathbf{C}_k = 1$ one can find functions $R_k(r_k)$, $(k = 1, 2)$:

$$\begin{aligned} R_1(r_1) &= \sqrt{R_i^2 - \frac{a_1^2 + r_1^2}{\lambda}}\ , \quad R_i = R_1(a_1), \\ R_2(r_2) &= \sqrt{R_e^2 - \frac{b_2^2 + r_2^2}{\lambda}}\ , \quad R_e = R_2(b_2). \end{aligned} \tag{1}$$

Neo-Hook model with equal shear modulus for both cylinders is used:

$$\mathbf{D}_k = \mu \mathbf{C}_k + p_k(r_k)\mathbf{C}_k^{-T}, \quad k = 1, 2. \tag{2}$$

Here $\mathbf{D}_k$ are Piola stress tensors, $\mu$ is the shear modulus, $p_k(r_k)$ are functions of hydrostatic pressure in incompressible bodies $(k = 1, 2)$. Equilibrium equations for both cylinders are

$$\nabla \cdot \mathbf{D}_k = 0, \quad k = 1, 2. \tag{3}$$

Here $\nabla$ is the nabla-operator in non-deformed state.

Boundary conditions are the following. The inner and the outer lateral surfaces of compound cylinder are considered free from loads:

$$\mathbf{D}_{1,rr}(a_1) = 0; \quad \mathbf{D}_{2,rr}(b_2) = 0. \tag{4}$$

Further, the Caushy-Green stress $\sigma_R$ of actual configuration and the radial coordinate are considered to be equal at bordering lateral surface:

$$\frac{b_1}{\lambda R_1(b_1)}\mathbf{D}_{1,rr}(b_1) = \frac{a_2}{\lambda R_2(a_2)}\mathbf{D}_{2,rr}(a_2); \quad R_1(b_1) = R_2(a_2). \tag{5}$$

Conditions (5) mean that there are no gaps between two parts while they are deforming.

Using Eq. (3) and boundary conditions (4)-(5) functions of hydrostatic pressure are found as follows:

$$p_2(r_2) = -\mu \left[ \frac{b_2^2}{\lambda^2 R_e^2} + \frac{(R_e^2 - b_2^2)(R_2^2(r_2) - R_e^2)}{2\lambda^2 R_e^2 R_2^2(r_2)} + \frac{1}{\lambda} \ln \frac{b_2 R_2(r_2)}{r_2 R_e} \right], \tag{6}$$

$$p_1(r_1) = p_2(a_2) - \mu \left[ \frac{b_1^2 - a_2^2}{\lambda^2 R_1^2(b_1)} + \frac{(R_i^2 - a_1^2)(R_1^2(r_1) - R_1^2(b_1))}{2\lambda^2 R_1^2(b_1) R_1^2(r_1))} + \frac{1}{\lambda} \ln \frac{b_1 R_1(r_1)}{r_1 R_1(b_1)} \right]. \tag{7}$$

Substituting $R_1(r_1)$, $R_2(r_2)$ from (1) to the second boundary condition (5) one get relation between inner radius $R_i$ and outer radius $R_e$ of compound cylinder:

$$R_i(R_e) = \sqrt{R_e^2 + \frac{a_1^2 + a_2^2 - b_1^2 - b_2^2}{\lambda}} \ . \tag{8}$$

The value $P$ of the shrinking force is determined by formula

$$P = 2\pi \left( \int\limits_{a_1}^{b_1} \sigma_{Z,1}(r_1) r_1 \ dr_1 + \int\limits_{a_2}^{b_2} \sigma_{Z,2}(r_2) r_2 \ dr_2 \right);$$

$$\sigma_{Z,k}(r_k) = \mathbf{e}_z \cdot \left( \mathbf{C}_k^T \cdot \mathbf{D}_k \right) \cdot \mathbf{e}_z, \quad k = 1, 2.$$

Here $\sigma_{Z,\ k}(r_k), k = 1, 2$ are normal stresses along the axis of cylinder within the inner and the outer part, respectively; $\mathbf{e}_z$ is the frame vector along the axis of compound cylinder. Using formulas (6)–(8) and boundary conditions (4), one can get the relation between elongation ratio $\lambda$ and the outer radius $R_e$. Thus, $P$ is a function of $\lambda$ and radii $a_1$, $b_1$, $a_2$, $b_2$. The final formula of $P$ is bulky enough, that is why it doesn't appear in the paper.

## 3 Neutral Balance

Let us consider the equilibrium intense-deformed state of compound cylinder, which is determined by the position vector $\mathbf{r}$ of a particle, the subcritical state. We shall assume, that alongside with it there is an infinitely closed equilibrium state which is defined by the position vector $\mathbf{r} + \eta\mathbf{w}$, where $\mathbf{w}$ is the vector of additional displacement, $\eta$ is infinitesimal parameter. Neutral balance of incompressible body is described as follows [1, 2]:

$$\nabla \cdot \mathbf{D}_k^\bullet = 0, \quad \mathrm{tr}\left( \mathbf{C}_\mathrm{k}^{-1} \cdot \nabla \mathbf{w}_\mathrm{k} \right) = 0, \quad k = 1, 2 \ ; \tag{9}$$

$$\mathbf{D}^\bullet = \left[ \frac{d}{d\eta} \mathbf{D}\left( \mathbf{r} + \eta\mathbf{w} \right) \right]_{\eta=0} . \tag{10}$$

Linearised boundary conditions are following:

$$\mathbf{e}_r \cdot \mathbf{D}_1^\bullet(a_1) = 0; \quad \mathbf{e}_r \cdot \mathbf{D}_2^\bullet(b_2) = q \ \mathbf{e}_r \cdot \left( \mathbf{C}_2^{-T}(b_2) \right)^\bullet ; \tag{11}$$

$$\left( \mathbf{D}_1 \frac{d\sigma}{d\Sigma} \right)^\bullet \Bigg|_{r_1=b_1} = \left( \mathbf{D}_2 \frac{d\sigma}{d\Sigma} \right)^\bullet \Bigg|_{r_2=a_2} ; \quad \mathbf{w}_1(b_1) = \mathbf{w}_2(a_2). \tag{12}$$

Here $\mathbf{e}_r$ is the radial basis vector in subcritical state; $d\sigma$, $d\Sigma$ are elementary material plates in undeformed and deformed state, respectively. From Eqs (2), (10) one derives

$$\mathbf{D}_k^\bullet = \mu \nabla \mathbf{w}_k + p \left( \mathbf{C}_k^{-T} \right)^\bullet + q_k \mathbf{C}_k^{-T}; \quad q_k = p_k^\bullet, \ k = 1, 2. \tag{13}$$

Componental representations of vectors $\mathbf{w}_k$ and tensors $\mathbf{D}_k^\bullet$ $(k = 1, 2)$ in frame $\mathbf{e}_r$, $\mathbf{e}_\varphi$, $\mathbf{e}_z$ are the following:

$$\mathbf{w}_k = u_k \mathbf{e}_r + v_k \mathbf{e}_\varphi + w_k \mathbf{e}_z \ , \quad \mathbf{D}_k^\bullet = D_{k,rr}^\bullet \mathbf{e}_r \mathbf{e}_r + D_{k,r\varphi}^\bullet \mathbf{e}_r \mathbf{e}_\varphi + \ldots \ , \quad k = 1, 2. \tag{14}$$

From Eqs (9), (13), (14) one obtains two systems of four equations (9), each of them contains four unknown functions $u_k, v_k, w_k, q_k$, $(k = 1, 2)$. Both systems allow following solutions:

$$\begin{aligned} &u_k = U_k(r_k)\cos(n\varphi)cos(\alpha z), \quad v_k = V_k(r_k)\sin(n\varphi)cos(\alpha z), \\ &w_k = W_k(r_k)\cos(n\varphi)sin(\alpha z), \quad q_k = Q_k(r_k)\cos(n\varphi)cos(\alpha z), \quad k = 1, 2. \end{aligned} \tag{15}$$

Here $n = 0, 1, 2, 3, \ldots$ and $\alpha$ is real number.

Using Eq. (15), variables $\varphi$, $z$ are separating, and the boundary value problem appears for two systems of four ordinary equations with unknowns $U_k$, $V_k$, $W_k$, $Q_k$, $(k=1, 2)$ and boundary conditions (11),(12). Excluding unknown functions $W_1, Q_1$ and $W_2, Q_2$ from appropriate systems, one derives two systems of six ODEs. Matrix form of these systems is the following:

$$\begin{aligned} &\mathbf{X}'^i + \mathbf{A}^i(\rho)\,\mathbf{X}^i = 0, \quad \mathbf{X}^i = \left\{U_1, U_1', U_1'', V_1, V_1', V_1''\right\}, \\ &\mathbf{X}'^e + \mathbf{A}^e(\rho)\,\mathbf{X}^e = 0, \quad \mathbf{X}^e = \left\{U_2, U_2', U_2'', V_2, V_2', V_2''\right\}. \end{aligned} \tag{16}$$

Here $\mathbf{X}^i$, $\mathbf{X}^e$ are column vectors of unknown functions; $\mathbf{A}^i(\rho)$, $\mathbf{A}^e(\rho)$ are coefficient matrices; prime sign $'$ denotes derivation with respect to radial coordinate $r_1$ or $r_2$, respectively. Applying finite-difference form [3] and using boundary conditions (12), both systems (16) can be reduced to system of linear algebraic equatioins

$$\mathbf{S} \cdot \mathbf{Y} = 0, \tag{17}$$

where $\mathbf{Y}$ is column vector of unknown values $U_1(a_1)$, $U_1'(a_1)$, $V_1(a_1)$, $U_2(b_2)$, $U_2'(b_2)$, $V_2(b_2)$. The other values $U_1''(a_1)$, $V_1'(a_1)$, $V_1''(a_1)$, $U_2''(b_2)$, $V_2'(b_2)$, $V_2''(b_2)$ could be found using $\mathbf{Y}$ components and boundary conditions (11). The system (17) is homogeneous concerning unknowns required. The non-trivial solution of such system exists if

$$\det \mathbf{S} = 0. \tag{18}$$

Criterion (18) is the characteristic equation for obtaining critical values of axial shrinking force $P$. The criterion makes possible to find values of $\lambda$, $R_e$, $a_1$, $b_1$, $a_2$, and $b_2$, which initiate instability.

## 4 Numerical Results

Rod buckling modes was studied, it means that $n = 1$ in Eq. (15). A new parameter $\nu = \alpha b_2$ was introduced for numerical calculations. If $\alpha = \pi m/l$, where $l$ is initial length of compound cylinder and $m$ is the number of half-waves along an element of cylinder, then one can consider $\nu$ as relative diameter of cylinder. Graphs were obtained for $m = 1$ since greater values of $m$ yield same results as smaller values of $l$ if their ratio $m/l$ remains constant. Values of axial force are dimentionless, i. e., $P_* = 2P/\pi\mu b^2$.

The stability area is a part of space of parameters $(d, P_*)$, that lies below neutral curve. In Fig. 2 solid curves represent compound cylinder, while dashed curves represent a homogenious hollow cylinder with inner and outer radii equal to $R_i$ and $R_e$, respectively. The homogenious cylinder is introduced for detection of initial stress influence, similar to accessory ring in [4].

Results are presented for relatively long cylinder, $\nu = 0.1$. That is, the ratio of diameter to length is $1/5\pi$ with $m = 1$. It is quite easy to notice that slight (less than 2%) increasing

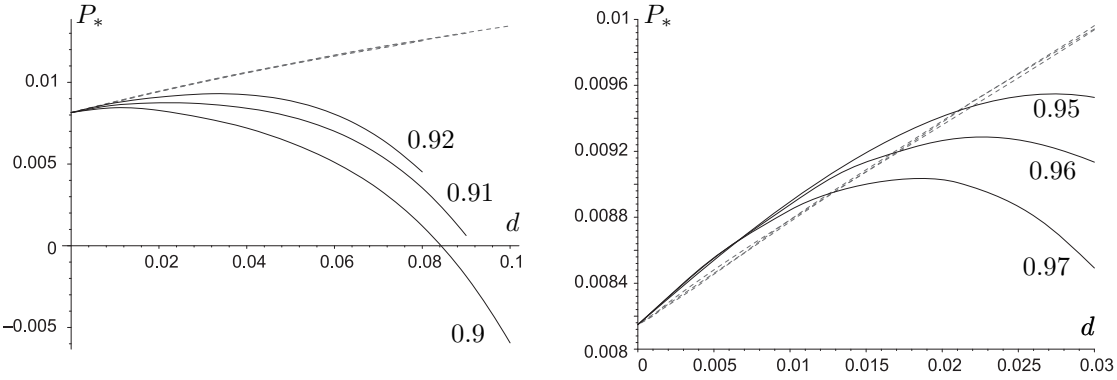


Figure 2: Neutral curves for shrinking force in case of long thin-wall cylinder with $\nu = 0.1$, $a_1 = 0.9$, $a_2$ values appear near appropriate curves. Other values: $b_2 = 1$, $b_1 = a_1 + d$.

of critical values of shrinking force takes place in rather narrow range of parameters $d$ and $a_2$, e. g., see right graph in Fig. 2. With many other values of $d$ and $a_2$ the presence of internal stress due to difference of $b_1$ and $a_2$ leads to decreasing of critical values of $P_*$. Moreover, the cylinder studied can buckle even with no load applied, but because of internal stress. For example, see left graph in Fig. 2 with $a_2 = 0.9$ and $d \approx 0.084$. Thus, long thin-wall double-layer cylinder is mainly less stable under axial shrinking in comparison to homogenious cylinder with the same values of inner and outer radii but without any internal stress.

## Acknowledgements

*This work was supported by the Federal target programme "Research and Pedagogical Cadre for Innovative Russia" for 2009–2013 years (state contract No P-596).*

## References

[1] Lurye, A. I. Theory of Elasticity (in Russian). Nauka, Moscow, 1970.

[2] Lurye, A. I. The Non-Linear Theory of Elasticity (in Russian). Nauka, Moscow, 1980.

[3] Zubov, L. M., and Moiseyenko, S. I. The Buckling of an Elastic Cylinder Under Torsion and Compression (in Russian). Izv. Acad. Nauk SSSR, Mekh. Tverd. Tela. 1981. **5**. Pp. 78–84.

[4] Zubov, L. M., and Popov A. V. The stability of a ring with initial strain (in Russian). Izv. vuzov. Severo-Kavkaz. Region. Estest. nauki. 2008. **1**. Pp. 32–36.

*Alexander V. Popov, Milchakova ul. 8a, Rostov-na-Donu, Russia*

# Influence of the nonequilibrium distribution function on dynamics of gas-surface scattering

Evelina V. Prozorova Alexander V. Shadrin
prozorova@niimm.spbu.ru

**Abstract**

We considered different aspects of interaction gas with aluminum plate. Computer simulation by dynamic methods of nonequilibrium gas and surface molecules interact in little district (2.5 of the lattice constant of the crystal structure) near surface. The distribution function is reconstructed. We investigate the long tail of destruction function on process of taking out molecules from surface.

Keywords: Boltzmann equations, Chapman-Enskog method, conjugate problem the Navie-Stokes, the molecular dynamics method.

## 1 Introduction

The important question for the problem of layer near a moving spacecraft is boundary conditions. It is necessary to know aerodynamic characteristics. These conditions are known badly for rarefied gas and for turbulence streams. To solute the Boltzmann equation is more difficult than Navier-Stokes equations. So better to solute Navier-Stokes equations. Usually for the classical case near the surface the Knudsen layer is considered. This layer has the length of order free path. M. Lunc, J. Luboncki, V.C.Liu , R.G. Patterson, W. Bule, F.O.Goodman, H.Y.Wachman, R G. Barantsev, Yu. A.Ryzhev, G.V. Dubrovskii and the others investigated the interaction molecules with surface near freely-molecular simulations. At present majority experimental and theoretical results were received for dispersion of monovelocity beam of atoms. Conjugated conditions at surface without the Knudsen layer are written to count friction and heat flow to the surface by solution the Boltzmann equation without collision integral in thin layer and by solution the Navie-Stokes equations with addition new terms with influence of an angular momentum variation in an elementary volume. The boundary conditions are made more accurate for rarefied gas and for transition flow regime. The molecular dynamics method is used to investigate the influence of the profile of the equilibrium distribution function on the exfoliation of the surface layer of aluminum for moving surface. This is the first step.

## 2 Influence of the dispersion near the surface

The problem for moving gas near the surface has some singularities. The modified Boltmann and Navier-Stokes equations are needed boundary conditions. To solute the Boltzmann equation is more difficult than Navier-Stokes equations. So better to solute Navier-Stokes equations [1-9]. In our case the equation for two-part distribution function near the

surface is

$$\frac{\partial f_2}{\partial t}+\sum_{i=1}^{2}\left\{\xi_i\cdot\left[\frac{\partial f_2}{\partial x_i}\right]+\xi_i\cdot\frac{\partial}{\partial x_i}\left[x_j\frac{\partial f_2}{\partial x_j}\right]-\frac{X_i}{m}\frac{\partial f_2}{\partial \xi_i}\right\}+X_{12}\cdot\frac{\partial f_2}{\partial \xi_1}+X_{21}\cdot\frac{\partial f_2}{\partial \xi_2}+X_{22}\frac{\partial f_2}{\partial \xi_2}=0.$$

Integrating in $\xi$ we obtain the equation for one-particle distribution function with interaction force gas molecule with surface molecules. Suggested algorithm is easily than classical. For $\xi_2$= 0 in solid body (without movement of the surface molecules) we have trajectory problem i.e. the usual of DSMC code**.**

## 3 The method of investigation

To simulate the interaction of gas with the crystal surface method has been applied molecular dynamics (MD), based on the solution of the equations of Newton [10]. In the first stage of modeling is the initial distribution of particles in space (spatial configuration of the crystal structure and the gas phase) and initial distribution of particle velocities corresponding to the mechanical and thermal motion of the system in the initial state. The generation of initial conditions occurs at the macro and micro levels. At the macroscopic level, wondered the geometric dimensions of the area in which calculations were carried out ( $L_x$, $L_y$, $L_z$) and the macroscopic velocity. Under the macroscopic velocity of the bombarding mean directional velocity of the gas stream. At the microscopic given level of packing particle structure (fcc lattice of the crystal surface) and the velocity distribution of the thermal motion of gas particles and the crystal structure. The thermal velocity distribution at the initial time is generated according to the Maxwell distribution

$$\mathrm{f}\,(\upsilon)=\frac{4}{\sqrt{\pi}}\left(\frac{m}{2kT}\right)^{3/2}\upsilon^2 e^{-\frac{m\upsilon^2}{2kT}}$$

where m is mass of atom, k is Boltzmann constant and T gas temperature.

The rate of gas particles at the initial moment of time is made up of directed macroscopic velocity and thermal velocity. The second stage computes the values of the coordinates and velocities of particles (describing the evolution of the system over time), which were carried out using the MD equations of motion integration algorithms with predetermined conditions based on the scheme Varlet [10]. The time step was chosen to be 5 fs, which is comparable with the period of molecular vibrations of the lattice.

The trajectories of the particles were calculated in a macroscopic ensemble under the thermodynamic conditions: constant number of particles, constant volume and constant temperature. The constancy of temperature in the system provides an introduction Noze-Hoover thermostat [12]. The number of gas particles was chosen to be 25, which corresponds to the pressure 1 atm in the computational volume $10^6$ ang. at 290 K. The number of particles in the structure of the computational domain is chosen equal to 10000. In this paper, the interaction between particles of type structure-structure described by a Morse potential [11]

$$U\left(r_{ij}\right)=D_0\left[e^{-2\alpha(r-r_0)}-2e^{-2\alpha(r-r_0)}\right],$$

where $r_0$ is the equilibrium internuclear separation and $D_0$, The well depth, is the dissociation energy of the molecule, $\alpha$ is an adjustable shape parameter.

For particles such as gas-gas and gas-structure described by Lennard-Johnes potential

$$U\left(r_{ij}\right) = 4\varepsilon\left[\left(\frac{\sigma}{r_{ij}}\right)^{12} - \left(\frac{\sigma}{r_{ij}}\right)^{6}\right],$$

where $\varepsilon$ is well depth $\sigma$ is affective atom diametr.

The potential parameters for the structure of the gas-particles were calculated using the formula [10]

$$\sigma_{gs} = \frac{\sigma_g + \sigma_s}{2}$$

and

$$\varepsilon_{gs} = \sqrt{\varepsilon_g + \varepsilon_s}$$

Theqradius of the particle interaction is chosen to be 2.5 of the lattice constant of the crystal structure.

Due to the limited computing resources the distribution function of gas particles is divided into a region of the velocities. For each region MD calculation was processed and distribution function was reconstructed (Fig. 1). Some particles due to the directional velocity received energy that enough to penetrate into the crystal structure (Fig. 2).

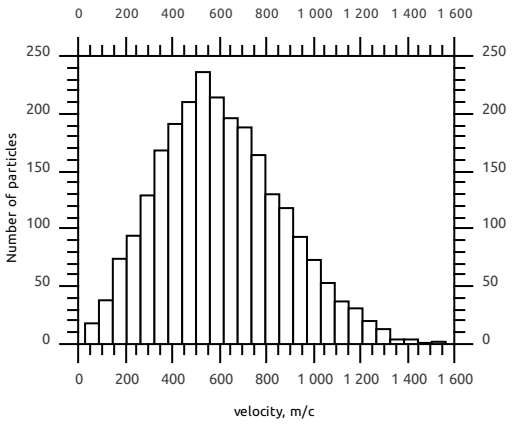


Figure 1: Gas distribution function

## Conclusion

Verified the absence of collisions between a gas in a narrow layer adjacent to the surface even for the normal pressure. Displaying the introduction of the gas molecules and the presence of fatigue effects in the case of directional velocity at the outer boundary. Proved the possibility of rejection of the Knudsen layer.

## References

[1] S. V. Vallander. The equations for movement viscosity gas. DAN SSSR .1951. V. LXX šššš, N 1

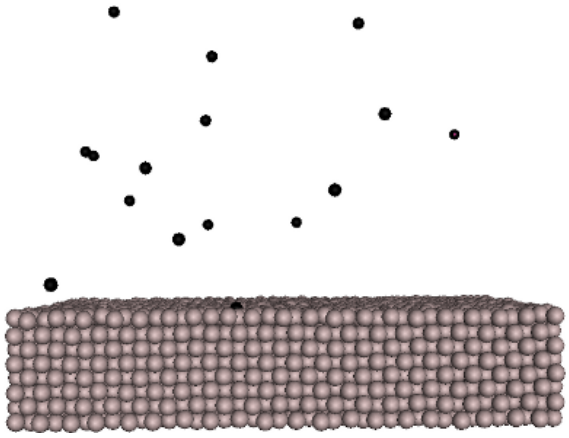

Figure 2: Penetration atom into crystal structure

[2] Alexeev. Generalized Boltzmann Physical Kinetics. Elsevier, Amsterdam, 2004

[3] C. Cercignani, Mathematical methods in kinetic theory Macmillan. 1969

[4] J.H. Ferziger, H.G. Kaper, Mathematical theory of transport processes in gases./ Amsterdam-London.1972.

[5] J.O. Hirschfelder, C.F. Curtiss, R.B. Bird, The molecular theory of gases and liquids. New-York, 1954.

[6] M.N. Kogan, The dynamics of the rarefied gases. M.: Nauka, 1967.( Russian)

[7] E.V. Prozorova, *Influence of dispersion in mechanics*. Seventh International Workshop on Nondestructive testing and Computer Simulations in Science and Engineering, edited by Akexander I. Melker, Proceedings of SPIE Vol.5400 (SPIE, Bellingham, WA, 2004) pp.212-219.

[8] E.V.Prozorova. Influence of the dispersion in nonequilibrium models for continuous mechanics. Proceedings of XXXVIII Summer School "Advanced Problems in Mechanics", pp. 568-574, Spb. 2010

[9] E.V. Prozorova. Influence dispersion and cross flux in continuous mechanics. THE EUROPEAN conference for aerospace scinces. (Russia, Saint Petersburg, 2011), id365 www.eucass.ru/cs/upload/gF76bMq/papers.zip

[10] M. P. Allen and A. K. Tildesley Computer Simulation of Liquids. – Oxford: Clarendon Press. 1987

[11] L. A. Girifalco, G. V. Weizer Application of the morse potential function to cubic metals // Phys. Rev. 114(3): p. 687 1959

[12] W. G. Hoover Cononical dynamics: Equilibrium phase-space distribution // Phys. Rev. A. 1992 V. 31. P. 1695-1697

# Influence of the dispersion in theory of continuous mechanics

Evelina V. Prozorova
prozorova@niimm.spbu.ru

**Abstract**

For continuous mechanics formulation of equilibrium of angular momentum conditions are suggested. In present time formulation of equilibrium force conditions are used. These give us symmetric pressure tensor and disturbance of continuous medium. In this work this question is discussed. Conditions of the existence of A.N. Kolmogorov inertia interval is established.

**Keywords**: Angular momentum, conservation laws, nonsymmetrical stress tensor, Boltzmann equations, Chapman-Enskog method, conjugate problem the Navie-Stokes, the molecular dynamics method.

## 1 Introduction

Many experimental facts tell us about the importance of gradients of physical values (density, linear momentum, energy). In the previous studies, the problem of influence of dispersion on the models and equations of continuum mechanics was considered carefully for various applications [1-4]. In those papers one can find also historical facts concerning different approaches to this problem, as well as some examples: in particular, modified Navier-Stokes equations, connection to kinetic theory, boundary layer, shock waves, numerical solutions, asymptotical methods, etc. So, there is no need to repeat all the details and discuss the importance of these equations.

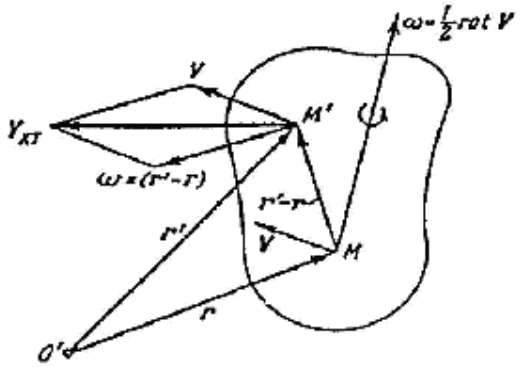


Figure 1: Velocity distribution near the point M

Presented in previous papers the equations of motion, energy and angular momentum were obtained before, but the use of force equilibrium conditions didn't require the calculation of angular momentum. When choosing the equilibrium conditions since the last

equation to determine the degree of asymmetry of the stress tensor. The issue arose when writing the law of conservation of density. Try to get it out of the equation by using phenomenological principle.

## 2 Equation for the density

The modified equation for the density was received from the kinetic theory in the form

$$\frac{\partial \rho}{\partial t} + \frac{\partial \rho u_i}{\partial x_i} + \frac{\partial}{\partial x_i}\left(x_i \frac{\partial \rho u_i}{\partial x_i}\right) = 0.$$

where $u_i$ - velocity, $\rho$ - dencity, $x_i$ - position.

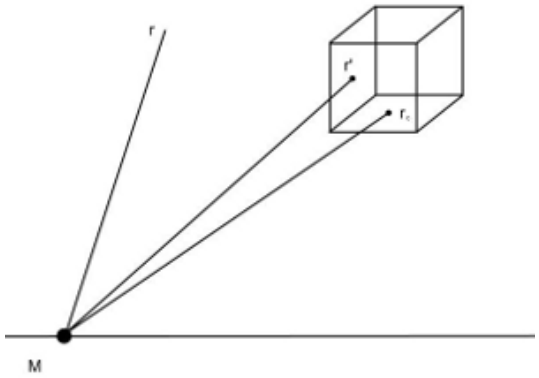


Figure 2: The influence of rotation of the elementary volume

The figure shows that the linear velocity v=$\omega \times \left(r' - r\right)$ is the velocity with respect to M for quasi-solid movement around axis without div $(\rho u)$. However, the point M can be very involved in the rotation. Consequently, the cross product will appear if the axis of rotation is chosen $r' - r$. The point M may itself be involved in the rotation. For an elementary volume v=$\omega \times \left(r' - r\right)$ formula means a rotation around the axis of the velocity at centre of inertia but axis of moving of elementary volume can be lie outside it. So we have for twisting an elementary volume. Consider the conclusion of the last term of the equation of continuity.

$$\int_{(s)} \nabla \rho \mathbf{u} \left(\mathbf{r'} - \mathbf{r_c}\right) \mathrm{ds} = \int_{(s)} \mathrm{div}\left(\nabla \rho \mathbf{u}\right) \left(\mathbf{r'} - \mathbf{r_c}\right) \mathrm{dv}$$

$\mathbf{r}$ - axis of rotation,$\mathbf{r_c}$ - center of gravity. After integration, the mention expression was received.

## 3 Infinite plate

The Blasius problem was considered by numerical and analytical. Some results for infinite plate will be formulated here. The equation for this case is

$$\frac{d}{dy}\left(\mu \frac{du}{dy}\right) + \frac{d}{dy}\left(\mu y \frac{d^2 u}{dy^2}\right) = 0.$$

Boundary conditions are

$$u = 0, \qquad \mu\frac{du}{dy} = \tau_w, \qquad y = 0, \qquad u = U_\infty, \qquad y \to \infty.$$

Integrating gives

$$\mu\frac{du}{dy} + \mu y\frac{d^2u}{dy^2} = Const = \tau_w.$$

Where $y$-coordinate, $\rho$-density, $u$-velocity, $\mu$-viscosity. Index "$w$" is relative to surface. From boundary condition we have $Const = \tau_w$. $\tau_w$ is skin friction. Integral of the equation is

$$u = C\ln y + \frac{\tau_w}{\mu}y + Const.$$

Possible variant to satisfy boundary conditions is that under the $y = \frac{\nu}{v_*}$, where $\nu = \frac{\mu}{\rho}$, $v_* = \left(\frac{\tau_w}{\rho_w}\right)^{1/2}$ we have $\ln = 0$. Later on diminution velocity takes place up zero, derivative can be very large but zero velocity observes between surface and $y$. So layer of the rest liquid is formed. Thickness of this layer is $10^{-3}$cm. We have not reliable measurements there. Probably for laminar layer there is no layer with zero velocity. Near the edge the gradient of the velocity tends to work. It works near the rebuilding region too. Far from edge friction strives to zero. It does not follow from the theory for semi-infinite plate that the value of the friction is finite but if we suggest zero friction in the first integral we can get the Karman formula for the mixture length. Equality $\tau_w = 0$ provides $u = 0$ as $y = 0$ and $u = U_\infty$ as $y \to \infty$ and leads to rebuilding of the flow. The profile of the velocity becomes more completed than near the edge. The region with $\tau_w = 0$ formulated the inertial layer( N.A. Kolmogorov). This case relies to logarithm profile for boundary layer. It is interesting that asymptotic friction for half- infinite plate has not the value for infinite plate. In my opinion we have similar situation for tubes.

## 4 Conclusion

We consider influence the angular momentum variation in an elementary volume near the surface and influence the cross flows through the sides of an elementary volume for great gradients of the physical values. Some examples are investigated.

## References

[1] L.G.Loyotinskiy. Mechanics of fluids and gas. M.: Nauka. 1970 ( Russian).

[2] E.V. Prozorova, Influence of dispersion in mechanics. Seventh International Workshop on Nondestructive testing and Computer Simulations in Science and Engineering, edited by Akexander I. Melker, Proceedings of SPIE Vol.5400 (SPIE, Bellingham, WA, 2004) pp.212-219.

[3] E.V.Prozorova. Influence of the dispersion in nonequilibrium models for continuous mechanics. Proceedings of XXXVIII Summer School "Advanced Problems in Mechanics", pp. 568-574, Spb. 2010.

[4] E.V. Prozorova. Influence dispersion and cross flux in continuous mechanics. THE EUROPEAN conference for aerospace scinces. (Russia, Saint Petersburg, 2011), id365 www.eucass.ru/cs/upload/gF76bMq/papers.zip.

# Complex variable Fast Multipole Method for modelling hydraulic fracturing in inhomogeneous media

Ewa Rejwer Liliana Rybarska-Rusinek Alexander Linkov
ewarejwer@o2.pl

**Abstract**

The work aims to develop a numerical method for modelling hydraulic fractures in strongly inhomogeneous rocks. We employ the complex variable (CV) boundary integral equations specially tailored for blocky systems with multiple interfaces. Their numerical implementation is carried out by including the CV boundary element method (BEM) in frames of the fast multipole method (FMM) to solve systems with large (up to millions) number of unknowns. Recurrent analytical quadrature rules are used for increasing the robustness and accuracy of calculations. They are obtained for higher order approximations of the density at straight and circular-arc, ordinary, tip and multi-wedge elements. Conclusions are drawn on the accuracy of the method developed.

## 1 Introduction

Hydraulic fracturing is one of the major techniques of reservoir stimulation employed by the petroleum and gas industry. In practice this method is used in rock mass, which is strongly inhomogeneous. Meanwhile, analytical studies and available numerical codes do not account for this factor because of extreme mathematical difficulties. The most advanced code by the Schlumberger Company models only a vertical fracture propagating across a few horizontal elastic layers. This work aims to develop a numerical method, which may serve for accounting for strong inhomogeneity. As a basis, we employ boundary integral equations (BIE) in a form specially tailored to model blocky systems with complicated interfacial conditions at contacts of structural elements and containing pores, inclusions and growing cracks [1], [2]. For such structures, solving the BIE by the boundary element method (BEM) is superior over the finite element method. The main difficulty when employing this method for strongly inhomogeneous rock is very large number (up to millions) unknowns. To overcome the difficulty, we follow the line of combining the BEM with the fast multipole method (FMM) (see, e.g. [3]). In this work the combined BEM-FMM is developed for plane problems in complex variables (CV). In contrast with known applications of the BEM-FMM, we employ (i) the mentioned special forms of the BIE, (ii) combinations of circular-arc and straight boundary elements providing continuous tangent when approximating smooth parts of external boundaries and contacts, (iii) special singular elements accounting for singular behaviour of fields near singular points like common apexes of structural elements, (iv) approximations of higher order for circular-arc and straight boundary elements both ordinary and singular, (v) analytical recurrent formulae for integrals defining *influence coefficients* of the BEM and *multipole moments* of the FMM. We focus on the log-type kernels as the most difficult for evaluation. Results of numerical tests highlight efficiency of the CV-BEM-FMM developed.

## 2 Evaluation of influence coefficients to solve CV-BIE for inhomogeneous media

The CV-BIE, specially derived for solving 2D potential and elasticity problems concerning with blocky systems with multiple interfaces, cracks, inclusions and pores, contain seven standard integrals [1], [2]. After representing the contour by boundary elements, the integrals to be evaluated over a boundary element $L_e$ are:

$$\int\limits_{L_e} \frac{f(\tau)}{\tau - z} d\tau, \int\limits_{L_e} \frac{f(\tau)}{(\tau - z)^2} d\tau, \int\limits_{L_e} f(\tau) \frac{\partial k_1}{\partial z} d\tau, \int\limits_{L_e} f(\tau) \frac{\partial k_2}{\partial z} d\tau,$$

$$\int\limits_{L_e} f(\tau) dk_1(\tau, z) d\tau, \int\limits_{L_e} f(\tau) dk_2(\tau - z) d\tau, \int\limits_{L_e} f(\tau) \ln|\tau - z| ds, \tag{1}$$

where $f(\tau)$ is the density, $z = x + iy$ is the CV coordinate of a filed point, $\tau$ is the CV coordinate of an integration point, $ds$ is the length increment of the integration path, $k_1 = Ln(\frac{\tau - z}{\overline{\tau} - \overline{z}})$, $k_2 = \frac{\tau - z}{\overline{\tau} - \overline{z}}$. The recurrent analytical quadrature rules, serving for efficient evaluation of the first six of them over straight and circular-arc, ordinary, tip and multi-wedge boundary elements may be found in [1], [4].

Below we focus on evaluation of the last (log-type) integral in (1), which presents the main difficulty when considering harmonic problems. They arise from the fact that in these problems the density is *real* what complicates using the *complex* variables when deriving recurrence analytical formulae for curvilinear singular boundary elements (see, e.g. [2], [5]). Having this integral evaluated, analytical quadrature rules for singular and hypersingular integrals are obtained by direct differentiation with respect to $z$, what in its turn serves for efficient evaluation of the remaining integrals.

We consider two major forms of boundary elements, which allow one to represent a smooth part of a contour by a curve with continuous tangent. These are (i) straight and (ii) circular-arc elements. By linear transformation, integration over such an element is reduced to that over a standard element.

(i) A straight element of the length $2l$ is transformed into the standard element along the real axis [-1,1] in the variable $\tau'$ by the transformation $\tau = \tau_C + l \exp(i\alpha_C)\tau'$, where $\tau_C$ is the center of an element, $\alpha_C$ is its angle with the $x$-axis. For the points of a transformed straight element we have $\tau' = \overline{\tau'}$, where the overbar denotes complex conjugation.

For a density $f(\tau')$ on a standard straight element, the recurrent quadrature rules allow us using approximation of an arbitrary order, accounting, when appropriate, for power-type asymptotics near end point $\tau' = 1$. As a rule, it is sufficient to use approximation of the second order. Then

$$f(\tau') = \sum_{k=1}^{3} f_k \sum_{j=0}^{2} c_{kj} \tau'^j (1 - \tau')^\beta, \tag{2}$$

where $f_k$ $(k = 1, 2, 3)$ are the nodal values of an approximated function, $c_{kj}$ $(j = 0, 1, 2)$ are the Lagrange coefficients. For an ordinary (non-singular) element, $\beta = 0$. For a singular element, in numerical applications we assume $\beta$ to be negative in cases when the density enters the log-type integral: $\beta = -\alpha$, with positive rational $\alpha = m/n$ $(m < n)$. When considering singular and hypersingular integrals, the exponent $\beta$ in the density may be positive rational itself: $\beta = m/n$ $(m < n)$. The value of $\beta$ for a particular problem is found by using the method suggested in [6] (for details, see [7]).

(ii) A circular-arc element with the angle $2\theta_0$ and radius $R$ is transformed into the standard circular-arc element of unit radius, having the same angle and located symmetrically with respect to the $x$-axis: $\tau = \tau_C - iR\exp(i\alpha_C)\tau'$. Herein, $\tau_C$ is the center of the arc and $\alpha_C$ is the angle of the tangent at the midpoint of the arc with the $x$-axis. For points of the transformed circular-arc element we have $\tau' = 1/\overline{\tau'}$. The approximation used on the standard circular-arc element is:

$$f(\tau') = \sum_{k=1}^{3} f_k \sum_{j=-1}^{1} \widetilde{c}_{kj}\tau'^{j}\mathrm{Re}((e^{i\theta_0} - \tau')^{\beta}), \tag{3}$$

where $\widetilde{c}_{kj}$ $(j = -1, 0, 1)$ are coefficients of the form-functions at the arc of unit radius (see, e.g. [1]). The exponent $\beta$ is prescribed similar to that for a straight ordinary or singular element.

Below the approximations (2), (3), suggested for evaluation of influence coefficients, serve us for evaluation of multipoles, as well.

## 3 Building quad-tree for FMM

A detailed description of the FMM algorithm may be found in [3]. Here we present the specific features of its numerical implementation adjusted to the particular forms of the CV-BIE. They are developed to minimize computer time and memory expense. Firstly, as all our computations are performed in the CV, the input data on the geometry of boundary elements is prescribed in the CV, as well. Thus a CV array of input data contains the CV coordinates of the central points of boundary elements. These data are repeatedly employed in further operations. In particular, an element is assumed to belong to a cell if its central point belongs to the cell.

The input information for building the hierarchical quad-tree consists of (i) these data on the coordinates of central points and (ii) a prescribed maximal number $N_{max}$ of elements, which may be in a leaf.

In our procedure, following the well-known general line (e.g.[3]), we avoid looking through the entire input data matrix. Rather, at each level, only branches are taken into consideration, and for each branch we consider only those points, which belong to the branch. This tends to reduce memory and time expense. To reach this goal, we use special *renumeration* of elements. The renumeration is performed as follows. We consider a parent-branch at some level. For it, we have prescribed the total number $M$ of points belonging to it. The points are numerated in growing order from $N_1$ to $N_2$, so that $N_2 = N_1 + M - 1$, and for each point, its number in the starting global numeration is known.

The parent-cell is divided into four child-cells, numerated form 1 to 4. The $M$ points are analized to find the child, to which a point belongs. As a result, we attribute each of $M$ points to a child-cell and find the total number of points in each of the children. Denote the total number of points in the $k$-th child $M_k$; obviously, $M = M_1 + M_2 + M_3 + M_4$. If $M_k = 0$, the corresponding child is empty and it is excluded from further analysis. Points of the first non-empty child $k_1$ with the total number of points $M_{k_1}$ obtain numbers from $N_1$ to $N_1 + M_{k_1} - 1$; points of the second non-empty child $k_2$ (if it exists) with the total number of points $M_{k_2}$ obtain numbers from $N_1 + M_{k_1}$ to $N_1 + M_{k_1} + M_{k_2} - 1$, and so on. Note, that in the new numeration, the first element of the first non-empty child-cell has the number $N_1$, while the last element of the last non-empty child-cell obtains the number $N_2$. Hence, the renumeration does not influence the numeration of elements in other cells on a

considered level and on all preceeding levels. As a result, for each child, which becomes a parent on the next level, the situation is reproduced: we have prescribed the total number of points belonging to it and numerated in growing order, which does not influence the numeration of points in other cells on the considered and preceeding levels. Finally, the totality of points in all leaves coincides with the points of the input array; now these points are numbered in that order, in which leaves appear in the dividing process.

In the course of dividing, we also save data on the number of a parent of a non-empty cell, total number of leaves and branches at each level, CV coordinates of centroids of non-empty cells, etc. These data are used later on for iterative solving the system of the CV-BEM in subroutines performing standard translations (Moment-to-Moment, Moment-to-Local and Local-to-Local) of the FMM (e.g. [3]). At each of the iterations, the multipole moments of each of leaves should be known. Their evaluation is performed by using analytical recurrence formulae, derived by the authors and presented in the next section.

## 4 Evaluation of multipole moments

As mentioned, we focus on the integral with log-type kernel. When a collocation point $z$ is far away from a boundary element of integration $L_e$, the expansion of the potential $G(\tau, z) = -\frac{1}{2\pi}\ln|\tau - z|$ into the Taylor series, yields:

$$-\frac{1}{2\pi}\int\limits_{L_e} f(\tau)\ln|\tau - z|ds \approx \frac{1}{2\pi}\mathrm{Re}\left(\sum_{q=0}^{R_q} O_q(z-\tau_0)\int\limits_{L_e} I_q(\tau-\tau_0)f(\tau)ds\right), \tag{4}$$

where $\tau_0$ is the *global* CV coordinate of the center of that leaf, to which the element $L_e$ belongs, $z$ is the CV coordinate of a collocation point, $R_q$ is the prescribed maximal degree of multipole moments, which are kept in multipole expansions. The functions $O_q(z-\tau_0)$ and $I_q(\tau-\tau_0)$ are defined as (e.g. [3]):

$$O_0(z-\tau_0) = -Ln(z-\tau_0),\ O_q(z-\tau_0) = \frac{(q-1)!}{(z-\tau_0)^q} \text{ for } q \geq 1,$$

$$I_q(\tau-\tau_0) = \frac{(\tau-\tau_0)^q}{q!} \text{ for } q \geq 0.$$

An integral with the integrand $I_q(\tau-\tau_0)f(\tau)$, containing the $q$-th degree of $\tau-\tau_0$, is called the multipole moment of order $q$. To evaluate the moments, we use the same transformations of coordinates, which have been employed when evaluating the influence coefficients.

For a straight boundary element, with the density function (2), we obtain:

$$M_{LS}^q(\tau_0') = \frac{1}{q!}\sum_{k=1}^{3} f_k \sum_{j=0}^{2} c_{kj} l (l e^{i\alpha_C})^q \int\limits_{-1}^{1} \tau'^j (1-\tau')^\beta (\tau'-\tau_0')^q d\tau'. \tag{5}$$

For a circular-arc element with the density function (3), we have:

$$M_{LC}^q(\tau_0') = \frac{1}{q!}\sum_{k=1}^{3} f_k \sum_{j=-1}^{1} \widetilde{c}_{kj}(-iR)(-iRe^{i\alpha_C})^q \int\limits_{e^{-i\theta_0}}^{e^{i\theta_0}} \tau'^{j-1}\mathrm{Re}((e^{i\theta_0}-\tau')^\beta)(\tau'-\tau_0')^q d\tau', \tag{6}$$

In both cases, $\tau_0'$ is the *local* CV coordinate of the leaf centroid.

Denote $M_q^j$ a typical integral on the right-hand side of equations (5) and (6),

$$M_q^j = \int_a^b w(\tau')\tau'^j(\tau' - \tau_0')^q d\tau', \tag{7}$$

Herein, $w(\tau')$ is a real weight function, accounting for behaviour of the density near the end point $b$; for an ordinary straight or circular-arc element, $w(\tau') = 1$; for a singular straight element ($b = -a = 1$), $w(\tau') = (1 - \tau')^\beta$; for a singular circular-arc element ($b = a^{-1} = e^{i\theta_0}$), $w(\tau') = \mathrm{Re}((e^{i\theta_0} - \tau')^\beta)$. When using three-node elements, we consider $j = 0, 1, 2$ for a straight element and $j = -2, -1, 0$ for a circular-arc element. As $(\tau' - \tau_0')^q = (\tau' - \tau_0')^{q-1}(\tau' - \tau_0')$, equation (7) yields the recurrence formula:

$$M_q^j = M_{q-1}^{j+1} - \tau_0' M_{q-1}^j. \tag{8}$$

Although equation (8) may be employed for evaluation of all the moments, it does not provide robust procedures for a straight element, because it requires using all the terms $M_0^{2+q}$ when calculating $M_q^2$ with $q$ running from 1 to $R_q$. Meanwhile, as shown below, we need to use equation (8) when considering negative degrees $j = -1, -2$, which appear in moments for circular-arc elements.

An alternative, more convenient recurrence equation for non-negative degrees $j$ ($j = 0, 1, 2$) employs binomial representation of $\tau'^j$, written as $\tau'^j = [(\tau' - \tau_0') + \tau_0']^j$. Denote

$$\widetilde{I}_q = \int_a^b w(\tau')(\tau' - \tau_0')^q d\tau'. \tag{9}$$

In many cases these coefficients are promptly evaluated recurrently in an analytical form. Then for $j = 0, 1, 2$ we obtain:

$$M_q^0 = \widetilde{I}_q,\ M_q^1 = \widetilde{I}_{q+1} + \tau_0'\widetilde{I}_q,\ M_q^2 = \widetilde{I}_{q+2} + 2\tau_0'\widetilde{I}_{q+1} + \tau_0'^2\widetilde{I}_q. \tag{10}$$

Equations (9) and (10) provide efficient evaluation of moments for straight elements.

For circular-arc elements, we firstly find

$$M_0^{-1} = \int_a^b w(\tau')\frac{1}{\tau'}d\tau',\ M_0^{-2} = \int_a^b w(\tau')\frac{1}{\tau'^2}d\tau'. \tag{11}$$

Then all higher-order moments are found recurrently by using (8), ( 9):

$$M_q^0 = \widetilde{I}_q,\ M_q^{-1} = \widetilde{I}_{q-1} - \tau_0' M_{q-1}^{-1},\ M_q^{-2} = M_{q-1}^{-1} - \tau_0' M_{q-1}^{-2}. \tag{12}$$

Equations (9), (11), (12) provide evaluation of moments for circular-arc elements.

## 5 Numerical experiments

We used exact analytical formulae for integrals over a closed or open circular contour (see, e.g. [1]) to (i) check that the derived formulae and developed procedures were correct, (ii) study the influence of the highest order $R_q$ of moments employed on the accuracy of calculations. We considered both log-type and singular integrals.

For a field point outside a closed contour, the singular integral with constant density is zero. Application of FMM and the moments of the form (5) and (6) gave this result with high accuracy. Specifically, when approximating the contour by four straight or circular-arc boundary elements, under the assumption that the field point is located at a distance $0.05\pi$ from the contour, the evaluated value was $10^{-17}$ for both types of elements. Approximations by a larger number of elements do not affect this accuracy notably.

In another example, we considered an open contour represented by the circular crack with the angle $2\theta_0 = \frac{\pi}{3}$, radius $R = 0.025$, and the center of the circle at the point $\tau_C = 0.3(1 + i)$. The length of the crack is $L = 2R\theta_0 = \pi R/3$. The distance from the center of the crack to the field point is $R + nL$ with $n = 1(3, 9)$. The relative distance is $r = \frac{R}{R+nL}$. Table 1 contains the obtained data on the accuracy of the CV-FMM-BEM for various $r$ and $R_q$.

Table 4: Relative error of CV-BEM-FMM for various relative distance of field point and for various number of moments

| | $M_{LC},\ \beta = 0.0$ | | | | $M_{SC},\ \beta = 0.0$ | | | |
|---|---|---|---|---|---|---|---|---|
| $R_q$ | 5 | 8 | 12 | 16 | 5 | 8 | 12 | 16 |
| r=1/3 | | | | | | | | |
| relative error | 3E-5 | 2E-5 | 7E-7 | 4E-8 | 1E-2 | 6E-4 | 4E-5 | 2E-6 |
| r=1/9 | | | | | | | | |
| relative error | 1E-6 | 1E-8 | 1E-8 | 1E-8 | 1E-4 | 3E-7 | 1E-10 | 1E-13 |
| r=1/19 | | | | | | | | |
| relative error | 1E-7 | 1E-8 | 1E-8 | 1E-8 | 2E-6 | 1E-9 | 1E-12 | 3E-13 |

The data of Table 1 show that, as could be expected, the accuracy grows with growing distance and the number of moments held in calculations. It can be also seen that to the accuracy commonly provided by the conventional CV-BEM in calculations with double precision (5-6 significant digits, at most), for $r = 1/3$ $(1/9,\ 1/19)$, it is sufficient to hold the moments of the degree $R_q = 5$ $(4,\ 3)$ and $R_q = 12$ $(6,\ 4)$, respectively, for ordinary log-type and singular-type circular-arc element.

## 6 Acknowledgment

*The first and the third of the authors (E. R. and A. L.) gratefully acknowledge the support of the European Research Agency (FP7-PEOPLE-2009-IAPP Marie Curie IAPP transfer of knowledge programme, Project Reference # 251475). The second auther (L. R.-R.) appreciates the support of the Polish Ministry of Science and Higher Education (Scientific Project N N519 440739 for 2010- 2012).*

## References

[1] Linkov A. M. Boundary Integral Equations in Elasticity Theory, Kluwer Academic Publishers, 2002.

[2] Dobroskok A. A., Linkov A. M. Complex variable equations and numerical solution of harmonic problems for piece-wise homogeneous media. J. Appl. Math. Mech., 2009, 73 (3), 313-325.

[3] Liu Y. J., Nishimura N. The fast multipole boundary element method for potential problems: A tutorial. Eng. Anal. Bound. Elem., 2006, 30, 371-381.

[4] Linkov A. M., Koshelev V. F., Blinova V. G. Tip, corner and wedge Elements: A regular way to increase accuracy of the BEM, IABEM, UT Austin, TX, USA, 2002.

[5] Linkov A. M., Szynal-Liana A. CV circular-arc ordinary and (multi-) wedge elements for harmonic problems, Eng. Anal. Bound. Elem., 2009, 33, 611-617.

[6] Blinova V. G., Linkov A. M. A method to find asymptotic forms at the common apex of elastic wedges. J. Appl. Math. Mech., 1995, 59 (2), 187-195.

[7] Linkov A. M., Koshelev V. F. Multi-wedge points and multi-wedge elements in computational mechanics: evaluation of exponent and angular distribution. Int. J. Solids and Structures, 2006, 43, 5909-5930.

*Ewa Rejwer, Liliana Rybarska-Rusinek, Alexander M. Linkov, Rzeszow University of Technology, Powstancow Warszawy 12, 35-959 Rzeszow, Poland.*

# Deformation mechanisms of wood at the ultrastructural scale

Erick I. Saavedra Flores Michael I. Friswell
e.i.saavedra-flores@swansea.ac.uk

**Abstract**

This paper investigates the deformation mechanisms of wood at the ultrastructural scale. At this level, wood is composed of a periodic alternation of amorphous and crystalline cellulose fractions, embedded in a soft hemicellulose-lignin matrix. The mechanical response of wood is calculated under tensile loading conditions by means of the computational homogenisation of a representative volume element (RVE) of material. Three potential mechanisms of failure are suggested: axial straining of the crystalline fraction of cellulose, accumulation of plastic strain in the amorphous portion of cellulose and tensile rupture in the hemicellulose-lignin matrix due to cellulose fibres separation. In order to validate the present multi-scale framework, we assess successfully our numerical predictions for ultimate strains at the instant of failure with experimental values.

## 1 Introduction

Wood microstructure can be understood as the result of an optimisation process developed by nature over hundreds of millions years of evolution. One of its main features is its hierarchical nature distributed across multiple spatial scales, from submicrometer dimensions to macroscopic scales. This important feature has been a subject of intensive research over the last few years in applied and computational mechanics circles [1, 2, 3]. Nevertheless, despite the increasing interest in this subject and the considerable effort devoted to its description, the complete understanding of the deformation and failure mechanisms of this material at very small scales, and their implications on the macroscopic response, is still an issue which remains open at present.

The constitutive description of wood at several scales has been widely investigated by means of computational multi-scale constitutive models. In the context of elastic response, several works have been presented. Holmberg *et al.* [1] studied the mechanical behaviour of wood by means of a homogenisation-based multi-scale procedure, incorporating growth rings, irregularity in the shape of cells and anisotropy in the layered structure of cell-walls. Hofstetter *et al.* [4, 5] suggested five elementary phases for the mechanical characterisation of wood. These were hemicellulose, lignin, cellulose, with its crystalline and amorphous portions, and water. They proposed a multi-scale model and validated their numerical predictions with experimental data. Qing and Mishnaevsky Jr. [6, 7] proposed a model taking into account several scale levels and investigated the influence of microfibril angles, shape of the cell cross-section and wood density on the elastic properties of wood. Recently, Qing and Mishnaevsky Jr. [3] extended their model by incorporating progressive damage to the homogenised elasticity matrix. Additional works in this field can be found, for instance, in Ref. [8].

In spite of this extensive work, a review of the current literature shows that little research has been done in the context of irreversible processes and microscopic dissipative phenomena taking place in wood at several scales. In Ref. [2], the authors investigated the non-linear irreversible behaviour of wood cell-walls. By adopting a finite element-based computational multi-scale approach, it was shown that one important mechanism of dissipation under tensile loading is the shear plastic deformation in the hemicellulose-lignin matrix due to the reorientation of cellulose fibres induced by their alignment with respect to the loading direction.

Due to its relevance in the macroscopic mechanical response of wood and wood-based materials, our main objective in this paper is to investigate the ultrastructural mechanisms of deformation and failure in wood under tensile loading conditions by means of a computational multi-scale approach. We study the local mechanisms of deformation in wood for a wide range of initial orientation of fibres. Here, we study the failure mechanisms associated with axial straining of the crystalline cellulose fraction, accumulation of plastic strain in the amorphous portion of cellulose and tensile rupture in the hemicellulose-lignin matrix due to cellulose fibres separation. We validate the present model by comparing our numerical predictions for the strains at the instant of failure with experimental data for wood under tension.

## 2 Ultrastructural mechanical properties of wood

At the ultrastructural scale [9, 10, 11], the wall of wood cells contains three fundamental constituents: cellulose, hemicellulose and lignin. These constituents form a spatial arrangement called microfibril which can be represented as a periodic unit building block of rectangular cross-section (refer to Figure 1).

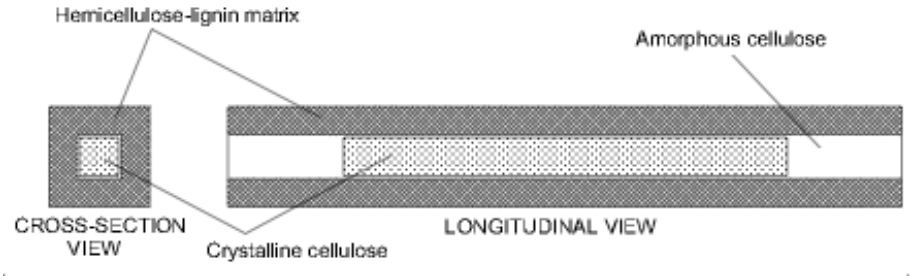


Figure 1: Schematic representation of the microfibril and basic constituents. The cross-section on the left of the figure shows the crystalline cellulose in the centre covered with an outer surface layer made up of amorphous cellulose [12], embedded in the hemicellulose-lignin matrix [13]. The longitudinal view on the right illustrates a typical periodic arrangement of crystalline and amorphous cellulose along the length of the microfibril.

Cellulose, hemicellulose and lignin constitute approximately 30%, 32.5% and 37.5%, respectively, of the total volume of wood substance for *compression wood* cells [2]. The cellulose is a long polymer composed of glucose units which is organised into periodic crystalline and amorphous regions along its length [14] (refer to Figure 1 for a representative portion of this periodic amorphous-crystalline cellulose arrangement). This periodic arrangement is further covered by an outer surface made up of amorphous cellulose [12]. The (volumetric) degree of crystallinity is defined as the ratio between the volume of crystalline cellulose and the total volume of (crystalline and amorphous) cellulose. Normally, its value varies between 0.49 and 0.60 in wood cells of Scots pine and Norway spruce, with

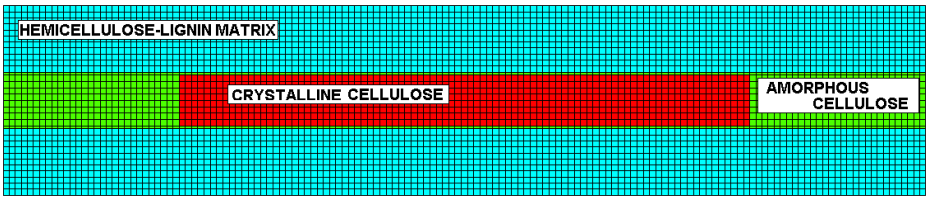


Figure 2: Typical RVE finite element mesh adopted for the computational homogenisation of wood at the ultrastructural scale.

an average value of 0.52 [15]. The specific orientation of microfibrils with respect to the longitudinal cell axis is called the microfibril angle (MFA) and is one of the most important parameters controlling the balance between stiffness and flexibility in trees. Hemicellulose is a polymer with little strength built up of sugar units, with mechanical properties highly sensitive to moisture changes. Despite its partially aligned molecular structure, it can be modelled isotropically. Lignin is an amorphous polymer whose purpose is to cement the individual cells together and to provide shear strength. Its amorphous structure makes possible the assumption of isotropy. Since the distribution of the hemicellulose and lignin in the matrix is not important, it is possible to adopt a single equivalent material for the description of the lignin-hemicellulose matrix [13]. In Ref. [16], the authors showed how the hemicellulose-lignin matrix in wood tissue and in individual cells undergoes large shear strains without apparent damage. This self-healing mechanism present in wood cells allows the assumption of no limit for the maximum shear strain in the hemicellulose-lignin matrix. Nevertheless, a maximum tensile strain of 15% can be adopted for the matrix [17], as a limit strain for the separation between cellulose fibres. For further information about the mechanical properties of the wood cell-wall constituents, we refer to Refs. [2, 19, 18].

## 3 Multi-scale finite element model

In this section, we consider the fully coupled two-scale finite element modelling of wood at the ultrastructural scale, subject to in-plane tensile loading conditions. The computational homogenisation scheme adopted here corresponds to the *periodic boundary displacement fluctuations* model [20], typically associated with the modelling of (heterogeneous) periodic media.

The procedure described in the following consists of modelling the mechanical response of wood at the ultrastructural scale by means of one single layer, with cellulose fibres oriented in one single direction.

The (microscopic) RVE consists of a two-dimensional periodic arrangement of crystalline and amorphous cellulose fibres embedded in the hemicellulose-lignin matrix. Figure 2 shows a typical RVE finite element mesh adopted for the computational homogenisation of the microstructure. It contains 4768 F-bar four-noded quadrilateral elements with a total number of 4950 nodes. To eliminate volumetric locking, the F-Bar methodology [21] is adopted throughout. For all of the finite element analyses we assume plane strain conditions under large strains regime.

The crystalline cellulose is assumed to be elastic. The amorphous cellulose and the hemicellulose-lignin matrix are modelled with an elastic-perfectly plastic von Mises law. For details about the mechanical properties of the basic constituents, we refer to [19].

The macroscopic problem consists of a $10 \times 10$ mm portion of material whose constitutive law is defined by the computational homogenisation of the above microstructure. Since

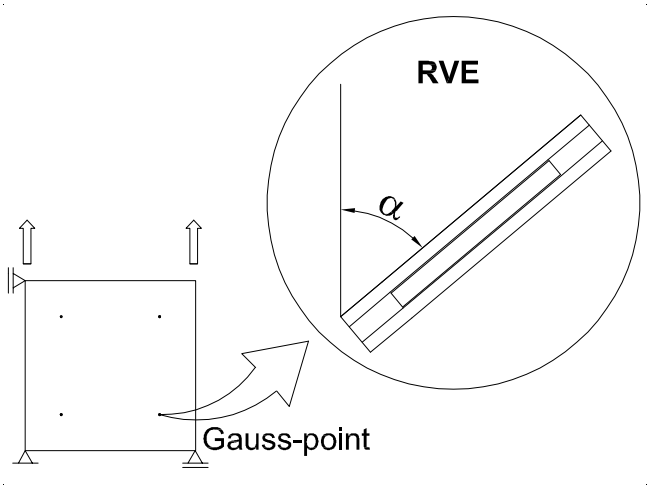


Figure 3: Macroscopic finite element mesh adopted for the computation of the actual tensile strain state at a Gauss-point.

we are interested in the mechanical response of the material, one single F-bar four-noded quadrilateral element is adopted to determine the actual tensile strain state at a macroscopic Gauss-point as illustrated in Figure 3. We note that the same approach was used by Govaert *et al.* [22] to investigate the time-dependent failure behaviour of off-axis loaded composites. Appropriate boundary constraints are imposed on the element as shown in Figure 3. In addition, since the in-plane shear strain is prevented in the wood cell-wall composite due to the interlocking between two or more adjacent cells in the wood tissue [16], the shear deformation is also prevented here by enforcing identical displacements in the $x$-direction at the two nodes on the left of the element (in all of the cases, $x$ and $y$-axes coincide respectively with the horizontal and vertical directions).

The loading programme consists of applying a prescribed displacement in the $y$-direction, sufficiently large to fail the material. The total prescribed displacement is applied in 20 incremental steps. However, when no convergence is detected in the solution of the RVE equilibrium problem at any macroscopic Gauss-point, smaller load increments are taken to ensure the success of the whole macroscopic loading programme. During tensile loading conditions, the (initial) MFA will evolve into a smaller angle $\alpha$ as shown in Figure 3. In order to investigate the reorientation of the cellulose fibres in wood, we select a wide range of MFAs for our study, between 0 and $90^o$ with respect to the loading direction.

In this investigation, the total failure of wood at the ultrastructural scale is assumed to be associated with the local failure of one of the basic constituents (crystalline or amorphous cellulose, or hemicellulose-lignin matrix). When the (microscopic) strain exceeds the maximum value or ultimate strain in at least one of the constituents, the whole cell-wall composite is assumed to have failed and the corresponding numerical simulation is stopped.

The following potential mechanisms of failure [23] are suggested in this investigation. The first failure mechanism is associated to the longitudinal straining of the crystalline cellulose fraction. In this particular failure mode, the longitudinal tensile strain in the crystalline cellulose reaches the ultimate strain of 0.0014 [19]. For each load step, the longitudinal tensile strain is computed in the crystalline fraction of the microscopic finite element mesh as the change in length per unit *reference* length.

The second potential mechanism of failure is the accumulation of plastic deformation in the amorphous fraction of cellulose. The condition of failure is assumed to occur when the volume averaged equivalent plastic strain reaches the value of 0.13 [19].

A third type of failure mechanism can occur under a dominant state of tensile deformation in the hemicellulose-lignin matrix, which is normally represented by the condition of cellulose fibres separation. Here, the failure is assumed to occur when a maximum total tensile strain of 0.15 is found [19].

## 4 Numerical results

Our purpose in this section is to validate the present multi-scale model with published experimental data. For all the cases, the variation of the MFA during straining is computed at each load step as the current orientation of the crystalline fraction of cellulose with respect to tensile loading axis. Similarly, the macroscopic strain is calculated at each load step as the current prescribed displacement divided by the initial length of 10 mm.

Figure 4 illustrates the maximum (macroscopic) strains obtained from our multi-scale

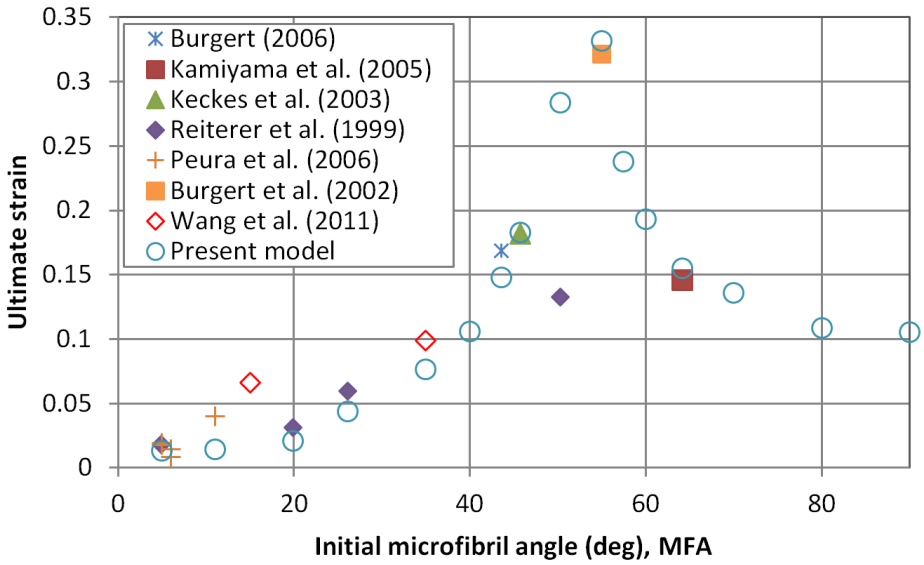


Figure 4: Ultimate tensile strains versus the MFA. Numerical predictions and some experimental results obtained from Refs. [24, 25, 16, 26, 27, 28, 29].

finite element model at the instant of failure along with some experimental values reported for a wide range of initial MFAs.

Despite the large scatter found in the mechanical properties of wood, our numerical model reveals a reasonably good agreement with the reported data. For a very small initial MFA, equal to $5^o$, our numerical model predicts an ultimate strain of 0.013, which is very similar to the experimental value reported by Peura *et al.* and Reiterer *et al.*, as shown in Figure 4. Similarly, for a MFA close to $20^o$, our model predicts an ultimate strain of 0.02, which is in good agreement with the result provided by Reiterer *et al.*, for the same initial MFA. We note that, the results shown in Figure 4 have been calculated with a volume fraction of cellulose equal to 50% (following Refs. [30, 31] for $S_2$-layer) when the MFA is smaller or equal than $20^o$. For larger MFAs, we have adopted a value of 30% [32, 33].

For larger MFAs, between 20 and $45^o$, our numerical results match the experimental data reasonably well. We emphasise the almost perfect matching with those values calculated for initial MFAs close to $45^o$, when compared with Burgert [34] and Keckés *et al.* [16]. In fact, the exponential trend described by our multi-scale model coincides qualitatively with the trend shown by the experimental data, with small fracture strains for small MFAs

and with larger strains for MFAs approaching $45^o$. It is also interesting to note that for initial MFAs smaller than $30^o$, the dominant mechanism of failure is related to the axial tensile straining of the crystalline cellulose.

We note that the published experimental data for MFAs larger than $45^o$ is very scarce. When compared to the value reported by Reiterer *et al.*, for an MFA close to $50^o$, our model overestimates the response with an ultimate strain of about 0.28. However, when compared to the fracture strains published by Burgert *et al.* and Kamiyama *et al.*, our proposed model provides an almost perfect matching. For an angle of $55^o$, the predicted maximum strain is near 0.33, and for $64.2^o$, the predicted value is 0.155, which are in good agreement with the experimental results shown in Figure 4.

Unfortunately, tensile experiments on wood samples with MFAs larger than $65^o$ have not been reported to the best of our knowledge. Therefore, more information on fracture strains as function of the MFA is needed here, probably on tissue of the $S_1$-layer, in which the MFA is near $90^o$ [35].

For very large MFAs, over $70^o$, the prevailing failure mode is associated with the tensile rupture of the matrix due to the separation of cellulose fibres. In general, for values of MFA between 30 and $70^o$, the failure mechanism is associated with the inelastic yielding of the amorphous portion of cellulose.

As suggested by Reiterer *et al.* [26], one of the main reasons for larger fibrillar angles in the wood cell wall is the optimisation of extensibility. For instance, the ability to develop large deformations is a fundamental feature in the branches of a tree. In order to allow large strains without failure, plants have evolved in time by adapting their microstructure to withstand mainly wind loads, self-weight and snow. At the same time, their microstructure must facilitate growth strains and adaptation to environmental conditions. For example, *compression wood* cells are typical fibres which can be found in branches of conifers. Normally, their MFA is larger than $45^o$ [36]. Burgert *et al.* reported initial MFAs for *compression wood* cells between 50 and $60^o$ [28]. Reiterer *et al.* [26] and Gindl *et al.* [37] published a value of $50^o$. Burgert *et al.* [38] determined by X-ray scattering a value of $52^o$. Remarkably, by observing Figure 4, we can find that our model predicts the maximum ultimate strains within this interval, at about 50-55$^o$. Any initial MFA out of this range will result in a smaller ultimate strain and therefore, in reduced extensibility. Consequently, our model is able to provide new clues into the understanding of how trees and plants optimise their microstructure in order to develop larger strains without apparent damage. The requirement of extensibility is of paramount importance when the material is deformed by the combined action of internal growth processes and environmental loading conditions.

## 5 Conclusions

This paper has investigated the deformation mechanisms of wood at the ultrastructural scale by means of a computational multi-scale approach. Three potential mechanisms of failure have been suggested under tensile loading conditions. These are: axial straining of the crystalline cellulose fraction, accumulation of plastic strain in the amorphous portion of cellulose and tensile rupture in the hemicellulose-lignin matrix due to cellulose fibres separation. Our numerical predictions for the ultimate strains in the material have been validated successfully with published experimental data. For initial MFAs smaller than $30^o$, the dominant mechanism of failure is related to the axial tensile straining of the crystalline cellulose whereas for very large MFAs, over $70^o$, the prevailing failure mode is associated with the tensile rupture of the matrix due to the separation of cellulose fibres. For inter-

mediate values of MFA, the failure mechanism is associated with the inelastic yielding of the amorphous portion of cellulose. We believe that the present modelling strategy, with the appropriate support of experimental work, can provide a robust platform for further investigations with a particular view to clarify unsolved issues with the microscopic dissipative mechanisms, and their influence on the macroscopic response, which still remain open at present.

## Acknowledgements

*E.I. Saavedra Flores and M.I. Friswell acknowledge the support of the European Research Council through project 247045 entitled "Optimisation of Multi-scale Structures with Applications to Morphing Aircraft". E.I. Saavedra Flores also acknowledges gratefully the support of the Department of Civil Engineering, University of Santiago, Chile.*

## References

[1] S. Holmberg, K. Persson, H. Petersson, Nonlinear mechanical behaviour and analysis of wood and fibre materials, Computers and Structures 72 (4-5) (1999) 459–480.

[2] E. I. Saavedra Flores, E. A. de Souza Neto, C. Pearce, A large strain computational multi-scale model for the dissipative behaviour of wood cell-wall, Computational Materials Science 50 (3) (2011) 1202–1211.

[3] H. Qing, L. Mishnaevsky Jr., A 3D multilevel model of damage and strength of wood: Analysis of microstructural effects, Mechanics of Materials 43 (9) (2011) 487 – 495. doi:10.1016/j.mechmat.2011.05.007.

[4] K. Hofstetter, C. Hellmich, J. Eberhardsteiner, Development and experimental validation of a continuum micromechanics model for the elasticity of wood, European Journal of Mechanics A/Solids 24 (6) (2005) 1030–1053.

[5] K. Hofstetter, C. Hellmich, J. Eberhardsteiner, Micromechanical modeling of solid-type and plate-type deformation patterns within softwood materials. a review and an improved approach, Holzforschung 61 (4) (2007) 343–351.

[6] H. Qing, L. Mishnaevsky Jr., 3D hierarchical computational model of wood as a cellular material with fibril reinforced, heterogeneous multiple layers, Mechanics of Materials 41 (9) (2009) 1034–1049.

[7] H. Qing, L. Mishnaevsky Jr., 3D multiscale micromechanical model of wood: From annual rings to microfibrils, International Journal of Solids and Structures 47 (9) (2010) 1253–1267.

[8] L. Mishnaevsky Jr., H. Qing, Micromechanical modelling of mechanical behaviour and strength of wood: State-of-the-art review, Computational Materials Science 44 (2) (2008) 363 – 370. doi:10.1016/j.commatsci.2008.03.043.

[9] D. Fengel, G. Wegener, Wood: chemistry, ultrastructure, reactions, Walter de Gruyter, Berlin, 1989.

[10] H. Harada, W. Côté, Biosynthesis and biodegradation of wood components, in: Structure of wood, FL: Academic Press, Orlando, 1985, p. 679.

[11] R. Neagu, E. Gamstedt, S. Bardage, M. Lindström, Ultrastructural features affecting mechanical properties of wood fibres, Wood Material Science and Engineering 1 (3-4) (2006) 146–170.

[12] P. Xu, L. A. Donaldson, Z. R. Gergely, L. A. Staehelin, Dual-axis electron tomography: a new approach for investigating the spatial organization of wood cellulose microfibrils, Wood Science and Technology 41 (2) (2007) 101–116.

[13] T. Nilsson, P. J. Gustafsson, Influence of dislocations and plasticity on the tensile behaviour of flax and hemp fibres, Composites Part A: Applied Science and Manufacturing 38 (7) (2007) 1722–1728.

[14] S. Andersson, A study of the nanostructure of the cell wall of the tracheids of conifer xylem by x-ray scattering, Ph.D. thesis, University of Helsinki, Finland (2006).

[15] S. Andersson, H. Wikberg, E. Pesonen, S. L. Maunu, R. Serimaa, Studies of crystallinity of scots pine and norway spruce cellulose, Trees - Structure and Function 18 (3) (2004) 346–353.

[16] J. Keckés, I. Burgert, K. Frühmann, M. Müller, K. Kölln, M. Hamilton, M. Burghammer, S. Stanzl-Tschegg, P. Fratzl, Cell-wall recovery after irreversible deformation of wood, Nature Materials 2 (2003) 811–814.

[17] M. C. Jarvis, Plant cell walls: supramolecular assembly, signalling and stress, Structural Chemistry 20 (2009) 245–253.

[18] J. Dinwoodie, Timber – Its nature and behavior, Von Nostrand Reinhold, New York, 1981.

[19] E. I. Saavedra Flores, M. I. Friswell, Ultrastructural mechanisms of deformation and failure in wood under tension, Submitted to International Journal of Solids and Structures.

[20] E. A. de Souza Neto, R. Feijóo, Variational foundations of large strain multi-scale solid constitutive models: Kinematical formulation, in: M. V. Jr., E. de Souza Neto, P. M. oz Rojas (Eds.), Advanced multi-scale material modelling: From classical to multi-scale techniques, Wiley: Chichester, 2010.

[21] E. A. de Souza Neto, D. Perić, M. Dutko, D. R. J. Owen, Design of simple low order finite elements for large strain analysis of nearly incompressible solids, International Journal of Solids and Structures 33 (1996) 3277–3296.

[22] L. E. Govaert, H. J. Schellens, H. J. M. Thomassen, R. J. M. Smit, L. Terzoli, T. Peijs, A micromechanical approach to time-dependent failure in off-axis loaded polymer composites, Composites: Part A 32 (2001) 1697–1711.

[23] E. I. Saavedra Flores, M. I. Friswell, Multi-scale finite element model for a new material inspired by the mechanics and structure of wood cell-walls, Journal of the Mechanics and Physics of Solids 60 (7) (2012) 1296 – 1309. doi:10.1016/j.jmps.2012.03.007.

[24] I. Burgert, Exploring the micromechanical design of plant cell walls, American Journal of Botany 93 (10) (2006) 1391–1401.

[25] T. Kamiyama, H. Suzuki, J. Sugiyama, Studies of the structural change during deformation in cryptomeria japonica by time-resolved synchrotron small-angle x-ray scattering, Journal of Structural Biology 151 (1) (2005) 1 – 11. doi:10.1016/j.jsb.2005.04.007.

[26] A. Reiterer, H. Lichtenegger, S. Tschegg, P. Fratzl, Experimental evidence for a mechanical function of the cellulose microfibril angle in wood cell walls, Philosophical Magazine A 79 (9) (1999) 2173–2184.

[27] M. Peura, I. Grotkopp, H. Lemke, A. Vikkula, J. Laine, M. Müller, R. Serimaa, Negative poisson ratio of crystalline cellulose in kraft cooked norway spruce, Biomacromolecules 7 (2006) 1521–1528.

[28] I. Burgert, J. Keckés, K. Frühmann, P. Fratzl, S. E. Tschegg, A comparison of two techniques for wood fibre isolation - Evaluation by tensile tests on single fibres with different microfibril angle, Plant Biology 4 (1) (2002) 9–12.

[29] G. Wang, S. Q. Shi, J. Wang, S. Cao, H. Cheng, Microtension test method for measuring tensile properties of individual cellulosic fibers, Wood and Fiber Science 43 (3) (2011) 1–11.

[30] A. Bergander, L. Salmén, Variations in transverse fibre wall properties: Relations between elastic properties and structure, Holzforschung 54 (6) (2000) 654–660.

[31] A. Bergander, L. Salmén, Cell wall properties and their effects on the mechanical properties of fibers, Journal of Materials Science 37 (1) (2002) 151–156.

[32] T. Timell, Recent progress in the chemistry and topochemistry of compression wood, Wood Science and Technology 16 (2) (1982) 83–122.

[33] T. Timell, Compression wood in gymnosperms, Springer, Berlin, 1986.

[34] I. Burgert, J. Keckés, P. Fratzl, Mechanics of the wood cell wall, in: Characterization of the cellulosic cell wall, Blackwell Publishing, Oxford, 2006, pp. 30–37.

[35] J. Brändström, Microfibril angle of the $s_1$ cell wall layer of Normay spruce compression wood tracheids, IAWA Journal 25 (4) (2004) 415–423.

[36] J. R. Barnett, V. A. Bonham, Cellulose microfibril angle in the cell wall of wood fibres, Biological Reviews 79 (2) (2004) 461–472.

[37] W. Gindl, H. S. Gupta, T. Schoberl, H. C. Lichtenegger, P. Fratzl, Mechanical properties of spruce wood cell walls by nanoindentation, Applied Physics A 79 (2004) 2069–2073.

[38] I. Burgert, M. Eder, N. Gierlinger, P. Fratzl, Tensile and compressive stresses in tracheids are induced by swelling based on geometrical constraints of the wood cell, Planta 226 (4) (2007) 981–987.

*Erick I. Saavedra Flores*
*College of Engineering, Swansea University, Singleton Park, Swansea SA2 8PP, United Kingdom.*
*Departamento de Ingeniería en Obras Civiles, Universidad de Santiago de Chile. Av. Ecuador 3659, Santiago, Chile.*

*Corresponding author. Tel: + 44 (0)1792 205678, Fax: + 44 (0)1792 295157.*

*Michael I. Friswell*
*College of Engineering, Swansea University, Singleton Park, Swansea SA2 8PP, United Kingdom.*

# Effective dynamical model of barotropic gas with rapidly oscillating initial data

Sergey A. Sazhenkov
sazhenkovs@yandex.ru

**Abstract**

We consider the classical three-dimensional Navier–Stokes equations of viscous compressible gas in a smooth bounded domain. The equations are supplemented with the no-slip conditions on a fixed boundary and with rapidly oscillating initial distributions of density. The state equation of the gas is the equation of a barotropic medium. We strictly justify a homogenization procedure, as frequencies of oscillations tend to infinity. As a result, we build up an effective homogenized limiting model of barotropic viscous gas. This model consists of four equations. They are the momentum and mass equations, which are the same as in the original model; the state equation, which differs from the original equation of barotropic gas; and an additional kinetic equation, which endows the model and holds the complete information about evolution of oscillations.

## 1 Problem formulation

We consider the system consisting of the balance of mass equation

$$\frac{\partial \rho}{\partial t} + \operatorname{div}_x(\rho \mathbf{u}) = 0, \quad (\mathbf{x}, t) \in \Omega \times (0, T), \tag{1a}$$

the momentum equation

$$\frac{\partial (\rho \mathbf{u})}{\partial t} + \operatorname{div}_x(\rho \mathbf{u} \otimes \mathbf{u}) - \mu \Delta_x \mathbf{u} - \xi \nabla_x \operatorname{div}_x \mathbf{u} + \nabla_x P = \rho \mathbf{g}, \quad (\mathbf{x}, t) \in \Omega \times (0, T), \tag{1b}$$

and the state equation of barotropic gas

$$P = a\rho^\gamma, \quad (\mathbf{x}, t) \in \Omega \times (0, T). \tag{1c}$$

The system is supplemented with the no-slip condition on the boundary $\partial\Omega$,

$$\mathbf{u}|_{\partial\Omega} = 0, \quad t \in (0, T), \tag{1d}$$

and with the initial data

$$\rho|_{t=0} = \rho_0^\varepsilon, \quad \mathbf{u}|_{t=0} = \mathbf{u}_0^\varepsilon, \quad \mathbf{x} \in \Omega. \tag{1e}$$

The domain $\Omega \subset \mathbb{R}^3$ is bounded. Its boundary $\partial\Omega$ is smooth. In the problem (1), $(\rho, \mathbf{u}, P)$ are the sought functions, the constants $\mu > 0$, $\xi > -\mu$, and $a > 0$ are given, the function $\mathbf{g}$ is a given density of distributed mass forces. In line with [1, formula (7.2)], we suppose that $\mathbf{g}$ belongs to the space $L^1(0, T; L^{2\gamma/(\gamma-1)}(\Omega)) \cap L^2(0, T; L^r(\Omega))$, where

$\frac{1}{r}+\frac{1}{\gamma}+\frac{1}{6}=1$. The adiabatic exponent $\gamma$ is supposed to be greater than three. The initial data depend on the small parameter $\varepsilon>0$ and satisfy the following properties and limiting relations:

$$\mathbf{u}_0^\varepsilon \in L^{2\gamma/(\gamma-1)}(\Omega), \quad \rho_0^\varepsilon \geq 0 \quad \text{a.e. in } \Omega, \quad \rho_0^\varepsilon \in L^\gamma(\Omega), \tag{2a}$$

$$\rho_0^\varepsilon \underset{\varepsilon\searrow 0}{\longrightarrow} \rho_0^* \quad \text{weakly in } L^\gamma(\Omega), \tag{2b}$$

$$\mathbf{u}_0^\varepsilon \underset{\varepsilon\searrow 0}{\longrightarrow} \mathbf{u}_0^* \quad \text{strongly in } L^{2\gamma/(\gamma-1)}(\Omega). \tag{2c}$$

The limiting relation (2b) models an effect of rapidly oscillating initial data. According to the current theory of compressible Navier–Stokes equations [1, 2], for a fixed $\varepsilon>0$ the problem (1) has a generalized solution $(\rho^\varepsilon, \mathbf{u}^\varepsilon, P^\varepsilon)$, where $P^\varepsilon := a\cdot(\rho^\varepsilon)^\gamma$. The very important observation that motivates the present study is outlined by P.-L. Lions in [1, remark 5.9]. In [1, remark 5.9] it is noticed that the limits of the family of solutions, arising as $\varepsilon\searrow 0$, cannot be solutions of the problem (1) because if a limit of $(\rho^\varepsilon, \mathbf{u}^\varepsilon, P^\varepsilon)$ is a solution of the problem (1) then necessarily there should be that $\rho_0^\varepsilon \underset{\varepsilon\searrow 0}{\longrightarrow} \rho_0^*$ strongly. But this limiting relation contradicts the limiting relation (2b).

The aim of the work is to study properties of the limiting points of the sequence $(\rho^\varepsilon, \mathbf{u}^\varepsilon, P^\varepsilon)$ as $\varepsilon\searrow 0$. As the results of this study, we construct a limiting homogenized model and strictly justify the homogenization procedure.

The notion of generalized solution of the problem (1) is introduced exactly as in [1, section 5.1], [2].

**Definition 1.** A triple of functions $(\rho^\varepsilon, \mathbf{u}^\varepsilon, P^\varepsilon)$ is called a generalized solution of the problem (1), if it satisfies the conditions

$$\rho^\varepsilon \geq 0 \text{ a.e. on } \Omega\times(0,T), \tag{3a}$$

$$\rho^\varepsilon \in L^\infty(0,T;L^\gamma(\Omega))\cap C([0,T];L^p(\Omega)) \text{ for } 1\leq p<\gamma, \tag{3b}$$

$$\mathbf{u}^\varepsilon \in L^2(0,T;H_0^1(\Omega)),\ \rho^\varepsilon|\mathbf{u}^\varepsilon|^2 \in L^\infty(0,T;L^1(\Omega)), \tag{3c}$$

$$\rho^\varepsilon\mathbf{u}^\varepsilon \in C([0,T];L^{2\gamma/(\gamma+1)}_{weak}(\Omega)), \tag{3d}$$

the state equation (1c), the integral equality

$$\int_0^T\int_\Omega\Big[\rho^\varepsilon\mathbf{u}^\varepsilon\cdot\frac{\partial\varphi}{\partial t}+(\rho^\varepsilon\mathbf{u}^\varepsilon\otimes\mathbf{u}^\varepsilon+P^\varepsilon\,\mathbb{I}-\mu\nabla_x\mathbf{u}^\varepsilon-\xi\mathrm{div}_x\mathbf{u}^\varepsilon\,\mathbb{I}):\nabla_x\varphi\Big]d\mathbf{x}dt$$
$$=-\int_0^T\int_\Omega\rho^\varepsilon\mathbf{g}\cdot\varphi d\mathbf{x}dt-\int_\Omega\rho_0^\varepsilon\mathbf{u}_0^\varepsilon\cdot\varphi(\mathbf{x},0)d\mathbf{x} \tag{3e}$$

for any vector-field $\varphi\in C^1(\Omega\times(0,T))$, vanishing on $\partial\Omega$ and in the neighborhood of the plane $\{t=T\}$, and the integral equality

$$\int_0^T\int_\Omega\Big[b(\rho^\varepsilon)\frac{\partial\psi}{\partial t}+b(\rho^\varepsilon)\mathbf{u}^\varepsilon\cdot\nabla_x\psi+\psi(b(\rho^\varepsilon)-b'(\rho^\varepsilon)\rho^\varepsilon)\mathrm{div}_x\mathbf{u}^\varepsilon\Big]d\mathbf{x}dt$$
$$=-\int_\Omega b(\rho_0^\varepsilon)\psi(\mathbf{x},0)d\mathbf{x} \tag{3f}$$

for any differentiable function $b$ with a bounded derivative $b'\in C(\mathbb{R})$ and for an arbitrary function $\psi\in C^1(\Omega\times(0,T))$, vanishing in the neighborhood of the plane $\{t=T\}$.

In (3d) we use the following notation. By $C([0,T];L^{2\gamma/(\gamma+1)}_{weak}(\Omega))$ we denote the space of functions $\varphi \in L^\infty(0,T;L^{2\gamma/(\gamma+1)}(\Omega))$ such that the mapping $t \mapsto \varphi(\cdot,t)$ is weakly continuous on the interval $[0,T]$ with values in $L^{2\gamma/(\gamma+1)}(\Omega)$. In other words, for an arbitrary test function $\psi \in L^{2\gamma/(\gamma-1)}(\Omega)$ the mapping $t \mapsto \int_\Omega \psi(\mathbf{x})\varphi(\mathbf{x},t)d\mathbf{x}$ is continuous on $[0,T]$.

**Remark 1.** In the distribution sense, (3f) is equivalent to the so-called *renormalized balance of mass equation*

$$\frac{\partial b(\rho^\varepsilon)}{\partial t} + \mathrm{div}_x(b(\rho^\varepsilon)\mathbf{u}^\varepsilon) + (b'(\rho^\varepsilon)\rho^\varepsilon - b(\rho^\varepsilon))\mathrm{div}_x\mathbf{u}^\varepsilon = 0. \tag{4}$$

Formally this equation follows from (1a) by multiplication on $b'(\rho^\varepsilon)$ and by use of the chain rule.

In [1, section 7.2] (see also in [2]) the following existence result was established.

**Proposition 1.** *For any fixed $\varepsilon \searrow 0$ there exists a generalized solution $(\rho^\varepsilon, \mathbf{u}^\varepsilon, P^\varepsilon)$ of the problem (1) in the sense of Definition 1.*

*Moreover, $\rho^\varepsilon$ belongs to $L^{\tilde p}(K\times(0,T))$, where $\tilde p = \gamma + \frac{2}{3}\gamma - 1$ and $K$ is an arbitrary compact subset of $\Omega$. Also, the generalized solution admits the energy inequality*

$$\int_\Omega \Big[\frac{1}{2}\rho^\varepsilon|\mathbf{u}^\varepsilon|^2 d\mathbf{x} + \frac{a}{\gamma-1}(\rho^\varepsilon)^\gamma\Big]d\mathbf{x} + \int_0^t ds\int_\Omega(\mu|\nabla_x\mathbf{u}^\varepsilon|^2 + \xi|div_x\mathbf{u}^\varepsilon|^2)d\mathbf{x}$$
$$\le \int_\Omega \frac{1}{2}|\mathbf{u}_0^\varepsilon|^2\rho_0^\varepsilon d\mathbf{x} + \int_\Omega \frac{a}{\gamma-1}\rho_0^\gamma d\mathbf{x} + \int_0^t ds\int_\Omega(\rho^\varepsilon\mathbf{u}^\varepsilon\cdot\mathbf{g})d\mathbf{x} \tag{5}$$

*for almost every $t\in[0,T]$.*

## 2 Uniform bounds with respect to $\varepsilon$. Limiting relations as $\varepsilon \searrow 0$

Implementing the standard technics for derivation of a priori bounds on solutions of the Navier–Stokes equations, from (5) we rather easily deduce that

$$\operatorname*{ess\,sup}_{\tau\in[0,T]}\int_\Omega\Big[\frac{1}{2}\rho^\varepsilon|\mathbf{u}^\varepsilon|^2 d\mathbf{x} + \frac{a}{\gamma-1}(\rho^\varepsilon)^\gamma\Big]d\mathbf{x} \le C_1(T;\|\mathbf{g}\|), \tag{6}$$

$$\|\mathbf{u}^\varepsilon\|_{L^2(0,T;H^1_0(\Omega))} \le C_2(T,\Omega,C_1), \tag{7}$$

$$\|\mathbf{u}^\varepsilon\|_{L^2(0,T;L^6(\Omega))} \le C_3, \tag{8}$$

$$\left\|\frac{\partial\rho^\varepsilon}{\partial t}\right\|_{L^\infty(0,T;W^{-1,2\gamma(\gamma+1)}(\Omega))} \le C_4, \tag{9}$$

$$\left(\left\|\frac{\partial(\rho^\varepsilon\mathbf{u}^\varepsilon)}{\partial t}\right\|_{L^\infty(0,T;W^{-1,1}(\Omega))}, \left\|\frac{\partial(\rho^\varepsilon\mathbf{u}^\varepsilon)}{\partial t}\right\|_{L^2(0,T;H^{-1}(\Omega))}\right) \le C_5, \tag{10}$$

where the constants $C_1$–$C_5$ do not depend on $\varepsilon$.

In [1, theorem 7.1] the following rather delicate result was established.

**Proposition 2.** *Let $(\rho^\varepsilon, \mathbf{u}^\varepsilon, P^\varepsilon)$ be a generalized solution of the problem (1). Let $\rho^\varepsilon \in L^{\tilde p}(K\times(0,T))$, where $\tilde p = \gamma + \frac{2}{N}\gamma - 1$ and $K$ is an arbitrary compact subset of $\Omega$. Then $\rho^\varepsilon$ is bounded in $L^{\tilde p}(K\times(0,T))$ by a constant, which depends only on the data of the problem and does not depend on $\varepsilon$.*

The above stated bounds allow us to use the result of [1, theorem 5.1, part 1] and establish the limiting relations

$$\rho^\varepsilon \mathbf{u}^\varepsilon \underset{\varepsilon\searrow 0}{\to} \rho^* \mathbf{u}^* \qquad \text{weakly in } L^{2\gamma/(\gamma+1)}(\Omega\times(0,T)), \tag{11}$$

$$\rho^\varepsilon u_i^\varepsilon u_j^\varepsilon \underset{\varepsilon\searrow 0}{\to} \rho^* u_i^* u_j^* \qquad \text{in } \mathcal{M}(\Omega\times(0,T)), \tag{12}$$

$$\text{weakly* in } L^\infty(0,T;L^1(K))\cap L^1(0,T;L^\beta(K)), \tag{13}$$

$$\sqrt{\rho^\varepsilon}\mathbf{u}^\varepsilon \underset{\varepsilon\searrow 0}{\to} \overline{\sqrt{\rho}}\mathbf{u}^* \qquad \text{weakly in } L^{2\gamma/(\gamma+1)}(\Omega\times(0,T)) \tag{14}$$

for an appropriate subsequence of $\{\varepsilon \searrow 0\}$. Here $(\rho^*, \mathbf{u}^*) := \text{w-}\lim\limits_{\varepsilon\searrow 0}(\rho^\varepsilon, \mathbf{u}^\varepsilon)$ and $\overline{\sqrt{\rho}} := \text{w-}\lim\limits_{\varepsilon\searrow 0}\sqrt{\rho^\varepsilon}$ (in the space $L^{2\gamma}(\Omega\times(0,T))$). The exponent $\beta$ is greater than one and depends on $\gamma$. In (13) $\mathcal{M}$ is the space of Radon measures, i.e., the dual space to the space of continuous functions.

The following convergence property of the so-called *effective viscous flux* [1, remarks 5.13, 5.18], [2, section 3.4] is very important for limiting transitions in (1).

**Proposition 3.** *Let $B$ be an arbitrary continuous on the semi-axis $[0,+\infty)$ function such that $B$ and $B'$ are bounded. Then the limiting relation*

$$B(\rho^n)\{(\mu+\xi)div_x\mathbf{u}^n - a\cdot(\rho^n)^\gamma\} \underset{n\nearrow\infty}{\to} \bar{B}\{(\mu+\xi)div_x\mathbf{u}^* - P^*\} \quad \text{in } \mathcal{D}'(\Omega\times(0,T)) \tag{15}$$

*holds true.*

Here we denoted $\bar{B} := \text{w-}\lim\limits_{n\nearrow\infty}\beta(\rho^n)$, $P^* := a\text{w-}\lim\limits_{n\nearrow\infty}(\rho^n)^\gamma \equiv \text{w-}\lim\limits_{n\nearrow\infty}P^n$.

In order to describe effectively superpositions of nonlinear functions and weakly convergent sequences, we use Ball's fundamental theorem on a version of Young measures, which reads as follows [3] (see also in [4]).

**Proposition 4.** *Let $\Omega$ be a bounded open subset of $\mathbb{R}^3$. Suppose a sequence of measurable functions $\{\rho^n\}_{n\geq 1}$ is bounded in $L^\gamma(\Omega)$, $1<\gamma<+\infty$.*

*Then there exist a subsequence still denoted by $\{\rho^n\}_{n\geq 1}$ and a measurable set of probability measures $\sigma_{x,t}\in\mathcal{M}(\mathbb{R})$, $(\mathbf{x},t)\in\Omega\times(0,T)$ with the distribution function $f(\mathbf{x},t,\lambda) := \sigma_{x,t}(-\infty,\lambda]$ such that*

*(1) for a.e. $(\mathbf{x},t)\in\Omega\times(0,T)$ the function $\lambda\mapsto f(\mathbf{x},t,\lambda)$ is right continuous and has the limits 1 and 0, as $\lambda\to\pm\infty$;*

*(2) for any Carathéodory function $G:\Omega\times(0,T)\times\mathbb{R}\mapsto\mathbb{R}$ satisfying the condition*

$$\lim_{|\lambda|\to\infty}\frac{\|G(\cdot,\cdot,\lambda)\|_{C(\Omega\times(0,T))}}{|\lambda|^\gamma} = 0,$$

*the sequence $G(\cdot,\cdot,\rho^n)$ converges weakly in $L^1(\Omega\times(0,T))$ to the function*

$$\bar{G}(\mathbf{x},t) = \int_{\mathbb{R}} G(\mathbf{x},t,\lambda)d_\lambda f(\mathbf{x},t,\lambda).$$

*Moreover, the mapping $(\mathbf{x},t)\mapsto\int_{\mathbb{R}}|\lambda|^\gamma d_\lambda f(\mathbf{x},t,\lambda)$ from $\Omega\times(0,T)$ into $\mathbb{R}$ belongs to $L^1(\Omega\times(0,T))$.*

**Definition 2.** The probability measures $\sigma_{x,t}$ are called *the Young measures* associated with the chosen subsequence $\{\rho^n\}_{n\geq 1}$.

By $d_\lambda f$ we denote the standard Stieltjes measure on $\mathbb{R}_\lambda$ generated by the function $\lambda\mapsto f(\mathbf{x},t,\lambda)$ for a.e. $(\mathbf{x},t)\in\Omega\times(0,T)$.

## 3 Formulation of the homogenized effective model

The following theorem and formulation of the homogenized effective model of dynamics of viscous barotropic gas with rapidly oscillating initial data are the main results of the work.

**Theorema H.** *(On homogenization of equations of viscous barotropic gas with rapidly oscillating initial data.) Let* $\{(\rho^\varepsilon, \mathbf{u}^\varepsilon)\}_{\varepsilon>0}$ *be a family of generalized solutions of the problem* (1) *corresponding to the rapidly oscillating initial data* (1e).

*Then there exist a quadruple of functions* $(\rho^*, \mathbf{u}^*, P^*, f)$ *and a subsequence* $\{\varepsilon \searrow 0\}$ *such that*

$$\rho^\varepsilon \underset{\varepsilon\searrow 0}{\to} \rho^* \qquad \text{weakly in } L^\gamma(\Omega\times(0,T))\cap L^{\tilde p}(K\times(0,T)), \tag{16}$$

$$\mathbf{u}^\varepsilon \underset{\varepsilon\searrow 0}{\to} \mathbf{u}^* \qquad \text{weakly in } L^2(0,T;H^1_0(\Omega)), \tag{17}$$

$$P^\varepsilon \underset{\varepsilon\searrow 0}{\to} P^* \qquad \text{weakly in } L^{1+\kappa}(\Omega\times(0,T)), \tag{18}$$

*and the quadruple of functions* $(\rho^*, \mathbf{u}^*, P^*, f)$ *is a solution of Problem H formulated immediately below.*

**Problem H.** In the domain $(\mathbf{x}, t, \lambda) \in \Omega\times(0,T)\times\mathbb{R}_\lambda$ it is necessary to find an effective density $\rho^* = \rho^*(\mathbf{x}, t)$, an effective velocity field $\mathbf{u}^* = \mathbf{u}^*(\mathbf{x}, t)$, an effective pressure $P^* = P^*(\mathbf{x}, t)$, and the right continuous and monotonously nondecreasing in $\lambda$ distribution function $f = f(\mathbf{x}, t, \lambda)$ such that $0 \le f \le 1$ a.e. in $\Omega\times(0,T)\times\mathbb{R}_\lambda$, satisfying the balance of mass equation

$$\frac{\partial\rho^*}{\partial t} + \operatorname{div}_x(\rho^*\mathbf{u}^*) = 0, \quad (\mathbf{x}, t)\in\Omega\times(0,T), \tag{19}$$

the momentum equation

$$\frac{\partial(\rho^*\mathbf{u}^*)}{\partial t} + \operatorname{div}_x(\rho^*\mathbf{u}^*\otimes\mathbf{u}^*) - \mu\Delta_x\mathbf{u}^* - \xi\nabla_x\operatorname{div}_x\mathbf{u}^* + \nabla_x P^* = \rho^*\mathbf{g}, \quad (\mathbf{x}, t)\in\Omega\times(0,T), \tag{20}$$

the kinetic equation

$$\frac{\partial f}{\partial t} + \operatorname{div}_x(f\mathbf{u}^*) - \frac{\partial}{\partial\lambda}(\lambda f\operatorname{div}_x\mathbf{u}^*) + \frac{\partial}{\partial\lambda}(\lambda M(f)) = 0 \quad (\mathbf{x}, t, \lambda)\in\Omega\times(0,T)\times\mathbb{R}_\lambda, \tag{21}$$

where the nonlinear operator $f \mapsto M(f)$ is defined by the formula

$$(\mathcal{M}(f))(\mathbf{x}, t, \lambda) := \frac{1}{\mu+\xi}\int_\lambda^\infty (as^\gamma - P^*(\mathbf{x}, t))d_s f(\mathbf{x}, t, s),$$

the state equation

$$P^*(\mathbf{x}, t) = a\int_{[0,\infty)}\lambda^\gamma d_\lambda f(\mathbf{x}, t, \lambda) \equiv a\gamma\int_{[0,\infty)}\lambda^{\gamma-1}(1 - f(\mathbf{x}, t, \lambda))d\lambda \quad (\mathbf{x}, t)\in\Omega\times(0,T), \tag{22}$$

the initial data

$$\rho^*|_{t=0} = \rho_0^*(\mathbf{x}), \quad \mathbf{u}^*|_{t=0} = \mathbf{u}_0^*(\mathbf{x}), \quad f|_{t=0} = f_0(\mathbf{x}, \lambda), \tag{23}$$

where $f_0$ is the distribution function of the Young measure associated with a subsequence $\{\rho_0^\varepsilon\}_{\varepsilon\searrow 0}$, and the no-slip boundary condition

$$\mathbf{u}^*|_{\partial\Omega} = 0, \quad t\in(0,T). \tag{24}$$

The solution of Problem H is understood in the sense of distributions. That is, the balance of mass equation (19) and the initial condition $(23)_1$ are understood in the sense of the integral equality

$$\int_0^T \int_\Omega \rho^* \Big[ \frac{\partial \psi}{\partial t} + \mathbf{u}^* \cdot \nabla_x \psi \Big] d\mathbf{x}dt = - \int_\Omega \rho_0^*(\mathbf{x}) \psi(\mathbf{x}, 0) d\mathbf{x} \tag{25}$$

for an arbitrary test-function function $\psi \in C^1(\Omega \times (0,T))$ vanishing in the neighborhood of the plane $\{t = T\}$, the momentum equation (20) and the initial condition $(23)_2$ are understood in the sense of the integral equality

$$\begin{aligned} &\int_0^T \int_\Omega \Big[ \rho^* \mathbf{u}^* \cdot \frac{\partial \varphi}{\partial t} + (\rho^* \mathbf{u}^* \otimes \mathbf{u}^* - \xi \mathrm{div}_x \mathbf{u}^* \mathbb{I} - \mu \nabla_x \mathbf{u}^*) : \nabla_x \varphi \\ &+ \Big( \int_{\mathbb{R}_\lambda} \gamma a \lambda^{\gamma - 1} (1 - f(\mathbf{x}, t, \lambda)) d\lambda \Big) \mathrm{div}_x \varphi \Big] d\mathbf{x}dt \\ &\qquad = - \int_0^T \int_\Omega \rho^* \mathbf{g} \cdot \varphi d\mathbf{x}dt - \int_\Omega \rho_0^* \mathbf{u}_0^* \cdot \varphi(\mathbf{x}, 0) d\mathbf{x}, \end{aligned} \tag{26}$$

where $\varphi \in C^1(\Omega \times (0,T))$ is an arbitrary test-function vanishing on $\partial\Omega$ and in the neighborhood of the plane $\{t = T\}$, and the kinetic equation (21) and the initial condition $(23)_3$ are understood in the sense of the integral equality

$$\begin{aligned} &\int_0^T \int_\Omega \int_{\mathbb{R}_\lambda} \Big\{ \frac{\partial \Phi}{\partial t} + \mathbf{u}^*(\mathbf{x}, t) \cdot \nabla_x \Phi - \lambda \frac{\partial \Phi}{\partial \lambda} \mathrm{div}_x \mathbf{u}^*(\mathbf{x}, t) \Big\} f(\mathbf{x}, t, \lambda) d\lambda d\mathbf{x}dt \\ &\qquad + \int_0^T \int_\Omega \int_{\mathbb{R}_\lambda} \frac{\partial \Phi}{\partial \lambda} \lambda \mathcal{M} d\lambda d\mathbf{x}dt = - \int_\Omega \int_{\mathbb{R}_\lambda} \Phi(\mathbf{x}, 0, \lambda) f(\mathbf{x}, 0, \lambda) d\lambda d\mathbf{x}, \end{aligned} \tag{27}$$

where $\Phi \in C^1(\Omega \times (0,T) \times \mathbb{R}_\lambda)$ is an arbitrary test function vanishing in the neighborhood of the plane $\{t = T\}$ and for large $|\lambda|$.

**Remark 2.** (Comments about derivation of the equations (19)–(22).) The balance of mass equation (19) and the momentum equation (20) follow directly from the equations (1a) and (1b) thanks to the limiting relations (11)–(13) and (18). The state equation (22) follows directly from the state equation of barotropic gas (1c) on the strength of Proposition 4 due to the uniform bound (6) on $(\rho^\varepsilon)^\gamma$. The derivation of the kinetic equation (21) is rather sophisticated. In order to construct (21), in the present work we follow the ideas of P. Plotnikov and J. Sokolowski [5]. The kinetic equation appears as the result of the limiting transition as $\varepsilon \searrow 0$ in the renormalized balance of mass equation (4). The justification of the limiting transition is heavily based on Proposition 4 and some additional facts from the Young measure theory and on Proposition 3 on effective viscous flux.

**Remark 3.** (On an alternative formulation of Problem H.) On the strength of Proposition 4, the effective density $\rho^*$ has an explicit representation in terms of the distribution function $f$ in the form of an additional state equation

$$\rho^*(\mathbf{x}, t) = \int_{[0,\infty)} \lambda d_\lambda f(\mathbf{x}, t, \lambda) \equiv \int_{[0,\infty)} (1 - f(\mathbf{x}, t, \lambda)) d\lambda \quad (\mathbf{x}, t) \in \Omega \times (0,T). \tag{28}$$

In turn, this equation along with the kinetic equation (21) yield the balance of mass equation (19). Consequently, in the formulation of Problem H the balance of mass equation can be equivalently substituted by the state equation (28).

## Acknowledgements

*The work was partially supported by the Russian Foundation for Basic Research (grant 10-01-00447) and by the Federal special-purpose program "Scientific and pedagogical-scientific brainpower of innovative Russia", 2009-2013 (contract no. 02.740.11.0617).*

## References

[1] Lions P.-L. Mathematical topics in fluid mechanics, vol. 2: compressible models. Oxford: Oxford University Press, 1998.

[2] Feireisl E., Novotný A., Petzeltová H. On the existence of globally defined weak solutions to the Navier–Stokes equations // J. Math. Fluid Mech. 2001. V. 3. P. 358–392.

[3] Ball J.M. A version of the fundamental theorem for Young measures // In: PDEs and Continuum Models of Phase Transitions. Lecture Notes in Physics. Vol. 344. (Springer-Verlag, Berlin, Heidelberg, New York, 1989) 241–259.

[4] Malek J., Nečas J., Rokyta M., and Ružička M. Weak and Measure-valued Solutions to Evolutionary PDEs. London, Chapman and Hall, 1996.

[5] Plotnikov P.I. and Sokolowski J. Stationary solutions of Navier-Stokes equations for diatomic gases // Russian Mathematical Surveys. 2007. V. 62. P. 561–593.

*Sergey A. Sazhenkov, Lavrentyev Institute of Hydrodynamics, Prospekt Lavrentyeva 15, and Novosibirsk State University, Pirogova Street 2, Novosibirsk 630090, Russia*

# Structural changes in filled elastomers subjected to stretching and recovery of their properties in thermostating

Vladimir V. Shadrin
shadrin@icmm.ru

**Abstract**

An experimental study showed that the growth of damage in rubbers subjected to repeated loading was not the only reason for hysteresis losses. The viscoelastic properties of elastomeric material also contributed to the hysteresis losses. Owing to these properties, the material is capable of partial or complete recovery of its mechanical properties after a long while or during heat treatment.

Numerous experiments on cyclic high-amplitude loading of rubbers have shown substantial hysteresis losses to occur during the first loading cycle; in the subsequent cycles, the losses decrease and the material becomes less stiff [1, 2]. This phenomenon is known as the Mullins effect and is attributed to a growth in damage of rubbers [3, 4]. The cause of these losses may also be the viscoelastic properties of the elastomer. The objective of this investigation was to study the viscoelastic properties in filled elastomers.

We performed experiments in which a specimen was subjected to cyclic stretching until the stabilization of hysteresis losses was reached. Then the specimen was held at a fixed temperature. Depending on the holding temperature, the mechanical properties of the rubber were recovered partially or completely.

The elastomer used in the study had a carbon-black volume fraction of 50% and a breaking extension of 250%.

Specimens were prepared in the form of a ring of 50 mm outer diameter, 4 mm width, and 2 mm thickness. The ring was put on round grips designed for this purpose and stretched. The merit of this shape of specimens was that they could not slip out of the grip fixtures at large strains or be damaged by clamping.

Special measures were taken (labels were attached) to control the base distance during the removal of the sample from the grips and its thermostatting for a given period of time.

Specimens prepared for testing were preliminarily annealed at 100°C for 72 h to stabilize their properties and to remove stresses induced during their preparation and storage. The specimens were stretched at 20°C with a speed of 100 %/min in a 2167 P-50 tensile-testing machine.

Experiments were performed on several specimens of identical geometrical dimensions, which were subjected to identical thermal treatment prior to testing. At the beginning of testing, the specimens were cyclically loaded to the same deformation. The plots of cyclic stretching were identical for all the specimens. After preconditioning the specimens were thermostatted for different periods of time. Note that the recovery of their properties after long-term thermostatting was complete.

Figure 1a presents the stress-strain plots under cyclic loading of a specimen to an extension ratio of 50% and the plots for specimens held at 100°C for 1 and 72 h.

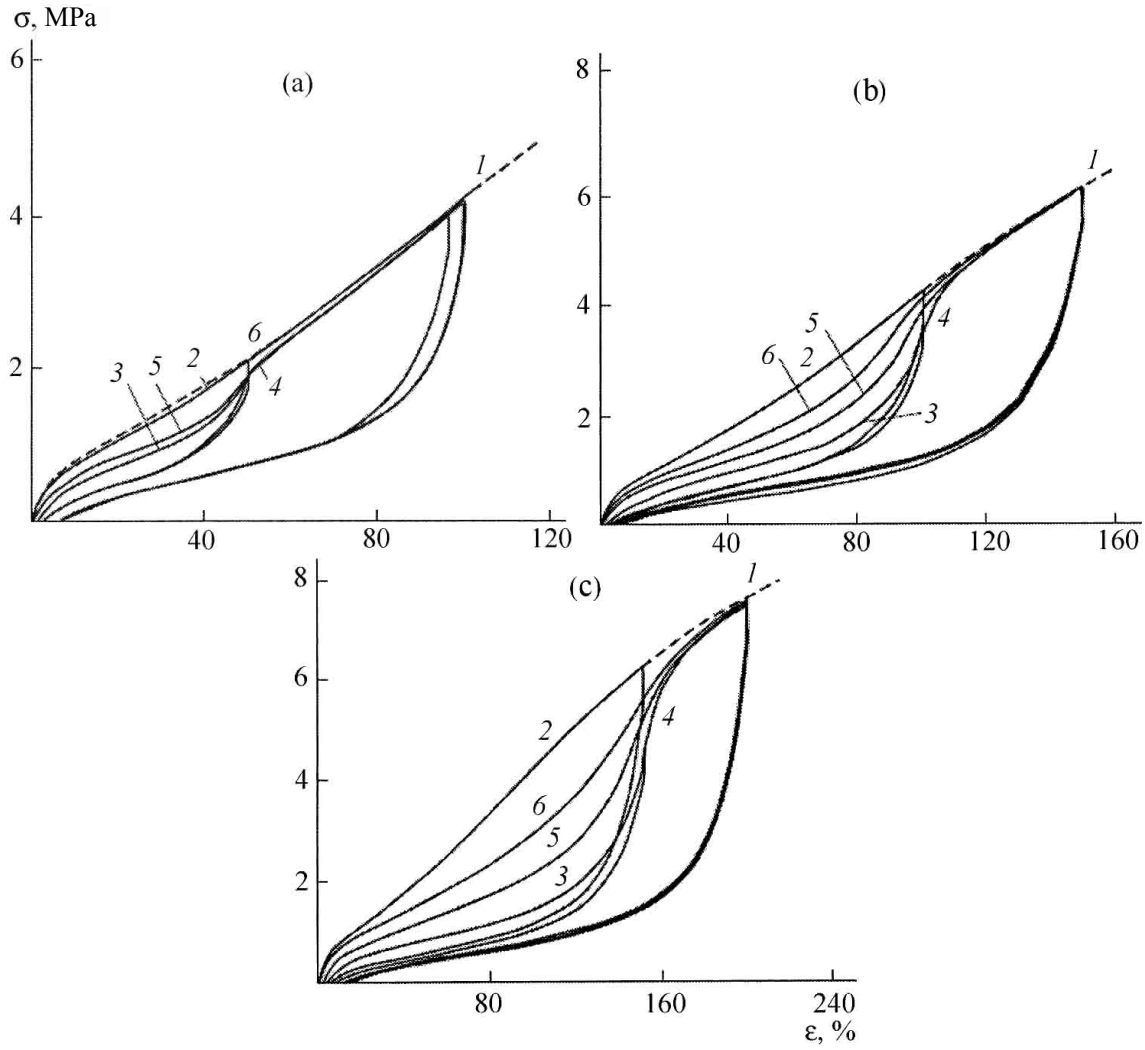


Figure 1: Tensile loading-unloading curves of thermo-statted specimens. Specimen preconditioning at an extension ratio of (a) 50, (b) 100, and (c) 150%: (1) single-stretching curve, (2) first loading of the virgin specimen, (3) the last cycle of specimen loading during conditioning, (4) immediate (without thermo-statting) stretching of the specimen to an extension ratio greater than the preconditioning extension, (5) stretching of the preconditioned specimen after thermostatting for 1 h, and (6) the same after 72-h thermostatting.

Figures 1b and 1c show similar plots. In these cases, the specimen was preliminarily subjected to cyclic stretching to 100 and 150%. The specimens thus aged were thermostatted for 1 and 72 h and then stretched to a higher extension ratio.

From Fig. 1, it is seen that the specimens thermostatted for 1 h partially recovered their mechanical properties.

Thermostatting for a long period of time (to 72 h) leads to the maximum recovery of properties. At a low preliminary extension level (to 50% in the given case), the specimen completely recovers its properties. However, if a specimen is conditioned at a higher extension ratio, there is no complete recovery of the properties.

It may be assumed that there are two possible ways of evolution of the structure of material — free and forced. The forced evolution of the material structure manifests itself

when the stretching of a specimen causes the tightening of loops in molecular chains at the molecular level, the slipping of chains, and their debonding from filler particles. This evolution occurs under an external load. In turn, unloading leads to the loosening of loops and the crawling of chains over or their adhering to inclusions. Under these conditions, the kinetic energy of motion of polymer chain units is insufficient for the reverse process of recovery to occur at the same rate as upon loading.

The loops tied to very tight knots take a very long time to disentangle and the formation of the initial polymer-network morphology is very slow. Let us call this the free evolution of the material structure. The softening of the material strongly depends on the volume fraction of filler and is substantially less dependent on the elastomer-crosslink density [5]. After a long rest (tens or even hundreds of days) at room temperature, the initial properties of rubbers may be recovered [6] (Fig. 2). The same takes place after thermostatting the specimens for a certain time — 3 days in our experiments. This suggests that the defects induced are either healed or the softening effect has a nature other than damaging, for example, thixotropic (as a consequence of desorption of taut chains from the filler surface [7], phase transition in the elastomer matrix near filler particles [8], or slippage of polymer chains on the filler surface [9]).

Fukahori [10] reported experimental data suggesting that filled elastomers have a much more complex structure than was anticipated. The complex structure has a softening nature due to different causes associated with both viscoelastic mechanisms (thixotropic properties) and damage buildup.

Figure 2 depicts a tensile stress-strain curve after resting a specimen at room temperature for 256 days. These data confirm that the recovery of the elastomer properties takes place at room temperature as well. The process is due to the thermal motion of molecules, and this takes time. Heating only accelerates the thixotropic processes.

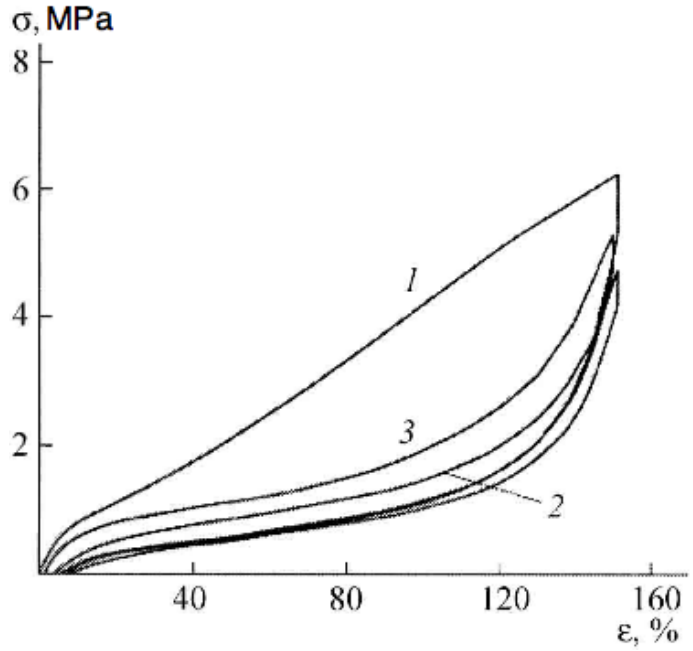


Figure 2: Recovery of the mechanical properties after 256 days of rest: (1) first stretching of the specimen to 150%, (2) the last cycle of stretching the specimen during its conditioning, and (3) specimen stretching after resting for 256 days.

From the data presented in Figs. 1b and 1c, it is seen that, at large extension ratios (more than 50% in our case), other processes that are presumably due to damage buildup occur in the elastomer along with the changes related to the viscoelastic properties. The greater the extension ratio during the preliminary cycling, the greater the amount of damage that is not healed with time (upon thermostatting).

What is noteworthy in Fig. 1 is that the material "remembers" its ultimate strain. When the specimens are stretched to an extension ratio that is higher than the one at which a specimen was conditioned, the stress-strain curve very rapidly reaches the level of the single stretching of the virgin specimen. This phenomenon is easy to explain in terms of both viscoelastic properties and damage buildup. However, the complete recovery of the initial properties of the specimen stretched to an extension ratio of more than 50% does not take place even after long-term thermostatting. The stress-strain curve after thermostatting lies below the first-stretching curve (Figs. 1b, 1c). This indicates that the changes associated with the structure recovery are not accomplished to the full extent at large deformations and the damage buildup process occurs simultaneously with thixotropic changes.

The results obtained in these experiments show that, in addition to damage buildup during deformation of rubbers, a considerable contribution to hysteresis losses is made by the viscoelastic properties of the elastomer matrix.

## Acknowledgements

This research was supported by the Russian Foundation for Basic Research (grant 12–08–00740-a) and the RAS Program 12–C–1–1015.

## References

[1] Svistkov A.L. Mechanical properties and mass transfer of viscoelastic deformable media // Int. J. Eng. Sci., 2001. V. 39. P. 1509–1532. (in english)

[2] Mullins L., Tobin N.R., 1965. Stress softenings in natural rubber vulcanizates, Part I. // J. Appl. Polym. Sci., 1965. V. 9. P. 2993–3010. (in english)

[3] Harwood J.A.C., Mullins L., Payne A.R. 1965. Stress softening in natural rubber vulcanizates, Part II. // J. Appl. Polym. Sci., 1965. V. 9. P. 3011–3021. (in english)

[4] Govindjee S. and Simo J.C. A micro-mechanically based continuum damage model for carbon black-filled rubbers incorporating Mullins' effect. // J. Mech. Phys. Solids, 1991. V. 39(1). P. 87–112. (in english)

[5] Schapery R.A. A theory of mechanical behavior of elastic media with growing damage and other changes in structure. // J. Mech. Phys. Solids, 1990. V. 38. P. 215–253. (in english)

[6] Bergstrom J.S., Boyce M.C. Constitutive modelling of the large strain time-dependent behavior of elastomers // J. Mech. Phys. Solids, 1998. V. 46. P. 931–954. (in english)

[7] Bueche F. Mullins effect and rubber-filler interaction. // J. Appl. Polym. Sci., 1961. V. 5(15). P. 271–281. (in english)

[8] Aleksandrov A.P and Lazurkin Yu.S.// Dokl. Akad. nauk SSSR, 1944. V. 45, S. 308–312. (in russian)

[9] Mullins L., Tobin N.R. Theoretical model for the elastic behavior of filler-reinforced vulcanized rubbers // Rubb. Chem. and Technol., 1957. V. 30. P. 555–571. (in english)

[10] Fukahori Y. The mechanics and mechanism of the black reinforcement of elastomers // Rub. Chem. Tech., 2003. V. 76. No. 2. P. 548–565. (in english)

*Vladimir V. Shadrin, Institute of Continuous Media Mechanics, Perm, Russia*

# The lift force of a wing moving in compressible fluid near a rigid surface

M. N. Smirnova A. V. Zvyaguin
wonrims@inbox.ru

**Abstract**

The problem of thin body motion in gas parallel to the boundary is regarded. In particular, the lift force in thin body motion parallel to rigid surface is determined and compared with existing solution for the lift force in case of an infinite space. The solution is determined under the assumption of fluid being ideal and compressible. The Chaplygin-Zhukovsky hypothesis of rear-edge-limited solution is taken into consideration. The solution of a problem is first reduced to singular integral equation and then to the Fredholm equation, which is solved numerically. The generalization of Zhukovski solution was obtained, which provides the lift force dependence on the altitude of the flight. The behavior of the lift force is very peculiar: it increases on decreasing altitude above the rigid surface. The screen effect becomes essential on moving wing altitude being smaller than the wing's length. The effect was detected experimentally before and gave birth to construction of a special flying vehicle named "ecranoplan". It is shown in the paper that the lift force could increase several orders of magnitude. This effect could be used in developing flying high-speed vehicles, which could be used in the territories of smooth surface: steppes, deserts, lakes, swamps, etc.

## 1 Introduction

It was observed that the lift force of a wing moving near flat surface increases strongly in comparison with free flight. An article about screen effect by B.N. Juriev [1] was published in 1923 in the USSR. That fact was used in creation of new flying devices - screen-flights, which got the Russian name "ekranoplan". In 1932 Finnish engineer T. Kaario proceeded to test his flying apparatus that used a screen effect. Then (1963 - 1976) a Soviet constructor R.L. Bartini created a screen-flight project SVVP-2500 that took off in 1974. The first Soviet manned jet screen-flight SM-1 was created in collaboration with R. Alekseev in 1960 - 1961 [2]. Giant screen-flight KM was finished by 1966 and "Orlyonok" type screen-flights were built from 1974 to 1983. Designing of new flying devices continues in many countries.

L.I. Sedov obtained an analytical solution for the lift force of a wing moving near rigid surface in terms of Weierstrass functions [3] using the theory of a complex variable. Approximate analytical solution of the problem of non-steady plane moving near rigid surface was obtained by K.V. Rozjdestvensky [4] with the help of asymptotic expansion. Theoretical investigation of a wing moving near rigid surface was made by A.N. Panchenkov [5, 6], but the obtained solutions incorporated free constants. Experimental results are shown in [7].

The problem of theoretical investigation of a wing's behavior near a surface is still far from being finalized. The present paper provides a theoretical solution for the two-

dimensional linearized problem of a thin wing motion near rigid surface in compressible fluid.

## 2 Mathematical statement of the problem

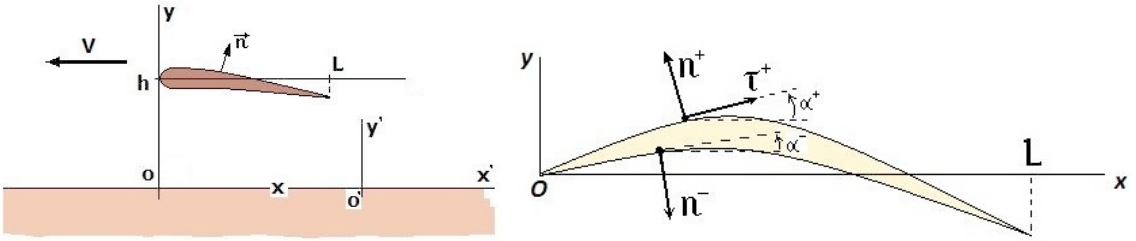


Figure 1: Schematic picture for thin wing motion above rigid surface.

The two-dimensional problem of thin body motion in the presence of rigid surface is regarded. The coordinate system and flow scheme are shown in Fig. 1. It is assumed that the wing is moving with constant velocity in an ideal compressible fluid near a motionless surface $y' = 0$ . In a motionless coordinate system $x', 0', y'$ adiabatic gas flow is described by the continuity and Euler equations. The angle $|\alpha^{\pm}| \ll 1$ and mass forces are considered to be negligibly small. These assumptions make the flow field to be potential. Streaming condition of the equality of normal velocity component should be satisfied on the rigid surface and on the body surface contacting fluid.

In movable coordinate system $x = x' + Vt, y = y'$ connected with the wing the gas flow can be considered stable. After transfer to another independent variable $\tilde{x} = \frac{x}{\delta}, \delta = \sqrt{1 - M^2}$ the equations and boundary conditions describing the gas flow take the following form:

$$\frac{\partial^2 \varphi}{\partial \tilde{x}^2} + \frac{\partial^2 \varphi}{\partial y^2} = 0; \tag{1}$$

$$0 \le \tilde{x} \le \frac{L}{\delta}, y = h^{\pm}: \quad \frac{\partial \varphi(\tilde{x}, h^{\pm})}{\partial y} = V\alpha^{\pm}(\delta\tilde{x}); \tag{2}$$

$$-\infty < \tilde{x} < \infty, y = 0: \quad \frac{\partial \varphi}{\partial y} = 0; \tag{3}$$

$$p = p_0 - \frac{\rho V}{\delta}\frac{\partial \varphi}{\partial \tilde{x}}. \tag{4}$$

Boundary conditions should be supplemented with function behavior at the infinity for the uniqueness of the solution. Thus an analytical function satisfying boundary conditions and decreasing at the infinity should be developed.

## 3 Problem solution

The solution of the Laplas equation can be developed in the form of a real part for the analytical function of a complex variable $\varphi(\tilde{x}, y) = Re\Phi(z), z = \tilde{x} + iy$ . Actually, it is necessary to develop first derivative of the analytical function, which could be denoted as: $iT(z) = \Phi'(z)$ . The development of the analytical function is reduced to the following

boundary problem [8]:

$$0 \le \tilde{x} \le \frac{L}{\delta}, y = h^{\pm}: \quad ReT(\tilde{x} + ih) = -V\alpha^{\pm}(\delta\tilde{x}) = -V\tilde{\alpha}^{\pm}(\tilde{x}); \tag{5}$$

$$-\infty < \tilde{x} < \infty, y = 0: \quad ReT^{+}(\tilde{x}, 0^{+}) = 0. \tag{6}$$

The pressure can be developed from the following formula:

$$p(\tilde{x} + iy) = p_0 + \frac{\rho V}{\delta} ImT(\tilde{x} + iy) \tag{7}$$

For the uniqueness of the solution boundary conditions should be supplemented with function behavior at the infinity and at the ends of the segment $0 \le \tilde{x} \le \frac{L}{\delta}$ . It is considered that the function tends to zero at the infinity and is limited at the rear edge of the wing, which is the result of the Chaplygin-Zhukovsky hypothesis [9].

The solution is developed with the help of the symmetry principle. The following non-dimentional variables are introduced $\tilde{\tilde{x}} = \frac{\tilde{x}}{\tilde{L}}, \tilde{\tilde{y}} = \frac{y}{\tilde{L}}, \tilde{\tilde{h}} = \frac{h}{\tilde{L}}, \tilde{L} = \frac{L}{\delta}$.

The development of the analytical function is reduced to the following boundary problem:

$$0 \le \tilde{\tilde{x}} \le 1, \tilde{\tilde{y}} = \tilde{\tilde{h}}^{\pm}: \quad ReT(\tilde{\tilde{x}} + i\tilde{\tilde{h}}) = -V\alpha^{\pm}(L\tilde{\tilde{x}}) = -V\tilde{\tilde{\alpha}}^{\pm}(\tilde{\tilde{x}}); \tag{8}$$

$$-\infty < \tilde{\tilde{x}} < \infty, \tilde{\tilde{y}} = 0: \quad ReT^{+}(\tilde{\tilde{x}}, 0^{+}) = 0. \tag{9}$$

The tildes will be omitted in the following equations.

The solution of the problem can be derived in the form of Cauchy type integral [8]:

$$T(z) = X_1(z)[\frac{1}{2\pi i}\int_0^1 \frac{1}{X_1^{+}(t)}\frac{\mu(t)}{t + ih - z}dt] + \frac{1}{2\pi i}\int_0^1 \frac{\zeta(t) + i\eta(t)}{t + ih - z} - \tag{10}$$

$$-X_2(z)[\frac{1}{2\pi i}\int_0^1 \frac{1}{X_2^{+}(t)}\frac{\mu(t)}{t - ih - z}dt] + \frac{1}{2\pi i}\int_0^1 \frac{\zeta(t) - i\eta(t)}{t - ih - z}, \tag{11}$$

where

$$X_1(z) = \sqrt{\frac{z - z_1}{z - z_2}} = \sqrt{\frac{R_{11}}{R_{12}}}e^{i\frac{\theta_{11} - \theta_{12}}{2}}, z_1 = 1 + ih, z_2 = ih; \tag{12}$$

$$X_2(z) = \sqrt{\frac{z - \bar{z_1}}{z - \bar{z_2}}} = \sqrt{\frac{R_{21}}{R_{22}}}e^{i\frac{\theta_{21} - \theta_{22}}{2}}, \bar{z_1} = 1 - ih, \bar{z_2} = -ih \tag{13}$$

Arguments $\theta_{11}, \theta_{12}, \theta_{21}, \theta_{22}$ are chosen according to the rule shown in Fig. 2.

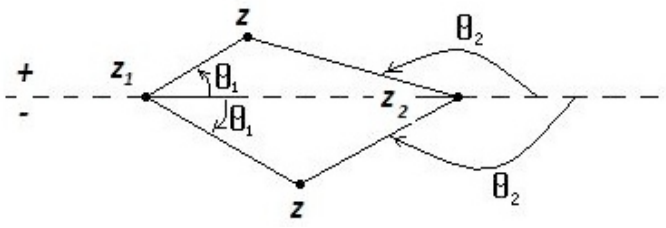


Figure 2: Rule to choose arguments $\theta_1 = arg(z - z_1), \theta_2 = arg(z - z_2)$.

The function $T(z)$ satisfies the boundary condition $-\infty < x < \infty, y = 0, T^{+}(x, 0^{+}) = 0$. It is assumed that $\mu(t) = -V(\tilde{\tilde{\alpha}}^{+} + \tilde{\tilde{\alpha}}^{-}), \zeta(t) = -V(\tilde{\tilde{\alpha}}^{+} - \tilde{\tilde{\alpha}}^{-})$ . The function $T(z)$ will

satisfy the boundary condition $0 \leq x \leq 1, y = h^{\pm} \quad ReT(x+ih) = -V\tilde{\tilde{\alpha}}^{\pm}(x)$, if the following singular integral equation will be fulfilled:

$$\frac{1}{2\pi}\int_0^1 \frac{\eta(t)}{t-s}dt - \frac{1}{2\pi}\int_0^1 \frac{(t-s)\eta(t)}{(t-s)^2+4h^2}dt - \frac{Vh}{\pi}\int_0^1 \frac{\tilde{\tilde{\alpha}}^+(t)-\tilde{\tilde{\alpha}}^-(t)}{(t-s)^2+4h^2}dt -$$
$$- R(s)\sin\alpha(s)\frac{V}{2\pi}\int_0^1 \sqrt{\frac{t}{1-t}}\frac{(t-s)}{(t-s)^2+4h^2}(\tilde{\tilde{\alpha}}^+(t)+\tilde{\tilde{\alpha}}^-(t))dt +$$
$$+ R(s)\cos\alpha(s)\frac{Vh}{\pi}\int_0^1 \sqrt{\frac{t}{1-t}}\frac{1}{(t-s)^2+4h^2}(\tilde{\tilde{\alpha}}^+(t)+\tilde{\tilde{\alpha}}^-(t))dt = 0, \quad (14)$$

where

$$\alpha(s) = \frac{1}{2}[\arctan(\frac{2h}{1-s}) + \arctan(\frac{2h}{s})], R(s) = \sqrt[4]{\frac{(1-s)^2+4h^2}{s^2+4h^2}}. \quad (15)$$

## 4 The case of wing being a plate

If the wing has a shape of a plate $\tilde{\tilde{\alpha}}^{\pm} = -\gamma$ the singular integral equation takes the following form:

$$\frac{1}{\pi}\int_0^1 \frac{\eta(t)}{t-s}dt - \frac{1}{\pi}\int_0^1 \frac{(t-s)\eta(t)}{(t-s)^2+4h^2}dt +$$
$$+ R(s)\sin\alpha(s)\frac{V\gamma}{\pi}\int_0^1 \sqrt{\frac{t}{1-t}}\frac{(t-s)}{(t-s)^2+4h^2}dt -$$
$$- R(s)\cos\alpha(s)\frac{2Vh\gamma}{\pi}\int_0^1 \sqrt{\frac{t}{1-t}}\frac{1}{(t-s)^2+4h^2}dt = 0. \quad (16)$$

The third and the fourth integrals can be taken analytically using the theory of residues [10]. The following singular integral equation can be determined:

$$\frac{1}{\pi}\int_0^1 \frac{\tilde{\eta}(t)}{t-s}dt = \frac{1}{\pi}\int_0^1 \frac{(t-s)\tilde{\eta}(t)}{(t-s)^2+4h^2}dt - F(s), \quad (17)$$

where

$$\tilde{\eta}(s) = \frac{\eta(s)}{V\gamma}, F(s) = R(s)\sin\alpha(s) - 1, R(s) = \sqrt[4]{\frac{(1-s)^2+4h^2}{s^2+4h^2}}, \quad (18)$$
$$\alpha(s) = \frac{1}{2}[\arctan(\frac{2h}{1-s}) + \arctan(\frac{2h}{s})]. \quad (19)$$

## 5 The case of wing being convex

If the wing has a convex shape $y^+(x) = -\gamma x^2, y^-(x) = -\gamma x$ :

$$\tilde{\tilde{\alpha}}^+(x) = -2\gamma x, \tilde{\tilde{\alpha}}^-(x) = -\gamma, \quad (20)$$
$$\tilde{\tilde{\alpha}}^+(x) + \tilde{\tilde{\alpha}}^-(x) = -2\gamma(t+\frac{1}{2}), \quad (21)$$
$$\tilde{\tilde{\alpha}}^+(x) - \tilde{\tilde{\alpha}}^-(x) = -2\gamma(t-\frac{1}{2}). \quad (22)$$

The singular integral equation takes the following form:

$$\frac{1}{\pi}\int_0^1 \frac{\eta(t)}{t-s}dt - \frac{1}{\pi}\int_0^1 \frac{(t-s)\eta(t)}{(t-s)^2+4h^2}dt + \frac{2\gamma Vh}{\pi}\int_0^1 \frac{t-\frac{1}{2}}{(t-s)^2+4h^2}dt+$$
$$+ R(s)\sin\alpha(s)\frac{V\gamma}{\pi}\int_0^1 \sqrt{\frac{t}{1-t}}\frac{(t-s)}{(t-s)^2+4h^2}(t+\frac{1}{2})dt-$$
$$- R(s)\cos\alpha(s)\frac{2\gamma Vh}{\pi}\int_0^1 \sqrt{\frac{t}{1-t}}\frac{1}{(t-s)^2+4h^2}(t+\frac{1}{2})dt = 0. \quad (23)$$

The third, the fourth and the fifth integrals can be taken analytically using the theory of residues [10]. The following singular integral equation can be determined:

$$\frac{1}{\pi}\int_0^1 \frac{\tilde{\eta}(t)}{t-s}dt = \frac{1}{\pi}\int_0^1 \frac{(t-s)\tilde{\eta}(t)}{(t-s)^2+4h^2}dt - F(s), \quad (24)$$

where

$$\tilde{\eta}(s) = \frac{\eta(s)}{V\gamma}, \quad (25)$$

$$F(s) = \frac{h}{\pi}\ln\frac{(1-s)^2+4h^2}{s^2+4h^2} + \frac{1}{\pi}(s+\frac{1}{2})[\arctan\frac{1-s}{2h} + \arctan\frac{s}{2h}]+$$
$$+ \frac{1}{2}(R(s)\sin\alpha(s)-1) + (s+\frac{1}{2})R(s)\sin\alpha(s) - 2hR(s)\cos\alpha(s)- \quad (26)$$
$$- \frac{(1-s)}{R^2(s)}[\cos 2\alpha(s) + \frac{2h}{1-s}\sin 2\alpha(s)],$$

$$R(s) = \sqrt[4]{\frac{(1-s)^2+4h^2}{s^2+4h^2}}, \alpha(s) = \frac{1}{2}[\arctan(\frac{2h}{1-s}) + \arctan(\frac{2h}{s})]. \quad (27)$$

The solution for the integral equations $\frac{1}{\pi}\int_0^1 \frac{\varphi(t)}{t-s}dt = \psi(s)$ which is limited in the point $x = 1$ and has a singularity in the point $x = 0$ is developed in the following form [22]:

$$\varphi(x) = -\sqrt{\frac{1-x}{x}}\frac{1}{\pi}\int_0^1 \sqrt{\frac{s}{1-s}}\frac{\psi(0)}{s-x}ds. \quad (28)$$

The mentioned form of solution for the integral equation is used to regularize the singular integral equation and to reduce it to the Fredholm equation [11]:

$$\tilde{\eta}(x) + \int_0^1 \tilde{\eta}(t)K(x,t)dt = G(x), \quad (29)$$

where

$$K(x,t) = \frac{1}{4\pi}\sqrt{\frac{1-x}{x}}\frac{\sin[\alpha(t)-\delta(x,t)]}{R(t)\sqrt{[t(1-x)-x(1-t)]^2+4h^2}}, \quad (30)$$

$$G(x) = \sqrt{\frac{1-x}{x}}\frac{1}{\pi}\int_0^1 \sqrt{\frac{s}{1-s}}\frac{F(s)}{s-x}ds, R(s) = \sqrt[4]{\frac{(1-s)^2+4h^2}{s^2+4h^2}}, \quad (31)$$

$$\alpha(t) = \frac{1}{2}[\arctan(\frac{2h}{1-t}) + \arctan(\frac{2h}{t})], \delta(x,t) = \arctan\frac{2h}{t(1-x)-x(1-t)}. \quad (32)$$

The following formula is used to determine the lift force:

$$F = \int_0^L [p^-(s) - p^+(s)]ds = \delta\int_0^{\frac{L}{\delta}} [p^-(\tilde{s}) - p^+(\tilde{s})]d\tilde{s}. \quad (33)$$

The pressure is derived from the problem statement:

$$p(\tilde{s}) = p_0 + \frac{\rho V}{\delta} ImT(\tilde{s}), \qquad p^-(\tilde{s}) - p^+(\tilde{s}) = \frac{\rho V}{\delta}(Im(T^-(\tilde{s}) - T^+(\tilde{s}))). \tag{34}$$

In the case of a plate:

$$Im(T^-(\tilde{\tilde{s}}) - T^+(\tilde{\tilde{s}})) = V\gamma[\sqrt{\frac{1-\tilde{\tilde{s}}}{\tilde{\tilde{s}}}}\frac{2}{\pi}\int_0^1 \sqrt{\frac{t}{1-t}}\frac{dt}{t-\tilde{\tilde{s}}} - \tilde{\eta}(\tilde{\tilde{t}})], \tag{35}$$

$$p^-(\tilde{\tilde{s}}) - p^+(\tilde{\tilde{s}}) = \frac{\rho V^2\gamma}{\delta}[2\sqrt{\frac{1-\tilde{\tilde{s}}}{\tilde{\tilde{s}}}} - \tilde{\eta}(\tilde{\tilde{t}})], \tag{36}$$

$$F = \int_0^L [p^-(s) - p^+(s)]ds = L\int_0^1 [p^-(\tilde{\tilde{s}}) - p^+(\tilde{\tilde{s}})]d\tilde{\tilde{s}} = \frac{\pi\rho LV^2\gamma}{\delta}[1 + \frac{1}{\pi}\int_0^1 [-\tilde{\eta}(\tilde{\tilde{s}})]d\tilde{\tilde{s}}]. \tag{37}$$

The derived lift force differs from its analog for boundless surface by an extra summand which decreases with the increase of the height.

In the case of a convex wing:

$$F = \frac{\rho LV^2\gamma}{\delta}[\int_0^1 \sqrt{\frac{1-s}{s}}\frac{1}{\pi}\int_0^1 \sqrt{\frac{t'}{1-t'}}\frac{2t'+1}{t'-s}dt'ds - \int_0^1 \tilde{\eta}(s)ds] = \\ = \frac{\pi\rho LV^2\gamma}{\delta}[\frac{5}{4} - \frac{1}{\pi}\int_0^1 \tilde{\eta}(s)ds]. \tag{38}$$

## 6 Results and discussions

The dependence of the reduced lift force $\frac{F\delta}{\pi\rho LV^2\gamma}$ upon the altitude $\tilde{h} = \frac{h}{L}$ is shown on Fig.3, Fig.4.

As it is shown on Fig.3, Fig.4 the lift force decreases with the increase of the height above the rigid surface until the force reaches its magnitude in a boundless medium.

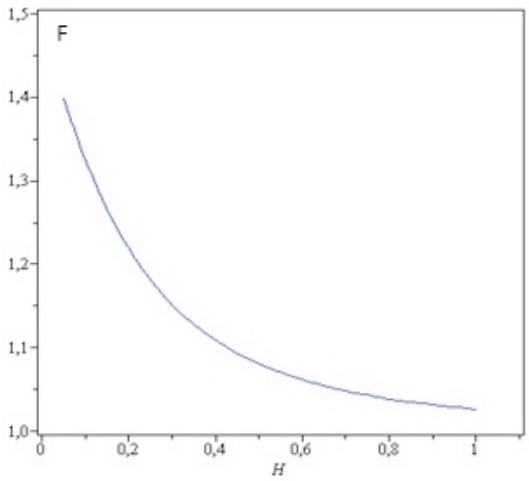


Figure 3: The dependence of the reduced lift force $\frac{F\delta}{\pi\rho LV^2\gamma}$ of a plate upon the altitude $H = \tilde{h} = \frac{h}{L}$.

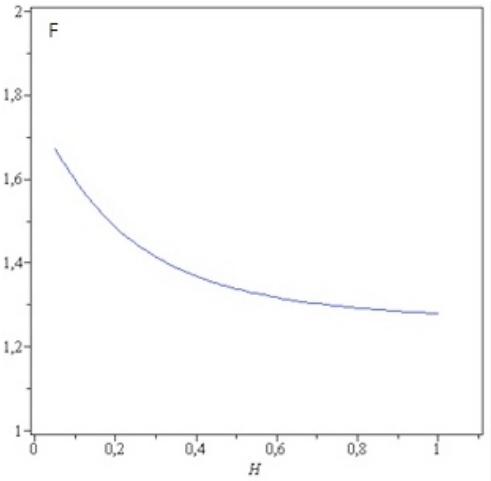


Figure 4: The dependence of the reduced lift force $\frac{F\delta}{\pi\rho LV^2\gamma}$ of a convex wing upon the altitude $H = \tilde{h} = \frac{h}{L}$.

## 7 Conclusion

A linear problem of thin wing motion near rigid surface is reduced to the Fredholm equation which is developed numerically as a system of linear equations. So the problem is solved almost analytically.

The behavior of the lift force and the point of its application evolution depending on the distance from the rigid surface are examined. It is shown that the lift force increases with the decrease of the wing distance from the plane surface. It can be seen that a rigid surface affects the lift force only on the altitude which is smaller than the length of a wing. If the altitude above the surface surpasses the wing span the screen effect practically disappears and the lift force tends to its value in an unbounded space determined by the classical Zhukovsky solution.

The obtained solution evidently shows, that the increase of lift force near the screen in the orders of magnitude allows developing flying vehicles carrying much more cargo at lower fuel consumption.

The obtained solution would be useful for designing giant screen-flight vehicles, because it is necessary to take into account the essential variation of lift force application center and its value depending on altitude.

The effect could be used for developing vehicles for operation on other planets having not very dense atmosphere and relatively smooth surface (like Mars). Flights in such an atmosphere are energy consuming, while using the effect of lift force increase near the surface could be very effective.

## Acknowledgements

Russian Foundation for Basic Research (RFFI) is acknowledged for financial support.

## References

[1] Juriev B.N. Earth impact on the aerodynamical characteristics of a wing. “Air fleet herald” No1, 1923.

[2] Belavin N.I. Screen-flights (ecranoplan). Moscow: “Shipbuilding” Publ, 1977.

[3] Sedov L.I. Plane problems of hydrodynamics and aerodynamics. Moscow: “Science” Publ., 1980.

[4] Rozjdestvensky K.V. Asymptotic theory of a wing moving on small distances from a rigid wall. Mechanics of liquid and gas, No6, 1977.

[5] Panchenkov A.N. Hydrodynamics of an underwater wing. Kiev: book printing house No5, 1964.

[6] Panchenkov A.N. Theory of optimal supporting surface. Novosibirsk: “Science” Publ, 1983.

[7] Serebriisky Y.M., Biyachuev S.A. The study of horizontal steady wing motion in a pipe. TSAGI papers (Central Aero Hydrodynamic Institute), issue 437, 1939.

[8] Gahov F. D. Boundary problems. Moscow: “Science” Publ, 1977.

[9] Kochin N. E., Kibel I. A., Roze N. V. Theoretical hydromechanics. Moscow: Physmathgys, 1963.

[10] Lavrent'ev M.A., Shabat B.V. Theory of functions of a complex variable. Moscow: "Science" Publ, 1987.

[11] Verlan A.F., Sizikov V.S. Methods of solving integral equations with programs for computers. Kiev "Science". 1977.

*M. N. Smirnova, A. V. Zvyaguin, Department of Mechanics and Mathematics, Moscow M.V. Lomonosov State University, Moscow 119992, Leninskie Gory 1, RUSSIA*

# Analysis of one-dimensional systems with spatially modulated parameters as dissemination of the concept of vibrational mechanics

Vladislav S. Sorokin
slavos87@mail.ru

**Abstract**

The paper is devoted to the study of averaged processes, which take place in fast varying periodic structures. Particularly, oscillations of a string and bending oscillations of a beam with variable cross-sections are considered. The method of direct separation of motions and the concept of vibrational mechanics [1,2] are used for the analysis of these systems. Thus, the applicability range of this method is broadened. The influence of "fast" spatial modulations on the effective values of systems parameters is revealed and described. Particularly, it is obtained that the variability of beam's cross-section, along with other effects, leads to the emergence of the additional "slow" longitudinal force. It is noted that the order of equations, which describe the averaged processes in the examined periodic structures, under certain conditions may be different from the order of corresponding equations, which characterize systems in the absence of modulations.

## 1 Introduction

Continua composed of periodically repeated elements (cells) are used in many fields of science and technology. Examples of such continua are composite materials, consisting of alternating volumes of substances with different properties. Use of these materials enables, in particular, to achieve the effect of heat or sound isolation. The simplest example is material such as felt, which has long been used for these purposes. Various frame structures, e.g. building frames and trusses of bridges, cranes and industrial constructions, railway tracks and compound pipes are also periodic systems. Study of such structures is of particular interest in connection with the problem of optimization of their properties.

Widely used approaches for wave examination in periodic systems are methods, based on the utilization of the Floquet theory [3,4,5]. The so-called frequency stop bands, i.e. frequencies ranges, in which a wave does not propagate through the considered structure, can be determined by its means. However, in the framework of this theory it is problematic to incorporate the (external) boundary conditions. Numerical approaches to study and optimization of periodic structures, particularly, WFE method [6,7] and topology optimization method [8,9,10], are based on finite-element models of the considered structures, and only approximate solution of a problem can be obtained by their means.

The present paper is devoted to the analysis of the averaged processes in spatially periodic structures, particularly, to the study of long wave propagation in a string and a beam with variable cross-sections. The aim of the research is to identify the effective (averaged) properties of the considered systems in relation to these "slow" processes. The averaging

procedure for stationary and non-stationary processes in periodic structures (composite materials) based on the multiple scales method [11] combined with the averaging method [12] was proposed in the monograph [13]. In the present paper the method of direct separation of motions (MDSM) is used for the analysis of the considered mechanical systems. This method facilitates solution of various challenging problems of action of high frequency vibrations on nonlinear mechanical systems [1,2]. The advantages of the MDSM over methods [11,12] are the simplicity in application and the transparency of the physical interpretation. Thus, the applicability range of the MDSM is broadened in the paper.

## 2 Oscillations of a string with variable cross-section

The equation of oscillations of a string with variable cross-section $S = S_0(1 + \alpha \sin kx)$, $0 \leq \alpha < 1$ ,$k >> \pi/l$, where $l$ is the length of the string, is considered

$$\rho S \frac{\partial^2 u}{\partial t^2} - \frac{\partial}{\partial x}\left(T \frac{\partial u}{\partial x}\right) = 0 \tag{1}$$

here $\rho$ is the density of the string material, $T$ is the tension force, $u(x,t)$ is a lateral deflection of the string. The boundary conditions are homogeneous: $u|_{x=0} = u|_{x=l} = 0$. Partial solution of equation (1) is sought in the form $u(x,t) = A(x)B(t)$. The following equations for the new variables $A(x)$ and $B(t)$ are obtained

$$\ddot{B} = -C_1 B; \frac{d^2 A}{dx^2} + \frac{C_1 \rho S_0}{T}(1 + \alpha \sin kx)A = 0 \tag{2}$$

Here $C_1$ is a constant. The concept of vibrational mechanics and the MDSM [1,2] are used for solving the second of these equations in the following manner: its solutions are searched in the form

$$A = A_1(x) + \psi(x, kx) \tag{3}$$

where $A_1$ is "slowly varying", and $\psi$ is "fast varying", $2\pi$-periodic in dimensionless ("fast") spatial coordinate $x_1 = kx$ variable, with period $x_1$ average being equal to zero: $\langle \psi(x, x_1) \rangle = 0$. Angle brackets denote averaging by $x_1$. The following equation is obtained for variable $A_1$ by averaging the second of equations (2) by $x_1$

$$\frac{d^2 A_1}{dx^2} + \frac{C_1 \rho S_0}{T} A_1 = -\frac{C_1 \rho S_0}{T} \alpha \langle \psi \sin x_1 \rangle \tag{4}$$

The boundary conditions are $A_1|_{x=0} = A_1|_{x=l} = 0$. The equation for variable $\psi$ is available from equation (2) by subtracting equation (4). Its solution has the form

$$\psi = A_1 \alpha \left( f_1(C_1\mu) \sin x_1 + \alpha f_2(C_1\mu) \cos 2x_1 + \alpha^2 f_3(C_1\mu) \sin 3x_1 + O(\alpha^3) + ... \right) \tag{5}$$

where $\mu = \rho S_0 / (Tk^2) << 1$, $f_1, f_2, f_3...$ are functions of $C_1\mu$, expressions for which depend on the number of retained terms in series (5). Employing the obtained relation for variable $\psi$, the following equation is composed for variable $A_1$

$$\frac{d^2 A_1}{dx^2} + \frac{C_1 \rho S_0}{T} \left(1 + \alpha^2 \frac{f_1(C_1\mu)}{2}\right) A_1 = 0 \tag{6}$$

Based on this equation, it may be concluded that modulations of string cross-sectional area lead to a change of the effective (averaged) value of this parameter. To satisfy the boundary conditions for variable $A_1$ the following equality should hold true

$$\sqrt{\frac{C_1\rho S_0}{T}\left(1+\alpha^2\frac{f_1(C_1\mu)}{2}\right)}=\frac{n\pi}{l} \tag{7}$$

Retaining only the first term in series (5), that is justified for small $\alpha$ ($\alpha < 0.5$), we obtain expression $f_1(C_1\mu)=\frac{C_1\mu}{1-C_1\mu}$ for function $f_1$, while equation (7) will have two roots, one of which is much greater than the other. So, formally the two values of the string oscillations frequency $\sqrt{C_{1(1)}}$, $\sqrt{C_{1(2)}}$ correspond to the one value of the wave number $n\pi/l$. Such result indicates a change of the order of the considered equation (1) owing to modulations of the string cross-section. The accounting of the other terms in solution (5) leads to the emergence of the additional values of the frequency $\sqrt{C_1}$, which correspond to the one wave number $n\pi/l$, every next of which exceeds the previous.

Series of numerical experiments was conducted to verify this conclusion. As an illustrative example, the dependence of the acceleration of the middle of the string $\ddot{u}(l/2,t)$ on time at parameters $\rho S_0/T = 1\,(\mathrm{s/sm})^2$, $l = 5$ sm, $\alpha = 0.5$, $k = 2.6$ 1/sm and simple initial conditions $u|_{t=0} = \sin \pi x/l$, $\dot{u}|_{t=0} = 0$ is presented in Figure 1.

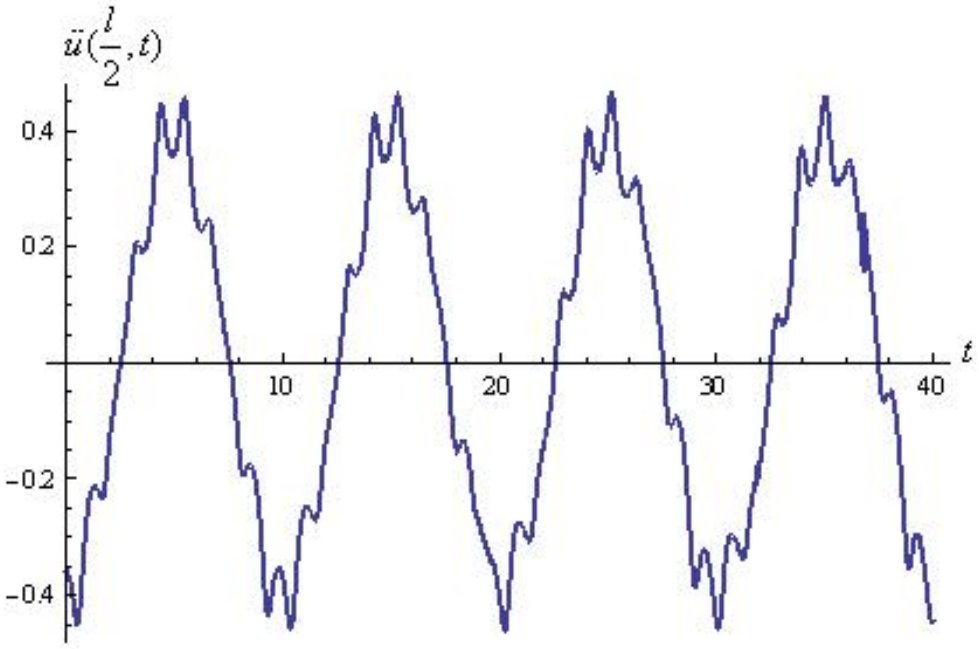


Figure 1: The dependence of the acceleration of the middle of the string on time.

As is seen from Figure 1, modulations of string cross-section indeed lead to the emergence of a spectrum of additional eigenfrequencies, which corresponds to the same wave number $n\pi/l$. Thereby, analitical results were confirmed by numerical experiments.

## 3 Bending oscillations of a beam with variable cross-section

We consider bending oscillations of a beam with variable cross-section, which are described by the equation

$$\rho S \frac{\partial^2 w}{\partial t^2} + \frac{\partial^2}{\partial x^2}\left(EJ\frac{\partial^2 w}{\partial x^2}\right) = 0 \tag{8}$$

Here $\rho$ is the density and $E$ is the Young's modulus of the beam's material, $w(x,t)$ is beam's deflection, $S = S(x) = S_0(1 + \alpha \sin kx)$ is the cross-sectional area, $J = J(x) = J_0(1 + \alpha_1 \sin kx)$ is the moment of inertia of the cross-section. Employing the approach, used above, for solving equation (8), we compose the equation for the slow variable $A_1$. Based on this equation it may be concluded that modulations of beam's cross-section lead to: the decrease of the effective moment of inertia of its cross-section, the emergence of the additional "slow" longitudinal force, and the increase of the effective cross-sectional area. As in the case of a string, satisfying the boundary conditions, we obtain an equation for the constant $C_1$, which has a number of roots.

Based on these results the conclusion is drawn that modulations of the beam cross-section lead, firstly, to the change of the value of the fundamental eigenfrequency $\sqrt{C_{1(1)}}$ in comparison with its non-modulated value, and, secondly, to the emergence of a spectrum of additional eigenfrequencies, which corresponds to the same wave number $n\pi/l$, i.e. to a change of the order of the initial differential equation.

## 4 Conclusions

The equations, which describe the averaged, long-wave processes in a beam and a string with variable cross-sections, are derived by means of the MDSM. Thus, the applicability range of this method is broadened to the cases, when separation of variables can be performed not in time, but, rather, in spatial coordinate. Based on the derived equations the influence of "fast" spatial modulations on the systems' effective (averaged) parameters is detected. Particularly, it is shown that modulations of string cross-sectional area lead to the increase of the effective value of this parameter, and the variability of beam's cross-section, along with other effects, leads to the emergence of the additional "slow" longitudinal force. It is noted that the order of differential equations, which describe the averaged (slow) processes in the considered periodic structures, under certain conditions may differ from the order of the corresponding equations in the absence of modulations.

## Acknowledgements

*The author is grateful to Professor I.I. Blekhman for specifying the research subject and comments to the paper.*

## References

[1] I.I. Blekhman (2000) Vibrational Mechanics. World Scientific, Singapore at al.

[2] I.I. Blekhman (2004) Selected Topics in Vibrational Mechanics. World Scientific, Singapore at al.

[3] L. Brillouin (1953) Wave Propagation in Periodic Structures second edition. Dover Publications, New York

[4] D.J. Mead (1973) A General Theory of Harmonic Wave Propagation in Linear Periodic Systems with Multiple Coupling. Journal of Sound and Vibration, 27, 235-260

[5] D.J. Mead (1996) Wave Propagation in Continuous Periodic Structures: Research Contributions from Southampton. Journal of Sound and Vibration,190 (3), 495-524

[6] B.R. Mace, D. Duhamel, M.J. Brennan, L. Hinke (2005) Finite Element Prediction of Wave Motion in Structural Waveguides. Journal of the Acoustical Society of America, 117, 2835-2843

[7] A. Soe-Knudsen, S. Sorokin (2011) On Accuracy of the Wave Finite Element Predictions of Wavenumbers and Power Flow: A Benchmark Problem. Journal of Sound and Vibration, 330, 2694-2700

[8] M.P. Bendsøe, N. Kikuchi (1988) Generating Optimal Topologies in Structural Design Using a Homogenization Method. Computer Methods in Applied Mechanics and Engineering, 71(2), 197-224

[9] M.P. Bendsøe, O. Sigmund (2003) Topology Optimization - Theory, Methods and Applications. Springer-Verlag, Berlin Heidelberg New York

[10] O. Sigmund, J.S. Jensen (2003) Systematic Design of Phononic Band-gap Materials and Structures by Topology Optimization. Philosophical Transactions of the Royal Society London, Series A (Mathematical, Physical and Engineering Sciences), 361, 1001-1019

[11] Ali H. Nayfeh, D.T. Mook (1979) Nonlinear Oscillations. Wiley-Interscience, New York

[12] N.N. Bogoliubov and Y.A. Mitropolski (1961) Asymptotic Methods in the Theory of Non-linear Oscillations. Gordon and Breach, New York

[13] N.S. Bakhvalov, G.P. Panasenko (1984) Averaging of Processes in Periodic Media (in Russian). Nauka, Moscow

*Vladislav S. Sorokin, Saint Petersburg, Russia*

# Application of hybrid algorithms to computational diagnostic problems for hydromechanical systems

V. D. Sulimov P. M. Shkapov
spm@bmstu.ru

**Abstract**

Reliable mathematical modeling in hydromechanical system dynamics is very important for studies related to the safety of significant objects in the nuclear power industry. Consideration is being given to problems of identification of anomalies in the phase constitution of the coolant circulating throw the reactor primary circuit. Main dynamical characteristics of the object under diagnosing are considered as continuous functions of the bounded set of control variables. Possible occurrence of anomalies in the phase constitution of the coolant can be detected owing to changes in dynamical characteristics of the two-phase flow. As the normal state of the coolant and anomalous one are characterized by different spectra, then it is necessary to minimize simultaneously individual differences between spectral components. So, the diagnostic problem is formulated as the inverse spectral problem. Two novel hybrid algorithms for solving the corresponding global minimization problem are proposed. The first algorithm M-PCALMS combines the stochastic Multi-Particle Collision Algorithm (scanning of the search space) and deterministic gradient algorithm (local minimization) with smoothing approximations of the error function. The second algorithm M-PCASFC implements the local search procedure using the space-filling curve method. Results of successful computational experiments are presented to illustrate the efficiency of the approach.

## 1 Introduction

Modern methods for solving practical problems relating to trouble free, efficient and prolonged operation of complex systems are presumed the application of computational diagnostics [1]. The investigations are concerned with mechanical and hydromechanical systems which are constituents of nuclear power plants, aerospace structures, chemical process equipment. Computational diagnostic methods make it possible to study properties of the object under diagnosing on base of circumstantial measured data [2–4]. Input data for diagnosing usually contain the results of experimental measurements of the system certain investigatory characteristics; among them may be registered parameters of oscillatory motion or impact process. It needs to evaluate causal characteristics like the dynamic equation coefficients, boundary conditions, geometrical and other characteristics. The diagnostic procedure is founded on the solution of the corresponding inverse spectral problem; the problem in many cases may be reduced to a minimization of an appropriate error criterion. Eigenvalues from the direct problem for the mathematical model and useful measured data for the system are used in order to construct the criterion. When solving these inverse problems, consideration must be given to following special features: the error criterion may be represented by nondifferentiable and multiextremal function. In the general case it is necessary to solve the problem using inaccurate incomplete experimental data.

Possible availability of repeated or very close eigenvalues one should take into account. It is well known that the above problem is often ill posed, so that small perturbations in the data can result in large changes of the solution. Regularization technique is a standard method of transforming the initial problem into well-posed form [5, 6]. Implementation of special procedures is required for finding regularization parameters. Incompleteness of the spectral data results in the error crterion being non-convex. As the error function has numerous local minima, it is necessary to use global optimization methods.

Vibration monitoring methods are cost-effective and reliable tools for early failure detection and preventive maintenance in the up-to-date nuclear power industry. One of the most severe accidents in nuclear power generation is loss of coolant, where the re-circulating coolant of the pressurized water reactor may flash into steam [7, 8]. The standard reactor instrumentation can register signals caused by pressure fluctuation of the coolant. The problem at hand is an interpretation of the registered spectra and useful data extraction for diagnostics. Methods of solving the problem for computational models of the VVER-1000 primary circuit are under consideration. Possible occurrence of anomalies in the phase constitution of the coolant can be detected owing to changes in dynamical characteristics of the two-phase flow. Mathematical models for numerical analysis of acoustical oscillations in two-phase coolant have been developed [9]. As the normal state of the coolant and anomalous one are characterized by different spectra, then it is necessary to minimize simultaneously individual differences between spectral components. These differences can be described by an appropriate error function. The goal is to find a set of controlling variables, which will minimize the error function and determine current phase constitution of the coolant. So, the diagnostics problem is formulated as the inverse spectral problem.

Implementation of the approach with the use of hybrid global optimization algorithms is discussed. As usual hybrid algorithms combine stochastic and deterministic algorithms in order to achieve better computational properties. Two novel stochastic algorithms have been proposed recently: the Particle Collision Algorithm PCA [10] and the Multi-Particle Collision Algorithm M-PCA [11]. The NMPCA is a good example of the hybridization method [12]. The hybrid NMPCA performs as follows: first, a wide search in the solution space is carried out using a stochastic optimization algorithm (the PCA), and then scanning the promising areas is made with a deterministic local search technique (Nelder-Mead Simplex). This searching is performed iteratively until a certain number of fitness function evaluations is reached. However, it is well-known that the convergence theory for Nelder-Mead simplex method is far from completion; so the method can fail to converge or converge to non-stationary points [13]. As an alternative to the NMPCA two novel hybrid algorithms are introduced. These algorithms combine the M-PCA and the deterministic gradient techniques with smoothing approximations for fitness functions or the space-filling method throw the local search.

The plan of the remainder of this paper is as follows. The section following contains statement of the diagnostics problem. Section 3 provides brief descriptions of the hybrid global optimization algorithms. In section 4 successful computational experiments for identifying anomalies of the VVER-1000 equipment components and the phase constitution of the coolant in the primary circuit are presented to illustrate peculiarities of the approaches. Section 5 gives conclusions and discussion on further work.

## 2 Formulation of the problem

It is supposed that a set of performance index values associated with a computational model to be updated is defined by a set of controlling variables. Experimental spectral data

registered by permanent instrumentation may be incomplete. So the goal is to determine vectors of controlling variables using only measured data on natural frequencies of the object. The standard approach is to set the inverse spectral problem and then to solve the corresponding least squares problem

$$\min_{x \in X \subset R^n} f(x), \tag{1}$$

where $f(x) = \sum_{i=1}^{N} w_i(\zeta_i(x) - \zeta_i^*)^2$; $x$, $X$ — the vector of controlling variables and its feasible domain of the error function $f(x)$ respectively; the $w_i$ stand for weighting factors that reflect the confidence level in the measurements; $N$ is the number of eigenvalues under consideration; $\zeta_i(x)$ and $\zeta_i^*$ denote the eigenvalues that correspond to computed (solutions of the direct problem) and to measured natural frequencies respectively;

$$X = \left\{ x_i \,\middle|\, x_i^L \le x_i \le x_i^U;\ i = \overline{1,n} \right\}; \tag{2}$$

here $x_i^L$, $x_i^U$ — the lower and upper bounds on the $i$th controlling variable.

As practical observations show, the error function in the considered problem is often multiextremal. Therefore, it is necessary to turn to methods of global optimization. It is clear that if the measured spectral data exactly match to the computational model then the solution of the minimization problem will cause error function to take its global minimum value of zero. Let us suppose that there is a unique solution of the ill-posed inverse spectral problem and that this corresponds to the global minimum of the error function. However, the fact is that the theoretical question of the uniqueness of solutions of the problem may not be relevant to practical applications in which there is the additional complication of accuracy of experimental measurements. Furthermore, some complications may arise due to incompleteness of measured spectral data, influence of the two-phase interference on the flow dynamics, the presence of noise, etc. Within the scope of this work we take it as a convenient and reasonable assumption that global minimization of the error function in the above inverse problem will yield correct model updating for objects under consideration.

# 3 Hybrid global optimization algorithms

## 3.1 The Particle Collision Algorithm (PCA)

The modern Particle Collision Algorithm [10] has some essential advantages in relation to well known stochastic global optimization algorithms such as the Genetic Algorithm, Simulated Annealing, Fast Simulated Annealing, etc. Specifically, the PCA does not require any additional parameters other than the number of iterations; the algorithm is extremely easy to implement and can be applied to both continuous and discrete optimization problems. The PCA performs using the analogy with nuclear particle collision reactions, in particular scattering and absorption. So, a particle that hits a high-fitness "nucleus" would be "absorbed" and would explore the boundaries. Otherwise, a particle that hits a low-fitness region would be scattered to another region. This reasoning makes it possible to simulate the exploration of the search space and the exploitation of the most promising areas of the fitness landscape throw successive scattering and absorption collision events.

The original PCA works as follows. First an initial configuration is chosen, then a modification of the old configuration into a new one is implemented. The qualities of the two configurations are compared. A decision then is made on whether the new configuration is acceptable. If it is, the current configuration acts as the old configuration for the

next step. If it is not acceptable, the algorithm proceeds with a new change of the old configuration. It is pertinent to note that acceptance of current trial solution with certain probability may avoid the convergence to local optima.

However, the PCA is in its early stages. In spite of its advantages over Genetic Algorithm and Simulated Annealing in solving test problems, practical application of the PCA is restricted because of solutions remain too expensive. As possible development, the local search procedure in the algorithm could be improved. It seems promising to use gradient methods for local minimization of the error function. But in so doing the problem of non-differentiability of the function should be taken into account.

### 3.2 The Multi-Particle Collision Algorithm (M-PCA)

The modern Multi-Particle Collision Algorithm is based on the canonical PCA, but a new characteristic is introduced: the use of several particles, instead of only one particle to act over the search space [11]. So, the new outer loop for the particle control has been added to the basic global optimization algorithm. Thanks to use of several particles the M-PCA can better explore the search space, avoiding convergence to a local minimum. Coordination between the particles was achieved throw a blackboard strategy, where the Best_Fitness information is shared among all the particles in the process.

Similar to PCA, M-PCA also has only one parameter to be determined, the number of iterations. But in this case, the total number of iterations is divided by the number of particles which will be used in the process. The division of the task is the great distinction of the M-PCA, which leads to a great reduction of required computing time.

The pseudo code brief description of the M-PCA algorithm is as follows.

```
0 Generate an initial solution Old_Config
Best_Fitness = Fitness (Old_Config)
Update Blackboard
  For n = 0 to # of particles
    For n = 0 to # of iterations
      Update Blackboard
      Perturbation( )
      If Fitness (New_Config) > Fitness (Old_Config)
        If Fitness (New_Config) > Best_Fitness
          Best_Fitness := Fitness (New_Config)
        End If
        Old_Config := New_Config
        Exploration( )
      Else
        Scattering( )
      End If
  End For
End For
2. Exploration( )
  For n = 0 to # of iterations
    Small_Perturbation ( )
    If Fitness (New_Config) > Fitness (Old_Config)
      If Fitness (New_Config) > Best_Fitness
        Best_Fitness := Fitness (New_Config)
      End If
```

```
        Old_ Config := New_ Config
      End If
    End For
  Return
  3. Scattering( )
    p_scatt = 1−( Fitness (New_Config)) / (Best_ Fitness)
    If p_scatt > random(0, 1)
      Old_ Config := random solution
    Else
      Exploration ( )
    End If
  Return
  Perturbation( )
    For i = 0 to (Dimension-1)
      Upper = Superior_Limit[i]
      Lower = Inferior_Limit[i]
      Rand = Random(0, 1)
      New_ Config[i] = Old_ Config[i] – ((Upper – Old_ Config[i])*
      Rand) – ((Old_ Config[i] – Lower)*(1 – Rand))
      If (New_ Config[i] > Upper)
        New_ Config[i] = Superior_ Limit[i]
      Else          If (New_ Config[i] < Lower)
          New_ Config[i] = Inferior_ Limit[i]
        End If
      End If
    End For
  Return
  Small_Perturbation( )
    For i = 0 to (Dimension-1)
      Upper = Random(1.0, 1.2) – Old_ Config[i]
      If (Upper > Superior_ Limit[i])
        Upper = Superior_ Limit[i]
      End If
      Lower = Random(0.8, 1.0) – Old_ Config[i]
      If (Lower > Inferior_ Limit[i])
        Lower = Inferior_ Limit[i]
      End If
      Rand = Random(0, 1)
      New_ Config[i] = Old_ Config[i] – ((Upper – Old_ Config[i])*
      Rand) – ((Old_ Config[i] – Lower)*(1 – Rand))    End For
  Return
```

### 3.3 The smoothing technique for local optimization

Inverse problems are considered to be substantially difficult because of the kinks connected with presence of the multiple frequencies in registered spectra of acoustical oscillations in two-phase coolant. The difficulty motivated the development of algorithms for the solution of the minimization problem via some smooth approximation, which could be minimized by using any of the efficient classical approaches for smooth optimization. Several

approximations to smooth out the kinks may be introduced. One of them results in a continuously differentiable approximate function, whereas another one leads to a twice continuously differentiable approximate function. Two-parametric smoothing approximations were successfully used to solve problems of multi-criterion optimization of mechanical and hydro-mechanical systems with continuous but not everywhere differentiable functions [14].

### 3.4 The hybrid algorithm M-PCALMS

As an alternative to the NMPCA a novel hybrid algorithm M-PCALMS is introduced. In this new version of the global optimization algorithm the local search mechanism is a standard deterministic linearization method. Inverse problems are considered to be substantially difficult because of the kinks connected with presence of the repeated or very close frequencies in registered spectra for the computational model under updating. The difficulty motivated the development of algorithms for the solution of the minimization problem via some smooth approximation, which could be minimized by using any of the efficient classical approaches for smooth optimization. Several approximations to smooth out the kinks may be introduced. One of them results in a continuously differentiable approximate fitness function, whereas another one leads to a twice continuously differentiable approximate function. These approximations replace the original function in some neighborhoods of directional differentiability points. Moreover, this approach preserves such important property of the original function as its convexity. It is clear that the approach makes it possible to implement efficient gradient techniques in the solution process. In general case the error function is not differentiable everywhere, so the implementation of the smoothing technique may be quite pertinent. Computational experiments show the principal applicability of the proposed hybrid algorithm M- PCALMS for solving the inverse spectral problems.

### 3.5 The hybrid algorithm PCASFC

Some powerful algorithms for multi-extremal non-convex optimization problem are based on reducing the initial multi-dimensional problem to the equivalent problem of one dimension. This reduction can be executed by applying Peano-type space-filling curves mapping a unit interval on the real axis onto a multi-dimensional hypercube [15, 16].. The Peano curve development maps the segment [0, 1] of the real axis $R^1$ into the hypercube $X \subset R^1$ determined in (2). Actually, this is the case of continuous single-valued mapping that offers finding point $x(z) = \big(x_1(z), \ldots, , x_n(z)\big)^T \in X$ for each point $z \in [0, 1]$:

$$\min_{x \in X} f(x_1, \ldots, x_n) = \min_{0 \le z \le 1} \phi(z).$$

So, the initial multi-dimensional minimization problem (1) is equivalent to the above one-dimensional problem of finding the global minima of the discontinuous multi-extremal function $\phi(z)$. The Hilbert technique is used here for building the development of the Peano space-filling curve depending on parameter $m$ that stands for the number of subdivision levels.

The approach needs not any derivatives of the function to be minimized with updating parameters. Some disadvantage of this approach is in the fact that one-dimensional problem obtained by the above reduction leaks some information on the closeness of iteration points in the initial multi-dimensional space.

Algorithm SFC: reduction of the problem dimension using the space-filling curve method.

0. Set formally the point $x^*$ of local minimum. Let two small numbers $\gamma_1 > 0, \quad \gamma_2 > 0$, and the vector of constraints $\beta \in R^n$ be given. Let $k = 0$, $m = 1$.

1. The local minimization phase: find new point $x^*$ (after $l$ sub-iterations); set $k = k + l$. If $f\left(x^k\right) = 0$ then go to step 2. If $f\left(x^k\right) < \gamma_1$ and $x_i^k > \beta_i$ for some $i \in I^x, \quad I^x = \{1, 2, ..., n\}$, then build the effective sub-vector $x_{eff}^k$, reduce the multi-dimensional problem to the one-dimensional form and go to step 2. Else, go to step of stochastic scanning.

2. Set $m = m + 1$. If $m \leq m_{\max}$ then go to step 3. Else, go to step 4.

3. Define the current value $z_*$ using the development of the Peano curve and calculate the current approximation of $\phi(z_*)$. If $\phi(z_*) \geq \gamma_2$ then go to step 2.

4. Reconstruct $x^*$ and $f(x_*)$ using $z_*$ and $\phi(z_*)$.

5. Define the point of local minimum $x^{LM} = x^*$, stop.

The pseudo code brief description of the hybrid M-PCASFC algorithm that combines the PCA and the deterministic space-filling curve method is as follows.

```
0 Generate an initial solution Old_ Config
Best_ Fitness = Fitness (Old_ Config)
Update Blackboard
For n = 0 to # of particles
  For n = 0 to # of iterations
    Update Blackboard
    Perturbation( )
    If Fitness (New_ Config) > Fitness (Old_ Config)
      If Fitness (New_ Config) > Best_ Fitness
        Best_ Fitness := Fitness (New_ Config)
      End If
      Old_ Config := New_ Config
      Exploration( )
    Else
      Scattering( )
    End If
  End For
End For

2. Local search( )
  Apply procedure of local search
  using the Space-Filling Curve Method
Return

3. Scattering( )
  p_scatt = 1−( Fitness (New_Config)) / (Best Fitness)
  If p_scatt > random(0, 1)
    Old_ Config := random solution
  Else
    Exploration ( )
  End If
Return
```

## 4 Computational results

In this section two numerical examples of hybrid algorithms M-PCALMS and M-PCASFC applications to inverse spectral problems for VVER-1000 nuclear reactor equipment are presented. First example is devoted to the steam pipe finite element model updating. In the second example the updating of the computational model of the coolant two-phase flow dynamics in the primary circuit is carried out.

**Example 1.** The computations were performed in connection with the problem of identification of the coolant phase constitution in the VVER-1000 primary circuit. Appearance of the second phase is possible: in a coolant heating zone (pressure tank of the pressurizer), in an exit volume of the reactor pressure vessel (RPV), in a core barrel of the RPV, in exit volumes of main circulating pumps. In order to formulate the inverse problems two vectors of relative acoustic velocities in a coolant flowing throw the specified zones are introduced. Let now the anomalous coolant state constitution be characterized by second vector of controlling variables: $x_1^* = 79.0\%$; $x_i^* = 100\%$, $i = \overline{2, 4}$. The error function is determined using ten lower spectral components. Table 1 displays the known spectral data for the considered model upating problem. Here we have: $i$ — mode number; $\omega_i$ — natural $i$th frequency of the coolant oscillation under normal conditions (without appearance of the second phase in the coolant); $\omega_i^*$ — natural $i$th frequency of the coolant oscillation with the availability of anomalies in coolant phase constitution.

Table 1: Given spectral data for Example 1

| $i$ | 1 | 2 | 3 | 4 | 5 | 6 | 7 | 8 | 9 | 10 |
|---|---|---|---|---|---|---|---|---|---|---|
| $\omega_i$, Hz | 0.89 | 6.77 | 9.82 | 15.44 | 15.96 | 18.94 | 24.57 | 26.69 | 27.07 | 30.52 |
| $\omega_i^*$, Hz | 0.84 | 6.77 | 9.82 | 15.44 | 15.96 | 18.87 | 21.44 | 26.67 | 27.06 | 30.52 |

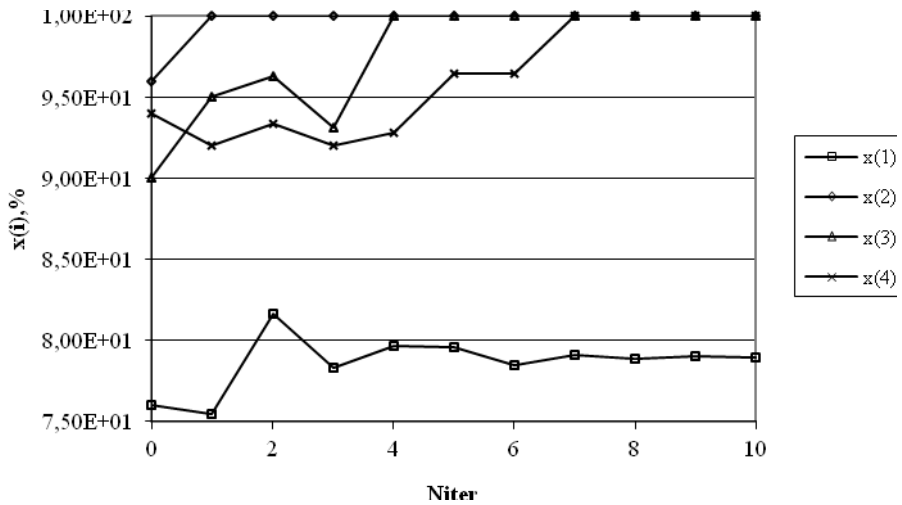


Figure 1: Number of final iterations of the M-PCALMS vs. relative velocities (Example 1)

The approximate solution reached by using the PCAHS algorithm is: $x_1^* \approx 78.9\%$; $x_i^* = 100\%$, $i = \overline{2, 4}$. Fig. 1 and Fig. 2 illustrate the solution history (final iterations of the hybrid algorithm). The inaccuracy of the relative acoustical velocity computing is about 1%. As follows from the results obtained in this example the coolant phase constitution anomalies are conditioned by boiling process in the coolant heating zone.

**Example 2.** Let now the anomalous coolant state constitution be characterized by

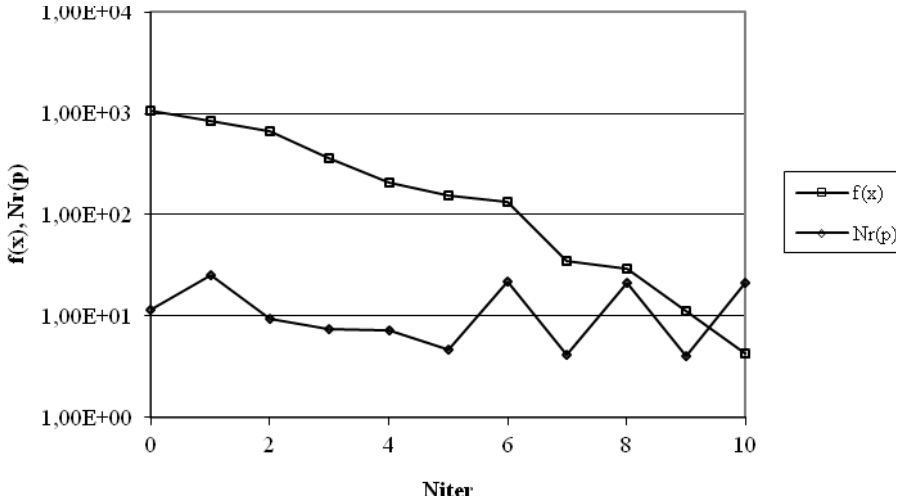


Figure 2: Number of final iterations of the M-PCALMS vs. error function and search gradient norm (Example 1)

second vector of controlling variables: $x_1^* = 77.5\%$; $x_2^* = 88.0\%$; $x_3^* = 82.5\%$; $x_4^* = 100\%$. The error function is determined using ten lower spectral components. Table 2 displays the known spectral data for the considered model diagnostic problem.

Table 2: Given spectral data for Example 2

| $i$ | 1 | 2 | 3 | 4 | 5 | 6 | 7 | 8 | 9 | 10 |
|---|---|---|---|---|---|---|---|---|---|---|
| $\omega_i$, Hz | 0.89 | 6.77 | 9.82 | 15.44 | 15.96 | 18.94 | 24.57 | 26.69 | 27.07 | 30.52 |
| $\omega_i^*$, Hz | 0.82 | 6.77 | 9.36 | 15.33 | 15.96 | 18.86 | 21.22 | 26.67 | 26.93 | 29.41 |

The approximate solution reached by using the PCALMS algorithm is: $x_1^* \approx 77.53\%$; $x_2^* \approx 87.58\%$; $x_3^* \approx 83.23\%$; $x_4^* = 100\%$. Fig. 3 and Fig. 4 illustrate the solution history (final iterations of the hybrid algorithm). The inaccuracy of the relative acoustical velocity computing is about 1%. As follows from the results obtained in this example the coolant phase constitution anomalies are conditioned by boiling process in the coolant heating zone, in the exit volume of the reactor pressure vessel and in the core barrel of the RPV.

## 5 Conclusions

Two novel global optimization algorithms combining a Metropolis-based stochastic algorithm M-PCA and deterministic gradient technique or space-filling curve method for local search are presented. Smoothing approximations are introduced during the local search that makes it possible to expand the M-PCALMS algorithm on the class of non-differentiable problems. The M-PCASFC algorithm being introduced here does not require any gradient information. Both the algorithms were used for solving inverse spectral problems in connection with computational model updating for the two-phase coolant flow in the nuclear reactor primary circuit and for the steam pipe supporting units. Numerical experiments show the principal applicability of the proposed hybrid algorithms for solving the above model updating problems. The future work will be devoted to increasing the computational efficiency of tools for solution the model updating problems with regard to noisy data.

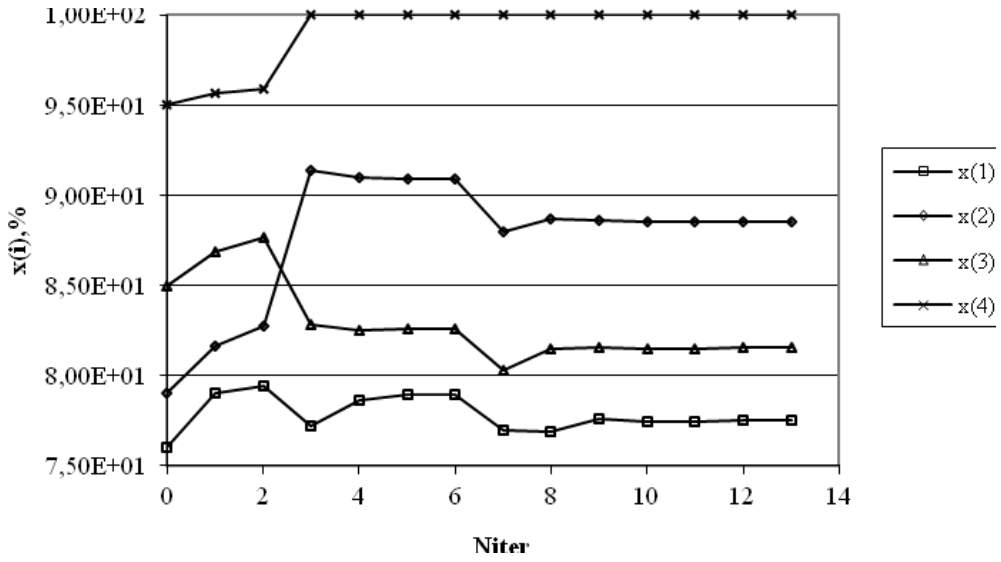


Figure 3: Number of final iterations of the M-PCALMS vs. error function and search gradient norm (Example 2)

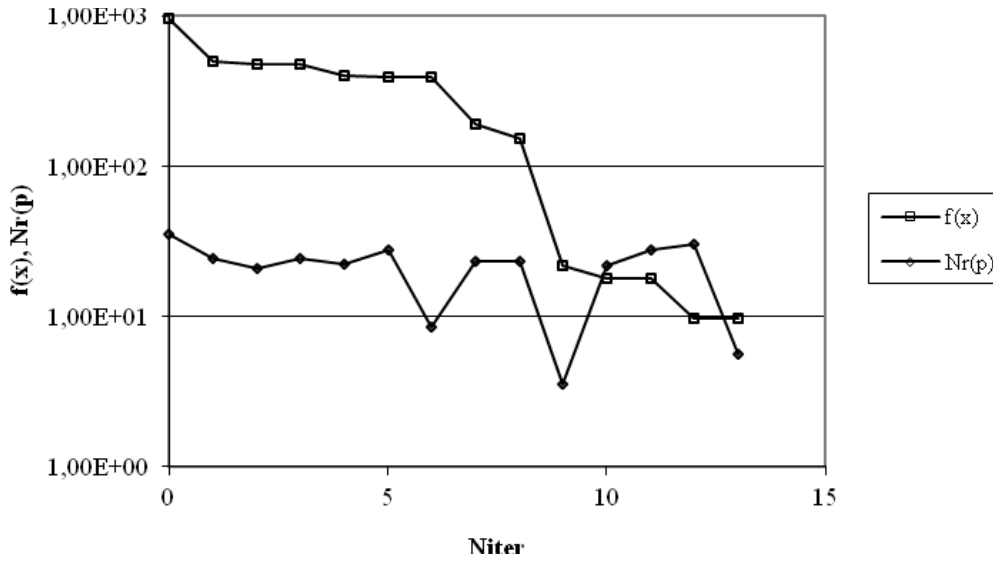


Figure 4: Number of final iterations of the M-PCALMS vs. error function and search gradient norm (Example 2)

## Acknowledgements

*This research is partially supported by the program "Leading Scientific Schools" of Russian Federation (the grant NSh-4748.2012.8).*

## References

[1] K. Wang. Intelligent Condition Monitoring and Diagnosis Systems: A Computational Intelligence Approach. IOS Press, Amsterdam, 2003.

[2] T. Pulecchi, F. Casella, M. Lovera. Object-oriented modeling for spacecraft dynamics: Tools and applications. Simulation Modelling Practice and Theory 18, 63–86, 2010.

[3] J.K. Sinha, A. Rama Rao, R.K. Sinha. Realistic seismic qualification using the updating finite element model for in-core components of reactors. Nuclear Engineering and Design 236, 232–237, 2006.

[4] D.G. Cople, E. S. Brick. A simulation framework for technical systems life cycle cost analysis. Simulation Modelling Practice and Theory 18, 9–34, 2010.

[5] H. Ahmadian, J.E. Mottershead, M.I. Friswell. Regularization methods for finite element model updating. Mechanical Systems and Signal Processing 12, 47–64, 1998.

[6] S. Kindermann, A. Neubauer. On the convergence of the quasioptimality criterion for (iterated) Tikhonov regularization. Inverse Problems and Imaging 2, 291–299, 2008.

[7] A. Poullikkas. Effects of two-phase liquid-gas flow on the performance of nuclear reactor cooling pumps. Progress in Nuclear Energy 42, 3–10, 2003.

[8] J.W. Park. Analytical evaluation of two-phase natural circulation flow characteristics under external reactor vessel cooling. Annals of Nuclear Energy 36, 1668–1675, 2009.

[9] V.G. Kinelev, P.M. Shkapov, V.D. Sulimov. Application of global optimization to VVER-1000 reactor diagnostics. Progress in Nuclear Energy 43, 51–56, 2003.

[10] W.F. Sacco, C.R.E. de Oliveira. A new stochastic optimization algorithm based on particle collisions // Proceedings of the 2005 ANS Annual Meeting. Transactions of the American Nuclear Society 92, 657-659, 2005.

[11] E.F.P. da Luz, J.C. Becceneri, H.F. de Campos Velho. A new multi-particle collision algorithm for optimization in a high performance environment // Journal of Computational Interdisciplinary Sciences 1, 3-10, 2008.

[12] W.F. Sacco, H.A. Filho, N. Henderson, C.R.E. de Oliveira. A Metropolis algorithm with Nelder-Mead Simplex applied to nuclear reactor core design. Annals of Nuclear Energy 35, 861–867, 2008.

[13] K.I.M. McKinnon. Convergence of the Nelder-Mead simplex method to a non-stationary point. SIAM J. Optimization 9, 148–158, 1998.

[14] V.D. Sulimov. A local smoothing approximation in a hybrid algorithm for optimization of hydro-mechanical systems. Vestnik MGTU. Estestvennye Nauki 3 (38), 3–14, 2010 (in Russian).

[15] H. Sagan. Space-Filling Curves. Kluwer Academic Publishers, Dordrecht, 1994.

[16] R.G. Strongin, Y.D. Sergeev. Global optimization: fractal approach and non-redundant parallelism. Journal of Global Optimization 27, 25–50, 2003.

*V.D. Sulimov, Baumanskaya $2^{nd}$ str. 5, Moscow, 107005, Russia.*
*P.M. Shkapov, Baumanskaya $2^{nd}$ str. 5, Moscow, 107005, Russia.*

# Account of capillary effects in the simulation of the atomic force microscope work

Alexander L. Svistkov Nadezhda I. Uzhegova
svistkov@icmm.ru, uzhegova@icmm.ru

**Abstract**

The aim of this study is to show that effect caused by the curvature of the surface under the action of the Laplace forces needs to be taken into account when materials are investigated by the Atomic force microscope (AFM). Indentation the probe of AFM into the fluid is considered. The equation of the boundary of fluid in the axisymmetric task is presented. It is analyzed different cone angle of the probe of the AFM and different scales. The contribution of effect caused by the curvature of the surface under the action of the Laplace forces is examined and it is found that the attenuation of surface curvature near the probe caused by the Laplace forces is occurred on the length 1 mm.

## 1 Introduction

There are many different methods and tools for studying the nanoworld. The important role belongs to the AFM. The AFM is used to obtain information about topology of material structure and about mechanical properties. The interaction forces, for example van der Waals force, electrostatic interaction, adhesion forces, capillary effects, need to be taken into account when we investigate material at nanoscale.

In this paper we examined the effects caused by the curvature of the surface under the action of the Laplace forces.

The Laplace law in total case is given as

$$\Delta p = \alpha \left( \frac{1}{r_1} + \frac{1}{r_2} \right),$$

where $r_1$ and $r_2$ – the principal surface curvatures, $\alpha$ – the surface tension, $\Delta p$ – the pressure difference in neighboring phases, which are separated by a curved surface, or the capillary pressure.

In the simplest case of a spherical surface (bubble or drop of fluid in the weightless) both the principal radius of curvature $r$ are equal and constant along the entire surface. In this case the Laplace law is given as:

$$\Delta p = \frac{2\alpha}{r}.$$

## 2 Equation of fluid boundary

The cylindrical system of coordinate and initial configuration is considered. The unit basis vectors of the coordinate axes in the cylindrical system of coordinate is denoted as $\mathbf{i}_r, \mathbf{i}_\theta, \mathbf{i}_z$

and properties of the unit basis vectors are known as

$$\frac{\partial \mathbf{i}_r}{\partial \theta} = \mathbf{i}_\theta,$$

$$\frac{\partial \mathbf{i}_\theta}{\partial \theta} = -\mathbf{i}_r.$$

The boundary between phases is modeled by a constant thickness thin membrane (Figure 1). The Level set method [2] is used.

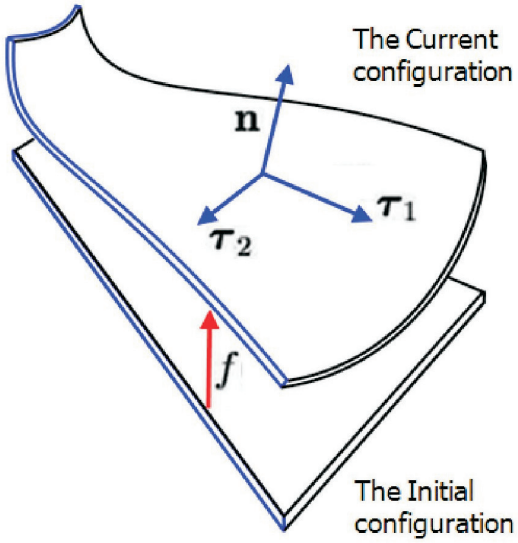


Figure 1: Modeling the thin membrane

Let us denote $\xi$ - the curvature of the membrane.

$$\xi = f(r) + \gamma(r)z,$$

where $\gamma(r)$ – the parameter, which is responsible for the membrane thickness, $f(r)$ – the parameter, which is responsible for the movement of the membrane. The derivatives of this function is denoted as

$$\xi' = \frac{\partial \xi}{\partial r},$$

$$\xi'' = \frac{\partial^2 \xi}{\partial^2 r}.$$

Let us denote $\mathbf{x}$ – the position vector of membrane points

$$\mathbf{x} = r\mathbf{i}_r + \xi \mathbf{i}_z.$$

The gradient of deformation in the initial configuration in the cylindrical coordinates is given by

$$\text{Grad } \mathbf{x} = \mathbf{i}_r \otimes \mathbf{i}_r + \mathbf{i}_\theta \otimes \mathbf{i}_\theta + \gamma \mathbf{i}_z \otimes \mathbf{i}_z + \xi' \mathbf{i}_z \otimes \mathbf{i}_r. \tag{1}$$

Now we can define the tangent vectors

$$\boldsymbol{\tau}_1 = \frac{(\text{Grad } \mathbf{x})\ \mathbf{i}_r}{\left|(\text{Grad } \mathbf{x})\ \mathbf{i}_r\right|} = \frac{1}{\sqrt{1+(\xi')^2}}\mathbf{i}_r + \frac{\xi'}{\sqrt{1+(\xi')^2}}\mathbf{i}_z \tag{2}$$

$$\boldsymbol{\tau}_2 = \mathbf{i}_\theta. \tag{3}$$

The surface unit tensor $\mathbf{I}_s$ is given by

$$\mathbf{I}_s = \boldsymbol{\tau}_1 \otimes \boldsymbol{\tau}_1 + \boldsymbol{\tau}_2 \otimes \boldsymbol{\tau}_2. \tag{4}$$

Using Eq.(2) and (3), we can write Eq.(4) as

$$\mathbf{I}_s = \frac{1}{1+(\xi')^2}\mathbf{i}_r \otimes \mathbf{i}_r + \mathbf{i}_\theta \otimes \mathbf{i}_\theta + \frac{(\xi')^2}{1+(\xi')^2}\mathbf{i_z} \otimes \mathbf{i}_z + \frac{\xi'}{1+(\xi')^2}\left(\mathbf{i}_r \otimes \mathbf{i}_z + \mathbf{i}_z \otimes \mathbf{i}_r\right). \tag{5}$$

Let us move from initial configuration to current one. We can use next formula

$$J\mathrm{div}\mathbf{I}_s = \mathrm{Div}\left(J\mathbf{I}_s(\mathrm{Grad}\mathbf{x})^{-\mathrm{T}}\right). \tag{6}$$

We should find $J$ - the third invariant and after that we can use Eq. (6).

$$J = \det\left(\mathrm{Grad}\mathbf{x}\right) = \gamma \tag{7}$$

We substitute Eq. (1), Eq. (5), Eq. (7) into the right hand side Eq. (6) and we obtain

$$\mathrm{Div}\left(J\mathbf{I}_s\left(\mathrm{Grad}\mathbf{x}\right)^{-\mathrm{T}}\right) = \gamma'\frac{1}{1+(\xi')^2}\mathbf{i}_r + \gamma\frac{\partial}{\partial r}\left(\frac{1}{1+(\xi')^2}\right)\mathbf{i}_r + \gamma'\frac{\xi'}{1+(\xi')^2}\mathbf{i}_z + \\ +\gamma\frac{\partial}{\partial r}\left(\frac{\xi'}{1+(\xi')^2}\right)\mathbf{i}_z + \frac{1}{r}\gamma\frac{1}{1+(\xi')^2}\mathbf{i}_r - \frac{1}{r}\gamma\mathbf{i}_r + \frac{1}{r}\gamma\frac{\xi'}{1+(\xi')^2}\mathbf{i}_z.$$

So divergence of the surface unit tensor is calculated as

$$\begin{aligned}\mathrm{div}\mathbf{I}_s &= \frac{\partial}{\partial r}\left(\frac{1}{1+(\xi')^2}\right)\mathbf{i}_r + \frac{\partial}{\partial r}\left(\frac{\xi'}{1+(\xi')^2}\right)\mathbf{i}_z - \frac{(\xi')^2}{r(1+(\xi')^2)}\mathbf{i}_r + \\ &+ \frac{\xi'}{r(1+(\xi')^2)}\mathbf{i}_z + \frac{\gamma'}{\gamma(1+(\xi')^2)}\mathbf{i}_r + \frac{\xi'\gamma'}{\gamma(1+(\xi')^2)}\mathbf{i}_z.\end{aligned} \tag{8}$$

We can write boundary conditions in total case as

$$\mathbf{T}\ \mathbf{n} = \mathbf{f} + \mathrm{div}(\alpha\mathbf{I}_s), \tag{9}$$

where $\mathbf{T}$ – the Cauchy stress tensor, $\mathbf{n}$ – the exterior unit normal, $\mathbf{f}$ – the external forces acting on the unit surface, $\alpha$ – the surface tension, $\mathbf{I}_s$ – the surface unit tensor. The equilibrium of fluid equation is given by

$$\mathrm{div}(\mathbf{T}) = \rho g, \tag{10}$$

where $\rho$ – the density of fluid , $g$ – the acceleration of free fall. We consider case without the external forces acting on fluid. In this case boundary condition Eq. (9) could be represented by

$$\mathbf{T}\ \mathbf{n} = \mathrm{div}(\alpha\mathbf{I}_s). \tag{11}$$

Now we can find scalar product Eq.(11) with the exterior unit normal

$$\mathbf{T}\ \mathbf{n}\cdot\mathbf{n} = \mathrm{div}(\alpha\mathbf{I}_s)\cdot\mathbf{n}. \tag{12}$$

Look at the left hand side Eq.(12), we can write it as

$$\mathbf{T}\ \mathbf{n}\cdot\mathbf{n} = -p\ \mathbf{I}\ \mathbf{n}\cdot\mathbf{n} = -p, \tag{13}$$

where $\mathbf{I}$ – the unit tensor, $p$ – the pressure. The exterior unit normal is defined as

$$\mathbf{n} = -\frac{\xi'}{\sqrt{1+(\xi')^2}}\mathbf{i}_r + \frac{1}{\sqrt{1+(\xi')^2}}\mathbf{i}_z.$$

Now we can find the right hand side Eq. (12)

$$\mathrm{div}\mathbf{I}_s \cdot \mathbf{n} = -\frac{\xi'}{\sqrt{1+(\xi')^2}}\frac{\partial}{\partial r}\left(\frac{1}{1+(\xi')^2}\right) + \frac{1}{\sqrt{1+(\xi')^2}}\frac{\partial}{\partial r}\left(\frac{\xi'}{1+(\xi')^2}\right) + \frac{\xi'}{r(1+(\xi')^2)} \quad (14)$$

We simplify Eq. (14) and the final form is

$$\mathrm{div}(\alpha\mathbf{I}_s)\cdot\mathbf{n} = \frac{\alpha}{\sqrt{1+(\xi')^2}}\left(\frac{\xi''}{1+(\xi')^2} + \frac{\xi'}{r}\right). \quad (15)$$

Using Eq. (13) and Eq. (15), pressure is found

$$p = -\frac{\alpha}{\sqrt{1+(\xi')^2}}\left(\frac{\xi''}{1+(\xi)^2} + \frac{\xi'}{r}\right). \quad (16)$$

**Verification of formula.** The boundary of the top half of drop is given by

$$\xi|_{z=0} = \sqrt{R^2 - r^2}.$$

The derivatives of this function is denoted as

$$\xi'\big|_{z=0} = -\frac{r}{\sqrt{R^2-r^2}}, \quad (17)$$

$$\xi''\big|_{z=0} = -\frac{R^2}{(R^2-r^2)^{1.5}}. \quad (18)$$

Using Eq. (17) and Eq. (18), we can write Eq. (16) as

$$p = \frac{2\alpha}{R}. \quad (19)$$

Thus, we have the familiar Laplace formula. So Eq. (16) is true.

**Consequence.** The boundary conditions is considered

$$\gamma = \sqrt{1+(\xi')^2}\Big|_{z=0}. \quad (20)$$

$$\frac{\gamma'}{\gamma} = \frac{\xi'\xi''}{1+(\xi')^2}\Big|_{z=0}. \quad (21)$$

We can find scalar product $\mathrm{div}\mathbf{I}_s$ with $\boldsymbol{\tau}_1$, using Eq. (2) and Eq. (8)

$$\mathrm{div}\mathbf{I}_s \cdot \boldsymbol{\tau}_1 = -\frac{\xi'\xi''}{\sqrt{1+(\xi')^2}(1+(\xi')^2)} + \frac{\gamma'}{\gamma\sqrt{1+(\xi')^2}}.$$

Using Eq. (20) and Eq. (21), one can be write

$$\mathrm{div}\mathbf{I}_s \cdot \boldsymbol{\tau}_1 = 0.$$

Similarly we can find scalar product $\mathrm{div}\mathbf{I}_s$ with $\boldsymbol{\tau}_2$

$$\mathrm{div}\mathbf{I}_s \cdot \boldsymbol{\tau}_2 = 0.$$

So, at the boundary between phases does not appear additional shear strength.

## 3 Solution

Introduction of the conical probe into the water at the temperature $20^0$ $C$ is considered as an example. The density of fluid is $\rho = 998$ kg/m$^2$. The acceleration of free fall is $g = 9.8$ m/s$^2$. The pressure acting on fluid is $p = -\rho g \xi$. The surface tension is $\alpha = 72.8 * 10^{-3}$ N/m. The wetting angle is $8^0$, for example.

Equation of the boundary of fluid in the axisymmetric task is given by

$$\xi'' = -(1 + (\xi')^2) \left( \frac{-\rho g \xi}{\alpha} \sqrt{1 + (\xi')^2} + \frac{\xi'}{r} \right). \tag{22}$$

Eq. (22) is solved numerically with respect to $\xi$. Figure 2 shows the change in the geometry of fluid surface by the Laplace forces, where the cone angle of the probe is $20^0$.

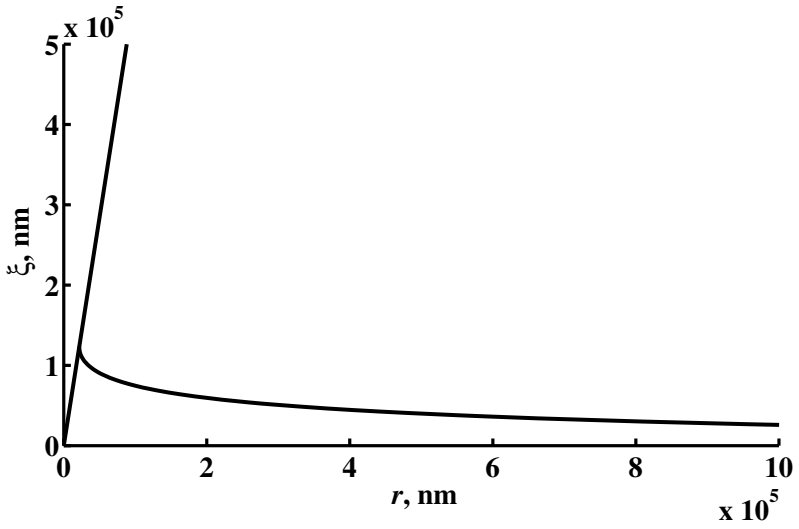


Figure 2: The change in the geometry of fluid surface at the nanolevel

Table 5 compares the depth of probe indentation and the height of fluid lifting.

| Depth of probe indentation (m) | Height of fluid lifting (m) |
|---|---|
| $-1.53 \cdot 10^{-4}$ | $4.15 \cdot 10^{-4}$ |
| $7.76 \cdot 10^{-6}$ | $6.45 \cdot 10^{-5}$ |
| $3.08 \cdot 10^{-6}$ | $8.75 \cdot 10^{-6}$ |
| $5.38 \cdot 10^{-7}$ | $1.11 \cdot 10^{-6}$ |
| $7.68 \cdot 10^{-8}$ | $1.34 \cdot 10^{-7}$ |
| $9.88 \cdot 10^{-9}$ | $1.56 \cdot 10^{-8}$ |
| $1.17 \cdot 10^{-9}$ | $1.74 \cdot 10^{-9}$ |

Table 5: The depth of probe indentation and corresponding the height of fluid lifting

The obtained solution shows that the indentation of a probe into the fluid at 10.7 nm is the cause of rising of fluid to a height of 20.2 $\mu m$. Thus, effect caused by the curvature of the surface under the action of the Laplace forces needs to be taken into account.

Surface profiles were calculated for different scales and cone angle of a probe. It is found that changing the geometry of the fluid surface caused by the Laplace forces is occurred on the length 1 mm. Figure 3 shows the attenuation of surface curvature near the probe on a nanolevel.

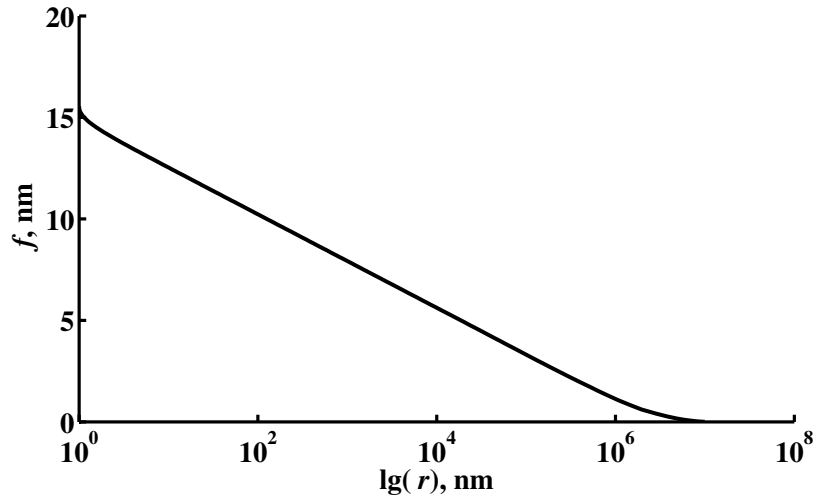


Figure 3: The attenuation of surface curvature near the probe caused by the Laplace forces

## 4 Conclusions

It is built model which is taken into account effect caused by the curvature of the surface under the action of the Laplace forces. Surface profiles were calculated for different scales.The calculations shows that changing the geometry of the fluid surface caused by the Laplace forces is occurred on the length 1 mm.

## Acknowledgements

*This work is executed at a financial support of the Russian fund of basic researches the Grant 11-08-96001-r urals a and the Grant of the state support of leading scientific schools SS-5389.2012.1.*

## References

[1] V.I. Roldugin. Physicochemistry of the surface. Publishing House “Intellect”, 2008.

[2] J.A. Sethian. Level Set Methods and Fast Marching Methods - Evolving Interfaces in Computational Geometry, Fluid Mechanics, Computer Vision, and Materials Science//European Journal of Mechanics (2000), V. 19, P. 531-532.

*Alexander L. Svistkov, Institute of Continuous Media Mechanics, Perm, Russia*
*Nadezhda I. Uzhegova, Institute of Continuous Media Mechanics, Perm, Russia*

# New criteria for rock brittleness estimation at triaxial compression

Boris G. Tarasov
boris.tarasov@uwa.edu.au

**Abstract**

Brittleness is one of the most important mechanical properties of intact rock; however, the concept of brittleness in rock mechanics is yet to be precisely defined. Many brittleness criteria have been proposed to characterise rock behaviour under triaxial compression $\sigma_1 > \sigma_2 = \sigma_3$, but there is no consensus as to which criteria is the most suitable. It was shown recently that increasing $\sigma_3$ can lead to contradictory intact rock behaviour within different ranges of $\sigma_3$. For example, rock behaviour can be changed from Class I to Class II and then to Class I again, based on Wawersik and Fairhurst classification. Brittleness in this case can vary within the range from absolute brittleness to absolute ductility. This paper shows that no one existing criteria can describe properly the variation of brittleness in this situation.

Two new criteria are proposed in the paper. These criteria are based upon the balance between the post-peak elastic energy withdrawn from the material during the rupture process and two other forms of post-peak energy associated with the failure process: the rupture energy and the excess (released) energy. The brittleness indexes based on the ratio between these parameters allow for the representation of the two classes of rock behaviour (Class I and Class II) in the form of continuous, monotonic and unambiguous scale of brittleness unlike other existing criteria.

## 1 Introduction

Brittleness is a very important mechanical property of intact rock because it has a strong influence on the failure process and on the rock mass response to mining or tunnelling activities. However, the concept of brittleness in rock mechanics is yet to be precisely defined. Several brittleness criteria have been proposed to characterise material behaviour under compression [1-19]. Difficulties in reaching a consensus can be explained by the existence of two alternative failure mechanisms, tensile and shear fracturing, taking place under different compressive loading conditions. Also brittleness can be treated in two ways: as an intrinsic material property or as the material behaviour under the effect of an external loading system contributing additional energy to the failure process.

Large seismic events are often produced when rock masses are submitted to triaxial compression generating violent shear failures. The correct determination of brittleness at such loading conditions is important to better understand these dynamic events. Unlike the generally accepted idea that rising confining pressure $\sigma_3$ makes rocks less brittle, the reality is more complex. Recently published papers [1-3] showed that increasing $\sigma_3$ can lead to contradictory rock behaviour within different ranges of $\sigma_3$. In fact, rock behaviour can be changed from Class I to Class II and then to Class I again, based on Wawersik and Fairhurst [20] classification. The range of brittleness variation in this case can vary from

absolute brittleness to absolute ductility. No one existing criteria can describe properly the variation of brittleness in this situation.

The paper proposes two new criteria allowing for the representation of the two classes of rock behaviour (Class I and Class II) in the form of continuous, monotonic and unambiguous scale of brittleness unlike other existing criteria. These criteria rely upon energy balance and are based on sound physics principles [1-3].

## 2 Rupture process at triaxial compression

Shear is the only form of large-scale rock failure at triaxial compression in nature and laboratory experiments. We will discuss features of the failure process on the basis of laboratory experiments obtained at stress conditions $\sigma_1 > \sigma_2 = \sigma_3$. Shear rupture development represents a localized failure process. Figure 1 shows four stages of shear rupture propagation in a specimen when subjected to triaxial compression. The real shear resistance and displacement along the future failure plane are very non-uniform. Three specific zones can be distinguished (see Figure 1(ii)): (1) the process zone (or rupture head) where the failure process is in progress; (2) the core frictional zone located behind the head where the full friction is mobilized, and (3) the intact zone in front of the head where the resistance is determined by the cohesive strength. With fracture propagation the cohesive strength of decreasing zone (3) is substituted by the frictional resistance of increasing zone (2). This process is accompanied by the decrease in bearing capacity of the specimen from the cohesive strength to the frictional (residual) strength.

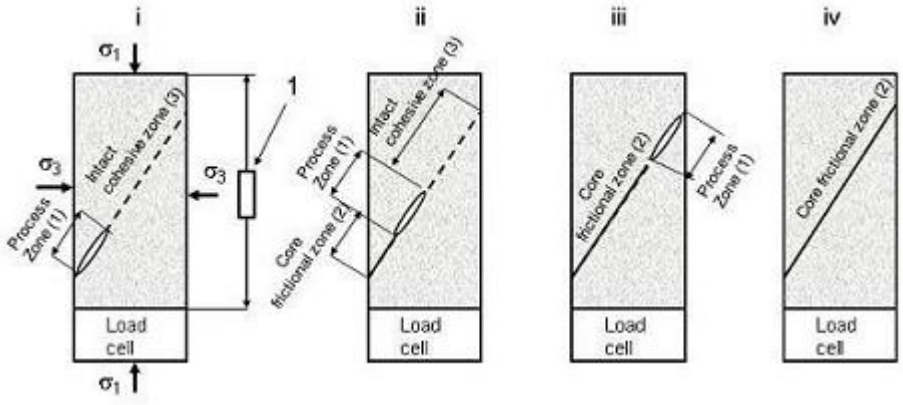


Figure 1: Four stages of shear rupture development in a specimen at triaxial compression and specific zones of shear resistance.

In common experiments the specimen is equipped with a load cell and an axial gauge 1 as shown in Figure 1(i). These gauges are capable to measure only the average load bearing capacity and the strain of the specimen during the loading procedure. On the basis of data provided by these gauges in experiments with different levels of confining stress $\sigma_3$ a set of stress $\sigma$ – strain $\varepsilon_1$ curves can be plotted; where $\sigma = \sigma_1 - \sigma_3$ is the differential stress and $\varepsilon_1$ is the axial strain. Figure 2 shows symbolically two sets of $\sigma - \varepsilon_1$ curves illustrating two types of rock behaviour in the post-peak region with rising confining stress from $\sigma_{3(0)}$ up to $\sigma_{3(6)}$. The development of shear rupture is mainly associated with the post-peak part of $\sigma - \varepsilon_1$ curves. The residual strength (horizontal parts of the curves) represents the frictional resistance of the completed fault (Figure 1(iv)).

It is generally accepted that increase in confining stress $\sigma_3$ increases an angle $\gamma$ located

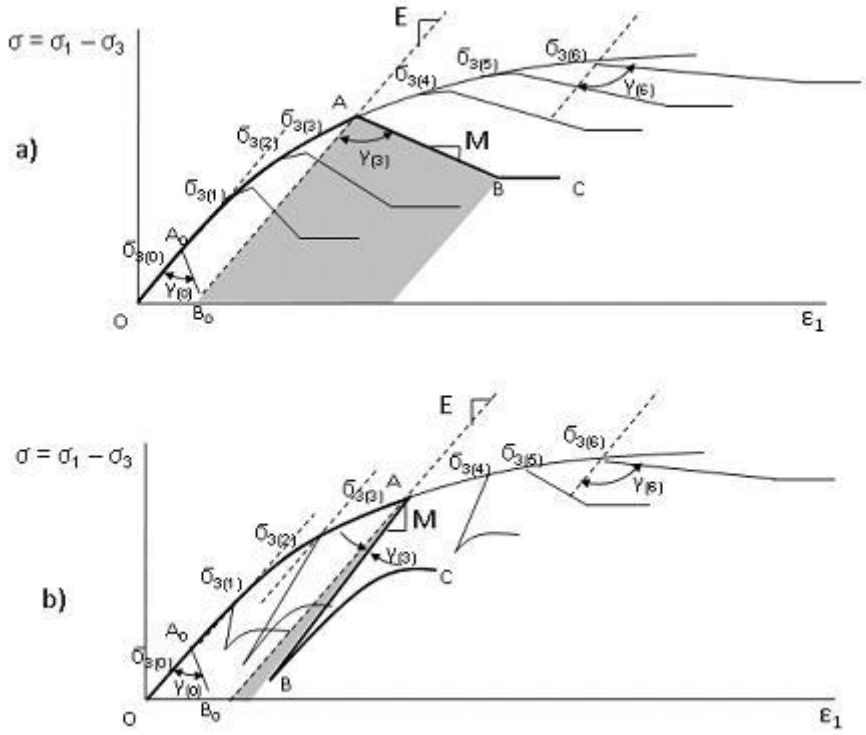


Figure 2: Two sets of stress $\sigma$ – strain $\varepsilon_1$ curves illustrating two types of rock behaviour in the post-peak region with rising confining stress from $\sigma_{3(0)}$ up to $\sigma_{3(6)}$.

between the elastic modulus $E = d\sigma/d\varepsilon_1$ and the post peak modulus $M = d\sigma/d\varepsilon_1$ (see Figure 2a). This indicates the increase in the post-peak rupture energy (shaded area for OABC curve) and the increase in stability of the failure process. However, such behaviour is typical for relatively soft rocks only. For hard rocks increasing $\sigma_3$ can cause very significant decrease of angle $\gamma$ within a certain range of $\sigma_3$ (see Figure 2b). This can be followed by the dramatic decrease in both: the post-peak rupture energy (shaded area for OABC curve in Figure2b) and in the stability of the failure process. The variation of angle $\gamma$ with rising $\sigma_3$ for hard rocks follows a typical pattern of initially decreasing, reaching a minimum and then ultimately increasing since all rocks become ductile at very high $\sigma_3$. The post-peak modulus M in this situation can vary from negative to positive value and then to negative value again indicating the variation of rock behaviour from Class I to Class II and then to Class I again, based on Wawersik and Fairhurst classification [20]. It must be emphasized that bearing capacity of the specimen determined by the shear rupture at the end of the failure process (point B on the curve OABC in Figure 2b) can be very low and the fully frictional resistance corresponding to the applied $\sigma_3$ is mobilized after point C only.

Rock behaviour illustrated by Figure 2a is very well studied and theoretically grounded. To explain features of hard rock behaviour shown in Figure 2b the following rupture model was proposed [1-3]. It is known that a shear rupture can propagate in its own plane due to the creation of short tensile cracks in front of the rupture tips [21-23]. This forms the universal structure of shear ruptures represented by an echelon of blocks (or slabs) separated by tensile cracks – known as 'book-shelf' structure [21-25] or Ortlepp shears [26,27]. A model of shear rupture involving this mechanics is shown in Figure 3a. The initial angle $\beta_0$ of the tensile crack and block inclination to the shear rupture plane is about 30–40$^o$ [28]. Shear displacement along the fault causes rotation of the blocks of the

'book-shelf' structure between the rupture surfaces [1-3,22-25].

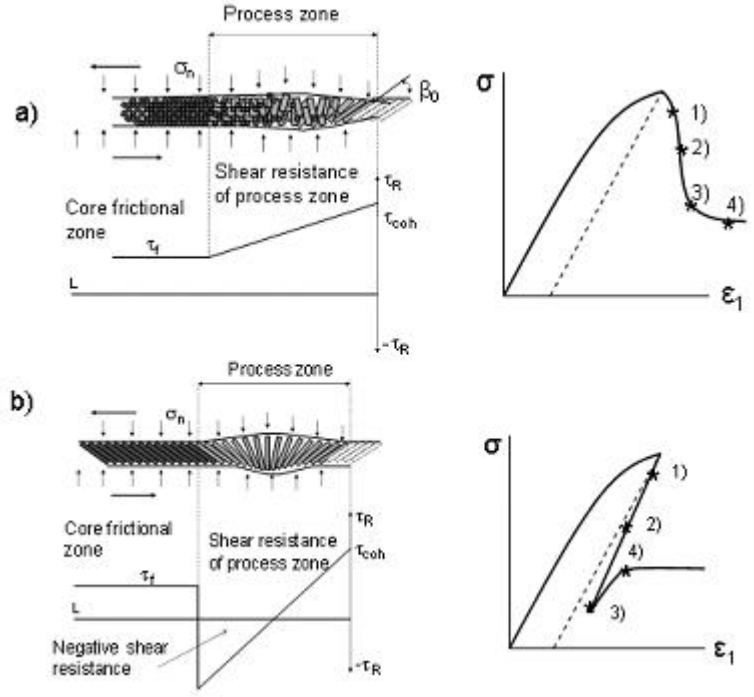


Figure 3: Illustration of rupture mechanisms at a) frictional and b) frictionless conditions of shear fracture development.

Figure 3(a) illustrates the essence of the shear rupture mechanism providing large rupture energy. Blocks located in the front part of the head create significant resistance to shear; however, they collapse with rotation providing gradual transformation of shear resistance within the head zone from cohesive to frictional levels. A graph under the shear rupture in Figure 3(a) shows the shear resistance variation along the fault head. The crushing and comminution of blocks within the head zone can absorb large amounts of energy. This is expected since the development of shear fractures requires displacement to occur along the total fault. This form of rupture development is classified as a crack-like mode. Such a rupture mechanism normally produces Class I material behaviour in the post-peak region. Four points on the stress–strain curve on the right correspond to the four stages of deformation shown in Figure 1.

Figure 3(b) illustrates a model where rotating blocks can withstand the rotation without collapse by behaving as hinges (see details in [1-3]). Due to consecutive formation and rotation of the blocks, these should form a fan structure within the rupture head. A remarkable feature of the rotating blocks (hinges) in the second half of the fan structure (where $\beta > 90°$) is the creation of active forces under the effect of normal stress applied. A graph under the shear rupture in Figure 3(b) shows the shear resistance variation along the fault head. The bottom part of the graph represents active forces (negative resistance) acting in the second half of the head and assisting the fault displacement. In the core zone represented by blocks that have completed their rotation the normal residual friction is restored.

The fan structure represents a self-equilibrating mechanism and can move spontaneously as a wave with very small shear resistance. In the idealised fan-head model, the resistance to rupture propagation is determined only by the tensile strength of the ma-

terial associated with consecutive formation of blocks in front of the propagating rupture. It is important that the fan head can propagate independently of the core zone, which can remain immobile due to high frictional resistance. Hence, this mechanism creates conditions for a pulse-like mode of fracture propagation. In this situation the rupture energy is determined by shear resistance of the fan head only. The fan-head rupture mechanism represents the most energy efficient shear rupture mechanism.

This mechanism is responsible for Class II behaviour with extremely small rupture energy. At stage iii (Figure 1) of the fracture propagation, the bearing capacity of the specimen can be less than at stage iv. It is because the shear resistance of the head (process) zone can be close to zero, decreasing the bearing capacity of the specimen. The longer the relative rupture head (process zone (1) in Figure 1) is, the smaller the shear resistance at stage iii of the rupture propagation. The full frictional resistance is mobilised at stage iv after the head completely propagates through the specimen. The stress-strain curve in Figure 3b (right) illustrates post-peak features providing by the discussed fan-head rupture mechanism.

We can conclude that fracture mechanisms operating within the process zone play the key role in the character of transformation from the cohesive to frictional strength which determines the shape of post-peak curves, the post-peak rupture energy and stability of the failure process. Experiments conducted on hard rocks showed that within a certain range of high confining stress $\sigma_3$ the post-peak modulus M can approach the elastic modulus E making angle $\gamma$ close to zero and the post-peak rupture energy extremely low [1-3]. The rupture control in this situation becomes absolutely impossible despite the use of extremely stiff and servo-controlled testing machine. The failure process in this case inevitably has an explosive like character.

## 3 Brittleness estimation

Traditionally the failure process associated with tensile crack formation is considered as brittle while shear rupture development is treated as ductile behaviour. The failure process in rocks subjected to triaxial compression has very complicated character: macroscopically the failure zone is represented by a shear plane the structure of which on the micro-level is formed due to tensile cracks. Such dual rupture mechanism creates difficulties in determination of rock brittleness at triaxial compression. Several brittleness criteria have been proposed [4-19], however, the concept of brittleness in rock mechanics is yet to be precisely defined. Below we propose new brittleness indexes which characterise degree of intrinsic macroscopic instability of rock specimen at failure. The loss of stability can take place at the post-peak stage of the loading process only. The proposed criteria are based upon the balance between the post-peak elastic energy withdrawn from the specimen body at the rupture development and two other forms of post-peak energy associated with the failure process: the rupture energy and the excess (released) energy.

Figure 4 shows a stress-strain curve illustrating the essence of the proposed criteria. The failure process between points B and B' is accompanied by the following variation in the energy balance. The elastic energy $dW_e$ withdrawn from the material body corresponds to the area ABCC'B'A'. The corresponding rupture energy $dW_r$ is represented by the area ABB'A'. The area C'B'BC represents the excess (released) energy $dW_a$. The mentioned forms of energy can be calculated on the basis of elastic modulus E and post-peak modulus M. It is known that these modules can vary significantly with the fracture development. However, two infinitely near points located on a post-peak curve (for example points B and B') can be characterised by the same value of E, while the corresponding modulus M

can be unambiguously determined on the basis of a tangent line.

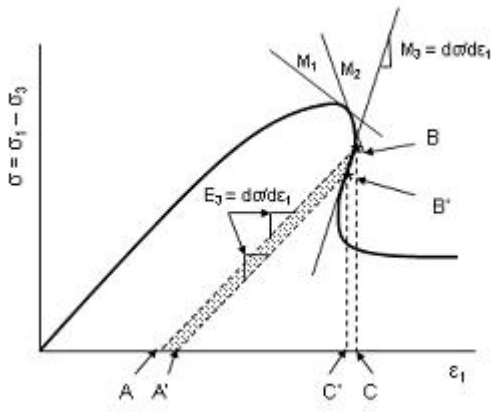


Figure 4: Principle of the current brittleness estimation by brittleness indexes $K_1$ and $K_2$.

Equations (1), (2) and (3) describe the mentioned above forms of energy associated with the rupture development between points B and B' in Figure 4. Equation (3) describing the post-peak rupture energy $dW_r$ takes into account the sign of post-peak modulus M for Class I and Class II behaviour:

$$dW_e = \frac{\sigma_B^2 - \sigma_{B'}^2}{2E} \tag{1}$$

$$dW_a = \frac{\sigma_B^2 - \sigma_{B'}^2}{2M} \tag{2}$$

$$dW_r = dW_e - dW_a = \frac{(\sigma_B^2 - \sigma_{B'}^2)(M - E)}{2EM} \tag{3}$$

The brittleness index $K_1$ below is determined by the ratio between the post-peak rupture energy and the withdrawn elastic energy:

$$K_1 = \frac{dW_r}{dW_e} = \frac{M - E}{M} \tag{4}$$

The brittleness index $K_2$ represents the ratio between the excess (released) and the withdrawn elastic energy:

$$K_2 = \frac{dW_a}{dW_e} = \frac{E}{M} \tag{5}$$

Brittleness indexes $K_1$ and $K_2$ characterize unambiguously the rock brittleness at different loading conditions. Figure 5 shows scales of rock brittleness indexes $K_1$ and $K_2$ with brittleness increasing from left to right [1-3]. The complete curves (differential stress $\sigma$ versus axial strain $\varepsilon_1$) illustrate how the different curve shapes describe a variation in brittleness. It is assumed, for simplicity, that the pre-peak parts of the curves are the same. Areas defined by the large dotted triangles correspond to elastic energy $W_e$ stored within the rock material at the peak stress, while the smaller white triangles on the right side of the curves represent the unconsumed portion of the stored elastic energy, within the material, after failure. The post-peak parts of the curves, which are characterized by the post-peak modulus M, are different for each curve. The grey areas represent the post-peak

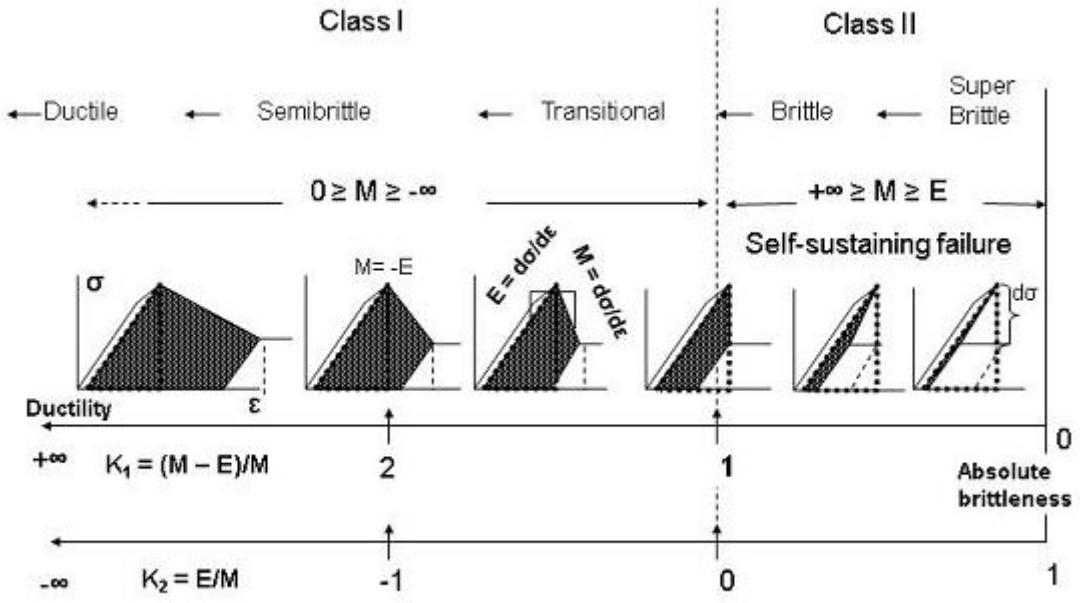


Figure 5: Scale of brittleness indexes $K_1$ and $K_2$ with characteristic shapes of complete stress–strain curves [1-3].

rupture energy $dW_r$ associated with strength degradation at failure from the peak stress to the residual strength (horizontal part of the post-peak curves).

Figure 5 shows variation in brittleness from absolute brittleness to ductility if read from right to left. The absolute brittleness has the following characteristics and parameters:

1. The post-peak modulus is the same as the elastic modulus M = E.
2. There is no portion of the stored energy transformed into post-peak rupture energy $dW_r = 0$.
3. The withdrawn elastic energy is entirely transformed into excess energy $dW_e = dW_a$.
4. $K_1 = 0$.
5. $K_2 = 1$.

Within the range of brittleness indexes $1 > K_1 > 0$ and $0 < K_2 < 1$ the elastic energy $dW_e$ withdrawn from the specimen material during stress degradation on the value $d\sigma$ exceeds the corresponding rupture energy $dW_r$, leading to self-sustaining failure (brittle Class II behaviour). The self-sustaining failure normally has a spontaneous character even for a hypothetically perfectly stiff testing machine. The greater the difference between $dW_e$ and $dW_r$ the closer the material behaviour is to absolute brittleness and the more violent is the self-sustaining failure. It should be noted that the use of very stiff and servo-controlled loading machines allow in many cases controllable failure for rocks characterized by the positive post-peak modulus M due to the extraction of the excess elastic energy from the material body. For the range of brittleness indexes $+\infty > K_1 > 1$ and $-\infty < K_2 < 0$

the rupture development is not self-sustaining (Class I behaviour). Variation in failure regimes corresponding to an increase in the rock brittleness is indicated in the upper part of Figure 5. These regimes are: ductile, semi-brittle, transitional, brittle and super-brittle. The characteristic features of the super-brittle regime are discussed in [1-3].

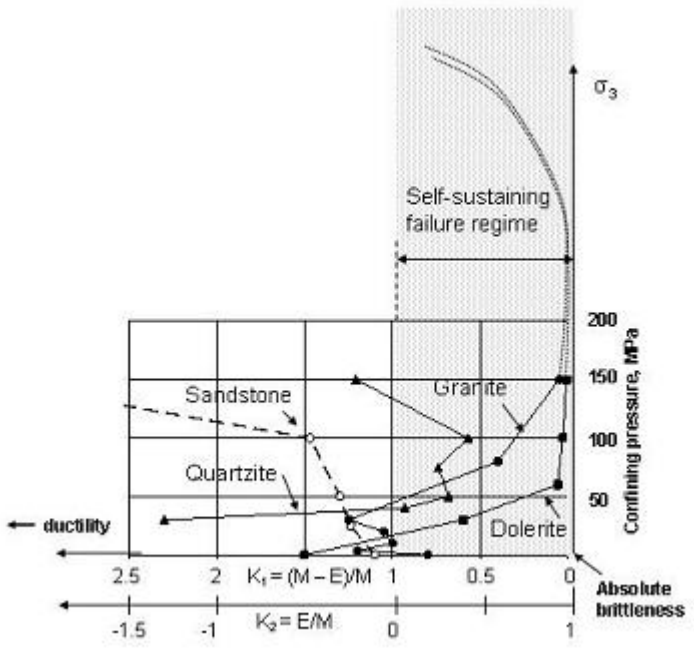


Figure 6: Variation of brittleness indexes $K_1$ and $K_2$ versus confining pressure $\sigma_3$ for rocks of different hardness (modified from [1-3]).

Figure 6 shows the variation of brittleness index $K_1$ and $K_2$ for four rocks exhibiting different responses to rising confining pressure $\sigma_3$ [1-3]. The self-sustaining failure regime corresponds to $1 > K_1 > 0$ and $0 < K_2 < 1$. The sandstone curve indicates that an increase in confinement $\sigma_3$ makes the rock less brittle. This behaviour is typical for softer rocks. For the quartzite, increase in confinement $\sigma_3$ within the range of 0–100 MPa makes the material more brittle. At greater confinement the brittleness decreases. For the granite, increase in $\sigma_3$ within the range of 0–30 MPa makes it less brittle. When $\sigma_3 > 30\ MPa$, the brittleness increases dramatically. The dolerite curve also shows very severe rock embrittlement. At $\sigma_3 = 75\ MPa$, according to the brittleness index $K_1$, the dolerite became 250 times more brittle when compared to uniaxial compression ($K_1(0) = 1.5; K_1(75) = 0.006$). At $\sigma_3 = 100$ and 150 $MPa$ the brittleness increased significantly, further approaching absolute brittleness. The dotted lines indicate the expected brittleness variation for granite and dolerite at greater values of $\sigma_3$: the brittleness continues to increase until it reaches a maximum at some level of $\sigma_3$ and then decreases, as all rocks become ductile at very high confining stresses. It is estimated in [1-3] that the maximum brittleness for granite is reached at $\sigma_3 = 300\ MPa$. For rocks that as hard as quartzite, the mode of brittleness variation is similar, but the maximum brittleness is lower and the range of confining pressure where embrittlement takes place is smaller.

Brittleness indexes similar to $K_1$ and $K_2$ were proposed earlier in [4-8]:

$$k_3 = \frac{M}{E + M}, [4, 5] \tag{6}$$

$$k_4 = \frac{M}{E}, [5-8] \tag{7}$$

However, the brittleness indexes $k_3$ and $k_4$ include some uncertainties which can lead to conflicting results for estimating the brittleness at different loading conditions. Also these indexes do not allow the creation of continuous and unambiguous scale of brittleness similar to the one presented in Figures 5 and 6. Two scales of brittleness for $k_3$ and $k_4$ are shown in Figure 7.

Both scales of brittleness are stretched between $-\infty$ and $+\infty$, and the extreme points of each scale ($-\infty$ and $+\infty$) are characterized by the same shape of stress–strain curves. Another zone of discontinuity is located in a central part of the scales between conditions of the absolute brittleness and absolute ductility. Hence, the brittleness indexes $k_3$ and $k_4$ are not ideal for brittleness characterisation at different levels of confining pressure.

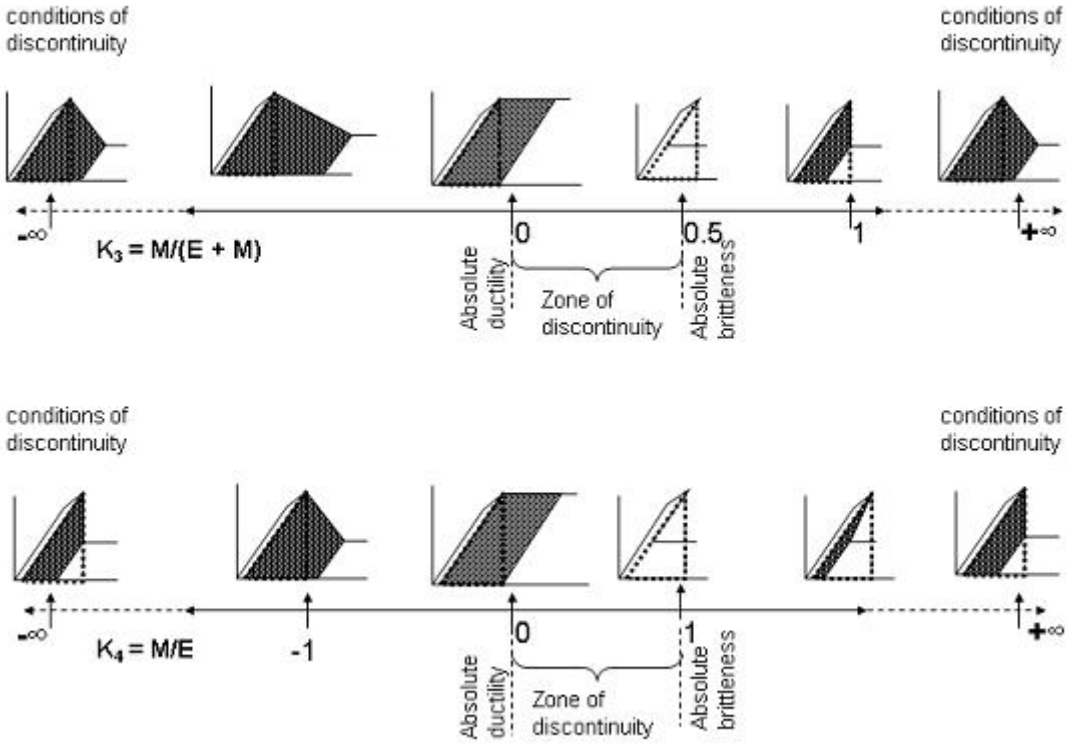


Figure 7: Scales of brittleness indexes $k_3$ and $k_4$ with characteristic shapes of complete stress–strain curves.

All other existing brittleness indexes representing ratios of different combination between pre-peak and post-peak strain [9-11]; involving parameters associated with the pre-peak irreversible deformation only [12-15]; based on ratios between compressive and tensile strengths [16-18]; determining brittleness from Mohr's envelope [13] and others give also conflicting results when samples are tested under triaxial compression at different levels of $\sigma_3$.

## 4 Conclusions

The applicability of various criteria for assessing rock brittleness under triaxial compression has been analyzed. It is shown that only two criteria proposed in this paper can describe properly the intrinsic material brittleness within the whole range of brittleness variation from the absolute brittleness to ductility. These criteria are based upon the balance between post-peak elastic energy withdrawn from the material body at the failure development and two other forms of post-peak energy associated with the failure process: the rupture energy and the excess (released) energy. The brittleness indexes based on the ratio between these parameters allow for the representation of the two classes of rock behaviour (Class I and Class II) in the form of continuous, monotonic and unambiguous scale of brittleness. Other existing criteria do not provide unambiguous characterisation of rock brittleness at different loading conditions under triaxial compression.

## Acknowledgements

*This work was supported over a number of years by the Centre for Offshore Foundation Systems at the University of Western Australia, which was established under the Australian Research Council's Special Research Centre scheme and is now supported by the State Government of Western Australia through the Centre of Excellence in Science and Innovation program. This support is gratefully acknowledged.*

## References

[1] Tarasov BG.Superbrittleness of rocks at high confining pressure. In: Proceedings of the 5th International seminar on deep and high stress mining; 2010. p. 119-33.

[2] Tarasov BG.Universal scale of brittleness for rocks failed at compression. In: Proceedings of the 13th International conference of the international association for computer methods and advances in Geomechanics; 2011. p. 669-73.

[3] Tarasov BG, Randolph MF.Superbrittleness of rocks and earthquake activity. Int JRock Mech Min Sci 2011; 48:88-98.

[4] Batougina IM, Petoukhov IM, Vinokur BS, Smirnov VA, Rabota EN.Methodological instructions for rockburst prophylaxis accounting the deposit geodynamics. Leningrad, VNIMI 1983.

[5] Stavrogin AN, Protossenia AG.Rock strength and excavation stability in great depth. Moscow, Nedra 1985.

[6] Petoukhov IM, Linkov AM.Mechanics of rockburst and outburst. Moscow, Nedra 1983.

[7] Manjikov BT, Mansourov VA, PougachevaTN, Tileguenov KT.Laboratory estimation of rockbursting danger. SSDRRMODMA, Frounze, Ilim 1983; p. 106-16.

[8] Bergman SGA, Still H.Rockburst problems in a 2.6 million m3 underground crude oil storage in granite. In: Proceedings of the 5th Congress ISRM; 1983, D302-D309.

[9] Andreev GE.Brittle failure of rock materials. Rotterdam, Balkema; 1995.

[10] Recommendation for determining the total Mohr strength envelope and deformability for rock. Leningrad, VNIMI 1988.

[11] He C, Okubo S, Nishimatsu Y.A study on the class II behaviour of rock. Rock Mechanics and Rock Engineering 1990; 23: p. 261-73.

[12] Coates DF.Experimental criteria for classification of rock substances. Int J Rock Mech Min Sci 1966; 3: p.181-89.

[13] Hucka V, Das B.Brittleness determination of rocks by different methods. Int J Rock Mech Min Sci 1974; 11:p. 389-92.

[14] Baron LI, Loguntsov BM, Posin IZ.Determination of rock properties. Moscow, NTILGD 1962.

[15] Walsh JB, Brace WF. A fracture criterion for brittle anisotropic rock. J Gephys Res 1964; 69: p. 3449-56.

[16] Vardoulakis I.Rock bursting as a surface instability phenomenon. Int J Rock Mech Min Sci 1984; 21: p. 137-44.

[17] Hajiabdolmajid V, Kaiser P, Martin CD.Mobilised strength components in brittle failure of rock. Geotechnique 2003; 53:3, p.327-36.

[18] Wawersik WR, Fairhurst C.A study of brittle rock fracture in laboratory compression experiments. Int J Rock Mech Min Sci 1970; 7: p.561-75.

[19] Reches Z. Mechanisms of slip nucleation during earthquakes. EPSL 1999; 170: p. 475-86.

[20] Cox SJD, Scholz CH. On the formation and growth of faults: an experimental study. J Struct Geol 1988; 10: p. 413-30.

[21] Reches Z, Lockner DA. Nucleation and growth of faults in brittle rocks. J Geophys Res 1994; Vol. 99, No. B9, p 18159-73.

[22] Peng S, Johnson AM. Crack growth and faulting in cylindrical specimens of Chelmsford granite. Int J Rock Mech Min Sci 1972; 9: p.37-86.

[23] King GCP, Sammis CG. The mechanisms of finite brittle strain. PAGEOPH 1992; 138, 4: p.611-40.

[24] Van Aswegen G. Ortlepp shears – dynamic brittle shears of South African Gold Mines. In: Proceedings of the 1st Southern Hemisphere International Rock Mechanics Symposium; 2008, p.111-19.

[25] Ortlepp W.D. Rock fracture and rockbursts. SAIMM, Johannesburg, 1997.

[26] Horii H, Nemat-Nasser S. Compression-induced microcrack growth in brittle solids: Axial splitting and shear failure. J Geophys Res 1985; 90: p.3105-25.

*Boris G. Tarasov The University of Western Australia, Perth, Australia*

# Distribution of the equilibrium positions of a shaft and defining the angular speed of the ring in a floating ring bearing

Nguyen Van Thang D. G. Arseniev A. K. Belyaev
thangspbstu@mail.ru

**Abstract**

Today, rotors of high-speed turbomachines are commonly supported by hydrodynamic journal bearings. Like other types of fluid bearings, rotors supported by floating ring bearings may become unstable with increasing speed of rotation due to self-excited vibrations. In order to study the stability of rotor, we have to define the angular speed of the ring in the floating ring bearing since the speed of the ring appears in the formulas of the nonlinear bearing forces, which are modeled by applying the short bearing theory for both fluid firms with the considering of the allowance of the lubrication hydrodynamics and the centrifugal force. Additionally, the analytical results are obtained from the condition of the equality of the torques acting on the ring under the allowance of the both fluid firms.

## 1 Introduction

The theory of short bearing researches the rotation of the shaft in the bearing, which is fixed in space. The gap between the rigid bodies is covered by incompressible fluid (commonly known as Newton fluid). In the scope of this article, a more difficult model of the floating bearing that is proposed in the research includes 3 parts (as in the figure 1): the first part is the floating shaft rotating with angular velocity $\omega_1$, the second part is the floating ring rotating with angular velocity $\omega_2$ and the third part is the fixed cylinder (bearing housing). The gap between the rigid bodies is covered by incompressible fluid, where 4–1 and 4–2 are denoted the inner and outer fluid firm.

Dynamic of rotor in the floating bearing have been researched in the classical short -– bearing theory, but all of them use the classical equation to describe the flow in the gap, i.e. Reynolds equations, without the allowance of centrifugal force. As the result, the rotation of the shaft is studied only under the allowance of the hydrodynamic forces [2] or the allowance of the hydrodynamic forces and the friction of fluid [5].

The main point of this article is to define the angular speed of the ring in the floating ring bearing with allowance of lubrication hydrodynamics and centrifugal force, which its influence must be obtained in case of high speed shaft. The dependence of pressure on the position of shaft in the gap is given by the equation describing the flow of the fluid (Reynolds equations). By the short- bearing theory, the expression of the forces and the torques is given by the following tract: the force acting on the shaft is defined by integrating the function of pressure on the surface of shaft and the torques acting on the shaft and the ring are defined by integrating the function of the shearing stress $\tau_{r\varphi}$ in the cylindrical system of coordinates. In this case (as in fig. 1), when defining the torque acting on the

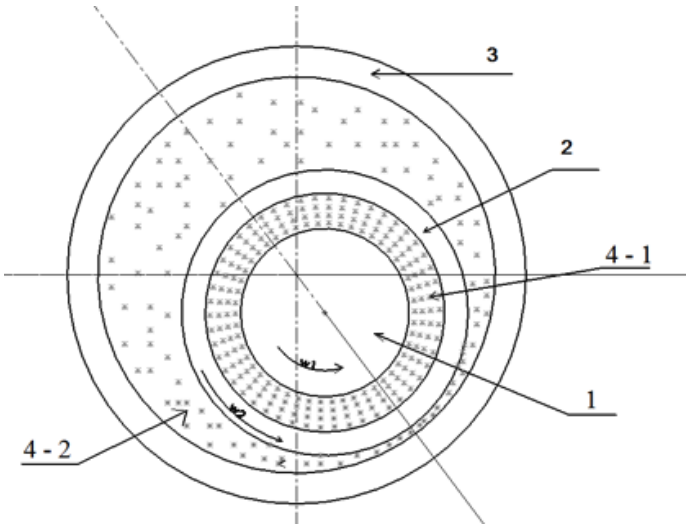


Figure 1: Mechanical model of rotor supported by floating ring bearing: 1 – floating shaft; 2 – floating ring; 3 – fixed bearing housing; 4 – incompressible fluid (4–1 – inner fluid firm, 4–2 outer fluid firm); $\omega_1$, $\omega_2$ are angular velocities of elements 1 and 2.

ring, we have to integrate the function of the shearing stress $\tau_{r\varphi}$ on the both sides of the ring in the floating ring bearing. The angular velocity of the ring $\omega_2$ which is considered as a constant is defined by the condition of the equalization of the torques from both sides of the ring.

## 2 Definition of the border of a lubricant layer

Without the influence of an external field of fluid 4-2, we shall consider only system "the ring – shaft". The system coordinates is fixed in the centre of the ring. Then in this system, incompressible oil 4-1 is in a gap between the ring $(O_2, R_2)$ that its axis of rotation is fixed and a rotating floating shaft$(O_1, R_1)$, see fig. 2. The ring rotates with angular speed $\omega_2$, and the shaft rotates with angular speed $\omega_1$.

It is noted: $h_{01} = R_2 - R_1$ is a nominal gap, $e_1 = e_{P1}(t)$ is eccentricity of the centre of a floating shaft and $\gamma_1 = \gamma_1(t)$ is an angle describing the position of a line of centre of the floating shaft and the centre of the rotating ring. The motion of a shaft on a lubricant layer is non-stationary, i.e. position and speed of its centre depend on time so the external loading and the reaction of the lubricant layer also depend on time.

In work [7] the expression for width of the gap (thickness of a lubricant layer) is received:

$$h_1(\theta_1, t) = h_{01} - e_1(t).\cos\theta_1. \tag{1}$$

And force on unit of the length, acting on the shaft:

$$q_{01} = \frac{1}{L}\int_{-L/2}^{L/2} \left(p_{01} - p_{01}^*\right) dz \; = \frac{\mu L^2(\omega_1 + \omega_2)}{2h_{01}^2}\,\overline{q}_{01}, \tag{2}$$

where

$$\overline{q}_{01} = \frac{\left(\frac{2\dot{\gamma_1}}{\omega_1+\omega_2} - 1\right)\varepsilon_1 \sin\theta_1 + \frac{2\dot{\varepsilon_1}}{\omega_1+\omega_2}\cos\theta_1}{\left(1 - \varepsilon_1\cos\theta_1\right)^3}\,,\; \varepsilon_1 = \frac{e_1}{h_{01}} \tag{3}$$

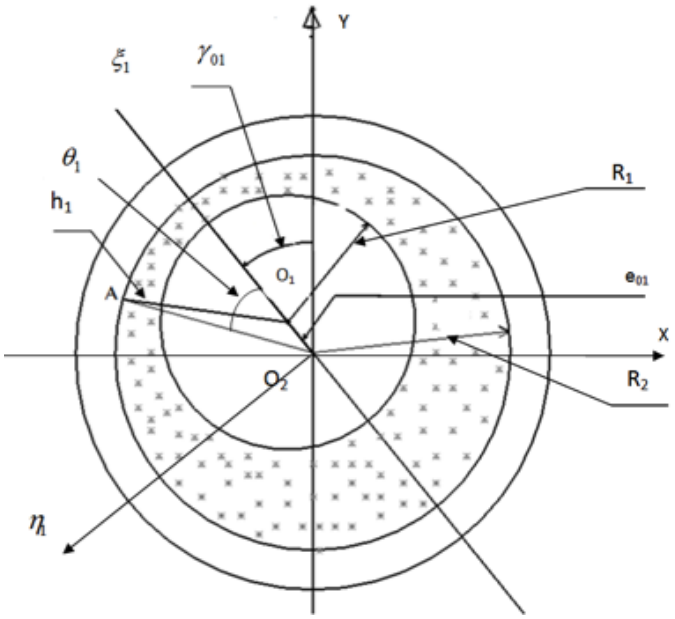


Figure 2: The denoting schema for system “the ring - shaft”.

and $p_{01} = p_{01}(r, \varphi, z, t)$ is the function of the pressure in the internal firm 4-1, $p^*_{01} = p^*_{01}(r, \varphi, t)$ is the function of pressure on the ends of the bearing, $\mu$, $L$ are the accordingly dynamic viscosity of the fluid and the length of the bearing.

In a local system of coordinates$(O_2\xi_1, O_2\eta_1)$, where the direction$O_2\xi_1$ corresponds$\theta_1 = 0$ $(\varphi = \gamma_{P1})$, projections of the force$F_1^P$acting on a shaft from a lubricant layer are written as the following form:

$$F^P_{1\xi} = L \int\limits_{\overline{\theta_1}}^{\overline{\theta_2}} (R_2 - h_1) q_{01} \cos\theta_1 d\theta_1, \qquad F^P_{1\eta} = L \int\limits_{\overline{\theta_1}}^{\overline{\theta_2}} (R_2 - h_1) q_{01} \sin\theta_1 d\theta_1. \tag{4}$$

The question on the borders of a lubricant layer now is unsolved, despite of a significant amount of works on this question. In the theory of the dynamic loaded bearings usually use one of the two following hypotheses:

1. The value of angle that is used to define the beginning and the end of the lubricant layer is determined at the positions where the pressure is equal to zero, i.e. in the positions where the thickness of a gap is narrowest or widest; often being denoted $\overline{\theta_1} = 0$, $\overline{\theta_2} = \pi$, i.e. only half of the gap [5], [6] are accepted.

2. The value of angle $\overline{\theta_1} = 0$, $\overline{\theta_2} = 2\pi$, i.e. a lubricant layer surrounds all the shaft. According to this hypothesis, there is a negative pressure that equal to the positive pressure on the absolute value.

In the present work the second hypothesis is used, i.e. the lubricant layer is full of the gap.

## 3 Distribution of equilibrium positions of the shaft and the ring in the lubricant layer in the floating ring bearing

As a result of integrating in the formulas (4), we receive the projections of the force $F_1^P$ acting on a shaft from a lubricant layer:

$$F_{1\xi}^P = \frac{2\mu L^3 \dot{\varepsilon}_1}{h_{01}^2}\left[\int_0^\pi \frac{R_1.\cos^2\theta_1}{(1-\varepsilon_1\cos\theta_1)^3}d\theta_1 + \int_0^\pi \frac{e_1.\cos^3\theta_1}{(1-\varepsilon_1\cos\theta_1)^3}d\theta_1\right],$$

$$F_{1\eta}^P = \frac{\mu L^3(\omega_1+\omega_2)\varepsilon_1}{h_{01}^2}\left(\frac{2\dot{\gamma}_1}{\omega_1+\omega_2}-1\right)\left[\int_0^\pi \frac{R_1.\sin^2\theta_1}{(1-\varepsilon_1\cos\theta_1)^3}d\theta_1 + \int_0^\pi \frac{e_1.\cos\theta_1.\sin^2\theta_1}{(1-\varepsilon_1\cos\theta_1)^3}d\theta_1\right]. \tag{5}$$

Let the shaft $(O_1, R_1)$ loaded with a constant external force $\overrightarrow{Q^P}$. In case $(\varepsilon_1^*, \gamma_1^*)$ denotes the coordinates of equilibrium position of the shaft in the bearing then $\dot{\varepsilon}_1^* = 0$, $\dot{\gamma}_1^* = 0$. It is assumed that the external force $\overrightarrow{Q^P}$ is directed vertically downwards, the condition of the equality forces shows that $\left|\overrightarrow{Q^P}\right|$ is proportional to angular speed of the shaft $\omega_1$. External loading $\overrightarrow{Q^P}$, for example, can be the gravity of the shaft. The set of equilibrium positions of the centre of the shaft in the lubricant layer is a horizontal line segment $O_2M$ (on fig. 3 it is marked bold), in which $\varepsilon_1^* \in [0,1]$ depends on the external loading $\overrightarrow{Q^P}$ on the shaft. If we use the first hypothesis, the curve of equilibrium positions of the centre of the shaft $O_1$ is a half of a circle, on fig. 3 this curve is marked as a dotted line. Here we notice that $O_2M = O_2M' = h_{01} = R_2 - R_1$.

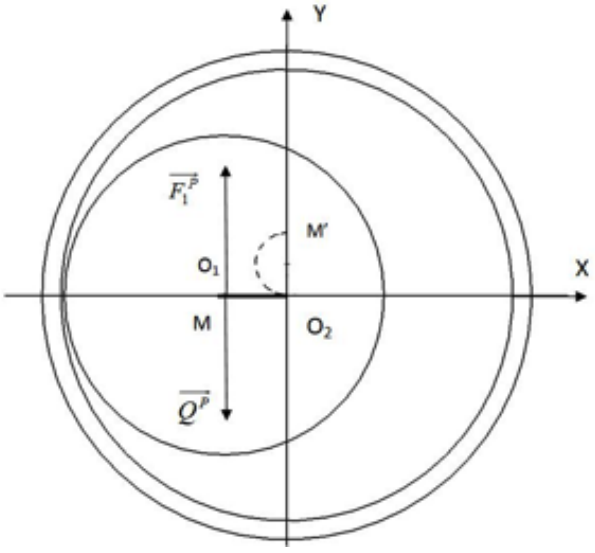


Figure 3: A curve of equilibrium positions of the centre of the shaft.

Up to now we only considered system "the ring - shaft" and neglected the influence of an external field of fluid 4-2. Now we shall consider the bearing which consists of three rigid elements, as shown in figure 1. Similarly we receive the projections of the reaction $F_2^B$ acting on the ring $(O_2, R_2)$ from the external field of fluid 4-2 in local coordinate system $(O\xi_2, O\eta_2)$, where the direction $O\xi_2$ corresponds $\theta_2 = 0$ $(\varphi = \gamma_{B2}(t_0))$, see the figure 4:

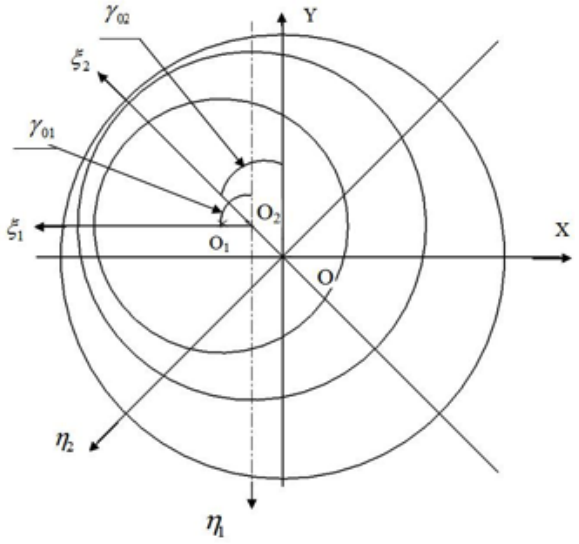


Figure 4: Schematic of designations for the floating ring bearing.

$$
\begin{aligned}
F_{2\xi}^{B} &= \frac{2\mu L^{3}\overset{\bullet}{\varepsilon}_{2}}{h_{02}^{2}}\left[\int_{0}^{\pi}\frac{R_{2}.\cos^{2}\theta_{2}}{\left(1-\varepsilon_{2}\cos\theta_{2}\right)^{3}}d\theta_{2}+\int_{0}^{\pi}\frac{e_{2}.\cos^{3}\theta_{2}}{\left(1-\varepsilon_{2}\cos\theta_{2}\right)^{3}}d\theta_{2}\right],\\
F_{2\eta}^{B} &= \frac{\mu L^{3}\omega_{2}\varepsilon_{2}}{h_{02}^{2}}\left(\frac{2\overset{\bullet}{\gamma}_{2}}{\omega_{2}}-1\right)\left[\int_{0}^{\pi}\frac{R_{2}.\sin^{2}\theta_{2}}{\left(1-\varepsilon_{2}\cos\theta_{2}\right)^{3}}d\theta_{2}+\int_{0}^{\pi}\frac{e_{2}.\cos\theta_{2}.\sin^{2}\theta_{2}}{\left(1-\varepsilon_{2}\cos\theta_{2}\right)^{3}}d\theta_{2}\right]
\end{aligned}
\tag{6}
$$

Here it is denoted:$h_{02} = R - R_2$ - a nominal gap, $e_2 = e_2(t)$ - eccentricity of the centre of a floating ring and $\gamma_2 = \gamma_2(t)$ - a angle describing position of a line of centre of bearing – housing and the centre of rotating floating ring. Similarly we receive the projections of the reaction$F_1^B$ acting on the floating ring$(O_2, R_2)$ from the internal field of fluid 4-1 in local coordinate system$(O\xi_2, O\eta_2)$:

$$
\begin{aligned}
F_{1\xi}^{B} &= -\frac{\mu L^{3}(\omega_{1}+\omega_{2})R_{2}}{2h_{01}^{2}}\int_{0}^{2\pi}\frac{\sin\theta_{1}.\cos\left(\theta_{1}+\gamma_{1}^{*}-\gamma_{2}^{*}\right)}{\left(1-\varepsilon_{1}^{*}\cos\theta_{1}\right)^{3}}d\theta_{1},\\
F_{1\eta}^{B} &= -\frac{\mu L^{3}(\omega_{1}+\omega_{2})R_{2}}{2h_{01}^{2}}\int_{0}^{2\pi}\frac{\sin\theta_{1}.\sin\left(\theta_{1}+\gamma_{1}^{*}-\gamma_{2}^{*}\right)}{\left(1-\varepsilon_{1}^{*}\cos\theta_{1}\right)^{3}}d\theta_{1}.
\end{aligned}
\tag{7}
$$

Where $(\varepsilon_1^*, \gamma_1^*)$ and $(\varepsilon_2^*, \gamma_2^*)$accordingly denote the coordinates of equilibrium position of the rotating shaft and the floating ring. When the centre of the rotating shaft and the centre of the floating ring are in the equilibrium position then$\gamma_1^* = \frac{\pi}{2}$, $\varepsilon_1^* \in [0, 1]$. Each equilibrium position of the shaft $(\varepsilon_1^*, \gamma_1^*)$ in the gap corresponds to a curve of equilibrium positions of the centre of the floating ring, which is defined by the equation:

$$
tg\gamma_{2}^{*} = -\frac{F_{1\eta}^{B}(\varepsilon_{1}^{*},\frac{\pi}{2})+F_{2\eta}^{B}(\varepsilon_{2}^{*},\gamma_{2}^{*})}{F_{1\xi}^{B}(\varepsilon_{1}^{*},\frac{\pi}{2})+F_{2\xi}^{B}(\varepsilon_{2}^{*},\gamma_{2}^{*})}.
\tag{8}
$$

## 4 Definition of constant speed of rotation of the ring in the floating ring bearing

Let the shaft $(O_1, R_1)$ rotates with the given constant angular speed $\omega_1$, and the floating ring $(O_2, R_2)$ rotates with unknown constant angular speed $\omega_2$. This angular speed $\omega_2$ is included into expressions for all forces acting on the shaft and the floating ring. To define the motions of elements of the bearing, it is necessary to investigate the dependence of speed of rotation of the floating ring $\omega_2$ on the speed of rotation of the shaft $\omega_1$. Up to now, the speed of rotation of the floating ring $\omega_2$ was determined only by an experimental method [9], [10]. In this work we shall receive an analytical dependence of $\omega_2$ on $\omega_1$. We notice that the moment of friction only exists in the field of positive pressure of the fluid. At the equilibrium position $\overset{\bullet}{\varepsilon}{}_1^* = 0$, $\overset{\bullet}{\gamma}{}_1^* = 0$, $\overset{\bullet}{\varepsilon}{}_2^* = 0$, $\overset{\bullet}{\gamma}{}_2^* = 0$, from the equations (2), (3) it is received that the pressure is positive in the area $\theta_1 \in [\pi, 2\pi]$ and similar in the area $\theta_2 \in [\pi, 2\pi]$.

In the article [7], the expression for the torque acting on the floating ring from the internal firm of the fluid in the short bearings theory is given:

$$M_1 = \frac{\mu\left(\omega_1+\omega_2\right)\varepsilon_1^* L^3 R_2}{8h_{01}^2}\int_\pi^{2\pi} T_1\frac{\partial Q_1^*}{\partial\theta_1}\,d\theta_1 - R_2 L\int_\pi^{2\pi} S_1\,d\theta_1, \tag{9}$$

where $T_1 = 1 - \frac{2\ln\left(\frac{R_2}{R_2-h_1}\right)}{\left(\frac{R_2}{R_2-h_1}\right)^2-1}$, $S_1 = \frac{2\mu(\omega_1-\omega_2)}{\left(\frac{R_2}{R_2-h_1}\right)^2-1}$, $Q_1^* = \frac{\sin\theta_1}{\left[1-\varepsilon_1^*\cos\theta_1\right]^3}$.

The expression for the torque acting on the floating ring from the external firm of the fluid in the short bearings theory:

$$M_2 = \frac{\mu\omega_2\varepsilon_2^* L^3}{8h_{02}^2}\int_\pi^{2\pi}\left(R-h_2\right)T_2\frac{\partial Q_2^*}{\partial\theta_2}\,d\theta_2 - L\int_\pi^{2\pi} S_2\left(R-h_2\right)\,d\theta_2, \tag{10}$$

where $T_2 = 1 - \frac{2\ln\left(\frac{R}{R-h_2}\right)}{1-\left(\frac{R-h_2}{R}\right)^2}$, $S_2 = \frac{2\mu\omega_2}{1-\left(\frac{R-h_2}{R}\right)^2}$, $Q_2^* = \frac{\sin\theta_2}{\left[1-\varepsilon_2^*\cos\theta_2\right]^3}$.

Rotation of the floating ring around its axis is submitted by the below equation:

$$M_1^B - M_2^B = J_B\overset{\bullet}{\omega}_2.$$

In case we assume the floating ring rotates with a constant angular speed $\omega_2$ then $\overset{\bullet}{\omega}_2 = 0$, so we get:

$$M_1^B - M_2^B = 0. \tag{11}$$

The equations (9), (10) and (11) lead to the expression for definition of angular speed of the ring $\omega_2$. In order to making a diagram, we take a numerical calculation with the following parameters: radius of the bearing housing $R = 0,05$, radius of the floating ring $R_2 = 0,048$, radius of the floating shaft $R_1 = 0,046$.

This paper is devoted to define the speed of rotation of the ring in the floating ring bearing with the considering of the allowance of lubrication hydrodynamics and centrifugal force. By integration a component of tensor stress on a surface of the gaps, we received obvious expressions for forces and the torques acting on the shaft and on the ring of the floating ring bearing. Distribution of the equilibrium positions of the shaft in lubricant layer in mobile coordinate system is researched. The dynamic analysis for the floating ring is defined by analogy. Other parts of this article are devoted to define the speed of rotation

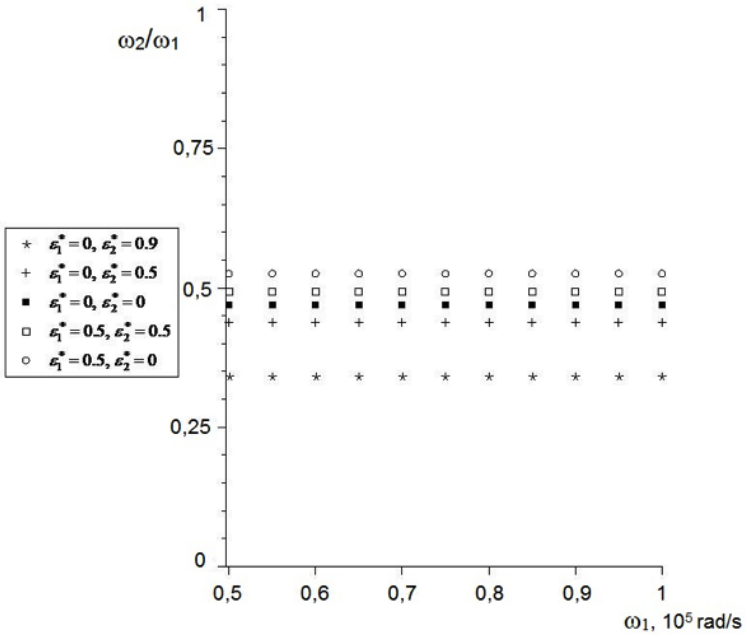


Figure 5: Diagrams of the dependence of the relation of angular speed of the floating ring to angular speed of the shaft $\frac{\omega_2}{\omega_1}$ from equilibrium position of the shaft and the floating ring in the bearing at different values of angular speed of the shaft $\omega_1$.

of the ring in the floating ring bearing. The given problem is important for definition of the forces acting on the shaft as they depend on angular speed of rotation of the floating ring. Angular speed of rotation of the ring in the floating ring is received within the framework of the short bearing theory from a condition of equality of the torque acting on the floating ring from the fluid firms both outside and inside. Numerical calculation has shown that angular speed of rotation of the floating ring in the floating ring bearing can vary in enough wide limits.

## References

[1] L.G. Loitsyansky. The mechanics of a liquid and gas. Nauka, 1987.

[2] G.B. Dubois and F.W. Ocvirk. Analytical derivation and experimental evaluation of short-bearing approximation for full journal bearing. Cornell Univ. Report, 1953.

[3] A.K. Belyaev, Nguyen Van Thang. Forces and moments acting on the rapidly rotating floating bearing. 36th International Summer School- Conference APM, 2008.

[4] K.A. Hatakenaka, K. Suzuki. Theoretical analysis of floating bush journal bearing with axial oil film ruptures being considered. Journal of tribology, 2002.

[5] S.P. Maximov. The self-oscillations of rotors caused by an oil layer of floating bearings. Journal of Kotloturbostroenie, 1964.

[6] J.V. Peshti. Designing of floating bearings with gas greasing. MVTU, 1973.

[7] Nguyen Van Thang. Forces and moments acting on a rapidly rotating floating bearing with allowance of centrifugal force. Scientific and technical statements SPbSPU, series "Physical and mathematical sciences", 2011.

[8] M.V. Korovchinsky. Theoretical bases of work of rotating floating bearings. Moscow, 1959.

[9] A. Boyaci, H. Hetzler, W. Seemann, C. Proppe, J. Wauer. Analytical bifurcation analysis of a rotor supported by floating ring bearings. Nonlinear Dynamics, Springer, 2009.

[10] O.R. Lang, W. Steinhilper. Gleitlager. Springer, Berlin, 1978.

*Nguyen Van Thang, Saint Petersburg State Politechnical University, Grazhdansky st., Saint Petersburg, Russia*

# Investigation of the dynamics of a surface phase formation in multicomponent solutions of surfactants

A. I. Trofimenko (A. I. Lutsik) A. I. Mizev D. A. Bratsun
Lutsik@icmm.ru

**Abstract**

The surface properties and dynamics of the formation of a surface phase in individual and binary aqueous solutions of surface-active substances by the Wilhelmy plate with the Langmuir-Blodgett barrier system are studied experimentally and theoretically. Salts of fatty organic acids are used as the surfactants - potassium laurate and potassium kaprilat, which are members of the same homologous series, but differing in properties. The properties of both one- and two-component solutions depending on both total concentration of all surfactants and relative contribution of each surfactant in the solution are investigated. The maximum surface pressure versus concentration at different speeds of the barriers are plotted. It is revealed that these curves have characteristic maximum. To interpret the results, a theoretical model allowing to study kinetic characteristics of adsorption/desorption processes is proposed.

## Introduction

The Langmuir-Blodgett barrier system was developed a hundred years ago specifically to study the surface properties of insoluble surfactant. In the last few decades it has been applied for studying solutions of soluble surfactant films. This study investigates the processes of formation of the surface phase in monosolutions of surfactants and in binary systems containing two surfactants. Such systems have not been adequately explored because with an increase in the number of solution components the number of physicochemical parameters also increases, which can influence the behavior of the system. The situation is further complicated if the components are mutually soluble. Nevertheless, interest in these systems is increasingly growing because of their common occurrence in nature and numerous applications in industrial processes, in power engineering, chemical and petroleum industry, medicine, etc.

Presently existing models of time-dependent mass transfer require thorough experimental verifications. A lot of publications devoted to the study of surface properties of combined systems are based on the study of equilibrium states [1]. The inadequacy of the equilibrium approach is especially evident in the processes with dynamically variable conditions for the existence of the free surface. In this respect, the approach applied in monographs [2, 3] seems to be more promising. The dynamic properties of the surface phase formation were investigated experimentally and theoretically in a series of works by Yossi, the results of which were summarized in monograph [2]. We can also mention the work [3], the authors of which concentrate their attention on the dynamics of adsorption/desorption processes.

The authors of this paper believe that the classical Langmuir-Blodgett method has not yet exhausted its potential and can be successfully used to study the dynamic properties

of the surface phase formation of one or more surfactants.

## Description of the experimental setup, materials and measuring method

Studies were performed with the use of the Langmuir-Blodgett barrier system and the Wilhelmy balance (KSV Ltd., Finland) [4]. The setup allows studying the surface properties of the solutions in a wide range of lifetime of the surface phase (from a few seconds and for much longer time) and is characterized by high sensitivity at concentrations much lower than the concentration of micelle formations. The dependence of the surface tension on the time provides information about the rate of adsorption/desorption of surfactants and allows us to estimate the characteristic times of mass exchange between the volume and surface phases.

The experiments were carried out with solutions of potassium salts of fatty acids - caprylic acid, propionic acid, and lauric acid prepared on the basis of an aqueous solution of potassium alkali of molar concentration. These surfactants have different lengths of the molecule, which leads to substantial differences in the ways they manifest their surface-active properties. For preparation of solutions we used water of the first degree of purity according to Russia state standard 52501-2005. The tray and setup barriers were cleaned before each experiment. Purity of the surface was checked against that of deionized water by indications of the Wilhelmy balance, which determine the force of pulling in the Wilhelmy plate submerged into a liquid. At the time when the barriers are brought close together the change in the surface pressure should not exceed 0.2 mN/m. After cleaning the water is pumped out and the tray is filled with test solution. Before each measurement the solution is kept in the tray for 20 minutes. The measurements were performed at a constant temperature of samples of $(23.0 \pm 0.3)^{\circ}C$. During all experiments the velocity of the barrier motion was kept constant. The barriers located on the surface of the tray filled with the test solution, first moved closer together with a certain fixed velocity, and then, after reaching a given position, stopped and, without immediately began to move with the same velocity in the opposite direction. Indications of the balance and the position of barriers were transferred in real time to a computer.

The Wilhelmy plate being constantly immersed in the solution registers the magnitude of the capillary force exerted by thesurface of the solution. Thus, during the experiment the scales record changes of the surface tension compared to the initial equilibrium value as a result of changes in the surface density of the surfactant due to an increase or decrease of the surface area of the solution. This quantity is called the surface pressure. At the beginning of each experiment, the indications of the balance were set to zero, i.e. the surface pressure was measured with respect to the equilibrium value of the surface tension.

## Discussion of results

The plots of surface pressure as a function of the surface area per one cycle of compression-extension obtained for monosolutions of potassium laurate and potassium caprylate are given below. Different curves correspond to various velocities of the barriers at the same molar concentration of the surfactant.

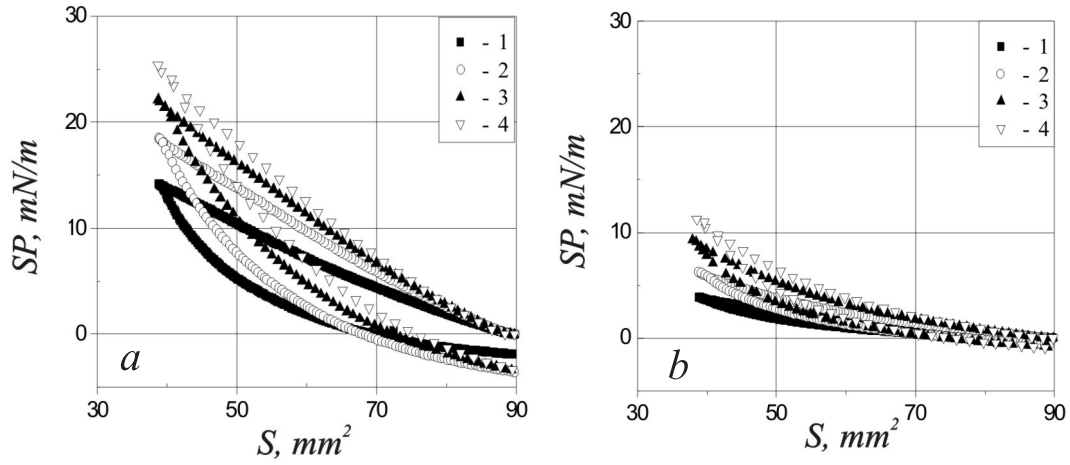


Fig.1 Variation of the surface pressure with the surface area for solutions of potassium laurate *a*), caprylate *b*) potassium molarconcentration of $C$ = 0.0036 mol/l for various velocities of barrier movement: $v$, mm/min: 1 - 10; 2 - 25; 3 - 50; 4 - 100

The graphs show that as the barriers approach each other the surface pressure increases, which is associated with an increase in the surface concentration of the surfactant due to a decrease in the surface area. However, the curves corresponding to a convergence and divergence of barriers do not coincide because part of the surfactant molecules has enough time to diffuse into the solution. With the growth of the compression rate the surface pressure varies more strongly. The higher the rate of barrier convergence, the smaller number of surfactant molecules have time to pass into the mass phase due to desorption. This leads to a larger value of the maximum change in the surface pressure recorded during each experiment. These data were used to construct curves of the maximum pressure change versus the volume concentration of potassium laurate and potassium caprylate in a molar KOH solution at different velocities of barrier motion. All curves show a pronounced maximum, the position of which depends on the barrier velocity.

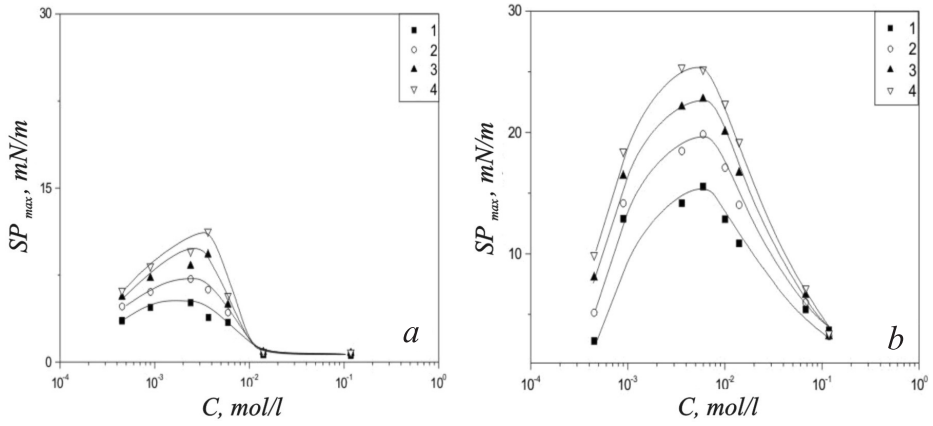


Fig.2 The dependence of the maximum value of pressure variation on the volume concentration of a) the potassium laurate, b) the potassium caprylate at different barriers velocities $v$, mm/min

The existence of the extremum is associated with the competition between two mechanisms, depending differently on the volume concentration. On the one hand, an increase in the volume concentration leads to an increases in the surface concentration of the surfactant, and, consequently, to a more significant change in the surface pressure during compression of the surface. Therefore, at low concentration this dependence is directly proportional. At a limiting value of the surface concentration, observed at different volume concentrations of various substances, a further increase in the surface pressure due to barrier compression does not occur, and the curve approaches saturation. On the other hand, the rate of mass transfer between the volume and surface phases monotonically increases with increasing volume concentration.

This leads to a decrease in the maximum value of the surface pressure in the experiments where the barriers are brought close together, so that instead of saturation one can observe a descending part of the curve.

In the second series of experiments, measurements were made at a constant velocity of the barrier motion, but for binary solutions containing both surfactants. At some fixed molar concentration of surfactants, defined as the total number of molecules of both surfactants in a unit volume of the solution, their relative content (the number molecules of each surfactant per unit volume of the solution determined by the mole fraction of each surfactant) changes:

$$X = \frac{\nu_1}{\nu_1 + \nu_2}$$

where $\nu_1$ and $\nu_2$ is the number of moles of the first and second surfactant in the mixture.

On the dependencies of the maximum change in the surface pressure on the mole fraction of potassium laurate at various total molar concentrations of the surfactant and velocities of barrier motion we saw that at higher concentrations of the surfactants in the solution the maximum change of the surface pressure is of monotonic character. Thus, the variation in the composition of the mixture monotonically changes its surface properties, which have intermediate values with respect to the values typical for the homogeneous mixtures. However, at low concentrations the plots have a minimum, i.e., in the case of a mixture, the molecules diffuse from of the surface layer into the solution faster than in the case of a mono-component mixture. The rate of desorption depends on the mixture composition.

## The mathematical model

Here we shall construct a theoretical model, describing the time-dependent processes of diffusion and adsorption/desorption of surfactants at the interface and near it under the conditions of dynamical changing surface area of the solution. The coordinate system is arranged in such a way that the x-axis is directed along the interface and the z-axis is perpendicular to it so that the condition $z$=0 specifies the surface, and the axis itself goes into the liquid. We shall restrict our consideration to the case of a two-dimensional problem. The volume and surface concentrations will be denoted by $C(t, x, z)$ and $\Gamma(t, x)$ respectively. The constitutive relation defining the dynamics of dissolved surfactant is a diffusion equation, valid for the bull of solution, taking into account a lead to surfactant transfer along the boundary and in adjacent viscous skin layer:

$$\frac{\partial C}{\partial t} + \Theta(t) z \frac{\partial C}{\partial z} = D \frac{\partial^2 C}{\partial z^2.} \tag{1}$$

where $D$ - is the diffusion coefficient of a surfactant in a liquid. Since we do not deal with the problem of convective mass transfer, we may omit the corresponding term in (1). Here $S$ denotes the surface area, and $\Theta$ - the rate of deformation. Relation (1) was derived under the requirement of fluid incompressibility.

The diffusion equation (1) for a surfactant found in the bulk solution must be supplemented by two equations for the surface concentration $\Gamma(t,x)$, which are considered as its boundary condition. Since the relaxation of the surface is fast enough in this system, we can omit the term corresponding to the diffusion of the surfactant along the surface in the equation. One of these equations for the examined system geometry is written as:

$$\frac{d\Gamma}{dt} + \Theta(t)\Gamma = D\frac{\partial C}{\partial z}\,|_{z=0} \tag{2}$$

However, boundary condition (2) for equation (1) is insufficient for an adequate description of the transport processes, since equation (2) introduces a new function $\Gamma(t,x)$ into consideration, and we need another relation, which relates surfactant concentrations at the surface and in the solution. To determine the type of this relationship it is necessary to compare the characteristic times of diffusion and adsorption/desorption. If the characteristic diffusion time is much longer than the time of establishment of the material equilibrium between the surface and near-surface layers due to adsorption/ desorption, we are dealing with the *diffusion kinetics* [2,3]. In this case, the delivery of the surfactant molecules to the surface at any variation of the solution thickness occurs almost instantaneously, and the system is in the state of thermodynamic equilibrium. The specific form of the relationship between $\Gamma$ and $C$, depends on the choice of the isotherm. For the problem under consideration it is convenient to use the Langmuir isotherm:

$$\Gamma = \Gamma_\infty \frac{C_0}{K_2/K_1 + C_0} \tag{3}$$

where $\Gamma_\infty$ - is the limiting surface concentration of the monolayer for a given surface-active substances, $C_0$ - is the value of the molar concentration of the surfactant in the near-surface layer, $K_1$ and $K_2$ - are the coefficients of adsorption and desorption, respectively.

If the balance of the characteristic times in the system is opposite, i.e., the diffusion processes occur much faster than the processes of adsorption/desorption, there is no equilibrium in the system and we need to introduce the dynamic relationship between the concentrations. In this case the Langmuir equation is used most commonly:

$$\frac{d\Gamma}{dt} = K_1 C_0 \left(1 - \frac{\Gamma}{\Gamma_\infty}\right) - K_2 \frac{\Gamma}{\Gamma_\infty} \tag{4}$$

In the case of the *adsorption kinetics* (4) the diffusion occurs so quickly that the concentration of the surfactant in the near-surface layer $C_0$ is held constant, since the diffusion always has time to remove extra molecules from the surface in the case of desorption, or to carry new molecules to the surface in the case of adsorption. It is readily seen that equation (3) is simply a stationary solution of equation (4).

Finally, if it is impossible to give preference to a certain kind of mass transfer process one should refer to mixed kinetics [2, 3]. It is the most complex case for the analysis, since the Langmuir equation takes the following form:

$$\frac{d\Gamma}{dt} = K_1 C(t,0) \left(1 - \frac{\Gamma}{\Gamma_\infty}\right) - K_2 \frac{\Gamma}{\Gamma_\infty} \tag{5}$$

Equation (5) can not be solved independently, since in this case the near-surface surfactant concentration is non-stationary.

Suppose that the processes in the system occur according to the diffusion kinetics scenario. In this case, to evaluate the evolution of the system we must solve equation (1) for the boundary conditions (2, 3) and the following initial conditions:

$$t = 0 : \Gamma = \Gamma_e, C = C_0. \tag{6}$$

Here $\Gamma_e$ - is the equilibrium value of the surface concentration of the surfactant at the beginning of the barrier movement. Consider the specific case of dynamically changing surfaces. Let the area of the surface phase is compressed with the constant rate $V$. To solve, we use the method developed by Yossi in [2]. As a result, we obtain an expression

$$\Gamma(\tau) = (1 - Vt)\left(\Gamma_e + 2\sqrt{\frac{D}{\pi}}\int_0^{\sqrt{\tau}}\left(C_0 - C(\tau - \lambda, 0)\right)d\sqrt{\lambda} + 2V\int_0^{\tau}\Gamma(\tau)d\tau\right), \tag{7}$$

using the initial conditions (6). The approximation $C_0 - C(\tau - \lambda, 0) \approx (\Gamma_e - \Gamma(\tau - \lambda))dC/d\Gamma$ can be used to solve equation (7) with respect to $\Gamma$, and the integrals can be replaced by the approximate expressions according to the mean value theorem.

The numerical calculations have been performed in the paper [2]. They show that this assumption does not introduce significant errors. Expressing in (7) the function of $\Gamma(\tau)$, and assuming that the deviations from the equilibrium $\Pi - \Pi_e \approx (\Gamma - \Gamma_e)d\Pi/d\Gamma$ are small, we arrive at the final expression for the evolution of the surface pressure:

$$\Delta\Pi(s) = \sqrt{\frac{\pi V}{4D}}\frac{RTC_0\Gamma_\infty^2}{\left(C_0 + \frac{K_2}{K_1}\right)^2}\frac{(1 - s)}{\sqrt{s}(G\sqrt{s} + \sqrt{1 - s})}. \tag{8}$$

Here $T$ - is the temperature $s$ - is the dimensionless area of the interface $s(t) = 1 - Vt$, which varies in the range from 1 to 0.

To construct equation (8) we used the expression for the Langmuir isotherm (6) and Gibbs isotherm, $d\Pi/dC = \Gamma_e RT/C_0$ The transformations made in (8) result in the appearance of the dimensionless parameter $G$ which is equal to the ratio of the characteristic diffusion time to the characteristic time of the barrier motion:

$$G = \frac{\sqrt{\pi}}{2}\sqrt{\frac{\tau_D}{\tau_V}} = \frac{\sqrt{\pi}}{2}\frac{d\Gamma}{dC}\sqrt{\frac{V}{D}}.$$

If the surface is compressed quickly, and $G >> 1$ relation (15) at the beginning of evolution becomes close to a liner expression: $\Delta\Pi(s) \approx (1 - s)/s$. For another limiting case $G << 1$ when the motion of the barriers is so slow that the diffusion processes have time to relax, we get $\Delta\Pi(s) \approx (1 - s)/s$ In both cases the curve has no extremums and the surface pressure varies monotonically.Assuming that the examined system evolves according to the scenario of diffusion kinetics we can use the above experimental data to estimate the value of the parameter $G$in the experiments with potassium caprylate: $G \approx 0.19\sqrt{\upsilon}$ , where $\upsilon$ - is the dimensional velocity of the barriers(mm/min).Taking into account these observations, we compared the theoretical curves calculated by formula (8) with the experimental data described by the curve of surface pressure versus surface area for the solutions used ($b$). The results for different velocities of the barrier motion (for the sake of comparison with experiment the surface area is expressed in $mm^2$ are shown in the figure as surface pressure versus surface area curves for a solution of potassium caprylate.

It is seen that for potassium caprylate there is a good agreement between the experimental and theoretical data for all velocities of the barrier motion set during experiments. There exists a value of $C$, for which an increase in the surface pressure during the motion of the barriers is maximum (see Fig.3).

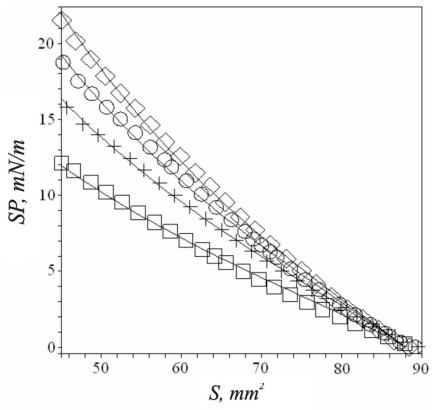


Fig.3 Variation of the surface pressure with the surface area for the solution of potassium caprylate. The experimental data (dots) are compare with the theoretical data (solid lines) calculated by formula (15) at a fixed molar concentration of the solution $C$ =0.0036 mol/l. The curves correspond to different velocities of the barrier motion: $v$, mm/min: 10 (□); 25 (+); 50 (○); 100 (◇).

Using (8) we shall try to clarify the physical meaning of the appearance of extremum on the plot of the maximum surface pressure as a function of volume concentration of the surfactant solution, shown on the dependence of the maximum change in pressure on the mass concentration (Fig.4). For this purpose we fix a value $s$=0.5 and see how the experimental points fit the theoretical curve, for example for the barrier velocity $v$=100 mm/min.

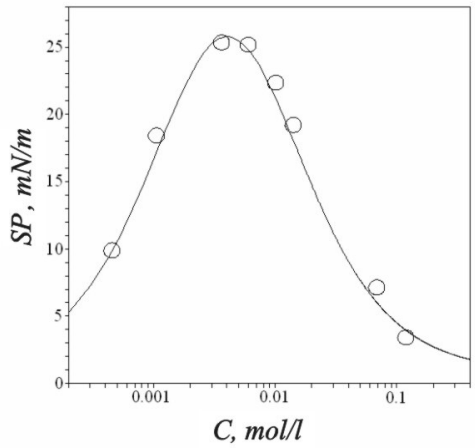


Fig.4 The dependence of the maximum pressure variation of the volume concentration of potassium caprylate.It is a comparison of experimental data (○) and theory (line), calculated by the formula (15) at a fixed speed barrier, $v$=100 mm/min.

If we differentiate (8) with respect to $C_0$, you can get the value of concentration at the curve maximum:

$$C_0^* = \frac{K_2}{K_1} \approx 0.4 \cdot 10^{-3} \tag{9}$$

Thus, the maximum of the curve corresponds to the case when concentration of the surfactant in the solution is equal to the Langmuir-Shishkovsky constant $a$=$K_2/K_1$. The latter is

the ratio of the desorption coefficient to the adsorption coefficient. The physical meaning of the constant follows from the Langmuir isotherm (3): it is an initial concentration of the surfactant in a mixture, at which after the establishment of the equilibrium the monolayer is exactly half full. Relation (9) can be used to estimate based on the experimental data the ratio of the adsorption to the desorption coefficients: $K_2 = K_1 C_0 \approx 0.4 \cdot 10^{-3} K_1$. In the framework of diffusion kinetics it is impossible to determine separately the adsorption and desorption coefficients, because a priori the diffusion time is much longer than the characteristic time of adsorption. Just this assumption has been used to derive formula (8).

## Conclusion

A theoretical model has been proposed to interpret the experimental data on the dynamics of formation of the adsorbed film of a single surfactant. It allows us to describe the time-dependent processes of diffusion and adsorption-desorption of a surfactant at the interface and near it under the conditions of dynamically changing surface area of the solution. Good agreement between the experimental and theoretical results (see surface pressure versus surface area curve and curves of maximum change in pressure plotted as a function of volume concentration), provides the basis for determining the type of kinetics of the examined surfactant.

However, the kinetics scenario can be predicted without making a complex mathematical analysis. Let us estimate the following dimensionless parameter:

$$R = \frac{\Gamma_\infty^2 \hat{K}_2}{a^2 D}, \tag{10}$$

This parameter is the ratio of the characteristic diffusion time to the characteristic time of adsorption-desorption. If the parameter R is large, the kinetics of the system is of diffusion type, if it is small, the kinetics is of the adsorption type. As for the values entering into relation (10) we can characterize them as follows. The reduced coefficient of desorption $\hat{K}_2 = \frac{K_2}{\Gamma_\infty}$ at times to 20 ms is almost independent of the type of material and is equal to 100 $s^{-1}$ [2]. The value of the saturation of the monolayer is also weakly dependent on the material and is approximately equal to 5 $\cdot 10^{-10}$ mol/sm$^2$. The Langmuir coefficient is determined from the experiment (9). The diffusion coefficient of potassium caprylate can be estimated as $10^{-6}$ sm$^2$/s. As a result, we obtain: $R \approx 2$. This means that potassium caprylate ($C_8H_{15}KO_2$) with some reservations can be attributed to the substances governed by the diffusion kinetics. A similar analysis performed for the potassium laurate ($C_{12}H_{23}KO_2$), leads to a larger value of: $R \approx 20$. The point is that the maximum of the curve for laurate is shifted toward lower concentration (which is readily seen from the dependence of the maximum change in pressure on the volume concentration). In general, these results correlate well with the observations of Yossi, who stated that a surfactant composed of heavier molecules of a homologous series, shows more pronounced diffusion kinetics [2].

Thus, we offer three possible variants of representing boundary conditions, which correspond to different types of kinetics of mass transfer processes at the surface of the solution: adsorption-desorption, diffusion, and mixed kinetics. It has been shown that on the basis of preliminary experimental data we can evaluate the type of kinetics inherent in a particular surfactant. A reasonable explanation has been given for the nonmonotonic dependence of the increment of the surface pressure on the volume surfactant concentration observed in the experiment. It has been found that the curve maximum corresponds to the case

in which the surfactant concentration in the solution is exactly equal to the Langmuir-Shishkovsky constant. The proposed approach for determining the Langmuir-Shishkovsky constant is new and is not described in the literature.

## Acknowledgements

*The work was supported by the RFBR (project № 10-01-96009), the Program of RAS Department (project No 01-T-1-1005), the Federal Program (project No 14.740.11.0352) and the Joint Project of SB.UB and F-EB of RAS (project No 12-C-1-1006).*

## References

[1] Mixed surfactant systems / ed. by Keizo Ogino and Masahiko // Surfactant science series. 1993. V. 46. P. 450.

[2] Joos P. Dynamic Surface Phenomena, VSP BV, AH Zeist, The Netherlands, 1999. P. 360.

[3] Dukhin S.S., Kretzschmar G., Miller R. Dynamics of Adsorption at Liquid Interfaces: Theory, Experiment, Application, in "Studies of Interface Science", Vol. 1, Elsevier, Amsterdam, 1995. P. 581.

[4] Official company sate: http://www.ksvltd.com

[5] Hansen R.S. The theory of diffusion controlled absorption kinetics with accompanying evaporation // J. Phys. Chem. 1960. V. 64. P. 637-641.

*Institute of Continuous Media Mechanics, Ural Branch of Russian Academy of Sciences, Acad. Korolev Str. 1, 614013 Perm, Russia.*

# Instability of solutocapillary flow in the presence of insoluble surfactant

A. I. Trofimenko (A. I. Lutsik) A. I. Mizev
Lutsik@icmm.ru

**Abstract**

The stability of the solutocapillary Marangoni flow initiated by a localized concentration source in the presence of an adsorbed layer of insoluble surfactant is investigated experimentally. It has been established that the main axisymmetric flow becomes unstable with respect to azimuthally periodic disturbances, which leads to the appearance of the surface flow with a multi-vortex structure. The structure of the secondary flow is investigated depending on the intensity of the main flow and the surface density of the surfactant. It has been shown that the azimuthal wave number increases with the growth of the Marangoni number and decreases with the growth of the surface density of the surfactant. A threshold value of the surface density of the surfactant, at which the Marangoni flow does not occur, has been defined.

## Introduction

The presence of the surface tension gradient induced by heterogeneities in temperature, chemical composition or electric potential along the surface of the fluid gives rise to a surface (or capillary) flow. The resulting surface motion is called, respectively, thermal, solutal or electrocapillary Marangoni flow. Interest in this subject is related, first of all to a wide class of both fundamental and applied problems, in which this class of flows has been intensively studied during last few decades.

The structure of surface flows reflects the configuration of heterogeneity distribution at the interface that provokes the appearance of surface tension gradient. As a rule, the structure of such flows is easy to predict, and it can be modelled relatively well based on theoretical and numerical studies. However, there are a number of experimental works, in which the structure of the observed surface flows differs significantly from that predicted theoretically and stemming from the problem symmetry. For example, experimental investigation of the thermal and solutocapillary convection from a concentrated source made in [1 - 3] revealed the occurrence of a multivortex flow on the surface, whereas the numerous experimental and theoretical studies showed the formation of a steady-state axisymmetric radial flow in this situation.

In our opinion, these discrepancies are most likely caused by surfactants (frequently uncontrolled in experiments), which generate an adsorption layer at the interface. For example, it was shown in [4] that the use of anti-wetting covering in the problems of the liquid bridge leads to its partial dissolution in the working fluid and, consequently, to the appearance of the adsorbed film, which changes dramatically the results of the experiments. The results gained by a series of qualitative experiments [5 - 6] have shown that thorough cleaning of the water/air interface lead to the formation of flow structures predicted by theoretical models and consistent with the symmetry of the problem. The content of even

small amounts of surface-active impurities at the interface, specifically deposited on the surface [5] or associated with inadequate fluid purification [6], leads to instability of the initial surface flow and the formation of more complex secondary structures at the interface. A more detailed experimental investigation and theoretical description of this phenomenon has not yet been done.

The idea of the influence of adsorbed layers of surfactants a well-studied on the problem of rising bubbles in the solution of surfactants. The explanation was first given by Frumkin and Levich [7]. To date, their hypothesis has been successfully verified in several experimental studies conducted with highly purified water and aqueous solutions of surfactants [8 - 11]. However, no direct experimental observation of the distribution of concentration and velocity on the bubble surface has been performed due to the small (a fraction of a millimeter) size of the region under study. Numerical simulation that has been carried out to take into account the adsorption-desorption process of surfactant molecules on the surface of the bubble shows qualitatively good agreement with the available experimental results [12 - 13]. Quantitative comparison of the results is a rather complicated procedure because much effort is required to measure accurately such parameters of adsorbed films as the rate of adsorption/desorption, characteristic relaxation time of the layer, etc.

In some studies the problem of the interaction of surfactant films with convective flows on the surface [14 - 16] it was found that surfactants exert a destabilizing effect at the early stage of thermocapillary convection, whereas in the other papers the presence of a surfactant has a stabilizing effect at the beginning of convection, leading to an increase in the threshold of the Marangoni number [17 - 19]. No attempts have been made to carry out experimental studies of the layer stability in the context of the Pearson problem.

It is seen that the proposed situation, in which the development of the surface flow is complicated by the presence of the adsorbed layer of surface-active impurities is widely met in practice, but is still poorly explored. The existence of the adsorbed film of surface-active impurities leads to a change in the boundary conditions (surface tension, surface rheology). The redistribution of the surfactant molecules by a convective flow can lead to inhomogeneous boundary conditions and, consequently, to loss of symmetry of the main flow. From this point of view there is a need of making a more comprehensive study of the evolution and stability of the surface flows in the presence of adsorbed surfactant films, which will allow us to formulate the boundary conditions suitable for such problems. The main purpose of the study is the investigation of the interaction in the context of a simple model situation: the stability of an axially symmetric solute-capillary flow induced by a concentrated source located at the surface. The paper presents the results of experimental study into the structure and evolution of solutocapillary flow on the surface of the liquid, depending on the intensity of convective motion (the solutal Marangoni number-la) and the surface concentration of surface-active impurities.

## Experimental setup and methods.

The main difficulty in the experimental investigation of this class of problems is the establishment of the "zero" surface, i. e., the surface, which is initially free of molecules of other substances, which can be used to generate the required surface flow and eliminate the influence of complicating factors. The existence of initially pure "zero" surface is also a prerequisite for the creation of the surface layer with controlled properties and concentration. There are two ways of creating such conditions. The first is to select a sample liquid. To extend the scope of research we used water as a base fluid. Out of commonly used fluids (except molten metals and salts) water possesses the largest surface tension, which makes

the choice of surfactant practically unlimited. However, preparation of a "zero" surface for water is quite a challenge. To solve this problem, we applied the second method, which includes thorough cleaning of the liquid and experimental setup and constant observation of the state of the interface.

A high level of water purification was achieved by applying successively the processes of Bi distillation and deionization, which enable us to remove practically all impurities. For the removal of impurities was accomplished by employing a Langmuir - Blodgett barrier system and aspirator. The degree of contamination of the surface is controlled by Wilhelmy balance. After completing the procedures of surface cleaning, par of water was pumped out. The water - air interface dropped to about the middle height of the cuvette, where the cuvette walls were transparent, which allowed us to apply the optical methods of structure visualization. The solutocapillary Marangoni flow was created in the following way. On the free surface of a horizontal layer of water (1, Fig.1) we placed a thin slice (0.9 mm outer diameter) of a stainless steel tube 2, through which a weakly concentrated aqueous solution of ethyl alcohol is feed by pump 3. Even small concentrations of the ethyl alcohol solution substantially lowers the surface tension, which leads to the appearance of convective flow at the interface, directed oppositely to a concentration gradient, i.e., from the center to the periphery of the cuvette. Ethyl alcohol is also a surfactant, but in weakly concentrated solutions it does not form stable adsorbed films capable of affecting the stability of solutocapillary flow.

Experiments have shown that the convective flow created at the surface in such a way remains stable, i.e., preserves the axial symmetry throughout the experiment. Changing concentration of the solution of ethyl alcohol and flow rate we can change the intensity of convective flow. For flow visualization we used the standard knife- edge technique in combination with light-scattering particles suspended in solution - glass, hollow spherical particles of neutral buoyancy. The particles undergo pre-treatment to remove contaminants from their surface. Knife-edge, created by laser 4 (wavelength 532 nm, power 200 mW) and lens system 5 moved along the surface of the liquid. The flow patterns were recorded by camera 6.

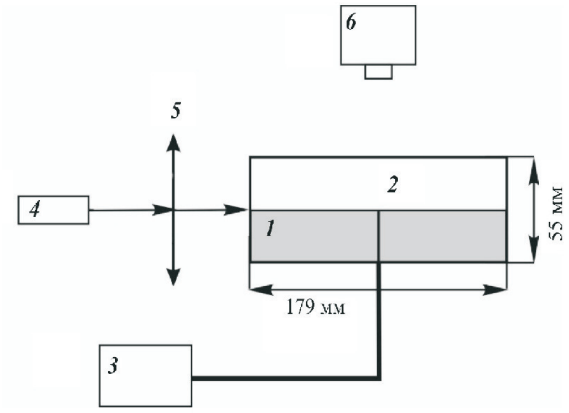


Fig.1 Scematics of experimental setup: 1 - water layer, 2 - a tube for feeding aqueous solution of ethyl alcohol, 3 - feeding pump, 4 - laser, 5 - lens system, 6 - photo camera

To create a film of surfactant on the surface of water we used insoluble surfactant (oleic acid). In this case, the molecules of surface-active impurities are located on the surface and do not penetrating into the liquid, which makes it possible to create a constant and

controllable surface concentration. The fluid motion at the interface can only lead to a redistribution of the molecules within the surface phase, which may change the local, but not the total concentration of molecules on the surface. To create a film on the surface of water we dissolved the surfactant in highly volatile and water - insoluble organic solvent - hexane. With the help of a microsyringe the solution was injected onto the surface of water. It rapidly spread over the surface covering all available area. As the solvent evaporates, a homogeneous surface layer is formed. At the beginning of each experiment, we specified the feed rate of the solution, its concentration and the surface density of the surfactant molecules. These quantities were used to form two dimensionless governing parameters of the problem: the degree of saturation of the layer by the molecules of surface-active impurities.

$$\frac{\Gamma}{\Gamma_e}$$

where $\Gamma$ - surface concentration of impurities, $\Gamma_e$ - surface concentration of the saturated mono-layer of a surfactant. The effective Marangoni number is.

$$Ma = \frac{q}{D\eta^2} \cdot \frac{d\sigma}{dC} \cdot C$$

where $q$ - dimensional mass flux of the surfactant solution, $\eta$ - dynamic viscosity, $D$ - diffusion coefficient, $\sigma$ - surface tension, $C$ - volume concentration. During experiment we investigated the structure of arising flow as a function of these dimensionless parameters.

## The results of experiments and discussion

The structure of the concentration-capillary motion on the surface essentially depends on the intensity of the Marangoni flow and the surface density of the surfactant. In the absence of the surfactant an axially symmetric flow (radial flow) stable over the entire range of the Marangoni numbers used in experiments is formed at the interface. Such a structure of the flow formed in the absence of the surfactant served as additional criterion of the water surface purity at the beginning of each experiment. The deviation of the flow structure from the axial symmetry was the reason for of interrupting the test and repeating the procedure of water purification and setup cleaning. The presence of a surfactant of any surface density leads to instability of the main flow and the formation of secondary structures in the form of a multivortex flow, periodic in the azimuthal direction.

The characteristic structures obtained experimentally for a fixed of $\Gamma/\Gamma_e$=0.35 and different values of the Marangoni number $Ma$ are given in (Fig.2). It is seen that at small value of the Marangoni number the developed flow has a two-vortex structure ($a$). With an increase in the flow velocity the structure loses stability at some value of $Ma$, giving way to a four-vortex structure ($b$). A further increase of the mass flux leads to the appearance of a more complicated structure with a greater number of vortices (6 and 8 vortices in Fig.2 ($c$) and ($d$), respectively). The value of the interval, in which there exists a stationary two-vortex flow decreases with increasing wave number. Moreover, with increasing intensity of the convective motion and at a constant surfactant content, in the vicinity of the source one can observe the formation of the zone of axially symmetric flow, which increases with the growth of Marangoni number. Similar evolution of the surface flow is observed at a fixed value of the Marangoni number and variable value of $\Gamma/\Gamma_e$ (Fig.3).

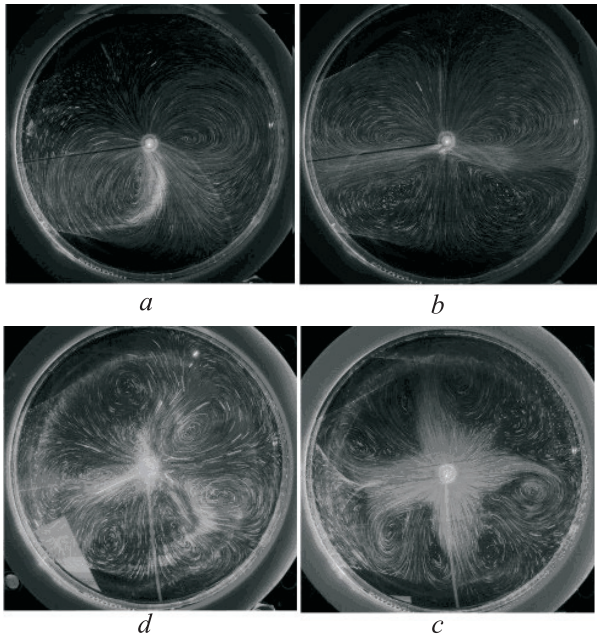


Fig.2 Characteristic flow patterns 1 at $\Gamma/\Gamma_e$=0.35 and $Ma \cdot 10^7$ : 0.5 ($a$), 1.0 ($b$), 2.5 ($c$), 4.0 ($d$)

In this case, the number of vortices decreases with the growth of the surfactant content at the surface.

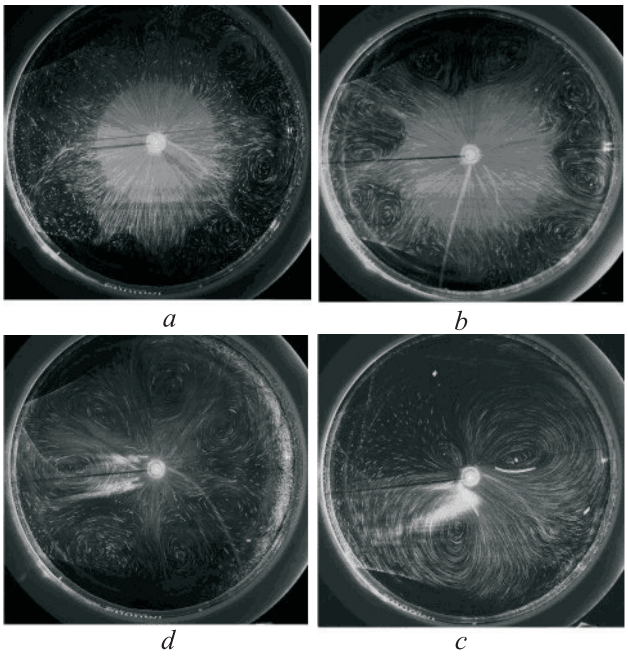


Fig.3 Characteristic flow patterns 2 at $Ma = 0.5 \cdot 10^7$ and $\Gamma/\Gamma_e$: 0.2 ($a$), 0.25 ($b$), 0.3 ($c$), 0.35 ($d$)

When $\Gamma/\Gamma_e$ approaches a certain threshold value depending on the Marangoni number, no surface flow is formed at the surface. It is also seen that the size of the region of the axially symmetric flow in the central part of the cuvette reduces with an increase in the

quantity of the surfactant at the interface. On the basis of the character of the multivortex flow described above, its symmetry and structure of the initiated flow we can derive a wave number, which is defined as $k_\varphi = 2\pi/\varphi$ , (where $\varphi$ is the angular dimension of the structure). It essentially depends on the Marangoni number and surface density of the surfactants.

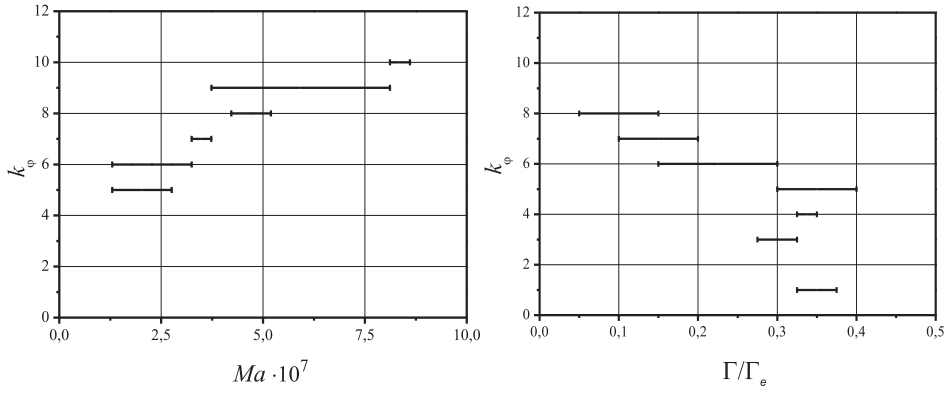


Fig.4 Azimuthal wave number as a function of the Marangoni number (left picture, $\Gamma/\Gamma_e$= 0.15) and the surfactant surface density (right picture, $Ma$=0.19·10$^7$)

The plots of azimuthal wave number as a function of the Marangoni number and surface density of the surfactant were constructed based on the results of experiments and are given in (Fig.4). It should also be noted that in the presence of surfactant at the interface there is a threshold value of the Marangoni number, at which a convective flow is initiated. At lower threshold values the flow on the surface is not formed. This threshold value depends strongly on the surface concentration of the surfactant.

## Conclusion

The results of experimental studies presented in this paper show that the flow structures observed in some studies [1 - 6], contradict the results predicted theoretically in compliance with the symmetry of the problem. This can be explained by the existence of uncontrolled content of surface-active impurities involved in the formation of the adsorbed layers at the interface. Experiments show that the presence of even small amounts of surfactant molecules on the surface leads to instability of the main flow. The structure of the secondary flow is determined by the geometry of a particular problem. In the case examined in this paper, an axisymmetric flow becomes unstable with respect to multivortex flow, which is periodic in the azimuthal direction. Moreover, the azimuthal wave number depends on the intensity of the flow and content of the surfactant.

The mechanism of the instability of the basic flow is as follows. Initially, a uniform distribution of particles on the surface is disturbed by the arising axially symmetric radial flow, which transports surfactant molecules to the periphery. However, compression of the adsorbed layer of insoluble impurities leads to the appearance of the surface pressure in the layer. Because it is directed against the flow, it slows down the main flow. This results in the formation of a peripheral zone, into which the flow does not penetrate. The boundary of this zone sets new boundary conditions for the flow, instead of conditions previously existing at the solid boundaries of the cuvette. Any violation of the symmetry of the moving boundary leads to breaking of the main flow symmetry due to the presence of feedback between the surface density of surfactant in the selected azimuthal direction

and intensity of the main flow in the same direction. The resulting heterogeneity in the distribution of the surfactant in the peripheral layer will increase leading to the instability, whose azimuthal wave number will depend on the control parameters of the problem. Of course, the proposed instability mechanism is hypothetical and should be tested in the theoretical study, which is scheduled for the near future.

## Acknowledgements

*The work was supported by the RFBR (project No 12-01-00258), the Department of Science and Education of Perm region (project C-26-210), the Federal Program (project No 14.740.11.0352) and the Joint Project of SB,UB and F-EB of RAS (project No 12-C-1-1006).*

## References

[1] Pshenichnikov A.F., Yatsenko S.S. Convective diffusion from the concentrated source of a surfactant // Proceedings of PSU. No 316. Hydrodynamics. V. 1974. P.175 - 181.

[2] Nagy P. and Neitzel G. Failure of thermocapillary-driven permanent nonwetting droplets // Physics of Fluids. 21 (2009), 112106.

[3] Priede J., et al. Experimental and numerical study of anomalous thermocapillary convection in liquid gallium // Physics of Fluids. 11 (1999), 3331-3339.

[4] Schwabe D., Mizev A.I. Particles of different density in thermocapillary liquid bridges under the action of travelling and standing hydrothermal waves // Eur. Phys. J. ST. 192 (2011), 13 - 27.

[5] Linde H., Friese P. Experimental evidence of new hydrodynamic surface instability // Z. Phys.Chem. (Leipzig), 247 (1971), 225 (in German).

[6] Mizev A. Influence of an adsorption layer on the structure and stability of surface tension driven flows // Physics of Fluids. 17 (2005), 122107.

[7] Frumkin A., Levich V. J of Physical chemistry 21 (1947). P. 1183.

[8] Krzan M., Malysa K. Profiles of local velocities of bubbles in n-butanol, n-hexanol and n-nonanol solutions // Coll. Surf., A 207 (2002), 279.

[9] Loglio G. et al. Rising of gas bubbles in aqueous medium in presence of surfactants // Il Nuovo Cimento. 12 (1989), 289.

[10] Takagi S. et al. Surfactant effect on the bubble motion // Fliud Dyn. Res. 41 (2009), 065003.

[11] Griffith R. The effect of surfactants on the terminal velocity of drops and bubbles // Chem.Eng.Sci., 17 (1962), 1057 - 1070.

[12] Takagi S. The effect of surfactant on rising bubbles // Phil.Trans.R.Soc., A 366 (2008), 2117 - 2129).

[13] Harper J. On spherical bubbles rising steadily in dilute surfactant solutions, Q J Mechanics Appl Math, 27 (1974), 87 - 100.

[14] Ryabitskiy E.A. The oscillatory thermocapillary instability of a plane layer in the presence of a surfactant // Transactions of RAS. Fluid Mechanics. No 1. 1993. P. 6 - 10.

[15] Ryabitskiy E.A. Thermocapillary instability of the plane layer equilibrium in the presence of soluble surfactant // Fluid mechanics. 1996. No 1.P. 3 - 8.

[16] Nauka. 2000. P. 280.

[17] Berg J., Acrivos A. The effect of surface active agents on convection cells induced by surface tension // Chem.Eng.Sci., 20 (1965), 737 - 745.

[18] Nepomnyaschy F., I. Simanovsky Thermocapillary convection in two-layer system in the presence of surfactant at the surface / / Izv. USSR Academy of Sciences. Fluid Dynamics. 2 (1986).

[19] Mikishev A., Nepomnyashchy A. Long-wavelength Marangoni convection in a liquid layer with insoluble surfactant // Microgravity Sci.Technol., 22 (2010), 415 - 423.

*Institute of Continuous Media Mechanics, Ural Branch of Russian Academy of Sciences, Acad. Korolev Str. 1, 614013 Perm, Russia.*

# Stability analysis of the 2D electroconvective charged flow between parallel plates using Discontinuous Galerkin Finite Element methods

P. A. Vázquez A. Castellanos
pvazquez@us.es

**Abstract**

We explore the capability of Discontinuous Galerkin Finite Element methods to solve numerically the charge transport equation in EHD convective problems. These methods are especially suited to treat purely hyperbolic problems. We compute both the electric and velocity fields in the case of strong injection. The numerical solution compares very well to the analytical solution for the hydrostatic situation, as well as with the theoretical linear stability criterion. The results are very promising for future research of complex electroconvection problems.

## 1 Introduction

Electrohydrodynamics (EHD) is an interdisciplinary area dealing with the interaction of fluids and electric fields or charges. It lies at the heart of several important industrial important processes[1] . In this paper we analyze the classical problem of the 2D flow between two parallel plates immersed in a dielectric liquid. When a high voltage is applied, the electrodes inject electric charge into the liquid, and the Coulomb force put the liquid into motion. Experiments and theoretical analysis show that the pattern of convection is made of hexagonal cells similar to those of Rayleigh-Bénard convection[2, 3]. The onset of the global motion is controlled by a non dimensional parameter involving the applied electric potential, the mobility of the charge carriers and the properties of the fluid.

The transport of electric charge involves three different mechanisms: drift by the electric field, convection by the velocity and th fluid and diffusion. In EHD, diffusion is only relevant inside a very thin boundary layer near the electrodes, and it is not relevant for phenomena developing in the bulk. So in our case the electric charge is transported only by the electric and velocity fields. The problem becomes purely hyperbolic, and special numerical treatments are needed.

In previous works we have simulated the time evolution of the 2D case using Particle-In-Cell(PIC) methods to deal with the distribution of electric charge[4, 5]. The numerical diffusion introduced by PIC methods is minimal, so they do a good job describing the electric charge distribution. However, they have problems too. They are numerically expensive, as a great number of particles are needed to simulate the problem. This is specially true for 3D problems. Also, special care must be taken to assures the value of the boundary condition for the charge near the injector.

Others methods have been used to simulate EHD problems: FE-FCT[4, 5], finite volumes[6], etc. In this paper, we explore the application of Finite Elements Discontinuous Galerkin methods to solve numerically the charge transport equation. We obtain

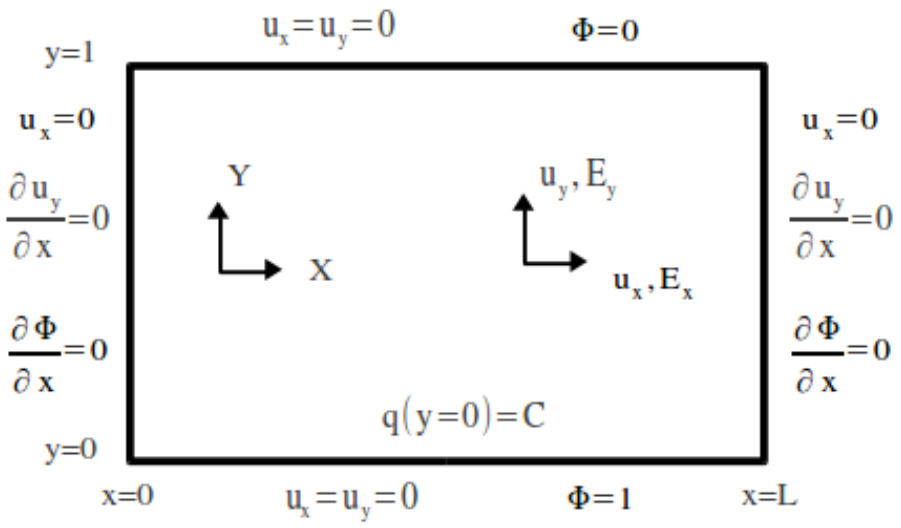


Figure 1: Non-dimensional computational domain and boundary conditions for the problem.

the linear stability analysis criteria for strong injection and compare the computed value with the analytical one[2, 3]. We will see that the Discontinuous Galerkin elements are able to reproduce very accurately the value for the linear stability criterion with much less CPU computing time than PIC methods.

## 2 Problem formulation

Two plane electrodes a distance $d$ apart immersed in a non-conductive fluid are considered. An electric potential is applied between the plates so that injection of charge occurs. The electric field forces the charges away from the injector and in this way a space charge appears. The Coulomb force pushes the charges and the liquid with them. If the electric potential is high enough all the liquid is put into motion. Here we consider the 2D case, so the system is considered to be infinite along one of the direction parallel to the electrodes.

The fluid is considered to be incompressible, isothermal and insulating with mass density $\rho$, kinematic viscosity $\nu$ and permittivity $\varepsilon$. An electric voltage $\Phi_0$ is applied between the plates. The charge carriers are considered to be of the same type with an ionic mobility $K$ so they migrate along the liquid with a velocity $K\mathbf{E}$, where $\mathbf{E}$ is the electric field. Unipolar autonomous injection is assumed so the density of charge at the injector is constant and equal to $q_0$, and that the ions discharge instantaneously once they reach the opposite electrode.

There are three mechanisms responsible for the motion of ions: convection by the fluid, drift by the electric field and molecular diffusion. The last one can be neglected [1] so the current density is given by $\mathbf{J} = q(K\mathbf{E} + \mathbf{u})$, $\mathbf{u}$ being the velocity of the fluid and $q$ the electric charge density. The first term represents drift and the second one convection.

The scales for all the involved variables are

$$\begin{array}{lll} x, y \sim d & \Phi \sim \Phi_0 & E \sim \Phi_0/d \\ u \sim K\Phi_0/d & t \sim d^2/K\Phi_0 & p \sim \rho K^2 \Phi_0^2/d^2 \\ q \sim \varepsilon\Phi_0/d^2 & & \end{array} \tag{1}$$

$p$ being the pressure.

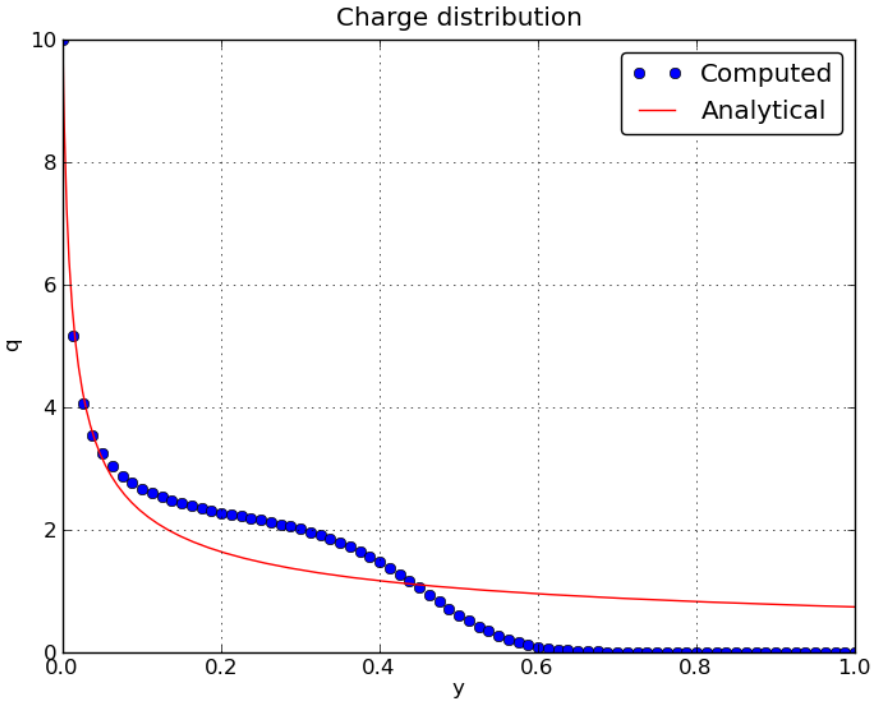


Figure 2: Charge density along the vertical central line of the domain for the hydrostatic solution for $C = 10$ and $t = 0.4$. The analytical solution and the outcome of the numerical simulation are shown.

The non-dimensional equation defining the problem are

$$\nabla^2\Phi = -q, \qquad \mathbf{E} = -\nabla\Phi, \tag{2}$$

$$\nabla \cdot \big[q(\mathbf{u}+\mathbf{E})\big] + \frac{\partial q}{\partial t} = 0, \tag{3}$$

$$\nabla \cdot \mathbf{u} = 0, \tag{4}$$

$$\frac{\partial \mathbf{u}}{\partial t} + (\mathbf{u}\cdot\nabla)\mathbf{u} = -\nabla p + \frac{M^2}{T}\nabla^2\mathbf{u} + M^2 q\mathbf{E}, \tag{5}$$

The non-dimensional parameters of the problem are

$$T = \frac{\varepsilon\Phi_0}{\rho\eta K}, \quad C = \frac{q_0 d^2}{\varepsilon\Phi_0}, \quad M = \frac{1}{K}\sqrt{\frac{\varepsilon}{\rho}} \tag{6}$$

$T$ is the ratio of the force term to the viscous term, and will be the stability paramenter. $M$ is the ratio of the hydrodynamic mobilty[7] and $C$ measures the injection strength.

In the linear stability analysis, the threshold value for the onset of the motion depends on the wavelength of the perturbation[2]. The minimum of these values is the absolute linear stability threshold. In the case of strong injection ($C = 10$), the critical wavelength turns out to be $k_{min} = 5.113$. We consider as domain a rectangle of size $L = \pi/k_{min} = 0.614$. This way, we solve the problem in one half of a convective cell. The non-dimensional domain and boundary conditions are shown in figure 1. At the lateral walls the perpendicular components of the electric and velocity field are null. The value of the charge density at the injector (the bottom plate) is $C$.

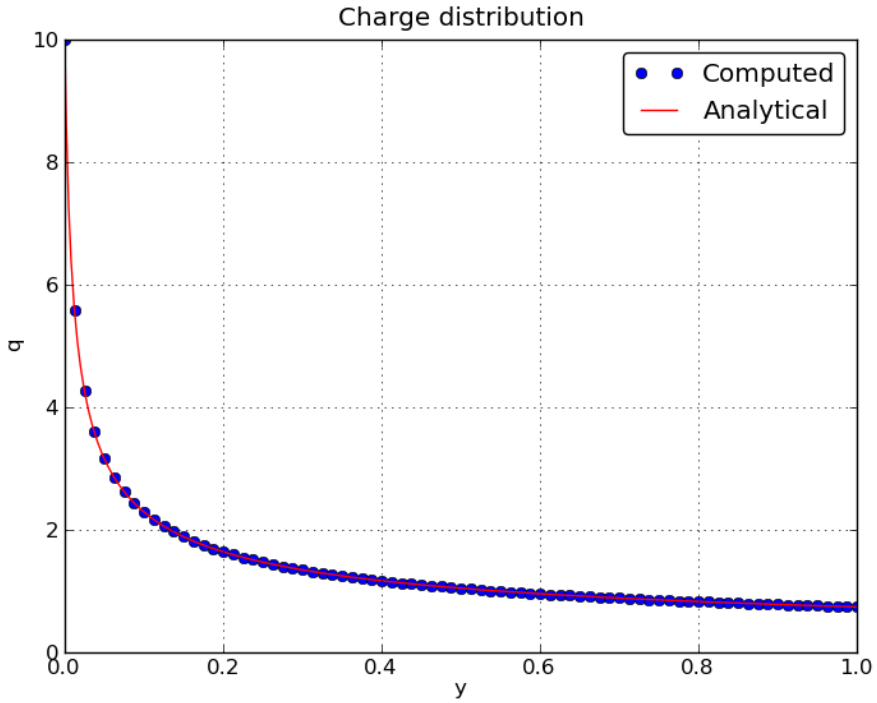


Figure 3: Charge density along the vertical central line of the domain for the hydrostatic solution for $C = 10$ and $t = 5.0$. The analytical solution and the outcome of the numerical simulation are shown.

## 3 Numerical algorithms

Both the electric field and the velocity field are computed using Continuous Galerkin Finite Elements(CG-FEM). We solve the Navier-Stokes equation using a Incremental Pressure Correction Scheme (IPCS)[8].

As described in the introduction, we use Discontinuous Galerkin Finite Elements (DG-FEM) to solve the charge transport equation. These methods were originally developed to deal with hyperbolic problems, but in recent years have been applied to all kind of problems involving partial differential equations[9]. The key idea is to consider internal degrees of freedom inside every element. The connection between elements is achieved using so called numerical fluxes. In this way, conservation is imposed locally. These methods have proved to be very stable when treating hyperbolic problems, and allow to work with complex geometries, as well as prescribing different orders of approximation inside each element.

We use a structured mesh made of triangles. We consider second order elements for the electric potential(CG-FEM) and the velocity field (CG-FEM). The pressure is approximated using first order CG-FEM, in order to comply with the LBB condition. The IPCS scheme is first order in time. For the charge density we use full upwind second order DG-FEM, with a backward scheme in time in order to enhance stability. The resulting numerical scheme is first order in time.

The algorithms have been implemented using the DOLFIN[10] Python library. This is an interface to FEniCS[11], a framework for automated solution of differential equations by the Finite Element method.

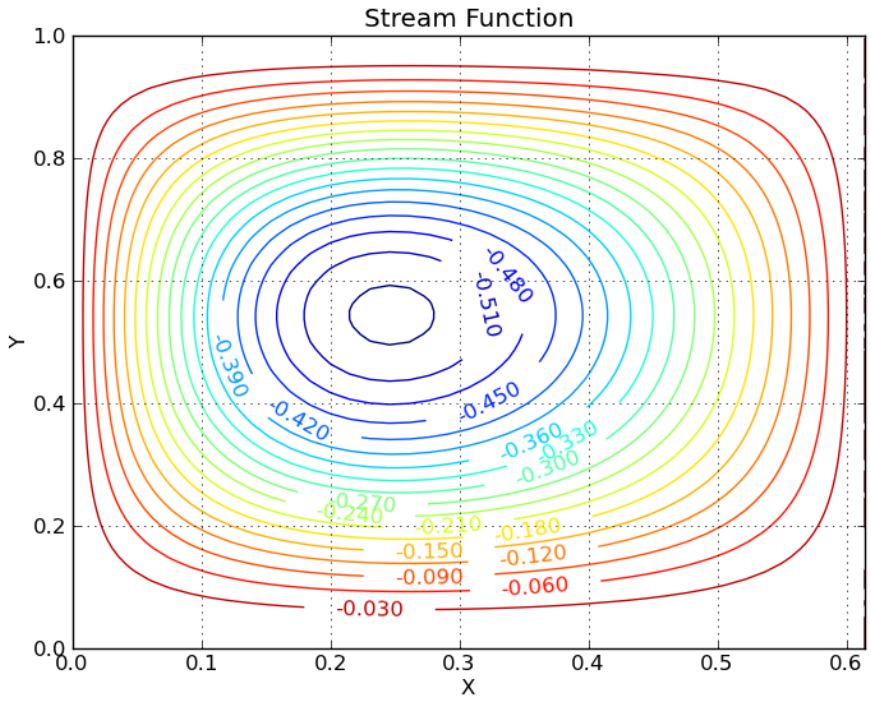


Figure 4: Contour plot of the stream function for for $t = 15$, $C = 10$, $M = 10$, $T = 200$.

# 4 Results

We present some results from simulations in 2D for the strong injection regime ($C = 10$). The bottom length of the rectangle is $L = 0.614$, which corresponds to the more unstable wavelength according to the linear stability analysis[2]. The mesh has 40 regular intervals along the X direction and 50 intervals along the Y direction, smaller near the injector at the bottom and coarser near the collector at the top. The mesh has 2091 nodes and 4000 triangular elements. The time step is $dt = 0.01$ for all simulations.

## 4.1 Hydrostatic regime

In order to verify the ability of the DG-FEM method to simulate the charge distribution, we have run simulations without computing the velocity. The results are compared with the analytical solution for $C = 10$

Figure 2 shows the charge density along a vertical line at non-dimensional time $t = 0.4$. The front of charge advancing towards the top electrode can be seen. The steady analytical solution is also plotted. The DG-FEM is able to describe this front of charge with no spurious oscillation near the region of the steepest gradient.

Figure 3 shows the computed and analytical charge densities along a vertical line when the steady state has been reached. The maximum difference between the computed value of the charge density and the analytical solution is less 0.5%. Also the values of the electric current computed at the injector and the collector differ in less than 0.1%.

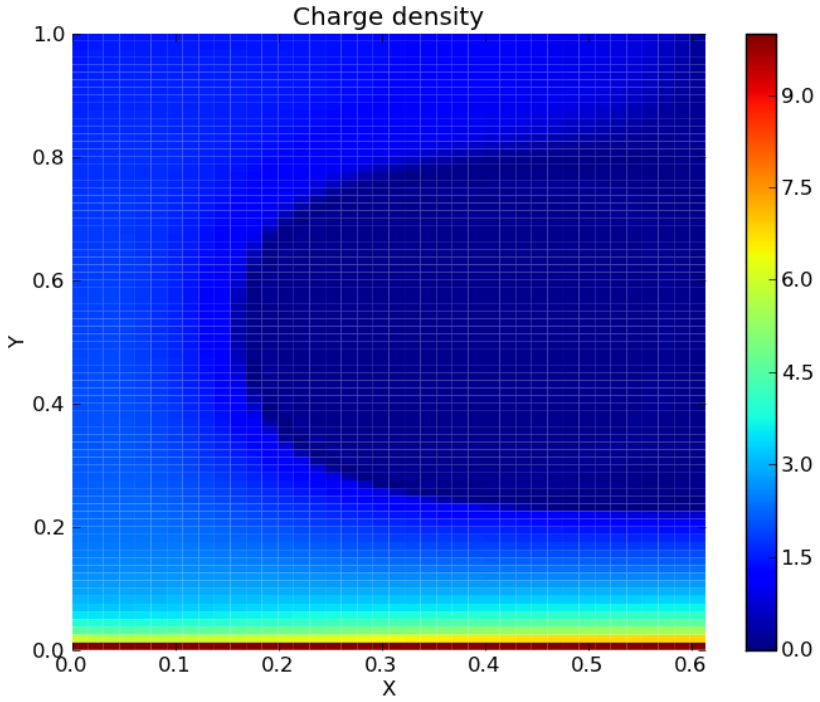


Figure 5: Charge density for $t = 15$, $C = 10$, $M = 10$, $T = 200$. The central region of the convective is void of electric charge.

### 4.2 Linear stability in the strong injection regime

In order to get the threshold value of the linear instability, we have run a set of simulations changing the value of the stability parameter $T$ for different fixed values of the mobility parameter $M$. As an initial condition for the charge density, we set the analytical profile for the hydrostatic regime. Then we compute the electric field and solve the Navier-Stokes equation. The electric and velocity fields obtained are used to advance the charge density. The process is repeated iteratively in time. All the simulations were done for the strong injection regime, $C = 10$.

If the value of $T$ is greater than the critical value $T_c$ a velocity roll appears, with a maximum velocity greater than the electric field ($v_{max} = 4$ for $T = 200$ and $M = 10$). The velocity roll pushes the charge away from the central region, where a region void of electric charge appears. Figure 4 show the contour plot of the stream function for $M = 10$ and $t = 15$. The velocity roll is fully developed here. Figure 5 shows the distribution of electric charge density for $M = 10$ and $t = 15$. The central region empty of charge is clearly seen.

Figure 6 plots the evolution in time for $M = 10$ and several values of $T$ of the global angular momentum of the convective cell, computed as $Lam = \int |(\mathbf{r} - \mathbf{r}_0) \times \mathbf{u}| \, d\mathrm{S}$, where $\mathbf{r}_0$ points to the center of the domain. This magnitude gives an idea of the strength of the velocity roll. For all values of $T$ the growth becomes exponential in a certain interval of time (this corresponds to the linear sections of the curve in the figure, as the scale of the $Y$ axis is logarithmic). In the linear stability analysis, in this region the angular momentum is considered to depend on time as $L_{am} = A\, e^{\sigma t}$, where $\sigma$ is the growth factor. The value of $\sigma$ depends on $T$. The critical value $T_C$ for the onset of the instability corresponds to $\sigma = 0$. Using a quadratic fit for the function $\sigma(T)$ the value of $T_c$ is obtained for the

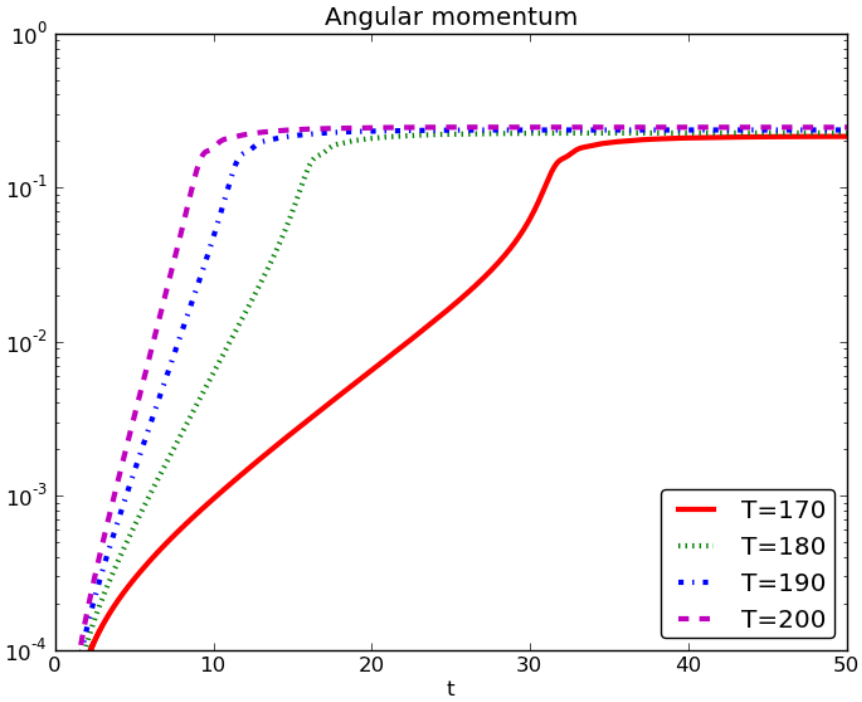


Figure 6: Evolution in time of the total angular momentum for $C = 10$ and $M = 10$. The critical value of $T$ can be estimated from the regions where linear growth is observed (the scale is logarithmic for the Y axis)

different values of $M$. Table 6 shows the values of $T_c$ obtained from our simulations for three different values of $M$.

These number are to be compared with $T_c^a = 164.1$, the critical value obtained from the linear stability analysis, independent of the value of $M$[2]. The computed values are very close to this theoretical number. The relative difference is only of 1.4%, which is consistent with the analytical result.

## 5 Conclusions

We have explored the possibility of using Discontinuous Galerkin Finite Element methods (DG-FEM) to solve numerically the charge transport equation in the 2D EHD convection between parallel plates in the strong injection regime. These methods are specially suited to deal with hyperbolic problems, as it is this case due to the negligible charge diffusion. We have used Continuous Galerkin Finite Element methods to solve the electric and hydrodynamic problems.

In the hydrostatic regime, the DG-FEM method is able to describe the advancing front of charge without spurious oscillations, and reproduces with a very good precision the analytical solution.

When the whole problem is considered, computing both the electric and velocity fields, the critical value for the onset of the linear instability obtained from the computation agrees extremely well with the analytical solution obtained from the linear stability analysis. It turns out to be essentially independent of the value of the mobility parameter, as it is

| $M$ | $T_c$ |
|---|---|
| 5 | 164.0 |
| 10 | 161.7 |
| 20 | 161.7 |

Table 6: Critical values for the onset of instability from the simulations for several values of $M$. The value obtained from the linear stability analysis is $T_c^a = 164.1$

predicted by the theory.

Further work is needed to validate the capacity of the DG-FEM methods to deal with EHD problems. In particular, the long term evolution of the charge density distribution has to be examined, in order to analyze the possible influence of the numerical diffusion that the method introduces, even if it is small. Also extensions to the 2D weak injection case, in the first place, and to the 3D dimensional problem is envisioned in future works.

## 6 Acknowledgements

This work has been supported by the Spanish Ministerio de Educación y Ciencia under contract FIS2011-25161 and the Junta de Andalucia under contract FQM-253.

## References

[1] Castellanos A ed 1998 *Electrohydrodynamics* (New York: Springer-Verlag).

[2] Atten P and Moreau R 1972 Stabilité électrohydrodynamique des liquides isolants soumis a une injection unipolaire *Journal de Mécanique* **11** 471–520.

[3] Atten P and Lacroix JC 1978 Electrohydrodynamic stability of liquids subjected to unipolar injection: non linear phenomena *Journal of Electrostatics* **5** 439–452.

[4] Vazquez P A, Georghiou G E and Castellanos A 2006 Characterization of injection instabilities in electrohydrodynamics by numerical modelling: comparison of particle in cell and flux corrected transport methods for electroconvection between two plates. *J. Phys. D: Appl. Phys.* **39** 2754 – 2763.

[5] Vazquez P A, Georghiou G E and Castellanos A 2008 Numerical analysis of the stability of the electrohydrodynamic (EHD) electroconvection between two plates *J. Phys. D: Appl. Phys.* **41** 175303 (10pp).

[6] Traoré Ph. and Pérez A.T. 2012 Two-dimensional numerical analysis of electroconvection in a dielectric liquid subjected to strong unipolar injection *Physics of Fluids* **24** 037102 doi 10.1063/1.3685721.

[7] Felici N 1969 Phénomenes hydro et aérodynamiques dans la conduction des diélectriques fluides *Rev. Gen. Electrostat.* **78** 717 – 734.

[8] Goda, K. 1979 A multistep technique with implicit difference schemes for calculating two- or three-dimensional cavity flows *Journal of Computational Physics* **30**(1) 76 – 95.

[9] Hesthaven J. S., Warburton T. 2008 *Nodal Discontinuous Galerkin Methods* Springer (Springer).

[10] Logg A. and Wells G.N. 2010 DOLFIN: Automated Finite Element Computing *ACM Transactions on Mathematical Software* **37**(2) doi:10.1145/1731022.1731030, arXiv:1103.6248.

[11] Logg A., Mardal, K. A. and Wells G.N. 2010 *Automated Solution of Differential Equations by the Finite Element Method* (Springer) doi:10.1007/978-3-642-23099-8.

*P. A. Vázquez, Dpto. de Física Aplicada III, E.S.I. Camino de los Descubrimientos s/n, 41092 Sevilla, Spain*

*P. A. Vázquez and A. Castellanos, Dpto. de Electrónica y Electromagnetismo, Facultad de Física, Avda. Reina Mercedes s/n, 41012 Sevilla, Spain*

# Particle dynamics simulation for supersonic heterogeneous flows around an obstacle

Vladimir V. Vinnikov Dmitry L. Reviznikov Andrew V. Sposobin
vvinnikov@list.ru

**Abstract**

This paper is concerned with numerical simulation of dispersed phase dynamics in supersonic dusty flows. Admixture equations are solved in Lagrangian variables due to staightforward handling of particle reflections from an obstacle. Two common approaches for particle simulation in path-following variables are discussed, namely: discrete trajectories method and discrete elements method respectively. Both methods yield particle concentrations and other required parameters for storage in arbitrary grids and further processing.

## 1 Introduction

Gas flows with dispersed admixture often occur in various physical processes and technical applications. Flow dynamics gains new qualities and shows new effects with the introduction of dispersed particles. New effects include compaction of a shock layer, intensification of convective heat flux to an obstacle surface, erosion of the exposed surface and screening effect, as well as radiative heat exchange between the obstacle surface and incoming particles. Almost every problem of two phase heterogeneous flows is quite complex and computationally expensive due to the difference of characteristic scales for carying and dispersed phases. There are two approaches to the numerical simulation of particle dynamics. The first one uses Eulerian description and treats admixture as continuous medium. The second one treats every particle in admixture independently and uses governing equations in Lagrangian variables. We use second approach, since it is more straintforward in simulation of consequent particle collisions with another particles and their reflections from the surface.

## 2 Discrete Trajectories and Discrete Element Methods

For given flow fields of carrying phase the dispersed phase dynamics is governed by partial differential equations in Lagrangian variables. Admixture particles are modeled as homogeneous isotermal hard spheres. The motion and heat transfer equations have the form:

$$m_p \frac{\mathrm{d}\mathbf{v}_p}{\mathrm{d}t} = \mathbf{f}_p, I_p \frac{\mathrm{d}\boldsymbol{\omega}_p}{\mathrm{d}t} = \mathbf{T}_\omega, c_{mp} m_p \frac{\mathrm{d}T_p}{\mathrm{d}t} = q_c + q_r$$

where $m_p$ is mass, $I_p$ – moment of inertia, $T_p$ – temperature, $\mathbf{v}_p$ – velocity, $\boldsymbol{\omega}_p$ – angular velocity, $c_{mp}$ – heat capacity of particle's material, $\mathbf{f}_p$, – external forces, $\mathbf{T}_\omega$ – torque, $q_c$ and $q_r$ – convective and radiative heat fluxes respectively. Integrating these eqiations one yields stream lines for the discrete trajectories method and individual particle trajectories

for the discrete element method. In the first method admixture propagates from inlow to outflow boundaries with constant concentration discharge rate along the stream lines. In the second method each computational particle travels independently and can participate in unsteady unique events, such as interparticle collisions.

The discrete element method is much more computationally consuming then its steady counterpart since it requires not just single particle per stream line, but regular inflow of particles to maintain the specified admixture volume concentration at the inlet. To simulate interparticle collisions on every computational step $\left[t^n; t^{n+1}\right]$ one constructs a trajectory approximation for each particle as the polynomial $\mathbf{r}(t) = \mathbf{r}_2 t^2 + \mathbf{r}_1 t + \mathbf{r}_0$. The condition for collision of pairs of particles $i$ and $j$ is expressed by the equation $\left|\mathbf{r}_i(t) - \mathbf{r}_j(t)\right|^2 = (r_{pi} + r_{pj})^2$, where $r_{pi}$, $r_{pj}$ are particles' radii.

## 3 Direct Collisions Simulation and Monte-Carlo method

The most accurate solution can be obtained by using an authors' full-scale version of the discrete element method [1], where each computational particle stands for a single real one. Parameters of paired interparticle encounters and collisions with an obstacle surface are computed using the above-said polynomial trajectory approximation. All particle impacts during one computational step $\left[t^n; t^{n+1}\right]$ are simulated sequentially in chronological order using the queue of collisions. Parameters for a pair of particles after collision as well as particle properties after reflection from a surface are calculated according to the model of hard spheres [3]. Processing of each collision event removes all subsequent encounters for this particle from the queue. Then one obtains particle parameters after collision at the instant $\tau \in (t^n; t^{n+1}]$, proceeds to integration of equations of movement and heat exchange on the interval $(\tau; t^{n+1}]$, approximates new trajectory and computes parameters for new collisions. Newly found encounters are placed in the global queue and treated in a consistent chronological order. It is necessary to put all collisions in the queue, not just the first one, since some of them, including early ones can be removed as not happened. This algorithm continues until the encounter queue is empty on the current computational step.

This approach allows to simulate complex heterogeneous flows with the best accuracy, including repeated mutual collisions of particles and their reflection from the obstacle surface. However, the implementation of this method involves considerable computational cost and parallelization is possible only for solving movement and heat equations. Collisions in the queue are handled sequentially and generally unsuitable for parallel processing. Therefore such numerical treatment of interparticle collisions is very computationally expensive.

There are means to decrease computational costs for interpaticle collisions and speed up simulation via some loss of spatial detalization for admixture. Two existing approaches are based on assumptions allowing to scale up particle dynamics from a single real particle to a group of them. Further simplification trades history of collisions for each computational particle on every timestep to random trials thus excluding unique deterministic trajectories and introducing stochastic averaged ones.

First approach to reduce the demands of discrete element mehod for computational resources is to represent every $F$ real particles by a single probe particle. The probe particle has physical characteristics of a single particle when solving the equations of motion and simulating interactions with other particles. One should take into consideration the factor $F$ for obtaining integral properties, such as an action of admixture on a carrier gas or an obstacle surface, or kinetic energy dissipation due to inelastic colli-

sions. To preserve the properties of the dispersed phase it is necessary to ensure that a probe particle has the same intensity of collisions along the trajectory, as a single real particle has. Therefore, the equation that determines the conditions of collision for a pair of probe particles is $\left|\mathbf{r}_i(t) - \mathbf{r}_j(t)\right|^2 = (r_{pi}\sqrt{F} + r_{pj}\sqrt{F})^2$. The results are the moments of time when a distance between centers of mass of the probe particles equals $r_{pi}\sqrt{F} + r_{pj}\sqrt{F}$. Parameters of particle pairs after collision are computed using a normalized vector defining the relative positions of the particles at the instance of the impact: $\mathbf{n}_{ij} = \left(r_{pi} + r_{pj}\right)\left(\mathbf{r}_j(\tau) - \mathbf{r}_i(\tau)\right)\left|\mathbf{r}_j(\tau) - \mathbf{r}_i(\tau)\right|^{-1}$

The distinctive feature of the direct collisions simulation algorithm is an essentially consequent way of processing the queue of collisions. Parallelization is straightforward to implement only for integration of equations of movement and heat exchange at each computational time step. At the same time the computational costs reduce nonlinearly at the stage of collisions simulation increasing the integration step expences in overall costs , which means the increase of parallelization efficiency for the problem solution in whole. Figure 1 shows plots of the computer time costs versus the factor $F$ for solving the problem in quasi-3D formulation. One can see that implementation of probe particles in combination with parallel computing reduces runtime up to a factor 10 while retaining the accuracy of full-scale solution (see Fig. 2). The problem was solved using PC based on Intel Xeon CPU with 4 cores.

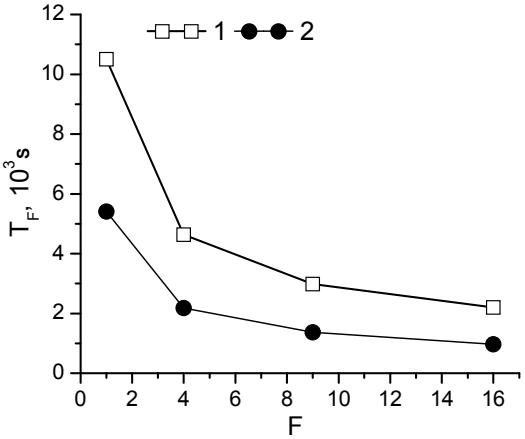


Figure 1: Runtime costs for the algorithms: 1 - successive, 2 - parallel

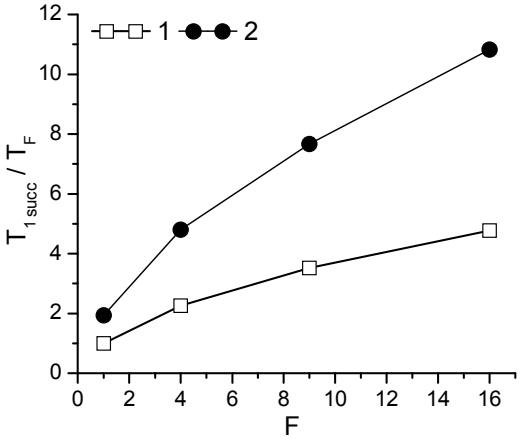


Figure 2: Runtime reduction for the algorithms: 1 - successive, 2 - parallel

Second approach to reduce computational costs is to use stochastic Direct Simulation Monte-Carlo methods (DSMC), e.g. [2]. In these methods particle dynamics on every timestep $\left[t^n; t^{n+1}\right]$ is simulated via consecutive advection and collision stages. On collision stage computational domain $U$ is split into nonintersecting cells $U = \bigcup_{m=1}^{M} U_m$. All particles contained in a one cell undergo statistical trials for possible collisions. A variety of Monte-Carlo methods is provided in [2, 4, 5]. We use one of the most popular variant of DSMC without time counter (No Time Counter, NTC) [2] with the following algorithm:

1. Compute the number of trials for collisions. $P_m = F\frac{N_m^n\left(N_n^m-1\right)}{2}\frac{\upsilon_{max}}{V_m}\left(t^{n+1} - t^n\right)$, where $\upsilon_{max} = \max_{i,j}\upsilon_{ij}$ for all particles $i$ and $j$ in the cell $U_m$, $\upsilon_{i,j} = \pi\left(r_{pi} - r_{pj}\right)^2\left|\mathbf{v}_i - \mathbf{v}_j\right|$, $r_p$ – particle radius, $\mathbf{v}$ – particle velocity, $N_n^m$ – number of particles in the cell, $V_m$ – cell volume, $F$ – ratio between real and computational particles.
2. Proceed trials $P_m$ times. On each trial select equiprobably a pair of particles $p_i$ and $p_j$ from cell $U_m$, then compute $\upsilon_{ij}$. Generate random number $\beta$, uniformly distributed

on $[0;1]$. If $\beta < \frac{v_{ij}}{v_{max}}$ then simulate a collision, otherwise proceed with next trial. In case of collision compute vector of relative positions $\mathbf{n}_{ij}$ and if particles are closing-in $\mathbf{n}_{ij}\left(\mathbf{v}_j - \mathbf{v}_i\right) < 0$ then change their parameters according to the model of collision.
There are several approaches to calculation of $\mathbf{n}_{ij}$ in literature:
1. Vector $\mathbf{n}_{ij}$ connects particles mass centers $\mathbf{n}_{ij} = \left(r_{pi} + r_{pj}\right)\frac{\mathbf{r}_j - \mathbf{r}_i}{|\mathbf{r}_j - \mathbf{r}_i|}$.
2. Vector direction is randomly uniformly distributed in space:
$\mathbf{n}_{ij} = \left(r_{pi} + r_{pj}\right)(\mathbf{i}\cos\chi + \mathbf{j}\sin\chi\cos\epsilon + \mathbf{k}\sin\chi\sin\epsilon)$, where $\cos\chi = 2\beta - 1$, $\sin\chi = \sqrt{1-\cos^2\chi}$, $\epsilon = 2\pi\alpha$, $\alpha$ and $\beta$ are uniformly distributed on $[0;1]$.
3. Projection $\mathbf{b}$ of vector $\mathbf{n}_{ij}$ on the plane orthogonal to relative velocity vector $\mathbf{v}_j - \mathbf{v}_i$ is distributed on $\left[0; r_{pi} + r_{pj}\right]$ proportionally $|\mathbf{b}|$ [2]:
$\mathbf{n}_{ij} = \left(r_{pi} + r_{pj}\right)\left(\mathbf{i}''\cos\chi + \mathbf{j}''\sin\chi\cos\epsilon + \mathbf{k}''\sin\chi\sin\epsilon\right)$, where $\cos\chi = \sqrt{\beta}$, $\sin\chi = \sqrt{1-\cos^2\chi}$, $\epsilon = 2\pi\alpha$, $\alpha$ and $\beta$ are uniformly distributed on $[0;1]$. Coordinate system $0x''y''z''$ is yielded by rotation of initial system $0xyz$, so that axis $0x''$ becomes collinear with vector of relative velocity : $i'' = \frac{\mathbf{v}_j - \mathbf{v}_i}{|\mathbf{v}_j - \mathbf{v}_i|}$

The DSMC variants are quite feasible for molecular dynamics simulation; however in case when gradients of particles concentration are large, statistical methods suffer from a loss of accuracy.

## 4 Results and Discussion

First, we consider a computational experiment for chaoticaly moving particles without carrying gas phase. At initial moment computational domain is filled with monosized particles uniformly distributed in space. Their velocity lengths are equal, and velocity directions are distributed uniformly. Domain has periodical boundary conditions. In general case particle collisions are inelastic. Distributions of collisions number against angle are shown on Fig. 3. This angle is the angle between vector of relative velocity and vector connecting particle mass centers at an instant of collision. First and second variants for vector $\mathbf{n}_{ij}$ yield similar results, yet they have qualitative differences from solutions, obtained by precise simulation and DSMC with the third variant of relative position vector $\mathbf{n}_{ij}$. The collisions number $N_a$ is non-dimentionalized by the number of particles entering computational domain through unit of surface per unit of time $N_s$. Dissipation of kinetic energy $E_{Kdisp}$ is scaled to summary kinetic energy of particles at the inflow $E_{K0}$ (Fig. 4).

Next we consider a problem of supersonic heterogeneous flow over a sphere. Gas phase is governed by a system of modified Euler equations. Gasdynamics equations are integrated numerically via HLL scheme. Boundary conditions for a solid curvilinear surface are approximated according to the ghost-cell immersed boundary method on rectangular grids. Parameters of a gas phase represent the atmospheric conditions at 10 km; Mach number $M_\infty = 6$. Admixture is represented by particles 10 $\mu m$ in diameter of aluminum dioxide $Al_2O_3$. Volume concentration for admixture is $C_{V0} = 10^4$. Sphere radius is 3 cm. It's necessary to note that regardless of axial symmetry for carrying gas flow, admixture simulation should be proceeded in three dimentions. To reduce computational costs for the full-scale discrete element method we used probe particles with various values of factor $F$.

Figures 5-7 show dynamical and energetical impact of admixture on the sphere surface in the case of inelastic interparticle collisions. Velocity restitution coefficient for hard spheres model was defined equal to 0.5. One can see that DSMC yields lower intensity of particle-surface collisions and, correspondingly, higher averaged particle normal velocity at the moment of collision with the surface (see Fig 5-6). Intensity of collisions is related to

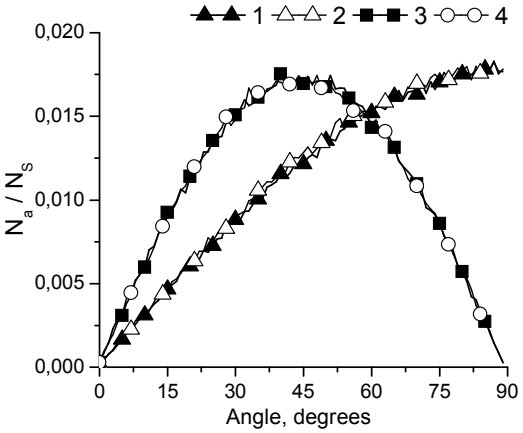


Figure 3: Distribution of collisions number vs. angle between vector of relative velocity and vector connecting particle mass centers at an instant of collision. 1-3 – DSMC, 4 – reference simulation by the full-scale discrete element method.

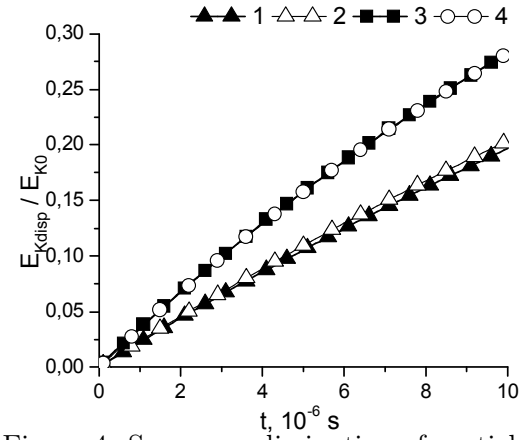


Figure 4: Summary dissipation of particles kinetic energy due to inelastic collisions. 1-3 – DSMC, 4 – reference simulation by the full-scale discrete element method.

intensity of inflow particles $I_\infty$ and averaged normal velocity $V_N$ is scaled to particle free streem velocity $V_\infty$.

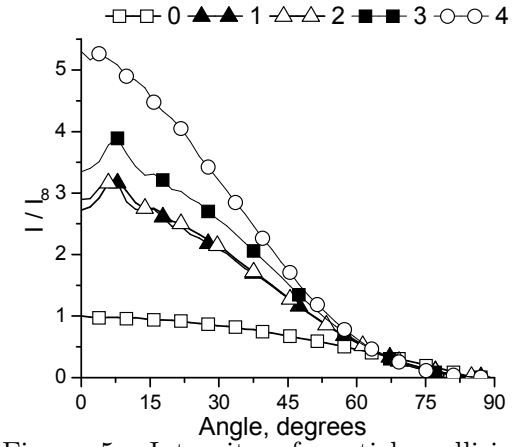


Figure 5: Intensity of particle collisions with the sphere surface. 0 – Discrete trajectory method without interparticle collisions, 1-3 – DSMC, 4 – reference simulation by the full-scale discrete element method.

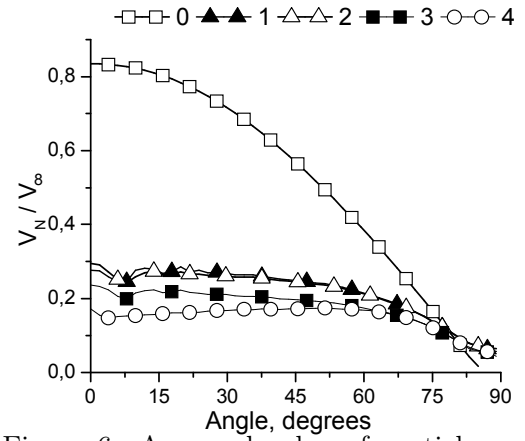


Figure 6: Averaged value of particle normal velocity at an instant of collision with the sphere surface. 0 – Discrete trajectory method without interparticle collisions, 1-3 – DSMC, 4 – reference simulation by the full-scale discrete element method.

The screening effect can be observed. It arises due to some kinetic energy dissipation for incident particles colliding with reflected ones and leads to lower impact of admixture on the surface. First and second variants for $\mathbf{n}_{ij}$ in DSMC give less intensive kinetic dissipation (see Fig. 4), what leads to underestimation of the screening effect compared to the reference results of the full-scale discrete element method. Third variant of $\mathbf{n}_{ij}$ is in close agreement with the accurate solution (see Fig. 7). The main drawback of all Monte-Carlo methods is that they prone to underestimate the number of subsequent collisions in the areas with strong macroscopic gradients of admixture concentration (Fig. 8) and

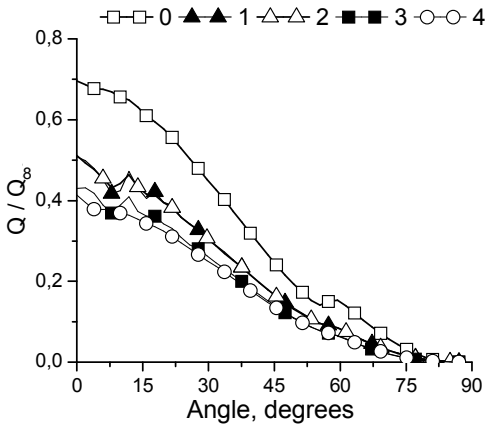


Figure 7: Energy flux density from admixutre to the surface of the sphere. 1-3 – DSMC, 4 – reference simulation by the full-scale discrete element method.

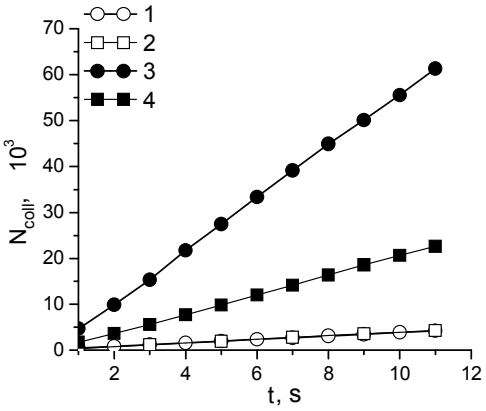


Figure 8: Summary number of interparticle collisions. 1, 2 – away from the surface ($d > 0.02R$), 3, 4 – in the vicinity of the surface ($d <= 0.02R$). 2, 4 – DSMC, 1, 3 – reference simulation by the full-scale discrete element method. Here $d$ – distance from particle to the obstacle surface, $R$ – sphere radius.

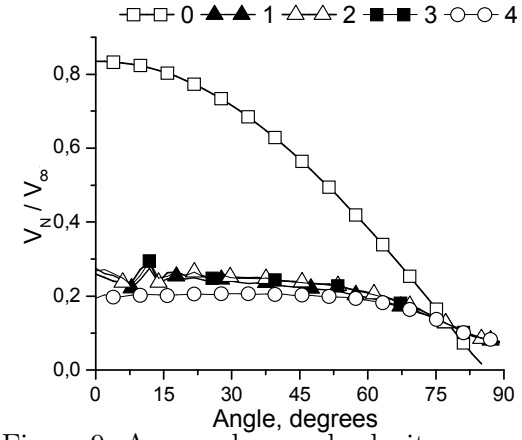


Figure 9: Averaged normal velocity component for a particle at an instant of collision with the surface. 0 – Collisionless simulation, 1-3 – DSMC, 4 – reference simulation by the full-scale discrete element method. Iinterparticle collisions are absolutely elastic.

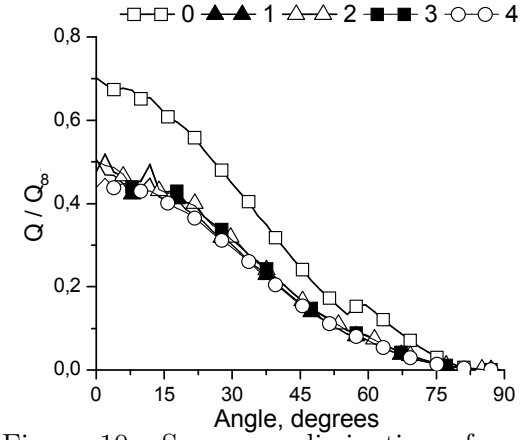


Figure 10: Summary dissipation of particles kinetic energy due to inelastic collisions. 1-3 – DSMC, 4 – reference simulation by full-scale discrete element method. Iinterparticle collisions are absolutely elastic.

so misrepresent dynamic action of admixture on the surface (see Fig. 5,6). Regardless of these numerical qualities the intergral parameters such as energy flux density (Fig. 7) yielded by the third DSMC method are quite accurate. It can be explained by the fact that the maximum energy dissipation occurs for the first collisions at high relative velocities. Represented energy flux density is scaled to $Q_\infty$ – energy flux density for free stream particles.

Similar computations were carried out for a case of absolutely elastic interparticle collisions.The plots for dynamical and energy impact of admixture on a surface are shown on Fig. 9-10. One can see that the diferences between various DSMC methods are nearly

vanish, since there is no kinetic energy dissipation in such collisions. In this case the screening effect arises only due to change of velocity direction for incident particles colliding with reflected ones.

## Conclusions

Two approaches to numerical simulation of collisional dynamics of dispersed admixture in heterogeneous flows are discussed, namely direct full-scale discrete element numerical simulation and statistical Monte-Carlo simulation. Implementation of probe particles in the discrete element method significantly extends application area by reducing demands for computer memory and runtime allowing to implement parallel computing algorithms. Therefore modifications of discrete-element method make numerical simulation of three-dimensional dusty flows past an obstacle quite plausible. It is shown that the DSMC method used for the problem of heterogeneous flow over the obstacle yields correct and accurate integral parameters of admixture impact on the surface such as particles energy flux density to the obstacle.

## Acknowledgements

*The work is supported by RFBR grant No 12-08-00867 and President's grant for support for young Russian scientists MK-179.2011.8.*

## References

[1] Reviznikov D.L. and Sposobin A.V. Direct numerical modeling of disperse phase flow of gas-particle mixture over a body [in Russian]// e-journal "Trudy MAI", 2007, No.26, 13 p.

[2] Bird G. A. Molecular Gas Dynamics and the Direct Simulation of Gas Flows. // New York, Oxford, Claredon Press, 1994, 476 p.

[3] Crowe C.T., Sommerfeld M. and Tsuji Y. Multiphase flows with droplets and particles. CRC Press LLC, 1998, 471 p.

[4] Bird G. A. Sophisticated DSMC. // Proceedings of the Notes from a short course held at the DSMC07 Conference, Santa Fe, USA, 2007.

[5] Volkov A.N., Tsirkunov Yu.M. CFD / Monte Carlo simulation of collision-dominated gas-particle flows over bodies. // Proceedings of ASME 2002 Fluids Engineering Division Summer Meeting, Montreal, Quebec, Canada, July 14-18, 2002.

[6] Mikhatulin D.S., Polezhaev Yu.V., Reviznikov D.L. Heat exchange and destruction of bodies in supersonic heterogeneous flows. [in Russian]. Moscow, Janus-K, 2007, 392 p.

[7] Vinnikov, V. and Reviznikov, D. and Sposobin, A. Two-phase shock layer in a supersonic dusty gas flow // Mathematical Models and Computer Simulations, 2010, Vol. 2, No. 4, pp. 514–525.

*Vladimir V. Vinnikov, Moscow Aviation Institute, Volokolamskoe sh. 4, 125993, Moscow, Russia*
*Dmitry L. Reviznikov, Moscow Aviation Institute, Volokolamskoe sh. 4, 125993, Moscow, Russia*
*Andrew V. Sposobin, Moscow Aviation Institute, Volokolamskoe sh. 4, 125993, Moscow, Russia*

# Convection and heat transfer in liquid with internal heat release in a rotating horizontal cylinder

Alexey A. Vjatkin vjatkin_aa@pspu.ru
Victor G. Kozlov kozlov@pspu.ru
Rustam R. Sabirov sabirov@pspu.ru

**Abstract**

The convection of heat-generating fluid in a rotating horizontal cylinder is experimentally investigated. The thresholds of thermal convection excitation, heat transfer in the cylinder and the structure of convective flows depending on the heat capacity, viscosity and relative length of the cavity are studied. Different modes of convection are revealed. In case of relatively rapid rotation due to the centrifugal force of inertia the temperature distribution is axially symmetric and has a maximum in the center of the cavity. The heat transfer, additional to the molecular one, in this case is provided by the inertial waves and the Ekman flows near the end walls of the cavity. With decrease of rotation velocity the convective flow arises in a threshold way in the form of vortex cells periodically arranged along the axis. The excitation of mean convection is caused by the action of termovibrational mechanism. In overcritical domain the stationary vortex regime is replaced by the oscillatory one (the fluctuations are associated with the periodic variation of the convective structures). For very slow rotation the quasi-stationary gravitational mechanism predominates.

## 1 Introduction

During the experiment a cylinder filled with a viscous heat-generating fluid rotates around its horizontal axis in a gravity field. The outer wall of the cylinder is isothermal, its temperature is maintained constant. In the cavity frame the gravity field oscillates. The frequency of oscillations coincides with the frequency of rotation. The averaged convection is caused by the nonisothermal liquid oscillations relative to the cavity caused by the gravity. This "vibrational" mechanism of averaged convection has been theoretically described in [1]. It is also shown that in case of liquid with internal heat release the averaged convection in the cavity rotating around a horizontal axis is characterized by a centrifugal Rayleigh number $Ra = \Omega^2 R^6 \beta q / \nu \chi^2 c_p \rho$, vibrational parameter $R_v = (g\beta R^3 q)^2 / 2\nu\chi^3 c_p^2 \rho^2 \Omega^2$ and dimensionless velocity of rotation $\omega = \Omega R^2/\nu$. Here $\beta$, $\nu$ and $\chi$ - coefficients of thermal expansion, kinematic viscosity and thermal diffusivity of fluid, $c_p$ - specific heat of fluid at constant pressure, $\rho$ - fluid density, $R$ - radius of the cylinder, $q$ - volumetric power of internal heat sources, $\Omega \equiv 2\pi n$ - angular velocity of rotation ($n$ - rotational speed of the cavity). The various problems of termovibrational convection in rotating cavities were investigated in [2] [3].

## 2 Experimental setup and technique

The cavity (Fig. 1) is made of a Plexiglas cylinder *1* with flanges *2* on both end sides. The length of the working part of the cell $l = 170$ mm, the internal diameter $d = 36$ or 44

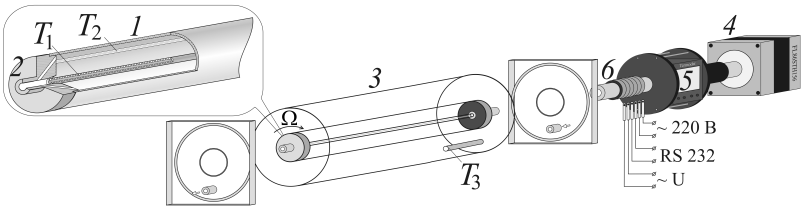


Figure 1: The sketch of the cavity.

mm. The water and glycerol-water solutions of different concentrations are used as working fluids. The internal heat generation is produced by the alternating electric current passing through the liquid. The flanges are equipped with the copper electrodes and the liquid is added with copper sulfate (not more than 5 proc.) for conductivity. The temperature in the cavity is measured with RTDs. The sensor $T_1$ is located on the axis of the cavity, $T_2$ - on the cylindrical wall. Both thermometers are made of copper wire and extend along the entire cell length, thus measuring the average temperature along the cell.

To provide the constant temperature of the external wall of the cell the last is placed in a Plexiglas cylinder *3* of a larger diameter, which is also closed with flanges. The water of desired temperature from the thermostat is pumped in the space between the walls of the cylinders. One more sensor T3 controls the temperature of liquid in this water shirt. Due to the system of bearings and seals the working cell can rotate freely. The rotation is given by the stepper motor *4*, the rate ranged from 0.01 to 2.00 revolutions per second.

The sensors data is processed by the Termodat device *5* which rotates with the cavity and transmits the signal to the computer. The connection to the computer is carried out with a multichannel electrical collector *6*. The collector is also used for providing the Termodat with power and internal heating of liquid in the cavity. The walls of the cell are transparent, which allows the visual observation and photography of convective structures. In experiments with photo recording the small amount of light scattering particles of Resine Amberlite is added in liquid. The particles diameter is 50 microns, the density is about the liquid density. The photos are made from the side of the cylinder. The longitudinal vertical light knife is used for illumination. The experiment starts with the relatively rapid cell rotation, electrical current is passed through the liquid. The measurements start after establishing of a stationary temperature distribution in the cavity. During the experiment the rotational velocity of the cylinder is reduced step by step.

## 3 Results of experiment

The rotation of the cavity around the axis of symmetry produces an axisymmetric field of the centrifugal forces of inertia $\rho\Omega^2\mathbf{r}$. In this case the temperature distribution $\Theta_0 = q(R^2 - r^2)/4\lambda$ corresponds to a stable equilibrium state of the liquid. Here $q$ - volumetric power of internal heat sources, $\lambda$ - coefficient of thermal conductivity, $r$ - distance from the axis of the cavity. This equation allows to determine the temperature at the center of the cavity relative to the wall $\Theta^{'} = qR^2/4\lambda$. At the beginning of the experiment the temperature in the center of the cavity is higher than the temperature at the cylindrical boundary, which leads to the nonuniformity of the thermophysical properties of fluids. It should be noted that when analyzing the experimental results all parameters are calculated

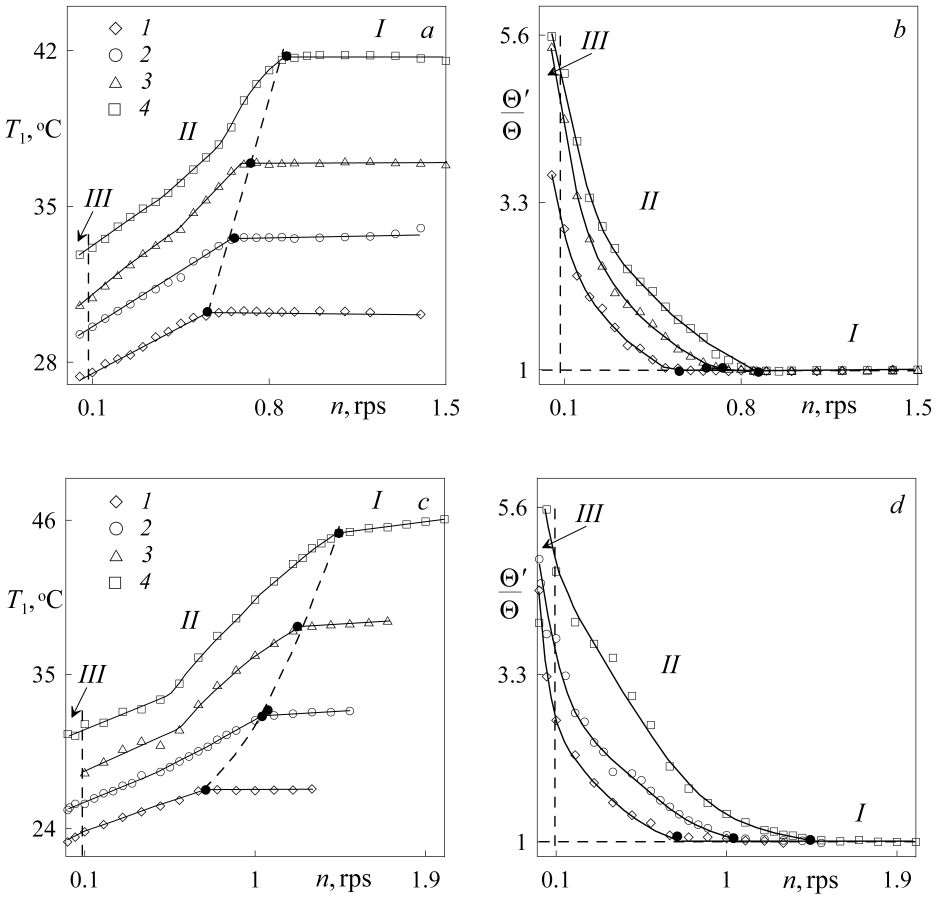


Figure 2: Temperature $T_1$ and dimensionless parameter $\Theta'/\Theta$ versus the speed of rotation; *a*, *b* - water, $R = 1.8$ cm, $q = 0.034$ (*1*), 0.050 (*2*), 0.063 (*3*) and 0.065 W/cm$^3$ (*4*); *c*, *d* - $C = 50$ %, $R = 1.8$ cm, $q = 0.030$ (*1*), 0.051 (*2*), 0.076 (*3*) and 0.103 W/cm$^3$ (*4*).

using the average temperature in the cavity.

The temperature $T_1$ variation with $n$ in liquids of different viscosities are presented in (Fig. 2, *a* and *c*). The curves of heat transfer corresponding to these experiments are shown in (Fig. 2, *b* and *d*). A dimensionless parameter chosen to characterize the heat transfer is $\Theta'/\Theta$, here $\Theta = T_2 - T_1$ - the experimental value of the fluid temperature at the cavity axis relative to the cylindrical wall. One can see a slight change in temperature $T_1$ with a decrease in speed (field *I*). With increasing the viscosity of liquid and its internal heating this change becomes more significant. In this case the temperatures $\Theta$ and $\Theta'$ are consistent only in the limit of high rotation speed. The flow visualization demonstrates that with the relatively rapid rotation when the heat transfer in the cavity nearly corresponds to the molecular one and the vortical structures in the volume of the cavity are absent, the powder settles on the inner wall of the cavity into thin rings (Fig. 3, *a*). As it will be shown below this is caused by slow averaged currents that are generated by an inertial wave that occurs near the ends of the cavity [4]. In experiments with a viscous fluid the rotation speed reduction leads to a greater increase in heat transfer. It is indicated by the decrease of the temperature $T_1$ (Fig. 2, *c* and *d*).

With further decreasing the velocity of rotation one observes the change in the regime

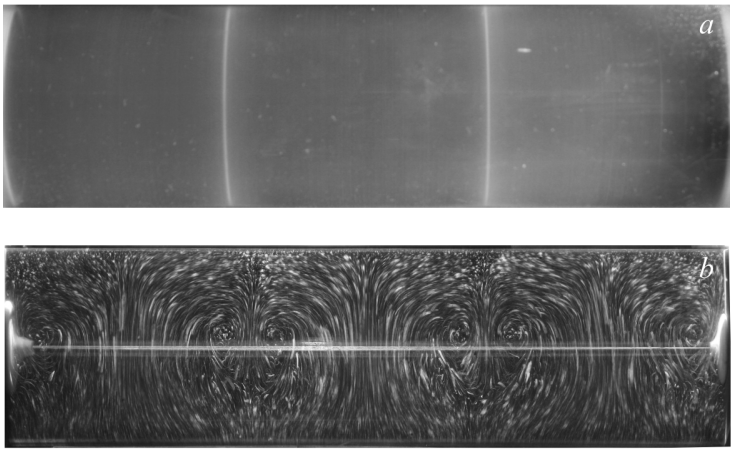


Figure 3: Pictures of structures: water, $R = 1.8$ cm, $q = 0.063$ W/cm$^3$, $n = 1.1$ ($a$) and 0.55 rps ($b$).

of convection, which is accompanied with a critical change in heat transfer (Fig. 2, the boundary of areas $I$ and $II$). The observations show that the critical temperature change is associated with the appearance of the periodic system of vortex cells (Fig. 3, $b$). The excitation of the convection is associated with the action of thermovibrational mechanism which is based on the fluctuations of non-isothermal fluid with respect to the cavity caused by the gravity force [1]. The picture shows the overcritical structure of convection, as the flows near the threshold are weak and their visualization is problematic. The structure of the currents in liquids of different viscosity is the same.

Experiments with water in the cell of larger radius show that the reduction in speed also leads to a crisis of heat transfer (Fig. 4, the boundary of areas $I$ and $II$). When the volumetric power of heat sources is relatively large the averaged convection looks like a system of vortex cells (Fig. 5) as in the experiments with the cavity of smaller radius. Another behavior is observed with decreasing of the rate of heating: one can see two critical transitions in heat transfer (Fig. 4, shaded area). In this range of values of $n$ the variation curves of heat transfer is different from other areas. It was problematic to determine the convective structures in this domain.

With further decrease of rotation speed the different modes of convection are observed. The order of regime change does not depend on the radius of the cell and fluid viscosity. The stationary vortex convection regime is replaced by the oscillatory one. In experiments with the liquids of relatively low viscosity the regular low-frequency oscillations of the temperature $T_1$ are detected. The observations show that these fluctuations are associated with shifts in convective flows, the vortexes develop and decay periodically. In the liquids of higher viscosity the structures also change periodically but their complete destruction does not occur and the temperature sensor in the center of the cavity captures the oscillations of low intensity.

For very slow rotation (Fig. 2, 4, the boundary of areas $II$ and $III$) the sensor detects oscillations of temperature $T_2$. The period of oscillation is equal to the period of rotation of the cavity and the amplitude reaches a few degrees at a very slow rotation. This indicates

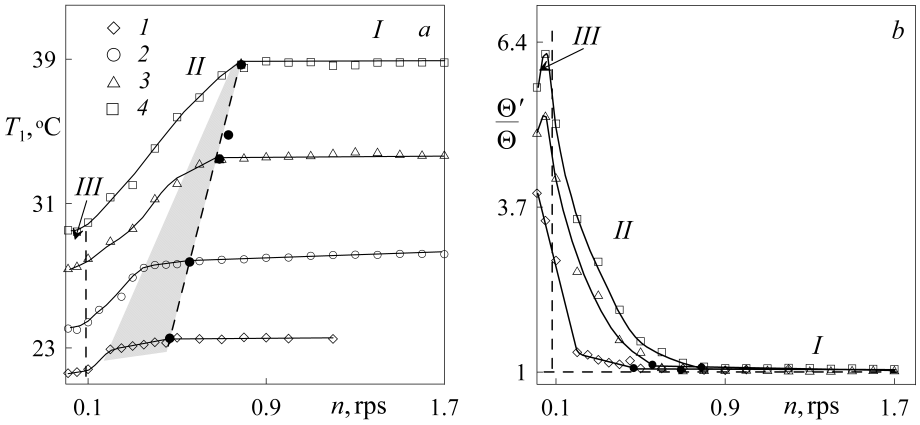


Figure 4: Temperature $T_1$ and dimensionless parameter $\Theta'/\Theta$ versus the rotation velocity; *a*, *b* - water, $R = 2.2$ cm, $q = 0.016$ (*1*), 0.030 (*2*), 0.050 (*3*) and 0.061 W/cm$^3$ (*4*).

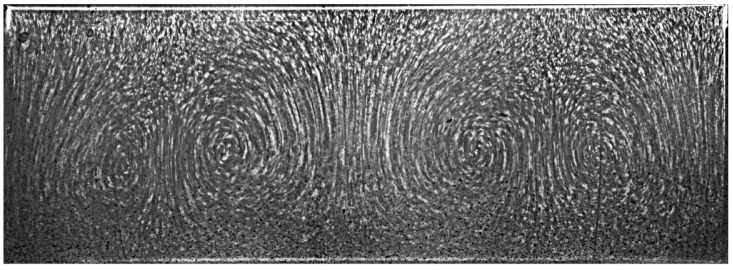

Figure 5: Photo of convective flows: water, $R = 2.2$ cm, $q = 0.065$ W/cm$^3$, $n = 0.5$ rps.

the predominance of the quasi-stationary gravitational mechanism of convection.

With increase of the heat release and temperature $\Theta$ the velocity of rotation corresponding to the threshold of convection excitation increases monotonically (Fig. 6). The instability areas are below the threshold curves (shaded). With increasing of the viscosity the threshold curves are shifted to the higher values of $n$.

## 4 Discussion of results

Consider the possible mechanism of formation of ring structures at large $n$. The rotation of the cavity filled with a nonuniformly heated fluid in a static external force field (gravitational in our case) results in fluctuations of the liquid relative to the cavity. In a rotating and simultaneously oscillating fluid the inertial waves can be excited [4]. Characteristic surfaces with intensive shear flows are specific for them. The angle between the characteristic surfaces and the axis of rotation is defined by the condition $\tan\varphi = (4/N - 1)^{-1/2}$. Here $N \equiv \Omega_{osc}/\Omega$ - dimensionless frequency of liquid oscillation ($\Omega_{osc}$ - radian frequency of liquid oscillation, $\Omega = 2\pi n$ - angular velocity of the cavity). In our case the fluctuations of fluid in the cavity frame occur with a frequency of rotation, that is $N = 1$. Thus, the tangent of the angle does not depend on the cell radius $R$ and equals to $1/\sqrt{3}$. The di-

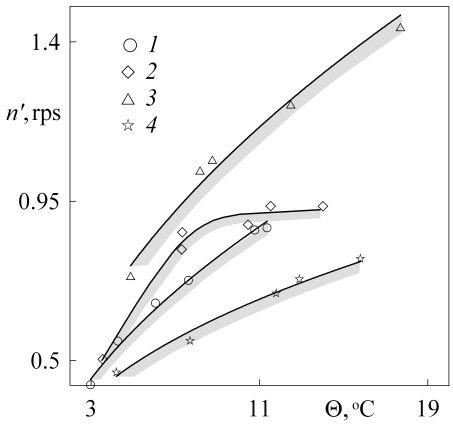


Figure 6: The dependency of the critical velocity on the temperature $\Theta$. $R = 1.8$ cm, water (*1*), $C = 25$ (*2*) и 50 % (*3*); $R = 2.2$ cm, water (*4*).

mensionless spatial period $\Lambda/R$ is $4\sqrt{3}$. Fig. 7 shows photographs of structures and the possible location of the characteristic surfaces (dashed lines). One can see that the characteristic surfaces determine the position of the rings on the cavity wall. The theoretical value $\Lambda/R$ agrees well with the experiment. The characteristic surface of excited wave is a cone. Liquid oscillates along the cone. Averaged flow leading to a redistribution of powder on the surface could be generated in the Stokes boundary layers by wave reflection from the cavity wall. In a thin cell (Fig. 7, *a*) the waves from the opposite ends of the cavity reflect from the walls being spatially coherent, so the structures they form are regular. In the cell of bigger radius (Fig. 7, *b*) such agreement is absent: the powder forms two rings at the lines of intersection of the characteristic surfaces of the opposing waves with the boundary of the cavity.

With the rapid rotation a weak radial motion of the fluid can also be generated in the viscous Ekman layers occurring near the end walls of the cylinder in the presence of differential azimuthal rotation of the fluid [4]. Thus the equilibrium state of the liquid subject to the rapid rotation may be disturbed by inertial waves and Ekman flows. This could explain the difference between the temperature field in the cavity from the case of rigid-body rotation of the entire system (Fig. 2 and 4).

In Fig. 8 (*a*) the threshold curves of the convection excitation are presented on the plane $Ra$,$R_v$. The area of quasi-equilibrium is marked by hatching. The points obtained for water and glycerin solution of a low concentration of 25 and 35 % agree with each other. With viscosity increase the noticeable discrepancy between the curves appears. This could be explained by the influence of the Coriolis force which is characterized by the dimensionless rotational speed $\omega$. It is known that the Coriolis force has a stabilizing effect on the three-dimensional vortex structures both in gravity [5] and vibrational [2] convection. Only in the case of two-dimensional vortices oriented parallel to the axis of rotation the Coriolis force has no effect. In this case the dependence on the dimensionless frequency is absent, as in [3]. Fig. 8 (*b*) shows the threshold values of vibration parameters $R_v$ versus the dimensionless velocity at a definite value of the centrifugal Rayleigh number $Ra = -4 \cdot 10^4$ (dashed line in Fig. 8, *a*). At large $\omega$ (experiments with water) the threshold of thermovibrational convection excitation (critical value of $R_v$) does not depend on the $\omega$. It can be assumed that the convective structures in the threshold are termovibrational

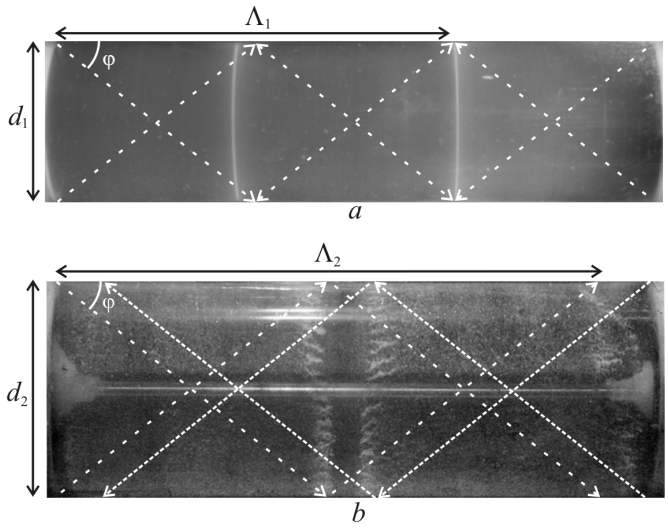


Figure 7: Photos of structures: water, *a* - $R = 1.8$ cm, $q = 0.063$ W/cm$^3$, $n = 1.1$ rps; *b* - $R = 2.2$ cm, $q = 0.065$ W/cm$^3$, $n = 1.5$ rps.

rolls elongated along the axis of rotation, similar to ones found in another problem [1].

## 5 Conclusion

Thermovibrational convection of heat-generating fluid in a horizontal cylinder with rotation is investigated experimentally. The effect of viscosity on the threshold of convection is studied. Heat transfer and the structure of convective flows at different regimes of convection are considered. It is shown that the threshold of the onset of convection is determined

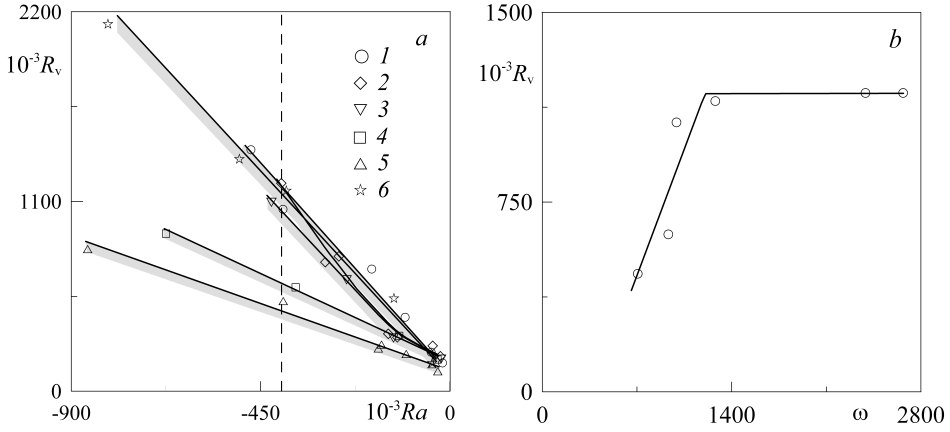


Figure 8: *a* - threshold curves in the plane of control parameters $Ra$,$R_v$; $R = 1.8$ cm, water (*1*), $C = 25$ (*2*) 35 (*3*), 40 (*4*) and 50 % (*5*); $R = 2.2$ cm, water (*6*); *b* - the critical vibrational parameter $R_v$ versus the dimensionless rotation velocity $\omega$ at $Ra = -4{\cdot}10^4$.

by the parameters $Ra$,$R_v$, and dimensionless speed of rotation.

## Acknowledgements

*The work is supported by Russian Foundation for Basic Research.*

## References

[1] Kozlov V.G. Thermal vibrational convection in rotating cavities // Fluid Dynamics. 2004. V. 39. N 1. P. 3-11.

[2] Ivanova A.A., Kozlov V.G., Rylova V.V. Thermal convection in a plane layer rotating about a horizontal axis // Fluid Dynamics. 2003. V. 38. N 1. P. 9-17.

[3] Vjatkin A.A., Ivanova A.A., Kozlov V.G. Convective stability of a nonisothermal fluid in a rotating horizontal coaxial gap // Fluid Dynamics. 2010. V. 45. N 1. P. 10-18.

[4] Greenspan H.P. The Theory of Rotating Fluids. Cambridge University Press, New York, 1968. 328 pp.

[5] 5. Gershuni G.Z., Zhukhovitsky E.M. Convective stability of incompressible liquid. M.: Nauka, 1972. 392 p. (Translated in English: Keter Publishing House Jerusalem Ltd., Jerusalem 1976).

*Victor G. Kozlov, Perm State Pedagogical University, Russia*
*Alexey A. Vjatkin, Perm State Pedagogical University, Russia*
*Rustam R. Sabirov, Perm State Pedagogical University, Russia*

# Vibrational motion of the cavity filled with perfect viscous gas

Anna V. Yakovenko Pavel T. Zubkov
pzubkov@utmn.ru

**Abstract**

The mathematical model of the vibrational motion of the cavity filled with viscous gas is defined. The numerical investigation of the heat and mass transfer processes in the cavity as a result of vibrations is performed. The maximum values of temperature and pressure of the gas on the walls of the cavity depending on the frequency of vibration were found. The cavity is filled by perfect viscous gas with air characteristics. The case is considered in a one-dimensional setting. The gas characteristics were chosen like the air characteristics.

## 1 Introduction. Problem formulation

As the technological expansion, people are more and more contact with the phenomena of vibration. Almost all machines are susceptible to mechanical vibrations in a varying degree. Even with a free flight of the spacecraft there is vibration from the operating equipment [1]. Vibration of machines may be a cause of abnormal operation of machinery and cause serious accidents. It is quite common to situations where there are cracks, pores or voids filled with air. Therefore, it is important to study gas influence to the boundaries of the cavity. We will numerically investigate the effects of the vibrating action with a constant frequency on the rectangular cavity filled with a viscous perfect gas. Due to the medium compressibility there is a forming of acoustic waves, which reinforce the heat and mass transfer. There are two frequencies: the natural frequency of the system and the oscillation frequency caused by the boundary conditions [2]. Specifying high-frequency vibration leads to appearance of shock waves. It is useful to determine the intensity of the impact of the waves on the boundary to avoid possible destructions of the product. Using this data (maximum pressure and maximum temperature near the boundary) we may calculate the maximum frequency of vibration for the other given characteristics.

## 2 Mathematical model

The cavity of length L filled with a viscous perfect gas with thermal properties of air is considered. At the initial moment the gas in the cavity stayed at rest with a constant temperature $T_0$ and a constant pressure $P_0$. The equilibrium state is disbalanced due to the vibrational effects of amplitude $A$ and frequency $\omega$. In the beginning the cavity was in the extreme right position. The boundaries are kept in temperature equal with the initial temperature. The thermal conductivity, the dynamic viscosity and the heat capacity are assumed to be constant.

The motion of the gas under these assumptions is described with the one-dimensional nonstationary system of equation in Cartesian coordinates, consisting of conservation laws of mass, momentum and energy. The Clapeyron ideal gas law is considered as the equation of state for gas. The system is written in the noninertial frame of reference associated with the vibrating cavity. Use the following formulas for the transition:

$$t = t', \tag{1}$$

$$x = x' - A\cos(\omega t), \tag{2}$$

$$u = \frac{\partial x}{\partial t} = u' + A\omega\sin(\omega t) \tag{3}$$

Here, $t$ is time in the noninertial frame of reference, $x$ is coordinate in the noninertial frame of reference, $u$ is the velocity in the noninertial frame of reference, $t'$ is time in the inertial frame of reference, $x'$ is coordinate in the inertial frame of reference, $u'$ is the velocity in the inertial frame of reference.

The system of dimensionless equations describing motion of such gas has the form

$$\frac{\partial\tilde{\rho}}{\partial\tau} + \frac{\partial\tilde{\rho}\tilde{u}}{\partial X} = 0, \tag{4}$$

$$\frac{\partial\tilde{\rho}\tilde{u}}{\partial\tau} + \frac{\partial\tilde{\rho}\tilde{u}\tilde{u}}{\partial X} = -\frac{\partial\tilde{P}}{\partial X} + \frac{4}{3}\frac{1}{Re}\frac{\partial^2\tilde{u}}{\partial X^2} + \tilde{\rho}A\Omega^2\cos(\Omega\tau), \tag{5}$$

$$\frac{\partial\tilde{\rho}\Theta}{\partial\tau} + \frac{\partial\tilde{\rho}\tilde{u}\Theta}{\partial X} = \frac{\gamma}{Pe}\frac{\partial^2\Theta}{\partial X^2} - \tilde{P}\frac{\partial\tilde{u}}{\partial X} + \frac{4}{3}\frac{1}{Re}(\frac{\partial\tilde{u}}{\partial X})^2, \tag{6}$$

$$\tilde{P} = \frac{\tilde{\rho}(\Theta+1)}{\gamma}, \tag{7}$$

The dimensionless variables are taken as:

$$X = \frac{x}{L},\ \tau = \frac{t\sqrt{\gamma RT_0}}{L},\ \tilde{u} = \frac{u}{\sqrt{\gamma RT_0}},\ \tilde{P} = \frac{P}{\gamma P_0},\ \tilde{\rho} = \frac{\rho}{\rho_0},\ \Theta = \frac{T-T_0}{T_0},$$

Dimensionless parameters:
$Re = \frac{\rho_0 L\sqrt{\gamma RT_0}}{\mu}$ - acoustical Reynolds number
$Pe = \frac{\rho_0 L c_p\sqrt{\gamma RT_0}}{k}$ - Peclet number
$\gamma = \frac{c_p}{c_v}$ - adiabatic exponent
$\Omega = \frac{\omega L}{\sqrt{\gamma RT_0}}$ - nondimensional vibration frequency
$\tilde{A} = \frac{A}{L}$ - nondimensional vibration amplitude
$\sqrt{\gamma RT_0}$ is adiabatic speed of sound in the region of the temperature $T_0$.

Here, $\rho$ is the density, $P$ is the pressure, $T$ is the temperature, $R$ is the gas constant, $\mu$ is the coefficient of dynamic viscosity, $k$ is the thermal conductivity coefficient and $c_v$ is the specific heat capacity at constant volume.

The initial conditions are as follows:

$$\tilde{u}|_{\tau=0} = 0, \Theta|_{\tau=0} = 0, \tilde{P}|_{\tau=0} = \frac{1}{\gamma}, \tilde{\rho}|_{\tau=0} = 1 \tag{8}$$

The boundary conditions are as follows:

$$\Theta|_{X=0} = 0, \tilde{u}|_{X=0} = 0, \Theta|_{X=1} = 0, \tilde{u}|_{X=1} = 0 \tag{9}$$

## 3 Parameters of calculation and numerical scheme

The main positions of the numerical method will be described here. In obtaining a numerical solution, we choose a number of locations (n grid points) and seek the solution there. The differential equations (4)-(7) with (8), (9) are solved by converting them into discretization equations (algebraic equations). The discretization equations are obtained by the control volume approach and the second-order treatment of the numerical scheme [3]. The system (4)-(7) is written as:

$$a_\Phi \Phi_i = b_\Phi \Phi_{i+1} + c_\Phi \Phi_{i-1} + d_\Phi \tag{10}$$

$$\tilde{\rho}_i = \tilde{\rho}_i(\Phi_i) \tag{11}$$

$$a_\Theta \Theta_i = b_\Theta \Theta_{i+1} + c_\Theta \Theta_{i-1} + d_\Theta \tag{12}$$

$$\tilde{P}_i = \tilde{P}_i(\Theta_i) \tag{13}$$

where

$$\Phi_i = \tilde{\rho}_i \tilde{u}_i \tag{14}$$

is the mass flux;$a_\Phi, b_\Phi, c_\Phi, d_\Phi, a_\Theta, b_\Theta, c_\Theta, d_\Theta$ are the known numeric functions, $i = 2..n-1$, (11) is the equation of continuity, (13) is the equation of state for gas. We use the staggered grid for the mass flux $\Phi$ and for the velocity $u$. In the staggered grid, the velocity components are calculated in points that lie on the faces of the control volume [4].

This is the sequence of operations:

1. Start with a guessed fields of velocity, pressure and density;
2. Calculate the coefficients for the equations (10), and solve this system to obtain $\Phi$ by the TriDiagonal-Matrix Algorithm [3];
3. Calculate the density by use of (11);
4. Calculate the coefficients for the equations (12), and solve this system to obtain $\Theta$ by the TriDiagonal- Matrix Algorithm [3];
5. Calculate the pressure by use of (13);
6. Calculate the velocity by use of (14);
7. Return to step 2 and repeat until convergence.

The computation grid was uniform and consisted of 1000 nods. The time step was taken to be $\Delta\tau = 0.1\Delta X$(i.e., on condition that the wave will pass a distance of $\Delta X$ or less during the time $\Delta\tau$ where $\Delta X$ is the size of control volume).

The dimensionless parameters were taken following:$\Omega = 0.144, 0.288, 0.432, 0.576, 0.720, 0.864, 1.008, 1.152, \tilde{A} = 2, Re = 100000, Pe = 80000, \gamma = 1.4$. We will use the dimensionless parameters for the analysis of the results.

## 4 Analysis of the results

We will first describe the behavior of the gas at the beginning of the vibration exposure. At the initial instant of time the cavity was situated at the rightmost position. Then the cavity begin to move to the left. Consequently, there are increasing of mass of the gas and a pressure jump near the right boundary. The calculations showed that the pressure to the right boundary at this time will be the maximum for all time of vibration. At the left boundary at the same time, however, there are great gas rarefaction and minimum pressure. Fig.1 shows the temperature at the nearest to the boundary points depending on time. Two frequencies are showed here. They are the natural frequency of the system

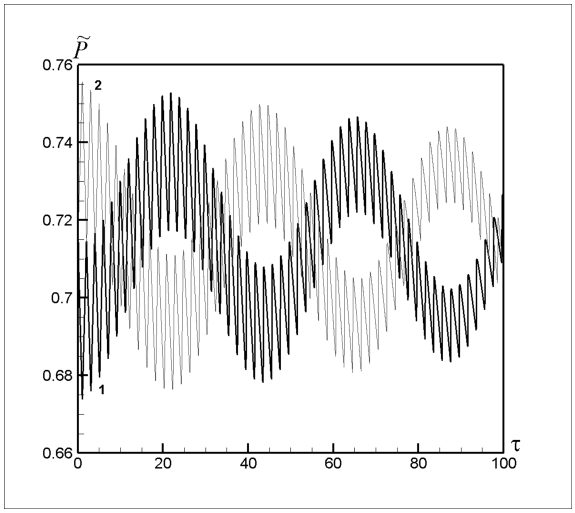


Figure 1: The time dependence of pressure: 1 - at the point $X = 0.0005$, 2 - at the point $X = 0.9995$

and the oscillation frequency caused by the boundary conditions ($\Omega = 0.144$)[2]. However, all further collision of waves with boundaries will cause less pressure jumps as compared with pressure jump at the right boundary which was a result of impact to the resting gas.With increasing frequency of vibration the maximum pressure in the boundary points is increased.

The numerical experiments showed that the maximum temperature in the nearest to borders grid points is not achieved at the same time with the maximum pressure. One reason for this is the influence of given constant wall temperature, which constrains the temperature jumps at the boundary. Let us consider the most intense vibration frequencies of the cavity since $\Omega = 0.720$. With such frequencies even the first acoustic wave is a shock wave. Therefore, it causes an intense temperature jump, and several less intense pressure jump. Following collision of shock waves cause a smaller increase in temperature, because the intensity of the shock wave decreases with time. Fig.2 and Fig.3 give the distributions

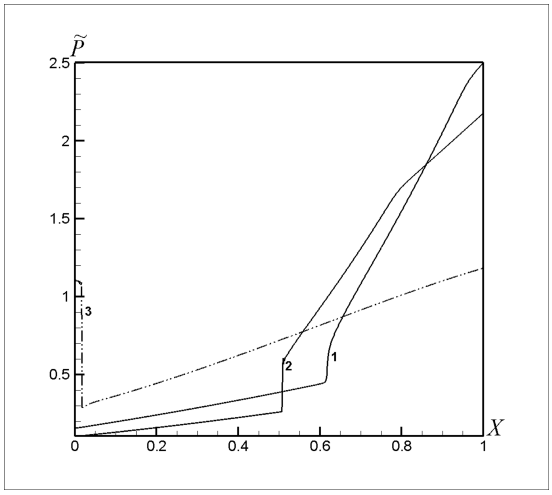


Figure 2: The pressure as a function of coordinate: 1 - $\tau = 0.74$, 2 - $\tau = 0.89$, 3 - $\tau = 1.38$

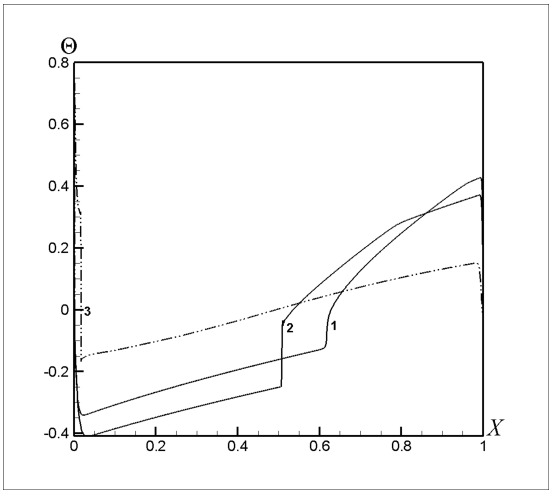


Figure 3: The temperature as a function of coordinate: 1 - $\tau = 0.74$, 2 - $\tau = 0.89$, 3 - $\tau = 1.38$

of pressure and temperature depending on coordinate at instants of time corresponding to

maximum pressure ($\tau = 0.74$), maximum temperature ($\tau = 1.38$) and intermediate time when where is a forming of the shock wave ($\tau = 0.89$).

With less intense vibration frequencies of the cavity the shock waves reach maximum intensity later than the first passage of the field. Therefore, the strongest collision of shock wave with the wall are later than with frequencies which more intensify than was considered earlier. The results are presented in Tab.1. Here for each of the considered frequencies are showed the period of cavity vibration T, maximum pressure $\tilde{P}_{max}$ near boundaries of the cavity, maximum pressure $\tilde{\Theta}_{max}$ near boundaries of the cavity and times when this values are showed ($\tau(\tilde{P}_{max})$ and $\tau(\Theta_{max})$).

Table 7:

| $\Omega$ | T | $\tilde{P}_{max}$ | $\tau(\tilde{P}_{max})$ | $\Theta_{max}$ | $\tau(\Theta_{max})$ |
|---|---|---|---|---|---|
| 0.144 | 43.617 | 0.756 | 0.99 | 0.006 | 55.57 |
| 0.288 | 21.809 | 0.884 | 0.96 | 0.045 | 11.52 |
| 0.432 | 14.539 | 1.111 | 0.91 | 0.114 | 5.50 |
| 0.576 | 10.904 | 1.456 | 0.85 | 0.190 | 3.49 |
| 0.720 | 8.723 | 1.940 | 0.79 | 0.305 | 1.41 |
| 0.864 | 7.270 | 2.593 | 0.74 | 0.897 | 1.38 |
| 1.008 | 6.231 | 3.445 | 0.68 | 1.413 | 1.30 |
| 1.152 | 5.4521 | 4.511 | 0.63 | 2.337 | 1.20 |

## 5 Conclusions

There are two frequencies: the natural frequency of the system and the oscillation frequency caused by the boundary conditions. The maximum values of the pressure and the temperature at the boundaries of the frequencies with investigated range are obtained. The time of observation of these values is found. The results provide an opportunity to determine the maximum frequency of vibration for given other vibration parameters, taking into account the specific properties of the material forming the wall of the cavity.

## References

[1] Frolov K.V. Vibration: Friend or Foe? New York: Hemisphere, 1990

[2] Yakovenko A. V., Zubkov P. T., Abdubakova L. V. Computation of vibrations in the area with perfect viscous gas // Proc. of XXXIX Summer School - Conference “Advanced Problems in Mechanics”, 2011. P. 532-542.

[3] Patankar S.V. Computation of conduction and duct flow heat transfer. USA, Innovative Research,1991

[4] Patankar S.V. Numerical heat transfer and flid flow. New York: Hemisphere, 1981

*Anna V. Yakovenko, Taymirskaya str. 74, Tyumen, Russia*
*Pavel T. Zubkov, Perekopskaya str. 15a, Tyumen, Russia*

# Scattering of SH wave in half-space with cavity of arbitrary shape and crack

Zailin Yang Yong Yang Yongquan Liu
yangzailin00@163.com

**Abstract**

We present a method to study the scattering of SH wave and the ground motion in the half-space containing a shallow buried cavity of arbitrary shape and a linear crack in any orientation. The methods of complex function and multi-polar coordinate system are utilized to construct a suitable Green's function, which is used for computing stress caused by the line source. Then a crack can be built with the crack-division technique, by loading force that are equal but opposite to the stress at the crack. The dynamic stress concentration factor around the cavity and the dynamic stress intensity factor at crack tips under varied conditions are calculated, and the results indicates that: the dynamic stress concentration factor can be changed greater with the difference of the shape of the hole, the incident angle, and/or the wave number, compared to the variety of the parameters of the crack. In general, the dynamic stress intensity factor at the crack tip is as the change of the wave number to a periodic fluctuation.

Key words: cavity of arbitrary shape, crack, scattering of SH wave, method of complex function, Green's function

## 1 Introduction

The problem of scattering of elastic waves by all kinds of defects is of considerable importance, in geophysics, fracture mechanics, explosion mechanics, ultrasonic testing and other areas, and it is therefore naturally to receive much attention[1]. Defects, such as cavities, cracks, inclusions and linings, can be existed individually [2-8] or collectively [9-10]. In principle, the defects with arbitrary shapes can be conformal mapped into circular ones, then the dynamic response of elastic wave can be obtained. However, when the defects are spindly, just like cracks, it cannot be calculated correctly using the wave function expansion method due to the extremely divergence of Bessel function. So we must take other measures, for example the ray method and the Integral Equation Method [9, 11-13], though they are relatively cumbersome. The interaction of cavities and cracks by SH wave has been studied by some researchers. For example, Liu et al. [14] has treated the scattering of SH wave by a crack originating at a circular hole edge. An approximate solution for the scattering of SH wave by a crack inside a circular inclusion was given by Lu et al. [15]. Until now, few efforts have been made to study the interaction of cavities and cracks when the crack is placed in any position and direction, especially when the cavity is of arbitrary shape.

In this paper, we study the scattering of SH wave and the ground motion in the half-space containing a shallow buried cavity of arbitrary shape and a linear crack in any orientation, using the Green's function method and multi-polar coordinate system. The

crack is built with the crack-division technique, by loading force that are equal but opposite to the stress at the crack. The dynamic stress concentration factor around the cavity and the dynamic stress intensity factor at crack tips under varied conditions are calculated.

## 2 Fundamental Equations

By introducing the complex variable $z = x + iy$, $\bar{z} = x - iy$ , the governing equation of the steady-state SH wave propagation can be expressed in the complex plane $(z, \bar{z})$as

$$\frac{\partial^2 W}{\partial z \partial \bar{z}} + \frac{k^2}{4} W = 0 \tag{1}$$

where $k$ is the wave number, $W$ is the amplitude of the displacement. The corresponding expressions of stress are given by

$$\tau_{r3} = \mu(\frac{\partial W}{\partial z} e^{i\theta} + \frac{\partial W}{\partial \bar{z}} e^{-i\theta}), \tau_{\theta 3} = i\mu(\frac{\partial W}{\partial z} e^{i\theta} - \frac{\partial W}{\partial \bar{z}} e^{-i\theta}) \tag{2}$$

where '3' represents the out-of-plane direction.

The method of conformal mapping $Z = w(\eta)$, $\eta = e^{i\theta}$ is used, the external region of the $z$ plane is mapped into the external region with a unit circle in $\eta$ plane, and the conformal mapping function can be generally expressed as

$$Z = w(\eta) = \frac{l\eta + m\eta^{-1}}{1 - n\eta^{-1}}, (|n| < 1) \tag{3}$$

where $l = l_1 + il_2$, $m = m_1 + im_2$, $n = n_1 + in_2$ . In particular, for elliptical holes, $l = \frac{a+b}{2}$, $m = \frac{a-b}{2}$,$n = 0$ , where $a$ and $b$ are the length of the major and minor axis, respectively; for square holes, the mapping function is $Z = w(\eta) = 1.11a(\eta - 1/9\eta^3)$, where $a$ is half of the length of the side; and for triangular holes, $Z = w(\eta) = c(\eta + m\eta^{-n})$, $(c > 0, 0 \leq m < \frac{1}{n})$.

Substituting the mapping function (3) into Eq.(1) and Eq.(2), we obtain

$$\frac{1}{w'(\eta)\bar{w}'(\eta)} \frac{\partial^2 W}{\partial \eta \partial \bar{\eta}} + \frac{k^2}{4} W = 0 \tag{4}$$

$$\tau_{r3} = \frac{\mu}{|w'(\eta)|}(\eta \frac{\partial W}{\partial \eta} + \bar{\eta} \frac{\partial W}{\partial \bar{\eta}}), \tau_{\theta 3} = \frac{i\mu}{|w'(\eta)|}(\eta \frac{\partial W}{\partial \eta} - \bar{\eta} \frac{\partial W}{\partial \bar{\eta}}) \tag{5}$$

Boundary conditions can be expressed as follows

$$\tau_{r3} = 0, \quad when \quad \eta = e^{i\theta} \tag{6}$$

$$\tau = 0, \quad at \quad the \quad surface \quad of \quad half \quad space \tag{7}$$

## 3 Green's Function

The Green's function here should meet Eq.(4), Eq.(6)and Eq.(7). In a complete half-space, the disturbance impacted by the line source loading $\delta(\underline{r} - \underline{r_0})$ can be described in this form

$$G^{(i)} = \frac{i}{4\mu} H_0^{(1)}(k|w(\eta)| - w(\eta_0)|) \tag{8}$$

where $H_0^{(1)}(\cdot)$ is the zero-order Hankel function of the first kind. The reflected wave is generated due to the surface of half-space, and it can be derived directly according to the characteristics of SH-wave,

$$G^{(r)} = \frac{i}{4\mu} H_0^{(1)}(k|w(\eta)| - \bar{w}(\eta_0)| - 2ih) \tag{9}$$

The expression of the scattered wave excited by the elliptic cavity should meet the governing equation (4), as well as the stress free condition at the surface of the half-place. It can be constructed in plane

$$G^{(s)} = \sum_{n=-\infty}^{+\infty} A_n\{H_n^{(1)}[k|w(\eta)|][\frac{w(\eta)}{\bar{w}(\eta)}]^n + H_n^{(1)}[k|w(\eta)-2ih|][\frac{w(\eta)-2ih}{\bar{w}(\eta)-2ih}]^n\} \tag{10}$$

The symmetry of the SH-wave, the method of complex function and multi-polar coordinate system are used in Eq.(14), in which $A_n$ are unknown coefficients to be determined by the boundary condition around the edge of the cavity, $H_0^{(1)}(\cdot)$ is the order-$n$ Hankel function of the first kind. Then we can get the Green's function by compositing those three components

$$G = G^{(i)} + G^{(r)} + G^{(s)} \tag{11}$$

Substituting Eq.(5) and Eq.(11) into Eq.(9), we have

$$\sum_{n=-\infty}^{\infty} A_n\varepsilon_n = \varepsilon \tag{12}$$

where

$$\varepsilon_n = \frac{\mu k}{2}\{[H_{n-1}^{(1)}(k|w(\eta)|)[\frac{w(\eta)}{|w(\eta)|}]^{n-1} - H_{n+1}^{(1)}(k|w(\eta)-2ih|)[\frac{w(\eta)-2ih}{|w(\eta)-2ih|}]^{-(n+1)}]$$
$$\cdot\frac{\eta w'(\eta)}{R|w'(\eta)|} - [H_{n+1}^{(1)}(k|w(\eta)|)[\frac{w(\eta)}{|w(\eta)|}]^{n+1} - H_{n-1}^{(1)}(k|w(\eta)-2ih|)$$
$$\cdot[\frac{w(\eta)-2ih}{|w(\eta)-2ih|}]^{-(n-1)}]\frac{\bar{\eta}\bar{w}'(\eta)}{R|w'(\eta)}\}$$
$$\varepsilon = \frac{ik}{8}H_1^{(1)}(k|w(\eta)-w(\eta_0)|)\cdot[\frac{\bar{w}(\eta)-\bar{w}(\eta_0)}{|w(\eta)-w(\eta_0)|}\frac{\eta w'(\eta)}{R|w'(\eta)|} + \frac{w(\eta)-w(\eta_0)}{|w(\eta)-w(\eta_0)|}$$
$$\cdot\frac{\bar{\eta}\bar{w}'(\eta)}{R|w'(\eta)|}] + \frac{ik}{8}\cdot H_1^{(1)}(k|w(\eta)-\bar{w}(\eta_0)-2ih|)\cdot[\frac{\bar{w}(\eta)-\bar{w}(\eta_0)+2ih}{|w(\eta)-\bar{w}(\eta_0)-2ih|}\frac{\eta w'(\eta)}{R|w'(\eta)|} -$$
$$\frac{w(\eta)-\bar{w}(\eta_0)-2ih}{|w(\eta)-\bar{w}(\eta_0)-2ih|}\frac{\bar{\eta}\bar{w}'(\eta)}{R|w'(\eta)|}]$$

Eq.(12) is a function containing infinite unknown coefficients $A_n$, we can transform it into infinite algebraic equations by multiplying $e^{-m\theta}$ on both sides of Eq.(12) and integrating over the interval $(-\pi, \pi)$, then we can get

$$\sum_{n=-\infty}^{\infty} A_n\varepsilon_{mn} = \varepsilon_m \tag{13}$$

where $\varepsilon_{mn} = \frac{1}{2\pi}\int_{-\pi}^{\pi}\varepsilon_n e^{-m\theta}d\theta$, $\varepsilon_m = \frac{1}{2\pi}\int_{-\pi}^{\pi}\varepsilon e^{-m\theta}d\theta$ . By intercepting finite terms, Eq.(13) converts to algebraic equations containing unknown coefficients $A_n$, which can be solved by the Gaussian method, then we can get the Green's function $G$.

# 4 The scattering of SH wave by the cavity and the crack

## 4.1 The first kind problem (SH wave incidences from below)

Just shown as Fig.1, there is an irregular cavity and a linear crack of arbitrary position and direction in half space, and SH wave incidences from below. It can be regarded as

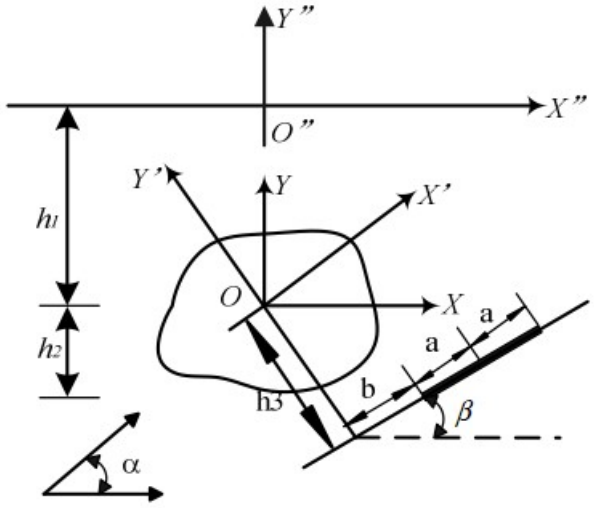


Figure 1: Model of half space with an arbitrary-shaped cavity and an crack when SH-wave incidences below

the Seismic problems of subsurface structures. To solve the problem, we should set up 3 coordinates $XOY$, $X'O'Y'$ and $X''O''Y''$, the relationship of them are

$$x' = x\cos\beta + y\sin\beta, y' = y\cos\beta - x\sin\beta,$$
$$x'' = x, y'' = y - h_1, h_3 = \frac{h_2 + b\sin\beta}{\cos\beta}$$

The incident wave and the reflected wave can be expressed as

$$W_1^{(i)} = W_0 \exp\{\frac{ik}{2}[(w(\eta) - ih)e^{-i\alpha_0} + (\bar{w}(\eta) + ih)e^{i\alpha_0}]\} \tag{14}$$

$$W_1^{(r)} = W_0 \exp\{\frac{ik}{2}[(w(\eta) - ih)e^{i\alpha_0} + (\bar{w}(\eta) + ih)e^{-i\alpha_0}]\} \tag{15}$$

In the same turn, the corresponding expressions of stress can be obtained by Eq.(5). When the displacement and the stress are obtained, then a crack can be built with the crack-division technique, by loading force that are equal but opposite to the stress at the crack. The additional wave field caused by the crack is

$$W_1^{(c)} = -\int_{(b,-h_3)}^{(2a+b,h_3)} \tau_{\theta z,1} G_1 dz'$$

Finally, in half space containing an irregular cavity and a linear crack of arbitrary position and direction, the wave field of the first kind problem is

$$W_1 = W_1^{(i)} + W_1^{(r)} + W_1^{(s)} + W_1^{(c)} \tag{16}$$

### 4.2 The second kind problem (SH wave incidences vertically from upside)

Just shown as Fig.2, there is an irregular cavity and a linear crack of arbitrary position and direction in half space, and SH wave incidences vertically from upside. It can be regarded as the anti-explosion problem of subsurface structures. For this problem, there

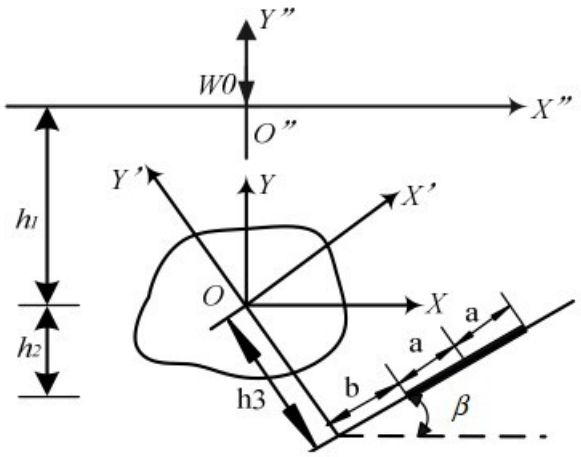


Figure 2: Model of half space with an arbitrary-shaped cavity and an crack when SH-wave incidences from upside

is no reflected wave, and the incident wave can be written as

$$W_2^{(i)} = W_0 \exp\{\frac{-k}{2}[(w(\eta) - ih) - (\bar{w}(\eta) + ih)]\} \tag{17}$$

Using similar methods, we can calculate the wave field of the second kind problem.

## 5 Dynamic Stress Concentration Factor (DSCF) and Dynamic Stress Intensity Factor (DSIF)

The dynamic stress around a shallow-buried cavity can be described by the dynamic stress concentration factor (DSCF) in the presence of the steady incident SH-wave

$$\tau_{\theta 3}^{*} = |\tau_{\theta 3}/\tau_0| \tag{18}$$

where $\tau_{\theta 3}$ is the hoop stress around the cavity, and $\tau_0 = \mu k W_0$ is the amplitude peak of the incident stress.

By picking the stress close enough to the crack tip as the nominal stress, we can get the dynamic stress intensity factor (DSIF) at the crack tip

$$K_3 = \frac{\tau_{r3}|_{\underline{r}\to\underline{r_1}}}{\tau_0 Q} \tag{19}$$

where $\tau_{r3}|_{\underline{r}\to\underline{r_1}}$ is the nominal stress of tiny distance from the crack tip, $Q = \sqrt{b/2}$ is the characteristic parameter,$b$ is the length of the crack.

## 6 Numerical Results and Discussion

In this section, numerical examples are provided to show the distribution of the DSCF around the cavity and the DSIF at the crack tip with the variation of various parameters, such as the wave number $k$, the incident angle $\alpha$, the shape of the cavity, the distance of the center of the circular cavity to the horizontal interface, the length of the crack etc.. Then we specialize the problem by setting the cavity as a circular one or by removing the crack, and the results are in conformity with published work available in the literature [6,7,10].

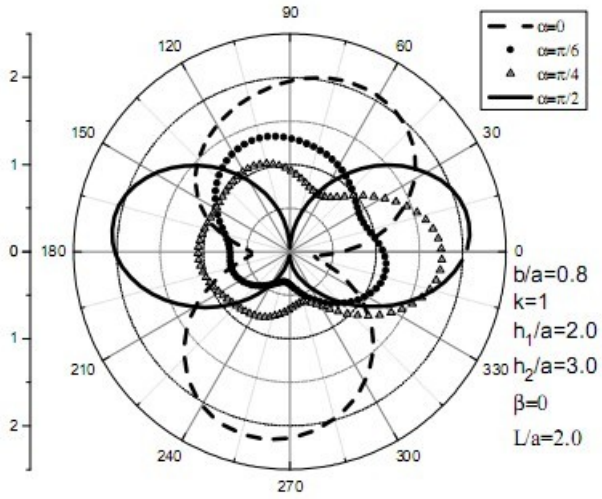


Figure 3: the DSCF around an ellipse cavity when SH-wave incidences from different directions

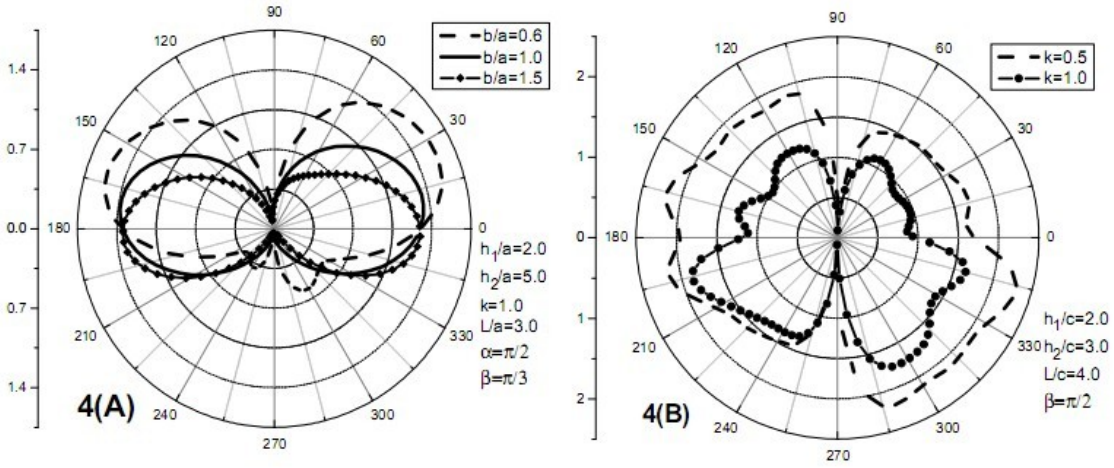


Figure 4: the DSCF around different shaped cavities for different wave numbers.

## 6.1 The DSCF around the cavity

(1) The results presented in Fig.3 show the variation of DSCF around the elliptic cavity with respect to the incident angle. We can see from it that the DSCF around the cavity varies widely, both for its amplitude and its shape, under deferent incident angle. (2) The distribution of DSCF around the cavity with respect to the change of the shape of the hole and the wave number is shown in Fig.4, where Fig.4(A) is the DSCF around a ellipse hole when the incident angle is 90°, Fig.4(B) shows the DSCF around a triangular cavity when the incident angle is 0°. The results indicate that the shape of the DSCF around the cavity varies widely for different cavities, and the amplitude of the DSCF can change a lot under different wave numbers. (3) Fig.5 shows the variation of DSCF around the elliptic cavity with respect to the distance of the center of cavity to the horizontal interface. Fig.5(A) shows the DSCF under the condition of $h_2/a$ is 5, 13, and with no crack, respectively. Fig.5(B) gives the calculation results of the variation of DSCF at $\theta = 90°$ vs. the depth of the crack. The results indicate that the value of DSCF decreases periodically with

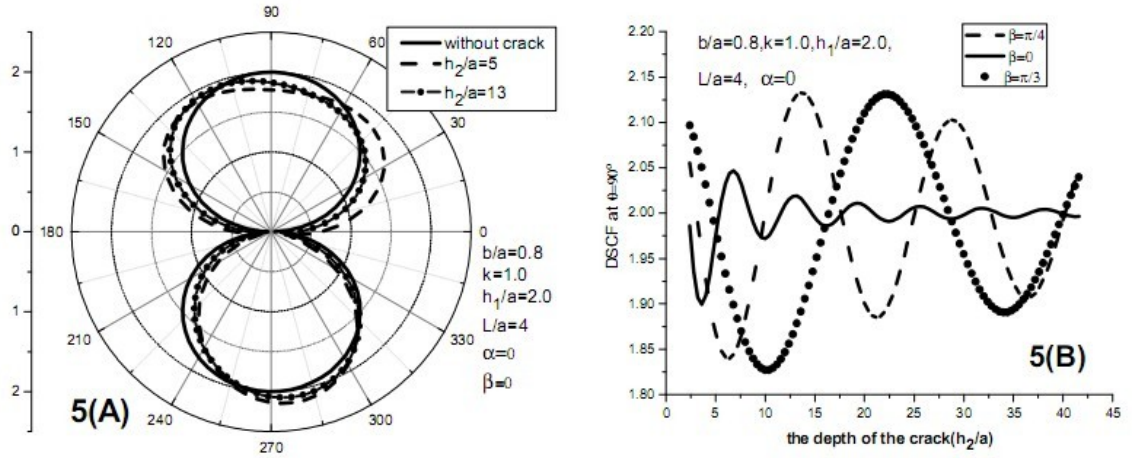


Figure 5: the DSCF with the variation of the depth of the crack.

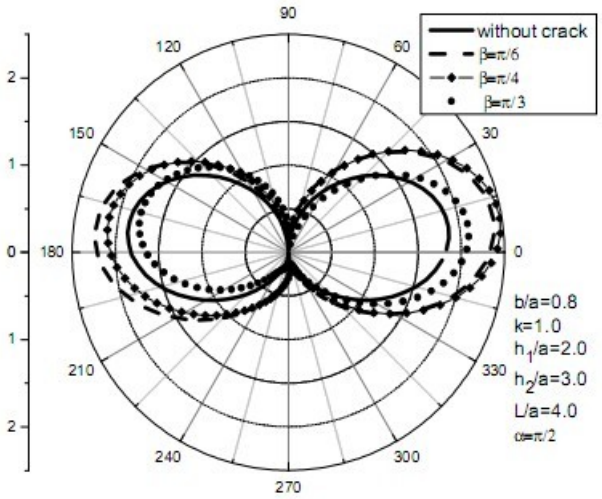


Figure 6: the DSCF around the cavity with different inclining angles of the crack

increasing distance, but the degradation is slight and related to the direction of the crack. (4) The magnitude of DSCF vs. inclining angles of the crack is plotted in Fig.6, and we can see that the effect of inclining angles to DSCF is less than those parameters such as the wave number, the incident angle and the shape of cavity.

## 6.2 the DSIF at the crack tip

(1) Fig.7 and Fig.8 demonstrate the effect of inclining angles of the crack and the incident angle on the DSIF, respectively. Fig.9 presents a qualitative analysis on the variation of DSIF vs. wave number with different length of the crack. This analysis indicates that the dynamic stress intensity factor at the crack tip is as the change of the wave number to a periodic fluctuation, and the change is more violent when the crack is longer.

(2) The variation of DSIF vs. the depth of the crack with different length of the crack is plotted in Fig.10, and the wave incidences vertically from upside. Generally speaking, the DSIF at the crack tip decrease gradually with the increase of crack depth, and the DSIF is proportional to the length of the crack.

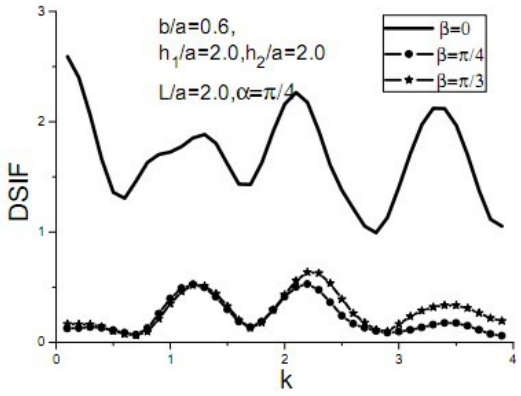


Figure 7: Variation of DSIF vs. wave number with different angles of the crack

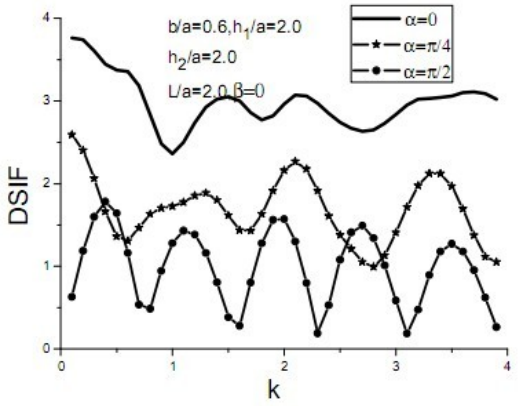


Figure 8: Variation of DSIF vs. wave number with different directions of the incident SH-wave

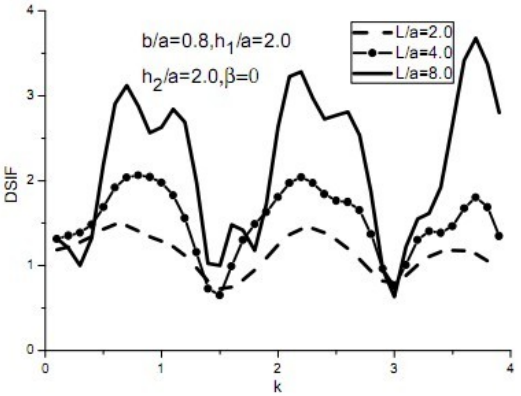


Figure 9: Variation of DSIF vs. wave number with different length of the crack

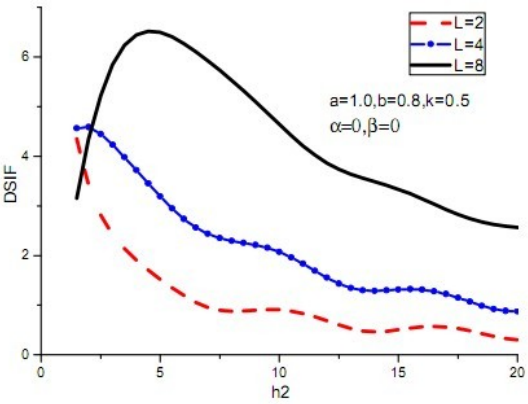


Figure 10: Variation of DSIF vs. depth of the crack with different length of the crack

## 7 Concluding remarks

This paper presented an analytical method to solve the scattering of SH wave by a cavity of arbitrary shape and a crack at arbitrary position and direction. The methods of complex function and multi-polar coordinate system have been used, and the crack is built with the crack-division technique. The numerical results were presented for both DSCF and DSIF under varied conditions, the results indicates that: the dynamic stress concentration factor can be changed greater with the difference of the shape of the hole, the incident angle, and/or the wave number, compared to the variety of the parameters of the crack. In general, the dynamic stress intensity factor at the crack tip is as the change of the wave number to a periodic fluctuation. An accurate investigation of the response is certainly an aid in the successful estimation of the detection of location, length, and depth of the crack. It is also a prerequisite for the inverse problem, and the method in the paper could be used to study some other correlative problem.

## Acknowledgements

*This work is supported by the National Science Foundation of China (10972064).*

## References

[1] Pao YH, Mow CC. Diffraction of Elastic Waves and Dynamic Stress Concentrations. Crane and Russak, New York, 1973. 114-304

[2] Liu Diankui, Liu Hongwei. Scattering and dynamic stress concentration of SH-wave by interface circular hole. Acta Mechanica Sinica, 1998, 30(5): 597-604 (in Chinese)

[3] Wang Yuesheng, Wang Duo. Diffraction of SH-waves by a circular cavity with a partially debonded liner. Acta Mechanica Sinica, 1994, 26(4): 462-468 (in Chinese)

[4] He Zhongyi, Fan Hongming, Liu Youjun, Scattering of SH-wave by an interface cavity. Acta Mechanica Sinica, 2002, 34(1): 68-75 (in Chinese)

[5] Yang Zailin, Liu Dankui. Scattering far field solution of SH-wave by movable rigid cylindrical interface. Acta Mechanica Solida Sinica, 2002, 15(3): 214-220

[6] Liu Diankui, Lin Hong. Scattering of SH-waves by a shallow buried cy lindrical cavity and the ground motion. Explosion and Shock Waves, 2003, 23(1): 6-12 (in Chinese)

[7] Chen Zhigang, Liu Diankui. Dynamic response on a shallowly buried cavity of arbitrary shape impacted by vertical SH-wave. Earthquake Engineering and Engineering Vibration, 2004, 24(2): 32-36 (in Chinese)

[8] Liang Jianwen, Li Yanheng, Vincent W Lee. A series solution for surface motion amplification due to underground group cavities: incident SH waves. Rock and Soil Mechanics, 2006, 27(10): 1663-1672(in Chinese)

[9] Lu Jianfei, Wang Jianhua, Shen Weiping. Interaction between antiplane circular inclusion and multiple circular holes and cracks. Chinese Journal of Computational Mechanics, 2000, 17(2): 229-234(in Chinese)

[10] Yang Zailin, Yan Peilei, Liu Diankui. Scattering of SH-wave and ground motion by an elastic cylindrical inclusion and a crack in half space. Acta Mechanica Sinica, 2009, 42(2): 229-235 (in Chinese)

[11] Sih G.C. Cracks in Composite Material. Mechanics of Fracture, 1981, 6: 485-491

[12] Wickham G.R. The Diffraction of Stress Waves by a Plane Finite Crack in Two Dimensions: Uniqueness and Existence. Proc.R.Soc, 1281, 378(1773): 241-261

[13] S. Itou. Diffraction of an Antiplane Shear Wave by Two Coplanar Griffith Cracks in an Infinite Elastic Medium. International Journal of Solids and Structures, 1980, 16: 1147-1153

[14] Liu Diankui, Liu Hongwei. Scattering of SH-wave by crack originating at a circular hole edge and dynamic stress intensity factor. Acta Mechanica Sinica, 1999,31(3): 292-299 (in Chinese)

[15] Lu Jianfei, Cai Lan, Liu Chuntu. Scattering of SH wave by a crack inside a circular inclusion. Acta Mechanica Sinica, 1999,35(5): 623-627 (in Chinese)

[16] M.A.Abdou, S.A. Aseeri. Goursat functions for an infinite plate with a generalized curvilinear hole in -plane. Applied Mathematics and Computation, 2009, 212:23-36

*Zailin Yang, Harbin Engineering University, Harbin 150001,China*
*Yong Yang, Harbin Engineering University, Harbin 150001,China*
*Yongquan Liu, Department of Mechanics and Engineering Science, Peking University, Beijing 100871, China*